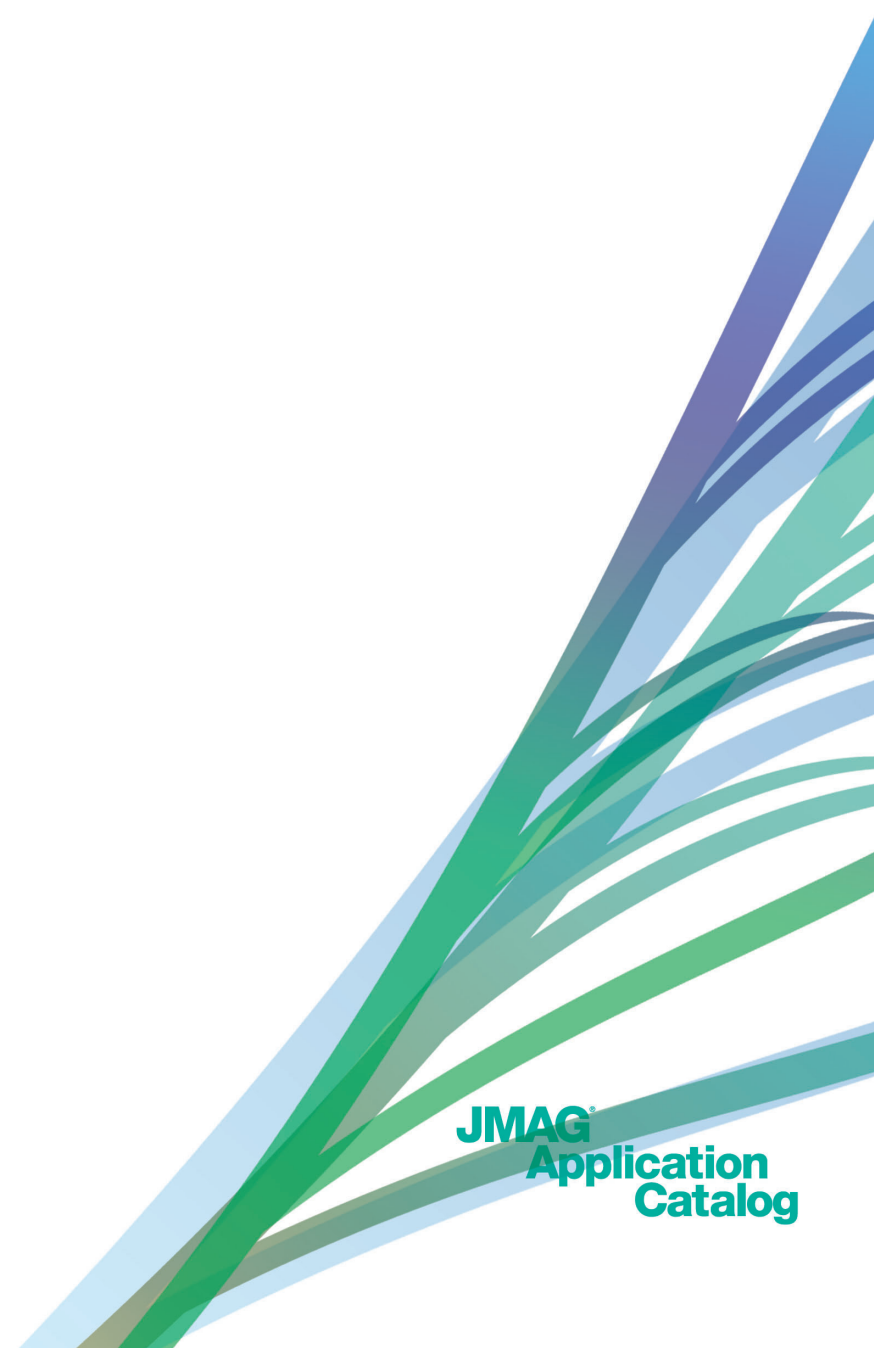


Sep 2023



JMAG[®]

Application Catalog



JMAG[®]
Application
Catalog

JMAG[®] Application Catalog

How To Use the Application Catalog

“Case studies performed using JMAG electromagnetic field simulation software”

JMAG is an electromagnetic field analysis software that is applicable to many analysis targets such as motors. It handles magnetic field analyses, and can also couple thermal and structural analyses thanks to enhancements in its multiphysics functions.

The Application Catalog on the JMAG website contains various case studies to introduce the applications and analysis functions that can be performed with JMAG to our customers.

We will introduce a few of them in this pamphlet.

We have also prepared Application Notes and model data on the JMAG users web site for those who are just beginning to work with analysis or are trying to work on a new analysis field.

Please try it if there are any analyses that you are considering or are interested in.

We will continue to introduce new cases and improve the content of the Application Notes and model data mentioned above in order to support our customers' analysis work.

<https://www.jmag-international.com/>

Contents

02 How To Use the Application Catalog



IPM Motor

- 14 Case 017 Inductance Analysis of an IPM Motor [DP]
- 15 Case 018 Thermal Analysis of an IPM Motor [HT, LS, TR]
- 15 Case 019 Analysis of the Centrifugal Force in an IPM motor [DS]
- 17 Case 022 Analysis of the Eddy Current in the Magnet of an IPM Motor [TR]
- 17 Case 023 Eccentricity Analysis of an IPM Motor [DP]
- 24 Case 037 Vector Control Analysis of an IPM Motor Using Control Simulator and the JMAG-RT [DP, RT]
- 35 Case 055 Integrated Magnetization Analysis of an IPM Motor [DP, ST]
- 37 Case 058 Efficiency Analysis of an IPM Motor [DP, LS]
- 38 Case 059 Iron Loss Analysis of an IPM Motor Accounting for PWM –Direct Link– [DP, LS]
- 43 Case 069 Iron Loss Analysis of an IPM Motor [DP, LS]
- 53 Case 087 Iron Loss Analysis of an IPM Motor Including the Effect of Shrink Fitting [DP, DS, LS]
- 55 Case 090 Analysis of the Effect of PWM on the Iron Loss of an IPM Motor [DP, LS]
- 55 Case 091 Iron Loss Analysis of an IPM Motor Including the Effects of Press Fitting Stress [DP, DS, LS]
- 73 Case 122 Inductance Analysis of an IPM Motor -d/q-axis Inductance Obtained by Actual Measurement- [DP]
- 77 Case 131 Stray Capacitance Analysis of a Motor [EL]
- 81 Case 142 Press Fit Analysis of a Divided Core [DS, DP, LS]
- 87 Case 156 Segregation Analysis of Torque Components for an IPM Motor [DP]
- 87 Case 157 Analysis of Eddy Currents in an IPM Motor Using the Gap Flux Boundary [DP, FQ]
- 90 Case 165 Creating IPM Motor Efficiency Maps [DP, LS]
- 94 Case 173 Basic Characteristic Analysis of an IPM Motor [DP, LS]
- 102 Case 188 Thermal Demagnetization Analysis of IPM Motors Accounting for Coercive Force Distribution of Magnets [DP]
- 108 Case 194 Analysis of High-Speed Rotation Motors Accounting for Eddy Current [DP, LS]
- 112 Case 200 Iron Loss Analysis of IPM Motor using Hysteresis Model [DP, LS]
- 116 Case 205 Analyzing the Torque Characteristics of IPM Motors Using a Thermal Equivalent Circuit [DP]
- 121 Case 211 IPM Motor Wire Joule Loss Analysis [DP]
- 123 Case 214 Monitoring the Radial Force Acting on the Teeth of IPM Motors Using Circuit Control Simulation [DP, RT]
- 124 Case 215 Simulation of an IPM Motor with a Delta Connection Using a Control Simulator and JMAG-RT [DP, RT]
- 129 Case 222 Irreversible Thermal Demagnetization Analysis of Incompletely Magnetized Magnets [DP, ST]
- 130 Case 223 Multi-Objective Optimization of an IPM Motor Accounting for Stress at High-Speed Rotation [DP, DS]
- 131 Case 225 Induced Voltage Analysis on Memory Motors Using Variable Magnets [ST, DP]
- 141 Case 237 AC Loss Analysis of an IPM Motor [TR]
- 142 Case 239 Fault Analysis in an IPM Motor [DP, LS, RT]
- 143 Case 240 NT Characteristics Analysis of an IPM Motor Using PAM Drive [DP]
- 153 Case 255 Evaluating the N-T Curve of an IPM motor Using 3D Correction [TR]
- 154 Case 257 IPM Motor Topology Optimization [DP, DS]
- 156 Case 259 Automatically Searching for Current Phase that Obtains Maximum Torque and Evaluating Torque Characteristics [DP]
- 159 Case 262 IPM Motor Thermal Demagnetization Analysis Accounting for Dy-Diffusion Magnet Incomplete Magnetization [DP, ST]
- 160 Case 263 IPM Motor Stress Analysis Taking Into Account Friction between Magnets and the Rotor Core [DS]
- 160 Case 264 Creating 6-Phase IPM Motor Efficiency Maps [DP, LS]
- 162 Case 267 IPM Motor Topology Optimization Using the Density Method [DP, DS]
- 166 Case 273 Creating IPM Motor Efficiency Maps Accounting for AC Loss [DP, LS]
- 168 Case 275 IPM Motor Iron Loss Analysis Accounting for the Effect of Residual Strain [DP]
- 169 Case 276 Six-Phase IPM Motor Harmonic Iron Loss Analysis [DP, LS]
- 172 Case 279 Thermal Analysis Accounting for Cooling of the IPM Motor [ExpressFR]
- 175 Case 286 IPM Motor Iron Loss Analysis Accounting for PWM : Evaluation with Different Modulation Methods [DP, LS]
- 178 Case 290 Design Exploration of IPM Motors, Including Evaluating Part Temperature and Stress [ExpressFR]



SR Motor

- 09 Case 006 Analysis of the SR Motor Torque Ripple [DP]
- 79 Case 138 Vibration Analysis of an SR Motor [DP, DS]
- 89 Case 162 Drive Simulation of an SR Motor using a Control Simulator and JMAG-RT [DP, RT]
- 96 Case 178 Analysis of SR Motor I-Psi Characteristics [DP]
- 97 Case 179 Analysis of SR Motor Static Characteristics [DP]
- 98 Case 180 Analysis of SR Motor Dynamic Characteristics [DP]
- 99 Case 181 Analysis of SR Motor Drive Characteristics [DP, LS]
- 113 Case 201 Iron Loss Analysis of an SR Motor [DP, LS]



Axial Gap Type Motor

- 10 Case 008 Analysis of an Axial Gap Motor [TR]
- 127 Case 219 Axial Gap Type Motor Cogging Torque Analysis [TR]
- 157 Case 260 Creating Axial Gap-Type Motor Efficiency Maps [LS, TR]
- 164 Case 271 Axial Gap Type Motor AC Copper Loss Analysis [TR]
- 170 Case 277 Vibration Analysis of Axial Gap-Type Motor [DS, TR]



SPM Motor

- 13 Case 015 Cogging Torque Analysis of an SPM Motor with a Step Skewed Magnet [TR]
- 16 Case 020 Sound Pressure Analysis of an SPM Motor [DP, DS]
- 16 Case 021 Iron Loss Analysis of an SPM Motor Including the Effect of Shrink Fitting [DS, DP, LS]
- 18 Case 024 Cogging Torque Analysis of an SPM Motor with a Skewed Stator [TR]
- 20 Case 029 Iron Loss Analysis of an SPM Motor with Overhanging Magnet [LS, TR]
- 21 Case 030 Magnetization Field Evaluation of an SPM motor [ST]
- 21 Case 031 Iron Loss Analysis of an SPM Motor Including the Effect of Press-fitting Stress [DS, DP, LS]
- 23 Case 034 Demagnetization Analysis of an SPM Motor [DP]
- 25 Case 040 Cogging Torque Analysis of an SPM Motor [DP]
- 30 Case 046 Sensitivity Analysis of the Magnetization Pattern of an SPM Motor [DP, ST]
- 49 Case 080 Cogging Torque Analysis of an SPM Motor with Skewed Magnetization [TR]
- 61 Case 103 Efficiency Analysis of a Permanent Magnet Synchronous Motor [DP, LS]
- 64 Case 108 Centrifugal Force Rupture Analysis of a Ring Magnet [DS]
- 68 Case 114 Vibration Analysis of an Outer Rotor Motor [DP, DS]
- 69 Case 115 Eccentricity Analysis of an SPM Motor [DP]
- 72 Case 120 Thermal Demagnetization Analysis of an SPM Motor [DP]
- 88 Case 159 Sensitivity Analysis of Dimensional Tolerance in an SPM Motor [DP]
- 90 Case 163 Torque-Current Curve Analysis of an SPM Motor [DP]
- 132 Case 226 Vibration Characteristics Analysis of SPM Motors [DP, DS]
- 135 Case 230 6-Phase SPM Motor Inverter Fault Simulation [DP, RT]
- 143 Case 241 Single-Phase Synchronous Motor N-T-I Characteristics Analysis [DP]
- 158 Case 261 SPM Motor Magnet Coercive Force Optimization For Obtaining Sinusoidal Magnetization [DP]
- 163 Case 268 SPM Motor Teeth Geometry Topology Optimization [DP]
- 167 Case 274 SPM Motor Thermal Demagnetization Analysis Using Bonded NdFeB Magnets [DP]
- 174 Case 285 Integrated Magnetization Analysis of an SPM Motor by Magnetizing Multiple Times [DP]





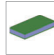


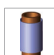





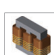





Basic Geometry

- 75 Case 128 Structural Analysis of a Cantilever [DS]
- 76 Case 130 Thermal Conductivity Analysis of Basic Geometry [HT]
- 80 Case 140 Analysis of Electromagnetic Repulsion Produced in Small Contact Bridges [TR]



RFID

- 47 Case 077 Inductance Analysis of an RFID Tag [FQ]

		High-Frequency Preheater			Sensor
149	Case 249	Dielectric Heating Analysis of a High-Frequency Preheater with Parallel Plate Electrodes [EL, HT]	20	Case 028	Magnetic Field Analysis of a Speed Sensor [TR]
150	Case 250	Dielectric Heating Analysis of a High-Frequency Preheater with Roller Electrodes [EL, HT]	60	Case 102	Magnetic Field Analysis of a Magnetic Sensor [ST]
		Condenser	145	Case 244	Magnetic Field Strength Analysis at a Sensor Position [DP]
45	Case 073	Analysis of the Capacitance of a Parallel Plate Capacitor [EL]			Electroplating
		Magnetic Head	110	Case 197	Electric field distribution Analysis of a Electroplating [EL]
19	Case 027	Head Field Analysis of a Recording Write Head That Accounts for Eddy Currents [TR]			Electromagnetic Forming
		Magnetic Shield	51	Case 084	Electromagnetic Forming Analysis of a Tube [DP]
34	Case 053	Magnetic Shielding Analysis of a Shield Room [FQ]			Electromagnetic Brake
155	Case 258	Magnetic Shield Geometry Optimization [ST]	19	Case 026	Braking Torque Analysis of an Electromagnetic Brake [TR]
		Piezoelectric Actuator			Electromagnetic Relay
26	Case 042	Displacement Analysis of a Piezoelectric Actuator [DS]	65	Case 109	Operating Time Analysis of an Electromagnetic Relay Accounting for Eddy Currents [TR]
		Magnetic Gear			Transformer / Reactor
118	Case 207	Transfer Torque and Efficiency Analysis of Magnetic Gear [DP]	8	Case 004	Sound Pressure Analysis of a Reactor [DS, TR]
		Magnet	22	Case 032	Analysis of a Transformer [FQ]
45	Case 072	Analysis of Attractive Force between Steel Plates and a Magnet [ST]	33	Case 052	Inductance Analysis of a Sheet Coil Transformer [FQ]
48	Case 079	Analysis of an Effect of Magnetic Field Orientation on Magnetization [ST]	39	Case 060	Superimposed Direct Current Characteristic Analysis of a Reactor [TR]
74	Case 126	Magnetization Analysis Accounting for Eddy Currents [ST, TR]	39	Case 061	Current Distribution Analysis of a Choke Coil [DP, TS, TRANSFORMER_TEMPLATE]
140	Case 236	Magnetic Circuit Optimization for Plastic Magnets in an Axial Magnetic Field [ST]	46	Case 075	Iron Loss Analysis of a Reactor [FQ, LS]
147	Case 246	Analysis of Electromagnetic Force Acting Between a Coil and a Magnet [ST]	47	Case 078	Loss Analysis of a Sheet Coil Transformer [FQ, LS]
148	Case 247	Magnetic Circuit Optimization for Plastic Magnets in a Radial Magnetic Field [ST]	49	Case 081	AL-value Analysis of a Choke Coil [ST, TRANSFORMER_TEMPLATE]
174	Case 284	Analysis of Minute Electromagnetic Forces Acting on a Magnet [TR]	57	Case 097	Sound Pressure Analysis of a Transformer [DS, FQ]
		Switching Gear / Breaker	58	Case 099	Superimposed Direct Current Characteristics Analysis of a High Current Reactor [TR]
83	Case 149	Analysis of Magnetic Force Acting on the Arc of a Vacuum Circuit Breaker [TR]	60	Case 101	AL-Value Current Characteristics Analysis of a Choke Coil [ST, TRANSFORMER_TEMPLATE]
84	Case 150	Electromagnetic Repulsion Analysis of a Vacuum Circuit Breaker [TR]	62	Case 105	Leakage Inductance Analysis of a Transformer [FQ, TS, TRANSFORMER_TEMPLATE]
		Synchronous Reluctance Motor	64	Case 107	Current Voltage Characteristics Analysis of Flyback Converters [DP]
50	Case 082	Analysis of a Synchronous Reluctance Motor [DP]	66	Case 110	Loss Analysis of a Choke Coil [FQ, LS, TS, TRANSFORMER_TEMPLATE]
136	Case 231	Vector Control Simulation of a Synchronous Reluctance Motor [DP, RT]	70	Case 117	Iron Loss Analysis of a Transformer [FQ, LS]
161	Case 265	Creating Synchronous Reluctance Motor Efficiency Maps [DP]	74	Case 123	Thermal Analysis of a Choke Coil [HT, TRANSFORMER_TEMPLATE]
176	Case 288	Synchronous Reluctance Motor Topology Optimization [DP]	77	Case 132	Loss Analysis of a Three-phase Transformer [FQ, LS]
		Stepper Motor	78	Case 133	Thermal Analysis of a Three-phase Transformer [HT]
11	Case 011	Pull-in/pull-out Analysis of a PM Stepper Motor Using a Control Simulator and the JMAG-RT [RT, TR]	81	Case 143	Inductance Analysis of an Air Core Coil [ST]
14	Case 016	Analysis of a Hybrid Stepper Motor [TR]	82	Case 146	Analysis of Stray Loss in a Transformer [FQ, HT, LS]
54	Case 089	Stiffness Torque Analysis of a PM Stepper Motor [TR]	83	Case 148	Loss Analysis of a Power Transformer (Flyback Converter) [TS, DP, ST, LS]
56	Case 094	Analysis of Detent Torque of a PM Stepper Motor [TR]	84	Case 151	Insulation Evaluation Analysis of a Power Transformer [EL]
76	Case 129	Analysis of a PM Stepper Motor Accounting for Magnetization [ST, TR]	85	Case 152	Electromagnetic Force Analysis of Short-circuited Power Transformer Coils [FQ]
		Speaker / Voice Coil Motor	88	Case 158	Superimposed Direct Current Characteristic Analysis of a Reactor That Accounts for Minor Hysteresis Loops [FQ, ST]
10	Case 009	Sound Pressure Analysis of a Loudspeaker [DS, TR]	100	Case 184	Reactor Sound Pressure Analysis taking Magnetostriction into Account [DS, TR]
41	Case 065	Static Thrust Analysis of a Voice Coil Motor [TR]	101	Case 185	Analysis of Stray Loss in a Power Transformer [FQ, LS]
145	Case 243	Voice Coil Motor Control Simulation Using a Control Simulator and JMAG-RT [DP, RT]	114	Case 202	Core Stray Loss Analysis of Power Transformer [FQ, LS]
			115	Case 203	No-Load Test Analysis of Power Transformer [FQ, LS]
			115	Case 204	Copper Loss Analysis of Switching Transformers using Litz Wire [TS]
			117	Case 206	Temperature Analysis of an Oil-Immersed Transformer Using a Coupled Magnetic Field and Thermal Fluid Analysis [FQ, LS]
			128	Case 221	Confirmation of the Influence from the Reduction of High-Frequency Resistance of a Magnetically Plated Wire Choke Coil [TS, FQ]
			137	Case 232	Reactor Joule Loss Analysis [FQ]
			139	Case 235	Reactor Core Stray Loss Analysis [LS, TR]
			141	Case 238	Hysteresis Loss Analysis in a Reactor with DC Bias [DP, LS]
			153	Case 254	Vibration Analysis of a Large Oil-Filled Transformer [DS, FQ]



Resistance Heating

- 28 Case 044 Resistance Heating Analysis of a Steel Sheet [HT, TR]
- 75 Case 127 Resistance Heating Analysis of Steel [FQ, HT]



Generator

- 18 Case 025 Analysis of a Claw Pole Alternator [TR]
- 73 Case 121 Output Analysis of a Salient-Pole Synchronous Generator [DP]
- 122 Case 212 AC Loss Analysis of a Claw Pole Alternator [TR]
- 125 Case 216 Simulation of a Claw-Pole Type Alternator Using a Control Simulator and JMAG-RT [RT, TR]
- 151 Case 251 Alternator Vibration Analysis [DS, TR]



Heater

- 11 Case 010 Thermal Analysis of a Radiant Heater [HT, TR]



Physical Property Testing

- 120 Case 209 Magnetic Measurement Analysis Accounting for Eddy Currents [TR]



Brush Motor / Universal Motor

- 8 Case 003 Analysis of a Permanent Magnet Brush Motor [DP]
- 44 Case 071 Basic Characteristic Analysis of a Motor with 2 Brushes, 6 Poles, and 19 Slots [DP]
- 56 Case 095 Analysis of a Universal Motor [DP]
- 63 Case 106 Iron Loss Analysis of a Brush Motor [DP, LS]
- 66 Case 111 Starting Performance Analysis of a Universal Motor [DP]



Wound-Field Synchronous Motor

- 122 Case 213 Circuit/Control Simulation of a Wound-Field Synchronous Motor [DP, RT]
- 175 Case 287 Analysis of Current Conditions for the Maximum Efficiency of a WFSM [DP, LS]
- 177 Case 289 Efficiency Map Creation for Wound-Field Synchronous Motors [DP, LS]



Linear Solenoid / Linear Actuator

- 40 Case 062 Attraction Force Analysis of a Solenoid Valve [DP]
- 42 Case 066 Operating Time Analysis of an Injector [DP]
- 57 Case 098 Response Analysis of a Solenoid Valve Using a Control Simulator and the JMAG-RT [DP, RT]
- 69 Case 116 Operating Time Analysis of an Injector by Evaluating the Reduction in Eddy Currents [TR]
- 103 Case 189 Response Characteristics Analysis of Injectors Accounting for Collision [DP]
- 106 Case 192 Response Characteristics Analysis of Solenoid Valves Accounting for Residual Magnetization [DP]
- 144 Case 242 Solenoid Valve Attractive Force Analysis Taking into Account Movable Part Motion [ST]
- 146 Case 245 Injector Control and Eddy Current Effects [DP]
- 152 Case 252 Geometry Optimization of a Solenoid Valve [DP]



Linear Motor

- 7 Case 002 Cogging Analysis of a PM Linear Motor [TR]
- 26 Case 041 Positioning Control Analysis of a Permanent Magnet Linear Motor Using the Control Simulator and the JMAG-RT [DP, RT]
- 34 Case 054 Analysis of the Cogging Force of a Moving Coil Linear Motor [TR]
- 41 Case 064 Thrust Force Analysis of a Coreless Linear Motor [TR]
- 61 Case 104 Thrust Force Analysis of a Linear Induction Motor [DP]
- 67 Case 112 Starting Thrust Force Analysis of a Linear Induction Motor [FQ]
- 78 Case 134 Speed Control Analysis of a Permanent Magnet Linear Motor Using the Control Simulator and the JMAG-RT [DP, RT]
- 165 Case 272 Thrust Analysis of Linear Actuator with a Curved Section [TR]



Induction Heating

- 12 Case 013 High-Frequency Induction Heating Analysis of a Shaft [FQ, HT]
- 29 Case 045 High-Frequency Induction Heating Analysis of an IH Cooking Heater [FQ, HT]
- 31 Case 047 High-Frequency Induction Heating Analysis of a Crankshaft [FQ, HT]
- 31 Case 048 High-Frequency Induction Heating Analysis of a Printer Roller [FQ, HT]
- 32 Case 049 High-Frequency Induction Heating Analysis of a Steel Sheet [FQ, HT]
- 32 Case 050 High-Frequency Induction Heating Analysis of a Steel Wire (Translational Induction Hardening) [FQ, HT]
- 33 Case 051 High-Frequency Induction Heating Analysis of a Gear [FQ, HT]
- 50 Case 083 Magnetic Shielding Analysis of an Induction Furnace [FQ]
- 51 Case 085 High-Frequency Induction Heating Analysis of a Constant Velocity Joint [FQ, HT]
- 59 Case 100 Surface Heating Analysis of a Steel Plate [FQ, HT]
- 93 Case 172 High-Frequency Induction Heating Analysis of a Test Piece (Rotational Induction Hardening) [FQ, HT]
- 99 Case 183 Agitation Force Analysis of an Induction Furnace [FQ]
- 102 Case 186 Gear Induction Hardening Analysis Using Two Frequencies [FQ, HT]
- 119 Case 208 High Frequency Induction Hardening Analysis Accounting for Deformation (Abaqus Link [FQ, ABAQUS2])
- 126 Case 218 High-Frequency Induction Hardening Analysis Accounting for Deformation [DS, FQ, HT]
- 127 Case 220 Analysis of the High-Frequency Induction Hardening and Cooling of a Gear [FQ, HT]
- 138 Case 233 Induction Heating Coil Optimization [FQ, HT]
- 173 Case 280 Topology Optimization of Induction Heating Coil [FQ, HT]









Induction Motor

- 7 Case 001 Torque Characteristic Analysis of a Three Phase Induction Motor [DP]
- 24 Case 038 Starting Performance Analysis of a Single Phase Induction Motor [DP]
- 25 Case 039 Torque Analysis of a Three Phase Induction Motor Accounting for the Skew [DP, TR]
- 36 Case 056 Torque Characteristics Analysis of a Self Starting Type Permanent Magnet Motor [DP]
- 40 Case 063 Analysis of Torque Characteristics of a Cage Induction Motor [FQ]
- 42 Case 068 Speed Versus Torque Characteristic Analysis of a Three-Phase Induction Motor [DP]
- 46 Case 074 Speed Versus Torque Analysis of a Single-Phase Induction Motor [DP]
- 71 Case 119 Torque Characteristic Analysis of a Three Phase Wound Rotor Induction Motor [DP]
- 86 Case 154 Calculation of Equivalent Circuit Parameters in a Three-Phase Induction Motor [DP]
- 89 Case 161 Line Start Analysis of a Three-phase Induction Motor [DP]
- 91 Case 166 Line Start Simulation of an Induction Machine Using a Control Simulator and the JMAG-RT [FQ, LS, RT]
- 92 Case 167 Iron Loss Analysis of a Three Phase Induction Motor [DP, LS]
- 95 Case 176 Drive Characteristic Analysis of a Three-Phase Induction Motor [DP, LS]
- 96 Case 177 Torque Characteristic Analysis of a Three Phase Induction Motor [DP, LS]
- 105 Case 191 Torque Analysis of Three-Phase Induction Motors Accounting for the Skew Using the Multi-slice Method [DP]
- 107 Case 193 Calculation of Equivalent Circuit Parameters in a Single-Phase Induction Motor [DP]
- 109 Case 195 Torque characteristics analysis of three-phase induction motors using 3D correction function [DP, TR]
- 125 Case 217 Creating Efficiency Maps for 3-Phase Induction Motors [FQ, LS, EFFICIENCYMAP]
- 133 Case 227 Circuit Control Simulation for Three-Phase Induction Motor [FQ, RT]
- 133 Case 228 Induction Motor Thermal Analysis [HT, LS, TR]
- 134 Case 229 Analysis of the Effect of PWM on the Iron Loss of an Induction Motor [DP, LS]
- 139 Case 234 Vibration Characteristics Analysis of an Induction Motor [DP, DS]
- 164 Case 269 Creating Three-Phase Induction Motor Efficiency Maps Accounting for Harmonics [DP, LS]
- 171 Case 278 Creating Six-Phase Induction Motor Efficiency Maps [FQ, LS]
- 179 Case 291 Control Simulation of Switching Number of Poles in a 6-Phase Induction Machine [DP, Pi]



Bus Bar

- 12 Case 014 Inductance Analysis of Bus Bar [FQ, Pi]
- 70 Case 118 Thermal Analysis of a Busbar [FQ, HT]
- 110 Case 198 Busbar Thermal Stress Analysis [FQ, DS, HT]

		Coreless Motor
27	Case 043	Torque Analysis of a Coreless Motor [TR]
		Spindle Motor
9	Case 007	Analysis of a Spindle Motor [TR]
		Cable
44	Case 070	Analysis of Impedance-Frequency Characteristics of a Cable [FQ]
		Bearing
77	Case 131	Stray Capacitance Analysis of a Motor [EL]
		Magnet Coupling
121	Case 210	Torque Decoupling of In-out Magnet Coupling [DP]
		Wireless Power Transfer
52	Case 086	Power Transmission Analysis of a Wireless Power Transfer System [FQ]
67	Case 113	Power Transmission Analysis of a Wireless Power Transfer System with Opposing Cores [FQ]
80	Case 139	Power Transmission Analysis Using Magnetic Resonance Phenomena [FQ]
104	Case 190	Arrangement Optimization of Wireless Power Supply System [FQ]
109	Case 196	Analysis of coil stray capacitance [EL]
111	Case 199	Efficiency Analysis of Wireless Power Transfer via Electromagnetic Induction Method using Resonance Circuits [FQ]
131	Case 224	Wireless Power Transfer Device Stray Loss Analysis [FQ]

Case 1 Torque Characteristic Analysis of a Three Phase Induction Motor

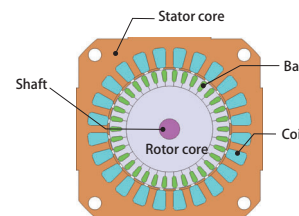
module: DP

Overview

An induction motor is a motor in which the rotating magnetic field of the stator coils causes induced current to flow in an auxiliary conductor, exerting force on the rotor in the rotational direction and causing it to spin. Induction motors are widely used in everything from industrial machines to home appliances because they have a simple construction and are small, light, affordable, and maintenance-free.

In an induction motor, the current induced by the auxiliary conductor exerts a large influence on its characteristics. It also causes strong magnetic saturation in the vicinity of the gap, in particular. With Finite Element Analysis (FEA), it is possible to investigate the characteristics that accurately evaluate the features listed above, so preliminary design evaluations are effective.

This Application Note introduces a case example of how to obtain the current density distribution of an auxiliary conductor and its rotation speed versus torque characteristics.



Current Density Distribution

The current density distribution at a rotation speed of 1050 r/min is shown in fig. 1. The torque in an induction motor is generated between the rotational flux stemming from the current flowing in the stator coil and the current induced in the auxiliary conductor, so the induced current has a large influence on the torque characteristics.

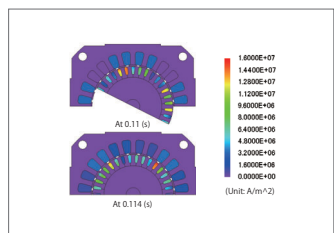


Fig.1. Current density distribution in the auxiliary conductor (rotation speed: 1050 r/min)

Speed-Torque Curve

The Speed-Torque curve is shown in fig. 2. The maximum torque is found to be near 1000 r/min. Based on the fact that the torque in the high speed region gets higher, it can also be seen that the auxiliary conductor's electric resistance in this induction motor is low. In the range labeled b in fig. 2, the speed change is only about 5%, with a 100% change in the torque, so the motor is rotating in a stable fashion.

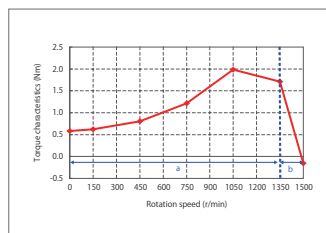


Fig. 2. Speed versus Torque

Case 2 Cogging Analysis of a PM Linear Motor

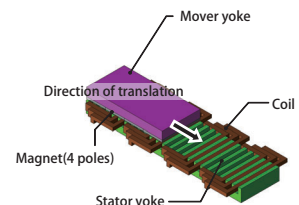
module: TR

Overview

Linear motors have been widely used in carrier devices and the drive units of machine tools due to their capability for high acceleration and deceleration, as well as their accurate positioning. As an issue for improving performance, people are trying to obtain a large thrust force in order to enhance responsiveness, but on the other hand it is also necessary to fulfill the demand for the trade-off of wanting to reduce thrust force variations and the attraction force.

In order to obtain a large thrust force, the material's nonlinear magnetic properties and the magnet's demagnetization characteristics need to be accounted for, and in order to evaluate thrust force variations, they need to be analyzed after modeling a detailed geometry. This is why they need to be studied with a magnetic field analysis simulation based on the finite element method (FEM).

This note presents how to obtain cogging, a cause of thrust variation, and evaluate the thrust force and attraction force during drive.



Cogging

Fig. 1 shows the cogging force waveform. To examine the cause of the cogging force, the flux density distribution at the position (timing) circled in blue in fig. 1 is shown in fig. 2.

Fig. 2 shows that the flux density at the end of the mover is not evenly distributed. This imbalance of the magnetic circuit is the key factor that causes large cogging ripples.

Thrust and Attraction Forces

The position versus thrust force is shown in fig. 3, and the position versus attraction force is shown in fig. 4.

The graphs show that the periods of thrust and attraction forces have the same interval as the period of cogging force. The cogging ripple influences the thrust variations, so the cogging ripple needs to be made smaller in order to reduce the thrust variations. The attraction force is also the same as the radial force in a rotating machine, meaning that it is influenced by the magnetic flux flow in the gap, so it can be reduced by lessening the magnetic flux that flows perpendicular to the gap by using changes in the slot geometry.

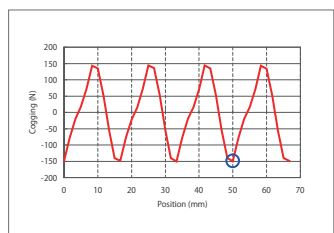


Fig. 1. Cogging Waveform

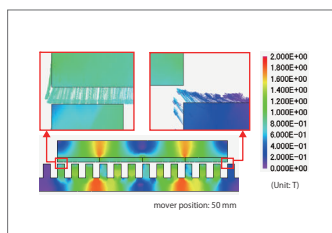


Fig.2. Magnetic flux density distribution

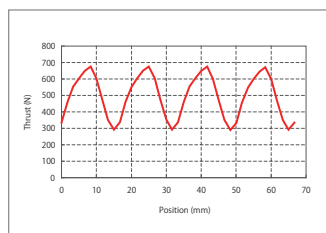


Fig. 3. Position versus Thrust Force

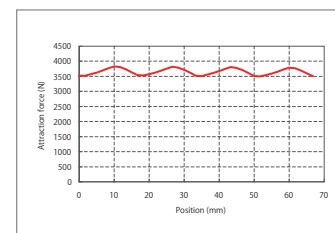


Fig. 4. Position versus Attraction Force

Case 3

Analysis of a Permanent Magnet Brush Motor

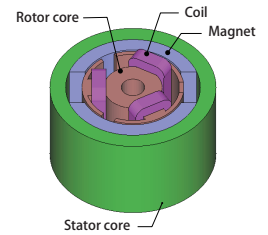
module: DP

Overview

A brush motor generates torque through the electromagnetic attraction and repulsion between its rotor and stator. They do not have many parts and do not require drive circuits, so they are widely used as a power source for compact equipment. A brush motor is composed of a magnetic circuit part, which actually generates torque via electromagnetic phenomena, and the brush/commutator part, which corresponds to the drive circuit. In order to aim at improving the performance of a brush motor, it is necessary to raise the usage efficiency of the magnetic circuit in each part and expertly utilize the nonlinear material characteristics. Proper placement of the brush/commutator that correspond to the drive circuit is also vital.

In order to evaluate the usage efficiency of the magnetic circuit, torque variations, current waveforms, etc. at the design stage, it is best to first do a detailed calculation of the magnetic flux density in each part, and then perform an electromagnetic field simulation using the finite element method (FEM), which can evaluate torque with high accuracy.

This document introduces how the characteristics of the brush-type PM motor can be obtained, including torque versus current (T-I), torque versus speed (T-N), and magnetic flux density distribution.



Speed-Torque Curve/Torque-Current Curve

Fig. 1 shows the Speed-Torque curve, and fig. 2 shows the Torque-Current curve. From both characteristic graphs it is possible to confirm that it has obtained the characteristics of a DC motor, such as the fact that the rotation speed and current are proportional to the torque. The controllable speed range in this motor can also be seen on the Speed-Torque curve.

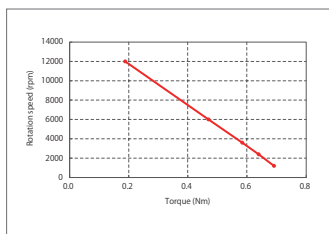


Fig. 1 Speed versus Torque

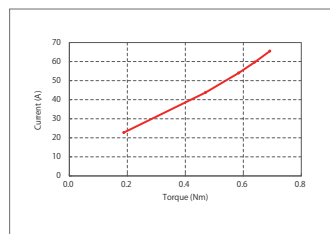


Fig. 2 Torque versus Current

Magnetic Flux Distribution

The magnetic flux density distribution at a rotation speed of 12000 rpm is shown in fig. 3. The magnetic flux density is particularly high in the regions circled in red. The magnetic flux from the rotor and the stator concentrate there. This magnetic flux produces torque. When magnetic flux leakage occurs due to magnetic saturation, the torque may be reduced.

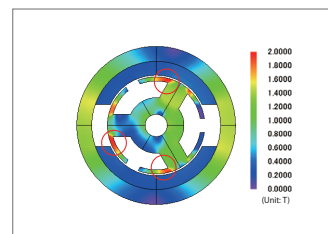


Fig. 3. Magnetic Flux Distributions at 12000 rpm

Case 4

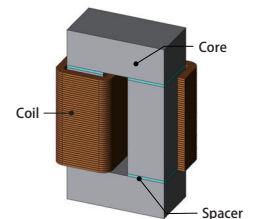
Sound Pressure Analysis of a Reactor

module: DS, TR

Overview

Reactors are used in a variety of electric power systems. For instance, they fill the role of making the current pulsation between an inverter and a motor more smooth. On the other hand, the sound that originates from a resonance phenomenon between an electromagnetic force and an eigenfrequency can become a problem. The reactor in this analysis has a gap in the magnetic circuit to prevent magnetic saturation. Due to the magnetic fields that occur with high frequency currents, electromagnetic force generates near the gap, and this electromagnetic excitation force in turn causes noise. Vibration and sound grow larger when the electromagnetic excitation force and the transformer's eigenmode resonate. In order to evaluate this phenomenon with good accuracy, it is necessary to find the electromagnetic force distribution and eigenmode in the high frequencies that become particular problems by using the finite element method (FEM).

This document introduces an example of an evaluation of a reactor's sound pressure when a part of a spacer has been removed.



Electromagnetic Force Distribution

Fig. 1 shows the distribution of the electromagnetic forces. The spacer is made of nonmagnetic material, which means that there are no changes in the magnetic circuit depending on whether or not it has been removed, so the electromagnetic force distribution is the same regardless of whether or not the spacer is present.

From the electromagnetic force distribution shown in fig. 1, it is apparent that the electromagnetic force is concentrated in the gap. This is because the air permeability in the core is different from the gap.

Eigenmode

Fig. 2 shows the eigenmode in the vicinity of the fundamental frequency (10 kHz) that carries electromagnetic force. Eigenmode in the vicinity of 10 kHz differs due to the spacers being stripped.

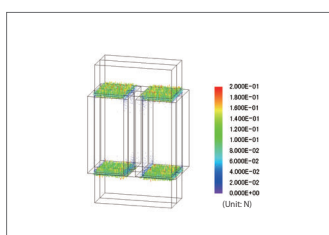


Fig. 1 Electromagnetic force distribution

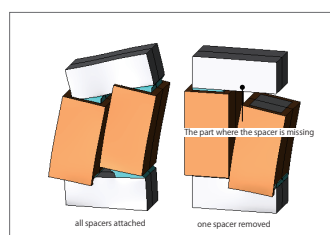


Fig. 2 The eigenmode of approximately 10 kHz

Acceleration

Fig. 3 shows the distribution of the acceleration. The electromagnetic force distribution does not change depending on the presence of the spacer, so differences in the acceleration distribution depend on differences in the eigenmode. Vibrations become larger in the vicinity of the missing spacer due to the spacer being stripped.

Sound Pressure Distribution

The distribution of the sound pressure is shown in fig. 4. The sound pressure distribution changes depending on the presence of the spacer.

While the core vibrates vertically when the spacer is present, when it is absent, the gap where it is missing vibrates longitudinally, so the distribution becomes dispersed. The vibration is also bigger when the spacer is absent, so the sound pressure gets bigger.

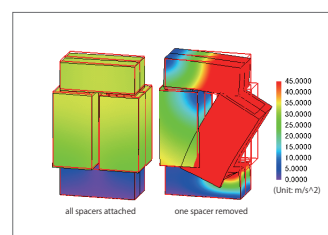


Fig. 3 Acceleration distribution

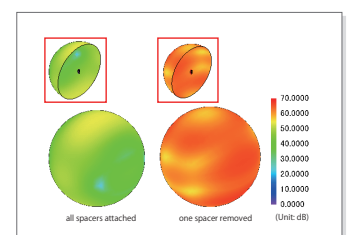


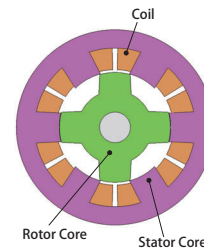
Fig. 4 Sound pressure distribution

Case 6 Analysis of the SR Motor Torque Ripple

module: DP

Overview

With the skyrocketing prices of rare earth magnets, expectations have been rising for SR (switched reluctance) motors because they have a motor format that does not use permanent magnets. SR motors have a simple structure that can achieve solid performance at a low price. However, torque generation depends only upon the saliency between the stator and rotor, so torque variations are extremely large and cause vibration and noise, meaning that the use applications are limited. On the other hand, because of the skyrocketing prices of rare earth metals, the improvement in current control technology, the possibility of optimized designs thanks to magnetic field analysis, and the rising ability to reduce challenges, SR motors are being reexamined. SR motors operate using the nonlinear region of a magnetic steel sheet, so the inductance displays nonlinear behavior that distorts the excitation current waveform a great deal, making it impossible to carry out advanced projections that are accurate with calculation methods that follow linear formulas. Consequently, it becomes necessary to use the finite element method (FEM), which can handle nonlinear magnetic properties in material and minute geometry as well as transient currents. This Application Note explains how to carry out a torque analysis that changes the switch conversion timing and evaluate both the torque ripples and average torque in an SR motor.



Torque Waveform

Fig. 1 shows the torque waveform when voltage is applied to U-phase at 50 deg and turned off at 80 deg. It is apparent that torque ripple peaks coincide with declines in torque that occur when the phase torque switches.

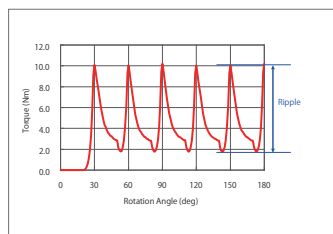


Fig. 1. Torque Waveform

Torque Ripple Comparison

Fig. 2 shows a graph comparing a load analysis at voltage switching angles of 55, 56, and 57 degrees in the U-phase with the torque waveform of a switching angle of 50 deg. A comparison of each of the average torques and the torque ripples at a voltage switching angle of 50 deg is listed in Table 1. Fig. 2 shows that the switch timing can significantly reduce the torque ripple. Comparing a 56 degree voltage switching angle with one of 50 degrees, the torque ripple has been contained by approximately 20%, but at the same time there has been a decline in the average torque, so further studies are necessary in order to improve the torque ripple without allowing the average torque to decline, such as considering increases in the overlap of the torque in each phase by changing either the number of phases or the width of the salient poles.

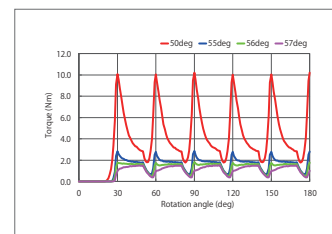


Fig. 2. A comparison of the torque using differences in the voltage switching angle in the U-phase (load analysis)

θ (deg)	Tave (θ) (Nm)	Tr (θ) (Nm)	Tave (θ) / Tave(50) (%)	Tr (θ) / Tr(50) (%)
50	4.51	8.44		
55	1.70	2.17	37.7	25.7
56	1.39	1.27	30.8	15.1
57	1.13	1.13	25.2	13.4

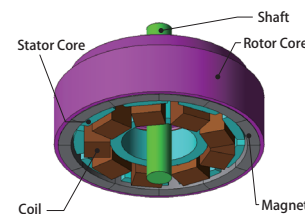
Table 1. The average torque Tave (θ s) and the average torque ripple Tr (θ s) according to changes in the voltage switching angle θ s

Case 7 Analysis of a Spindle Motor

module: TR

Overview

Spindle motors are often used as drive motors where limited space is an issue, as is the case with storage media like hard disks. They employ an outer rotor structure in order to obtain a large torque, but to do so they have to use a great deal of permanent magnets while remaining thin and compact. In order to reduce the number of parts used in their composition, the rotor core has functions that both bear the magnet's flux path and transfer the generated torque, which supports the magnet, to the shaft. For this reason the rotor core is composed of materials that are easy to produce, meaning that there is a possibility that its efficiency as a magnetic circuit will decrease. As motors get smaller, they require a design that accounts for flux leakage because it begins to affect the disc in the rotor. For this reason, spindle motors need electromagnetic field simulations that use the finite element method (FEM), which can account for detailed 3D geometry and magnetic saturation in materials, in order to carry out an accurate evaluation. In this example, how the Speed-Torque curve, the Torque-Current curve and the magnetic flux density distribution of a spindle motor can be obtained.



Speed-Torque Curve/Torque-Current Curve

Fig. 1 shows the Speed-Torque curve, and Fig. 2 shows the Torque-Current curve. The results show that the torque decreases as the speed increases, and increases as the current increases. From the Speed-Torque curve, it becomes apparent that the torque is almost directly inversely proportional to the rotation speed. From these results, it can be assumed that there is almost no influence from the inductance in the winding.

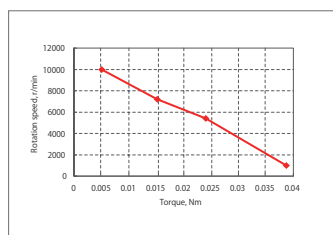


Fig. 1. Speed versus Torque

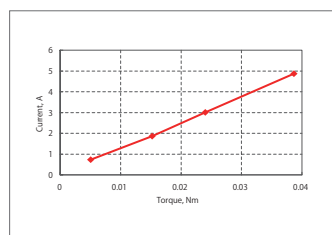


Fig. 2. Torque versus Current

Magnetic Flux Density Distribution

Fig. 3 shows the magnetic flux density distribution at a rotation speed of 7,200 r/min. It can be seen that, from the spindle motor's structure, it has magnetic flux density distribution in the rotor core's rotation axis direction. The magnetic flux density is high in the rotor core because the rotor core is thin in the magnet's magnetic flux direction. High magnetic flux density causes magnetic saturation, which can lead to a decrease in torque.

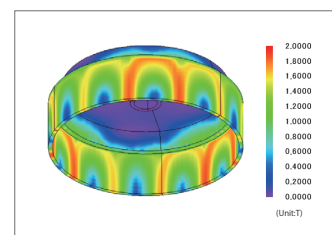


Fig. 3. Magnetic Flux Density Distribution at 7,200 r/min (0.00139 sec)

Case 8

Analysis of an Axial Gap Motor

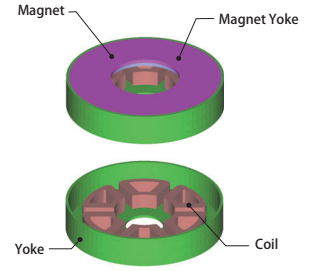
module: TR

Overview

Unlike typical cylindrical motors such as radial gap motors, axial gap motors have a structure in which the stator and the rotor, which is arranged on a disk, face each other and produce rotation. For that reason, because it is possible to arrange thinner parts than with a radial gap motor, they can respond to demands for miniaturization of equipment.

With axial gap motors, evaluations using the magnetic circuit method and empirical data are difficult because the magnetic flux that passes through the rotor and stator, which face each other, becomes a 3D magnetic circuit, meaning that a 3D electromagnetic field simulation using the finite element method (FEM) is necessary because it can carry out an accurate analysis.

In this example, how to use JMAG's 3D magnetic field analysis to carry out a load analysis of an axial gap motor, and then obtain the Torque-Speed curve and the Torque-Current curve.



Magnetic Flux Density Distribution

The magnetic flux density distribution at a rotation speed of 1,000 r/min is shown in Fig. 1. The axial gap motor has magnetic flux density distribution in the rotor coil's rotation axis direction because of its structure. It is also apparent that the magnetic flux density is greater in the vicinity between the magnetic poles. High magnetic flux density causes magnetic saturation, which can lead to a decrease in torque.

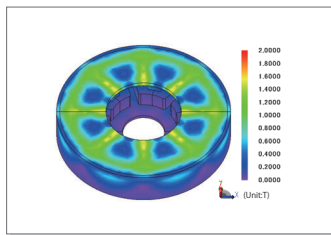


Fig. 1. Magnetic Flux Density Distribution

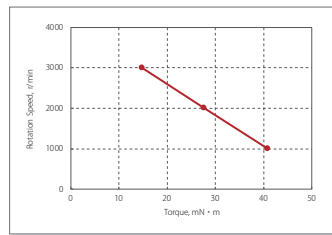


Fig. 2. Torque-Speed Curve

Torque-Speed Curve/Torque-Current Curve

Fig. 2 and Fig. 3 show the analysis results for the Torque-Speed and Torque-Current curves, respectively.

The axial gap motor torque decreases as the rotation speed increases, and increases as the current increases.

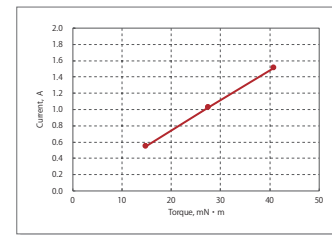


Fig. 3. Torque-Current Curve

Case 9

Sound Pressure Analysis of a Loudspeaker

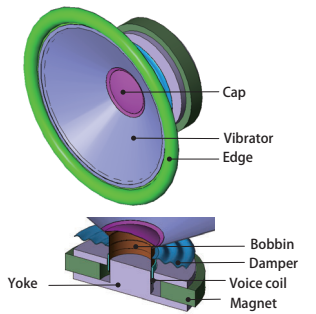
module: DS, TR

Overview

A loudspeaker produces sound when the voice coil makes the vibrator vibrate. The general requirement of the loudspeaker is to produce uniform sound over a wide range of the frequencies.

Lorentz force is generated in the coil when the magnetic field of a permanent magnet acts on the current flowing through the voice coil, and produces sound by making the vibrator vibrate. In order to evaluate the sound with good accuracy, it is necessary to handle the resonance phenomenon between the Lorentz force and the speaker's eigenmode properly. The eigenmode and Lorentz force distribution change depending on the place where the core and coil are wound, so high accuracy calculations need to be carried out using the finite element method (FEM).

This Application Note presents how the frequency characteristics of sound pressure can be obtained using the constant Lorentz force on the voice coil, regardless of the frequency.



Sound Pressure Level

The frequency characteristic of the sound pressure level at the front center of the loudspeaker is shown in fig. 1. The sound pressure distributions at frequencies of 200 Hz and 2000 Hz are shown in fig. 2.

It becomes apparent from the frequency characteristics of the sound pressure level that this speaker is able to obtain a fairly uniform output at over 100 Hz, and that it is not suited to usage in the low frequency region of below 100 Hz.

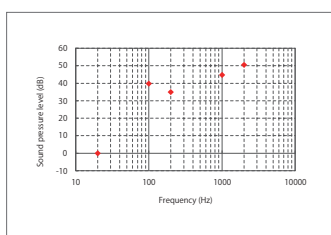


Fig. 1 Frequency Characteristics of the Sound Pressure Level

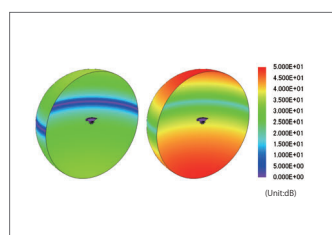


Fig. 2 Sound pressure level distribution (left: 200 Hz, right: 2,000 Hz)

Case 10

Thermal Analysis of a Radiant Heater

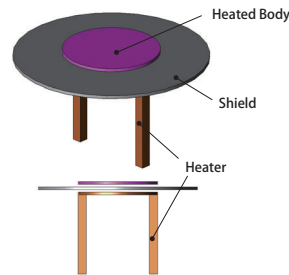
module: HT, TR

Overview

Quartz heaters, which are used in semiconductor manufacturing, are a kind of heating device that uses heat radiation phenomena. Thermal radiation is a mechanism of heat transfer, which is defined as the transport of heat through the transmission of electromagnetic waves between objects that have different temperatures, making transfer possible even through a vacuum. This objective is to transfer heat to a heated body uniformly by placing it near the heater, which has been heated by running current through the coil.

It is necessary to properly handle the effects of the 3D geometry of the heated body or the heat generated from the heater in order to see whether it is raising the temperature uniformly, so a thermal analysis is carried out.

This Application Note explains how to carry out a thermal analysis using the thermal radiation phenomenon between a heater and a heated body to obtain the differences in temperature distribution in the heated body with and without a shield.



Temperature Distribution

The temperature distributions of the heated body depending on the presence of a shield (the range is the same) are shown in figures 1 and 2, and the temperature difference with the center of the heated body surface (distance: 150 mm) is shown in fig. 3.

From these results it becomes apparent that, while there is a difference in the absolute value of the temperature depending on the presence of a shield, when there is no shield there are irregularities in the temperature because heat transfer is being carried out directly to the heated body through thermal radiation from the heater. On the other hand, when there is a shield heat transfer is carried out uniformly to the heated body through the shield's even heat distribution.

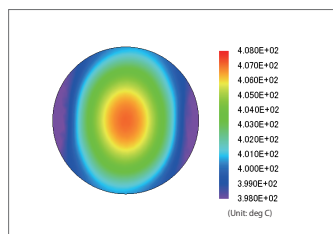


Fig. 1 Temperature distribution in the heated body (without a shield)

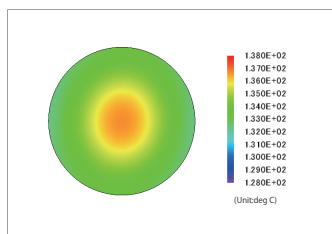


Fig. 2 Temperature distribution in the heated body (with a shield)

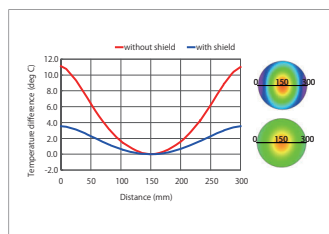


Fig. 3 Temperature difference with the center of the heated object's surface (distance: 150mm)

Case 11

Pull-in/pull-out Analysis of a PM Stepper Motor Using a Control Simulator and the JMAG-RT

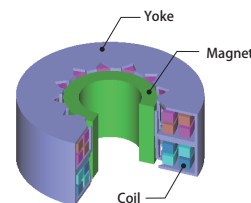
module: RT, TR

Overview

Stepper motors are commonly used for positioning in printers and digital cameras. With a PM stepper motor, there are excitation types such as one phase excitation, two phase excitation, and one-two phase excitation for the excitation system, and the accuracy for stepper motor positioning changes depending on which system is used. Pull-in and pull-out torques are important indicators that show the transient characteristics of a stepper motor, so it is vital to understand and study them in advance.

To measure them, begin to gradually reduce the load on the stepper motor from a stationary state, measure the pull-in torque when it begins to rotate, begin to gradually increase the load in sync with the pulses from a rotating state, and measure the pull-out torque when it loses synchronism. It is necessary to carry out transient analysis while changing the load in order to solve this phenomenon in magnetic field analysis. While it is possible to calculate it using an equation of motion with JMAG's 3D transient response analysis, such calculations take too much time. With JMAG, it is possible to create a motor model that is detailed and conforms to a real machine, and that accounts for spatial harmonics and magnetic saturation characteristics that are included in a stepper motor. By importing this motor model, a "JMAG-RT model," to the control/circuit simulator, it is possible to derive the stepper motor's pull-in and pull-out torques quickly and accurately because it accounts for the motor's magnetic saturation characteristics and spatial harmonics.

This note presents how JMAG-RT can be used to calculate holding torque and coil inductance that varies with current. The result is the JMAG-RT motor model used as a reference for a circuit / control simulator that runs a transient analysis to obtain pull-in and pull-out torques of the stepper motor. By also using a single JMAG-RT motor model and changing the circuit on the circuit/control simulator, it is possible to obtain the characteristics of two types of drives: a bifilar winding with a unipolar drive, and a monofilament winding with a bipolar drive. Other parameters are the same for both analyses.



Pull-In and Pull-Out Torques characteristics

The pull-in and pull-out torque characteristics are shown in fig. 1 and fig 2. Fig. 1 shows the result with bifilar winding and unipolar drive. Fig. 2 shows the result with monofilament winding and bipolar drive along with the result of fig. 1. The I-shape in each figure represents approximate error range of pull-in and pull-out torques at each point. Error range is shown in both figures.

The self starting region and slew region can be determined from fig. 1. These results indicate the correlation between the torque and pulse rate required for the motor to run on without losing synchronized stepping.

As shown in fig. 2, the result of bifilar winding with unipolar drive and the result of the monofilament winding with bipolar drive have similar pull-in and pull-out torques when other parameters are the same.

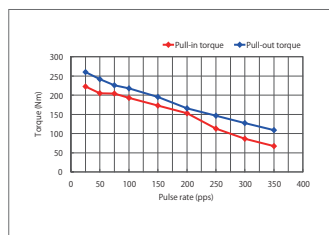


Fig. 1 Pull-in and Pull-out Torque Characteristics (bifilar winding / unipolar drive)

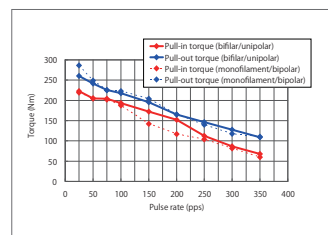


Fig. 2 Pull-in and Pull-out Torque Characteristics (monofilament winding / bipolar drive)

Case 13

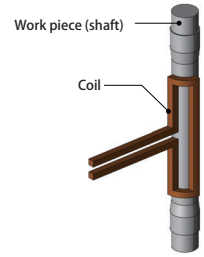
High-Frequency Induction Heating Analysis of a Shaft

module: FQ, HT

Overview

Shafts are used in parts like axles, which transfer power from the engine to rotate the tires, so the need to have sufficient strength to handle the torsion. They also need to have increased surface toughness to raise their degree of abrasion resistance in the areas that join with other parts, and they must maintain their interior toughness in order to obtain strength and fatigue resistance against torsion. By using high-frequency induction heating, which is a type of surface hardening method, the part is heated rapidly on only its surface by a high frequency power source. This process also has many other benefits, such as providing a clean working environment because it uses electrical equipment, being very efficient, and providing uniform results for each product. This is why it is being aggressively implemented in the field. Eddy currents generated by the high-frequency varying magnetic field occur in the surface of the shaft. The material properties also change due to the rising temperature. Examining detailed phenomena requires handling the phenomena that occur in the interior of the shaft in a numerical analysis based on the finite element method.

This Application Note explains how to create a numerical analysis model and analyze the elevated temperature process in order to use the coil geometry and current conditions (power supply frequency, current value) to verify whether or not the target temperature distribution is obtained.



Eddy Current Loss Density Distribution

Fig. 1 shows the eddy current loss density distribution produced in the shaft. The magnetic field generated by the coil produces eddy currents in the surface of the shaft. In areas where induction heating makes the temperature exceed the Curie point, the magnetic properties change and both the relative permeability and the electric conductivity grow smaller, which makes the eddy current loss density shrink as well.

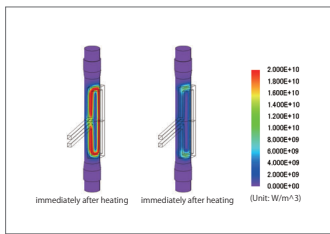


Fig. 1 Eddy current loss density distribution

Temperature Distribution

Fig. 2 shows the temperature distribution in the shaft at each time.

From fig. 2, it is apparent that rotating the shaft heats the surface of the shaft facing the coil uniformly in the circumferential direction.

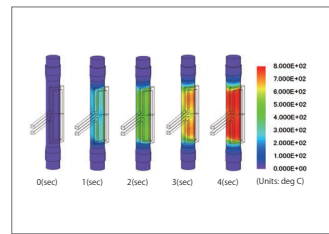


Fig. 2 Temperature distribution

Case 14

Inductance Analysis of Bus Bar

module: FQ, Pi

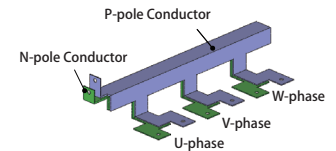
Overview

Voltage surges can damage the components in electrical equipment such as an inverter.

Busbar inductance can be a cause of surges. Therefore, it is important to reduce it to protect the electrical equipment.

Using FEM allows for the calculation of inductance based on the magnetic field and current distribution obtained from the magnetic field analysis.

This note presents a case study on the current distribution and the frequency versus inductance characteristic of the busbar.



Current Distribution in the Conductor

Fig.1 shows the current density distribution in the conductor when applying the current from +U phase to -W phase.

This current distribution is caused by the skin effect in which the current concentrates near the surface. This current distribution affects resistance and inductance.

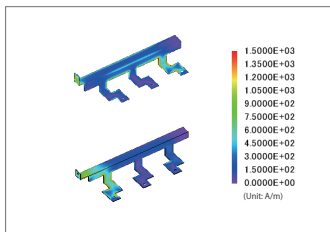


Fig.1 Current Density Distribution of the Conductor Surface (Upper: N-pole, lower: P-pole)

Inductance

Fig. 2 shows self inductance of the N and P pole conductors, Fig. 3 shows the mutual inductance between the N and P pole conductors, and Fig. 4 shows the Resistance of the N and P pole conductors.

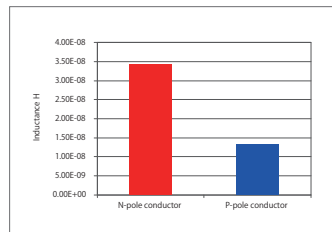


Fig.2 Self-inductance

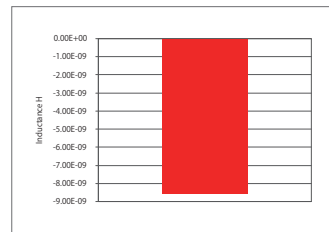


Fig.3 Mutual inductance

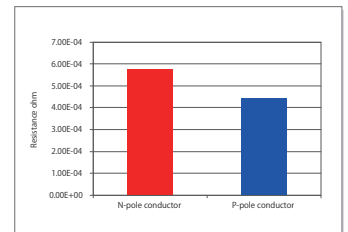
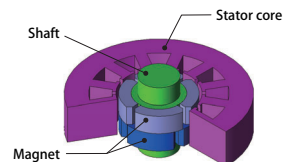


Fig.4 Resistance

Case 15

Cogging Torque Analysis of an SPM Motor with a Step Skewed Magnet

module: TR



Overview

Reductions in vibration and noise are being sought after because they are a cause of torque variations in motors, and demands for reduction are particularly strong with motors that are used in machine tools and power steering. Cogging torque, which is a torque variation that is produced when there is no current, is generated because the electromagnetic force, which is produced in the gap, changes in relation to the rotor's rotation, making it necessary to apply skew to the stator and rotor and improvise with the magnet and stator's geometry in order to limit said variations in electromagnetic force as a countermeasure for reducing the torque variations. When applying skew, force in the thrust direction is produced in exchange for a reduction in the cogging torque, meaning that there is the disadvantage of producing eddy currents from the magnetic flux that links in the lamination direction.

Consequently, in order to accurately evaluate a motor that has skew applied, one needs a magnetic field analysis simulation that uses the finite element method (FEM), which can account for a detailed 3D geometry, instead of studies that use the magnetic circuit method or a 2D magnetic field analysis.

This Application Note presents the use of magnetic field analysis to evaluate the magnetic flux density distribution and cogging torque in each part of an SPM motor with a step skewed magnet.

Magnetic Flux Density Distribution

Fig. 1 shows the magnetic flux density distribution at the rotation angle of 60 degrees, and fig. 2 shows the frequency component of the magnetic flux density waveform in the gap. The upper limit of the frequency component is 1440 Hz, and the primary component of the frequency is 120 Hz because there are 4 poles and the rotation speed is 30 rps. As shown in fig. 1, the magnetic circuit is changed by the application of the step skew. As shown in fig. 2, the ratio of the frequency component at 360 Hz, which is the fundamental frequency of the cogging torque, is 13 % when the magnet is not step skewed and 4 % when the magnet is step skewed, so the cogging torque may be reduced by applying the step skew.

Cogging Torque Waveform

Fig. 3 shows the cogging torque waveforms of Model A and Model B. When the magnet is step skewed, the peak value of the cogging torque is reduced by about 50 percent.

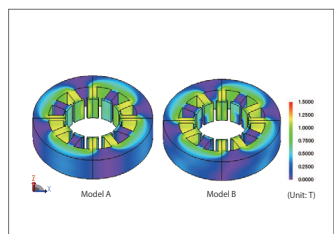


Fig. 1. Magnetic flux density distribution

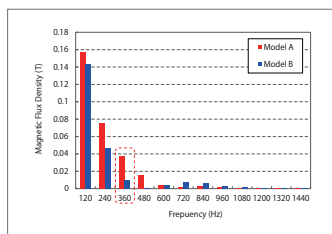


Fig. 2. Frequency Component of the Magnetic Flux Density Waveform in the Gap

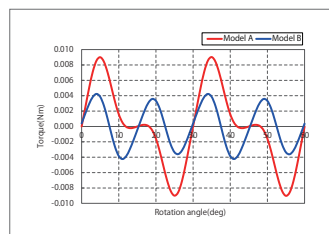
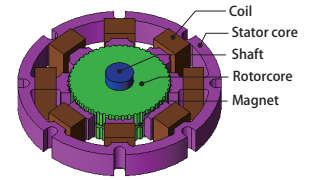


Fig. 3. Cogging torque waveform

Case 16

Analysis of a Hybrid Stepper Motor

module: TR



Overview

Hybrid stepper motors are used as actuators for equipment where position detection accuracy is required, such as the joints of robots or rotary tables for machine tools. The rotor has a construction that sandwiches a magnet that is magnetized in the axial direction between two rotor cores that have serrated teeth to create salient poles, and the tips of the stator core's teeth are shaped like gears as well. Because the rotation resolution is determined by the number of rotor teeth and the number of phases for the drive coil, the design uses large number of teeth, such as 50 or 100, so the angle resolution can be increased. The most important characteristics for a stepper motor are the controllability, the detent torque, which is a non-excitation holding torque, and the stiffness torque, which is an excitation holding torque, and not the motor's output.

The two-plated rotor core of a stepper motor has an N pole on one side and an S pole on the other, so a multipole magnet is achieved by deviating the saliency of the gear condition by 1/2 pitch. Consequently, the magnetic circuit is 3D. There are also times when the division pitch geometry of the teeth is complicated, so it is necessary to carry out a 3D electromagnetic field analysis using the finite element method (FEM) to proceed with an accurate preliminary study.

This document introduces how the detent torque and stiffness torque can be calculated for a hybrid stepper motor.

Detent Torque

The detent torque is shown in fig. 1, and the magnetic flux distribution in the XY-plane at the rotation position of 0.45 degrees is shown in fig. 2. A closer view to show the flux distribution in the gap is shown in fig. 3. These results reveal that the flux in both the rotor and stator is saturated even with no excitation. The flux leakage around the tips of the teeth, due to saturation, can be expected to have a large effect on the detent torque.

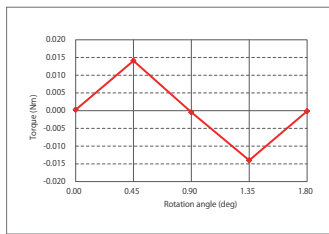


Fig. 1. Detent torque

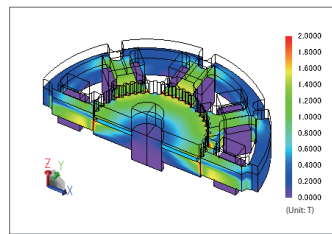


Fig. 2 Magnetic flux distribution at the rotation of 0.45 deg

Stiffness Torque

Fig. 4 shows the stiffness torque with one-phase excited and fig. 5 shows the stiffness torque with two-phase excited. The flux distribution in the gap of the XY-plane with one-phase excited is shown in fig. 6, and the flux distribution in the gap of the XY-plane with two-phase excited is shown in fig. 7. As with the detent torque, the magnetic flux around the teeth is saturated. The flux leakage caused by the saturation can be expected to also have a large effect on the stiffness torque.

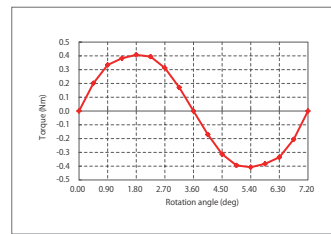


Fig. 4 Stiffness torque with one-phase excitation

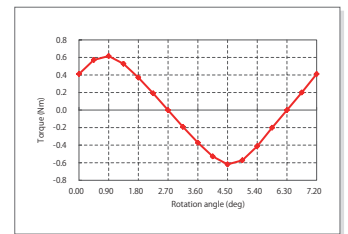


Fig. 5 Stiffness torque with two-phase excitation

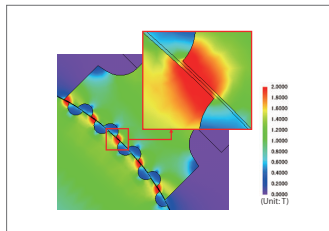


Fig. 3 Flux distribution in the gap at the rotation of 0.45 deg

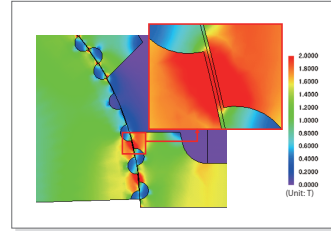


Fig. 6 Magnetic flux distribution of the gap with one-phase excitation at a rotation of 1.8 deg

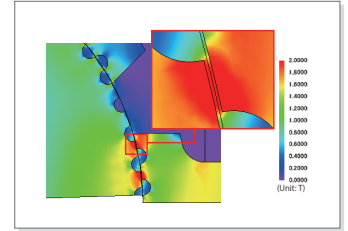
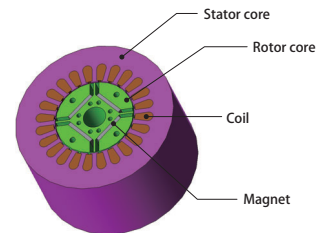


Fig. 7 Magnetic flux distribution of the gap with two-phase excitation at a rotation of 0.9 deg

Case 17

Inductance Analysis of an IPM Motor

module: DP



Overview

An IPM motor can use both magnet torque and reluctance torque, so by appropriately choosing the current phase it is possible to improve efficiency over a broad spectrum of drive range. It is a motor type that is often used in equipment with a wide operational range, from air compressors in air conditioners to motors that power vehicles. In many cases, strong rare earth magnets are used to increase output density, so it is necessary to have an IPM motor design that accounts for magnetic circuit saturation.

For this reason a study that considers the influence of saturation needs to be carried out in order to evaluate the IPM motor's design, so the study ends up carefully investigating variations in inductance characteristics due to current phase, geometry, or the material's nonlinear magnetic properties. An analysis based on the magnetic circuit method or a theoretical equation that assumes linear properties cannot predict these functions with good accuracy and therefore cannot derive them. Consequently, in order to perform an advanced projection of an IPM motor's design, an electromagnetic field simulation that uses the finite element method (FEM) is necessary.

This Application Note explains how to obtain the current phase angle characteristics of a dq axis inductance that accounts for magnetic saturation and flux leakage in an IPM motor.

Inductance

Fig. 1, and a current phase angle graph for the torque that was output from the inductance value is shown in fig. 2.

Fig. 1 shows that the d-axis inductance is smaller because the magnetic flux must pass through the low permeability magnet. It is less affected by magnetic saturation due to very large magnetic resistance. On the other hand, the q-axis inductance is larger than the d-axis inductance due to larger permeability, and it is also significantly affected by magnetic saturation because the magnetic resistance is much smaller.

Fig. 2 shows that the maximum torque for this IPM motor can be obtained when the current phase angle is around 20 deg.

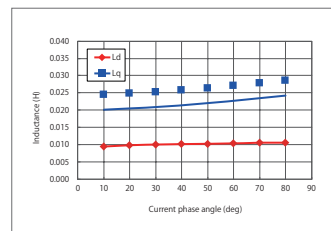


Fig. 1. Ld/Lq versus current phase angle

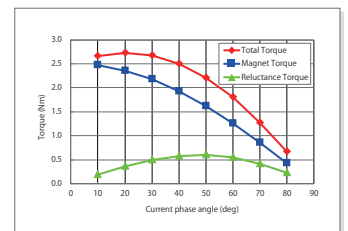


Fig. 2. Torque versus current phase angle

Case 18 Thermal Analysis of an IPM Motor

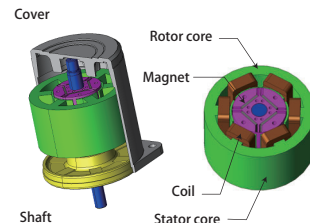
module: HT, LS, TR

Overview

Exactly how to resolve the problem of rising temperatures is a critical issue when trying to achieve an improvement in a motor's efficiency and output. In order to solve this problem it is important to investigate a magnetic design that reduces the losses themselves because they are a source of heat, but it is also important to study a thermal design that improves heat dissipation and does not let the temperature rise. Copper loss in the coils and iron loss in the core are the dominant heat sources, so this analysis mainly evaluates the effects of this heat. Changes in the magnet's properties due to temperature are large and its heat resistance is low, so it is necessary to design while paying careful attention to rising temperatures during operation. During operation, rated evaluations with a continuously operated constant load are run until a thermal balanced state has been reached. In addition to these rated evaluations, however, thermal transient evaluations that add a thermal cycle with an intermittently operated electrical overload are performed, as well.

In order to carry out an accurate thermal design, it is necessary to first correctly understand the heat generation amount and location, so it would be advantageous to calculate the losses in a magnetic field analysis simulation using the finite element method, and from there to carry out a thermal analysis using the resulting loss distribution.

In this example, how to evaluate a motor's temperature distribution by creating a thermal analysis model that can investigate the loss analysis and temperature distribution in order to obtain the motor's total loss distribution, and then analyzing the elevated temperature process.



Loss

The values of the losses in each part when a 2 A current is applied are shown in Table 1. The loss in the coil is relatively large, and it is expected to be the main source of heat.

Iron loss in the rotor core	Iron loss in the stator core	Eddy current loss in the magnet	Copper loss in the coil
0.23 W	4.5 W	0.015W	21W

Table 1. Loss in Each Part

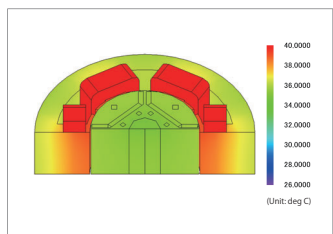


Fig. 1. Temperature Distribution at a Steady State

Temperature Distribution at Steady State

The distribution of temperature at the steady state when a 2 A current is applied is shown in Fig. 1.

The result shows that the temperature is transferred from the coil to the surrounding parts.

Temperature Variation

The points where the temperature is measured in each part and the temperature changes when a 2 A current is applied are shown in Fig. 2 and Fig. 3.

Fig. 3 shows that the temperature in each part reaches a steady state.

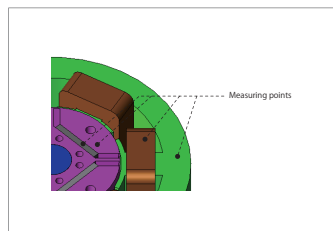


Fig. 2. Points of Measuring Temperature for Each Part

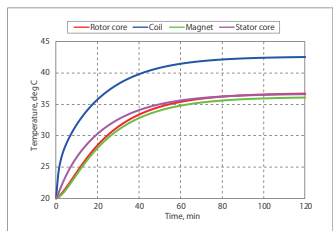


Fig. 3. Temperature variation

Current, A	2	6
Average torque, Nm	0.36	1.1

Table 2. Current and Average Torque

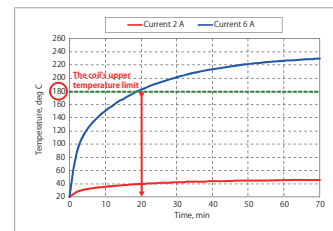


Fig. 4. Temperature Variation of the Coil with Various Currents

Consecutive Operating Time and Average Torque with Various Currents

The current was set at three times the rated value to increase the average torque to 1.0 Nm or above. The average torque and temperature variations in the coil are shown in Table 2 and Fig. 4 (see Fig. 2 for the points of measurement).

Although increasing the current produces a higher torque, at a motor drive time of 20 min the coil's temperature exceeds the upper temperature limit of 180 deg C.

By carrying out a magnetic field-thermal coupled analysis in this way, it is possible to evaluate the motor's properties and constraints with more detail.

Case 19 Analysis of the Centrifugal Force in an IPM motor

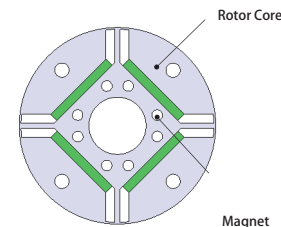
module: DS

Overview

While motors have started being combined with motor drives and used in a wide range of velocities, further changes toward high output and high efficiency are being demanded of them. While higher speed revolution has been given as a means of attaining higher output, the centrifugal force becomes larger with higher speed revolution and this requires evaluation from the point of mechanical strength.

IPM motors have a structure that embeds the magnet in the rotor. Centrifugal force kicks in during motor drive, so the magnet becomes pressed against the rotor core because it gets peeled off or displaced, making it so that a strong local stress begins to operate. It is necessary to correctly handle the phenomena of a magnet peeling off or becoming displaced in order to accurately obtain the local stress distribution. It is important to account for the adhesion and contact conditions between the magnet and rotor core in an analysis in order to do this.

This Application Note presents examples of cases that obtain changes and stress distribution from the centrifugal force in the rotor.



Mises Stress

Fig. 1 shows the mises stress distribution in the rotor.

Fig. 1 shows that the magnet drastically deforms the rotor core with centrifugal force in the radial direction. Also, the Mises stress increases at the bridge part of the rotor core. Mises stress allows the evaluation of the risks of damaged rotor cores and mechanical strength.

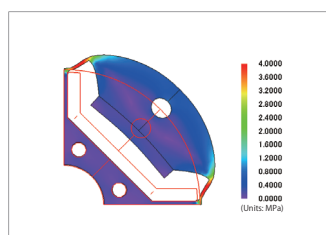


Fig. 1 Mises stress density distribution

Case 20

Sound Pressure Analysis of an SPM Motor

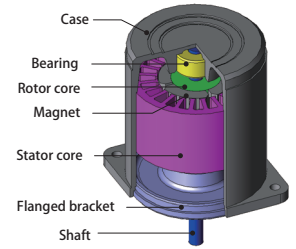
module: DP, DS

Overview

As electric motors are becoming more common, motors which create less noise are in high demand. Sound can be divided into categories of electromagnetic noise, mechanical noise, and draft noise, where electromagnetic noise is the most common for medium and small sized motors. Sound can be divided into categories of electromagnetic noise, mechanical noise, and draft noise, where electromagnetic noise is the most common for medium and small sized motors.

The electromagnetic force in a motor vibrates as an electromagnetic excitation force which creates noise. The vibration and noise are generated when the electromagnetic excitation force resonates with the motor's eigenmodes. In order to evaluate this phenomenon more accurately, it is necessary to understand the distribution of electromagnetic force that moves the stator core which is the basis for the radiated sound. The distribution of electromagnetic force or the eigenmodes in a model that depends on the geometry of a stator core is required for running an analysis such as for the finite element analysis.

In this example, an evaluation of a reactor's sound pressure, when acquiring electromagnetic force generated by a stator core for a SPM motor and linking the eigenmodes of a motor.



Electromagnetic Force

Fig. 1 shows the distribution of the electromagnetic force distribution. A strong output of electromagnetic force can be seen at the tips of the teeth. From these results, it can be expected that the stator core is generating a strong force in a radial direction.

The results of a resolution in a frequency component for an electromagnetic force in a radial direction on the tips of the teeth is shown in Fig. 2. From these results, the frequency component in 400 Hz is the most dominant. Also, can see that the frequency components above 5,000 Hz are very small.

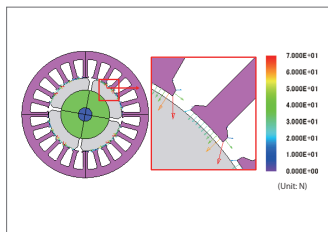


Fig. 1. Electromagnetic Force Distribution

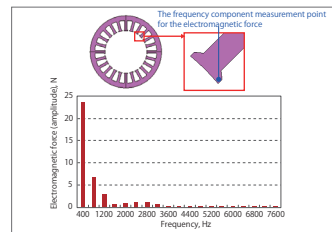


Fig. 2. Frequency Components of the Electromagnetic Force

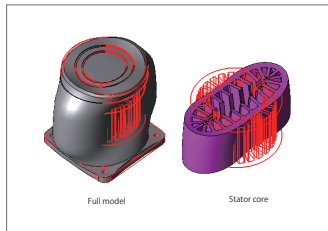


Fig. 3. The Eigenmode of Approximately 3,600 Hz (Red Line: Original Shape)

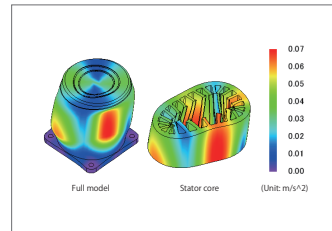


Fig. 4. Acceleration Distribution of 3,600 Hz

Eigenmode

The eigenmode near 3,600 Hz is shown in Fig. 3. It is apparent that a mode in deformation exists in a stator of ellipse near 3,600 Hz, and a large vibration is going to be generated from the resonance phenomenon between an eigenmode and an electromagnetic force.

Acceleration

Fig. 4 shows the distribution of the acceleration at 3,600 Hz. This is the frequency in which the mode that deforms elliptically (displayed in the eigenmode analysis) appears. At 3,600 Hz, it can be seen that electromagnetic resonance is occurring between the electromagnetic force and the eigenmode shown in Fig. 3.

Sound Pressure Distribution

The sound pressure distributions at 3,600 Hz are shown in fig. 5. Like with the distribution of acceleration, at 3,600 Hz an electromagnetic resonance occurs between the electromagnetic force and the eigenmode shown in fig. 3.

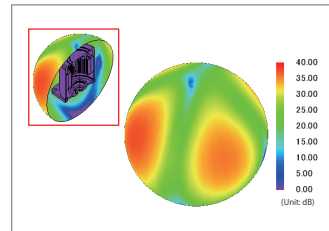


Fig. 5. Sound Pressure Level Distribution in 3,600 Hz

Case 21

Iron Loss Analysis of an SPM Motor Including the Effect of Shrink Fitting

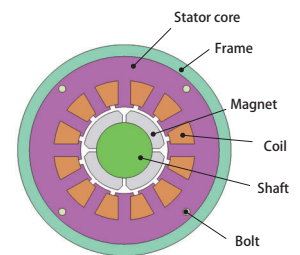
module: DS, DP, LS

Overview

A magnetic steel sheet is used for the iron core in a motor. A frame is shrunk into a stator core in order to sustain the laminated structure and to improve the strong joint between the frames. It is known that a compressive stress is generated during the shrinking process which increases the iron loss process. Therefore, it is important to account the affects of stress during iron loss evaluation. Therefore, it is important to account the affects of stress during iron loss evaluation.

An iron loss is generated by the magnetization field in displacement with a steel sheet. The size of the iron loss is dependent on the iron loss properties of a steel sheet. Iron loss characteristics of a steel sheet deteriorates when there is stress in shrinkage. The stress generated by the shrinkage is distributed in areas in which the section in the back yoke becomes large. In order to evaluate the iron loss with good accuracy, it is necessary to obtain the stress distribution for the magnetic flux, time variation, and steel sheet with accuracy.

This note presents an analysis to obtain the iron loss density of an SPM motor both including and not including the stress caused by shrink fitting.



Compressive Stress Distribution

The compressive stress distribution is indicated in Fig. 1. The compressive stress caused by the frame shrinking in the radial direction increases around the slots as indicated in Fig. 1. This is because the stress decreases towards the tips of the teeth while the stress is concentrated around the slots.

Iron Loss Density Distribution

The iron loss density distribution is indicated in Fig. 2. The iron losses increase up to 7 times depending on whether or not the stress is applied. An analysis that accounts for the thermal stress caused by shrink fitting needs to be performed to evaluate the iron losses more accurately because the iron losses increase when the thermal stress is applied.

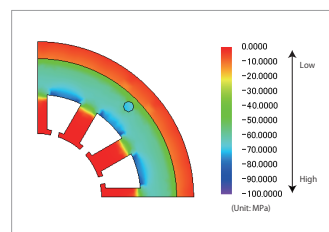


Fig. 1. Principal stress (compressive stress)

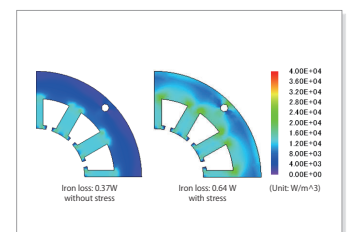


Fig. 2. Iron loss density distribution

Case 22

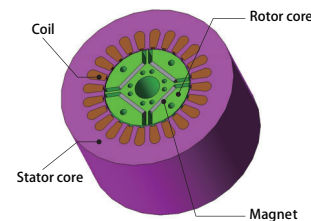
Analysis of the Eddy Current in the Magnet of an IPM Motor

module: TR

Overview

More and more permanent magnet motors are starting to use rare earth magnets, which have a high energy product, in order to achieve higher output density. Neodymium rare earth magnets contain a great deal of iron so they have a high electric conductivity, but when a varying magnetic field is applied they produce Joule loss from eddy currents. Due to the spread of IPM structure adoption and field weakening controls in recent years to speed up rotation, the frequencies and fluctuation ranges of varying fields applied to magnets have increased, and there has been a corresponding increase in Joule loss. By dividing the magnet, like one would a laminated core, to control eddy currents, one can obtain a method of lowering the apparent electric conductivity and lowering the eddy currents. Armature reactions in the stator occur before the eddy currents produced in the magnet, so the eddy currents are determined by the slot geometry of the stator core, the geometry of the rotor, the nonlinear magnetic properties of the core material, and the current waveform that flows through the coil. In order to examine these kinds of magnet eddy currents ahead of time, one has to account for things like these geometries and material properties precisely, so a magnetic field simulation using the finite element method (FEM), which can account for them, would be the most effective.

In this example, the use of a magnetic field analysis in a state of operation to obtain variations in magnet eddy current losses according to the number of divisions in the magnet.



Eddy Current Density Distribution in the Magnet

Fig. 1 shows the eddy current density distribution in the magnet. The eddy currents are concentrated on the surface of the magnet. Using a divided magnet breaks up the eddy current paths.

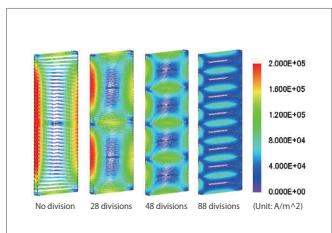


Fig. 1 Eddy current density distribution in the magnet

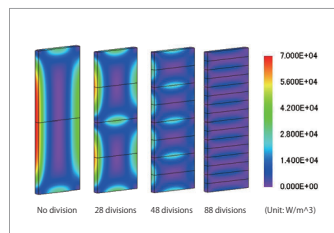


Fig. 2 Eddy current loss density distribution in the magnet

Change of the Loss in Divided Magnet

Fig. 2 shows the magnet's eddy current loss density distribution and Fig. 3 shows the eddy current loss.

By increasing the number of divisions in the magnet, the magnet increases the eddy current flow path and increases the electrical resistance. Because of this, the eddy current density in each divided magnet is reduced as well, making it so that the total amount of eddy current loss decreases.

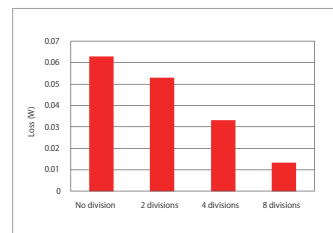


Fig. 3 Eddy current loss in the magnet

Case 23

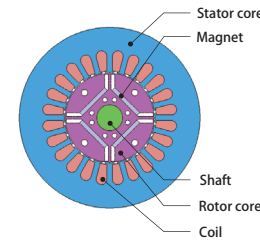
Eccentricity Analysis of an IPM Motor

module: DP

Overview

Rotor eccentricity is one cause of vibration and noise in motors. It is well known that motor torque is produced by electromagnetic attraction and repulsion between the stator and rotor, but not much attention is paid to the fact that electromagnetic attraction acts in the radial direction between the rotor and stator. This is because it seems that this electromagnetic force is canceled out and therefore not produced because the rotor and stator are normally arranged concentrically. However, if there are dimensional errors in the parts that support the shaft or stator and concentricity is not maintained, in other words if there is eccentricity, the electromagnetic force in the radial direction is not canceled out. In this case, friction increases due to the constant action of the radial load on the shaft bearings, causing vibration and noise. A certain amount of error from processing has to be expected. Processing error itself is not so large that the parts cannot be put together, but even assembly error can cause a minute eccentricity of around 1/10 mm. Analysis that can handle this level of precision is needed to evaluate this kind of minute geometry difference, and electromagnetic field analysis using the Finite Element Method (FEM) is useful because it has the sensitivity for detailed geometry differences.

This Application Note presents how to obtain variations in electromagnetic force according to changes in the amount of rotor eccentricity.



Electromagnetic Force on the Rotor

For each amount of eccentricity, the eccentricity direction component of the electromagnetic force acting on the rotor is indicated in fig. 1, and the perpendicular direction component of the eccentricity is indicated in fig. 2.

The graphs show the eccentricity amount becomes larger while the eccentricity direction component of the electromagnetic force becomes smaller. The balance for the orthogonal direction component of the eccentricity for an electromagnetic force is deformed and the amplitude becomes larger.

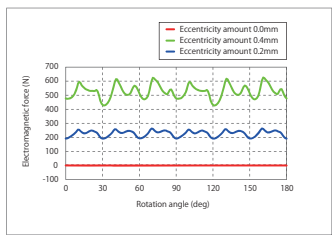


Fig. 1. Electromagnetic force acting on the rotor (Eccentricity direction component)

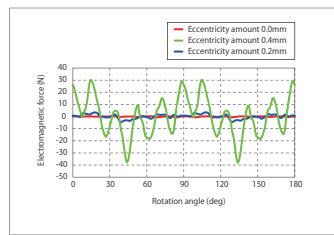


Fig. 2. Electromagnetic force acting on the rotor (Orthogonal direction component of the eccentricity)

Electromagnetic Force Acting on the Teeth

The electromagnetic force of the radial direction component that acts on the teeth where the gap length is most narrow is indicated in fig. 3, and the results for the frequency components of the electromagnetic force displayed in fig 3 is indicated in fig. 4. The radial direction is the positive center direction for a circle.

Fig. 3 shows the larger the eccentricity amount the faster the electromagnetic force changes and is the cause of deformation in the stator. The area in red square as shown in fig. 4 indicate that an increase in harmonic components based on eccentricity causes vibration and noise.

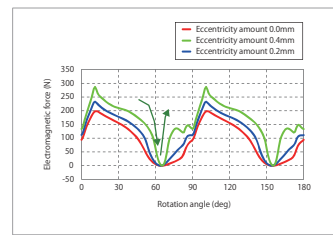


Fig. 3. Electromagnetic force acting on the teeth (radial direction component)

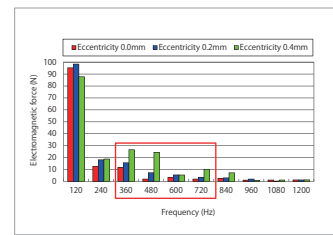


Fig. 4. Frequency component for the electromagnetic force acting on the teeth

Case 24

Cogging Torque Analysis of an SPM Motor with a Skewed Stator

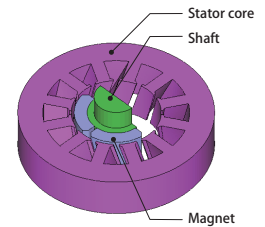
module: TR

Overview

Reductions in vibration and noise are being sought after because they are a cause of torque variations in motors, and demands for reduction are particularly strong with motors that are used in machine tools and power steering. Cogging torque, which is a torque variation that is produced when there is no current, is generated because the electromagnetic force, which is produced in the gap, changes in relation to the rotor's rotation, making it necessary to apply skew to the stator and rotor and improvise with the magnet and stator's geometry in order to limit said variations in electromagnetic force as a countermeasure for reducing the torque variations. When applying skew, force in the thrust direction is produced in exchange for a reduction in the cogging torque, meaning that there is the disadvantage of producing eddy currents from the magnetic flux that links in the lamination direction.

Consequently, in order to accurately evaluate a motor that has skew applied, one needs a magnetic field analysis simulation that uses the finite element method (FEM), which can account for a detailed 3D geometry, instead of studies that use the magnetic circuit method or a 2D magnetic field analysis.

This note presents the use of magnetic field analysis to evaluate the cogging torque of an SPM motor with a skewed stator.



Magnetic Flux Density Distribution

Fig. 1 shows the magnetic flux density distribution of the stator core, and fig. 2 shows the magnetic flux density waveform in the gap. The magnetic flux density waveform is the average of the three points that are indicated on the line in the axial direction shown in fig. 2. As shown in Fig 1, magnetic circuit changes with the application of the skew. Applying skew also deviates the phases of the magnetic flux density waveforms at the three points. Therefore, the variation in the average magnetic flux density waveform is smaller as shown in fig. 2, so the cogging torque may be reduced.

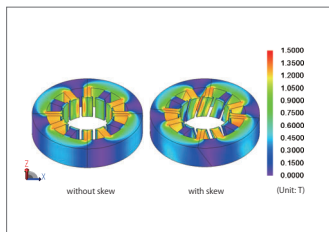


Fig. 1 Magnetic Flux Density Distribution

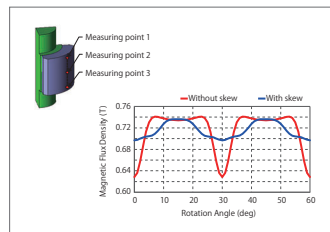


Fig. 2 Magnetic flux density waveform in the gap

Cogging Torque

Fig. 3 shows the cogging torque waveform of the SPM motor with the skewed stator and with the non-skewed stator. The peak value of cogging torque of the skewed stator is reduced by about 60 percent compared with that of the non-skewed stator.

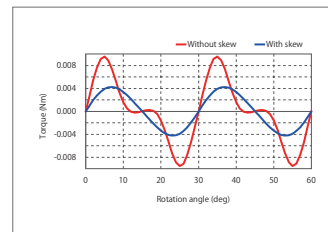


Fig. 3 Cogging Torque Waveform

Case 25

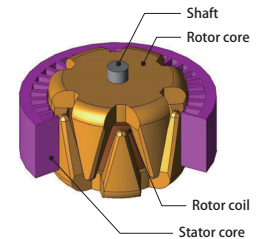
Analysis of a Claw Pole Alternator

module: TR

Overview

Demand for high fuel efficiency in vehicles has been growing every year, and auxiliary machines like power steering and coolant pumps have been switching to electrical operation to support those needs. This is why the amount of electrical power being used in typical gasoline vehicles is increasing with each passing year, and manufacturers are looking for high-output alternators that can supply this level of electricity. They need to increase the output density, however, because they cannot increase the size of the actuator to correspond with the added generation capacity. They also need to achieve higher efficiency. A claw pole alternator generates electricity in the coil on the stator side with the rotor side acting as an electromagnet. The excitation coil on the rotor side is a single phase, and the claw pole is arranged so that it wraps around this coil. The claws that extend from the inside of the coil and the ones that extend from the outside of the coil have poles with different polar characteristics, and they have the same polar structure as a magnet that is arranged with magnetization that alternates between North and South. Because the alternator needs to be designed with a 3D geometry to account for the claw poles and the analysis needs to consider eddy currents generated in the surface of the claw poles, which are made from a metal plate, an electromagnetic field analysis using the finite element method would be the most useful, as it can simulate detailed geometries and account for eddy currents.

This Application Note presents the use of an electromagnetic field analysis to evaluate the output capacity of a claw pole alternator operating at 1500 r/min while accounting for eddy currents in the rotor core.



Eddy Current Density Distribution/ Magnetic Flux Density Distribution

Fig. 1 shows the eddy current density distribution and fig. 2 shows the magnetic flux density distribution.

Eddy current is produced in the surface of the claw pole from the rotor core. These eddy currents produce eddy current losses and reduce the alternator's efficiency. The eddy currents also affect the magnetic flux density distribution, so they must be taken into account when studying a magnetic circuit at high output.

Output

Fig. 3 shows the current versus time characteristic taking into account the effect of a shunt resistance.

The transient phenomena that occur until a steady state are caused by influence from the stator coil's inductance and the rotor core's eddy currents, so ripples in a steady state are caused by the commutator circuit.

The alternator output is approximately 41 Ampere, which can be found from the average value of the current waveform at a steady state.

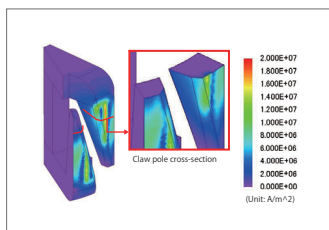


Fig. 1 Eddy current density distribution at 0.06 sec

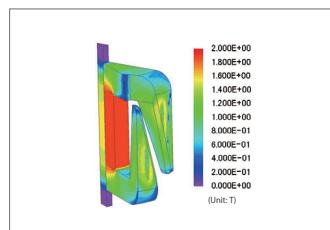


Fig. 2 Magnetic flux density distribution at 0.06 sec

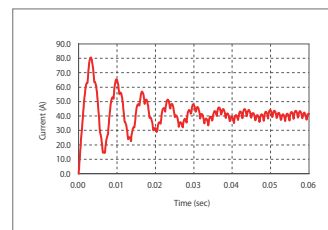


Fig. 3 Current versus time

Case 26 Braking Torque Analysis of an Electromagnetic Brake

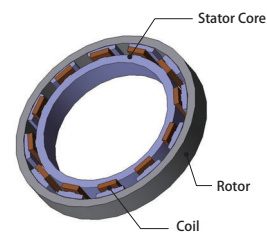
module: TR

Overview

An electromagnetic brake is an auxiliary brake device for large-scale vehicles like trucks and buses. It is fit onto the propeller shaft and applies a braking force. There are both hydraulic and electromagnetic types. With an electromagnetic brake, a magnetic field is produced in the stator coil, making eddy currents occur because of time variations in the magnetic flux density linking to the rotor. This, in turn, produces a braking torque. The range in which eddy currents occur in the rotor and the braking torque can vary a great deal according to the current flowing to the stator coil and the rotor's rotation speed.

In order to estimate the electromagnetic brake's performance accurately at the design stage, it is best to carry out an electromagnetic field analysis simulation using the finite element method (FEM) because it can approximate the material's nonlinear magnetic properties and can approximate the skin effect caused by current distribution, as well.

This Application Note shows how to obtain the braking torque of an electromagnetic brake during drive.



Eddy Current Density Distribution

Fig. 1 shows the eddy current density distribution of the rotor at different rotation speeds. Eddy currents flow on the inner surface of the rotor to interrupt the magnetic flux produced by the stator coil. When the rotation speed increases, the magnetic flux flowing in the rotor changes substantially, thereby increasing the eddy currents generated on the rotor.

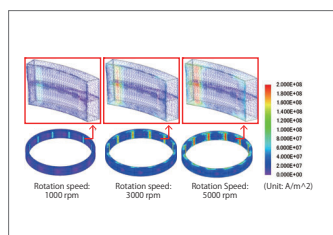


Fig. 1 Eddy current density distribution on the rotor at different rotation speeds

Dependency of Braking Torque on Rotation Speed

Fig. 2 shows the level of dependence of the braking torque on rotation speed. When the rotation speed increases, eddy currents are concentrated on the surface due to the skin effect, making the electric resistance grow larger and shrinking the amount that the eddy currents increase. As a result, increases in the braking torque also become smaller because it is caused by eddy currents.

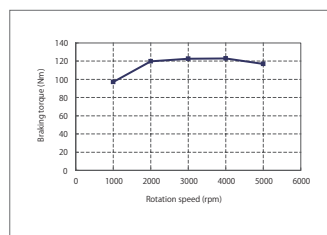


Fig. 2 Level of dependence of the braking torque on rotation speed

Case 27 Head Field Analysis of a Recording Write Head That Accounts for Eddy Currents

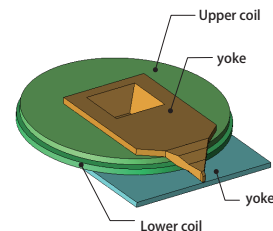
module: TR

Overview

Magnetic heads are devices that are used to record data on storage media, and are often found in hard disks. A magnetic head has both a recording head that writes data by magnetizing a round magnetic disk and a playing head that reads the data from the magnetic disk's magnetization pattern. For the recording head, the vital thing is an evaluation of the recording head field's responsiveness toward input electrical signals. This evaluation comes from a detailed evaluation of the magnetic flux density distribution around the head. To study these characteristics, the analysis needs to include the effect of eddy currents generated on the yoke.

In order to account for eddy current distribution that is produced in the fine part at the tip of the recording write head, a magnetic field analysis using the finite element method (FEM) is most effective.

This Application Note shows how to obtain the responsiveness of recording head field that is generated in the magnetic head.



Eddy Current Density Distribution / Magnetic Flux Density Distribution

Fig. 1 shows the eddy current density distribution around the head, and fig. 2 shows the magnetic flux density distribution. As shown in the eddy current density distribution, eddy currents are generated on the surface of the yoke. This eddy current interrupts the flow of the magnetic flux, resulting in reduced responsiveness of the head field to the magnetomotive force.

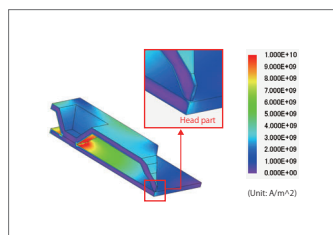


Fig. 1 Eddy current density distribution

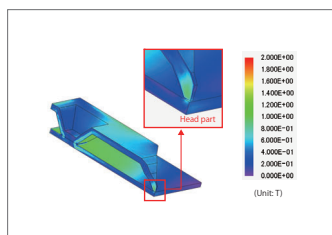


Fig. 2 Magnetic flux density distribution

Response Characteristics of the Recording Head Field

Fig 3 shows a graph of the response characteristics of the head field. The head field starts up more slowly than the magnetomotive force waveform. This is caused not by the coil inductance but also by the eddy currents on the yoke. When analyzing the response of the head field, the analysis must include the effects of eddy currents.

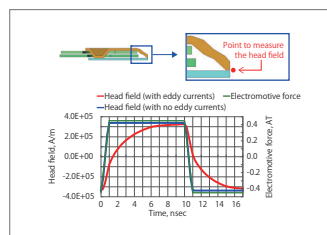


Fig. 3 Response characteristics of the head field

Reference:
 K. Fujiwara, F. Ikeda, A. Kameari, Y. Kanai, K. Nakamura, N. Takahashi, K. Tani, and T. Yamada, "Thin Film Write Head Field Analysis Using a Benchmark Problem," IEEE Trans. Magn., vol.36, no.4, pp.1784-1787, July 2000.

Case 28

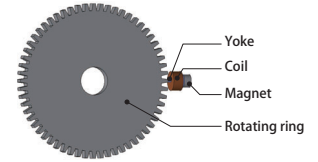
Magnetic Field Analysis of a Speed Sensor

module: TR

Overview

Antilock brake systems (ABS) have become a standard feature in vehicles, so speed sensors are attached to each wheel in order to measure their respective speeds. There are several methods of detecting rotation speed, but magnetic sensors are weather resistant and have a small number of parts because there only needs to be a gear on the rotation side, so they are widely used. The challenges from a design standpoint are the angle and relative distance between the gear's teeth and sensor, and how to ensure sensitivity and responsiveness when considering the magnetic influence of the surrounding air. In order to proceed with an advance study like this that considers a precise geometry and material properties, an electromagnetic field analysis using the finite element method (FEM) is effective.

This Application Note presents the use of magnetic field analysis to evaluate the variation of the voltage signal of a magnetic speed sensor for a range of air gap distances.



Magnetic Flux Density Distribution

Fig. 1 shows the magnetic flux density distribution at a rotation angle of 5.0 deg when the gap width is 0.5 mm.

The figures show how the magnetic flux from the magnet flows through the yoke and reaches the rotating ring. When the rotating ring rotates, the permeance in the magnetic circuit changes due to the moving teeth. This changes the amount of magnetic flux that passes through the yoke, thus generating the electromotive force in the coil.

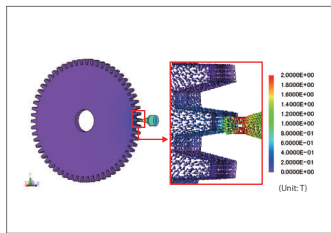


Fig. 1. Magnetic flux density distribution

Voltage Signal at Different Gap Widths

Fig. 2 shows the voltage signal waveform at each gap width, and fig. 3 shows the peak value of the voltage signal as a function of the gap width.

When the gap width is large, the voltage is small because the permeance is smaller compared with a small gap width, and then the magnetic flux amount that flows through the yoke and the coil becomes smaller.

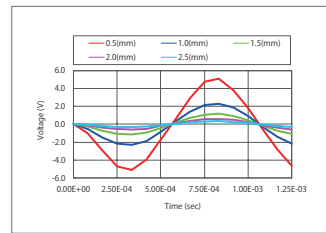


Fig. 2. Voltage Signal Waveform

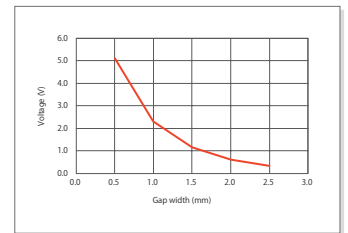


Fig. 3. Voltage Signal at Different Gap Widths

Case 29

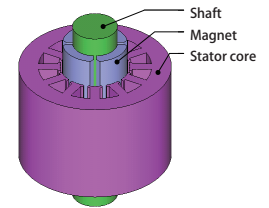
Iron Loss Analysis of an SPM Motor with Overhanging Magnet

module: LS, TR

Overview

There are times when permanent magnet motors are designed with a magnet made with overhang, in other words made longer than the stator's stack length, in order to strengthen the magnetic field that it creates. A space is necessary in the rotor if the rotor and stator have the same stack length, so a magnet is placed in this space with the objective of increasing the magnetic flux without making the magnet thicker. However, the magnetic field produced by the overhanging part of the magnet enters the stator at an angle, so magnetic flux is produced in the lamination direction, which creates a possibility of increasing eddy current loss by a wide margin. When the overhang is too big, the magnet's magnetic field goes to waste because it does not reach the stator. For this reason it is necessary to set up the overhang amount properly while looking at the trade-off between an increase in torque and an increase in losses. A magnetic field analysis using the finite element method (FEM), which can obtain the relationship between a three dimensional magnetic field and eddy currents, is an effective method for an advance study.

This Application Note presents the use of a no-load iron loss analysis of an SPM motor with and without an overhanging magnet.



Magnetic Flux Density Distribution, Eddy Current Density Distribution

Fig. 1 shows the flux density distribution of the stator core with and without overhanging magnet, fig. 2 shows the flux density distribution in the lamination direction, and fig. 3 shows the eddy current density distribution. The flux density is higher around the surface of the stator core because the overhanging magnet increased the flux in the in-plane direction and the lamination direction. The eddy currents generated around the surface of the tooth tips also penetrates into the interior of the stator core because of the increase in magnetic flux in the lamination direction.

Iron Loss Comparison with and without Overhanging Magnet

Fig. 4 show the values of the eddy current loss and hysteresis loss from the magnetic flux in the lamination direction and in-plane direction, which was obtained from a magnetic field analysis and an iron loss calculation. Fig. 5 shows the amount of increase in the losses from overhang.

Losses generated by magnetic flux in the lamination direction and in-plane direction both increased when overhang was applied.

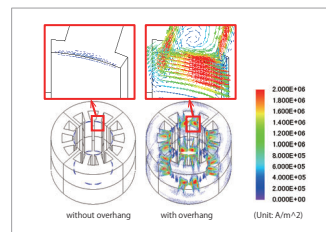


Fig. 3 Eddy current density distribution at 0.015 s

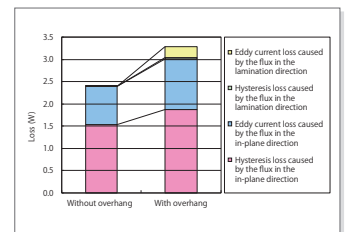


Fig. 4 Iron loss comparison

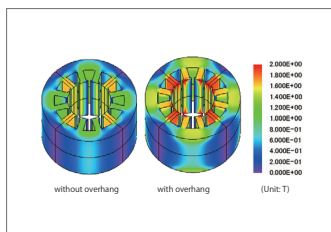


Fig. 1 Magnetic flux density distribution at 0.015 s

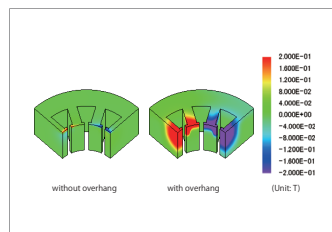


Fig. 2 Magnetic flux density distribution of the Z-component at 0.015 s

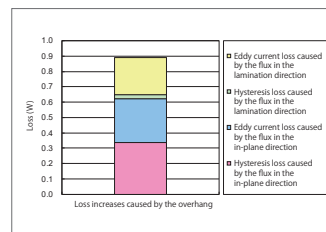


Fig. 5 Loss increases caused by the overhang

Case 30

Magnetization Field Evaluation of an SPM motor

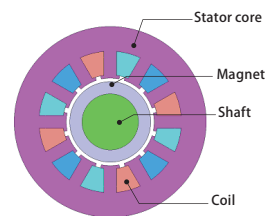
module: ST

Overview

A surface magnet type motor (SPM) has direct contact with a stator which generates torque through the interaction of magnetic fields generated by magnets and excitation coils. The magnetization state of a magnet is the main factor which determines the characteristics of a motor. It is important that motor designers adjust the magnetization pattern when designing a motor to restrain the higher components of an induced voltage to confirm the variation in characteristics. A general method of confirming the magnetization direction of a magnet is measuring the induced voltage waveform or the surface magnetic flux density of the magnet.

The characteristic such as magnetization device, magnetization of electric current, or magnetizing ration needs to be taken into account when evaluating the magnetic patterns. To evaluate the characteristics in advance, understanding the entire flow of magnetization is necessary, where a magnetic field analysis simulation using the finite element method which can obtain details on electromagnetic behavior from results is very useful.

In this example, carry out SPM motor's magnetization to obtain the magnetization field and magnet's surface magnetic flux density.



Magnetization Field

The magnetization field distribution during a magnetization field evaluation is shown in fig. 1. This figure shows the magnetization field distribution that is obtained by flowing current through the stator coil. The magnetization field between poles is smaller than at the center of the pole. The effective magnetization field distribution is obtained from this magnetization field and the orientation of the magnet.

Magnetization Ratio

Fig. 2 shows the magnetization distribution of the magnet after the magnetization influence from being used in the motor. It can be seen that near the magnetic poles on the outside of the magnet is fully magnetized, but between the poles on the inside of the magnet the magnet is not fully magnetized.

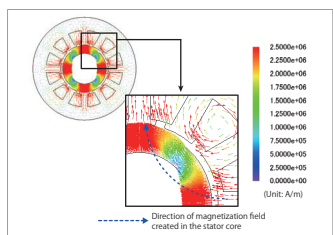


Fig. 1. Magnetization Field Distribution

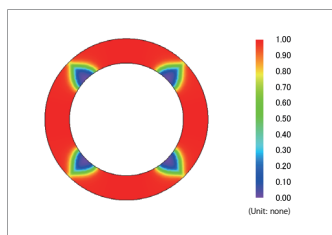


Fig. 2. Magnetization Distribution Ratio

Surface Magnetic Flux Density of the Magnet

Fig. 3 shows the surface magnetic flux density waveform of the magnet when the uniformly magnetized magnet is used and when the magnetization process is taken into account. The orientation direction of a magnet is in parallel direction. The surface magnetic flux density differs substantially between when the uniformly magnetized magnet is used and when magnetization process is taken into account near 45 deg where orientation components of the magnetization field decrease.

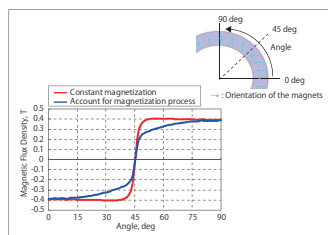


Fig. 3. Surface Magnetic Flux Density Waveform of the Magnet (at 0.25 mm above the magnet surface)

Case 31

Iron Loss Analysis of an SPM Motor Including the Effect of Press-fitting Stress

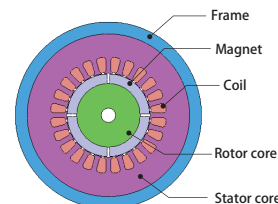
module: DS, DP, LS

Overview

The laminated structure of a core in a SPM motor can be sustained using press-fitting or shrink fitting. The press-fitting stress needs to be accounted for in the iron loss evaluation because the stress caused by press-fitting is known to increase the iron losses when a magnetic steel sheet is used for the core of the motor.

An iron loss is generated by the magnetization field in displacement with a steel sheet. The size of the iron loss is dependent on the iron loss properties of a steel sheet. The iron loss characteristics of a steel sheet deteriorates by stress from press fit coupling. The stress generated by the press fit coupling is distributed in areas in which the section in the back yoke becomes large. In order to evaluate the iron loss with good accuracy, it is necessary to obtain the stress distribution for the magnetic flux, time variation, and steel sheet with accuracy.

This note presents the use of the press fit condition to model a core and frame and obtains iron loss density for when the generated stress is used and not used.



Compressive Stress Distribution

The compressive force distribution is indicated in fig. 1, and the tensor display is indicated in fig. 2. The compression stress is large in the yoke when compared to the frame and teeth. The compression stress is concentrated in the yoke facing the slots because the stress decreases towards the tip of the teeth while the stress in the slots does not decrease. The compression stress is concentrated around the slots, and the tensile strength is concentrated around the frame as indicated in fig. 2.

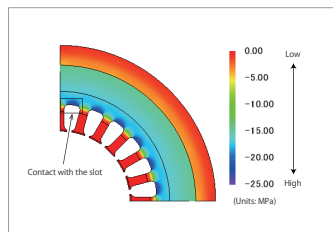


Fig. 1 Compressive stress distribution

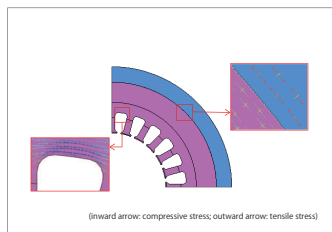


Fig. 2. Tensor display

Iron Loss Density Distribution

The iron loss density distribution is indicated in fig. 3. The iron loss density distribution varies depending on whether or not the stress is applied. The iron losses are increased by 15 % due to the stress. An analysis that accounts for the compressive stress caused by the press-fitting needs to be performed to evaluate the iron losses more accurately because the iron losses increase when the compressive stress is applied.

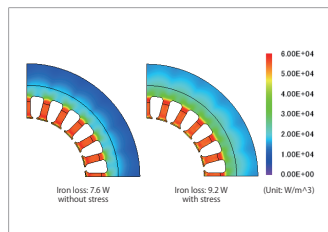


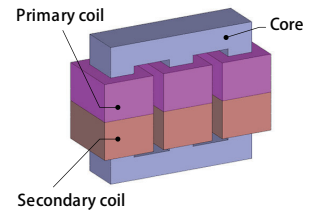
Fig. 3. Iron loss density distribution

Overview

A transformer is an electrical device that uses electromagnetic induction to convert the voltage level of alternating current power. In an ideal transformer the secondary voltage is constant regardless of the load, but in reality it tends to vary with the size of the load and the power factor. The size of a transformer's voltage variations is a vital output characteristic when considering constant voltage reception. It is also important to maintain a balanced state because an imbalance in the voltage and current in each phase can bring about a rise in the transformer's temperature or a fault in the device using the transformer.

A transformer's output characteristics depend on the leakage flux from the iron core. Leakage flux passes through the air instead of the iron core, so it is hard to predict accurately during the design phase. It is possible to handle magnetic flux passing through the air in a magnetic field analysis, meaning that it is also possible to evaluate a transformer's output characteristics, including the effects of leakage flux.

In this example, the use of a magnetic field analysis to evaluate changes in the secondary voltage caused by load variations in a low frequency transformer.



Secondary Voltage for the Load

Fig. 1 shows changes in the secondary voltage for the load. The ideal secondary voltage of the transformer used for this analysis is 14.1 V. When the load resistance decreases, the secondary current increases. Accordingly, the secondary voltage falls because the voltage drop increases due to the resistance of the secondary coil and the leakage reactance.

Induced Voltage in the Secondary Coil

Secondary coil's induced voltage amplitude and its phase are indicated in Table 1. Fig. 2 shows the vector plot for the induced voltage in the secondary coil, when the load resistance is large and small. The amplitude is shown by the vector length, and the phase is shown by the slope of the vector. When the load resistance is large the amplitude is almost the same and a phase difference of 120 deg is maintained, so the transformer is in a balanced state. On the other hand, when the load resistance is small there is a gap in amplitude between each phase, so the transformer is in an unbalanced state because the phase difference does not reach 120 deg.

Magnetic Flux Density - RMS Distribution

Fig. 3 shows the magnetic flux density - RMS distribution of the transformer when the load resistance large and small. When the load resistance is large the magnetic flux density is distributed almost symmetrically, but when it is small the current in each phase is unbalanced, which makes the magnetic flux density asymmetric.

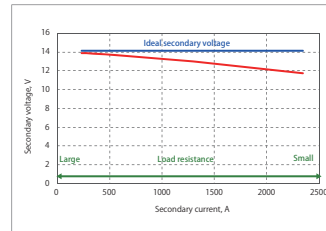


Fig. 1. Secondary Voltage for the Load

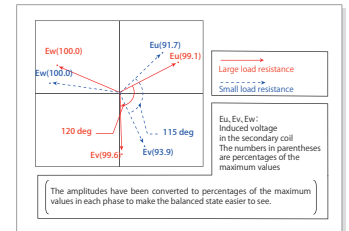


Fig. 2. Induced Voltage in the Secondary Coil

Load resistance ohm	Uphase		Vphase		Wphase	
	Amplitude V	Phase deg	Amplitude V	Phase deg	Amplitude V	Phase deg
0.005	21.61	132	22.12	247	23.56	10
0.01	23.12	140	23.59	257	24.29	19
0.02	23.79	145	24.09	263	24.42	25
0.03	23.99	146	24.21	266	24.42	26
0.04	24.09	147	24.26	267	24.41	27
0.05	24.14	148	24.28	267	24.40	28
0.06	24.17	148	24.29	268	24.39	28

Table 1. Induced Voltage in the Secondary Coil

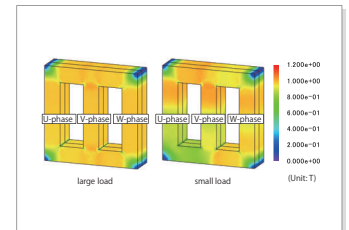
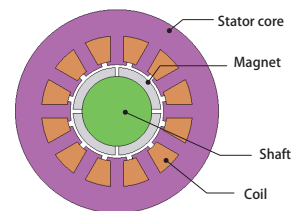


Fig. 3. Magnetic Flux Density - RMS Distribution

Case
34

Demagnetization Analysis of an SPM Motor

module: DP



Overview

Rare earth magnets have characteristics of large energy product, but decrease when used in an area exceeding a knee point, causing irreversible demagnetization. For motors, the possibility of thermal demagnetization through thermal stress may occur when the magnet temperature rises due to iron loss or copper loss during rotation. Large amounts of electric currents are run through an excitation coil where demagnetization may occur when a reverse magnetic field is applied to a magnet. Demagnetization of magnets in a motor is one of the causes of decrease in motor performance, where whether or not performance has decreased, demagnetization needs to be predicted. The magnetic field analysis simulation can handle magnetic fields or temperature generated in an internal magnet, which can evaluate demagnetization on the edges of a magnet accurately. This note presents the use of a magnetic field analysis to evaluate the demagnetizing ratio distribution of an SPM motor by changing the current flow.

Magnetic Flux Density Distribution

Fig. 1 shows the magnetic flux density for a current of 20 A and a rotation angle of 20 degrees. Demagnetization occurs at the end of the magnet because the orientation of the magnet and the direction of the flux generated by the rotating magnetic field are opposed.

Operating Point

The measuring points selected to confirm operating points are displayed in Fig. 2, and operating points for each measuring point at a current of 20 A are displayed in Fig. 3. Measuring point 1 in Fig. 3 is not set on a BH curve based on the operation point where irreversible demagnetization occurs. The size of the reverse magnetic field imposed upon each measuring point is also illustrated on the horizontal axis.

Permeance Coefficient Distribution

Fig. 4 shows the permeance coefficient distribution of the magnet when the motor is stationary with no load. The knee point's permeance is shown in two colors, red and purple. The knee point's permeance used for the analysis is 0.699. Fig. 4 shows that demagnetization hardly occurs when the motor is stationary with no load.

Demagnetizing Ratio Distribution

Fig. 5 uses the no-load static state as a benchmark to show the demagnetizing ratio distribution when rotating the rotor one period of electric angle with no load after demagnetization. As the current increases, both the demagnetizing area and demagnetizing ratio increase.

Induced Voltage Waveform

Fig. 6 shows the induced voltage waveform of the U-phase coil when rotating the rotor one period of electric angle with no load before and after demagnetization. When the amount of current is set to 20 A, it becomes apparent that demagnetization causes the induced voltage waveform to change.

* The demagnetizing ratio is the amount of demagnetization from the standard magnetization that is specified.

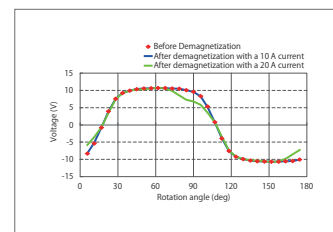
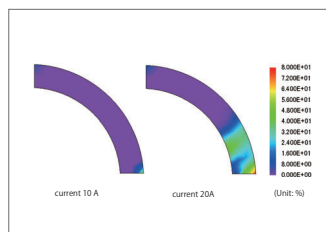
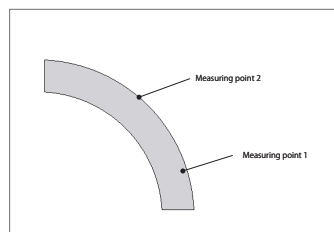
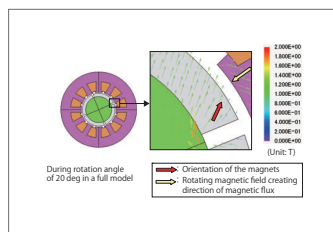
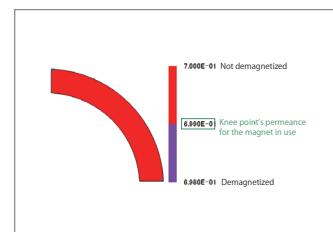
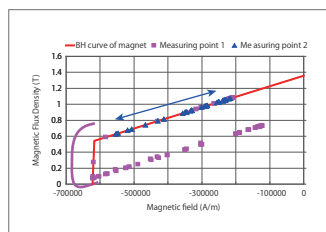


Fig. 1 Magnetic flux density distribution

Fig. 2. Measuring position of operating point

Fig. 5 Demagnetizing Ratio Distribution

Fig. 6 Induced Voltage Waveform

Case 37

Vector Control Analysis of an IPM Motor Using Control Simulator and the JMAG-RT

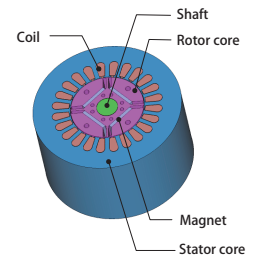
module: DP, RT

Overview

Traditionally, the design of a motor's controls and the design of the motor itself were often performed independently because coordinated designs were difficult to carry out. Motor control designs have been getting more advanced, however, so there has been an increasing demand for simulations that use detailed motor models that exhibit behavior that conforms to that of an actual machine.

With JMAG, it is possible to create a detailed model that conforms to a real machine and accounts for spatial harmonics and magnetic saturation characteristics that are included in a motor. Importing this motor model, a "JMAG-RT model," to a control/circuit simulator makes it possible to carry out a linked simulation that accounts for a motor's magnetic saturation and spatial harmonics as well as a motor drive's control characteristics.

The purpose of this Application Note is to demonstrate how to import a JMAG-RT model to a control/circuit simulator after using the JMAG-RT to obtain the inductance spatial harmonics of the torque and coil. The model is then used to run an analysis that controls the speed of an IPM motor to its target value.



Id and Iq Current Waveforms/ Torque Waveform

Fig. 1 shows the Id and Iq current waveforms from the vector control analysis, and fig. 2 shows the torque waveform. The JMAG-RT motor model accounts for the motor's geometry, so it is possible to display the current and torque waveforms, including the slot harmonic components. However, the ideal motor model does not include slot harmonic components. The evaluation for the q-axis current is also smaller than with the JMAG-RT motor model.

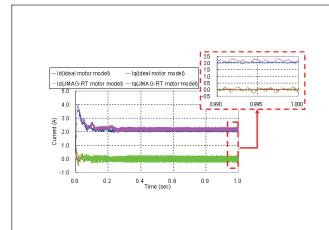


Fig. 1 Id and Iq current waveforms

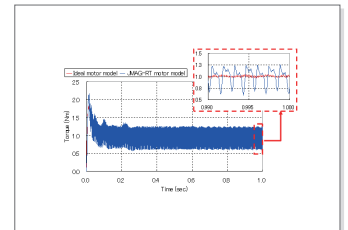


Fig. 2 Torque waveform

Case 38

Starting Performance Analysis of a Single Phase Induction Motor

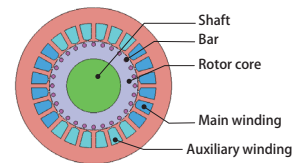
module: DP

Overview

Single phase induction motors are widely used as small output motors for the drives in household electrical appliances and office machinery, like fans and washing machines, because they can use single phase AC, the typical power source for home electronics. Unlike three phase AC, however, single phase AC cannot create a rotating magnetic field by itself, meaning that it cannot start a motor. For this reason, it needs to use an alternate method to generate a rotating magnetic field to start the motor.

It is important to verify whether or not torque is generated in the intended direction and continues to rotate stably ahead of time in the design phase. In order to carry out this verification, the conditions where the rotor follows the equation of motion according to the electromagnetic force mechanism and starts up need to be analyzed correctly.

The purpose of this Application Note is to introduce an example of a single phase induction motor that uses a capacitor to set up an auxiliary winding and show its rotation speed versus time, torque versus time, and the magnetic flux density distribution and current density distribution in the bar just after the motor starts.



Magnetic Flux Density Distribution, Eddy Current Density Distribution

Fig. 1 shows the magnetic flux density distribution right after the motor startup, and fig. 2 shows the eddy current density distribution of the secondary conductor bars.

The magnetic flux generated by the winding causes eddy currents in the secondary conductor bars, generating a rotating magnetic field.

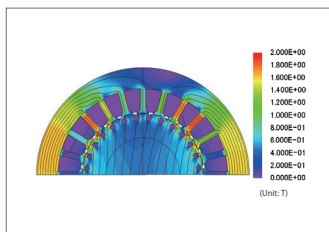


Fig. 1 Magnetic flux density distribution

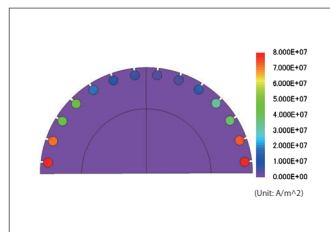


Fig. 2 Eddy current density distribution

Starting Performance

Fig. 3 shows the rotation speed versus time graph, and fig. 4 shows the torque versus time graph.

The time from motor startup until it reaches the synchronous speed is determined by the capacitance of the capacitor. The slip is very small when the motor reaches synchronous speed, so the average torque becomes zero.

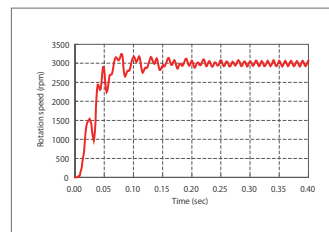


Fig. 3 Rotation speed versus time

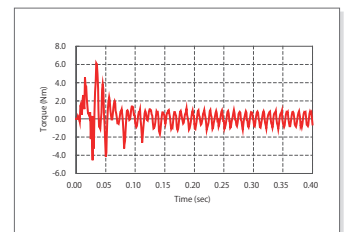


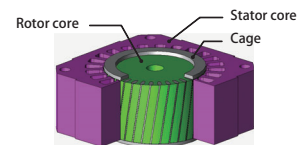
Fig. 4 Torque versus time

Case 39 Torque Analysis of a Three Phase Induction Motor Accounting for the Skew

module: DP, TR

Overview

An induction motor can utilize skew easily because the cage is constructed by metallic casting such as die casting. When skew is applied, it arranges the variations in the magnetic flux that links to the cage in a sinusoidal wave. This makes it possible to eliminate the harmonic components from the induction current that cause negative torque and contain things like the torque variations caused by influence from the slots. Applying skew generally affects the flow of magnetic flux in the axial direction, making it complex. This is why an analysis that can correctly verify the three dimensional magnetic flux flow is necessary to obtain an advance evaluation of the skew's effects. This Application Note presents a comparison of the torque waveforms of three phase squirrel cage induction motors with and without torque, and introduces the effects of using skew to reduce torque variations. Changes in the higher components caused by skew are also displayed by separating the frequencies of the secondary current, which causes the torque variations.



Torque Variations

The torque waveform with and without a cage that has skew is indicated in fig. 1, fig. 2, and fig. 3, and the size of the torque variations is indicated in Table 1. The results in fig. 1 are obtained with a 3D analysis. The results in fig. 2 are obtained with a 2D analysis. The results in fig. 3 combine the 2D analysis results with the skew angle. An induction motor produces torque from the rotating magnetic field of the stator coil and the induction current of the rotor. The torque variations can be reduced by using a cage that has skew. Fig. 3 shows that the superimposition of the 2D analysis and the skew angle makes it easy to display the reductions in torque ripple from skew and the approximate generated torque.

Current Density Distribution

Fig. 4 shows the secondary current density versus frequency, and fig. 5 shows the current density distribution of the cage. The harmonic components of the current produced by the harmonic magnetic flux in the stator are reduced by using a cage with skew as indicated by the secondary current density versus frequency. This is why the torque variations have been reduced as described above.

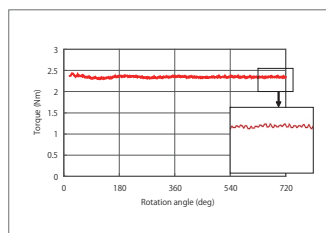


Fig. 3 Superimposed torque waveform accounting for the skew angle

With/without skew	Torque variations (Nm)
With skew	0.18
Without skew	0.41
Accounting for skew with superimposition	0.04

Table 1. Torque variations

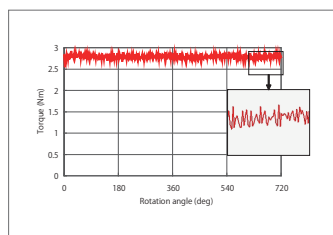


Fig. 1. Torque waveform with skew

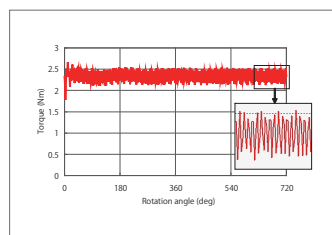


Fig. 2 Torque waveform without skew

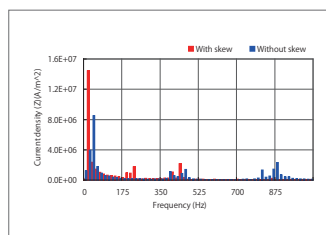


Fig. 4 Secondary current density versus frequency

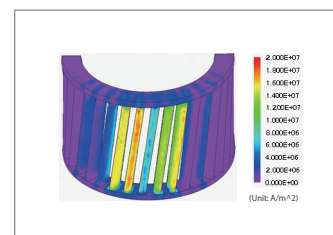


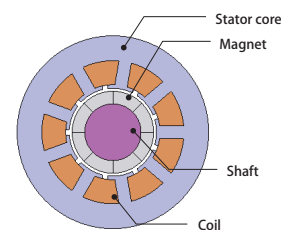
Fig. 5 Current density distribution (Z component) of the cage at a rotation angle of 630 deg

Case 40 Cogging Torque Analysis of an SPM Motor

module: DP

Overview

The rotor's rotation in a permanent magnet motor can generate positive and negative torque, even when there is no current flow. This torque is called "cogging torque." While output torque a center of focus in motors used in precision equipment, cogging torque reduction must be taken into account as well. Skew and fractional slots are means of reducing this cogging torque. Skew is a widely used technique that attempts to cancel out cogging torque by applying an appropriate amount of twist to the stator or rotor. This generates electromagnetic force in the thrust direction, however, which presents challenges such as a decrease in performance and an increase in manufacturing cost. Fractional slots do not have the drawbacks found in skew, but the winding pattern is different from that found with integer slots. This means that the torque generation becomes difficult to evaluate because the teeth geometry and the magnet's magnetization distribution are hard to design accurately. In order to carry out these evaluations, an electromagnetic field analysis using the finite element method (FEM) needs to be carried out because it can perform detailed evaluations of the electromagnetic force distribution produced in the magnetic circuit. This Application Note presents the use of magnetic field analysis to obtain the cogging torque of an 8-pole, 9-slot SPM motor, which has relatively small period.



Cogging Torque Waveform

Fig. 1 shows the cogging torque waveform. As shown in the waveform, the amplitude is about 5e-5 Nm. The period of the cogging torque is also determined from the number of slots and poles, which in this analysis are 8 (poles) and 9 (slots). By dividing 360 deg by 72, the least common multiple of 8 and 9, one arrives at the period of cogging torque, which in this case is 5 deg.

Magnetic Flux Lines

Fig. 2 shows the magnetic flux lines at rotation angles of 0 deg, 1 deg, and 4 deg. While the magnetic flux lines are symmetrical along a symmetry line at 0 deg, they are not symmetrical at 1 deg and 4 deg. This generates cogging torque.

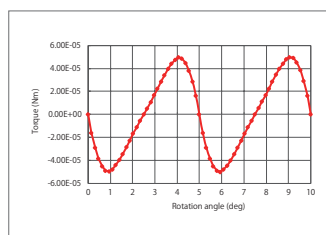


Fig. 1 Cogging torque waveform

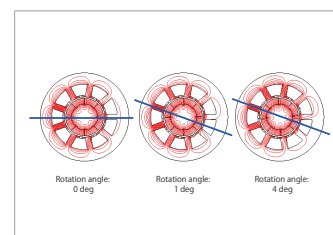


Fig. 2 Magnetic flux lines (symmetry line)

Case 41

Positioning Control Analysis of a Permanent Magnet Linear Motor Using the Control Simulator and the JMAG-RT

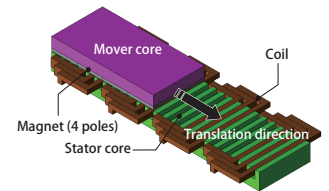
module: DP, RT

Overview

Linear motors are widely used for carrier devices and machine tools because of their high-speed performance, high acceleration and deceleration, and accurate positioning. A type of linear motor called a permanent magnet linear motor has harmonic components such as cogging and ripples in its thrust because of its structure and how it operates. These components have a large influence on velocity control and positioning accuracy. The thing that separates linear motors from rotating motors is that linear motors have edges, limiting how far they can move. This is why linear motors have different characteristics when the mover is positioned in the center of the stator and when it is at the edge. In order to create a more advanced control design, it is possible to use a control simulation to obtain a linear motor model that exhibits more detailed behavior than is based on an actual machine.

With JMAG, it is possible to create a linear motor model that is detailed and conforms to a real machine, and that accounts for spatial harmonics and magnetic saturation characteristics included in a permanent magnet linear motor. Importing this linear motor model, a "JMAG-RT model," to a circuit/control simulator makes it possible to run a linked simulation that accounts for the linear motor's magnetic saturation characteristics and spatial harmonics as well as the driver's control characteristics.

This Application Note presents how to use the JMAG-RT to obtain the space harmonics and current dependency of the thrust and coil inductance and import them to a circuit/control simulator as a JMAG-RT model. From there, it shows how to perform an analysis that controls the position of the permanent magnet linear motor to the desired value.



Response characteristic/Thrust Variation

Fig. 1 shows the mover position versus time, and fig. 2 shows the thrust force versus time. Fig. 1 shows the time taken for the mover to reach the command value. The JMAG-RT model accounts for the motor geometry, so the thrust varies according to the positional relationship between the mover and the slots.

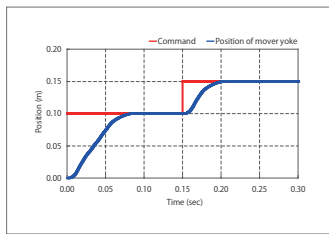


Fig. 1 Position of mover yoke versus time

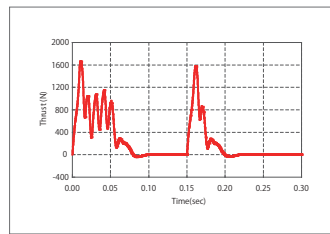


Fig. 2 Thrust force versus time

Case 42

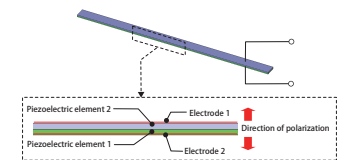
Displacement Analysis of a Piezoelectric Actuator

module: DS

Overview

Piezoelectric elements are used as actuators and sensors, as well as oscillator circuits and filter circuits in the analog electronic circuits. When the electric potential is applied, the piezoelectric element is deformed. This is called the converse piezoelectric effect. In JMAG, the analysis of the piezoelectric actuator using the converse piezoelectric effect can be performed by specifying the permittivity matrix and the electric potential for the material.

This note presents the use of structural analysis to evaluate the displacement of a bimorph piezoelectric actuator, caused by the inverse piezoelectric effect.



Displacement

Fig. 1 shows the state of displacement and the displacement vector. The part outlined in red is the piezoelectric actuator at the initial position. In this analysis, one edge of the piezoelectric actuator is secured, so the other edge can freely be displaced when the electric potential is applied.

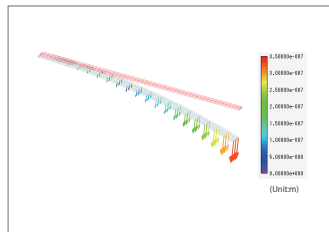


Fig. 1. Displacement

Electric Potential-Displacement Characteristics

Fig. 2 shows the electric potential-displacement characteristics. The displacement increases linearly with electric potential. The electric potential to obtain the target displacement can be estimated from the coefficient which is obtained from the slope of the line.

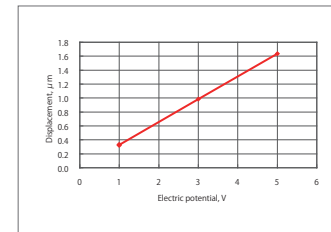


Fig. 2. Electric Potential-Displacement Characteristics

Case
43

Torque Analysis of a Coreless Motor

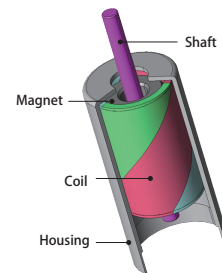
module: TR

Overview

As their name implies, coreless motors have a rotor that lacks a core and is made of only a coil. For this reason, there is no core to produce iron loss in the rotor, and its moment of inertia is small. They can be controlled easily because their characteristics are linear and they have small torque ripples, but they are not versatile enough to produce a large amount of torque. This is why they are often used in small precision equipment that requires high rotation speeds and good responsiveness. The rotor coil is hard to construct because it is made of only a coil. It is important to design the coil's twist angle to be able to produce torque. The model needs to be made precisely because coreless motors are used in compact equipment and because the detailed geometry of the parts can affect the characteristics.

In order to carry out these evaluations, the coil's twist needs to be accounted for accurately in three dimensions. An electromagnetic field analysis using the finite element method (FEM) is necessary to accomplish this because it can evaluate the distribution of the electromagnetic force produced in the magnetic circuit in detail.

This Application Note presents an evaluation of the torque waveform of a coreless motor when current is running.



Torque Waveform/Current Waveform

The torque waveform and current waveform are shown in fig. 1 and fig. 2. A smooth rotation can be achieved because the rotor doesn't have an iron core, as indicated in fig. 1. The average torque is also indicated at 0.022 mN · m. A ripple has occurred in the torque waveform calculated by this analysis, but this is caused by the varying contact of the brush and commutator as indicated in fig. 2.

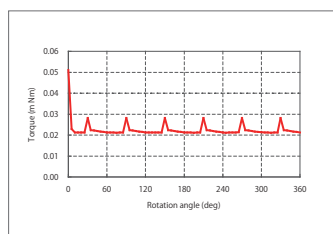


Fig. 1. Torque waveform

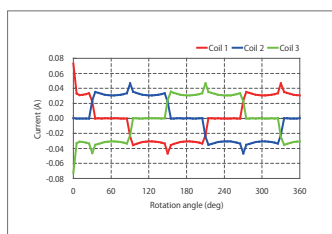


Fig. 2. Current waveform

Current Density Distribution/Lorentz Force Density Distribution

The current density distribution of the coil at a rotation angle of 360 deg is shown in fig. 3, and the Lorentz force density distribution is shown in fig. 4. A current flows in coil 1 and coil 3 without flowing in coil 2 when the rotation angle is 360 deg, as indicated in fig. 3. The currents also flow in opposite directions of one another. The box inside of fig. 4 shows that coil 3 generates force in the rotation direction, but coil 1 generates force both with and against the rotation direction. This occurs because the direction of the current differs while the directions of the magnetic fields for each phase coil are the same.

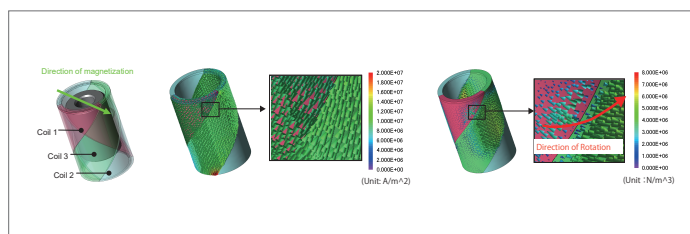


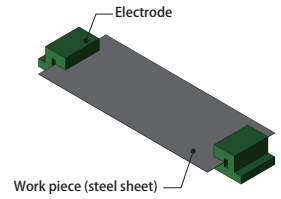
Fig. 3. Current density distribution (rotation angle: 360 deg)

Fig. 4. Lorentz force density distribution (rotation angle: 360 deg)

Overview

In treatments like hot formed pressing, a steel sheet needs to be heated uniformly as a part of pre-processing. Resistance heating is a method of uniform heating that uses a steel sheet's electric resistance. In resistance heating, current is run through electrodes placed on both sides of a steel sheet. The joule heat produced from the ensuing electric resistance is then used to heat the steel sheet. However, the uniformity of the range of heat generation changes depending on the arrangement of the electrodes, so whether or not the uniformity satisfies the heating conditions needs to be investigated ahead of time. Unevenness in the current distribution flowing from the electrodes through the steel sheet is determined from the geometry and the material's electric conductivity. Electric conductivity changes according to the temperature, though, so both the electromagnetic phenomena and the heat transfer phenomena need to be analyzed at the same time.

This Application Note presents how to obtain the calculate current density distribution, Joule loss distribution and temperature distribution of steel sheet.



Current Density Distribution and Joule Loss Density Distribution

Fig. 1 shows the current density distribution and current flux line of the work piece immediately after heating. Fig. 2 shows the Joule loss density distribution of the work piece immediately after heating. The electrodes are shorter than the work piece in the width direction, so the current density is not uniform at the edges of the work piece, as can be seen in fig. 1. It is high near the tips of the electrodes and gets lower at the four corners of the work piece. Joule loss comes from electric resistance in the work piece, so its density has the same distribution as the current density. Their distribution is almost uniform near the center of the work piece. This joule loss becomes the heat source.

Temperature Distribution

The work pieces temperature distribution is shown in fig. 3, and its work pieces temperature of 10 sec are shown in fig. 4 and fig. 5. Electric resistance generates heat in the work piece and heats it to about 400 deg C in 10 sec. The areas aside from the work piece's edges are heated uniformly.

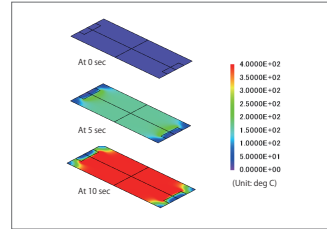


Fig. 3 Temperature distribution with a supply current of 16 kA

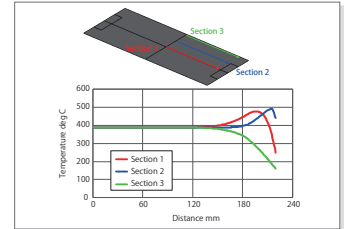


Fig. 4 Temperature of the work piece of 10 sec

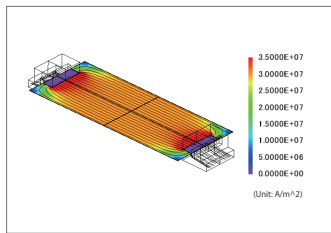


Fig. 1 Current density distribution and current flux line of the immediately after heating

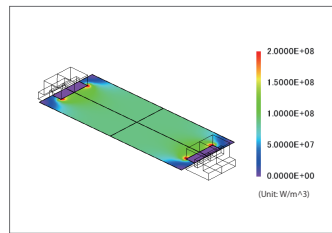


Fig. 2 Joule loss density distribution of the immediately after heating

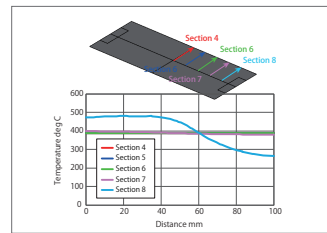


Fig. 5 Temperature of the work piece

Case
45

High-Frequency Induction Heating Analysis of an IH Cooking Heater

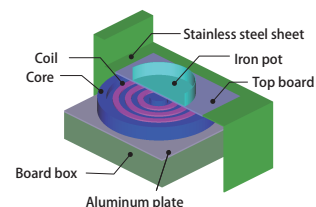
module: FQ, HT

Overview

An IH cooking heater cooks food by heating a pot that acts as a conductive body. It heats this pot with an induction heating method that uses electromagnetic induction. Eddy currents flow in the iron pot when a high frequency current is applied to the coil. These eddy currents produce joule loss, which acts as a heat source to raise the temperature of the iron pot. When designing the heating coil, the main points to look out for are: What kind of magnetic circuit design will raise heating efficiency, and whether it is generating uniform heat in the iron pot. Another factor is controlling leakage flux to the circuit component in the board box that surrounds the apparatus.

A magnetic field analysis simulation that uses the finite element method (FEM) is best for studying a three dimensional combination of the geometry, number, and alignment of the magnetic material that adjusts the magnetic circuit, and for quickly obtaining the electric circuit constant of the high frequency circuit that performs the heating.

This Application Note shows how to obtain the magnetic flux density surrounding an IH cooking heater that uses high frequency induction heating and the temperature distribution of its iron pot.



Magnetic Flux Density Distribution

Fig. 1 shows the magnetic flux density distribution of the IH cooking heater. The aluminum plate on the board box shields it from magnetic flux, reducing the amount of leakage flux that flows to it.

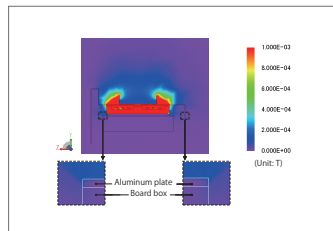


Fig. 1 Magnetic flux density distribution of the IH cooking heater

Eddy Current Loss Density Distribution and Temperature Distribution of the Iron Pot

Fig. 2 shows the eddy current loss density distribution of the iron pot. The magnetic field generated by the coil produces eddy currents on the surface of the iron pot. The iron pot is then heated because its electric resistance produces joule heat.

Fig. 3 shows the temperature distribution of the iron pot at 10 s, 30 s, and 60 s. The iron pot is heated by eddy currents. The temperature of the bottom of the iron pot rises over time, reaching 100 deg C at 60 s. In this analysis, the temperature rise of the bottom of the iron pot is not uniform. To heat the bottom of the iron pot uniformly during heating, the coil arrangement and the core geometry need to be improved.

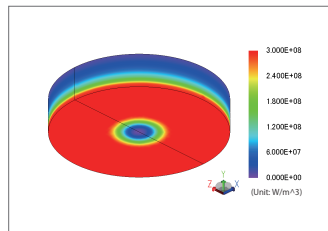


Fig. 2 Eddy current loss density distribution of the iron pot

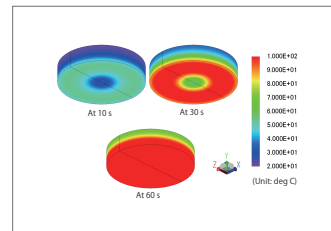
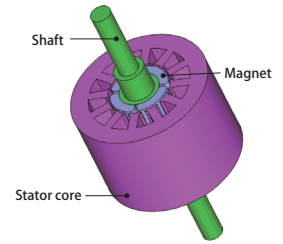


Fig. 3 Temperature distribution of the iron pot

Overview

The magnet in a surface permanent magnet (SPM) motor is arranged on the rotor's surface, facing the stator. The motor produces torque from the interaction between the magnetic field produced by the magnet and the magnetic field produced from the excitation coil. Cogging torque, which is generated during no-load rotation, depends largely on the magnet's magnetizing state. Adjusting the magnet's magnetization pattern makes it possible to reduce the cogging torque, which lowers efficiency and causes vibration and noise. In order to control the magnetization pattern in the magnet of an actual machine precisely, a great number of magnetization devices is required. This makes a real machine hard to control, but with a magnetic field analysis simulation that uses the finite element method (FEM), it is possible to estimate how the cogging torque in the physical phenomenon will change by simply setting the magnetization pattern. Once the optimum magnetization pattern has been found, studying the magnetization method can lead to a reduction in development cost. This Application Note presents the use of a magnetic field analysis to obtain the surface flux density for radial pattern, parallel anisotropic pattern, and polar anisotropy pattern magnets. It also displays the changes in induced voltage and cogging torque caused by differences in the magnetization patterns.



Surface Magnetic Flux Density

The surface magnetic flux density for magnets with a radial pattern, a parallel anisotropic pattern, and a polar anisotropy pattern are indicated in fig 1. Furthermore, the decay is compared between the radial pattern and parallel anisotropic pattern at 10 deg, 20 deg, and 30 deg. The polar anisotropy is compared by the distance from the center pole. When the magnetization directions of the magnets are compared, the radial pattern is closest to a trapezoid, but the waveform of the parallel anisotropy pattern and polar anisotropy pattern are the closest to sinusoidal waves. The waveform of the induced voltage and the flux linkage can be calculated as being closer to a sinusoidal waveform for the parallel anisotropy and polar anisotropy patterns than the radial pattern. Furthermore, the radial pattern and parallel anisotropy are closer to a sinusoidal waveform the larger the angle of the decay. The waveform of the polar anisotropic pattern is closer to a sinusoidal waveform the larger the distance is from the center pole. However, the distance from the center pole is optimum at 15.35 mm because the waveform when $r=16.35$ has a higher magnetic flux density around 45 deg.

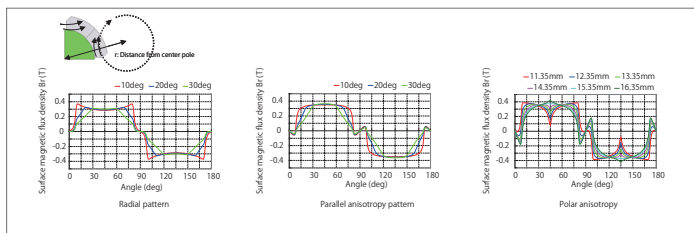


Fig. 1 Surface magnetic flux density

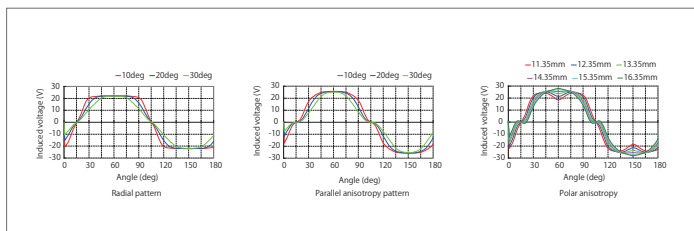


Fig. 2 Induced voltage

Induced Voltage, Flux Linkage, and Cogging Torque

The induced voltage for the radial, parallel anisotropy, and polar anisotropy are indicated in 2, the flux linkage in 3, and the cogging torque in 4. When the induced voltage waveform is compared for each pattern, the waveform for the radial pattern is closer to a trapezoid, while the waveforms for the parallel anisotropy and polar anisotropy patterns are closer to a sinusoidal waveform, just as predicted by the surface magnetic flux waveform. The waveforms for the flux linkage are also the same. Furthermore, as can be seen from the surface magnetic flux density, when the angle of decay and the distance from the center pole are compared, the induced voltage waveform and flux linkage waveform are closer to a sinusoidal waveform the larger the angle of decay, or the larger the distance from the center pole. Therefore, after comparing the magnetization patterns, the parallel anisotropy or polar anisotropy patterns have a smoother rotation that produces less cogging torque than the radial pattern. Furthermore, when comparing the angle of decay and the distance from the center pole, the cogging torque is the lowest with a radial pattern at 20 deg, a parallel anisotropy pattern at 30 deg, or for the polar anisotropy pattern, a distance when $r= 16.35$ mm.

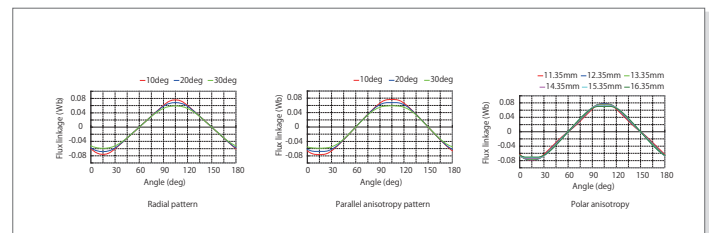


Fig. 3 Flux linkage

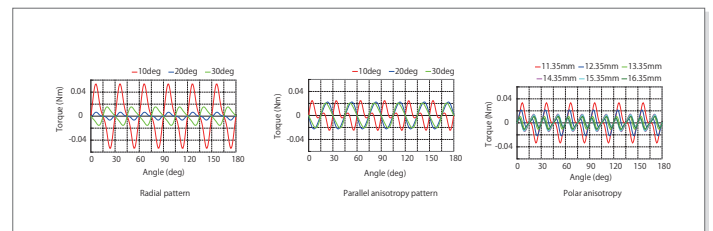


Fig. 4 Cogging torque

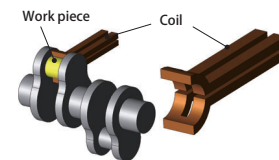
Case 47 High-Frequency Induction Heating Analysis of a Crankshaft

module: FQ, HT

Overview

Machine parts like shafts and gears are made to be resistant to wear and tear. This is accomplished by giving them a certain degree of flexibility by maintaining their interior toughness while increasing the hardness of their surfaces. By using high-frequency induction heating, which is a type of surface hardening method, the part is heated rapidly on only its surface by a high frequency power source. This process also has many other benefits, such as providing a clean working environment because it uses electrical equipment, being very efficient, and providing uniform results for each product. This is why it is being aggressively implemented in the field.

With induction hardening like the kind used on the work piece in this analysis, the main requirement is to heat a given surface uniformly and increase rigidity. Eddy currents generated by the high-frequency varying magnetic field occur in the surface of the work piece. Examining these phenomena in detail requires handling the phenomena that occur in the work piece itself in a numerical analysis based on the finite element method (FEM). This Application Note shows an example of an evaluation performed by creating a numerical analysis model, analyzing the elevated temperature process, and seeing whether or not the desired temperature distribution is achieved. Use this analysis when obtaining the optimum coil geometry, current conditions (power supply frequency, current value), and rotation speed.



Temperature Distribution, Temperature Variations, Joule Loss Density Distribution

This section shows the temperature distribution in fig. 1, temperature variations in fig. 2, and the joule loss density distribution in figures 3 and 4 as analysis results of the crankshaft's high-frequency induction heating.

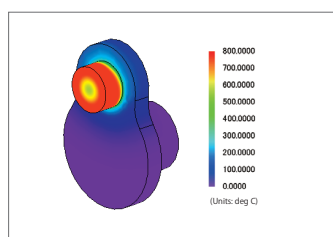


Fig. 1 Temperature distribution at Step 288

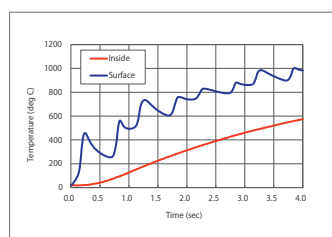


Fig. 2 Temperature variations in the surface and interior of the work piece

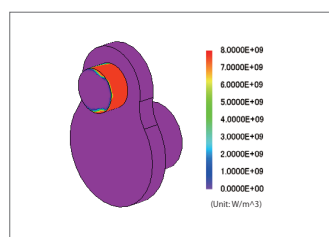


Fig. 3 Joule loss density distribution at Step 1

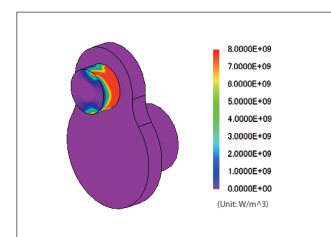


Fig. 4 Joule loss density distribution at Step 288

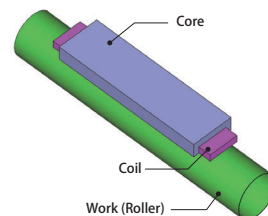
Case 48 High-Frequency Induction Heating Analysis of a Printer Roller

module: FQ, HT

Overview

A printer works by running a piece of paper with toner on it between a heated fuser roller and a pressure roller. The heated fuser roller then applies heat to fix the toner to the paper. The fuser roller needs to have uniform temperature distribution in order to handle various types of paper. It also requires the ability to heat up rapidly in order to shorten the standby time, allowing the person using the printer to print documents quickly. A magnetic field analysis using the finite element method (FEM) is useful in examining several aspects of the process, including: Differences in heating from the heating coil's geometry or placement, what kind of eddy currents are generated in the roller's thin surface and whether they provide uniform temperature, and how the magnetic flux flow spreads to the roller, air, and core.

This Application Note confirms the non-uniformity in temperature distribution produced by an assumed coil geometry, as well as the temperature elevation in each part caused by rotation.



Eddy Current Loss Density Distribution

The eddy current loss density distribution of the roller is shown in fig. 1. The magnetic field generated by the coil produces eddy currents on the surface of the roller. The eddy currents are distributed on the surface of the roller due to the skin effect, which is stronger at high frequencies.

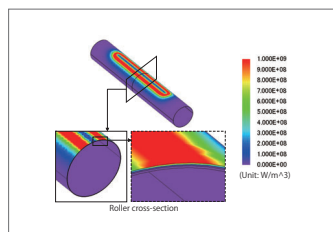


Fig. 1 Eddy current loss density distribution directly after starting heating

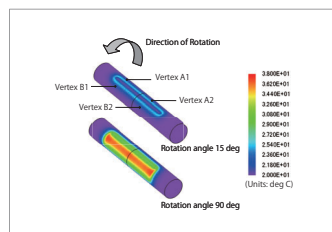


Fig. 2 Temperature distribution of the roller

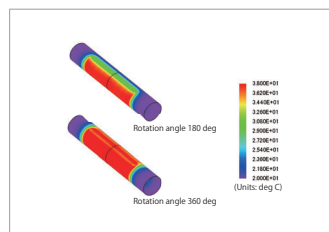


Fig. 3 Temperature distribution of the roller

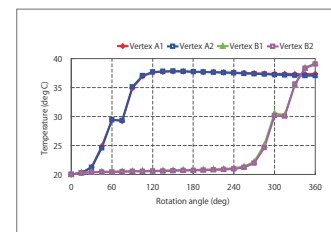


Fig. 4 Temperature variation at the surface of the roller

Temperature Distribution/Temperature Variation

The temperature distribution of the roller is indicated in figures 2 and 3, and the temperature variation of the roller surface is indicated in fig. 4. Fig. 4 indicates the temperature variation of the roller at the measuring points shown in fig. 2. The measuring points have been selected in order to be able to confirm the temperature variation in the circumferential direction and the rotation axis direction. The roller is normally heated to a temperature of approximately 200 deg C, but in this analysis it is only analyzed for one full revolution. From figures 2 and 3, it is apparent that the rotational motion causes the roller's surface to be heated in a strip. The temperature increase in the area being heated is fairly even on the axis direction of the roller, as indicated in fig. 4. On the other hand, the temperature is not distributed evenly in the circumferential direction due to timing differences in heating, and heat dissipation into the air. The coil's geometry does not allow it to generate heat in the center part, so the temperature elevation is not smooth.

Case 49

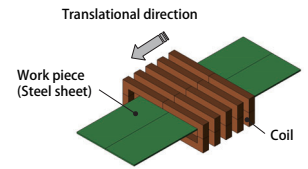
High-Frequency Induction Heating Analysis of a Steel Sheet

module: FQ, HT

Overview

The rolling process of steel sheets changes the strength and properties of the product, so heat treatment is used. High frequency induction heating is a type of heat treatment that uses a high frequency power source to produce rapid heating, allowing the equipment on the production line to be smaller. It also has a multitude of benefits, such as being highly efficient and providing a clean working environment. When the object being heated is a long steel sheet, this process heats it quickly while sending it through a heating coil. For this reason, there are several factors that need to be studied when assigning a heating amount to correspond to the speed at which the sheet passes through the coil. Examples of these are: the arrangement of the heating coil so that it can fulfill the necessary heating amount, and how to adjust the current's frequency and size. This Application Note presents a simulation of the heating conditions of a sufficiently long steel sheet that passes through a heating coil. The eddy currents produced from the high frequency's varying magnetic fields are uneven on the steel sheet's surface, so its material properties change due to increases in temperature. This is why it is necessary to approximate the amount of heat generated in a numerical analysis based on the finite element method (FEM) in order to handle the detailed phenomena.

This Application Note explains how to create a numerical analysis model when obtaining the optimum coil geometry, current conditions (power supply frequency, current value), and movement speed. It also shows how to evaluate whether the model fulfills the target heating speed by analyzing the elevated temperature process.



Eddy Current Loss Density Distribution

Fig. 1 shows the eddy current loss density distribution in the work piece's surface, as well as a cross section. Eddy currents are generated in the work piece by the magnetic field produced by the coil. Eddy currents generated by the skin effect are distributed through the surface of the work piece.

Temperature Distribution

Fig. 2 shows the temperature distribution in the work piece. The eddy currents generate heat in the work piece, and after having moved through the coil for 10 s it has been heated to a temperature of over 800 deg. Moving the work piece through the coil at 0.1 m/s heats it without almost no irregularities in temperature. Heat transmission heats the work piece's interior, as well.

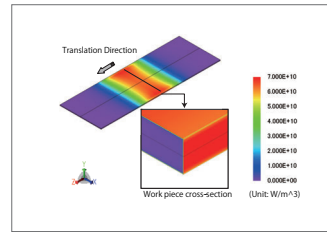


Fig. 1 Eddy current loss density distribution in the work piece at 0 s

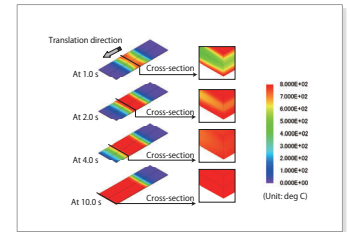


Fig. 2 Temperature distribution of the work piece

Case 50

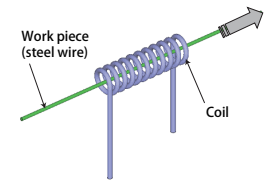
High-Frequency Induction Heating Analysis of a Steel Wire (Translational Induction Hardening)

module: FQ, HT

Overview

Steel wires are made to be resistant to wear and tear. This is accomplished by giving them a certain degree of flexibility by maintaining their inner toughness while increasing the hardness of their surfaces. By using high-frequency induction heating, which is a type of surface hardening method, the steel wire is heated rapidly on only its surface by a high frequency power source. This process also has many other benefits, such as providing a clean working environment because it uses electrical equipment, being very efficient, and providing uniform results for each product. This is why it is being aggressively implemented in the field. On the other hand, when the heating target is a long steel wire, it is heated rapidly while passing through the heating coil. For this reason, there are several factors that need to be studied when assigning a heating amount to correspond to the speed at which the wire passes through the coil. Examples of these are: the arrangement of the heating coils so that it can fulfill the necessary heating amount, and how to adjust the current's frequency and size. This Application Note presents a simulation of the heating conditions of a sufficiently long steel wire that passes through a heating coil. The eddy currents produced from the high frequency's varying magnetic fields are uneven on the steel wire's surface, so its material properties change due to increases in temperature. This is why it is necessary to approximate the amount of heat generated in a numerical analysis based on the finite element method (FEM) in order to handle the detailed phenomena.

This Application Note explains how to create a numerical analysis model when obtaining the optimum coil geometry, current conditions (power supply frequency, current value), and movement speed. It also shows how to evaluate whether the model fulfills the target heating speed by analyzing the elevated temperature process.



Eddy Current Loss Density Distribution

Fig. 1 shows the eddy current loss density distribution of the work piece and the coil. The magnetic field made by the coil changes with time, generating eddy currents in the work piece. In induction heating these eddy currents become heat sources and heat up the work piece. At high frequencies, the work piece is influenced by the skin effect, making it so that the eddy currents are distributed in the surface.

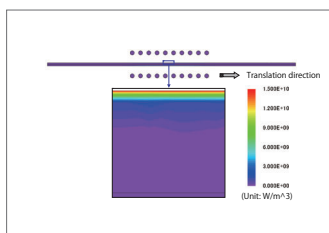


Fig. 1 Eddy current loss density distribution (cross-section)

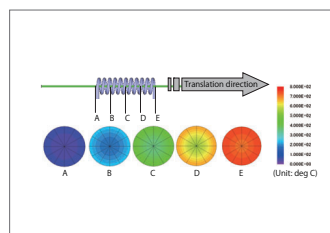


Fig. 2 Temperature distribution inside the work piece (cross-section)

Temperature Distribution of the Steel Wire

Fig. 2 shows the temperature distribution at each position of the work piece.

Temperature Variation of the Steel Wire

Fig. 3 shows the temperature variation at the surface and inside of the work piece. According to the graph, the maximum temperature is around 750 deg C both at the surface and inside the work piece. It is apparent that the surface is heated first.

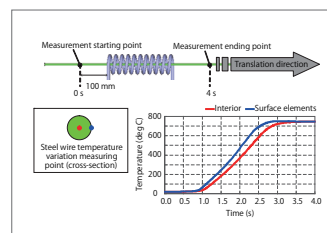


Fig. 3 Temperature variation of the work piece

Case 51

High-Frequency Induction Heating Analysis of a Gear

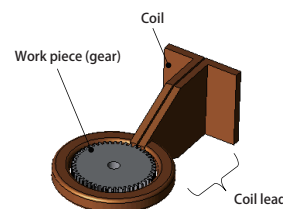
module: FQ, HT

Overview

Gears are created in such a way that the surfaces of their teeth are hard in order to resist the wear and tear that occurs when they come into contact with the teeth of other gears. However, this has to be accomplished while maintaining the gear's overall toughness. In the case of high-frequency induction heating, which is one of the surface hardening methods, just the surface of the teeth can be hardened by rapidly heating only the surface using a high-frequency power source. This process also has many other benefits, such as providing a clean working environment because it uses electrical equipment, being very efficient, and providing uniform results for each product. This is why it is being aggressively implemented in the field. On the other hand, there are several factors that need to be studied in order to heat the gear's surface uniformly, such as how to adjust the heating coil's geometry, arrangement, current frequency and size.

The eddy currents generated by high-frequency varying magnetic fields are uneven in the tooth surface, so the material properties change a great deal as the temperature rises. In order to handle the detailed phenomena, it is necessary to calculate the heat generation amount in a numerical analysis based on the finite element method (FEM).

This Application Note shows how to create a numerical analysis model when obtaining the optimum coil geometry and current conditions (power supply frequency and current value), analyze the elevated temperature process, and evaluate whether or not the model fulfills the target temperature distribution.



Eddy Current Loss Density Distribution of the Gear

Fig. 1 shows the eddy current loss density distribution of the surface of the gear and the cross-section of a tooth top. Each cross-section shown in the figure is at the midway position of the tooth width. The magnetic field generated by the coil produces eddy currents on the gear tooth surface. This eddy currents are distributed on the surface of the gear due to the skin effect.

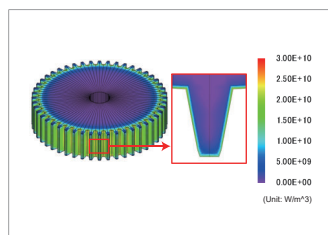


Fig. 1 Eddy current loss density distribution between 0.0 sec and 0.15 sec

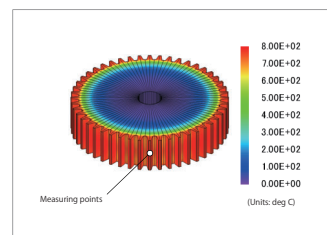


Fig. 2 Temperature distribution at 3.0 sec

Temperature Distribution and Variation of the Gear

Fig. 2 shows the temperature distribution of the gear, and fig. 3 shows the temperature variation versus time of the tooth tops. Fig. 3 shows the temperature variation of the tooth top at the measuring points shown in fig. 2. From the temperature distribution, it is apparent that the eddy currents generate heat in the tooth top.

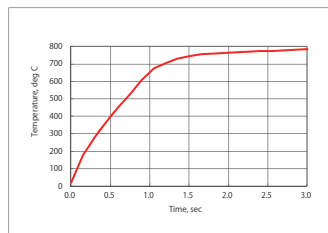


Fig. 3 Temperature versus time at tooth top

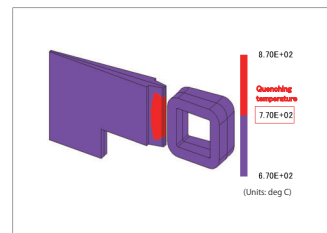


Fig. 4 Maximum achieving temperature distribution

Maximum Achieving Temperature Distribution

Fig. 4 shows the maximum temperature that each part reaches. This figure is a two color contour plot, where the parts exceeding 770 deg C are shown in red, and those below 770 deg C are shown in purple.

Case 52

Inductance Analysis of a Sheet Coil Transformer

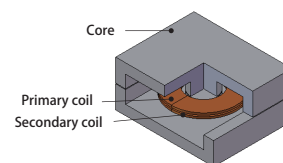
module: FQ

Overview

Power transformer requires large currents, so their geometry tends to be large. This means that they are particularly hard parts to miniaturize when electrical product designs get smaller. The sheet coil transformer introduced in this Application Note achieves thinner dimensions by winding its coil in a thin sheet.

Self-inductance and leakage inductance are critical items in a transformer's design requirements. The amount of inductance is dependent on the magnetic circuit, but the nonlinear characteristics of the magnetic properties make it so that the magnetic circuit changes when the operating point changes. The leakage inductance has all of the same properties, but it also has a flux path in non-magnetic regions, making it easily affected by the geometry and coil arrangement in addition to the core. This is why a magnetic field analysis using the finite element method (FEM) is necessary when evaluating these types of inductance.

This Application Note explains how to obtain the self-inductance and leakage inductance of a sheet coil transformer.



Magnet Flux Density Distribution

The magnetic flux density distribution used to calculate the self-inductance is indicated in fig. 1. The magnetic flux is concentrated at the center of the core, as indicated in the figure. The magnetic flux produced by the current flowing through the coil is split in two from the center core because the magnetic flux flows around the outer circumference of the core and then back to the center of the core.

The magnetic flux density is larger at the corners inside of the core than the outside of the core. This is because the magnetic flux flows through the shortest route of the core.

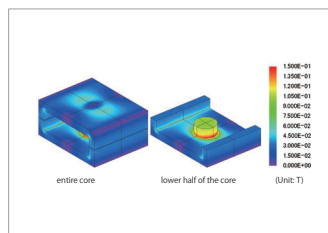


Fig. 1 Magnetic flux density distribution of the core during self-inductance calculation

Self inductance	30.13 μ H
Leakage inductance	0.832 μ H

Table 1 Inductance of the sheet coil transformer

Inductance

The inductance of the sheet coil transformer is indicated in table 1. The inductance can be obtained from the relationship between the voltage and current. The self-inductance is 30.0 μ H, and the leakage inductance is 0.755 μ H.

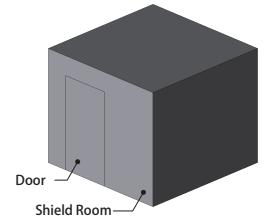
Case 53

Magnetic Shielding Analysis of a Shield Room

module: FQ

Overview

Shield rooms are meant to protect precision equipment from the influence of external magnetic fields, so they have to be an enclosed space that implements special processing in the walls that blocks magnetic flux. The effects of external magnetic fields inside the shield room depend on how they are generated, where the precision equipment is located, and the position of the shield room's opening and supply cable. A magnetic field analysis using the finite element method is necessary to perform an evaluation that deals with three dimensional and temporal variations to figure out how magnetic flux enters the shield room when several external magnetic fields have been applied. This Application Note explains how to handle the magnetic shielding phenomena used by the shield room when an external magnetic field is applied, and from there how to confirm the magnetic flux density distribution.



Magnetic Flux Density Distribution

The shield room and magnetic flux density distribution surrounding air region are shown in fig. 1. The external magnetic field is applied in the direction of the arrows in the figures. The magnetic flux from this field flows along the wall surface of the shield room, reducing the magnetic flux density inside of the room itself. The external field that is uniform in the Z-direction in the figures also tries to flow with the wall in the vicinity of the shield room, so the parts outlined in red are where the magnetic flux concentrates and gets more dense. The parts outlined in blue are where the magnetic flux density is less dense.

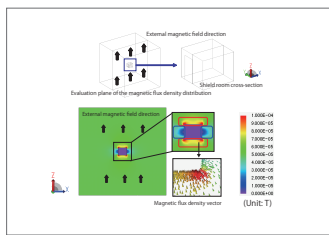


Fig. 1. Magnetic Flux Density Distribution

Magnetic Flux Density Waveform

The magnetic flux density waveforms for each evaluation axis are shown in figures 2 and 3. The shield room is between the positions of 12 m and 15 m, so the magnetic flux density is lower in that region compared to the outside because of the room's magnetic shielding qualities. For an external magnetic field of $50 \mu T$ the magnetic flux density inside of the shield room is $0.9 \mu T$, meaning that the magnetic shielding effect blocks out approximately 98%.

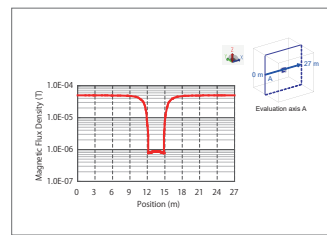


Fig. 2. Magnetic flux density waveform in evaluation axis A

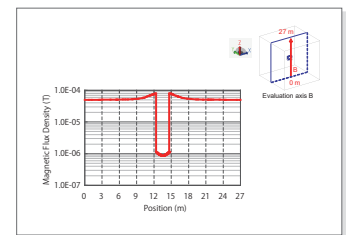


Fig. 3. Magnetic Flux Density Waveform at Evaluation Axis B

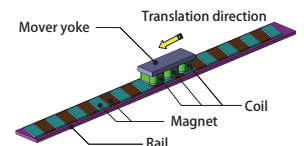
Case 54

Analysis of the Cogging Force of a Moving Coil Linear Motor

module: TR

Overview

Linear motors have been widely used in carrier devices and the drive units of machine tools due to their capability for high acceleration and deceleration, as well as their accurate positioning. In order to improve performance people are trying to obtain a large thrust force in order to enhance responsiveness, but one also needs to fulfill the demand for the trade-off of reducing thrust force variations and the attraction force. There are also times when skew is added to the magnets because of requirements to reduce thrust force variation. In order to obtain a large thrust force, the material's nonlinear magnetic properties and the magnet's demagnetization characteristics need to be accounted for, and they need to be analyzed after modeling a detailed geometry in order to evaluate thrust force variations. This is why the characteristics need to be studied with a magnetic field analysis simulation based on the finite element method (FEM). This Analysis Note explains how to obtain the magnetic flux density distribution and cogging in a moving coil linear motor with skew applied to its magnets.



Magnetic Flux Density Distribution

The magnetic flux density distribution at a translation distance of 36 mm is shown in fig. 1. Applying skew changes the magnetic circuit. It is anticipated that these changes in the magnetic circuit will affect the cogging torque.

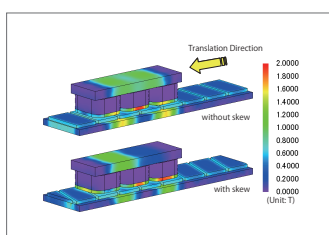


Fig. 1. Magnetic flux density distribution at a translation distance of 36 mm

Cogging Waveform

The cogging waveform is shown in fig. 2. When skew is applied, the cogging torque's peak value falls by approximately 50%.

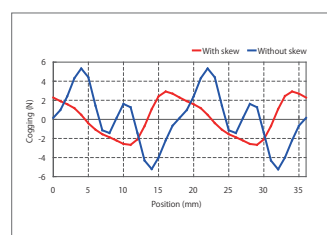


Fig. 2. Cogging Waveform

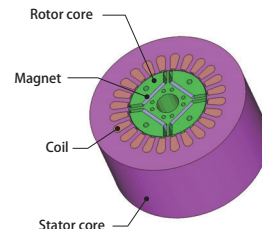
Case 55

Integrated Magnetization Analysis of an IPM Motor

module: DP, ST

Overview

Interior permanent magnet (IPM) motors often use strong rare earth magnets. They have poor workability, however, because the magnets are inserted into the rotor's small gaps during the assembly process. After the magnets have been inserted the rotor generates a strong magnetic field, which means that the workability when embedding it into the stator gets worse, as well. This is why in some cases they assemble the magnets while still in an unmagnetized state and magnetize them after they have been assembled. This construction method is called integrated magnetization. Using this means of construction can improve the assembly process a great deal, but there is also the possibility that the magnets will not be completely magnetized. Consequently, first one needs to confirm whether or not integrated magnetization is even possible, and then from there to estimate the electrical power that the equipment needs for magnetization. Using a magnetic field analysis simulation with the finite element method (FEM) provides the ability to change the making current amount and yoke geometry as magnetization conditions, as well as to account for magnetic saturation and evaluate whether or not the magnets are completely magnetized. This Application Note explains how to determine the changes that occur in a magnetizing field if the making current is changed during magnetization, as well as how to obtain the induced voltage and cogging torque in the motor using the aforementioned magnets.



Magnetization Field Distribution

The magnetization field distributions of the magnet during integrated magnetization at making currents of 1.0 kA, 1.5 kA, 2.0 kA, and 2.5 kA are shown in fig. 1. The strength of the magnetization field correlates to the size of the making current. On the other hand, the orientation of the magnetization field faces almost the same direction, regardless of the making current.

Magnetization Distribution inside the Magnet

Fig. 2 shows the magnetization distribution in two cases: An ideal magnetizing state with uniform magnetization through the entire magnet, and the magnetization field that occurs with making currents of 1.0 kA, 1.5 kA, 2.0 kA, and 2.5 kA. When the making current is 1.0 kA and 1.5 kA, the magnetization in the entire magnet is small. However, with a making current of 2.5 kA, there is almost no difference with the magnetization distribution in an ideal magnetizing state.

Induced Voltage Waveform, Cogging Torque Waveform

Fig. 3 shows the U-phase induced voltage waveform with uniform magnetization in the entire magnet as an ideal magnetization state, as well as when accounting for the magnetization field with making currents of 1.0 kA, 1.5 kA, 2.0 kA, and 2.5 kA. Fig. 4 shows the cogging torque waveform with uniform magnetization in the entire magnet as an ideal state, as well as when accounting for the magnetization field with making currents of 1.0 kA, 1.5 kA, 2.0 kA, and 2.5 kA. The magnetization distributions shown in fig. 4.1 affect the induced voltages and cogging torques. Figures 3 and 4 indicate that magnetization at 2.0 kA or higher provides mechanical characteristics equivalent to those when using a magnet with an ideal magnetizing state.

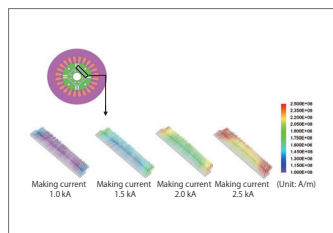


Fig. 1 Magnetization field distribution

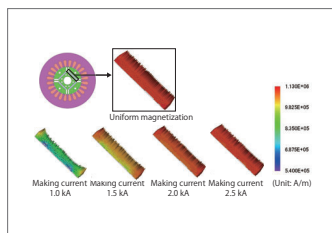


Fig. 2 Magnetization distribution in the magnet

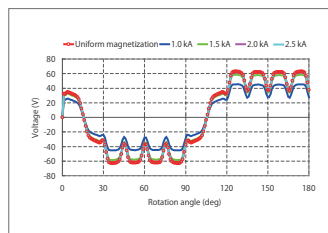


Fig. 3 U-phase induced voltage waveform

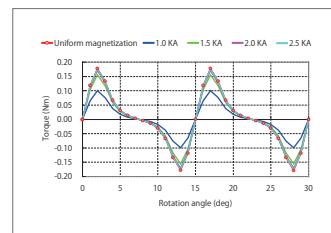


Fig. 4 Cogging torque waveform

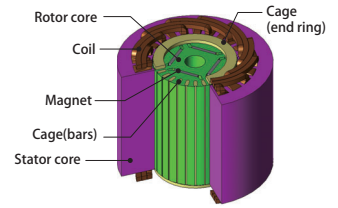
Torque Characteristics Analysis of a Self Starting Type Permanent Magnet Motor

module: DP

Overview

A self starting permanent magnet motor combines the characteristics of an induction motor and a permanent magnet motor, so it has higher efficiency than an induction motor even without a control device like an inverter. It behaves as an induction motor when it starts, generating torque when the rotor cage first slips against the rotating magnetic field created by the stator and then produces a secondary current. Consequently, this kind of motor has superior starting ability because there is no need to account for the rotor's start-up position or rotation speed. When the rotation speed increases and the motor synchronizes, the permanent magnet begins to generate the magnetomotive force and produce torque instead of the secondary current, so there is no secondary iron loss. This kind of motor has a weak point, however: The torque falls a great deal when the motor deviates from its synchronicity, and it gets out of step as a magnet motor so the torque variations are large. This is why self starting permanent magnet motors can achieve full-voltage starting with household current and are very efficient while in a synchronous state, but have drawbacks like relatively low starting torque and recovery once they have lost synchronization. These factors make it so that a magnetic field analysis simulation based on the finite element method is necessary to investigate whether the motor's characteristics meet the requirements ahead of time.

This Application Note shows how to obtain the current density distribution and slip versus torque curve.



Current Density Distribution

The current density distribution at a 0.8 slip is indicated in fig. 1.

If the slip is large, the motor operates as an induction motor. The induced current largely affects the torque characteristics because the torque is produced by the rotating magnetic field produced in the coils and the current induced in the rotor and cage.

Flux Lines

The flux lines at a 0 slip are indicated in fig. 2.

If the slip is 0, the motor operates as a synchronous motor. The torque is produced by the attractive force of the permanent magnet and the reluctance magnetic flux because the self starting permanent magnet motor operates as an IPM motor.

Slip vs. Torque Curve

The slip versus torque curve is indicated in fig. 3.

The torque of the self starting permanent magnet motor gets smaller as the slip gets larger, reaching a maximum torque at a 0.2 slip.

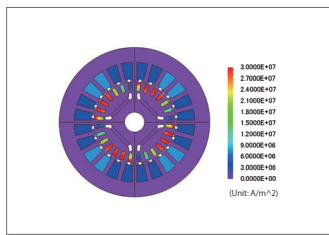


Fig. 1. Current density distribution for a 0.8 slip at 0.667 s

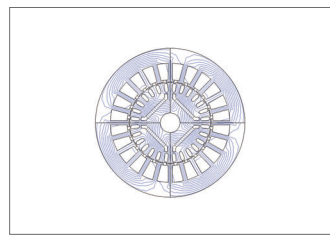


Fig. 2. Flux lines at 0 slip

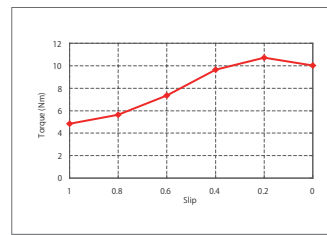


Fig. 3. Slip versus torque

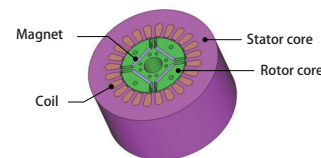
Case 58

Efficiency Analysis of an IPM Motor

module: DP, LS

Overview

An IPM motor's features are in its rotor geometry, where its magnets are embedded. When the stator's rotating magnetic field is applied in a direction that runs perpendicular to the rotor magnets (the q-axis) the motor operates like a normal SPM motor. When the current phase is displaced and the d-axis component is applied, however, the motor operates so that the magnetic fields in the rotor magnets are weakened. This is called field weakening. In an SPM motor the d-axis current operates enough to weaken the magnetic field, so the rotation speed increases but the torque decreases. However, the rotor geometry in an IPM motor is created so that there is a difference in inductance between the d-axis and q-axis, so it is possible to generate torque with the d-axis current, which weakens the magnets. This makes it possible to recover the part weakened by the flux. Consequently, an IPM motor achieves a greater range of operation by incorporating field weakening controls. For this reason an IPM motor's characteristics depend greatly on its rotor geometry, so studies using the magnetic circuit method are difficult. In order to perform an advance design study accurately, an electromagnetic field analysis using the finite element method is necessary. This Application Note presents the use of magnetic field analysis to obtain the efficiency of an IPM motor in each current phase with a rotation speed of 1800 rpm and the current amplitude of 4.0 A when the motor is driven by sinusoidal wave current.



Efficiency characteristics, loss by type, magnetic flux density distribution, the torque waveform

When the rotation speed is 1800 rpm and the current amplitude is 4.0 A, the efficiency characteristics per current phase are shown in fig. 1, the loss by type is shown in fig. 2, the magnetic flux density distribution is shown in fig. 3, the torque waveform is shown in fig. 4, and the average torque and torque ripple rate are shown in fig. 5. The results of the efficiency characteristics indicate that a maximum efficiency of 91% can be obtained at $\beta = 30$ deg. Adjusting the current phase can lower the magnetic flux density of the stator and reduce iron loss. Doing this, however, will reduce the average torque and increase torque ripple, which can lead to noise problems. This means that the current phase needs to be selected while accounting for the size of torque ripples in addition to the degree of efficiency.

Obtaining the efficiency by changing the rotation speed, current value, and current phase within the motor's range of possible operation makes it possible to create an efficiency map.

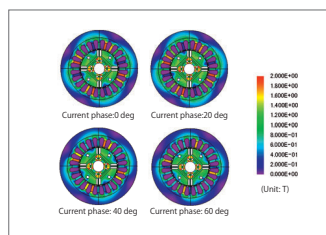


Fig. 3 Magnetic flux density distribution

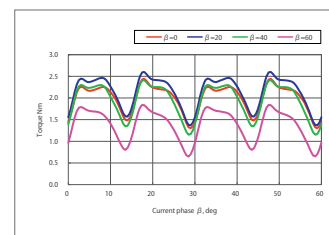


Fig. 4 Torque Waveform

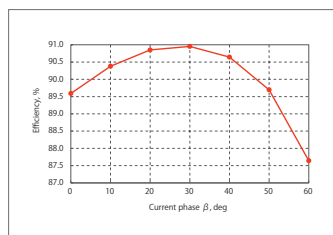


Fig. 1 Efficiency characteristics per current phase at a rotation speed of 1800 rpm and a current amplitude of 4.0 A

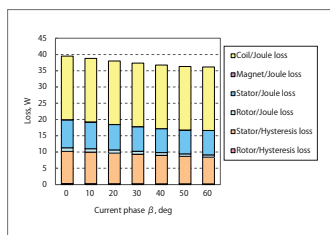


Fig. 2 Loss by type at each current phase

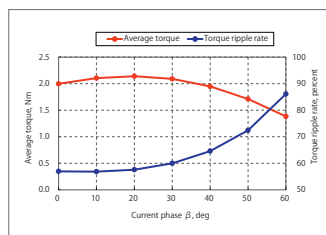
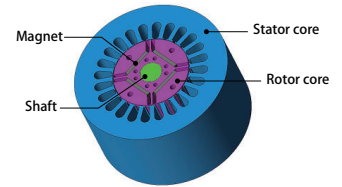


Fig. 5 Average torque and torque ripple rate per current phase



Overview

Vector controls using a PWM (Pulse Width Modulation) control are commonly included in the drive circuits of high efficiency motors. A PWM control makes it possible to adjust the phase or amplitude of a current according to load and rotation speed, so they can achieve high efficiency in a wide operation range. The control frequency of a PWM is called a carrier frequency. Carrier frequencies are often used up to almost 20 kHz. To form the current waveform supplied by the PWM control, the carrier harmonic current is superimposed on the basic wave current. This carrier harmonic current applies a high-frequency magnetic field to each part of the motor. As a result, core iron loss and magnet eddy current loss are generated. The total amount of these losses is not a dominant factor, but they can be a hindrance when trying to raise efficiency, so they need to be eliminated in the design process. In order to study these problems, both the motor's electromagnetic behavior and what kinds of controls the drive circuit performs have to be investigated.

In order to run an advance study of these phenomena in CAE, a high fidelity motor model and inverter model need to be coupled. There are three ways of accomplishing this: Directly linking with a circuit/control simulator, entering a current waveform obtained by using a JMAG-RT motor model and a circuit/control simulator, and entering actual current measurements.

In this analysis, the iron losses of the IPM motor that accounts for the carrier harmonic are obtained by directly linking to a circuit/control simulator.

Iron Losses

Comparisons of the iron losses, hysteresis losses, and joule losses when the IPM motor is driven by a PWM inverter and a sinusoidal current are shown in table 1.

The iron losses in both the rotor core and the stator core increase when the IPM motor is run using a PWM inverter. The joule losses increase the most severely, increasing 70% in the rotor core, and 40% in the stator core.

Joule Loss

The frequency components of the joule losses are indicated in figures 1 through 4. The joule loss density distribution is indicated in figures 5 and 6.

The fundamental frequency and harmonic component have almost the same amount of iron losses in both the rotor core and the stator core if a sinusoidal current or a PWM inverter is used with a fundamental frequency of 360 Hz for the rotor core and 60 Hz stator core. However, losses are only generated when the PWM inverter is used with a PWM fundamental frequency of 10 kHz and its harmonic component. (These values are indicated inside the green square in fig. 1.)

The increased joule losses when the motor is run using a PWM inverter are caused by the carrier harmonic. The effects of a carrier harmonic need to be accounted for to analyze the characteristics of an IPM motor in detail.

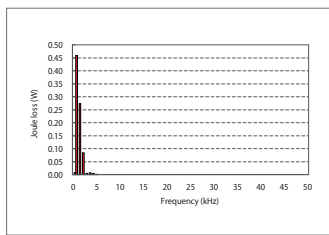


Fig. 1 Joule loss frequency component of the rotor core (sinusoidal current drive)

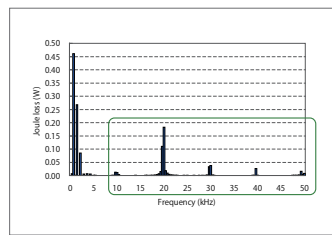


Fig. 2 Joule loss frequency component of the rotor core (PWM inverter drive)

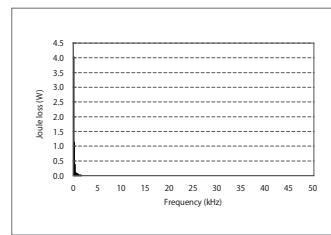


Fig. 3 Joule loss frequency component of the stator core (sinusoidal current drive)

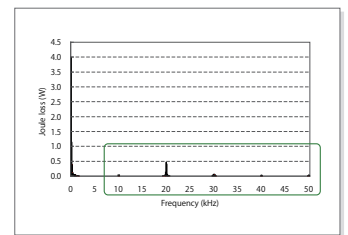


Fig. 4 Joule loss frequency component of the stator core (PWM inverter drive)

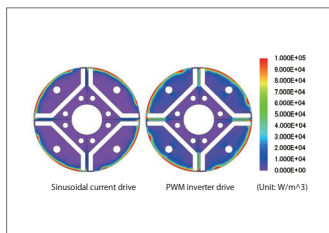


Fig. 5 Joule loss density distribution of rotor core

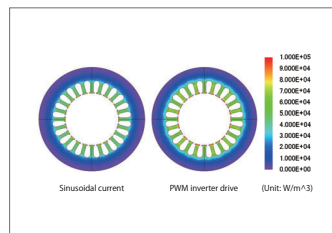


Fig. 6 Joule loss density distribution of the stator core

	Rotor core		Stator core	
	Sinusoidal current drive	PWM inverter drive	Sinusoidal current drive	PWM inverter drive
Iron Loss	1.14 W	1.89 W	14.44 W	16.80 W
Hysteresis Loss	0.18 W	0.20 W	8.28 W	8.35 W
Joule Loss	0.97 W	1.69 W	6.16 W	8.45 W

Table 1. Iron loss results

Case 60

Superimposed Direct Current Characteristic Analysis of a Reactor

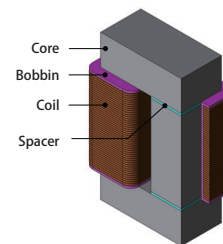
module: TR

Overview

A high-frequency reactor, used in equipment such as DC-DC converters, has a high-frequency current accompanying the switching direct current. The performance of a reactor is evaluated by a stable inductance in a wide direct current region. The gap that is designed to prevent magnetic saturation from the core largely affects the inductance, so it is a vital parameter of the reactor's design.

The magnetic resistance is determined by the gap when there is a large gap width, which is used as a parameter for the superimposed direct current of the inductance. This means that the resistance can be evaluated using the magnetic circuit method, but when the gap width is small, the current is large, and magnetic saturation has a large effect on the inductance, an advance study using a finite element analysis (FEA) is an effective tool.

This Application Note explains a case example that obtains the superimposed direct current characteristics of a high-frequency reactor when the gap width is changed.



Superimposed Direct Current Characteristics

From fig. 1, it is apparent that the inductance decreases more rapidly as the direct current increases. This is caused by influence from magnetic saturation, as shown in fig. 2. As the gap width grows larger, the gap becomes the dominant factor for magnetic resistance in the magnetic circuit, so the sensitivity of the inductance toward the current variation decreases.

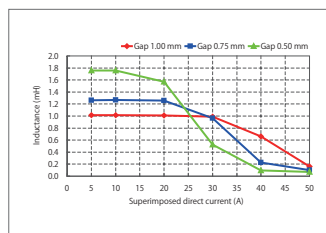


Fig. 1. Superimposed direct current characteristics

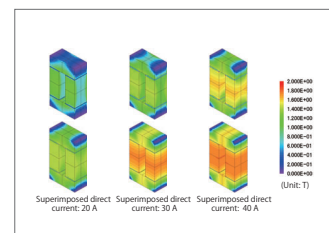


Fig. 2. Magnetic flux density distribution (top: gap width: 1.0 mm; bottom: gap width 0.5 mm)

Case 61

Current Distribution Analysis of a Choke Coil

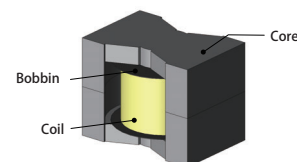
module: DP, TS, TRANSFORMER_TEMPLATE

Overview

A choke coil is an electric component that is intended to filter high-frequency current.

The current in a choke coil's interior produces local heat generation because of the skin effect, proximity effect, and current offsets caused by leakage flux near the gap. From a heat resistant design standpoint, visual confirmation of detailed current distribution using a finite element analysis (FEA) is useful because it provides feedback for the design.

This Application Note explains a case example that obtains the current distribution in a choke coil.



Current Density Distribution

The current waveform is shown in fig. 1, and the current density distribution in the coils at each time is shown in fig. 4.2. In order to evaluate in a steady state, fig. 1 shows the time from 40 μs to 80 μs .

From the figures, it is apparent that there are offsets in the current at 40 and 60 μs when the time variations in the current are severe, and that there is not much of an offset at 50 μs , when the time variations are mild. This is because variations in the magnetic field near the gap, which are the source of current offsets, cause variations in the coil current.

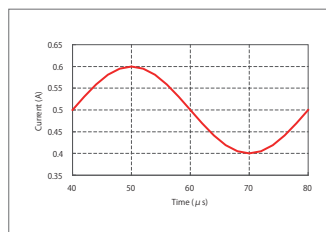


Fig. 1. Current waveform

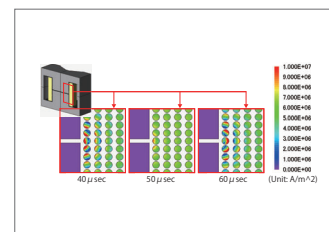


Fig. 2. Current density distribution

Case 62

Attraction Force Analysis of a Solenoid Valve

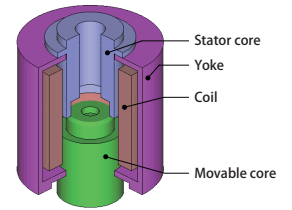
module: DP

Overview

Solenoid valves move their iron cores in a translational direction, and are used to adjust the inflow and outflow amounts of liquids and gasses. Running current through the coil forms an electromagnet, which generates an electromagnetic attraction force between the mover and stator. A high level of responsiveness is required to open and close the valve, so the power supply and valve used in the drive need to be evaluated to determine whether they fulfill the required responsiveness and attraction force.

The attraction force is determined from the size of the current, the arrangement of the iron core, and the material properties. However, the actual flow of magnetic flux is complex, and even if the current is increased, phenomena may occur such as the attractive force not being proportional to the current due to the effects of magnetic saturation in the core. A magnetic field analysis simulation using the finite element method (FEM) is useful in studying these kinds of behaviors.

This Application Note obtains the attraction force at each position of the movable core.



Magnetic Flux Density Distribution

Fig. 1 shows the magnetic flux density distribution at different movable core positions. The closer the movable core moves toward the stator core, the smaller the air gap becomes. So, the magnetic flux increases in the moving direction and the magnetic circuit changes. The magnetic circuit between the movable core and the stator core has a large effect on the attractive force.

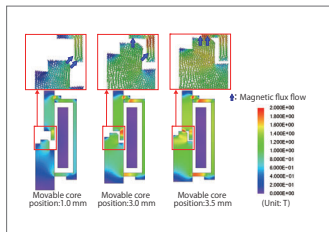


Fig. 1. Magnetic flux density distribution

Attraction Force Characteristics

Fig. 2 shows a vector plot of the surface force density produced in the movable core at each position, and fig. 3 shows the attraction force characteristics of the solenoid valve. When the movable core is in a position of 1.0 mm to 2.5 mm, a basically constant attraction force is obtained. As the movable core gets closer to the stator core the space between them shrinks, causing the magnetic resistance to change rapidly. This is why the attraction force generated in the direction of movement changes depending on the movable core's position when there is direct current excitation.

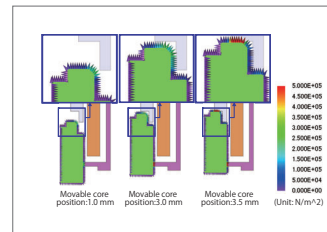


Fig. 2. Surface force density distribution at each position

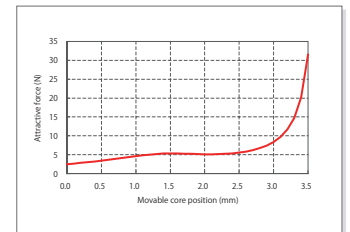


Fig. 3. Attraction force characteristics

Case 63

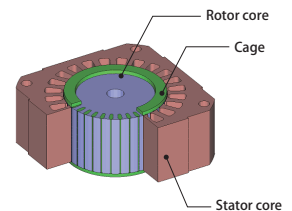
Analysis of Torque Characteristics of a Cage Induction Motor

module: FQ

Overview

Induction motors have been widely used for a long time in general industries because they have a simple structure, and are affordable, robust and highly efficient. When an induction motor rotates at synchronous speed, no torque is produced. However, when proper slip is caused, the maximum torque can be obtained. Losses are generated in a cage induction motor when current flows through the cage, so the pros and cons of continuous rotation depending on the amount of the heat generated need to be studied. In an induction motor, the current induced by the auxiliary conductor exerts a large influence on its characteristics. It also causes strong magnetic saturation in the vicinity of the gap, in particular. This is why a magnetic field analysis based on the finite element method (FEM) is useful when investigating the motor's characteristics for a design study.

This Application Note introduces a case example that obtains the Slip-Torque curve, Torque-Current curve, Current-Voltage curve at maximum torque, and the Current-Joule Loss curve for the cage.



Torque Characteristics

The Slip-Torque curves for each current amplitude are shown in fig. 1, the Torque-Current curve is shown in fig. 2, and the Current-Voltage curve is shown in fig. 3. As shown in fig. 1, the slip where the torque reaches its maximum value changes depending on the size of the current amplitude. The slip where the torque reaches its maximum value is determined by the coil's electric resistance, the cage's electric resistance, and the leakage reactance. Therefore, the changes in the leakage reactance due to an increase in current cause the changes in the slip where the torque reaches its maximum value. As can be seen from the slope of the Torque-Current curve in fig. 2, the torque constant of this induction motor is about 0.8 Nm/A. There is also a limit on the primary voltage that can be supplied, so the Current-Voltage curve needs to be used to investigate the primary voltage during maximum torque ahead of time.

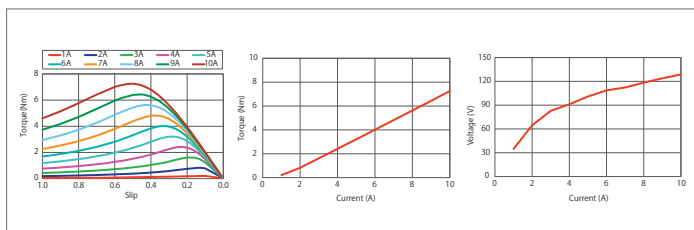


Fig. 1. Slip-Torque curve

Fig. 2. Torque-Current curve

Fig. 3. Current-Voltage curve

Eddy Current Density Distribution / Joule Loss

The eddy current density distribution when the current amplitude is 10 A is shown in fig. 4, and the joule loss in the cage for each current value is shown in fig. 5. Both of these are results at maximum torque. As shown in fig. 4, an excessive current with current density of over 2×10^7 A/m² flows through the bars, and the heat generation is large, so continuous operation is difficult. As shown in fig. 5, the joule loss increases quadratically against the current value. By estimating the heat generation from the loss, it is possible to understand the period of time when continuous operation is possible at the maximum torque. In this way, it is necessary to understand the current and losses in the cage when studying the maximum torque in a cage induction motor.

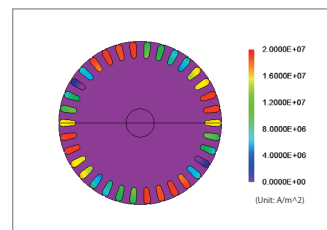


Fig. 4. Eddy current density distribution (rotor)

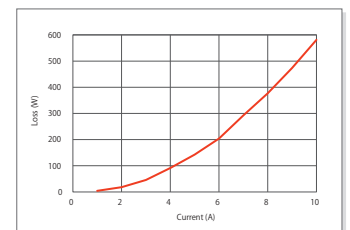


Fig. 5. Joule loss of the cage

Case 64

Thrust Force Analysis of a Coreless Linear Motor

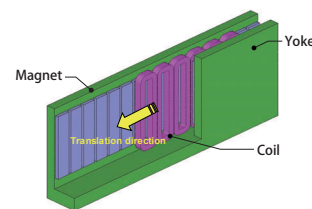
module: TR

Overview

Linear motors are widely used for carrier devices and machine tools because of their high-speed performance, high acceleration and deceleration, and accurate positioning. Among them there is a type of motor called a coreless linear motor. Coreless linear motors generally have a smaller thrust force than core linear motors, but they do not produce cogging, so they only have a small amount of thrust variation. They are used for linear motor stages and electronic packaging machines to make use of this property.

Because the thrust variations in linear motors are small, they can be hard to predict and measure at the design stage. With the finite element method (FEM), it is possible to obtain thrust variations with accuracy even when they are small, as is the case with a coreless linear motor.

In this example, explains how to obtain the thrust variations in a coreless linear motor when it is driven with a three-phase alternating current.



Lorentz Force Density Distribution

The Lorentz force density distribution at a translation distance of 21 mm is shown in Fig. 1. The Lorentz force is generated by the magnet's magnetic field when electricity flows through the coil. The strength of the Lorentz force is determined by the current value and the strength of the magnetic field. The direction of the Lorentz force is determined from the direction of both the current flow and the magnetic field.

When the translation distance is 21 mm current only flows through the U-phase and W-phase coils, so the Lorentz force density gets higher in the places in those coils that face the magnets. The Lorentz force occurs in the translation direction, becoming the thrust force.

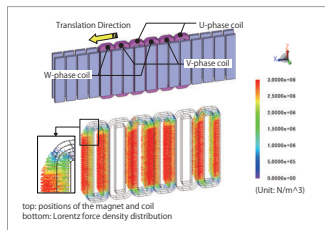


Fig. 1. Lorentz Force Density Distribution in the Coils at a Translation Distance of 21 mm

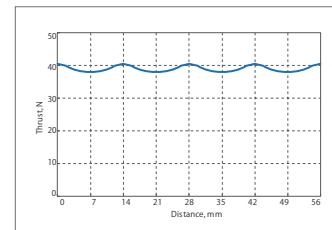


Fig. 2. Thrust Force Waveform

Thrust Force

The thrust force waveform is shown in fig. 2. Because there is no cogging the thrust variations are small, comprising about 6% of the average thrust force.

Case 65

Static Thrust Analysis of a Voice Coil Motor

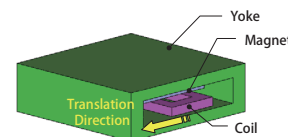
module: TR

Overview

Linear actuators are used in machine tools because of their high-speed performance, high acceleration and deceleration, and accurate positioning. There are coreless types of linear actuators, as well. They generally have a smaller thrust force than core linear actuators, but they do not produce cogging, so they only have a small amount of thrust variation. Because of this property, they are used in fields where high-accuracy positioning is necessary, like with head drives of packaging machines or the slight movements of precision stages.

Static thrust variations at the translation position of the actuator have an effect on determining the position accurately. The static thrust is determined by the amount of current, so its current characteristics need to be obtained.

This Application Note explains how to obtain the current characteristics and the translation position characteristics of the static thrust in a voice coil motor, which is a type of coreless linear actuator.



Translation Position Characteristics of Static Thrust

The translation position characteristics of the static thrust at a supply current of 0.05 A are shown in fig. 1. The Lorentz force density distribution and magnetic field distribution of the coil at translation positions of 0 mm and 1 mm are shown in figures 2 and 3. From fig. 1, it is apparent that the static thrust reaches its peak at a translation position of 1 mm, when the coil is directly beneath each magnetic pole. From fig. 2, it is apparent that the Lorentz force density inside the circle at the translation position of 0 mm is small compared to the translation position of 1 mm. From fig. 3, it is apparent that the magnetic field in the circle at the translation position of 0 mm is weak, and its direction is not perpendicular to the translation direction. Because the direction and size of the current in the coil is constant and the static thrust (Lorentz force) is determined from the strength and direction of the magnetic field, the static thrust is reduced by the magnetic field distribution in the coil.

Current Characteristics of Static Thrust

The current characteristics of the static thrust are shown in fig. 4. The figure shows the linearity of the static thrust against the supply current. According to the slope of this line, the thrust constant is 6 N/A. This means that it is possible to control the static thrust with the supply current value.

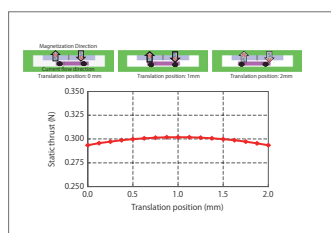


Fig. 1 Translation position characteristics of the static thrust

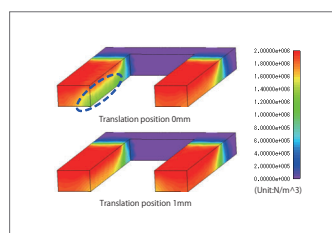


Fig. 2 Lorentz force density distribution (translation direction component)

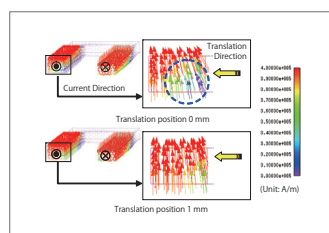


Fig. 3 Magnetic Field Distribution

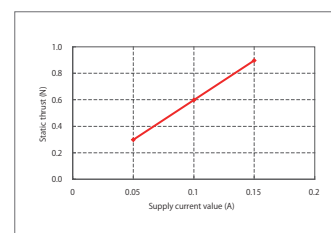


Fig. 4 Current characteristics of the static thrust

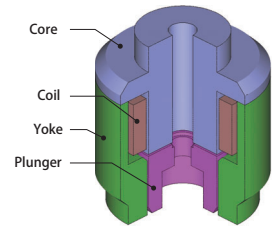
Case 66

Operating Time Analysis of an Injector

module: DP

Overview

A solenoid type injector used in engines opens a valve and injects fuel by moving a plunger with magnetic force created by an electromagnet. Injectors in engines need to respond quickly for applied voltage to improve fuel consumption by maintaining the amount of fuel flow. In solenoid injectors, one of the reasons that the response is delayed is eddy currents, which are produced when the magnetic flux generated by current flow undergoes time variations. The eddy currents are generated in a direction that inhibits changes in the magnetic flux, causing a delay in the initial rise of the attraction force when the current begins to flow. This reduces the injector's responsiveness. JMAG makes it possible to account for the effects from eddy currents and obtain an injector's responsiveness by running a transient response analysis. Identifying the places where eddy currents are generated enables a designer to study whether or not responsiveness can be improved. This Application Note explains how to apply direct current voltage to a solenoid injector and obtain its response characteristics by accounting for effects from eddy currents.



Response Characteristics

Fig. 1 shows the response characteristics of the plunger versus time. The plunger's displacement assumes the opening direction to be positive, and the valve is fully open when the displacement is 0.1 mm.

Fig. 1 demonstrates the difference in responsiveness of the plunger depending if eddy current is accounted for or not. Responsiveness is lower when eddy current is accounted for.

Attraction force characteristics

Fig. 2 shows the attraction force characteristics.

Fig. 2 shows attraction force is lower when eddy current is accounted for compared to when it isn't accounted for. Responsiveness decreases when eddy current is raised due to a decrease in attraction force.

Current characteristics

Fig. 3 shows response characteristics for current versus time.

Fig. 3 demonstrates the valve is open at 0.003(s) when eddy current is accounted for. However, when eddy current isn't accounted for, the valve is open at 0.0025(s). A slower responsiveness can be verified from the current flowing in the coil when eddy current is accounted for. Furthermore, when eddy current is accounted for, there is a lot of current flowing through the coil even though attractive force is lowered, compared to when it isn't accounted for.

Current Density Distribution

Fig. 4 shows the current density distribution when the current starts flowing 1 ms, when the plunger starts moving 2.3 ms and when the plunger moves one stroke 4.2 ms. The plunger moves in the direction that the valve opens in. When current flows in the coil, eddy currents are produced in the core, yoke and plunger. Magnetic flux flows rapidly when the current starts running, which causes eddy currents to concentrate in the surface of each part. However, eddy currents begin flowing in the interior of each part as time passes because the power supply is a direct current. These eddy currents lower the injector's responsiveness.

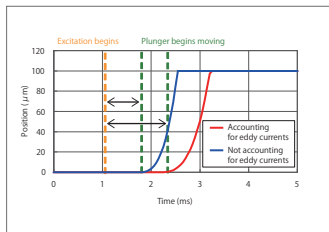


Fig. 1 Response characteristics

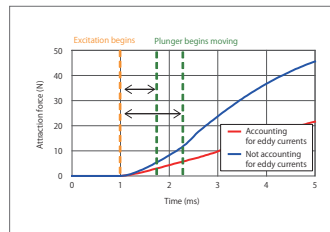


Fig. 2 Attraction force characteristics

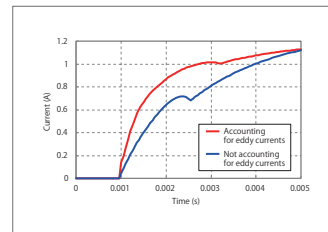


Fig. 3 Current characteristics

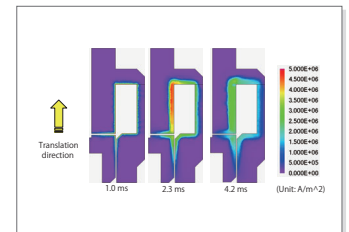


Fig. 4 Current density distribution

Case 68

Speed Versus Torque Characteristic Analysis of a Three-Phase Induction Motor

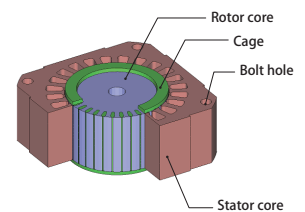
module: DP

Overview

An induction motor is a motor in which a rotating magnetic field in the stator coils causes induced current to flow in an auxiliary conductor. This current and magnetic field exert force on the auxiliary conductor in the rotation direction and cause the motor's rotor to rotate. Induction motors are widely used in everything from industrial machines to home appliances because they have a simple construction and are small, light, affordable, and maintenance-free.

In an induction motor, the current induced by the auxiliary conductor exerts a large influence on its characteristics. It also causes strong magnetic saturation in the vicinity of the gap, in particular. This is why a magnetic field analysis based on the finite element method (FEM) is useful when investigating the motor's characteristics for a design study.

This Application Note explains an analysis that confirms the Speed-Torque curve and current density distribution of an induction motor.



Current Density Distribution

The current density distribution at a rotation speed of 1050 r/min is shown in fig. 1. The rotating magnetic field created by the stator coils generates induced current in the rotor cage. Torque is generated from the magnetic flux and rotating magnetic field created by this induced current, so the current has a large effect on the torque characteristics.

Speed-Torque Curve

The Speed-Torque curve is shown in fig. 2. For this induction motor, the maximum torque can be obtained at the lower speed range. This means the induction motor has high resistance. In this case, changing the thickness of bars can reduce the electric resistance, and then the maximum torque can be obtained at the higher speed range.

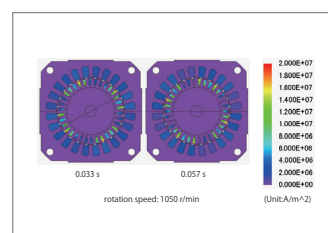


Fig. 1 Current density distribution

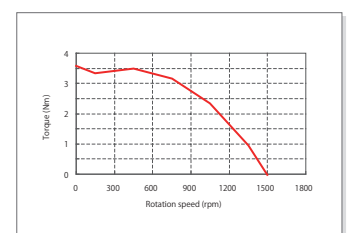


Fig. 2. Speed-Torque Curve

Case 69 Iron Loss Analysis of an IPM Motor

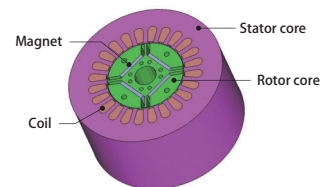
module: DP, LS

Overview

Demand for higher efficiency and smaller size in motors has grown from the need to accommodate devices that incorporate miniaturization and energy efficiency in their designs. In order to meet this demand, motors have to improve their output density and reduce their losses. One type of loss commonly found in motors is iron loss, which increases drastically at high rotation speeds and high magnetic flux densities. This increase can lead to a rise in temperature and a reduction in efficiency. Consequently, it is growing more important to predict iron loss levels at the motor design stage.

Unfortunately, it is not possible to obtain iron losses accurately in studies that use the magnetic circuit method or rules of thumb. In order to obtain them accurately, one needs to find the distribution and time variations of the magnetic flux density in each part of the motor after accounting for a fine geometry and the material's nonlinear magnetic properties. Using the finite element method (FEM) is essential in order to carry out this kind of a detailed analysis.

This Application Note explains a case example that obtains the iron loss and its distribution in a permanent magnet motor.



Magnetic Flux Density Distribution

The magnetic flux density distribution of the stator core and rotor core is shown in fig. 1, and the magnetic flux density waveforms of the magnetic flux density r-component at measuring points 1 and 2 is shown in fig. 2.

While both the value and amount of variation in the magnetic flux density at measuring point 1 are large, at measuring point 2 the magnetic flux density has a large value but a small amount of variation. These differences in magnetic flux density affect the iron loss.

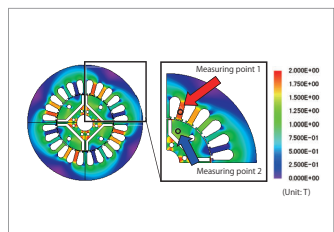


Fig. 1 Magnetic flux density distribution (1 rotation)

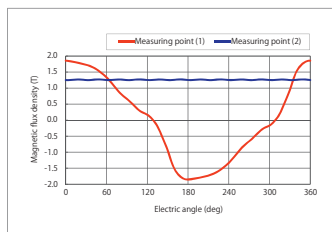


Fig. 2 Magnetic flux density waveforms (r-component)

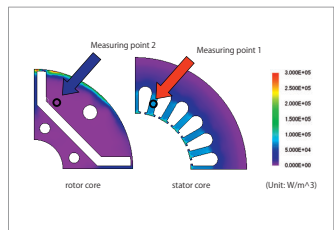


Fig. 3 Joule loss density distribution

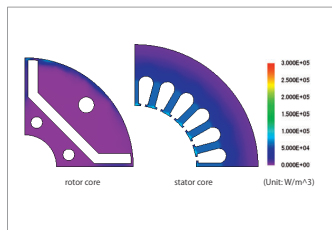


Fig. 4 Hysteresis loss density distribution

Joule Loss Density Distribution/Hysteresis Loss Density Distribution/Iron Loss Density Distribution

The joule loss density distributions for the stator core and rotor core are shown in fig. 3. The hysteresis loss density distributions for the stator core and rotor core are shown in fig. 4. The iron loss density distributions for the stator core and rotor core are shown in fig. 5.

The ratios of loss for the stator core and rotor core are shown in fig. 6. As shown in the magnetic flux density waveforms, joule losses are greater in places where the amount of variation in the magnetic flux density is large, compared to places where the amount of variation in the magnetic flux density is small. The same trend can be seen in the hysteresis losses as well, as shown in fig. 6 by the fact that the ratio of the joule and hysteresis losses taken up by the stator is large.

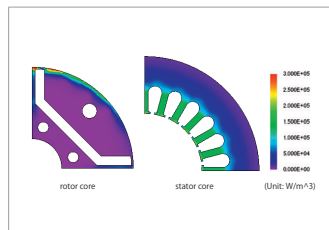


Fig. 5 Iron loss density distribution

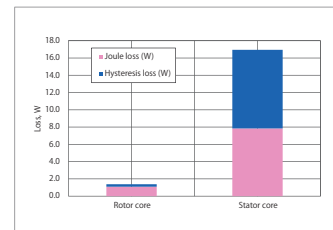


Fig. 6 Ratio of loss

Case 70

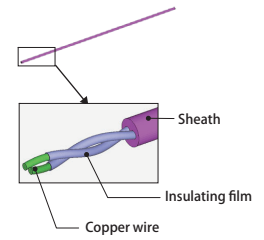
Analysis of Impedance-Frequency Characteristics of a Cable

module: FQ

Overview

Twisted pair cables are used in situations that require strict noise reduction like with signal lines and speaker cables because they are not affected by external noise and do not emit much noise of their own. The cable's performance relies on its electric properties, but these change depending on the state of the current that is flowing. For example, when the current frequency rises, the current is offset in the copper wires because of the skin effect and proximity effect. As a result, the apparent cross-sectional area of the current flow is reduced, causing the alternating current resistance to increase and the inductance to change. An increase in the resistance leads to an increase in losses, and changes in inductance result in distortions in the signal. This is why these frequency characteristics need to be understood in advance. The above phenomena occur in the interior of the copper wires, so an evaluation using a magnetic field analysis based on the finite element method (FEM) is useful because they can be difficult to predict with manual calculations.

This Application Note explains how to obtain the frequency characteristics of the resistance and inductance in twisted pair cables.



Current Density Distribution

The current density distribution of the copper wire is shown in fig. 1. At a frequency of 10 kHz the proximity effect causes offsets in the current, and at 100 kHz both the skin and proximity effects cause offsets in the current. It is anticipated that these offsets in current have an effect on the resistance and inductance.

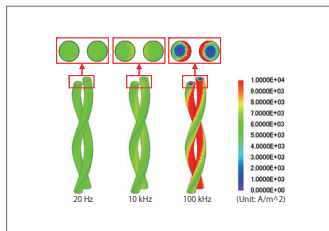


Fig. 1 Current density distribution in the copper wire

Resistance/Inductance Frequency Characteristics

The frequency characteristic of the resistance in the copper wire is shown in fig. 2, and the frequency characteristic of the inductance is shown in fig. 3. The resistance and inductance begin to change gradually at around 10 kHz due to the proximity effect, and the skin effect begins to increase as the frequency grows larger, so both resistance and inductance change rapidly. In order to reduce the skin and proximity effects, the structure needs to be studied so that the current in the frequency range being used can flow through the conductor uniformly.

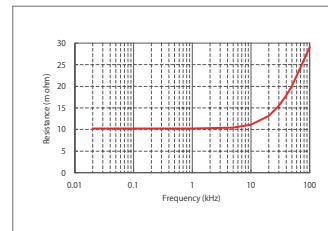


Fig. 2 Frequency characteristic of the resistance

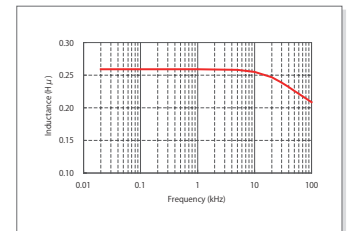


Fig. 3 Frequency characteristic of the inductance

Case 71

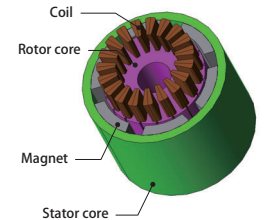
Basic Characteristic Analysis of a Motor with 2 Brushes, 6 Poles, and 19 Slots

module: DP

Overview

Small brush motors generally have a structure containing 2 poles and 3 slots, but there are times when a multi-pole structure is adopted in order to produce higher torque. The reason for this is because achieving a higher torque makes it possible to omit deceleration systems. Brush motors have a construction where the number of poles and number of slots are not divisible, with the objective of raising the rectification effect or limiting torque variations. In exchange for reducing torque variations, however, there is a drawback when it comes to torque output. This is why selecting the number of poles and slots have become a design theme, especially when it comes to small motors, which have a small number of slots. This makes the selection process difficult because the difference in distribution becomes large. The model for this analysis has 6 poles and 19 slots, so there are 3.16 slots per pole. They cannot be divided into decimals however, so there have to be either 3 or 4 slots for each magnetic pole. As a result, the induced voltage in each coil and the torque generated are unbalanced.

These evaluations need to be able to account for an accurate circuit geometry, and the current flowing through coil connected via a commutator needs to be handled accurately, as well. This is why an electromagnetic field analysis using the finite element method (FEM) is necessary to account for everything. This Application Note presents an analysis to obtain the speed versus torque and torque versus current for a motor that has 2 brushes, 6 poles, and 19 slots.



Speed-Torque Curve and Torque-Current Curve

Fig. 1 shows the speed versus torque curve and fig. 2 shows the current versus torque curve.

As shown in fig. 1, the torque in the DC brush motor decreases as the rotation speed increases. This is because the current flowing in the coil is reduced by the increase of reverse electromagnetic force produced as the rotation speed increases. As shown in fig. 2, the relationship between the current and torque is mostly linear, and the torque coefficient of this brush motor is 0.05 Nm/A.

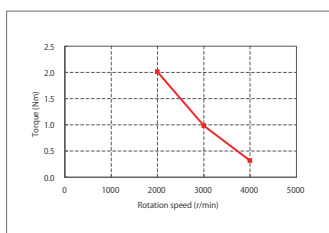


Fig. 1. Speed-Torque curve

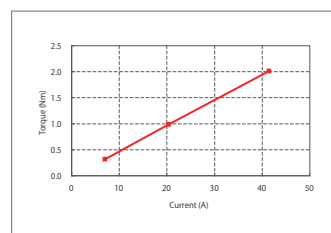


Fig. 2. Torque-Current curve

Magnetic Flux Density Distribution

Fig. 3 shows the magnetic flux density distribution at rotation speeds of 2000 r/min and 4000 r/min.

The magnetic flux density increases at a lower rotation speed, as indicated in the figure. This is because the current flowing in circuit is larger, as mentioned earlier. A motor and control design that does not allow magnetic saturation to occur at low rotation speeds is desirable because the performance of the motor worsens with magnetic saturation.

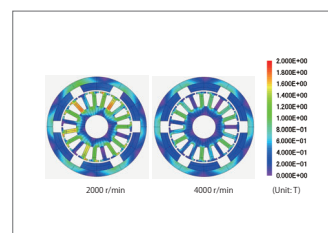


Fig. 3. Magnetic flux density distribution

Case 72 Analysis of Attractive Force between Steel Plates and a Magnet

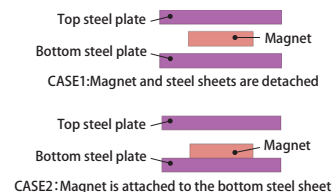
module: ST

Overview

Many electronic products that have movers use the attractive force generated between magnets and magnetic materials. Even magnetic materials that are not magnetized themselves take on magnetic properties when in the vicinity of a magnet, generating an attractive force between the two bodies.

In order to understand the phenomena where the magnet and magnetic material attract each other, it is helpful to visualize the magnetic flux flowing through the air. Using a magnetic field analysis makes it easy to visualize and understand these phenomena.

This Application Note explains how to obtain the magnetic flux density distribution and attractive force generated between a steel plate and a magnet.



Attractive Force Characteristics of CASE 1

The magnetic flux density distribution for CASE 1 is shown in fig. 4.1, and its attractive force characteristics are shown in fig. 4.2. The attractive force acting in the positive direction on the Y-axis is set to positive.

The relative positions of the magnet and steel plate allow the magnetic flux to be vertically symmetrical, meaning that the forces acting on the top steel plate and the bottom steel plate are the same, and almost no force is acting on the magnet.

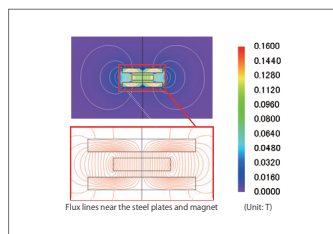


Fig. 1 Magnetic Flux Density Distribution of CASE 1

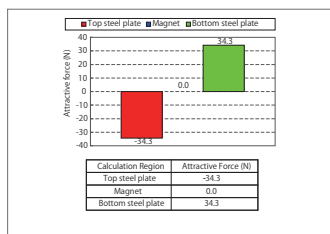


Fig. 2 Attractive Force Characteristics for CASE 1

Attractive Force Characteristics of CASE 2

The magnetic flux density distribution for CASE 2 is shown in fig. 3, and its attractive force characteristics are shown in fig. 4. In fig. 4, (4) is a value that represents the sum of the attractive forces of (2) Magnet and (3) Bottom steel plate. The attractive force acting in the positive direction on the Y-axis is set to positive.

In CASE 2 the magnet is touching the bottom steel plate, so the magnetic flux density is higher in the bottom steel plate than in the top steel plate, and the attractive force between the magnet and the bottom steel plate is larger than between the magnet and the top steel plate. This is why the magnet's attractive force in fig. 4 is shown acting in the negative direction, and the sum of (1) and (2) is equal to (3). (1) and (4) are also equal, so it is possible to confirm that the attractive force that the attractive force acting on the magnet and the bottom steel plate has been obtained correctly.

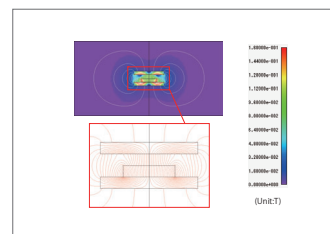


Fig. 3 Attractive Force Characteristics of CASE 2

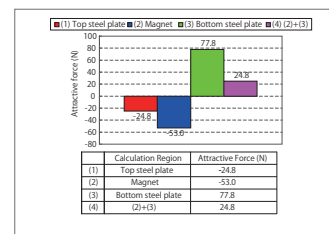


Fig. 4 Attractive Force Characteristics of CASE 2

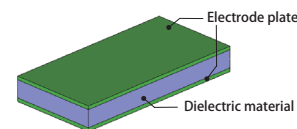
Case 73 Analysis of the Capacitance of a Parallel Plate Capacitor

module: EL

Overview

Capacitors are widely used as basic passive components in a variety of electric circuits. Parallel plate capacitors are taken up as the subject matter for how to obtain capacitance, a basic electric property, because they follow simple phenomena. Two electrode plates are placed in the air to face each other. When a constant electric potential difference is applied to them, they store an electric charge. The capacity of the charge stored in the electrode plates changes depending on the permittivity of the dielectric material between them.

This Application Note explains how to use JMAG to calculate the capacitance when the dielectric material is air and when it is a high permittivity material, while obtaining the amount of charge in each.



Electric Field Distribution

The magnetic field distributions generated between the two electrode plates when they are in parallel and an electric potential difference is applied to them are shown in fig. 1. When the dielectric material is air, there is a large magnetic field that extends from the opposing faces of the electrode plates to the air, so there is a large magnetic field generated locally at the corner of the electrode.

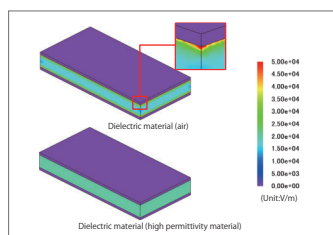


Fig. 1 Electric Field Distribution

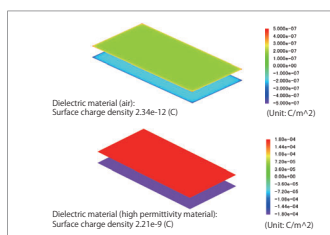


Fig. 2 Electric Charge Distribution of the Electrode Plate Surface

Capacitance Calculation

The electric charge distribution generated on the surfaces of the electrode plates is shown in fig. 2. When the high permittivity material is used, the amount of surface charge density is larger than that of air. The capacitance is calculated with the following formula by using the amount of surface charge density and the electric potential difference applied in the analysis. The result is shown in table 1.

$$C = \frac{Q}{V}$$

C : Capacitance, F
 Q : Electric charge, C
 V : Electric potential difference, V

	Dielectric material (air)	Dielectric material (high permittivity material)
Capacitance	0.47 pF	443 pF

Table1 Capacitance

Case 74

Speed Versus Torque Analysis of a Single-Phase Induction Motor

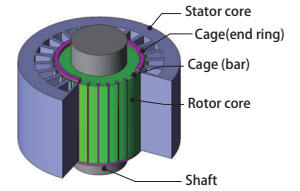
module: DP

Overview

Single-phase induction motors are widely used as small output motors for the drives in household electrical appliances and office machinery, like fans and washing machines, because they can use single-phase AC, the typical power source for home electronics. Unlike three-phase AC, however, single-phase AC cannot create a rotating magnetic field by itself, meaning that it cannot start a motor. For this reason, it needs to use an alternate method to generate a rotating magnetic field to start the motor.

The induced current flowing in the secondary conductor largely affect the performance of the motor because the motor rotates by using the interaction between this current and the magnetic field of the stator coils. Strong magnetic saturation distribution is also generated near the gap, so the nonlinear characteristics of the magnetic properties have a big influence on performance, as well. At the step before the design phase, it is helpful to run an analysis and evaluation using the finite element method (FEM) to understand a single-phase induction motor's characteristics by accounting for induced current and magnetic saturation characteristics.

This Application Note explains how to obtain the current density distribution and Speed-Torque curve created by auxiliary winding that uses a capacitor.



Current Density Distribution

The current density distributions for maximum torques at rotation speeds of 2,100 rpm are shown in fig. 1. The difference in speed between the rotor and rotating magnetic field becomes smaller as the rotor reaches high speed. This makes the variations in the magnetic field acting on the cage grow smaller, which in turn reduces the eddy currents flowing in the bars accordingly. The eddy current distribution in the bars largely affects the torque characteristics.

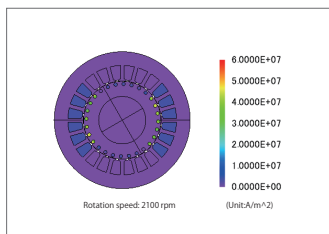


Fig. 1. Current density distribution

Speed-Torque Curve

The Speed-Torque curve is shown in fig. 2. The maximum torque can also be obtained at around 2000 rpm. The rotation region that provides maximum or high torque varies depending on the electric resistance, so changing the cage materials or geometry makes it possible to study the motor characteristics that most closely meet the goals of the design.

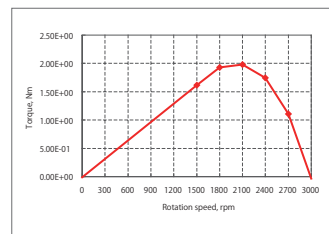


Fig. 2. Speed-Torque curve

Case 75

Iron Loss Analysis of a Reactor

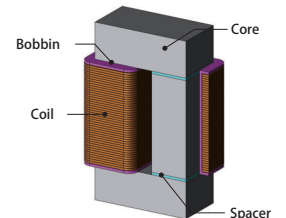
module: FQ, LS

Overview

Reactors are installed on the input or output side of inverter circuits. Because they are required for long-term operation, the ability to control running costs from losses is an important challenge for their design. Iron loss is one of the major types of losses in a reactor. It consumes electric power as heat in a magnetic body, so it causes heat to increase and efficiency to decrease in the reactor.

Using a finite element analysis (FEA) to confirm the distribution of iron loss density makes it possible to study a reactor's local geometry during its design, so it is useful in providing feedback about the design itself.

This Application Note analyzes the iron loss of a reactor.



Magnetic Flux Density Distribution/ Iron Loss Density Distribution

The core's magnetic flux density distribution and iron loss density distribution are shown in figures 1 and 2, respectively. The magnetic flux concentrates on the surface because it cannot flow easily in the direction of the laminations, increasing the iron losses accordingly. The magnetic flux also tries to flow through the shortest path in the magnetic circuit, so the magnetic flux density and iron loss are large at the top and bottom of the core, which are not wrapped by the coil.

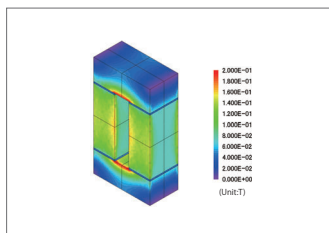


Fig. 1. Magnetic flux density distribution

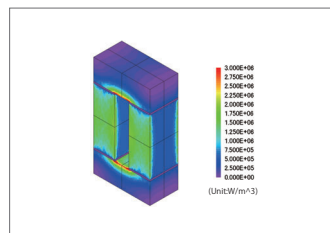


Fig. 2. Iron loss density distribution

Joule Loss Density Distribution/ Hysteresis Loss Density Distribution

The core's joule loss density distribution and hysteresis loss density distribution are shown in fig. 3, the ratio of losses is shown in fig. 4, and the losses are shown in table 1. As can be seen from the figures, the contribution of the joule loss toward the iron loss is large. The amount of core loss may be effectively decreased by reducing the amount of Joule losses.

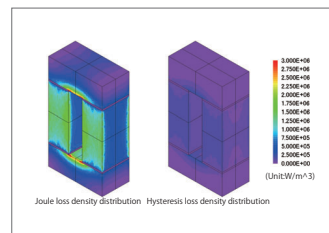


Fig. 3. Joule loss density distribution and hysteresis loss density distribution

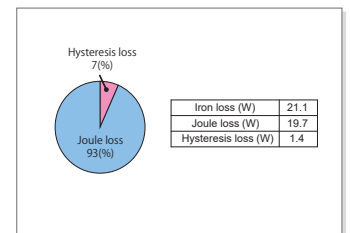


Fig. 4. Ratio of loss

Table 1. Losses

Case 77 Inductance Analysis of an RFID Tag

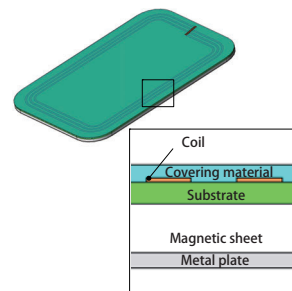
module: FQ

Overview

An RFID tag uses electromagnetic induction to communicate information by supplying electrical power to an IC chip from a reading device. In order to relay information in specific frequencies with a good degree of sensitivity, the RFID tag uses resonance between its internal coil antenna and capacitor.

The coil antenna's inductance and the capacitor's resonance frequency need to be estimated for resonance to be produced accurately at the specified frequency. When the capacitor is external, the inductance of the coil antenna needs to be obtained accurately and the capacitor's capacity needs to be identified. Some RFID tags have magnetic sheets or metallic films on them. The sheet's magnetic properties and eddy currents generated in the film can affect the inductance.

This Application Note performs a magnetic field analysis of an RFID tag that has a metallic film and a magnetic sheet with a resonance frequency of 13.56 MHz, and obtains the magnetic field distribution and the RFID tag's inductance.



Magnetic Field Distribution

The magnetic field distribution around the RFID tag is shown in fig. 1. The magnetic field is shielded toward the metal plate, as shown in fig. 1. This magnetic field distribution has a large effect on the inductance.

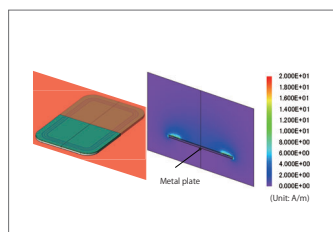


Fig. 1 Magnetic field distribution

Inductance

The inductance of the RFID tag and the capacity of the resonant capacitor are shown in table 1.

The inductance of this RFID tag can be obtained from the relationship between the voltage and current. In this analysis, it is 942 nH. The capacity of the external capacitor, calculated from the resonance frequency and inductance, is 146 pF.

Resonance frequency	13.56 MHz
Inductance	942 nH
Capacitance	146 pF

Table 1. Each value of the RFID tag

Case 78 Loss Analysis of a Sheet Coil Transformer

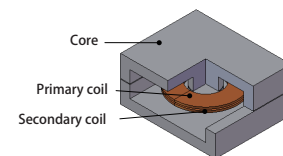
module: FQ, LS

Overview

Power transformers need to be able to operate over the long term, so they are always required to control running costs from losses. Iron loss is one of the main losses in a transformer, and it can lead to temperature increases and efficiency decreases because it consumes electric power as heat in a magnetic material.

Using a finite element analysis (FEA) to display the iron loss density distribution and obtain the iron loss values in a transformer makes it possible to study the local geometry and get design feedback at the design stage.

This Application Note shows how to obtain the iron loss of a sheet coil transformer.



Magnetic Flux Density Distribution/ Iron Loss Density Distribution

The core's magnetic flux density distribution and iron loss density distribution are shown in figures 1 and 2, respectively. The magnetic flux density distribution and iron loss density distribution are similar, as indicated in the figures. This is because the frequency of the magnetic flux density variations is constant, so the size of the iron losses is proportional to the size of the magnetic flux density variations.

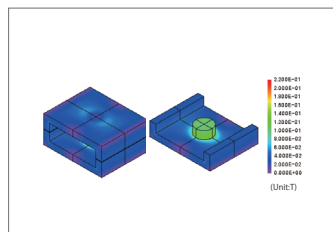


Fig. 1. Magnetic flux density distribution

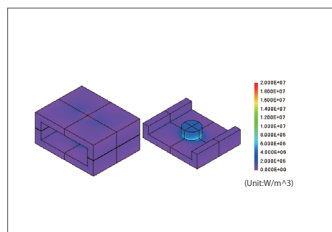


Fig. 2. Iron loss density distribution

Joule Loss Density Distribution/ Hysteresis Loss Density Distribution

The core's joule loss density distribution and hysteresis loss density distribution are shown in fig. 3, the ratio of losses is shown in fig. 4, and the losses are shown in table 1.

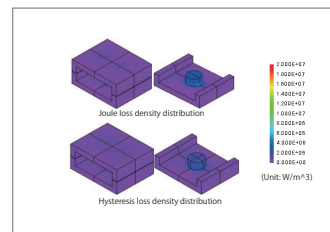


Fig. 3. Joule loss density distribution and hysteresis loss density distribution

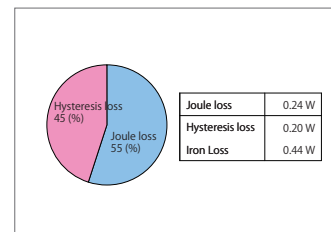


Fig. 4. Loss ratio

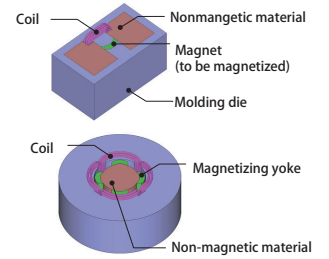
Table 1. Losses

Overview

A magnet's magnetizing state largely affects the characteristics of a device that uses permanent magnets. The manufacturing process of a magnet is divided into two parts: the orientation process and the magnetization process. In the orientation process, an orientation device is used at the stage where magnetic power is formed to align the growth direction of the magnetization. After this, the magnet is temporarily demagnetized. Next, in the magnetization process, a magnetization device achieves the desired state of magnetization in the magnet. Both the orientation process and the magnetization process need to be accounted for in order to evaluate a magnet's magnetization state accurately. Consequently, it is extremely difficult to study a magnetizing state by obtaining the behaviors of the molding die, magnetization device, and magnetization current with manual calculations. Running a magnetic field analysis simulation that uses the finite element method (FEM) it is possible to calculate the magnetic field orientation and magnetization field from the material properties, equipment geometry, and applied current. One can also run an analysis that uses the magnetization state inside the magnet based on these results. This Application Note explains how to obtain a magnet's surface magnetic flux density distribution while accounting for the orientation and magnetization processes.

Magnetic Field Orientation Distribution/ Magnetization Field Distribution

The magnetic field orientation distribution is shown in fig. 1, and the magnetization field distribution is shown in fig. 2. As can be seen in fig. 1, the magnetic field orientation distribution is almost entirely radial distribution. For this orientation, the magnetization state of the magnet is determined by applying the magnetization field shown in fig. 2.



Magnetization Distribution/ Surface Magnetic Flux Density Distribution

Fig. 3 shows the magnetization distribution in Magnets A and B. Magnet A is the magnet that was magnetized by accounting for the magnetic field orientation shown in fig. 1. Magnet B is a magnet that was magnetized with an ideal radial orientation. The magnetic flux density distribution at a distance of 0.5 mm from the surface of a magnet that has been placed in air is shown in fig. 4.

From fig. 3, it can be seen that there is greater magnetization at the ends of Magnet A than of Magnet B. This is because the orientation at the ends of Magnet A shown in fig. 1 is more similar to the magnetization field distribution shown in fig. 2 than with Magnet B. From fig. 4, it can be seen that the surface magnetic flux density is higher in Magnet B than Magnet A at the center of the magnetic poles. This is because the orientation at the center of the poles in Magnet A shown in fig. 1 differs more from the direction of the magnetization field shown in fig. 2 than it does with Magnet B. As can be seen from the results in fig. 3, the surface magnetic flux density distribution at the ends of the magnets differs greatly.

This is why in order to evaluate the magnetization state of a magnet accurately, the magnetic field orientation and magnetization field need to be taken into account.

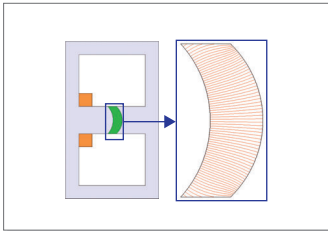


Fig. 1 Magnetic field orientation distribution (red lines: magnetic flux)

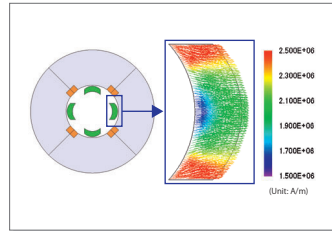


Fig. 2. Magnetization Field Distribution

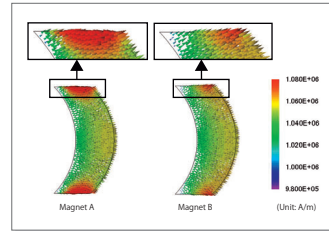


Fig. 3 Magnetization distribution in the magnet

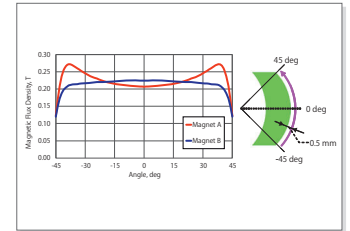
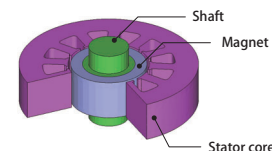


Fig. 4 Surface magnetic flux density of the magnet

Case 80 Cogging Torque Analysis of an SPM Motor with Skewed Magnetization

module: TR



Overview

Reductions in vibration and noise are being sought after because they are a cause of torque variations in motors, and demands for reduction are particularly strong with motors that are used in machine tools and power steering. Cogging torque, which is a torque variation that is produced when there is no current, is generated because the electromagnetic force produced in the gap changes according to the rotor's rotation. This makes it necessary to apply skew to the stator and rotor and come up with innovative geometry for the magnet and stator in order to reduce torque variations by limiting variations in the electromagnetic force. Applying skew reduces the cogging torque, but it also brings disadvantages such as producing force in the thrust direction and generating eddy currents from the magnetic flux that links in the lamination direction.

Consequently, in order to accurately evaluate a motor that has skew applied, one needs a magnetic field analysis simulation that uses the finite element method (FEM), which can account for a detailed 3D geometry, instead of studies that use the magnetic circuit method or a 2D magnetic field analysis.

This Application Note presents the use of a magnetic field analysis to obtain the flux density distribution, cogging torque, and induced voltage of an SPM motor that has skewed magnetization applied to its magnet.

Magnetic Flux Density Distribution

Fig. 1 shows the magnetic flux density distribution at the rotation angle of 90 deg. From fig. 1, it is apparent that the magnetic circuit changes when the magnet is skewed. These variations in the magnetic circuit have an effect on the cogging torque waveform.

Cogging Torque Waveform

Fig. 2 shows cogging torque waveforms at skew angles of 0 deg and 30 deg. The peak value of the cogging torque is reduced by approximately 90% when skew has been applied to the magnet.

Induced Voltage Waveform

The induced voltage waveforms of the U-phase at skew angles of 0 deg and 30 deg are shown in fig. 3, and the frequency components of the U-phase's induced voltage waveforms are shown in fig. 4.

The high frequency components are reduced when skew is applied to the magnet. The ratio taken up by the fundamental frequency of 60 Hz out of the total frequency components is 72% with a skew angle of 0 deg and 82% with a skew angle of 30 deg. According to these results, the induced voltage waveform is smoother at a skew angle of 30 deg than at an angle of 0 deg.

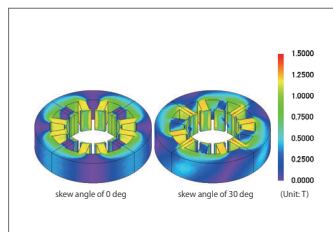


Fig. 1 Magnetic flux density distribution

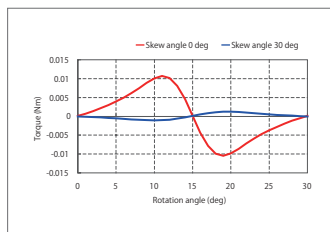


Fig. 2 Cogging torque waveform

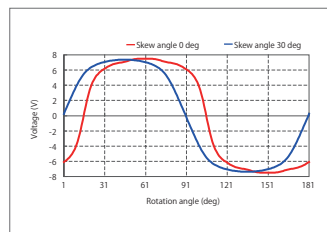


Fig. 3 U-phase induced voltage waveform

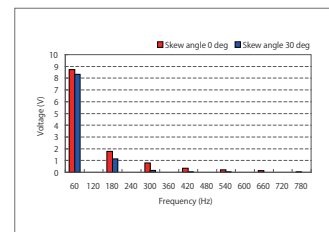
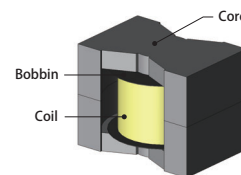


Fig. 4 Frequency components of the U-phase induced voltage waveform

Case 81 AL-value Analysis of a Choke Coil

module: ST, TRANSFORMER_TEMPLATE



Overview

A choke coil is an electric component that is intended to filter high-frequency current. The AL-value is a vital parameter in a choke coil design that determines the cutoff frequency of a high-frequency current.

The AL-value varies greatly depending on gap width, so it is effective for the advance study of a design to accurately obtain the AL-value dependency on the gap width (air gap versus AL characteristics) for the geometry of a choke coil by using a finite element analysis (FEA).

This Application Note explains a case example that obtains the air gap versus AL characteristics of a choke coil.

Air Gap-AL Characteristics

The air gap versus AL curve of the choke coil is shown in fig. 1. Fig. 1 demonstrates the relationship between the gap width and the AL-value. This makes it possible to obtain the AL-value from the gap width and estimate the number of turns to achieve the specified inductance.

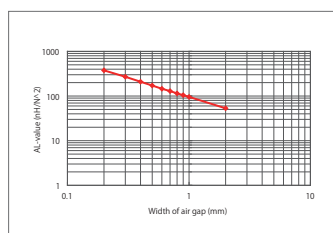


Fig. 1. Air gap versus AL-value

Case 82

Analysis of a Synchronous Reluctance Motor

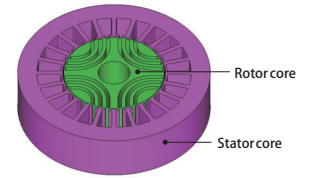
module: DP

Overview

Skyrocketing prices of rare earth magnets have led to rising expectations for synchronous reluctance motors (referred to below as SynRMs), which do not use permanent magnets. SynRMs have a simple structure that can achieve solid performance at a low price. However, torque is generated only by the rotor's saliency and the coil's magnetomotive force, so raising the torque density depends greatly on the core's nonlinear magnetic properties and the rotor geometry. This is why they have a different format than a typical motor. On the other hand, the aforementioned rising prices of rare earth magnets, improvements in current control technology, and the ability of optimization designs using magnetic field analysis have raised the possibility of lowering these barriers, giving SynRMs the chance to be reexamined.

SynRMs operate using the nonlinear region of a magnetic steel sheet, so the inductance expresses nonlinear behavior as well. This behavior distorts the excitation current waveform a great deal, making it impossible to run advanced projections that are accurate with calculation methods that follow linear formulas. Consequently, it becomes necessary to use the finite element method (FEM), which can handle nonlinear magnetic properties in material, detailed motor geometry, and transient currents.

This Application Note presents an evaluation of torque variations that occur when the phase of a sinusoidal wave current is changed.



Magnetic Flux Density Distribution and Average Torque per Current Phase

The magnetic flux density distribution at a rotation speed of 600 r/min and a current amplitude of 3.0 A is shown in fig. 1. The average torque at each current phase is shown in fig. 2. The magnetic flux density distribution changes with the current phase. When the current phase is 0 deg and 90 deg the average torque is 0, and when the current phase is 45 deg the torque reaches its peak.

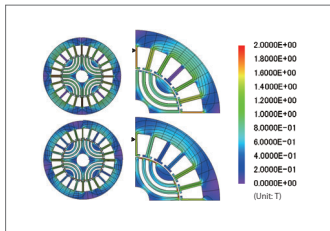


Fig. 1 Magnetic flux density (top: $\beta = 0$, bottom: $\beta = 45$)

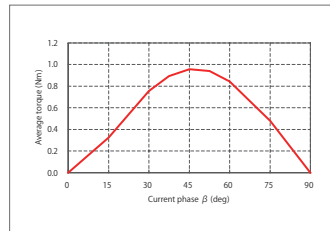


Fig. 2 Average torque per current phase

Case 83

Magnetic Shielding Analysis of an Induction Furnace

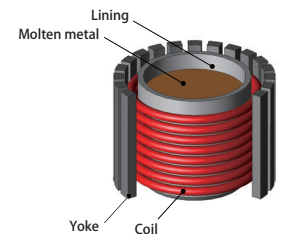
module: FQ

Overview

An induction furnace is an apparatus that uses high-frequency induction heating to melt metal. Running current through the coil surrounding the crucible starts electromagnetic induction phenomena, which generate current in the metal in the crucible. This current produces joule losses in the metal, which are used to heat and melt it. Magnetic yokes are arranged around the coil. The yokes are used as strong components that prevent the Lorentz force generated by the coil from damaging and deforming it. The magnetic yokes also reduce the leakage flux that flows out of the appliance, preventing unintended heating in surrounding structures. Keeping the amount of material used in the magnetic yokes to a minimum makes it possible to reduce the cost of the apparatus.

To understand the magnetic flux that spreads from the induction furnace, it is necessary to use the eddy current distribution and magnetic flux flow in the metal in the crucible, as well as the concentrations in magnetic flux caused by the positions of the yokes.

This Application Note displays magnetic flux density distribution to evaluate the differences in magnetic flux with and without yokes.



Magnetic Flux Density Distribution

The magnetic flux density distribution generated in the yokes and the air region is shown in fig. 1. When the yokes are present, there is less leakage flux than when they are not present. This means that it is possible to prevent a steel plate outside of the yokes from being heated.

Molten Metal Joule Loss

The joule loss values of the molten metal are shown in fig. 2. There is 5% more joule loss in the furnace with the yokes than without them, so it is applying energy to the molten metal efficiently.

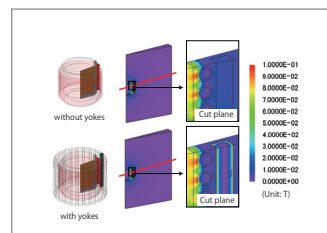


Fig. 1 Magnetic flux density distribution

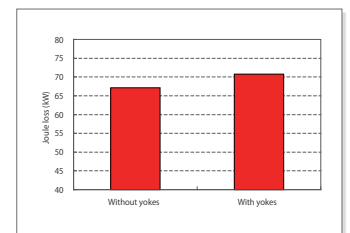


Fig. 2 Joule Loss of the Molten Metal

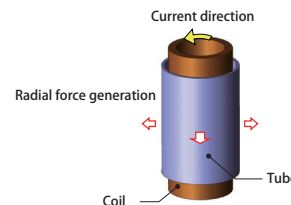
Case 84

Electromagnetic Forming Analysis of a Tube

module: DP

Overview

Electromagnetic forming is a process in which eddy currents are generated in a tube when a large, instantaneous current is run through a coil, creating a strong magnetic field. The tube is formed by using the Lorentz force produced by the interaction between these magnetic fields. This method is different from forming that uses plastic deformation with a press mold because it deforms with the power of the tube itself. This makes it possible to perform difficult forming, like with an object that will not fit into a normal press mold. However, the force generated in the tube is determined from induced eddy currents, which means that it is dynamic deformation, so the behavior of its deformation is known for being difficult to analyze. Using JMAG to properly analyze the Lorentz force distribution generated in the tube can assist with predicting the deformation behavior of the electromagnetic forming process. This Application Note explains how to obtain the Lorentz force density distribution generated in a tube when current is run through a coil.



Eddy Current Density Distribution

The eddy current density distribution generated in the tube at 125 μs is shown in fig. 1. Running high current through the coil creates a strong magnetic field around it, inducing eddy currents in the tube. More eddy currents are generated in the ends of the tube, as shown in fig. 1. This is because the magnetic flux concentrates near the ends of the tube.

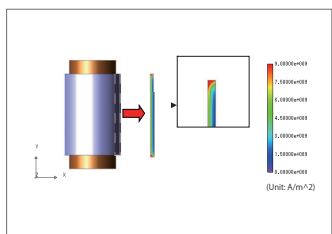


Fig. 1 Eddy current density distribution in the tube at 125 μs

Lorentz Force Density Waveform

The Lorentz force densities in the radial direction and the axial direction at each time are shown in figures 2 and 3. The tube expands with the positive values of Lorentz force density in the radial direction, and the tube shrinks with negative values of Lorentz force density in the tube. The Lorentz force that occurs in the radial direction at 65 μs and 125 μs is produced consistently around the center of the tube, and it becomes drastically larger at the ends, as indicated in fig. 2. This is because the eddy currents concentrate in the ends of the tube. When the current has declined to 187.5 μs , the Lorentz force that occurs shrinks the ends of the tube. The Lorentz force density in the axial direction only occurs within a 10 mm range at each end of the tube, and it is distributed symmetrically across the center position of 0. The Lorentz force generated works to shrink the tube as well as to expand it while current is flowing in the coil, so the Lorentz force density in the tube needs to be evaluated using a simulation at the design stage.

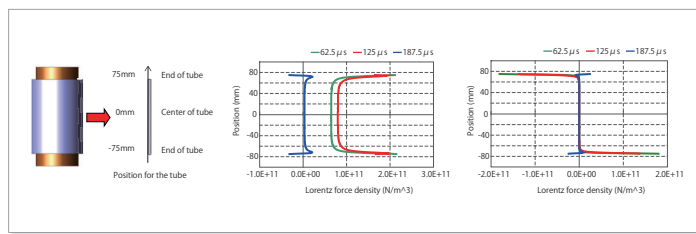


Fig. 2 Lorentz force density in the radial direction

Fig. 3 Lorentz force density in the axial direction

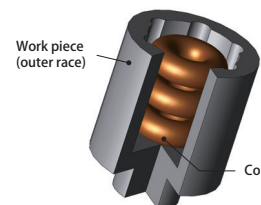
Case 85

High-Frequency Induction Heating Analysis of a Constant Velocity Joint

module: FQ, HT

Overview

Constant velocity joints are used in the connections at each end of a drive shaft in a vehicular drive system. The inside of the outer race of a constant velocity joint makes direct contact with steel balls or rollers on the inner race, so it needs to have increased hardness to improve its ability to resist wear and tear. On the other hand, its inside needs to retain its toughness in order to maintain its flexibility as a part. High-frequency induction hardening is used as a heat treatment method that hardens only the surface of a product. With this method, using a high-frequency power supply makes it possible to heat the surface locally and rapidly. This process also has many other benefits, such as providing a clean working environment because it uses electrical equipment, being very efficient, and providing uniform results for each product. This is why it is being aggressively implemented in the field. It is difficult to predict the hardening of the inside of a constant velocity joint because its uneven geometry makes eddy currents and magnetic flux flow in a complex manner. With interior hardening like the kind used in this example, the heating coil design must follow spatial constraints. The eddy currents that are generated from a high-frequency varying magnetic field are offset on the surface of the part's interior, so the material properties change a great deal as the temperature rises. This is why it is necessary to predict the amount of heat generated in a numerical analysis based on the finite element method (FEM) in order to handle the detailed phenomena. This Application Note shows how to run an analysis of the elevated temperature process by using the geometry of a coil to evaluate whether or not the target temperature conditions are fulfilled.



Joule Loss Density Distribution

The joule loss density distribution produced in the outer race is shown in fig. 1. Eddy currents are generated in the outer race by time variations in the magnetic field created by the coil. In induction heating, these eddy currents become a heat source for the work piece. At high frequencies the work piece is strongly affected by the skin effect, so the eddy currents are distributed near its surface.

Temperature Distribution

The temperature distribution of the outer race is shown in fig. 2. The eddy currents cause heat to generate in the outer race, so the temperature rises as time passes. At 2 s most of the inside of the outer race reaches the Curie point of 800 deg C, but there is variation in the temperature distribution. Improvements need to be made to the coil geometry in order to achieve uniform heating on the inside of the outer race.

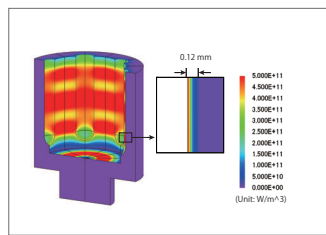


Fig. 1. Joule loss density distribution

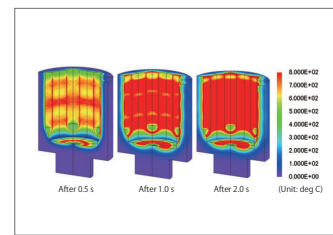
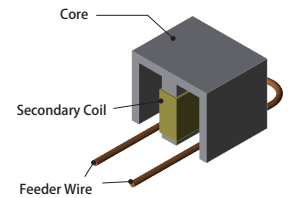


Fig. 2. Temperature distribution

Overview

A wireless power transfer system is a device which uses electromagnetic induction to provide electric power without physical contact. They can be used for various applications, such as moving or rotating devices, or devices sealed inside enclosed spaces. Because the primary and secondary sides do not touch, the power transmission efficiency and leakage flux vary depending on their positions relative to each other. Therefore, it is important at the design stage to understand how properties change according to their placement.

When evaluating the properties of a transformer whose primary and secondary sides are separated by a gap, it is helpful to use magnetic field analysis based on the finite element method (FEM), which allows precise modeling of the geometry of the parts and their relative positions, and makes it possible to visualize the leakage in the magnetic flux that is generated in the primary side and transmitted to the secondary side. This Application Note presents how to obtain the power transmission efficiency when the feeder wire's position is moved in both the horizontal and vertical directions from a reference position, and how to display the flow of magnetic flux.



Vertical Distance vs. Power Transmission Efficiency

Diagrams of the magnetic flux lines with the feeder wire moved in the vertical direction are shown in fig. 1, and the power transmission efficiency is shown in fig. 2. As the distance between the feeder wire and the core gets larger, the amount of leakage flux increases and the linkage flux in the secondary coil decreases. In this way, the power transmission efficiency is reduced.

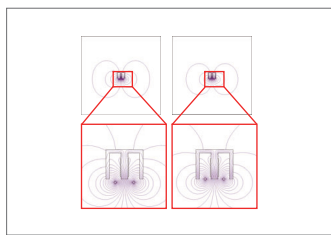


Fig. 1 Magnetic flux lines (left: primary coil moved downward vertically 15 mm; right: reference position)

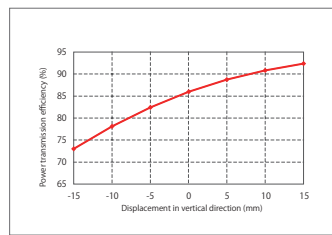


Fig. 2 Vertical distance vs. power transmission efficiency

Horizontal Distance vs. Power Transmission Efficiency

Diagrams of the magnetic flux lines with the feeder wire moved in the horizontal direction are shown in fig. 3, and the power transmission efficiency is shown in fig. 4. When the feeder wire is moved horizontally from the reference position, the balance of magnetic flux in the core becomes distorted to the left and right. Variations in the linkage flux in the secondary coil are small, and variations in power transmission efficiency are also small.

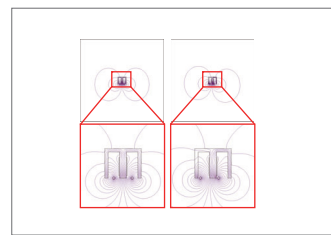


Fig. 3 Magnetic flux lines (left: reference position; right: primary coil moved horizontally 15 mm)

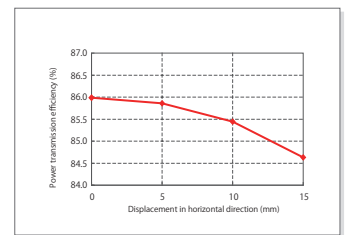
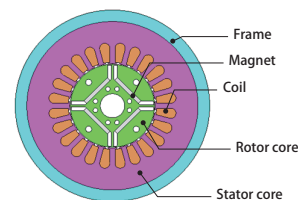


Fig. 4 Horizontal distance vs. power transmission efficiency

Case
87

Iron Loss Analysis of an IPM Motor Including the Effect of Shrink Fitting

module: DP, DS, LS



Overview

Magnetic steel sheet is used for the cores of drive motors for HEVs and EVs. This is to make them more compact, lighter, and more efficient. The main point for improving efficiency in an IPM motor's high rotation speed region is how to reduce iron loss. However, shrink fitting is used in order to strengthen the joint between frames and stator cores with laminated structure. The compressive stress generated during shrink fitting is known to increase iron loss. Therefore, it is important to account for the effects of this stress when evaluating iron loss.

Iron loss is generated when there are magnetic-field variations in steel sheet. Also, the amount of iron loss depends on the steel sheet's iron loss properties. These iron loss properties of steel sheet become worse when it is subjected to stresses such as shrink fitting. The stress caused by shrink fitting has its own distribution, and is particularly large in the back yoke. So, in order to evaluate the iron loss with good accuracy, it is necessary to correctly obtain the stress distribution for the magnetic flux, time variation, and steel sheet. In recent research, it has been mentioned that in order to increase the precision of stress dependency for iron loss, stress distribution is not the only requirement; evaluations accounting for changes in magnetic flux density over time for each primary axis of principle stress is also a requirement.

Based on the results of iron loss with no stress, this document will compare the results of iron loss accounting for only the size of stress, and iron loss accounting for changes in magnetic flux density over time for each principle stress. (hereafter referred to as iron loss accounting for stress tensor)

Principal stress distribution

Fig. 1 demonstrates compressive stress distribution and stress tensor for principle stress. It shows that compressive stress occurs in the back yoke and the direction is the circumferential direction. We learn that compressive stress caused by the frame compressing in the radial direction becomes bigger in the slot area. This is because the stress is damped towards the tips of the teeth, while it cannot be damped and concentrates at the slots.

Magnetic flux density (basic wave components) distribution

Fig. 2 demonstrates effective value distribution for the basic wave components (60Hz) of magnetic flux density when accounting for stress. The radial direction components of the magnetic flux density are the main components in the teeth, on the other hand, the circumferential direction components are the main components in the back yolk. Upon evaluating iron loss for stress dependencies, these differences in magnetic flux density distribution effect on the methods: if only the stress size is accounted for, or if changes in magnetic flux density over time for each principle stress are accounted for.

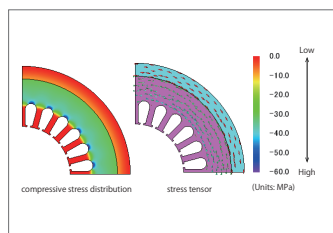


Fig. 1. Principal stress

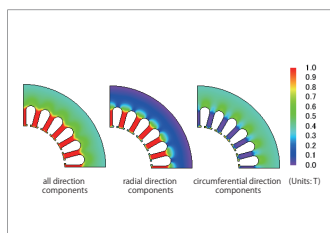


Fig. 2. Effective value distribution of magnetic flux density for basic wave (60Hz)

Iron Loss Density Distribution

Fig. 3 shows the iron loss density distribution. In order from the left: results of not accounting for stress, accounting for only stress size, and accounting for stress tensor. We learn that depending on if stress is accounted for or not, iron loss density distribution varies, and iron loss values increase approximately 60 percent. This is believed to be due to loss becoming greater from stress, and in order to match iron loss with actual measurements, an analysis accounting for stress due to shrink fitting is required. In the comparison regarding stress dependency methods, differences become visible with an analysis accounting for stress size only and an analysis accounting for stress tensors around the base of the teeth. This is due to magnetic flux density distribution around the base of the teeth greatly affects the radial direction components, and an analysis accounting only for compressive stress can be overestimated compared to an analysis accounting for variations of magnetic flux density over time for each principle stress.

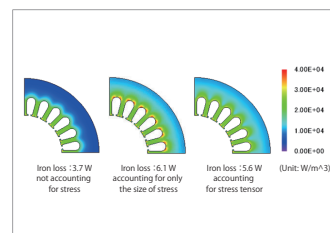
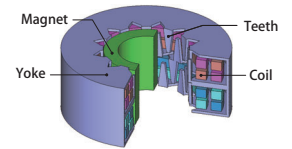


Fig. 3. Iron loss density distribution

Overview

PM stepper motors are commonly used for positioning of moving parts in small devices such as printers and video equipment. In order for its drive to function with an open loop, the most important characteristics for a stepper motor are controllability and holding torque, and not the motor's output. Therefore, the desired characteristics are detent torque, which is a non-excitation holding torque, and stiffness torque, which is an excitation holding torque. A PM stepper motor is made up of a multi-pole magnetized rotor and offset inductors for each phase. In order to reduce their size and number of parts, claw pole inductors are made from folded steel sheet. Because of this, the flow of magnetic flux is three dimensional, so it is necessary to carry out a 3D electromagnetic field analysis using the finite element method (FEM) to proceed with an accurate preliminary study.

This Application Note describes how the stiffness torque at 0.5 A of current can be calculated for a PM stepper motor.



Stiffness Torque

Fig. 1 shows the stiffness torque with one-phase excitation and fig. 2 shows the stiffness torque with two-phase excitation. Fig. 3 shows the magnetic flux density distribution of the yoke with one-phase excitation at a rotation angle of 5.5 deg. Fig. 4 shows the magnetic flux density distribution of the yoke with two-phase excitation at a rotation angle of 5.0 deg. A maximum torque of 0.26 Nm is obtained at 5.5 deg for one-phase excitation, and 0.27 Nm is obtained at 5.0 deg for two-phase excitation. The magnetic flux density is concentrated at the inductor regardless of the excitation.

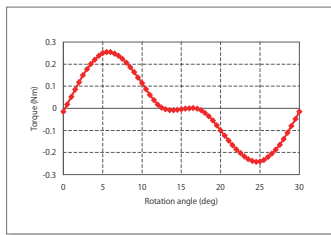


Fig. 1 Stiffness torque with one-phase excitation

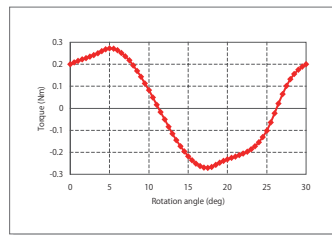


Fig. 2 Stiffness torque with two-phase excitation

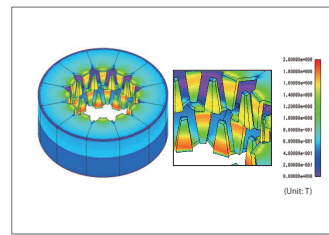


Fig. 3 Magnetic flux density distribution (at 5.5 deg) for one-phase excitation

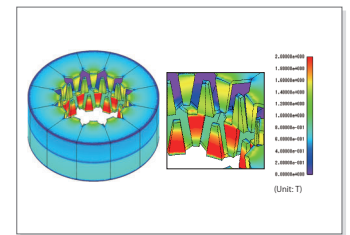


Fig. 4 Magnetic flux density distribution (at 5.0 deg) for two-phase excitation

Case 90 Analysis of the Effect of PWM on the Iron Loss of an IPM Motor

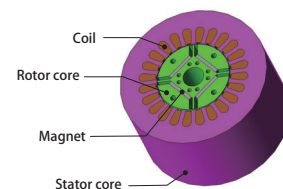
module: DP, LS

Overview

Current vector controls are generally used in interior permanent magnet synchronous motors (hereinafter referred to as IPMs), and among them PWM inverters are widely utilized to create a command current. It is vital to get a good understanding of iron losses in order to raise the efficiency of an IPM motor. However, iron losses increase when power is converted by the PWM inverter because the carrier harmonic created by the PWM becomes superimposed on the current and the magnetic flux density waveform in the IPM motor's core.

There are three methods to gain an understanding of iron loss that accounts for PWM carrier harmonics: There is the method of linking a control / circuit simulator that contains the PWM inverter with a magnetic field analysis by inputting the current waveform obtained from the simulation into the analysis, the method of inputting the actual measurements of a current into a magnetic field analysis, and the method of inputting the estimated harmonic current.

This Application Note demonstrates a case study where the effects of a carrier harmonic against an IPM motor's iron loss is confirmed using estimated harmonic current waveform as input.



Iron Loss

A comparison of the hysteresis losses, and joule losses when the IPM motor is driven by a PWM inverter and a sinusoidal current are shown in fig 1 and Fig. 2.

The iron losses in both the rotor core and the stator core increase when the IPM motor is run using a PWM inverter. The joule losses increase the most severely, increasing 70% in the rotor core, and 20% in the stator core.

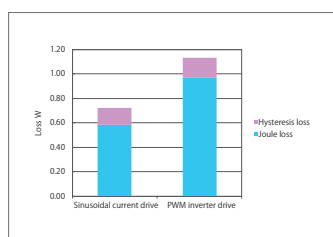


Fig. 1 Ratio of loss (Rotor core)

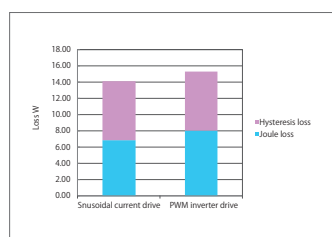


Fig. 2 Ratio of loss (Stator core)

Joule Loss/ Joule Loss Density Distribution

The joule loss frequency components are shown in Fig. 3 and Fig. 4, and the joule loss density distribution is shown in Fig. 5 and Fig. 6.

The fundamental frequencies (360 Hz in the rotor core and 60 Hz in the stator core) and harmonic components have almost the same amounts of iron loss in the rotor core and stator core whether a sinusoidal current drive or a PWM inverter drive is used. However, iron loss is only produced during PWM inverter drive for the PWM's fundamental frequency (10 kHz). (These values are indicated inside the green square in the Fig. 3 and Fig. 4.)

The increased joule losses when the motor is run using a PWM inverter are caused by the carrier harmonic.

The effects of a carrier harmonic need to be evaluated to analysis the characteristics of an IPM motor in detail.

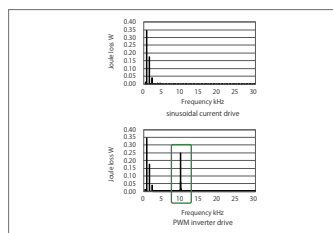


Fig. 3. Joule Loss Frequency Component of Rotor Core

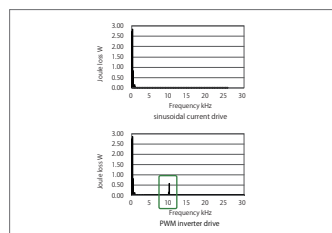


Fig. 4. Joule Loss Frequency Component of Stator Core

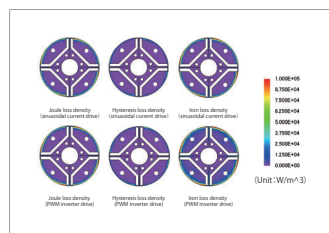


Fig. 5. Loss Density Distribution of Rotor Core

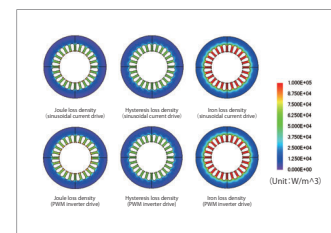


Fig. 6. Loss Density Distribution of Stator Core

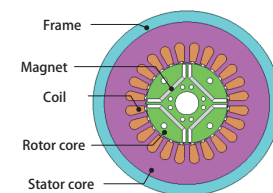
Case 91 Iron Loss Analysis of an IPM Motor Including the Effects of Press Fitting Stress

module: DP, DS, LS

Overview

One of the demands for IPM motors is higher efficiency over a wide range of rotation speeds in combination with motor drives, as reluctance torque can be used in addition to magnet torque. Iron loss makes up a particularly large proportion of total loss in the high rotation region, and how to make this smaller is a major design issue. Generally, IPM motor cores have laminated structures, and methods such as press fitting or shrink fitting are used to maintain them. For motors using magnetic steel sheet for their cores, the stress generated by press fitting can increase iron loss, so it is important to take this stress into account when evaluating iron loss. Iron loss is generated when there are magnetic-field variations in steel sheet. Also, the amount of iron loss depends on the steel sheet's iron loss properties. These iron loss properties of steel sheet become worse when it is subjected to stresses such as press fitting. The stress caused by press fitting has its own distribution, and is particularly large in the back yoke. So, in order to evaluate the iron loss with good accuracy, it is necessary to correctly obtain the stress distribution for the magnetic flux, time variation, and steel sheet.

This Application Note presents modeling the press fitting of a core and frame with the Press Fit condition and then obtaining the iron loss density of an IPM motor with and without accounting for the stress generated at that time.



Minimum Principal Stress Distribution

The minimum principal stress distribution is indicated in fig.1. Tensile stress occurs in the frame and teeth, but compressive stress that especially affects the iron losses is produced largely in the yoke. The compressive stress is especially large in the area of the model within the square in fig.1, but this is because of the slots' geometry.

Iron Loss Density Distribution

Fig.2 shows the iron loss density distribution. The iron loss density distribution varies depending on whether or not the stress is accounted for. The iron losses are increased by 10 % due to the stress. An analysis that accounts for the compressive stress caused by the press-fitting needs to be performed to evaluate the iron losses more accurately because the iron losses increase when the compressive stress is applied.

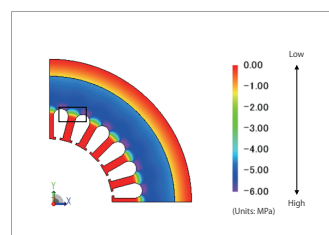


Fig. 1 Minimum principal stress distribution

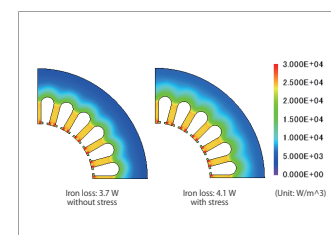


Fig. 2 Iron loss density distribution

Case 94

Analysis of Detent Torque of a PM Stepper Motor

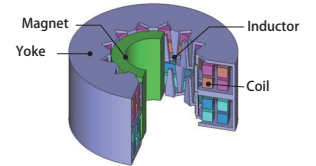
module: TR

Overview

PM stepper motors are commonly used for positioning of moving parts in small devices such as printers and video equipment. In order for its drive to function with an open loop, the most important characteristics for a stepper motor are controllability and holding torque, and not the motor's output. Therefore, the desired characteristics are detent torque, which is a non-excitation holding torque, and stiffness torque, which is an excitation holding torque.

A PM stepper motor is made up of a multi-pole magnetized rotor and offset inductors for each phase. In order to reduce their size and number of parts, claw pole inductors are made from folded steel sheet. Because of this, the flow of magnetic flux is three dimensional, so it is necessary to carry out a 3D electromagnetic field analysis using the finite element method (FEM) to proceed with an accurate preliminary study.

This Application Note describes how the detent torque can be calculated for a PM stepper motor.



Detent Torque/ Magnetic Flux Density Distribution

The detent torque is shown in fig. 1, and the magnetic flux density distribution in the yoke at a rotation of 7.5 deg is shown in fig. 2.

From the geometry, the detent torque seems to have a period of 7.5 deg, but due to the three dimensional flow of magnetic flux between the upper inductor and the lower inductor, the period is 15 deg.

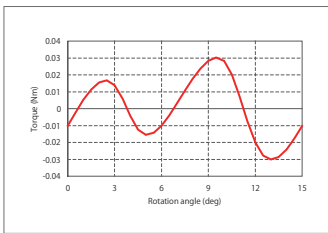


Fig.1. Detent Torque

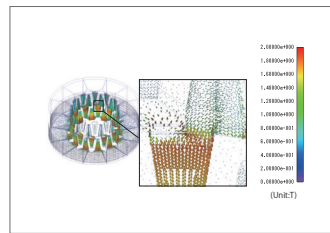


Fig. 2 Magnetic flux density distribution in the yoke (at rotation of 7.5 deg)

Case 95

Analysis of a Universal Motor

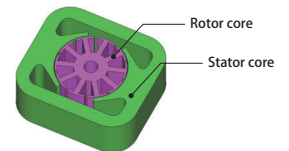
module: DP

Overview

Motors in electrical industrial equipment are often used for cutting and machining, so it is desirable for them to be usable at high rotation speeds. Induction motors cannot achieve high rotation speeds with commercial power supplies because their rotation speed is determined by alternating current frequency. DC brush motors can achieve high rotation speeds, but it is necessary to provide DC power for them, so they cannot be used with commercial power supplies. Universal motors, on the other hand, are designed to be connected to commercial power supplies, and because they can rotate at high rotation speeds with either direct or alternating current, they can fulfill purposes needing thousands of r/min, such as electric drills. Because of their high degree of versatility, they are widely used in everyday-life applications. Users of industrial tools often hold them in their hands, making reduced weight desirable in addition to low vibration and noise levels. Development to solve these issues is being carried out in universal motor design.

The basic structure is the same as in a brush motor, but when the supplied power is alternating current, the output itself varies periodically. Further, they are used under difficult conditions such as when inrush current occurs when a commercial power supply is directly connected from a stopped state. Therefore, electromagnetic field analysis using the finite element method (FEM), which can account for nonlinear magnetization properties of the materials, is useful in order to evaluate magnetic saturation during overload.

This note presents how the characteristics of a universal motor can be obtained, including torque versus current (T-I), torque versus speed (T-N), and magnetic flux density distribution.



Magnetic Flux Density Distribution

Fig. 1 shows the magnetic flux density distribution at rotation speeds of 4000 r/min and 8000 r/min.

More current flows in a universal motor during low rotation speeds than during high rotation speeds, so magnetic flux and torque are both higher. However, a magnetic circuit and motor design that does not allow magnetic saturation to occur at low rotation speeds is desirable because performance may be worse for a motor in which magnetic saturation occurs easily.

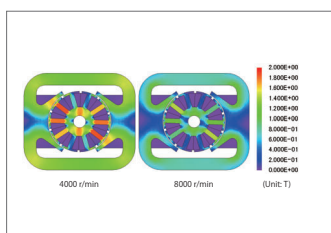


Fig. 1. Magnetic flux density distribution at a rotation angle of 1060 deg

Speed-Torque and Torque-Current Curves

The speed-torque curve is shown in fig. 2, and the torque-current curve is shown in fig. 3. As can be seen from the two graphs, in a universal motor, the torque gets smaller as rotation speed rises, and the torque gets larger as current increases.

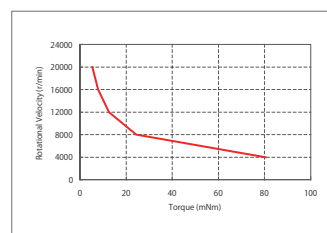


Fig. 2. Speed-Torque Curve

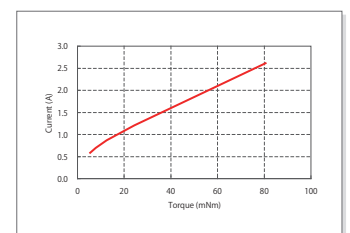
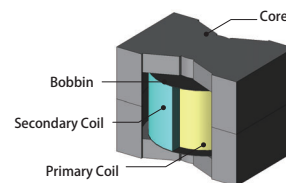


Fig. 3. Torque-Current Curve

Case 97

Sound Pressure Analysis of a Transformer

module: DS, FQ



Overview

In recent years, the demand to reduce vibration and noise is growing while the requirements for higher efficiency and smaller and lighter transformers grow with environmental conservation trends. The primary cause of noise for transformers is the electromagnetic vibrations and the resonance phenomena at the eigenfrequency of the structure. A sound pressure analysis can be performed with a coupled magnetic field and structural analysis that uses the electromagnetic force as excitation force. This example presents the use of a coupled magnetic field and structural analysis to obtain the sound pressure distribution accounting for the electromagnetic force of the core when the transformer is operating on a power supply frequency of 6 kHz.

Electromagnetic Force Distribution

Fig. 1 shows the electromagnetic force distribution of the core while driven. From the figure, it can be seen that a large force is generated in the Z-axis direction in the gap. Also, because this electromagnetic force works as an attraction force, the frequency is 12 kHz, double the power supply frequency.

Eigenmode

The Eigenmode of the transformer are indicated in fig. 2. This shows that there is not much deformation in the Z-axis direction in the low-order Eigenmode, relatively close to the electromagnetic force's frequency of 12 kHz. Modes where the area around the gap deforms in the Z-axis direction include 47 kHz and 66 kHz.

Acceleration Distribution

The acceleration distribution at 12 kHz is shown in fig. 3. The deformation modes are larger at 47 kHz and 66 kHz, as indicated in this figure. This is because the electromagnetic force generated near the core's gap and the deformation modes at 47 kHz and 66 kHz are in the same Z-axis direction. The figure also shows that the deformation in the core's sides increases with the attraction force in the gap. However, there are no resonance phenomena because the frequency of the electromagnetic force is sufficiently smaller than the Eigen frequency.

Sound Pressure Distribution

The sound level distribution at 12 kHz is shown in fig. 4. The sound pressure is higher in the Z-axis direction, in which the electromagnetic force works, and in the X-axis direction, in which the core's deformation is larger. The reason why the sound pressure levels are not too high is that the electromagnetic frequency of 12 kHz and the Eigen frequencies of the deformation modes that greatly influence the electromagnetic vibration are far apart.

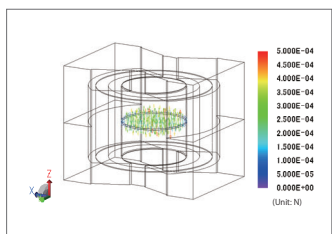


Fig.1. Electromagnetic force distribution

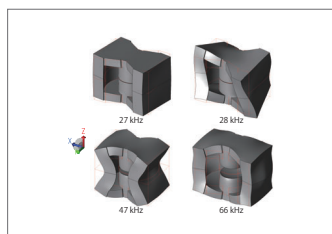


Fig.2. Eigenmode (red outline: original model)

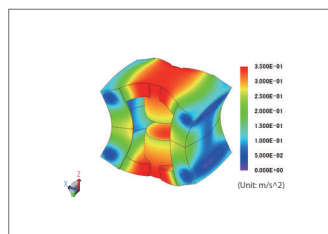


Fig.3. Acceleration distribution at 12 kHz

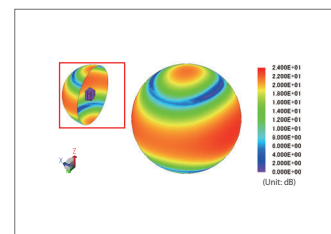
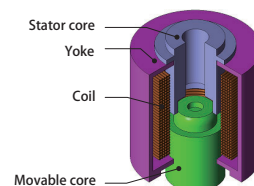


Fig.4. Sound pressure level distribution at 12 kHz

Case 98

Response Analysis of a Solenoid Valve Using a Control Simulator and the JMAG-RT

module: DP, RT



Overview

A solenoid valve opens and closes valves using the force of electromagnets. A valve that control s the amount of fluid flowing has various states of open and closed. For this reason, this analysis evaluates the response, such as the speed and position control, of a valve to commands. An analysis that accounts for both the magnetic circuit characteristics of solenoid valve and control characteristics are necessary to measure the response time of the solenoid valve or position controllability because both two characteristics have influences. JMAG enables you to create a detailed and actual-machine faithful solenoid valve model that accounts for attraction force contained in a solenoid valve, inductance harmonic, or current dependency. A link simulation that accounts for both the solenoid valve magnetic saturation, or spatial harmonic and the control characteristics of the motor drive can be run by importing this solenoid valve model "JMAG-RT model" in a circuit/control simulator. This note presents how JMAG-RT can be used to calculate attraction forces and coil inductance that varies with harmonic and current. The result is the JMAG-RT model used as a reference for a circuit / control simulator that runs a transient analysis to run an analysis that controls the solenoid valve position within the desired Value.

The position of the movable core and the excitation current versus time

The position of the movable core versus time is indicated in Fig.1. , and the excitation current versus time is indicated in Fig.2. The position of the movable core is moved from 0 mm to 1.5 mm, and then moved from 1.5 mm to 3.0 mm, as indicated in Fig.1. Even though the movable core moves 1.5 meters in both instances, the method to move the core differs due to the electromagnetic force, current dependency of the inductance, position, and the spring constant. A surge occurs the moment the movable core begins moving, as indicated in Fig.2. This surge should be investigated further if it is fairly large, because electrical equipment near the surge could be damaged.

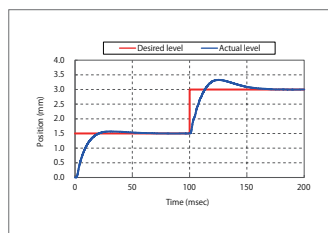


Fig. 1. Position of the movable core versus time

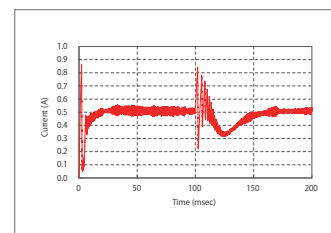


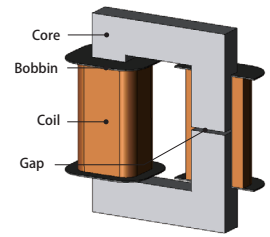
Fig. 2. Excitation current versus time

Superimposed Direct Current Characteristics Analysis of a High Current Reactor

module: TR

Overview

High-frequency, high-current reactors have a current composed of direct current with high-frequency ripple superimposed on it. In terms of reactor performance, stable inductance over a wide range of direct current is desirable. Also, the gap installed to prevent magnetic saturation in the core has a large effect on the inductance, and thus is a vital parameter in reactor design. Finite element method (FEM) analysis is useful for accurately estimating inductance over a wide current range, while also accounting for the effects of the gap's inductance and nonlinearity in magnetization properties, and applying this during design. This Application Note presents how to obtain a high-current reactor's superimposed direct current characteristics when the gap length is varied.



Superimposed Direct Current Characteristics

The relationship between the length of the flux path, the gap length, and the inductance when the direct current is 25 A is indicated in table 1, the superimposed direct current characteristics are indicated in fig. 1, and the magnetic flux density distribution is indicated in fig. 2. From table 1, it is apparent that the inductance decreases as the gap length becomes larger. This is because the magnetic resistance of the entire magnetic circuit is made up of the magnetic resistances in the core and the gap connected in series, and the magnetic resistance of the gap increases with gap length. From fig. 1, it can be seen that the direct current at which the inductance starts decreasing is smaller with a shorter gap. This is because the core becomes magnetically saturated more easily as the gap becomes shorter, as shown in fig. 2.

Flux path length (mm)	Gap length (mm)	Inductance (μH)
440	2	36.06
	3	26.96
	4	22.07

Table 1 Values at current of 25 A

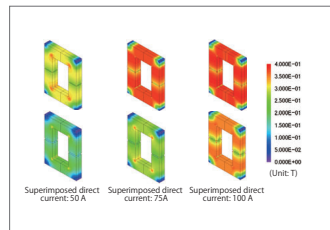


Fig. 2. Magnetic flux density distribution (top: gap length 2 mm ; bottom: gap length 4 mm)

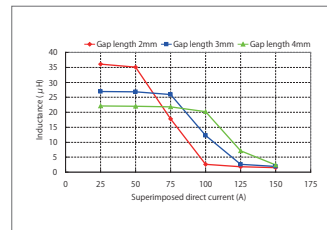


Fig. 1 Superimposed direct current characteristics

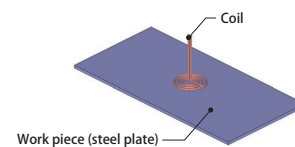
Case 100 Surface Heating Analysis of a Steel Plate

module: FQ, HT

Overview

High-frequency induction heating is one heating method used when heat treating the surface of a steel plate. With induction heating, the heating depth can be adjusted because it is possible to localize heating by modifying the coil's geometry and electrical power. The coil geometry, heating conditions, etc. must be designed correctly in order to achieve heating as desired, but the cost and time needed for prototyping can be a problem. To make accurate predictions, it is necessary to account for the temperature dependency of the thermal conductivity, the electrical conductivity, and the detailed coil geometry in order to find the heat generation distribution. Electromagnetic field simulation using the finite element method (FEM) is needed for this type of prediction.

This Application Note presents how to confirm the uniformity of the surface temperature distribution in the steel plate facing the coil and check for an eddy current loss density distribution that causes the temperature distribution to be uneven, when a mosquito-coil-shaped coil is in position.



Eddy Current Loss Density Distribution

The eddy current loss density distribution generated in the steel plate and the eddy current loss density distribution in a cross-section of the steel plate are shown in Fig. 1 and Fig. 2. The eddy currents generated by the magnetic field variations created by the coil are distributed to the surface of the steel plate by the skin effect.

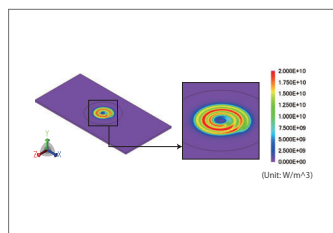


Fig. 1 Eddy current loss density distribution in the steel plate between 1.9 and 2.0 s

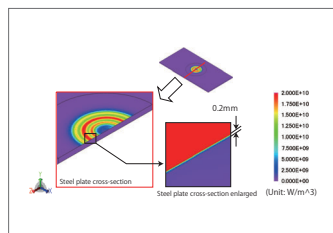


Fig. 2 Eddy current loss density distribution in the steel plate cross section between 1.9 and 2.0 s

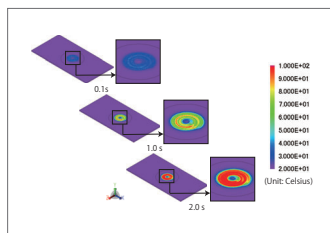


Fig. 3 Temperature distribution of the steel plate

Temperature Distribution

The temperature distribution of the steel plate at 0.1 s, 1.0 s, and 2.0 s is indicated in fig. 3. The temperature versus time is indicated in fig. 4, and the temperature distribution in the cross-section of the steel plate is indicated in fig. 5. The temperature of the surface of the steel plate rises over time, reaching about 100 deg C in the steel plate surface below the coil at 2.0 s. Heating occurs first in the surface, with the heat then transferred gradually to the inside of the steel plate, because the eddy currents are concentrated on the steel plate surface.

The temperature distribution of the steel plate is uneven because of the coil's geometry. Improvements need to be made to the coil geometry in order to achieve uniform temperatures in the steel plate.

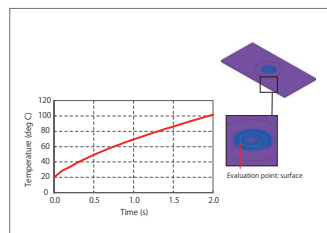


Fig. 4 Temperature variation of the steel plate surface

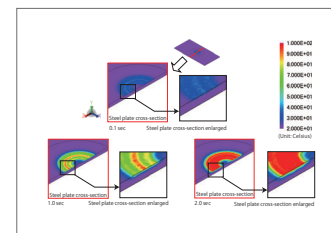


Fig. 5 Temperature distribution in the steel plate cross section

Case 101

AL-Value Current Characteristics Analysis of a Choke Coil

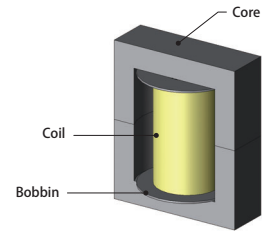
module: ST, TRANSFORMER_TEMPLATE

Overview

A choke coil is an electric component that is intended to filter high-frequency current. The AL-value is a vital parameter in a choke coil design that determines the cutoff frequency of a high-frequency current.

Because the AL-value is often set as a design specification and AL-value is a nonlinear magnetic property of the core, it varies widely according to the making current. Finite element analysis (FEA) enables accurate reflection of magnetic properties, and so can obtain AL-value current properties and provide feedback for design.

This note presents the use of a magnetic field analysis to obtain the AL-value current properties of a choke coil.



Magnetic Flux Density, Flux Linkage, and AL-value

The magnetic flux density distributions of the core for currents of 0.5 A and 0.7 A are indicated in fig. 1, the current characteristics of the flux linkage are indicated in fig. 2, and the current characteristics for the AL-value are indicated in fig. 3. If the current flowing in the coil increases, the flux linkage increases only minimally because of magnetic saturation in the core. Furthermore, the AL-value is smaller due to magnetic saturation in areas where the current is large because the AL-value is the inductance per turn in the coil.

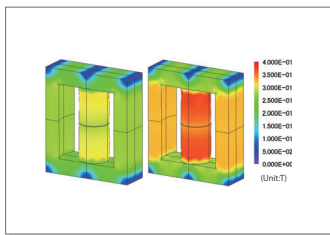


Fig. 1. Magnetic flux density distribution (left: current 0.5 A; right: current 0.7 A)

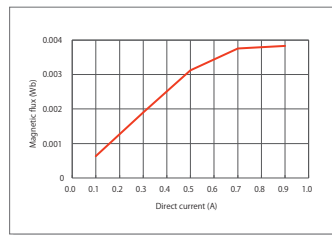


Fig. 2. Direct current versus flux linkage

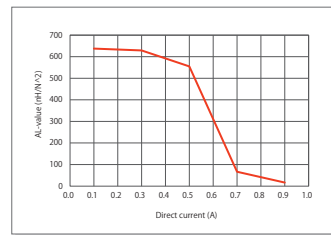


Fig. 3. Direct current versus AL-value

Case 102

Magnetic Field Analysis of a Magnetic Sensor

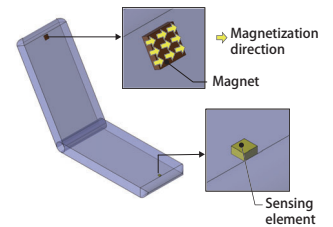
module: ST

Overview

With recent improvements in the functionality of electric devices and home appliances, magnetic sensors are being used more for contactless sensing of whether device doors, etc. are open or closed. An open/closed switch using a magnetic sensor switches between open and closed by sensing distance according to the size of the magnets' magnetic field. At the design stage, it is necessary to evaluate magnet type and position, sensor sensitivity, and other issues.

Magnetic field analysis simulation using the finite element (FEM) method is effective for accounting for differences in magnetic field strength due to three-dimensional positioning and interference from other magnetic parts.

This Application Note presents how to obtain the magnetic flux density distribution at points in the horizontal and vertical directions away from the magnet.



Magnetic Flux Density Distribution

The magnetic flux density distribution of the Z component produced around the magnet is indicated in fig. 1. The horizontal distance versus Z-component magnetic flux is indicated in fig. 2. The rotation angle versus θ component magnetic flux is indicated in fig. 3. Positive values are indicated in the positive direction of the Z-axis, and negative values are indicated in the negative direction of the Z-axis. The magnetic flux density value at a spatial coordinate is analyzed ignoring the volume of the sensing element.

As indicated in fig. 1, the magnetization direction of the magnet has negative values on the Z-axis in the vertical direction, and works in the opposite direction in the horizontal direction. For this reason, if the sensing element is moved in a horizontal direction, the magnetic flux density that has a negative value in its initial position weakens toward a positive value when the sensing element is moved away from the magnet, as indicated in fig. 2. The direction of the magnetic flux density does not change within a rotation angle range of 15 deg, and the θ -component magnetic flux density decreases when the sensing element is moved away from the magnet, as indicated in fig. 3.

The magnetic flux density distribution can be evaluated in detail, and the detection range of the magnetic flux density can be estimated from these results.

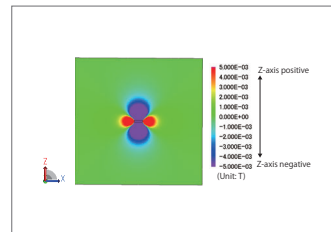


Fig. 1. Magnetic flux density distribution of the Z component

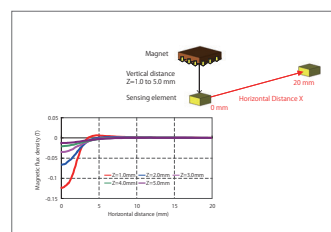


Fig. 2. Horizontal distance versus Z-component magnetic flux density

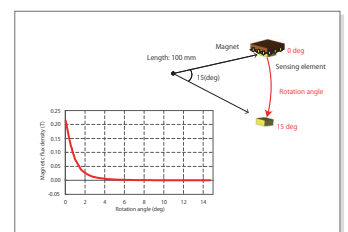
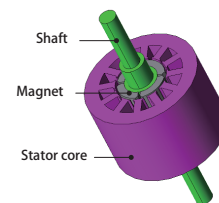


Fig. 3. θ -component magnetic flux density versus rotation angle (rotation radius: 100 mm)

Case 103 Efficiency Analysis of a Permanent Magnet Synchronous Motor

module: DP, LS



Overview

PM motors can achieve high efficiency over a wide range of drive regions compared to inductance and brush motors because they use the magnetic field from their magnets. Thinking of the motor as an energy converter, "efficiency" here means the degree of efficiency with which electric energy is converted to kinetic energy. The main indicators are the power factor, which can show whether electric power is being used effectively, and efficiency, which shows the ratio of input power to output power. Because a motor's characteristics vary widely according to its geometry and control, it is necessary to do an evaluation considering a number of parameters in order to improve efficiency. It is difficult to accurately evaluate a motor's characteristics in advance using the magnetic circuit method or other methods, therefore it is necessary to run an electromagnetic field analysis using the finite element method (FEM). In this example, how to obtain the efficiency with a sinusoidal wave voltage drive at a rotation speed of 1,800 r/min and voltage amplitude of 40 V.

Voltage Waveform/Current Waveform

The voltage waveform and current waveform for the U-phase are indicated in Fig. 1. The Fig. 1 shows that there is displacement between the phase voltage and phase current. This phenomenon occurs due to inductance. In addition, the apparent power is 78.9 VA when calculated from each effective value and converted to the three phases.

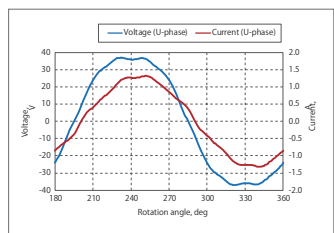


Fig. 1. U-phase Voltage Waveform and the Current Waveform

Active Power Waveform/Power Vector Plot

The U-phase active power waveform is shown in Fig. 2, and the power vector plot is shown in Fig. 3. When the U-phase average active power is calculated according to Fig. 2 and converted to the three phases, the value is 76.6 W. The power factor and power factor angle are calculated from the ratio of the active power and apparent power, which is 0.97 and 13.8 deg for this motor. The reactive power can be obtained from the apparent power and power factor angle and displayed in a vector plot as in Fig. 3.

Output Characteristics

The torque waveform is shown in Fig. 4 and the output characteristics value is shown in Table 1. The average torque 0.30 Nm can be obtained from Fig. 4. The motor output 55.7 W can be calculated from the obtained torque and rotation speed. Note that the copper loss consumed by the coil is 20.0 W. The efficiency of this motor, 70.0 % is calculated from the output, iron loss and copper loss.

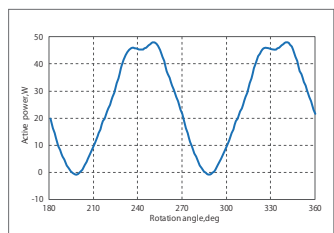


Fig. 2. U-phase Active Power Waveform

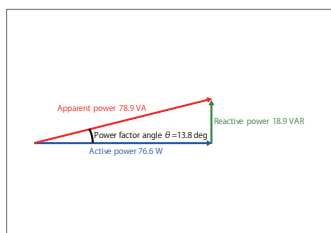


Fig. 3. Power Vector Plot

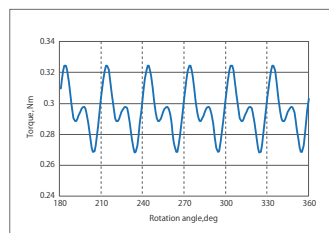


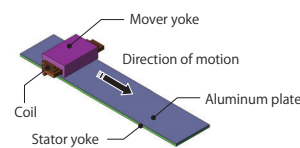
Fig. 4. Torque Waveform

Parameter	Value
Average Torque, Nm	0.30
Output, W	55.7
Iron loss, W	3.9
Copper Loss, W	20.0
Efficiency, %	70.0

Table 1. Output Characteristics Value

Case 104 Thrust Force Analysis of a Linear Induction Motor

module: DP



Overview

Linear motors are widely used for carrier devices and machine tools because of their high-speed performance, high acceleration and deceleration, and accurate positioning. One type of linear motor, the linear induction motor, can be constructed at low cost because it can use a primary side with coils, and a secondary side made of a conductor that is not magnetized, such as aluminum or copper. Linear induction motors have unique phenomena called end effects that cause reduced performance at low slip, so it is important to grasp thrust force characteristics, including end effects, using magnetic field analysis when evaluating these motors. This Application Note presents how to obtain thrust force characteristics for a linear inductance motor.

Eddy Current Density Distribution

The eddy current density distribution and magnetic flux lines are shown in fig. 1. Thrust force is produced through the interaction between the eddy currents and magnetic field when eddy currents occur in the aluminum sheet due to variations in the magnetic field created by the coils. More eddy currents remain behind the motor at a translation speed of 3.7125 m/s than at a translation speed of 1.2375 m/s, as indicated in fig. 1. This is because variations in magnetic flux to the rear of the motor increase as the translation speed is increased.

Thrust Force

The thrust force characteristics are shown in fig. 2. When this linear induction motor starts from a stationary state and accelerated to a synchronous speed, the thrust force reaches a maximum of 360 N at a translation speed of 1.2375 m/s and then falls thereafter. This is because the amount of variation in the magnetic flux in the aluminum sheet is reduced as the variation in the magnetic field generated by the coil reaches a synchronous speed.

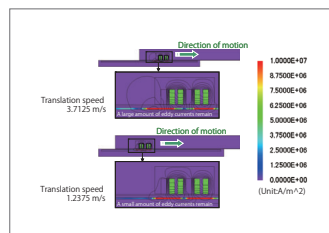


Fig. 1. Eddy current density distribution and magnetic flux lines at 0.16 s

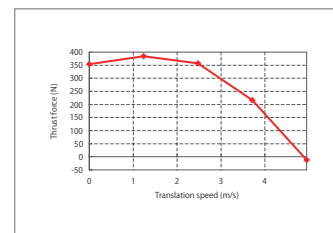


Fig. 2. Thrust force

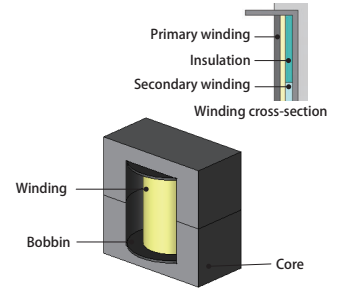
Case
105

Leakage Inductance Analysis of a Transformer

module: FQ, TS, TRANSFORMER_TEMPLATE

Overview

Inductance is an important physical quantity that determines a transformer's response characteristics against electric signals. Inductance is generally categorized into self-inductance and leakage inductance. Self-inductance is an indicator of to what extent the transformer can produce magnetic flux, and leakage inductance is an indicator of how much magnetic flux the transformer can send from the primary coil to the secondary coil without leaking. This is why self-inductance and leakage inductance are important items for transformer design requirements. The amount of inductance is dependent on the magnetic circuit, but the nonlinear characteristics of the magnetic properties make it so that the magnetic circuit changes when the operating point changes. The leakage inductance has all of the same properties, but it also has a flux path in non-magnetic regions, making it easily affected by the arrangement and geometry of the winding in addition to the core. This is why a magnetic field analysis using the finite element method (FEM) is necessary when evaluating these types of inductance. This Application Note explains how to obtain self-inductance and leakage inductance for two types of secondary coiling in a transformer: uniform coiling and close coiling.



Inductance

The inductance of the transformer when the secondary coil has a uniform coiling and close coiling is indicated in table 1. The model that has a secondary coil with a closed coiling has a larger leakage inductance.

Evaluating Leakage Inductance

The leakage inductance is obtained from the flux linkage of the primary coil when the secondary coil has a short circuit.

The flux linkage of the primary coil is evaluated as the flux leakage because the magnetic flux produced by the primary coil eliminates the flux linkage of the secondary coil. The variations of the flux leakage versus time can be evaluated from the voltage terminal of the primary circuit because they are induced voltage.

	Uniform coiling	Close coiling
Self-inductance	104 μ H	105 μ H
Leakage inductance	20 μ H	25 μ H

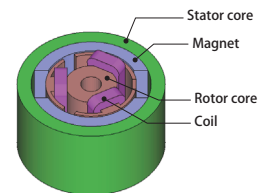
Table 1. Inductance of the transformer

	Uniform coiling	Close coiling
Voltage terminal connect to the current source	3.7 mV	3.8 mV

Table 2. Voltage terminal connect to the current source

Case 106 Iron Loss Analysis of a Brush Motor

module: DP, LS



Overview

Brush motors are used in many devices, particularly smaller-sized ones. With demands for energy-saving in recent years, higher efficiency is desired not only in high performance and large-scale motors used in HEVs and large appliances, but also in small-scale brush motors. To respond to these demands, it is important to reduce loss. Loss reduces efficiency directly, and also causes further reductions by increasing a device's temperature through heat generation, so it is necessary to know the amount and distribution of loss in order to create improved designs that suppress this loss. Motor loss is dominated by copper loss and iron loss, and copper loss can be more or less known from the current flowing in the coils. Iron loss, however, depends on material properties, drive conditions, and geometry, and is therefore difficult to evaluate through desktop calculation.

Magnetic analysis using the finite element method (FEM) is useful at the design stage because it can consider all electromagnetic behavior and motor geometry, and therefore makes estimation of the distribution and total amount of iron loss possible.

This note presents how to obtain the iron loss in the stator core and rotor core of a brush motor.

Magnetic Flux Density Distribution

The magnetic flux density distribution is shown in fig. 1, the r-component and theta component of the magnetic flux density waveform for measuring point 1 are shown in fig. 2, and the r-component and theta component of the magnetic flux density waveform for measuring point 2 are shown in fig. 3.

The magnetic flux density of the rotor core is greater than that of the stator core, as indicated in fig. 1. Figures 2 and 3 show that the amount of variation in the magnetic flux density at measuring point 1 is large, while the amount of variation in the magnetic flux density at measuring point 2 is small. This difference in the amount of variation has an effect on the iron loss.

Joule Loss Density Distribution/Hysteresis Loss Density Distribution/Iron Loss Density Distribution

The joule loss density distribution is shown in fig. 4, the hysteresis loss density distribution is shown in fig. 5, and the iron loss density distribution is shown in fig. 6. The proportions of the loss in the stator core and the rotor core are shown in fig. 7 and fig. 8.

The joule loss density is greater in areas that have larger variations in magnetic flux density compared to areas with smaller variations in magnetic flux density, as confirmed by the magnetic flux density waveform. The same trend can be seen with the hysteresis loss. Fig. 7 and fig. 8 confirms that the rotor core accounts for a greater proportion of the joule loss and hysteresis loss.

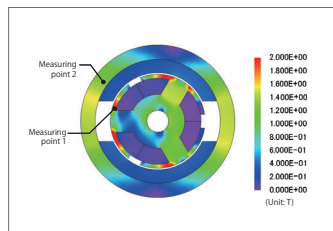


Fig. 1 Magnetic flux density distribution

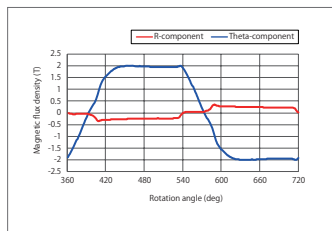


Fig. 2. Magnetic flux density waveform (measuring point 1)

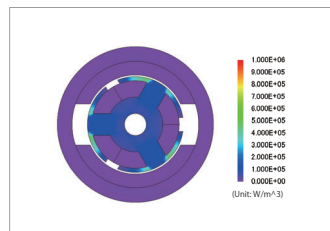


Fig. 5. Hysteresis loss density distribution

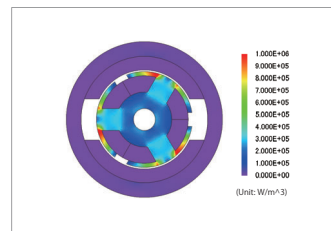


Fig. 6. Iron loss density distribution

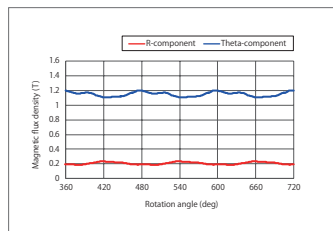


Fig. 3. Magnetic flux density waveform (measuring point 2)

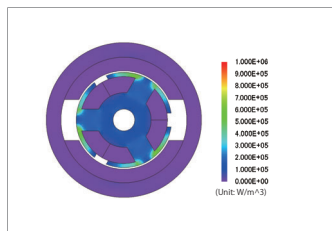


Fig. 4. Joule loss density distribution

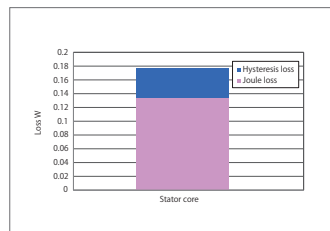


Fig. 7 Ratio of loss(Stator core)

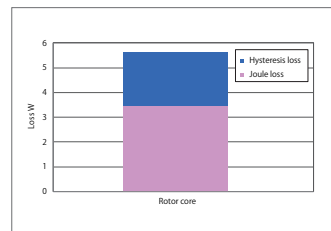


Fig. 8 Ratio of loss(Rotor core)

Case 107

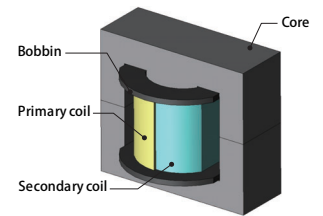
Current Voltage Characteristics Analysis of Flyback Converters

module: DP

Overview

DC-DC converters such as flyback converters control current of primary / secondary winding with switch operation, and transmit electrical power on the load side using diodes and condensers. Depending on its application, there is a need to satisfy current voltage characteristics but it is affected by magnetic saturation and skin effect. To accurately evaluate current voltage characteristics, it will be important to specifically account for the impact of skin effects and proximity effects, as well as leakage flux from the core gap. Especially for high switching frequencies, it will be necessary to control alternating resistance occurring in the winding due to switch period, and to accurately evaluate alternating resistance to design converters with low loss.

Magnetic field analysis using the finite element method is effective for accurate analyses of magnetic saturation and alternating resistance. By coupling external circuits and magnetic field analysis running switching, the current voltage characteristics of the converter can be obtained. In this example, this case study obtains the current waveform of the primary / secondary winding and the core magnetic flux density distribution, current density distribution inside the winding, joule loss density distribution at each time when the voltage is applied.



Current Waveform, Magnetic Flux Density Distribution

Primary current and secondary current waveform obtained in the time of one cycle in the steady state is shown in Fig. 1, and the magnetic flux density distribution of each time is shown in Fig. 2. While voltage is applied to the primary side when the switch is on, it can be confirmed that primary current is increasing. It can be confirmed that when the switch is off at 12.5 μ s, the current of the primary side will be 0 and that current is flowing in the secondary side at 13 μ s, it can be confirmed that the core magnetic flux density hits the maximum, and it is slowly discharged, reducing the magnetic flux density.

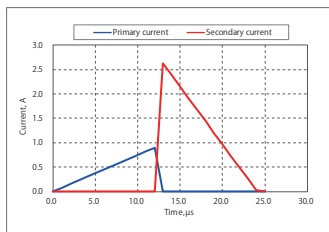


Fig. 1. Current Waveform

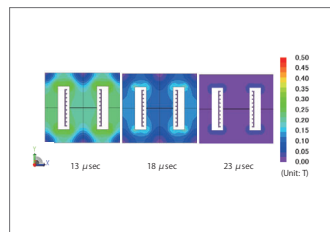


Fig. 2. Magnetic Flux Density Distribution

Voltage Characteristics

Primary coil terminal voltage and load voltage waveform obtained in the time of one cycle in the steady state is shown in Fig. 3. It can be confirmed that while the switch is on, the input voltage of 70 V is applied to the coil. It can be confirmed that the load voltage is a constant value of 21 V and has stepped down following the winding ratio.

Joule Loss Density Distribution

The joule loss density when current is applied to the secondary winding is displayed in Fig. 4. The Fig. 4 shows that joule loss inside secondary winding is concentrated on the outside of the winding. This may be caused by the skin effect due to current variations inside the winding and leakage flux from the core gap.

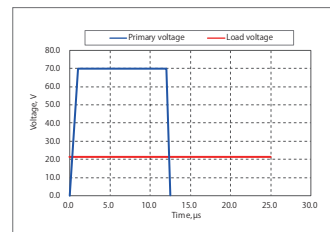


Fig. 3. Voltage Characteristics

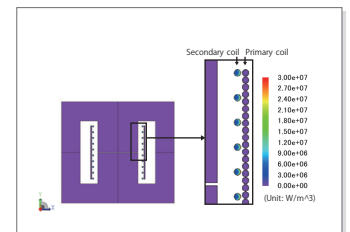


Fig. 4. Joule Loss Density Distribution

Case 108

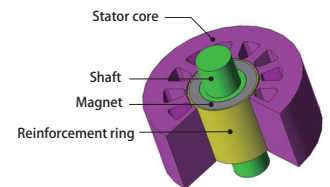
Centrifugal Force Rupture Analysis of a Ring Magnet

module: DS

Overview

As the applications for permanent magnet synchronous motors expand in the manufacturing sector, the development of high-speed-capable motors is continuing apace. One problem during high-speed operation is centrifugal force produced in the rotor, because, in an SPM using ring magnets, a magnet can rupture when the stress acting on it surpasses its mechanical strength. Analyzing the maximum rotation speed of a motor in advance to evaluate methods to prevent the magnet from rupturing, such as designing reinforcing rings, is highly advantageous during the design stage. When an SPM motor rotates, centrifugal force is generated, producing stress on the magnets. The stress distribution inside the magnets is not uniform. In addition to evaluating their mechanical strength, it is necessary to thoroughly investigate areas of stress concentration using the finite element method (FEM).

This Application Note presents how to obtain the stress distribution of a ring magnet in an SPM motor rotating at high speeds.



Tensile Stress Distribution by Rotation Speed

The tensile stress distributions of the magnet without a reinforcing ring under different rotation speeds are shown in fig. 1. It can be seen from the figure that, without a reinforcing ring, the tensile stress in the magnet becomes higher than its mechanical strength between 2,750 and 3,000 r/s, and the magnet will rupture.

Tensile Stress Distribution with and without a Reinforcement Ring

The tensile stress distribution with and without a reinforcing ring at a rotation speed of 3,000 r/s is shown in fig. 2. It can be seen from the figure that, with a reinforcing ring, the magnet does not exceed its tensile strength limit. This is because the reinforcing ring suppresses the deformation of the magnet. In this way, the motor can be driven at faster rotation speeds by using measures to prevent the ring magnet from rupturing.

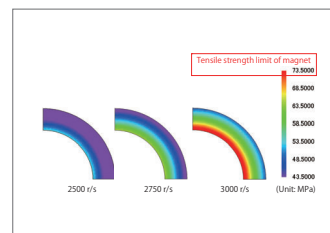


Fig. 1. Tensile stress distribution of the magnet

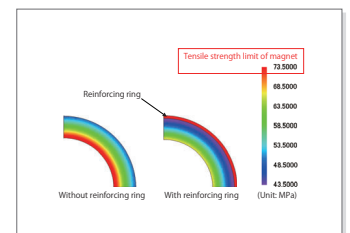


Fig. 2. Tensile stress distribution with and without the reinforcement ring

Case 109 Operating Time Analysis of an Electromagnetic Relay Accounting for Eddy Currents

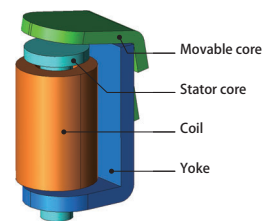
module: TR

Overview

Electromagnetic relays are devices that use an electromagnet to physically connect and disconnect contact points. Magnetic flux is generated from the magnetomotive force, which is expressed as the product of the number of turns in the coil and the current that is applied to the coil. This flux produces an attraction force in the movable core, making the relay close.

To put it simply, the attractive force is determined from the area of the gap between the movable core and the stator core and the size of the magnetic flux density produced in said gap. With a relay whose movable core does not move linearly, however, it is a difficult problem to predict the magnetic flux density in the gap because it does not become parallel. The nonlinear magnetic properties of the iron core and yoke also affect the magnetic flux density in the gap. With a JMAG magnetic field analysis, it is possible to obtain the attraction force of the movable core while accounting for these factors. One of the reasons that the response is delayed in electromagnetic relays is eddy currents, which are produced when the magnetic flux generated by current flow undergoes time variations. The eddy currents are generated in a direction that inhibits changes in the magnetic flux, causing a delay in the initial rise of the attraction force when the current begins to flow. This reduces the injector's responsiveness. JMAG makes it possible to account for the effects from eddy currents and obtain an electromagnetic relay's responsiveness by running a transient response analysis.

This Application Note presents the use of the motion equation function to evaluate the operating time of an electromagnetic relay with DC voltage drive. Eddy currents generated in the core are considered for this purpose.



Operating Time

The displacement versus time is indicated in fig. 1, the current versus time is indicated in fig. 2, and the attraction force versus time is indicated in fig. 3.

The current gradually increases after excitation starts, but it does not increase easily for around 2 ms because of the reverse electromotive force that comes with an increase in magnetic flux. Even after the excitation stops at 5 ms, the movable core still contacts the stator core because of the electromagnetic energy stored in the coil flowing through the diode, but when the elastic force of the spring becomes stronger than the attractive force at around 7 ms, the movable core returns to its initial position.

Magnetic Flux Density Distribution

The magnetic flux density distributions just before excitation stops, just after excitation stops, and just after the movable core begins to return to its initial position are indicated in fig. 4.

After excitation stops, the magnetic flux density decreases gradually because current is still flowing into the coil through the diode due to the effect of the electromagnetic energy in the coil as indicated in fig. 2.

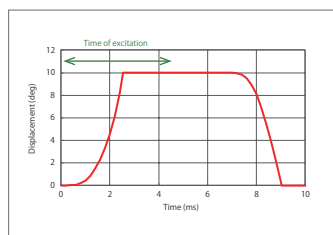


Fig. 1. Displacement versus time

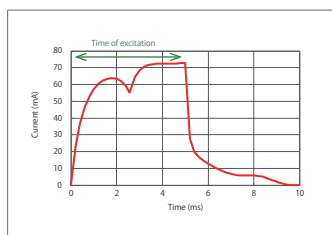


Fig. 2. Current versus time

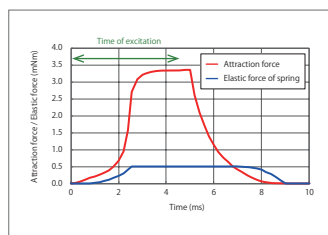


Fig. 3. Attraction force versus time

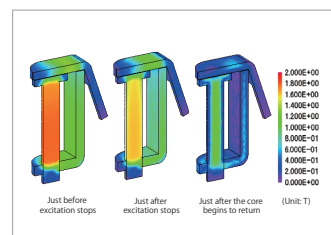
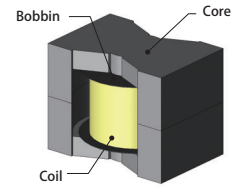


Fig. 4. Magnetic flux density distribution

Case 110

Loss Analysis of a Choke Coil

module: FQ, LS, TS, TRANSFORMER_TEMPLATE



Overview

A choke coil is an electric component that is intended to filter high-frequency current. Measures to evaluate the heat source as well as the core iron losses that occur within the choke coil and the copper losses of the coil that decrease efficiency need to be used for this analysis. The current generated in the choke coil has offsets caused by the skin effect, proximity effect, and leakage flux near the gap, so it is distributed both inside of and between the wires. Iron loss generated in the core is also distributed by offsets in the core's magnetic flux density. It is helpful to get tips for the design quantitatively and visually studying these detailed distributions, and an effective way of doing this is a magnetic field analysis that uses the finite element method (FEM).

This Application Note shows how to obtain the iron loss and copper loss in a choke coil.

Iron Loss Density Distribution

The iron loss density distribution is shown in fig. 1, the joule loss density distribution in fig. 2, and the hysteresis loss density distribution in fig. 3.

From fig. 1, it is apparent that iron losses increase in the inside corners. This is caused by the flow of magnet flux concentrating on the shortest path through the magnetic circuit. The hysteresis losses are the largest contributor to the iron losses, as indicated in figures 2 and 3.

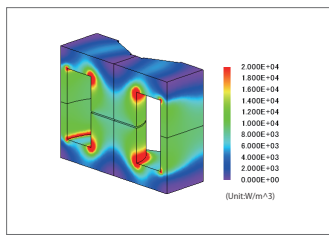


Fig. 1. Iron loss density distribution

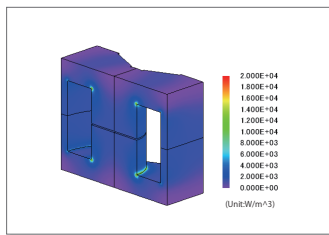


Fig. 2. Joule loss density distribution

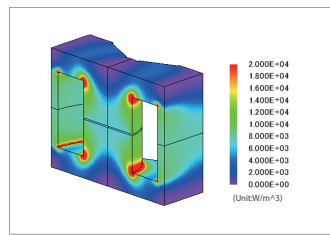


Fig. 3. Hysteresis loss density distribution

Copper Loss Density Distribution

Fig. 4 shows the joule loss density distribution in the coil. The joule losses are larger around the gap, as indicated in this figure. These joule losses are produced by the leakage flux from the gap that causes the current distribution in the wires to be uneven.

Percentage of Loss

The percentage of the iron and copper losses is indicated in fig. 5. As the table indicates, the hysteresis losses dominate the losses of the choke coil. However, when looking at the loss densities it becomes apparent that there is a region near the coil where they are high. In a heating design it is possible to resolve this issue and lower the heat generation density in the coil by changing the gap width or the coil arrangement.

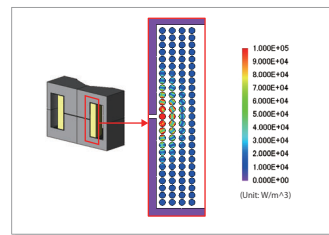


Fig. 4. Joule loss density distribution of the coil

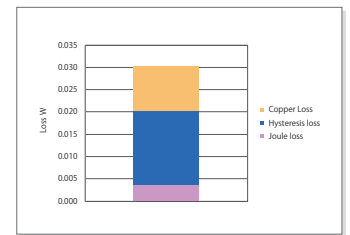
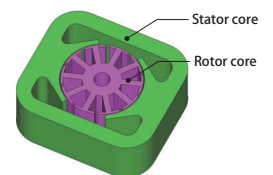


Fig. 5. Ratio of loss

Case 111

Starting Performance Analysis of a Universal Motor

module: DP



Overview

A universal motor is a motor that rotates on both direct and alternating currents. A universal motor is used in home appliances and industrial machines because these motors are robust, compact, light, and fast with a simple construction, and have a large starting torque. However, problems such as vibration and a reduction in starting torque caused by the cogging torque occur as the size of the motor becomes smaller. Evaluating the starting performance of a universal motor at the design stage is necessary to resolve these problems.

This document introduces the use of a magnetic field analysis to obtain the speed versus time graph, the current waveform, and the torque versus time graph for a universal motor.

Starting Performance

The speed versus time graph from when the motor starts to 0.4 seconds is indicated in Fig. 1, the current waveform of the stator coil is indicated in Fig. 2, and the torque versus time graph is indicated in Fig. 3.

The universal motor reaches a rotation speed of 6,000 rpm at approximately 0.35 seconds as indicated in Fig. 1. Furthermore, the larger the current flowing through the stator coil is, the larger the torque becomes when the motor is started. As the rotation speed increases, the current and torque decrease.

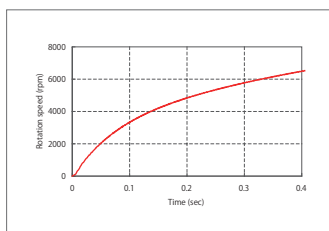


Fig.1. Speed versus time graph

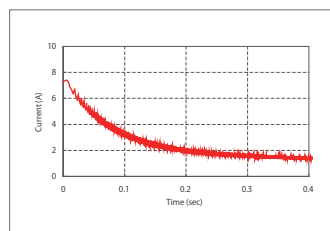


Fig.2. Current waveform of the stator coil

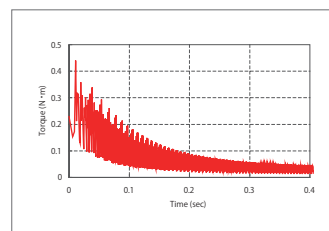


Fig.3. Torque versus time graph

Case 112 Starting Thrust Force Analysis of a Linear Induction Motor

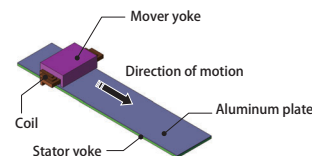
module: FQ

Overview

Linear motors are widely used for carrier devices and machine tools because of their high-speed performance, high acceleration and deceleration, and accurate positioning. One type of linear motor, the linear induction motor, can be constructed at low cost because it can use a primary side with coils, and a secondary side made of a conductor that is not magnetized, such as aluminum or copper.

There are some problems when building a linear inductance motor, such as complex eddy currents flowing in the secondary conductor sheet, and a large amount of leakage flux between the mover and stator. In order to improve linear inductance motor efficiency, therefore, it is important to gain an understanding of the paths of eddy currents and the leakage flux. Evaluation using the finite element method (FEM) is useful for this.

This Application Note presents how to obtain the starting thrust force for a linear inductance motor.



Eddy Current Density Distribution/ Frequency of the Aluminum Sheet vs. the Joule Losses

The eddy current density distribution for each power supply frequency is indicated in fig. 1, and the aluminum sheet's frequency vs. joule loss is indicated in fig. 2.

As indicated in fig. 1, eddy currents in the aluminum sheet increase as the power supply frequency becomes higher. This is because time variations in the magnetic flux acting on the aluminum sheet increase along with power supply frequency. As indicated in fig. 2, joule loss in the aluminum sheet increases as eddy currents increase.

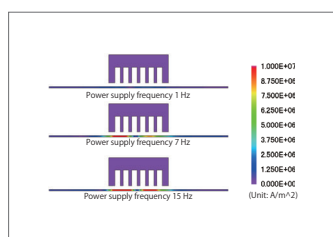


Fig.1 Eddy current density distribution

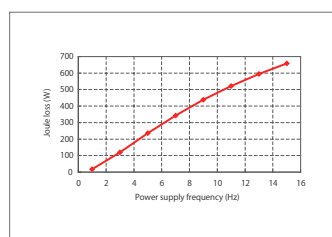


Fig.2 Aluminum sheet frequency vs. joule loss

Starting Thrust Force

The starting thrust force for power supply frequencies of 1 to 15 Hz is indicated in fig. 3. As the figure shows, thrust force increases as the power supply frequency gets higher. This is because eddy currents in the aluminum sheet increase with higher power supply frequencies as shown in fig. 1. The maximum starting thrust force of this linear induction motor is approximately 180 N.

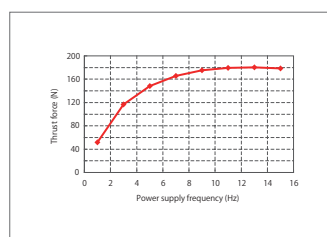


Fig.3 Starting thrust force

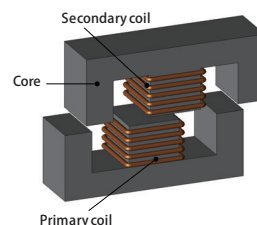
Case 113 Power Transmission Analysis of a Wireless Power Transfer System with Opposing Cores

module: FQ

Overview

A wireless power transfer system is a device which uses electromagnetic induction to provide electric power without physical contact. They can be used for various applications, such as supplying power to moving or rotating devices, or devices sealed inside enclosed spaces. Because the primary and secondary sides do not touch, the power transmission efficiency and leakage flux vary depending on their positions relative to each other. Therefore, it is important at the design stage to understand how properties change according to their placement.

When evaluating the properties of a transformer whose primary and secondary sides are separated by a gap, it is helpful to use magnetic field analysis based on the finite element method (FEM), which allows precise modeling of the geometry of the parts and their relative positions, and makes it possible to visualize the leakage in the magnetic flux that is generated in the primary side and transmitted to the secondary side. In this example, how to obtain the power transmission efficiency when the feeder wire's position is moved in both the horizontal and vertical directions from a reference position, and how to display the flow of magnetic flux.



Vertical Distance vs. Power Transmission Efficiency

Magnetic flux density distributions with varied vertical distance between the primary and secondary sides are shown in Fig. 1, and the vertical distance versus power transmission efficiency curve is shown in Fig. 2. The leakage flux increases and the magnetic flux inside the secondary side core falls with greater vertical distance, as indicated in Fig. 1. Approximately 80% of maximum efficiency can be achieved when the vertical distance is 2 mm, as indicated in Fig. 2. The efficiency falls basically linearly because the reduction in flux linkage in the secondary coil is caused simply by the increase of the vertical distance.

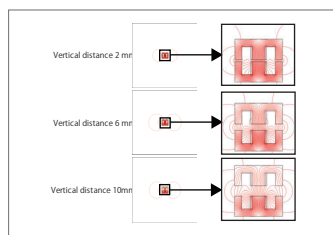


Fig. 1. Magnetic flux lines

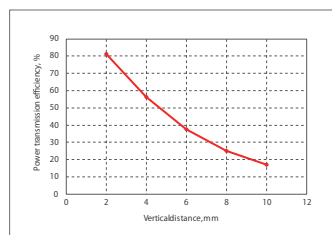


Fig.2. Vertical distance vs. power transmission efficiency

Horizontal Distance vs. Power Transmission Efficiency

Magnetic flux density distributions with a vertical distance of 2 mm and varied horizontal distance between the primary and secondary sides are shown in Fig. 3, and the horizontal distance versus power transmission efficiency curve is shown in Fig. 4. As indicated in Fig. 3, magnetic flux in the left side of the secondary side core falls with horizontal distance, and a flow channel that does not link the secondary coil is formed when the horizontal distance is 10 mm. The efficiency is reduced nonlinearly, as shown in Fig. 4. This is because the reduction in linkage flux in the secondary coil is due not only to distance, but also to changes in the way the magnetic flux flows.

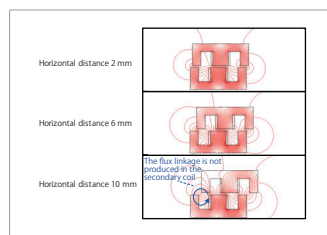


Fig.3. Magnetic flux lines

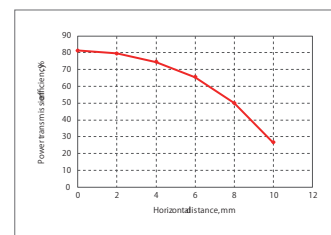
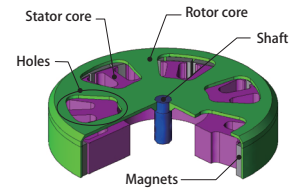


Fig.4. Horizontal distance vs. power transmission efficiency

Overview

An outer rotor motor has a magnetic rotor that rotates around a stator. The rotor radius of an outer rotor motor is large, so it can produce a larger amount of drive torque than an inner rotor motor with the same diameter, giving it a superior constant velocity. On the other hand, countermeasures for vibration and noise that occur during rotation are vital as well. The electromotive force is a cause of the vibration that occurs when a motor rotates. Additionally, when this electromotive force resonates with the motor's eigenmodes, it causes even larger vibrations and noise. Countermeasures such as changing the motor's eigenfrequency through processes like setting a hole in the rotor core have been taken with the objective of preventing resonance. In order to carry out these kinds of studies, it is necessary to get a precise, definite grasp of the electromotive force's spatial distribution, frequency analysis, and natural frequency.

This note presents the use of a magnetic field analysis and structural analysis to obtain the sound pressure caused by electromagnetic vibrations in an outer rotor motor with holes fabricated in the rotor core.



Electromagnetic Force Distribution

Fig. 1 shows the electromagnetic force distribution where the electromagnetic force is greatest among the frequency measurement component points, and Fig. 2 shows the frequency components of the electromagnetic force displayed at the points in Fig. 1. The frequency components of the electromagnetic force are concentrated at 180 Hz and the electromagnetic force is larger between the rotor core and poles.

Eigenmode

The eigenmode for a rotor core with and without fabricated holes are indicated in Fig. 3. This analysis confirms the minimum frequency for the mode that is deformed in the radial direction, which was 649 Hz with holes and was 677 Hz without them. A large amount of vibration is generated by the resonance phenomenon of the eigenfrequency and the electromagnetic force.

Acceleration (RMS) Distribution and Sound Pressure Level Distribution

The acceleration (R-RMS) distribution at 720 Hz is indicated in Fig. 4.4 and the sound pressure level distribution at 720 Hz is indicated in Fig. 4.5. The electromagnetic force takes effect, and it is possible to confirm a large acceleration and a high sound pressure level distribution due to the resonance phenomenon at an eigenfrequency of 720 Hz, a frequency close to the eigenfrequency shown in 4.2 "Eigenmode". Fig. 4.4 and Fig. 4.5 show that opening holes shown below can suppress acceleration in the R direction and reduce noise in this motor.

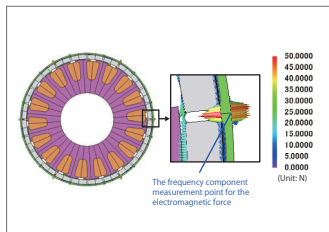


Fig.1. Electromagnetic force distribution

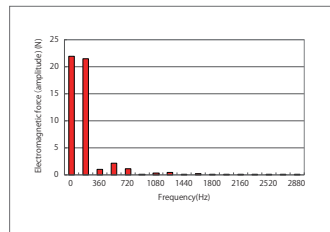


Fig.2. Frequency components of the electromagnetic force

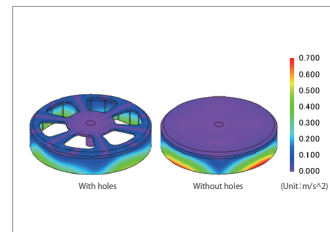


Fig. 4. Acceleration (intensity) distribution at 720 Hz

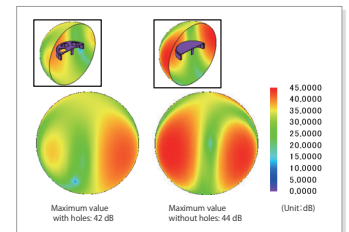


Fig. 5. Sound pressure level distribution at 720 Hz

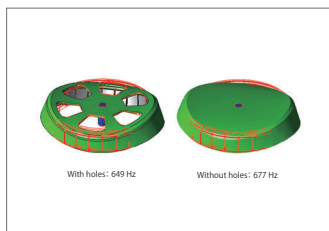


Fig. 3. Eigenmode deformation in the radial direction

Case 115 Eccentricity Analysis of an SPM Motor

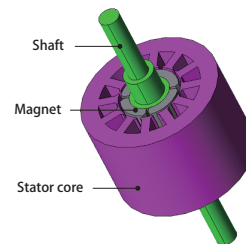
module: DP

Overview

Motors have many parts, which must be assembled correctly for a usable product. Even if each part is made within acceptable limits for manufacturing errors, when various parts with small errors are put together, the errors can have a cumulative effect. In particular, if eccentricity (deviation, deflection) occurs in the cylindrical axis of the rotor and stator, the magnetic flux density distribution and electromagnetic force can become unbalanced, causing vibration and noise. Ideally, parts would be manufactured without any errors, but in reality, error reduction requires precise mechanical manufacturing, which means a huge increase in costs. This is why it is necessary to figure out the tolerance zone of trade-off between settings and performance for each part at the design stage.

In order to grasp these at the design stage, highly precise evaluation sensitive to parts' manufacturing errors is needed, so electromagnetic field analysis using the finite element method (FEM) is effective.

This Application Note presents how to evaluate the cogging torque waveform and effects on the electromagnetic force acting on the stator in an SPM motor with and without eccentricity.



Torque Waveform/ Magnetic Flux Density Distribution

The torque waveform with and without eccentricity is indicated in fig. 1. The magnetic flux density distribution with a rotation angle of 180 deg at the largest difference in the position of the rotor is indicated in fig. 2. Torque variations occur with each one rotation of one period when eccentricity is applied, as indicated in fig. 1. The magnetic flux density increases in the direction of the eccentricity in the stator core, as indicated in fig. 2. This is how variations in the magnetic flux density distribution caused by eccentricity affect the torque waveform.

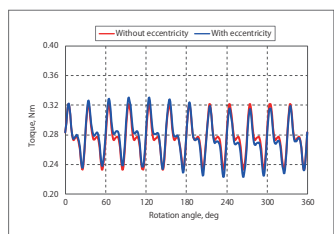


Fig. 1. Torque Waveform

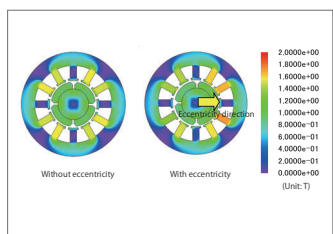


Fig. 2. Magnetic Flux Density Distribution (Rotation Angle: 180 deg)

Electromagnetic force acting on the stator

The eccentricity direction component of the electromagnetic force acting on the stator is indicated in fig. 3. The perpendicular direction component of the eccentricity is indicated in fig. 4. Each of the components has an electromagnetic force waveform with one period of one rotation due to eccentricity. Vibration and noise can be caused by electromagnetic resonance if the frequency component of the electromagnetic force acting on each part is close to the eigenmode of the motor.

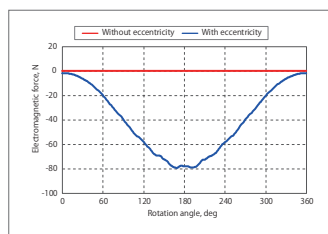


Fig. 3. Electromagnetic Force Acting on the Stator (Eccentricity Direction Component)

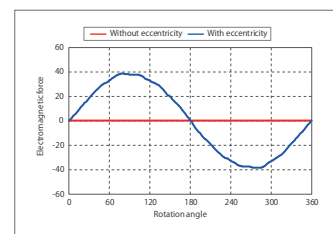


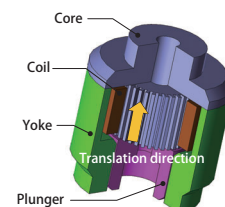
Fig. 4. Electromagnetic Force Acting on the Stator (Perpendicular Direction Component)

Case 116 Operating Time Analysis of an Injector by Evaluating the Reduction in Eddy Currents

module: TR

Overview

A solenoid type injector used in engines opens a valve and injects fuel by moving a plunger with magnetic force created by an electromagnet. Injectors in engines need to respond quickly to applied voltage in order to control the amount of fuel flow and improve fuel efficiency. In solenoid injectors, one of the reasons for slow response is eddy currents, which are produced when the magnetic flux generated by current flow undergoes time variations. The eddy currents are generated in a direction that inhibits changes in the magnetic flux, causing a delay in the initial rise of the attraction force when the current begins to flow. This reduces the injector's responsiveness. JMAG makes it possible to account for effects from eddy currents and obtain an injector's responsiveness by running a transient response analysis. Identifying the places where eddy currents are generated enables a designer to study how responsiveness can be improved. This Application Note explains how to apply direct current voltage to a solenoid injector and obtain its response characteristics by accounting for effects from eddy currents. The effectiveness of slots added to reduce eddy currents are evaluated by comparing the analysis results with a model without slots added.



Joule Loss / Current Density Distribution

The joule loss for each part is shown in fig. 1, and current density distributions at 1.3 ms, when the core's joule loss is at its approximate peak, are shown in fig. 2.

Fig. 1 shows that the joule loss is particularly different in the core, and the peak joule loss is reduced by 20%. Eddy currents are reduced by using a core with narrow slots installed, as shown in figures 2 and 3.

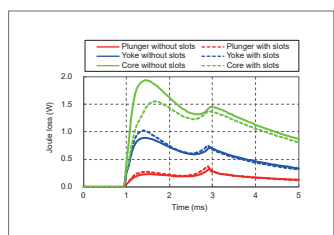


Fig. 1. Joule losses

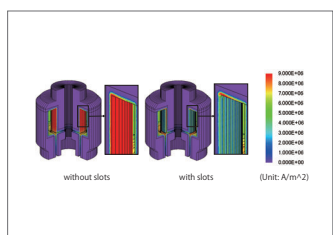


Fig. 2. Current Density Distribution

Response Characteristics

Fig. 3 shows the response characteristics, and fig. 4 shows the attraction force characteristics of the plunger versus time.

The displacement of the plunger is in the direction the valve opens, and the valve is fully open at a position of 0.1 mm. There is a constant fuel pressure of 5 N against the direction of the displacement. The plunger does not move right after the current is applied, but rather begins moving when the attraction force exceeds the fuel pressure, as indicated in the figures. The response characteristics and attraction force are improved by adding slots to reduce eddy currents.

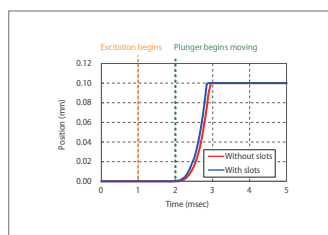


Fig. 3. Response characteristics

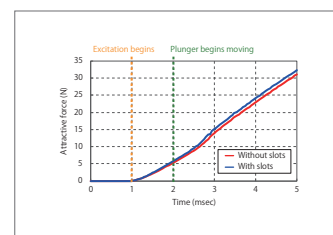


Fig. 4. Attraction force characteristics

Case 117

Iron Loss Analysis of a Transformer

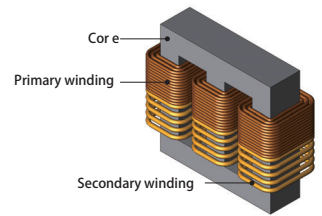
module: FQ, LS

Overview

Mid- and large-sized power transformers need to be able to operate over the long term, so they are always required to control running costs from losses. Iron loss is one of the main losses in a transformer, and it can lead to temperature increases and efficiency decreases because it consumes electric power as heat in a magnetic material.

Using finite element analysis (FEA) to confirm the distribution of iron loss density makes it possible to study a transformer's local geometry during design. Further, iron loss is divided into hysteresis loss caused by hysteresis in the core and joule loss caused by eddy currents, and analysis makes it possible to compare the relative contributions of each of these.

This Application Note presents how to obtain the iron loss and the ratio of hysteresis loss and joule loss within that iron loss for a three-phase transformer.



Magnetic Flux Density Distribution/ Iron Loss Density Distribution

The core's magnetic flux density distribution and iron loss density distribution are shown in figures 1 and 2, respectively. The magnetic flux density distribution and iron loss distribution are similar, as indicated in the figures. This is because the frequency of the magnetic flux density variations is constant, so the size of the iron losses is proportional to the size of the magnetic flux density variations.

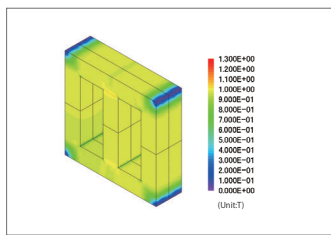


Fig. 1 Magnetic flux density distribution (winding is hidden)

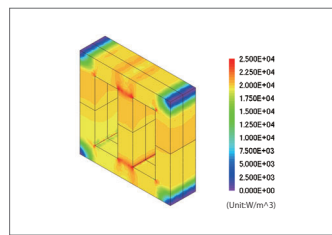


Fig. 2 Iron loss density distribution (winding is hidden)

Joule Loss Density Distribution/ Hysteresis Loss Density Distribution

The core's joule loss density distribution and hysteresis loss density distribution are shown in fig. 3, the ratio of losses is shown in fig. 4, and the losses are shown in table 1. As can be seen from the figures, the contribution of the hysteresis loss toward the iron loss is large. From this, it seems that investigating ways to reduce hysteresis loss would be effective in reducing iron loss.

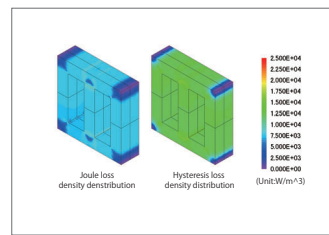


Fig. 3 Joule loss density distribution and hysteresis loss density distribution (winding is hidden)

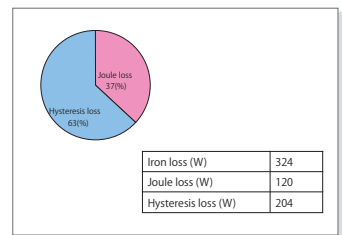


Fig. 4 Ratio of loss

Table 1. Iron loss

Case 118

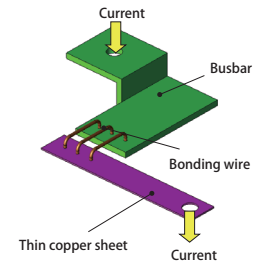
Thermal Analysis of a Busbar

module: FQ, HT

Overview

Current is supplied via busbars or wire bonding in power supply lines for power electronics devices such as inverters. Because inverters and similar devices operate with PWM carrier frequencies of several kHz, high-frequency current flows in their busbars. Influences from the skin effect cannot be ignored in this kind of high-frequency current, so increased resistance and loss become problems. A design that accounts for heat and temperature distributions at each frequency is vital because excess heat can cause a reduction in efficiency or even damage the device. Because a busbar's geometry is complicated, it is difficult to predict in advance where there will be unevenness in the current's flow while current is running, and whether this will cause heat generation. With magnetic field analysis using the Finite Element Method (FEM), it is possible to correctly obtain the unevenness in current distribution and the joule loss, and then predict the temperature distribution with these as causes of heat generation.

This Application Note presents how to obtain the temperature distribution in a busbar or the like with changes in the power supply frequency.



Current Density Distribution/ Joule Loss Frequency Characteristics

The current density distribution at each frequency is indicated in fig. 1, and the frequency characteristics of the joule loss are indicated in fig. 2. The current density in the bonding wires and the thin copper sheet increase as indicated in fig. 1. Joule loss increases as the frequency increases, as indicated in fig. 2. This is because the cross-sectional area where current is flowing decreases and the resistance increases due to the skin effect.

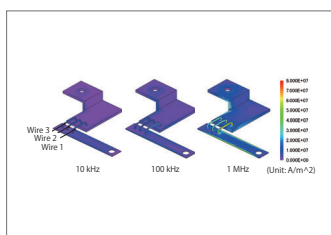


Fig. 1. Current Density Distribution

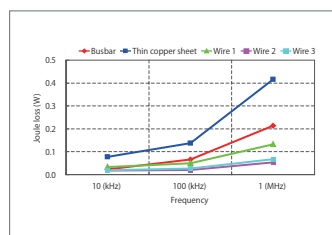


Fig. 2. Joule loss frequency characteristics

Temperature Distribution/ Average Temperature Frequency Characteristics

The temperature distribution of the busbar is indicated in fig. 3, and the frequency characteristics of the average temperature are indicated in fig. 4. The temperature increases in the bonding wires and thin copper sheet along with the current density at all of the frequencies. Also, the temperature increases drastically at 1 MHz compared to 10 kHz and 100 kHz. Caution needs to be taken because the increase in temperature can not only cause the busbar to burn out, but can also damage the device as thermal stress increases.

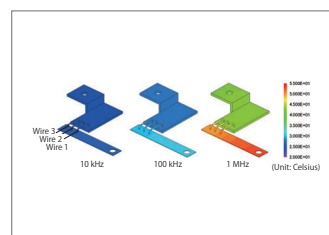


Fig. 3. Temperature distribution

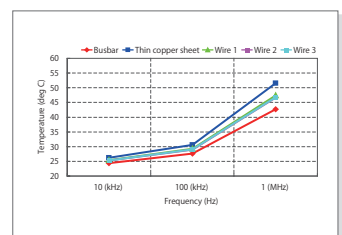


Fig. 4. Average temperature frequency characteristics

Case 119 Torque Characteristic Analysis of a Three Phase Wound Rotor Induction Motor

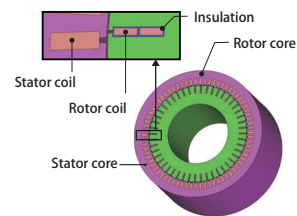
module: DP

Overview

A wound-rotor induction motor is a motor that causes induced current to flow in the secondary coil using a rotating magnetic field in the stator coil, and thus produces turning force through the interaction of the current and the rotating magnetic field. Because induced current flows through the coil, electric power can be extracted and regenerated via slip rings.

In an induction motor, the current induced by the secondary conductor exerts a large influence on its characteristics. It also causes strong magnetic saturation in the vicinity of the gap, in particular. For these reasons, analysis based on the finite element method (FEM) can accurately handle induced current and magnetic saturation, and is useful for understanding detailed characteristics in advance.

This Application Note shows how to obtain the current density distribution and slip-torque curve.



Current Density Distribution

The current density distribution at a 0.5 slip is indicated in fig. 1.

Induced current is generated in the rotor coil by the rotating magnetic field of the stator coil. Torque is generated from the magnetic flux and rotating magnetic field created by this induced current, so the current has a large effect on the torque characteristics.

Slip-Torque Curve

A graph of the slip-torque curve is shown in fig. 2.

The amount of torque that can be produced by this induction motor increases as the slip gets larger. It is necessary to investigate measures such as reducing the rotor's external resistance when attempting to obtain higher torque with a small slip, because the torque at each slip is determined by the induced current in the secondary side.

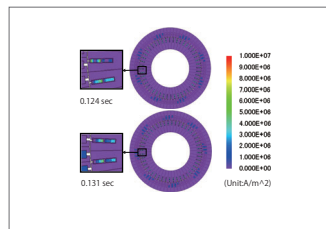


Fig. 1. Current density distribution at 0.5 slip

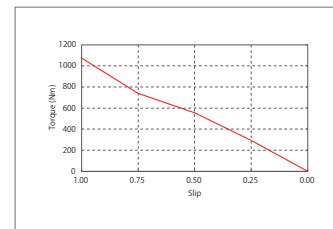
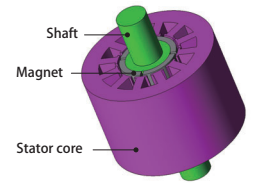


Fig. 2. Slip-torque curve



Overview

Exactly how to resolve the problem of rising temperatures is a vital issue when trying to achieve an improvement in a motor's efficiency and output. Among the materials used in a motor, the magnet experiences the greatest variations in properties in relation to temperature. In the case of rare-earth magnets, demagnetization can occur within tens of degrees above 100 deg C. Whether they demagnetize or not depends on the reverse magnetic field applied and the temperature. They still have some resistance if either the temperature is raised only or if a reverse magnetic field is applied only, but the combination of the two causes a great reduction in resistance. A large current flows in the coils when the motor is overloaded and is producing a lot of torque, which leads to a large reverse magnetic field and heat, increasing the possibility of demagnetization. Solutions to this problem include heat-resistant magnets and increased motor size, but these lead to trade-off issues during the design stage because of the larger size and higher cost.

In order to carry out a precise evaluation of demagnetization, it is necessary to get a definite grasp of areas where a reverse magnetic field occurs and the materials' demagnetization properties. With magnetic field analysis simulation using the finite analysis method (FEM), it is possible to calculate the reverse magnetic field and determine whether magnets and other parts demagnetize due to reverse magnetic field, taking material demagnetization properties into account.

This Application Note presents how to change the temperature of permanent magnets in an analysis, and then evaluate the effects on the torque waveform, magnetic flux density distribution, etc.

Torque Waveform

The torque waveform when the temperature of the magnet is varied from 60 deg C to 140 deg C and then back to 60 deg C for one period of electrical angle (180 deg of mechanical angle) is indicated in fig. 1.

The average torque is reduced due to thermal demagnetization when the magnet is at a temperature of 140 deg C, as indicated in fig. 1. Also, the irreversible demagnetization that occurred at 140 deg C is apparent in that the average torque is 17% lower when the temperature of the SPM motor is returned to 60 deg C.

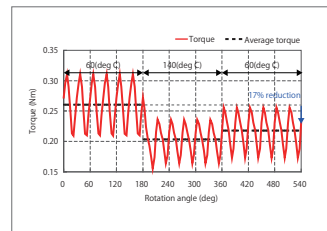


Fig.1. Torque waveform

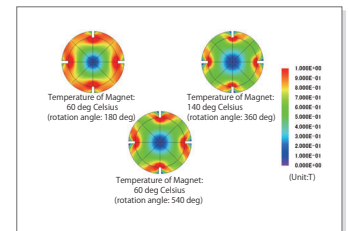


Fig.2. Magnetic flux density distribution

Magnetic Flux Density Distribution

The magnetic flux density distributions under the different conditions are shown in fig. 2. From the figure, it can be seen that the overall magnetic flux density is lower at 140 deg C compared to before the temperature is raised. It can also be seen that it does not return to its original state even after the temperature is returned to 60 deg C.

Demagnetizing Ratio Distribution

Fig. 3 shows the demagnetization ratio (*1) distribution after the temperature is returned to 60 deg C, with magnetization conditions prior to the raised temperature as a standard. The demagnetization shown here is irreversible demagnetization from going over the knee point, and indicates that the magnet properties have worsened.

It can be seen from the figure that even when the magnet is returned to 60 deg C, there is demagnetization across a wide range compared to before.

*The demagnetizing ratio is the amount of emagnetization with reference to magnetization that is specified.

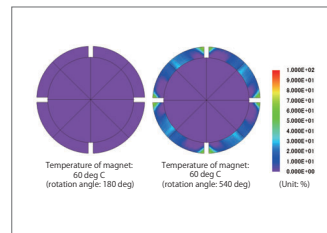


Fig.3. Demagnetizing ratio distribution

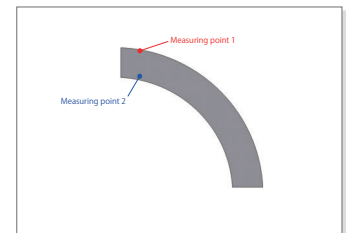


Fig.4. Measuring points for operating point

Operating Point

The measuring points selected to confirm operating points are shown in fig. 4, and the operating points are shown in fig. 5.

In fig. 5, it can be seen that irreversible demagnetization has occurred because the operating point exceeds the knee point at measuring point 1 after heat is added and the operating point does not return to the original B-H curve after the temperature is reduced to 60 deg C. The size of the reverse magnetic field acting on each element can also be seen on the horizontal axis.

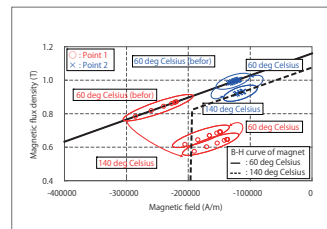
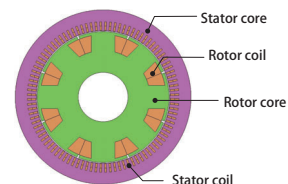


Fig.5. Operating point

Case 121 Output Analysis of a Salient-Pole Synchronous Generator

module: DP



Overview

Salient-pole synchronous generators are used in hydroelectric generators and the like. Power is generated in the stator coils (armature) by a field current flowing in the rotor coils and the rotor rotating. Reactions occur between the field current and the armature current that either strengthen or weaken the magnetic flux depending on the power factor of the connected load of a salient-pole synchronous generator. This causes the operating point of the magnetic circuit inside the generator to change, which affects the output. The core normally has nonlinear magnetic properties, so an evaluation of the magnetic circuit with magnetic field analysis, which can handle nonlinear magnetic properties, is useful. This Application Note presents the use of a magnetic field analysis to obtain the magnetic flux density distribution, no-load saturation curve, and output of a salient-pole synchronous generator.

No-load Saturation Curve/ Magnetic Flux Density Distribution

The no-load saturation curve is shown in fig. 1, and the magnetic flux density distributions for excitation currents of 75 A and 100 A at 0.005 s are shown in fig. 2. The slope of the no-load saturation curve begins to decrease after exceeding an excitation current of 75 A. The magnetic flux density increases in the teeth of the rotor core and stator core as the excitation current gets larger, and the slope of the no-load saturation curve decreases as magnetic saturation increases. The effective value of the induced voltage is obtained using the root mean square.

Output

The time versus current of the shaft resistance at an excitation current of 75 A is indicated in fig. 3. The output current of this salient-pole synchronous generator is 880 A.

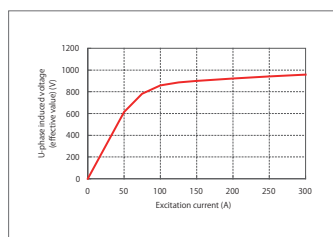


Fig.1. No-load saturation curve

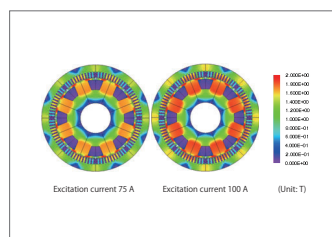


Fig. 2. Magnetic flux density distribution at 0.005 s

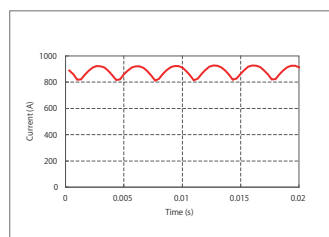
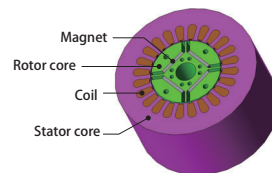


Fig. 3. Time versus current at excitation current 75 A

Case 122 Inductance Analysis of an IPM Motor - d/q-axis Inductance Obtained by Actual Measurement -

module: DP



Overview

Evaluating the inductance characteristics along the d/q-axis is important when analyzing the saliency of a rotor in an IPM motor. With actual measurements, it is possible to calculate the inductance in the d-axis and q-axis by measuring the no-load magnetic flux or the voltage and current with a three-phase current flowing when the motor is in actual operation. If it cannot be measured while the motor is operating, an LCR meter can be entered in two phases when the rotor is in a stationary state. However, current conditions are different between three phases and two phases, so the motor will express different characteristics during actual drive, especially when it is strongly affected by magnetic saturation. For this reason, the analysis contents need to be determined according to the situation of the actual measurements when comparing the measurements with an analysis. This Application Note presents an analysis that obtains d/q-axis inductance in an IPM motor while assuming actual measurements in a stationary rotor.

Ld/Lq versus current phase angle /Inductance

From fig. 1, it is apparent that the d-axis inductance hardly changes depending on the current phase angle. The reason for this is that the inductance is small because the d-axis magnetic flux passes through a magnet with low permeability, meaning that it is not very affected by the magnetic saturation of the iron core because the magnet's magnetic resistance makes a big contribution. On the other hand, the magnetic flux from the q-axis passes through the iron core, so the permeability is large compared with the d-axis, meaning that the inductance is large as well. The current phase also progresses, so when the magnetic flux is weaker the iron core's magnetic saturation is alleviated, meaning that the q-axis inductance increases.

However, a three-phase current is not run with the method of calculation using the line-to-line inductance, so it is not possible to obtain the variations in d-axis/q-axis inductance caused by the current phase angle. The magnetic saturation conditions of the iron core are also different when running a three-phase AC and a line-to-line current, so the q-axis inductance has been generally overestimated. In contrast, the contribution of the aforementioned magnet's magnetic resistance to the d-axis inductance is large, so there is not a big gap between the results of the two methods.

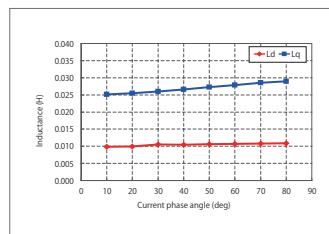


Fig. 1 Ld/Lq versus current phase angle (LdLq analysis model)

Parameter	Value
d-axis inductance Ld	0.010 H
q-axis inductance Lq	0.030 H

Table 1 Ld/Lq (line-to-line inductance model)

Case 123

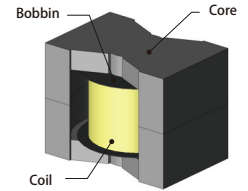
Thermal Analysis of a Choke Coil

module: HT, TRANSFORMER_TEMPLATE

Overview

A choke coil is an electric component that is intended to filter high-frequency current. The current generated in the choke coil has offsets caused by the skin effect, proximity effect, and leakage flux near the gap, so it is distributed both inside of and between the wires. Iron loss generated in the core is also distributed by offsets in the core's magnetic flux density. Iron loss in the choke coil's core and copper loss in its coil become a heat source in addition to reducing efficiency, so they need to be understood and reduced from a heating design standpoint. An analysis using the finite element method (FEM) is effective in getting more information about the design by quantitatively evaluating the heat generation phenomena with copper and iron losses as the heat sources.

This Application Note shows the use of a thermal analysis to obtain the temperature distribution using the iron losses and copper losses in the choke coil as the heat source.



Temperature Distribution

Fig. 1 shows its temperature distribution, and fig. 2 shows the maximum temperature in each part.

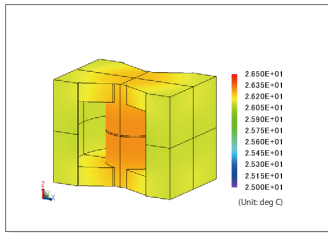


Fig. 1. Temperature distribution in the core

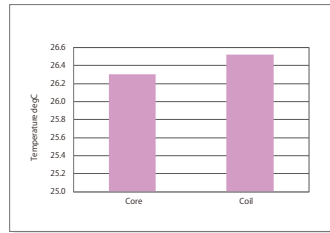


Fig. 2. Maximum temperature in each part

Case 126

Magnetization Analysis Accounting for Eddy Currents

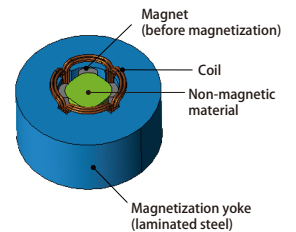
module: ST, TR

Overview

A magnet's magnetization state largely affects the characteristics of a device that uses permanent magnets. A magnetization device performs magnetization by applying an extremely strong magnetic field to a magnet. The capacity of the magnetization power supply is also determined by multiplying the magnetization current by time. The production process requires that magnetization be performed by running a large current through a magnetization coil in an extremely short period of time. However, eddy currents are generated in the magnetic material to be magnetized when the currents time variations are too severe, opening the possibility that the intended magnetization distribution cannot be obtained. On the other hand, when the current changes too slowly the magnetizing device's capacity needs to be expanded, leading to an increase in production cost. This is why the trade-off between production costs and whether sufficient magnetization can be carried out needs to be studied.

A magnetic field analysis using the finite element method (FEM) can handle the nonlinear magnetic properties of materials and eddy currents that are generated in the magnetic material to be magnetized when current flows through the coil. This makes it possible to discover how the magnetizing field will be generated and what effect it will have on the magnetization distribution.

This Application Note presents how to obtain the magnetization field distribution accounting for eddy currents in the magnetic material to be magnetized, the eddy current density distribution in the magnetic material to be magnetized, and the surface magnetic flux density of the magnet.



Magnetization Field/ Eddy Current Density Distribution/ Surface Magnetic Flux Density

This section shows the magnetization field in fig. 1, the eddy current density distribution in the magnetic material to be magnetized in fig. 2 and the magnet's surface magnetic flux density in fig. 3.

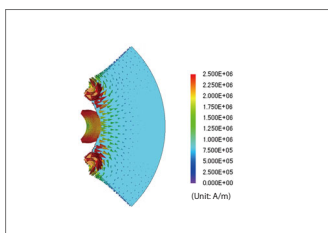


Fig. 1. Magnetization field distribution

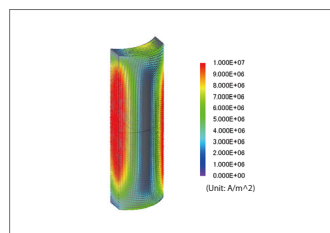


Fig. 2. Eddy current density distribution of the magnetic material to be magnetized

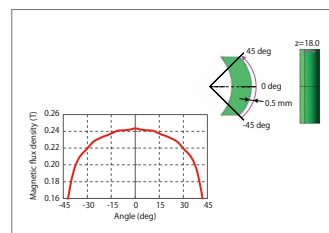


Fig. 3. Surface magnetic flux density waveform of the magnet (at 0.5 mm above the magnet surface)

Case 127 Resistance Heating Analysis of Steel

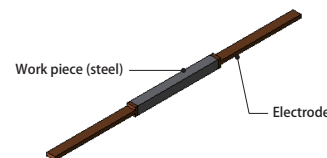
module: FQ, HT

Overview

Deformation occurs when large metal parts such as shafts undergo machining, causing their material properties to worsen. Because of this, these material properties are restored by eliminating machining deformations using thermal processing, which returns the metal structure to its standard condition. It is necessary to heat the whole part to the same temperature in order to restore the metal's overall properties with thermal heating, and ohmic heating is often used for this purpose. It is helpful to measure the temperature distribution in advance with an investigation of heating conditions.

Evaluation with analysis based on the finite element method (FEM) is necessary to find whether a product with a 3D geometry is heated uniformly by a given electrode configuration.

This Application Note presents how to obtain the temperature distribution, temperature variations, and heat flux distribution in a body heated by ohmic heating.



Temperature Distribution

The temperature distribution of the heated body is shown in fig. 1. From the figure, it is apparent that the central portion of the heated body has the highest temperature at all times.

Temperature Variations

Temperature variations at each measurement point A, A', B, B' are shown in fig. 2. In the figure, it can be seen that there is no temperature variation between the surface and the inside (A-A', B-B'). Also, there is a temperature variation between the ends and the central portion (A-B, A'-B') as seen in fig. 1, and this temperature variation is 200 deg C after 700 s of heating.

Heat Flux Distribution

The heat flux distribution at 700 s is shown in fig. 3. From the figure, it is clear that heat is conducted from the heated body to the electrodes, and that this is the cause of the temperature variation along the lengthwise direction of the heated body.

Some means of reducing this temperature variation in the lengthwise direction is necessary in order to uniformly heat the body and improve its properties.

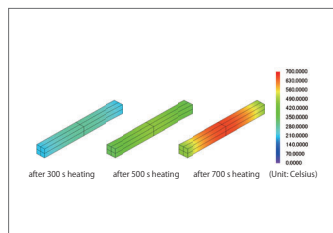


Fig.1. Temperature distribution

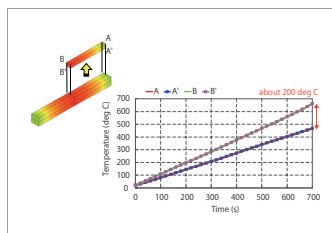


Fig.2. Temperature variations

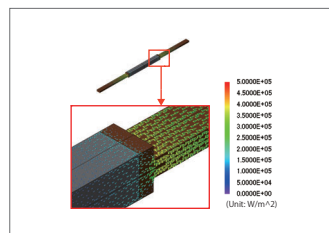


Fig.3. Heat flux distribution

Case 128 Structural Analysis of a Cantilever

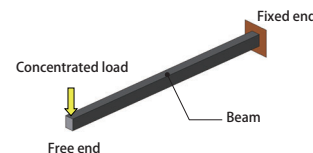
module: DS

Overview

As the importance of robust design in today's smaller and thinner electric devices continues to rise, so does the demand for ways of reducing vibration. In order to precisely evaluate an electric device's vibration characteristics and robustness, it is important to first evaluate these phenomena in the device's parts individually, because overall characteristics can often be understood by understanding the characteristics of each of its component parts. This Application Note presents how to evaluate the vibration characteristics and robustness of a basic cantilever beam, rather than of an actual electric device.

Electric devices and their individual component parts have eigenmodes that are determined by their mechanical properties and their geometry. Vibration increases when the excitation force resonates with the electromagnetic device's eigenmode. Also, electric devices and their component parts deform when a load is applied to them. Even in a simple form like a cantilever beam, the displacement direction differs depending on the direction of the load, its position, and the frequency. For this reason, it is necessary to evaluate the eigenmode and displacement for an electric device and its component parts in order to understand these phenomena.

In this Application Note, the displacement is obtained for three simple cantilever beam models with different mesh conditions when their eigenmode or a concentrated load is applied to them, and the displacement is then compared with theoretical values.



Eigenmode

The first-order eigenmodes for Models A (coarse mesh, first-order elements), B (fine mesh, first-order elements), and C (coarse mesh, second-order elements) are shown in fig. 1 and their first- through third-order natural frequencies are shown in table 1. These show that the deformation direction of the first-order eigenmode can be found even with a coarse mesh, but in order to keep the natural frequency including bending within around 5% off from the theoretical value, it is necessary to either use a finer mesh or use second-order elements.

Displacement

The Z-direction displacements for Models A, B, and C are shown in fig. 2, and their maximum Z-direction displacements are shown in table 2. These show that the deformation can be found approximately with a coarse mesh, but in order to keep the maximum displacement including bending within around 5% off from the theoretical value, it is necessary to either use a finer mesh or use second-order elements.

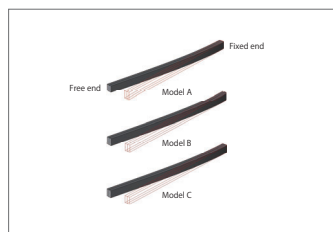


Fig. 1 First-order eigenmodes (red lines: original model)

		Theoretical value	Model A	Model B	Model C
1st-order mode	Natural frequency (Hz)	130.92	160.7	134.9	129.9
	Difference from theoretical value (%)	--	22.7	3.0	0.8
2nd-order mode	Natural frequency (Hz)	163.65	184.5	171.7	168.7
	Difference from theoretical value (%)	--	12.7	4.9	3.1
3rd-order mode	Natural frequency (Hz)	818.27	1008	839.7	808.1
	Difference from theoretical value (%)	--	23.2	2.6	1.2

Table 1. Natural frequency

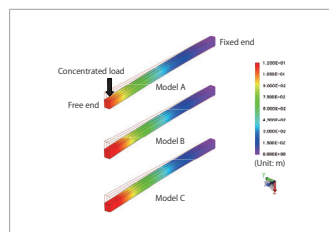


Fig.2. Displacement (red lines: original model)

		Theoretical value	Model A	Model B	Model C
Zdirection maximum displacement (mm)		139.23	116.38	134.28	139.14
Difference from theoretical value (%)		--	16.4	3.6	0.1

Table 2. Maximum displacement

Case 129

Analysis of a PM Stepper Motor Accounting for Magnetization

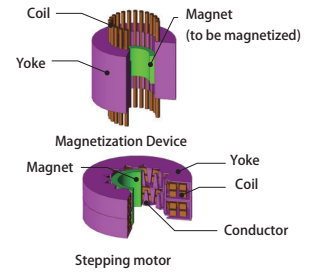
module: ST, TR

Overview

Stepper motors are commonly used for positioning in printers and digital cameras. In PM stepper motors, the motor's characteristics are determined through design of the magnetization state of the permanent magnet used. It is necessary to accurately evaluate this magnetization state in order to improve the precision of estimations of a PM stepper motor's characteristics.

Detailed measurements of the magnetization distribution inside a magnet are difficult to make. However, it is possible to accurately find the magnet's magnetization because it can be obtained through analysis of the magnetization field from the magnetization device, using the finite element method (FEM).

In this analysis, a magnetization device model is created and a magnet is magnetized. The magnetization distribution and surface magnetic flux density of the magnetized magnet, and the induced voltage of a PM stepper motor with the magnetized magnet integrated into it, are then obtained.



Magnetization Distribution and Surface Magnetic Flux Density of the Magnet

The magnetization distribution of the magnet magnetized by the magnetization device is shown in fig. 1, and fig. 2 shows the radial direction component of a two-pole span of the surface magnetic flux density at 0.2 mm from the magnet surface.

It can be seen from fig. 1 that magnetization is strong in all parts of the magnet under complete magnetization, and magnetization is weak toward the inner side of the magnet under incomplete magnetization. This is why in fig. 2, the maximum surface magnetic flux density value under complete magnetization is around 0.8 T, and is smaller at around 0.3 T under incomplete magnetization. This shows that it is necessary to consider the magnetization ratio and recoil relative permeability in order to grasp the magnetization state.

Induced Voltage Waveform

The induced voltage waveform of the stepper motor rotating at 1,000 r/min is shown in fig. 3. The figure makes it clear that the maximum induced voltage value goes down from around 7.5 V under complete magnetization to around 5.0 V under incomplete magnetization due to the difference in the strength of the magnet's magnetization, and the PM stepper motor's characteristics are different depending on whether the magnetization ratio and recoil relative permeability are accounted for or not.

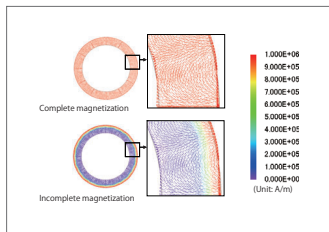


Fig. 1. Magnetization distribution in the magnet

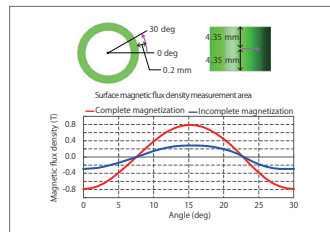


Fig. 2. Radial direction component of the magnet's surface magnetic flux density

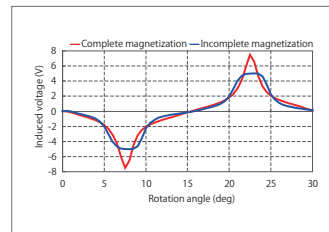


Fig. 3. Induced voltage waveform

Case 130

Thermal Conductivity Analysis of Basic Geometry

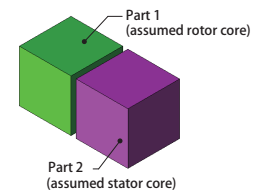
module: HT

Overview

With improvements in the miniaturization and increased output power of electric devices in recent years, demands for ways of dealing with heat are also increasing. It is of course important to reduce loss in order to prevent heat, but it is also important to find ways to expel any heat that is generated. The actual heat conduction and heat transfer phenomena in each part need to be accurately modeled in order to precisely evaluate an electric device's heat dissipation characteristics. In other words, if the thermal behavior of each part is accurately modeled, it becomes possible to grasp the thermal characteristics of the entire electric device.

Here, to make thermal analysis easier to understand, two basic cube-shaped objects are modeled as stand-ins for a rotating machine's rotor core and stator core, and a thermal conductivity analysis is carried out between them.

In this Application Note, the analysis accuracy is investigated by comparing the temperatures obtained through analysis in each part with theoretical values.



Temperature Distribution

The temperature distribution of part 1 and part 2 is shown in fig. 1. The temperature changes linearly from the outer to the inner side of each part.

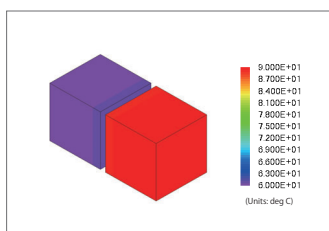


Fig. 1. Temperature distribution

Inner side temperature of each part

Analysis results and theoretical calculations for the inner side temperatures of part 1 and part 2 are shown in table 1. The analysis results are consistent with the theoretical calculations for both parts. This indicates that these analysis results are accurate.

	Temperature from analysis results (deg C)	Temperature from theoretical calculation (deg C)
Part 1	60.7	60.7
Part 2	89.3	89.3

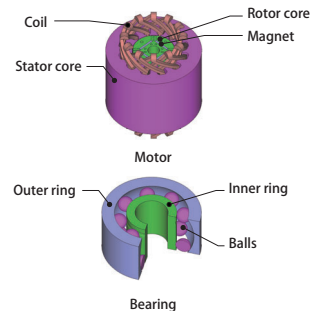
Table 1. Inner side temperature of each part

Case 131 Stray Capacitance Analysis of a Motor

module: EL

Overview

Motors driven by PWM inverters are widely used in household appliances. It is known that when a PWM inverter is used for drive, common mode current flows and axial voltage is produced in the motor's bearings. Electric corrosion is caused in the bearings by this axial voltage, which can reduce the motor's reliability and life. It is advantageous to use analysis to grasp the stray capacitance in advance, because the common mode current is produced by stray capacitance acting parasitically on the motor's parts. This note presents the use of analysis to obtain the stray capacitance between an IPM motor's coil and stator core, between its rotor core and stator core, and between the inner and outer rings of its bearings.



Electric Field Distribution

The electric field distribution when the electric potential difference is applied between the motor's coil and stator core, the motor's rotor core and stator core, and the inner and outer rings of the bearing are indicated in figures 1, 2, and 3. A large electric field is produced: in the air in the slots near the coil and stator core when the electric potential difference is applied between the coil and stator core; in the air in the gap when the electric potential difference is applied between the rotor core and the stator core; and through the balls, which are conductors, when the electric potential difference is applied between the inner and outer rings.

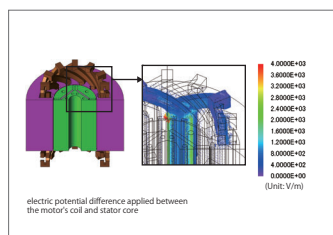


Fig. 1. Electric field distribution

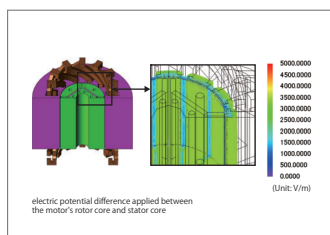


Fig. 2. Electric field distribution

Stray Capacitance

The stray capacitance between the motor's coil and stator core, between the motor's rotor core and stator core, and between the inner and outer rings of the bearings is indicated in table 1. Axial voltage is produced by the stray capacitance.

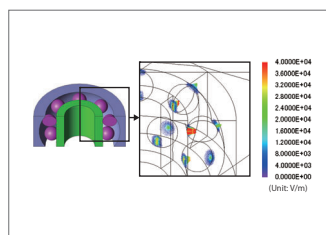


Fig. 3. Electric field distribution (electric potential difference applied between the inner and outer rings of the bearing)

	Between the motor's coil and stator core	Between the motor's rotor core and stator core	Between the bearing's inner and outer rings
Stray capacitance (pF)	40	78	8.2

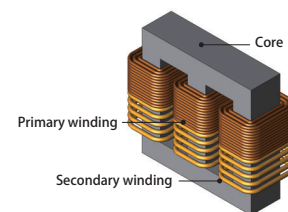
Table 1. Stray capacitance

Case 132 Loss Analysis of a Three-phase Transformer

module: FQ, LS

Overview

Mid- and large-sized power transformers need to be able to operate over the long term, so they are always required to control running costs from losses. Iron loss is one of the main losses in a transformer, and it can lead to temperature increases and efficiency decreases because it consumes electric power as heat in a magnetic material. Using finite element analysis (FEA) to confirm the distribution of iron loss density makes it possible to study a transformer's local geometry during design. Further, evaluating the ratio and distribution of the iron and copper losses through FEA becomes advantageous when designing a transformer. This note presents how to obtain the iron and copper losses of a three-phase transformer.



Iron loss Density Distribution

The iron loss density distribution of the core is shown in fig. 1, the joule loss density distribution of the core in fig. 2, and the hysteresis loss density distribution of the core in fig. 3. From fig. 1, it is apparent that iron losses increase in the inside corners. This is because the magnetic flux flows through the shortest route of the core. As can be seen from figures 2 and 3, a large percentage of the iron loss is hysteresis loss.

Current Density Distribution and Copper Loss Density Distribution

The current density distribution of the coil is shown in fig. 4, and the joule loss density distribution in fig. 5. From fig. 4, it is apparent that the current density distribution is approximately the same in each phase. Joule loss is higher in the secondary coil than the primary coil, as indicated in fig. 5. This is because the current is larger in the secondary coil.

Percentage of Loss

The percentages of the iron and copper losses are indicated in table 1. Table 1 shows that the ratio of iron loss in the total loss is large. Therefore, investigating ways to reduce iron loss would be effective in reducing the total amount of loss. Furthermore, finding ways to reduce hysteresis loss would be effective in reducing the iron loss.

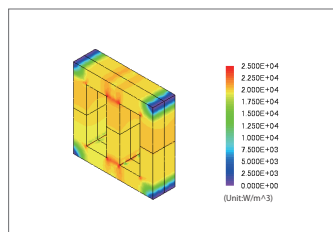


Fig. 1. Iron loss density distribution

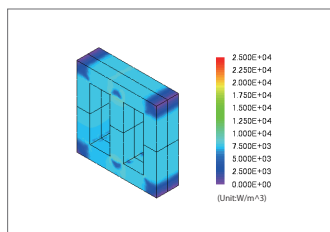


Fig. 2. Joule loss density distribution

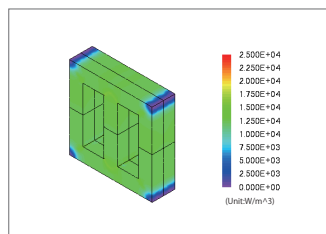


Fig. 3. Hysteresis loss density distribution

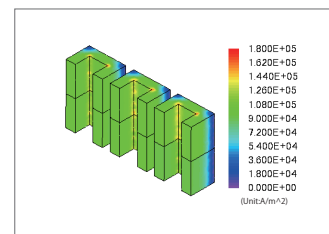


Fig. 4. Eddy current density distribution

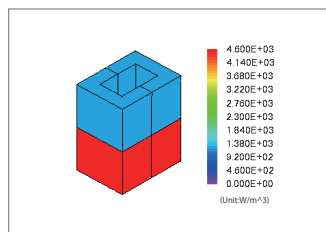


Fig. 5. Joule loss density distribution

Type of loss	Iron losses (W)	Percentage (%)
Iron loss	Joule loss	32
	Hysteresis loss	54
Copper Loss	52	14

Table 1. Ratio of loss

Case 133

Thermal Analysis of a Three-phase Transformer

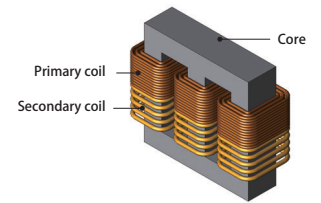
module:HT

Overview

One of the most important principles in transformer design is how low loss can be kept to during operation. Iron loss in the transformer's core and copper loss in its coil become heat sources in addition to reducing efficiency, so they need to be understood and reduced from the standpoint of heat resistant design for all parts, particularly the coil's insulation.

An analysis using the finite element method (FEM) is effective in getting more information about thermal design by quantitatively evaluating the heat generation phenomena with copper and iron losses as heat sources, including the temperature distribution.

This Application Note presents an example of how to confirm a temperature distribution using the iron and copper losses of a three-phase transformer as heat sources.



Heat Generation/Temperature Distribution

From fig. 1, it is apparent that the heat generation density is higher on the inside corners of the core. This is because the flow of magnet flux is concentrated in the shortest path through the magnetic circuit. The temperature around the bases of the core's center leg is higher because the heat generation density is higher there, as indicated in fig. 2(a). For this reason, the temperature of the winding at the center leg is also higher.

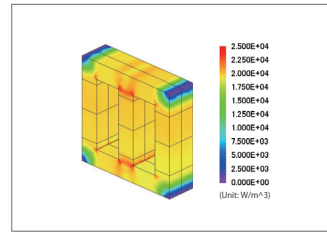


Fig. 1. Heat generation density distribution of the core

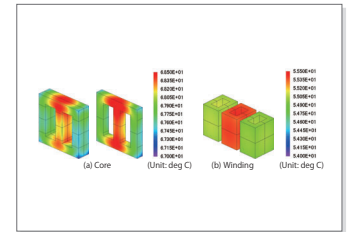


Fig. 2. Temperature distribution

Case 134

Speed Control Analysis of a Permanent Magnet Linear Motor Using the Control Simulator and the JMAG-RT

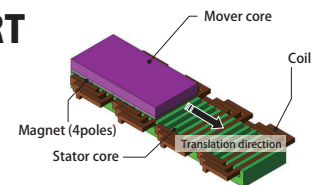
module: DP, RT

Overview

Linear motors are widely used for carrier devices and machine tools because of their high-speed performance, high acceleration and deceleration, and accurate positioning. A type of linear motor called a permanent magnet linear motor has harmonic components such as cogging and ripples in its thrust because of its structure and how it operates. These components have a large influence on velocity control and positioning accuracy. The thing that separates linear motors from rotating motors is that linear motors have edges, limiting how far they can move. This is why linear motors have different characteristics when the mover is positioned in the center of the stator and when it is at the edge. In order to create a more advanced control design, it is possible to use a control simulation to obtain a linear motor model that exhibits more detailed behavior that is based on an actual machine.

With JMAG, it is possible to create a linear motor model that is detailed and conforms to a real machine, and that accounts for spatial harmonics and magnetic saturation characteristics included in a permanent magnet linear motor. Importing this linear motor model, a "JMAG-RT model," to a circuit/control simulator makes it possible to run a linked simulation that accounts for the linear motor's magnetic saturation characteristics and spatial harmonics as well as the driver's control characteristics.

This Application Note presents how to use JMAG-RT to obtain the spatial harmonics and current dependency of the thrust and coil inductance, and import them to a circuit/control simulator as a JMAG-RT model. From there, it shows how to perform an analysis that controls the speed of the permanent magnet linear motor to the desired value. The system that creates a JMAG-RT model using magnetic field analysis is referred to as JMAG-RT.



Speed/ Mover position

The time variations in speed are shown in fig. 1 and the time variations in mover position are shown in fig. 2 for when there is a constant command value of 0.8 m/s. The fact that this linear motor is running at its command value of 0.8 m/s can be confirmed in that the speed oscillates around 0.8 m/s in fig. 1, and that the slope in fig. 2 is about 0.8.

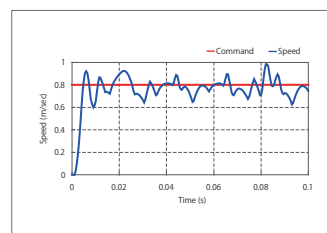


Fig. 1. Speed time variations

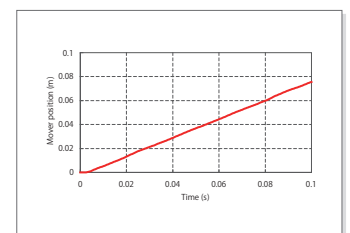


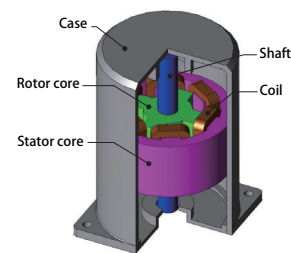
Fig. 2. Mover position time variations

Case 138 Vibration Analysis of an SR Motor

module: DP, DS

Overview

There are high hopes for SR motors to provide robustness and low cost, thanks to their relatively simple construction without permanent magnets. However, the large electromagnetic force produced by the saliency of their stator and rotor causes vibration and noise. The electromagnetic force working in an SR motor causes vibration and noise as an electromagnetic excitation force. Vibration and noise are caused when this electromagnetic excitation force resonates with the motor's eigenmode. In order to evaluate this phenomenon with acceptable precision, it is necessary to accurately ascertain the distribution of the electromagnetic force acting on the stator core, which is the source of radiated sound, and to obtain the eigenmode of the entire motor including its connected case. In this example, how to obtain the electromagnetic force generated in the stator core of an SR motor and evaluate the sound pressure by linking it to the motor's eigenmode.



Current Density Distribution and Electromagnetic Force Distribution

The contour plot of the current density distribution when the SR motor is at 45 deg of rotation and the vector plot of the electromagnetic force distribution of the stator core are indicated in Fig. 1. The frequency components of the electromagnetic force produced at the ends of the stator core's teeth are indicated in Fig. 2. The electromagnetic force at the stator core teeth tips gets very large from the timing of the current flow, as seen in Fig. 1. Fig. 2 shows that the 66.67 Hz frequency component is dominant in the electromagnetic force.

Eigenmode

The eigenmode at around 2,100 Hz is shown in Fig. 3. It can be seen that there is a mode at which the stator core is deformed to an ellipse at around 2,100 Hz. A great deal of vibration is likely to be caused by resonance phenomena between this eigenmode and the electromagnetic force.

Acceleration Distribution and Sound Pressure Distribution

Fig. 4 shows the acceleration distribution at 2,067 Hz, the frequency at which the mode occurs with elliptical deformation confirmed by eigenmode analysis. Fig. 5 shows the sound pressure level distribution. It can be seen that at 2,067 Hz, electromagnetic resonance occurs between the electromagnetic force and the eigenmode shown in Fig. 3.

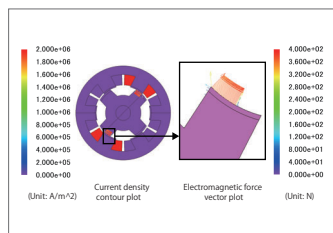


Fig. 1. Electromagnetic Force Distribution at a Rotation of 45 deg

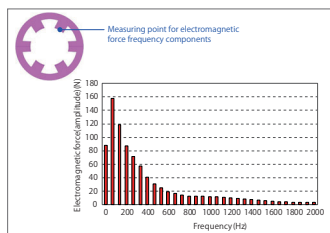


Fig. 2. Electromagnetic Force Frequency Components

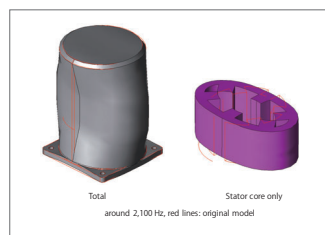


Fig. 3. Eigenmode with Deformation in the Radial Direction

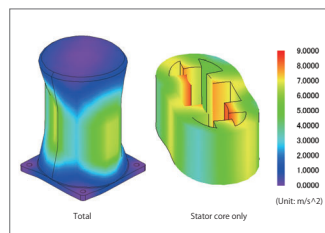


Fig. 4. Acceleration Distribution at 2,067 Hz

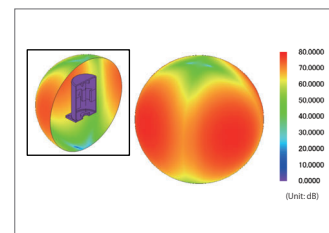
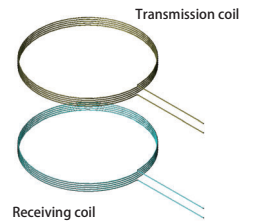


Fig. 5. Sound Pressure Level Distribution at 2,067 Hz

Case 139

Power Transmission Analysis Using Magnetic Resonance Phenomena

module: FQ



Overview

Recently, magnetic resonance is gaining attention as a new type of wireless transmission technology. Magnetic resonance differs from conventional types of electromagnetic induction transmission that are widely used today in that the axes of the transmission and receiving coils do not need to be aligned and in that it allows efficient transmission at a distance of several meters. A design for the coil geometry and circuit that is optimized for the frequency being used is necessary to make the transmitting and receiving sides resonate and thus transmit power. It is very difficult to use measurement to visualize how magnetic field is being generated, and is therefore transmitting power, in the space between the transmitting side and the receiving side. Reproducing the power transmission state using analysis can help with designing optimized coils.

This Application Note presents how to confirm the power transmission efficiency and the magnetic flux density distribution.

Power Transmission Efficiency

Graphs of power transmission efficiency for varying distances between the transmission and receiving coils are shown in figures 1 and 2. From fig. 1, it is apparent that with distances between the coils of 200 to 275 mm, there are peaks to each side of the resonance frequency of 17.5 MHz, at which a transmission frequency of nearly 100% is achieved. With a distance between the coils of 300 mm, there is one consolidated peak equal to the resonance frequency. Fig. 2 shows that with distances between the coils of 325 to 400 mm, power transmission efficiency does not reach 100% even at its peak, meaning reduced efficiency. Therefore, it can be said that the optimal distance for power transmission at a resonance frequency of 17.5 MHz is around 300 mm.

Magnetic Flux Density Distribution

Fig. 3 shows magnetic flux density distributions (amplitude) for 17.0 MHz, 17.5 MHz, and 18.0 MHz with distances between transmission and receiving coils of 200 mm, 300 mm, and 400 mm.

The figure makes it clear that, for each distance between transmission and receiving coils, magnetic flux density is larger near the receiving coil at a frequency with good power transmission efficiency. The size of the magnetic field can also be displayed in JMAG.

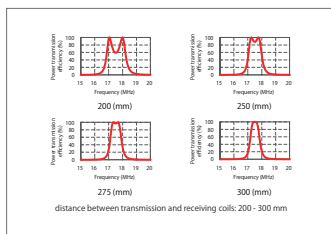


Fig. 1 Power transmission efficiency

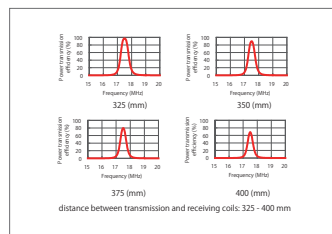


Fig. 2 Power transmission efficiency

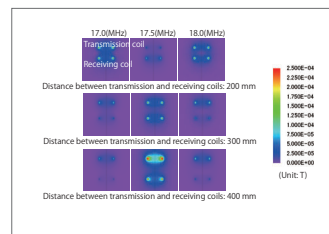
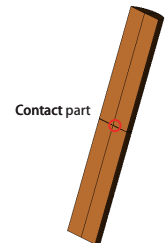


Fig. 3 Magnetic flux density distribution (amplitude)

Case 140

Analysis of Electromagnetic Repulsion Produced in Small Contact Bridges

module: TR



Overview

Electromagnetic repulsion is generated in the contact points of switches used in electrical equipment and current inflow points during resistance heating when contact terminals bridge through a small point. It is advantageous to investigate the size of the electromagnetic repulsion when designing a device, or to understand the phenomena that are actually occurring.

This Application Note presents the use of a magnetic field analysis to obtain the electromagnetic repulsion when a switch is closed, creating a contact bridge.

Current Density Distribution, Lorentz Force Density Distribution, Electromagnetic Repulsion

This section shows the current density distribution near the contact terminal in fig. 1, the Lorentz force density distribution in fig. 2, and the electromagnetic repulsion in fig. 3.

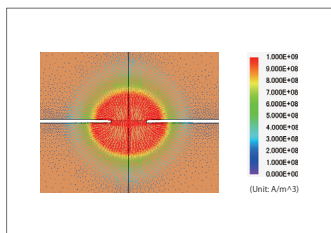


Fig. 1 Current density distribution

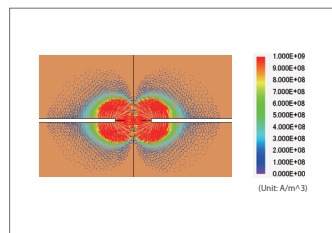


Fig. 2 Lorentz force density distribution

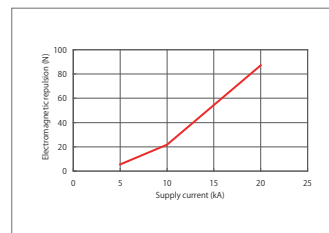


Fig. 3 Current characteristics of the electromagnetic repulsion

Case 142 Press Fit Analysis of a Divided Core

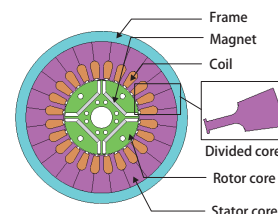
module: DS, DP, LS

Overview

Smaller size and higher output are being demanded of the motors used for applications such as air conditioning compressors. One production technique for achieving this is a higher lamination factor in divided cores. The stress caused by press-fitting a divided stator core into a frame is known to increase iron loss in a motor if magnetic steel sheet is used for the core.

Iron loss is affected by magnetic flux density and stress. Specifically, it increases in areas of high magnetic flux density with high frequency, and in areas of high stress. Further, the stress caused by press fitting has its own distribution, and is particularly large in the core and back yoke. So, in order to evaluate the iron loss with good accuracy, it is necessary to correctly obtain the magnetic flux density distribution, time variations, and stress distribution.

This Application Note presents how to use the Press Fit condition to model an analysis of the stress from fitting a core to a frame, and then obtain the iron loss density of an IPM motor under no load, with and without accounting for the stress.



Minimum Principal Stress Distribution

The minimum principal stress distribution is indicated in fig.1. Tensile stress occurs in the frame and teeth, but compressive stress that especially effects iron loss is produced largely in the contact faces between the divisions of the core. The compressive stress is especially large in the area of the model within the square in fig.1, but this is because of the slots' geometry.

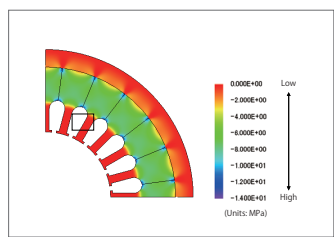


Fig. 1. Minimum principal stress distribution

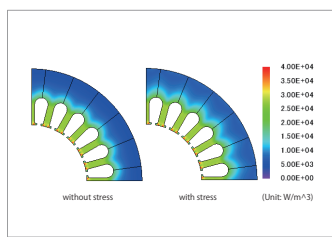


Fig. 2. Iron loss density distribution

Iron Loss Density Distribution

Fig.2 shows the iron loss density distribution, and Fig.3 shows the comparison of iron loss values. The iron loss density distribution varies depending on whether or not the stress is accounted for, with iron loss increased by around 10% due to the stress. An analysis that accounts for the compressive stress caused by the press-fitting needs to be performed to evaluate the iron losses more accurately because the iron losses increase when the compressive stress is applied.

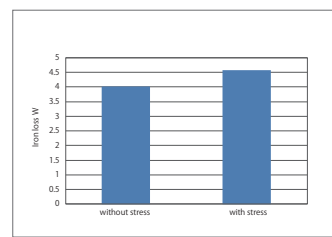


Fig. 3. Iron loss

Case 143 Inductance Analysis of an Air Core Coil

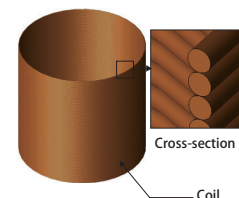
module: ST

Overview

Electric components such as choke coils and chip inductors are used for purposes such as reducing electromagnetic noise by taking advantage of their own inductance. Air core coils have smaller inductance than those with cores, but because they do not use cores with nonlinear magnetization properties, they maintain linearity in their inductance and can therefore be used in high-frequency filters and oscillators.

In a coil with a core, most of the magnetic flux flows in the core, but because the magnetic circuit in an air core coil is not as clearly structured as in a core, the inductance is easily influenced by the coil's dimensions and geometry. Because of this, it is necessary to accurately understand the inductance by analyzing the flow of magnetic flux in the air region.

This analysis shows how to obtain an air core coil's inductance through analysis and compare it with theoretical values.



Magnetic Flux Density Distribution/ Inductance

The magnetic flux density distribution in the coil and the air region around it is shown in fig. 1 and the coil's inductance is shown in table 1. The inductance from the analysis results is compared to theoretical values.

Fig. 1 shows that the density of the coil's flux linkage is higher in the center of the coil. The difference between the inductance obtained from the flux linkage and theoretical values is 0.28%. This confirms that essentially accurate inductance can be obtained using analysis.

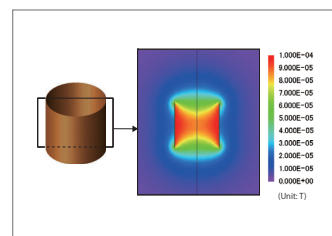


Fig.1. Magnetic flux density distribution

Analysis (H)	Theoretical (H)	Difference (%)
6.77e-03	6.79e-03	0.28

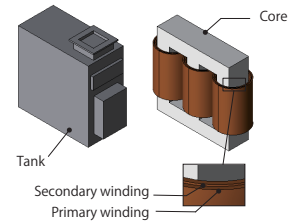
Table 1. Inductance

Overview

Transformers are made to be used long-term, so it has become an important design policy to control running costs from losses. These losses include copper loss in the coil and iron loss in the core. In high-capacity transformers, however, there is also stray loss in the tank from flux leakage from the core. From a safety standpoint, companies want to contain the heat produced from stray losses in the tank to well below the standards required for heat resistant design because they anticipate injuries from people touching the tank itself.

Predicting these losses and the heat that they generate is a vital component of transformer design, but it is difficult to estimate them from desktop calculations, so evaluations and detailed analyses using the finite element method (FEM) are indispensable.

This Application Note explains how to obtain losses in a transformer tank and use them to evaluate the temperature distribution in each part.



Joule Loss Density Distribution

Fig. 1 shows the magnetic flux density distribution, fig. 2 shows the current density distribution, and fig. 3 shows the joule loss density distribution in the tank. From fig. 1, it is apparent that magnetic flux is leaking from the transformer to the tank. This leakage flux generates eddy currents in the tank, as shown in fig. 2. Fig. 3 shows that joule losses get bigger in places with high current density.

Iron Loss Density Distribution

Fig. 4 shows the iron loss density distribution in the core. From fig. 4, it is apparent that iron losses increase in the inside corners. This is caused by the flow of magnet flux concentrating on the shortest path through the magnetic circuit.

Losses

Fig. 5 and Fig. 6 shows the losses in each part. Use these loss values as heat sources to run the thermal analysis.

Temperature Distribution

Fig. 7 shows the core's temperature distribution, fig. 8 shows the winding's temperature distribution, and fig. 9 shows the tank's temperature distribution. From fig. 7, it is apparent that the temperature in the outside of the core is lower than in the inside of the core. This is because the core is cooled by insulating oil. In the same way, from fig. 8 it is apparent that the primary winding on the outside has a lower temperature than the secondary coil on the inside. From fig. 9, it is apparent that the temperature of the tank has not risen higher than the temperature of the insulating oil.

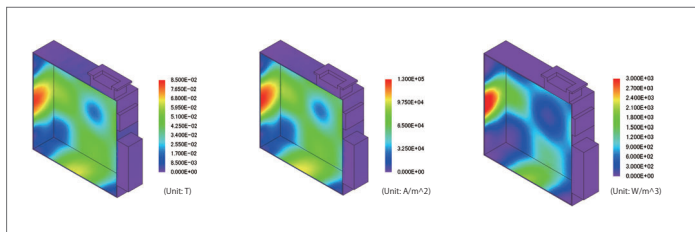


Fig. 1 Magnetic flux density distribution in the tank

Fig. 2 Current density distribution in the tank

Fig. 3 Joule loss density distribution in the tank

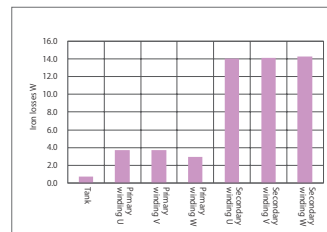


Fig. 6. Losses (Other than core)

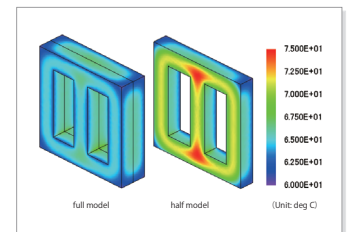


Fig. 7. Temperature distribution of the core

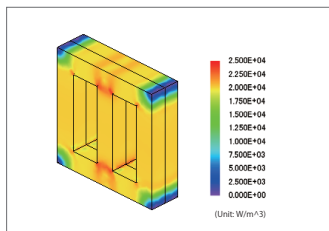


Fig. 4 Iron loss density distribution

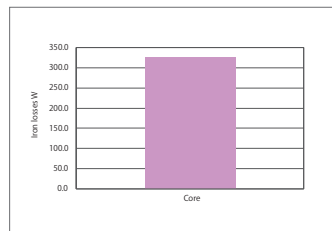


Fig. 5. Losses(Core)

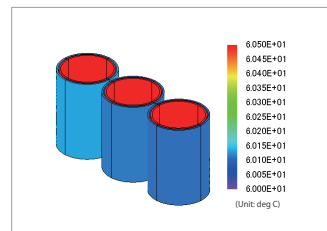


Fig. 8 Temperature distribution in the winding

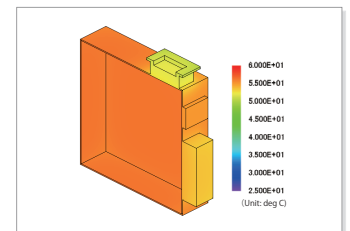


Fig. 9. Temperature distribution of the tank

Case
148

Loss Analysis of a Power Transformer (Flyback Converter)

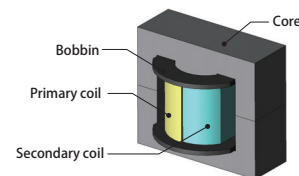
module: TS, DP, ST, LS

Overview

A flyback converter is a well-known system for small capacity power supplies in the several-dozen W class. They are cheap and have a simple structure, so they are widely used as converters for pressurization in home appliances. In recent years there has been a trend toward making small-scale switching transformers even smaller and higher-frequency, so it is not rare to see converters using the flyback system drive 100 kHz or more. Because of the higher frequencies and smaller scales of transformers, an important challenge of how to control their heat generation has emerged in the design process. The losses that produce heat can be separated into copper loss in the coil and iron loss in the core. Copper loss is distributed inside of the coils because of the proximity effect, which is caused by influence from the skin effect and leakage flux. This means that local heat generation in the coils becomes a problem.

Iron loss also has a complex distribution because it depends on the magnetic flux density distribution that accounts for the core's magnetic saturation, so the core's local heat generation becomes a problem as well.

A magnetic field analysis simulation based on the finite element method (FEM) can precisely evaluate the complex loss distributions of the coil and core, so it is optimal for an advance study of a switching transformer's thermal design.



Iron Loss Density Distribution

Fig. 1 shows the iron loss density distribution.

From the figure, it is apparent that iron losses increase in the inside corners. This is caused by the flow of magnet flux concentrating on the shortest path through the magnetic circuit.

Percentage of Loss

The percentages of the iron and copper losses are indicated in table 1. As the table indicates, the iron losses are dominant in this transformer.

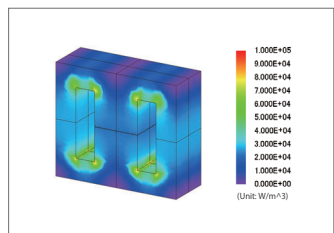


Fig. 1. Iron loss density distribution

Type of loss	Loss value (W)	Percentage (%)
Iron loss	1.56e-01	76.7
Copper loss	4.73e-02	23.3

Table 1. Ratio of loss

Copper Loss Density Distribution

Fig. 2 shows the coil's joule loss density distribution when the maximum current is flowing through the primary coil.

The joule losses are larger around the gap, as indicated in this figure. These joule losses are produced by the leakage flux from the gap that causes the current distribution in the wires to be uneven.

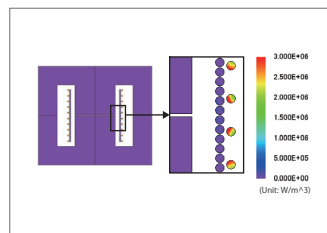


Fig. 2. Joule loss density distribution of the coil

Case
149

Analysis of Magnetic Force Acting on the Arc of a Vacuum Circuit Breaker

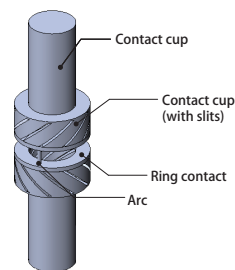
module: TR

Overview

Vacuum circuit breakers have the function of breaking the current when a large current flows due to a short circuit or other reason in distribution boards, etc. When the vacuum circuit breaker breaks the current, metal vapor is discharged from the contacts and becomes a plasma, producing an arc. Vacuum evaporation may occur due to this arc.

To avoid vacuum evaporation caused by an arc, a magnetic field is created by the arrangement of the contacts, and the arc is diffused with Lorentz force. Because the construction of the contacts is complex, it is important to analyze the magnetic field using the finite element method (FEM), which can handle complex geometries, to estimate whether the arc will be adequately diffused.

This Application Note presents how to calculate the current density and Lorentz force of a vacuum circuit breaker, and obtain its arc-diffusing force.



Lorentz Force

The direction of the Lorentz force generated in the arc is shown in fig. 1. A force of 6 N works in a direction -51 deg from an X-axis passing through the center of the arc.

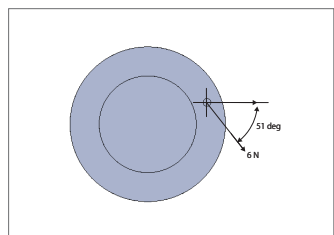


Fig. 1. Direction of Lorentz force

Current Density Distribution and Magnetic Flux Density Distribution

The current density distribution is shown as a vector plot in fig. 2, and the magnetic flux density distribution of a cross-section of the arc is shown as a contour plot in fig. 3. Current flowing in the contact cup as shown in fig. 2 causes magnetic flux to be generated as shown in fig. 3. The magnetic flux density to the upper left of the center of the arc is larger than the magnetic flux density to the lower right. Therefore, force is produced from the upper left to the lower right.

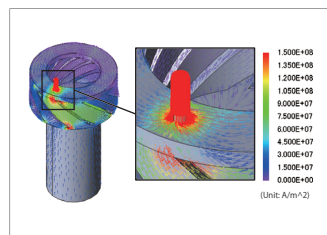


Fig. 2. Current density distribution

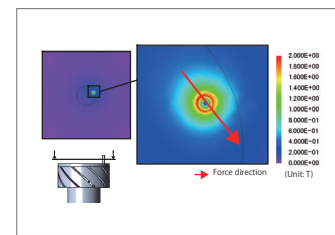


Fig. 3. Magnetic flux density distribution (arc cross-section)

Case 150

Electromagnetic Repulsion Analysis of a Vacuum Circuit Breaker

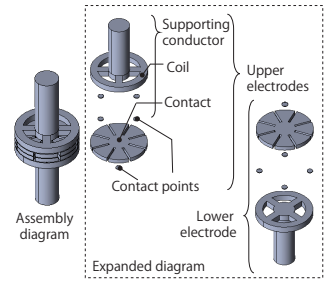
module: TR

Overview

Vacuum circuit breakers have the function of breaking the current when a large current flows due to a short circuit or other reason in distribution boards, etc. Contact pressure is applied to the contacts in a vacuum circuit breaker because it is necessary for the vacuum circuit breaker's contacts to be in contact and the electric circuit to be closed when normal current is flowing, unlike the large current from a short circuit.

Electromagnetic repulsion is produced by the current flowing in a vacuum circuit breaker's contacts when current flows through the vacuum circuit breaker. Therefore, it is necessary to evaluate the electromagnetic repulsion and set the contact pressure higher than the electromagnetic repulsion in order to maintain a closed state during normal current.

This Application Note presents how to obtain the electromagnetic repulsion in a circuit breaker from the Lorentz force when a 100 kA current is flowing.



Current Density Distribution

Current density distributions are shown in figures 1, 2, and 3. The current that flows into the supporting conductor of the lower electrode divides in the coil and flows to the contact via the contact points as shown in (a). Then, the current that has flowed into the contact is concentrated at the contact point as seen in (b). When current flows into the contact of the upper electrode from the narrow contact points, it tries to spread out as shown in fig. 3.

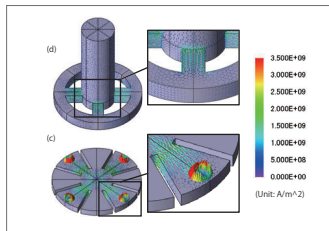


Fig. 1 Current density distribution (upper)

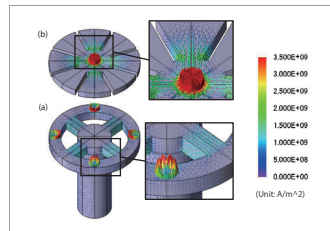


Fig. 2 Current density distribution (lower)

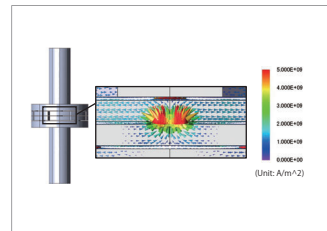


Fig. 3 Current density distribution (ZX plane around contacts)

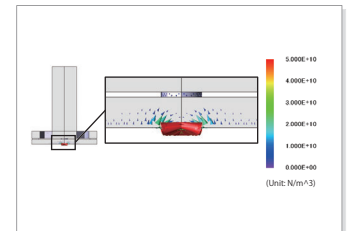


Fig. 4 Lorentz force density distribution (ZX plane around contacts)

Lorentz Force Density Distribution and Electromagnetic Force

The Lorentz force density distribution is shown in fig. 4. Vertically repulsive force is generated in the contacts by the current flowing as shown in fig. 3. Electromagnetic repulsion of approximately 700 N is generated in the contacts.

Case 151

Insulation Evaluation Analysis of a Power Transformer

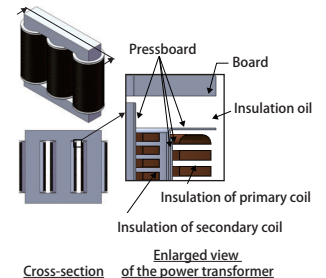
module: EL

Overview

A transformer is an electrical device that uses electromagnetic induction to convert the voltage level of alternating current power. Among transformers, power transformers that are used in power conversion have extremely high electric fields applied to their coils, so insulation technology like the winding structure, insulating materials, and insulation structure are vital in attaining miniaturization and higher capacity. In addition to normal power conversion, a transformer's insulation structure has to be designed to be able to withstand lightning strikes and excess voltage during short circuits.

A transformer's dielectric strength is dependent on the electric field intensity applied to the insulating material, so the electric field intensity needs to be examined before the safety factor for the insulation breakdown can be estimated.

This Application Note shows how to obtain the electric field intensity distribution when a lightning strike or short circuit occurs and the assumed maximum voltage is applied to the winding.



Electric Filed Distribution

Fig.1 shows the electric field distribution when a voltage difference is applied between the primary coil's insulating material and the secondary coil's insulating material. The maximum electric field intensity is about 8 kV/mm, which does not exceed the dielectric strength. From the distribution, it is also possible to confirm which parts large electric fields are generated in.

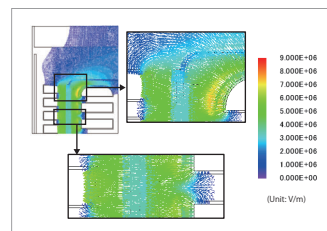


Fig. 1 Electric field distribution

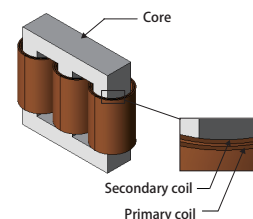
Case 152 Electromagnetic Force Analysis of Short-circuited Power Transformer Coils

module: FQ

Overview

A transformer is an electrical device that uses electromagnetic induction to convert the voltage level of alternating current power. Electromagnetic force is produced by the current and magnetic field in a transformer's coils while it is converting power. There is a risk that a large electromagnetic force can cause the coils to deform or rupture, particularly when something goes wrong and current flows in a short circuit. Electromagnetic force is produced by the current and magnetic field in a coil, but the coil is exposed to not only the magnetic field it produces by itself but also the magnetic field from other coils and leakage flux from the core. Because of this, it is important to evaluate in advance what kinds of forces are produced in what areas due to the arrangement of the coils and the positional relationship of the coils and core using magnetic field analysis.

This analysis uses different coil positions to evaluate the Lorentz force density and electromagnetic force produced in the coils during a short circuit in order to confirm the effects that the primary and secondary coils have on each other.



Lorentz Force Density

The Lorentz force density distribution vectors of the V-phase coil as seen from the X-axis are shown in fig. 1, and the Lorentz force density distribution vectors of the three phases as seen from the Z-axis are shown in fig. 2. From fig. 1, it can be seen that the direction of the force working on the coil varies according to how the coils are wound. Fig. 2 indicates that in models A and D, in which the deviation of the Lorentz force is large, the Lorentz force density to the inside grows large because it is influenced by the adjacent coils.

Electromagnetic Force

The electromagnetic force of the V-phase coil is shown in fig. 3. The Z-component graph shows that, in all of the models, repulsion force is produced that mutually separates the primary and secondary coils. In an actual machine, the Z-component force is canceled out by symmetry, but this force can be seen in analysis because only a half model is used. From the Y-component graph, it can be seen that a greater force is working in models A and B compared to the other models. When the balance of the coil's winding method is asymmetrical vertically, a large force is produced in the vertical direction in addition to the repulsion in the radial direction, as indicated by the Lorentz force density vectors in fig. 1. The overall force in model D is canceled out so its Y-component force is zero, but by looking at the Lorentz force density vector distribution, it can be seen that force is produced a direction that compresses the primary coil as a whole.

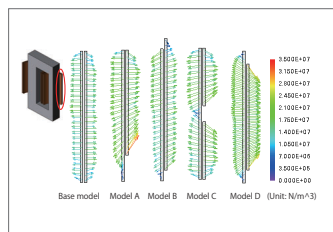


Fig. 1. Coil Lorentz force density distribution (V-phase, YZ plane)

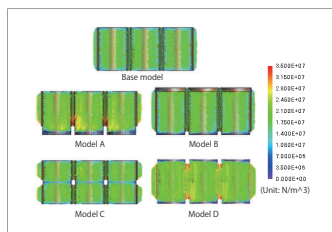


Fig. 2. Coil Lorentz force density distribution (XY plane)

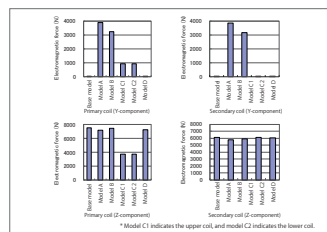
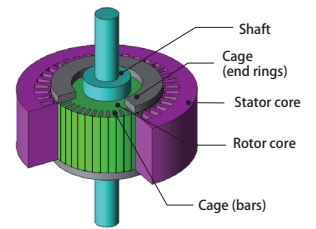


Fig. 3. V-phase coil electromagnetic force graphs



Overview

An induction motor is a motor in which the rotating magnetic field of the stator coils causes induced current to flow in an auxiliary conductor, exerting force on the rotor in the rotational direction and causing it to spin. Induction motors are widely used in everything from industrial machines to home appliances because they have a simple construction and are small, light, affordable, and maintenance-free. An induction motor's characteristics are influenced by leakage reactance and resistance, including resistance on the secondary side. These are referred to as equivalent circuit parameters, and they are important because they characterize a device's properties. Equivalent circuit parameters are greatly affected by both the current distribution induced in the auxiliary conductor and the magnetic saturation near the gap, so a finite element analysis (FEA) needs to be run in order to investigate these characteristics with precision.

This Application Note explains how to obtain the secondary resistance, leakage inductance, and excitation inductance of an induction motor when its power supply frequency has been changed with regard to its voltage and current controls.

Equivalent Circuit Parameter Frequency Characteristics (Voltage Control)

The secondary resistance when the power supply frequency in the voltage control has been changed is shown in fig. 1, the leakage inductance is shown in fig. 2, the magnetic flux density distribution during the lock test is shown in fig. 3, the current density distribution is shown in fig. 4, the excitation inductance is shown in fig. 5, and the magnetic flux density distribution during the no-load test is shown in fig. 6. The leakage inductance is the sum of the primary and secondary leakage inductances.

The equivalent circuit parameters change according to the frequency in each result. This is because the primary and secondary currents as well as the current distribution in the bars change according to the frequency.

Equivalent Circuit Parameter Frequency Characteristics (Current Control)

The secondary resistance when the power supply frequency in the current control has been changed is shown in fig. 7, the leakage inductance is shown in fig. 8, the magnetic flux density distribution during the lock test is shown in fig. 9, the current density distribution is shown in fig. 10, the excitation inductance is shown in fig. 11, and the magnetic flux density distribution during the no-load test is shown in fig. 12. The leakage inductance is the sum of the primary and secondary leakage inductances.

The equivalent circuit parameters change according to the frequency in each result. The excitation inductance also has a constant value. For current control, the excitation current during the no-load test does not change with the frequency and the excitation inductance is constant because induction current does not flow through the cage.

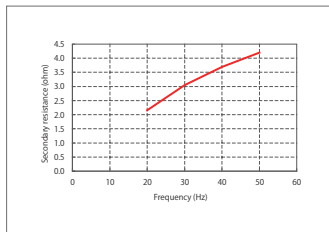


Fig. 1 Frequency characteristics of the secondary resistance

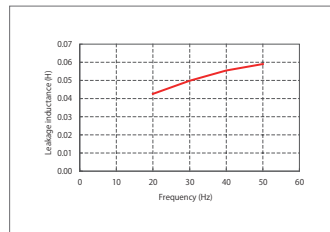


Fig. 2 Frequency characteristics of the leakage inductance

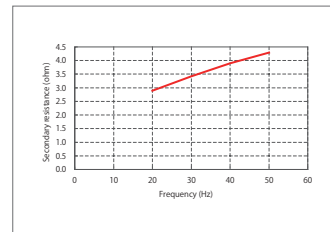


Fig. 7 Frequency characteristics of the secondary resistance

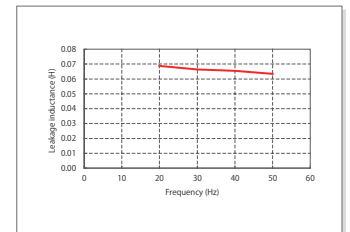


Fig. 8 Frequency characteristics of the leakage inductance

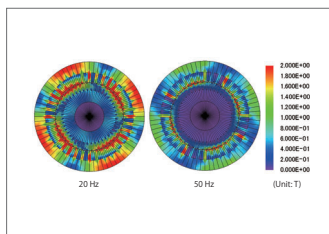


Fig. 3 Magnetic flux density distribution during lock test

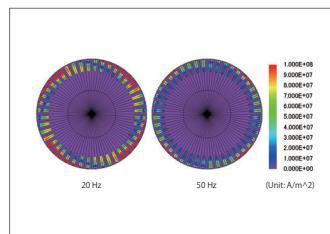


Fig. 4 Current density distribution during lock test

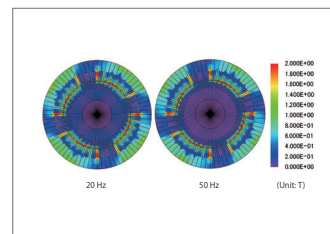


Fig. 9 Magnetic flux density distribution during lock test

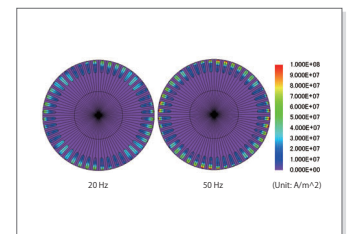


Fig. 10 Current density distribution during lock test

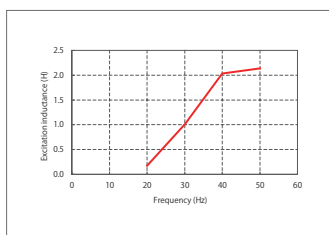


Fig. 5 Frequency characteristics of the excitation inductance

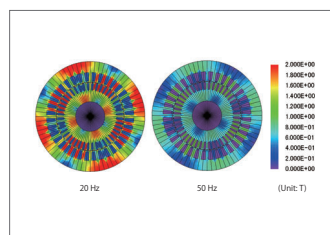


Fig. 6 Magnetic flux density distribution during no-load test

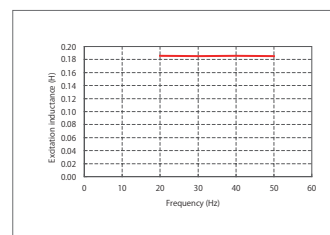


Fig. 11 Frequency characteristics of the excitation inductance

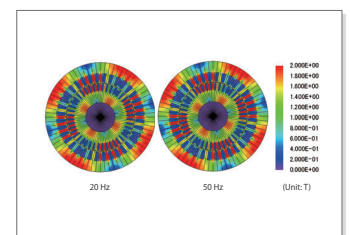


Fig. 12 Magnetic flux density distribution during no-load test

Case 156 Segregation Analysis of Torque Components for an IPM Motor

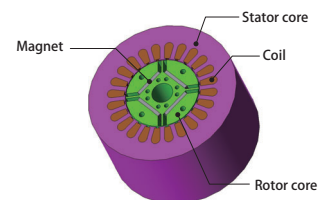
module: DP

Overview

IPM motors are often used as high performance motors because they are highly efficient and their structure makes it possible to achieve a wide range of operation. They are able to achieve high efficiency because they obtain maximum total torque by using their controls to adjust their magnet and reluctance torques. For this reason, it is important to find out the distribution of both of these torques during operation when the IPM motor is being designed. The motor's detailed geometry and the material's nonlinear magnetic properties need to be taken into account to obtain the torque characteristics, and it is even more difficult to segregate the torque into two components by using manual calculations.

In order to proceed with the design while looking into how much each one contributes, it needs to be studied with an electromagnetic field analysis that uses the finite element method (FEM).

In this Application Note, the torque components are separated and the magnetic flux density distributions created by each magnetomotive force are confirmed.



Torque Versus Current Phase Angle

Fig. 1 shows a graph of the torque versus current phase angle. As can be seen in the graph, the maximum torque is obtained when the current phase angle is near 20 deg. The magnet torque also takes up a bigger portion of the total torque.

Magnetic Flux Density Distribution, Magnetic Flux Lines

Fig. 2 shows a contour plot of the magnetic flux density distribution and magnetic flux lines.

As can be understood from these figures, it is possible to visualize the condition of the magnetic circuit in addition to segregating the torque values. From these, it is possible to confirm the effects on the torque of each magnetomotive force.

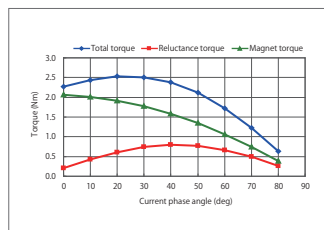


Fig. 1 Torque versus current phase angle

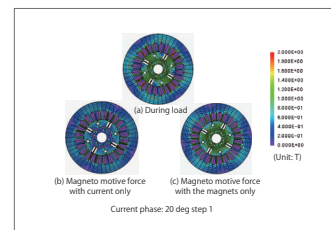


Fig. 2 Magnetic flux density distribution, magnetic flux lines

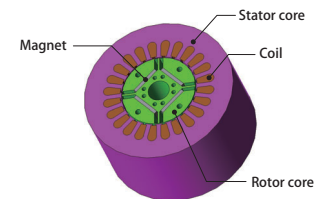
Case 157 Analysis of Eddy Currents in an IPM Motor Using the Gap Flux Boundary

module: DP, FQ

Overview

It is becoming increasingly common for permanent magnet motors to use rare earth magnets in order to achieve higher output density because they have a high energy product. Neodymium rare earth magnets have a high electric conductivity because they contain a great deal of iron, so when a varying magnetic field is applied to them they produce joule loss from eddy currents. IPM structure adoption and field weakening controls have become prevalent in recent years in order to allow faster rotation. This has led to an increase in the frequencies and fluctuation ranges of the varying fields applied to magnets, resulting in a corresponding increase in joule losses. By dividing the magnet like one would a laminated core to control eddy currents, one can obtain a method of raising the apparent electric conductivity while lowering the eddy currents. Armature reactions in the stator occur before the eddy currents produced in the magnet, so the eddy currents are determined by: The slot geometry of the stator core, the geometry of the rotor, the nonlinear magnetic properties of the core material, and the current waveform that flows through the coil. In order to examine these kinds of magnet eddy currents ahead of time, one has to be precise when accounting for things like these various geometries and material properties. This is why a magnetic field simulation using the finite element method (FEM), which can account for them, would be the most effective.

This Application Note explains how to use the gap flux boundary condition to evaluate the eddy current loss in the magnet by changing the number of magnet divisions. This will make it possible to obtain effective results in a shorter period of time than with a normal transient response analysis.



Change in the Losses of the Divided Magnet

Fig. 1 shows the magnet's eddy current losses and fig. 2 shows the eddy current loss density distribution.

From fig. 1, it is apparent that the losses are largest at 2880 Hz. This is caused by the effects from the slot harmonic components, which are decided by multiplying the rotation speed by the number of slots. From fig. 1 and 2, it is also apparent that the eddy current losses decrease as the number of magnet divisions increases.

By increasing the number of divisions in the magnet, the magnetic flux that links the individual magnets is reduced. Because of this, the eddy current density in each divided magnet is reduced as well, making it so that the total amount of eddy current loss decreases.

Eddy Current Density Distribution in the Magnet

Fig. 3 shows the eddy current density distribution in the magnet at 2880 Hz. It is apparent that dividing the magnet causes the eddy currents to decrease.

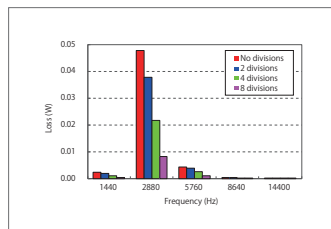


Fig. 1 Eddy current loss of the magnet

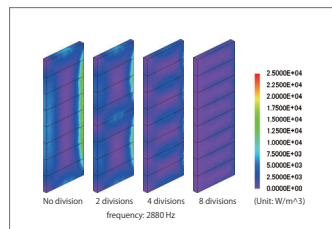


Fig. 2 Eddy current loss density distribution in the magnet

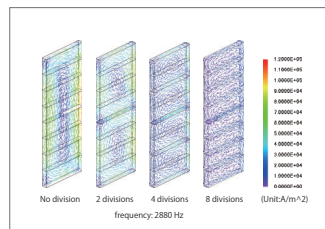


Fig. 3 Eddy current density distribution in the magnet

Superimposed Direct Current Characteristic Analysis of a Reactor That Accounts for Minor Hysteresis Loops

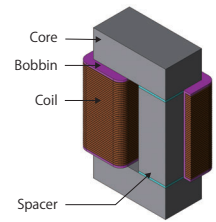
module: FQ, ST

Overview

High-frequency reactors used in equipment like DC-DC converters have a high-frequency current accompanying the switching direct current. The reactor's performance requires a stable inductance in a wide direct current region that is superimposed by alternating current components. If there is only a direct current, the magnetic flux is generated against the external magnetic field, following the magnetic steel sheet's DC magnetization curve. However, when there is a current waveform whose high-frequency components are superimposed on the direct current component, the response displays a minor loop against the external magnetic field. The values of the inductance in the reactor can have significant differences depending on the method used to measure them. This can make it difficult to carry out a performance prediction during an actual state of operation.

In order to handle the responsiveness of a magnetic field against a current waveform that is superimposed by a higher harmonic with a small amplitude for the direct current component, a magnetic field analysis that accounts for material modeling needs to be carried out. With a magnetic field analysis, it is possible to analyze the machine characteristics from the magnetic flux density distribution.

This Application Note presents the use of the frozen permeability condition to obtain the superimposed direct current characteristic that includes minor hysteresis loops of a high-frequency reactor.



Superimposed direct current characteristics, Magnetic flux density distribution

This section shows the superimposed direct current characteristics in fig. 1 and the core's magnetic flux density distribution in fig. 2 as analysis results of the reactor described. From fig. 1, it is apparent that the inductance decreases more rapidly as the direct current increases. This is caused by influence from magnetic saturation, as shown in fig. 2.

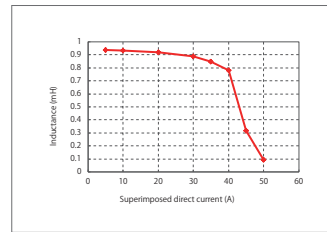


Fig. 1 Superimposed direct current characteristics

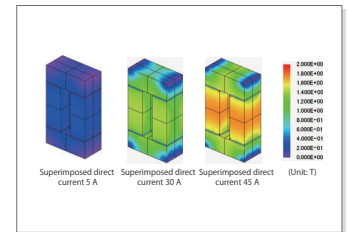


Fig. 2 Magnetic flux density distribution (during DC flow)

Sensitivity Analysis of Dimensional Tolerance in an SPM Motor

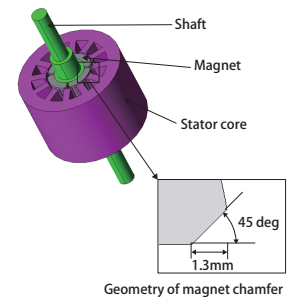
module: DP

Overview

The corners of magnets used in surface permanent magnet (SPM) motors can be filleted, chamfered, etc. However, it is difficult to maintain exactly the same production in the manufacturing process, and some variation among finished products will occur. Dimensional tolerance is set so as to eliminate the effects of these variations on motor performance.

There are tradeoffs between dimensional tolerance, performance, and cost, so it is important to investigate these at the design stage. With numerical analysis using the finite element method (FEM), it is possible to evaluate the sensitivity of motor performance, such as torque, by simply changing the dimensions.

This Application Note presents how to assume a dimensional tolerance of ± 0.4 mm for a chamfer, and find out whether changing dimensions within the tolerance range has an effect on motor performance by comparing cogging torque and induced voltage.



Cogging torque

The cogging torque waveform is shown in fig. 1, and the frequency components of the cogging torque are shown in fig. 2. Although the location of the peak value is different when the size of the chamfer is changed, the peak value is almost the same, as indicated in fig. 1. Differences at the fundamental frequency of 360 Hz are small when compared with higher harmonic components, as confirmed by the frequency components in fig. 2. From this, it can be determined that variations in the chamfer occurring within the tolerance range have little effect on the cogging torque.

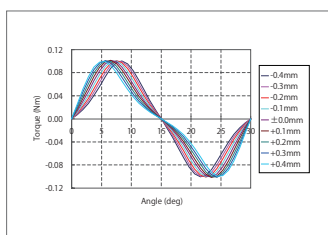


Fig. 1. Cogging torque

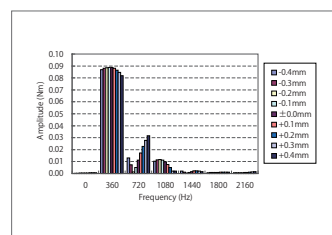


Fig. 2. Frequency components of cogging torque

Induced voltage

The induced voltage waveform is shown in fig. 3, and the frequency components of the induced voltage are shown in fig. 4. Even when the size of the chamfer is changed, the induced voltage value is almost the same, as indicated in fig. 3. Differences at the fundamental frequency of 60 Hz are small when compared with higher harmonic components, as confirmed by the frequency components in fig. 4. From this, it can be determined that there are few effects from the chamfer tolerance.

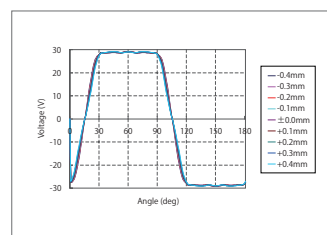


Fig. 3. Induced voltage

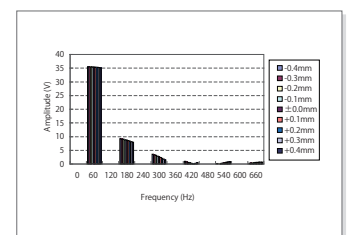
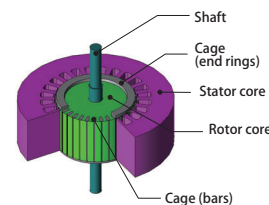


Fig. 4. Frequency components of the induced voltage

Case 161 Line Start Analysis of a Three-phase Induction Motor

module: DP



Overview

The simplest method for starting an induction motor is a line start that connects the motor to a direct power supply. For a line start, the static impedance is small compared to impedance during rated operation, so a large current flows during the initial start-up. The large current flowing through both the primary and secondary sides during start-up causes intense magnetic saturation near the induction motor's gap. This magnetic saturation results in reduced impedance, so the starting current grows even larger. The size of the starting current affects the voltage source capacity connected to the induction motor, as well as both the electromagnetic force and heat capacity that operate on the motor's coils. This is why it is beneficial to investigate the starting performance of an induction motor with the finite element method (FEM), which can account for local magnetic saturation. This Application Note presents an analysis that simulates the line start of an induction motor and obtains the starting performance of its rotation speed variations.

Rotation Speed Waveform

The rotation speed waveform when starting the induction motor is indicated in fig. 1. Fig. 1 shows that the motor accelerates rapidly at the initial start-up, and reaches a steady state at approximately 0.5 s.

Torque waveform

The waveforms of the drive torque and load torque when starting the induction motor are indicated in fig. 2. Fig. 2 shows that an extremely large drive torque is produced at the initial start-up. In a steady state, a drive torque that is almost constant is generated in order to achieve balance with the load torque.

Current waveform

The current waveform of the stator coil when the induction motor starts is indicated in fig. 3. Fig. 3 shows that an extremely large current is produced during the initial start-up. This is because the reverse voltage at initial start up is small and almost all of the power supply voltage is applied to the stator coils. At a steady state, the three-phase AC has an amplitude of less than 5 A.

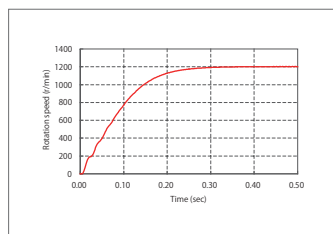


Fig. 1. Rotation speed waveform

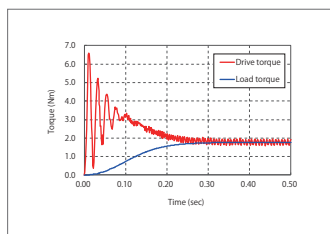


Fig. 2. Torque waveform

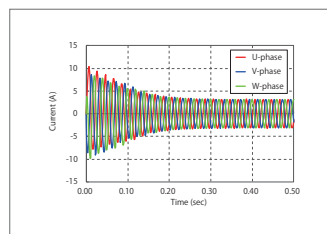
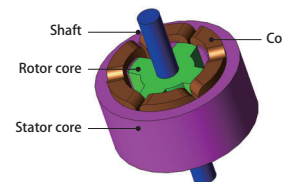


Fig. 3. Current waveform

Case 162 Drive Simulation of an SR Motor using a Control Simulator and JMAG-RT

module: DP, RT



Overview

SR motors are gaining attention as motors that do not use permanent magnets. However, torque pulsation is greater in SR motors because of the way their torque is generated, so it is seen as important to suppress torque pulsation not only with detailed design of magnetic circuits, but also using SR motor control. In order to evaluate suppression of torque pulsation with control simulation, it is necessary to have an SR motor model that shows behavior conforming to a real motor. With JMAG, it is possible to create a detailed model that conforms to a real machine and accounts for the torque's dependency on rotor angle and the magnetic saturation characteristics of the magnetic circuit in an SR motor. Importing this motor model, a "JMAG-RT model," to a control/circuit simulator makes it possible to carry out a linked simulation that accounts for an SR motor's detailed characteristics as well as a motor drive's control characteristics. This kind of operation makes control simulation to suppress an SR motor's torque pulsation possible. In this Application Note, after using JMAG-RT to obtain an SR motor's torque and inductance characteristics, the JMAG-RT model is imported into a circuit/control simulator, voltage is applied to drive the SR motor, and the torque pulsation is analyzed. By evaluating the obtained torque pulsation in detail, investigations can be carried out to reduce the torque pulsation (this Application Note does not incorporate actual attempts to reduce torque pulsation).

Rotation Speed Waveform/Torque Waveform/Current Waveform

Fig. 1 shows the rotation speed waveform, fig. 2 shows the torque waveform, and fig. 3 shows the current waveform when the SR motor is driven. A large phase current flows immediately after starting because the rotation speed is slow and the starting voltage is small, but this is suppressed to an upper limit by the current limit value. At this time, a lot of torque is generated, and the rotation speed increases rapidly. Once the rotation speed increases a certain amount, the rotation speed, torque, and current settle into a steady state because the starting voltage rises and the current limit becomes irrelevant. The rotation speed also oscillates because the torque ripple in the steady state is large. Evaluation of excitation timing and control of the current waveform itself are possibilities for ways to reduce this.

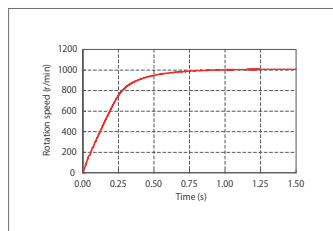


Fig. 1. Rotation speed waveform

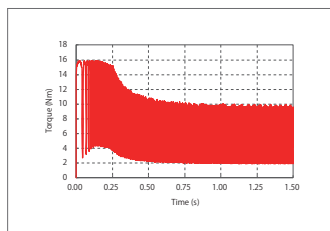


Fig. 2. Torque waveform

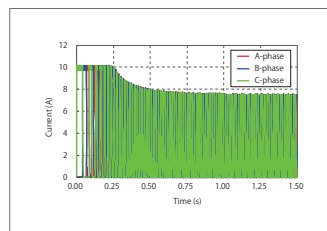
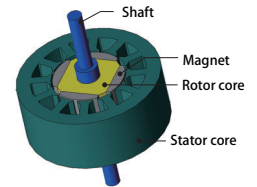


Fig. 3. Current waveform

Case 163

Torque-Current Curve Analysis of an SPM Motor

module: DP



Overview

One of the fundamental properties of a permanent magnet synchronous motor is the relationship between its current and torque (torque-current curve). The torque generated at each current value is uniform with increases in current up to a certain point, so the torque increases in a linear fashion. However, magnetic saturation effects occur with further current increases, and the torque generated with each increase in current begins to drop off.

Because a permanent magnet synchronous motor's torque-current curve is highly susceptible to saturation effects in the motor's magnetic circuit, it is helpful to obtain the torque-current curve with a magnetic field analysis taking saturation into account in order to evaluate the motor's design and drive characteristics.

This Application Note presents how to obtain the torque-current curve as a basic property of one type of permanent magnet synchronous motor, the surface permanent magnet synchronous (SPM) motor.

Magnetic Flux Density Distribution

Figures 1 and 2 show the magnetic flux density distribution at current amplitudes of 10 A and 200 A.

From the figures, it can be seen that there are differences in the flow of magnetic flux due to larger and smaller current amplitude, such as changes in the locations of teeth with high magnetic flux density. This is due to magnetic saturation in the teeth, and these changes in the flow of magnetic flux affect the torque.

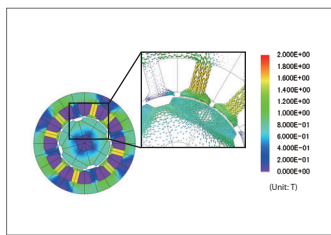


Fig. 1. Magnetic flux density distribution (current amplitude: 10 A)

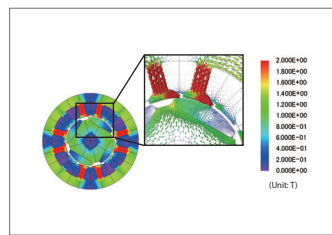


Fig. 2. Magnetic flux density distribution (current amplitude: 200 A)

Torque-Current Curve, Torque Constant-Current Curve

Figures 3 and 4 show the torque-current curve and torque constant-current curves. It can be seen from figures 3 and 4 that the ratio of torque increase declines with increased current. This is because the flow of magnetic flux changes, as seen in figures 1 and 2.

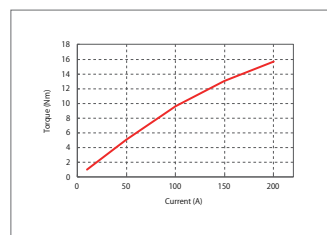


Fig. 3. Torque-current curve

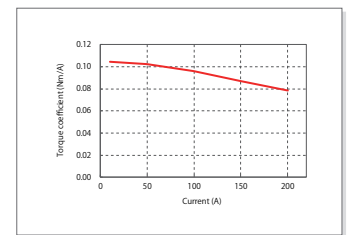
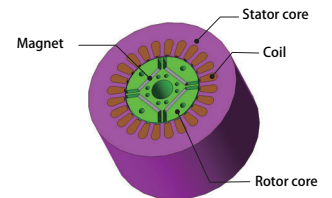


Fig. 4. Torque constant-current curve

Case 165

Creating IPM Motor Efficiency Maps

module: DP, LS



Overview

IPM motors use rare earth sintered permanent magnets because they have strong magnetic energy. They can use the magnetic torque from the magnet's field and the rotating magnetic field in addition to the reluctance torque that originates from the difference in inductance between the d-axis and q-axis, so they have a wide drive range and are highly efficient.

Their efficiency changes with their rotation speed and their load, so it is beneficial to create an efficiency map when designing the motor and its controls. However, the calculations required to create an efficiency map are typically huge, so it takes time to organize the results as well. Though it is possible to estimate the efficiency by using the motor's voltage equation and torque formula to calculate the torque, voltage, and current, one cannot use this method to estimate the iron loss or account for the effects of the nonlinear magnetic properties of the motor's iron core. The main problem is the difficulty of correctly calculating the efficiency. To help with this problem, an efficiency map that accounts for influence from iron loss and nonlinear magnetic properties can be easily obtained by creating a JMAG-RT model of the target and using JMAG-RT Viewer's efficiency map calculation function.

This Application Note presents the use of the JMAG-RT Viewer to create an efficiency map for an IPM motor.

Speed-Torque curve / Efficiency map

Fig. 1 shows the Speed-Torque curve, and fig. 2 shows the efficiency map.

As seen in fig. 1, in the low speed region the torque becomes constant. This is due to the current controls. The torque also decreases as speed increases. This is because the current flowing to the motor coil decreases due to back electromotive voltage.

In fig. 2 it is possible to get a grasp of the efficiency at each drive condition. The range that maps the torque's positive value and efficiency also becomes the possible range of output for this motor.

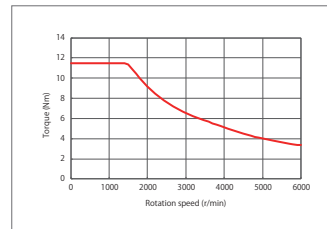


Fig. 1. Speed-Torque curve

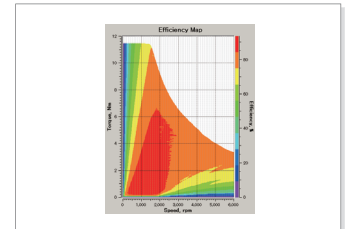
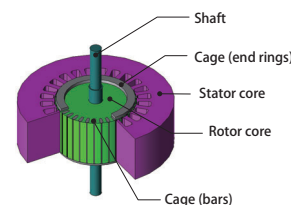


Fig. 2. Efficiency map

Case 166 Line Start Simulation of an Induction Machine Using a Control Simulator and the JMAG-RT

module: FQ, LS, RT



Overview

Collaborative design is difficult because the controls and motor are designed independently. However, it has become necessary to resolve challenges through high-accuracy simulations at the beginning of the development process in order to meet demands for more advanced motors. An effective way of achieving this is for the simulations to be performed while collaborating on the motor design circuit/control designs.

An induction motor's characteristics are influenced by leakage reactance and resistance, including resistance on the secondary side. The resistance on the secondary side is affected by the skin effect, so the finite element method (FEM) needs to be used to obtain the distribution of the secondary induced current. With JMAG, it is possible to use a magnetic field analysis to obtain the resistance and leakage reactance, and to create a model of an induction motor, as well. Incorporating this motor model, called a "JMAG-RT model," to a circuit/control simulator makes it possible to use JMAG-RT to run a linked simulation with it.

This Application Note explains how to use the JMAG-RT to create a JMAG-RT model of an induction motor, import it to a circuit/control simulator, and run an induction motor line start simulation.

Rotation Speed Waveform

The rotation speed waveform when starting the induction motor is indicated in fig. 1. From fig. 1, it is apparent that the motor accelerates rapidly at the initial start-up and moves to a more steady acceleration while transitioning to a steady state.

Torque waveform

The waveforms of the drive torque and load torque when starting the induction motor are indicated in fig. 2.

From fig. 2, it is apparent that a large drive torque is generated at initial start-up. Furthermore, the drive torque becomes almost constant as the load torque balances out in the steady state.

Current Waveform

The current waveform of the stator coil when the induction motor starts is indicated in fig. 3.

Fig. 3 shows that an extremely large current is produced during the initial start-up. This is because the back electromotive voltage at initial start-up is small and almost all of the power supply voltage is applied to the stator coils. At a steady state, the three-phase AC has an amplitude of less than 5 A.

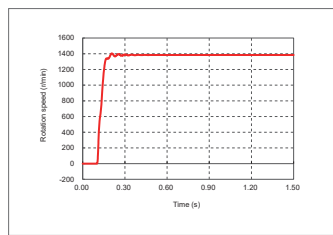


Fig. 1. Rotation speed waveform

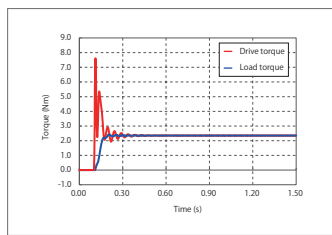


Fig. 2. Torque waveform

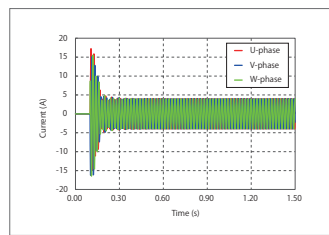
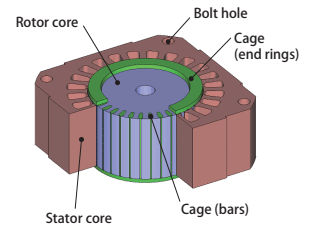


Fig. 3. Current waveform



Overview

An induction motor is a motor in which the rotating magnetic field of the stator coils causes induced current to flow in an auxiliary conductor, which produces force in the rotational direction. Induction motors are widely used in everything from industrial machines to home appliances because they have a simple construction without parts that experience wear from abrasion, and can be used simply by connecting them to a power source.

Improved efficiency in induction motors is an important theme. Iron loss, a cause of lower efficiency along with primary and secondary copper loss, must be reduced in order to improve efficiency. The relative importance of iron loss tends to grow especially with higher rotations due to the inverter drive, so it is helpful to estimate the complex iron loss distribution inside the core.

This Application Note presents an example of how to find the iron loss in the stator core and rotor core at a rotation speed of 3,300 r/min.

Magnetic Flux Density Distribution

The magnetic flux density distribution of the stator core and rotor core is shown in fig. 1, the magnetic flux density waveforms of the magnetic flux density R-component at measuring points 1, 2, 3, and 4 are shown in fig. 2, and a graph of the results from measuring point 2 after FFT is shown in fig. 3. Also, the steady-state torque and primary current amplitude are shown in table 1, and the secondary current flowing in the cage is shown in fig. 4.

Comparing measuring points 1 and 2, at measuring point 2 the magnetic flux density has a large value and amount of variation, but at measuring point 1 the magnetic flux density has a small value and amount of variation. For measuring points 3 and 4, it can be confirmed that the value is large at measuring point 3. Further, when measuring points 2 and 3 are compared, the amount of variation is seen to be larger at measuring point 2. These differences in magnetic flux density have an effect on iron loss.

120 Hz, the frequency of the power supply, is dominant at measuring point 2, as seen in fig. 3.

The frequency of the secondary current affects the magnetic flux density on the rotor side.

Joule Loss Density Distribution/Hysteresis Loss Density Distribution/Iron Loss Density Distribution

The joule loss density distributions for the stator core and rotor core are shown in fig. 5. The hysteresis loss density distributions for the stator core and rotor core are shown in fig. 6. The iron loss density distributions for the stator core and rotor core are shown in fig. 7. The ratios of loss for the stator core and rotor core are shown in fig. 8.

As shown in the magnetic flux density waveforms, joule losses are greater in places where the amount of variation in the magnetic flux density is large, compared to places where the amount of variation in the magnetic flux density is small. The same trend can be seen in the hysteresis losses as well, as shown in table 2 by the fact that the ratio of the joule and hysteresis losses taken up by the stator is large.

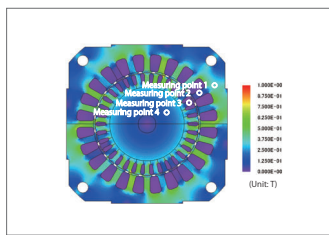


Fig. 1. Magnetic flux density distribution at a rotation of 1,800 deg

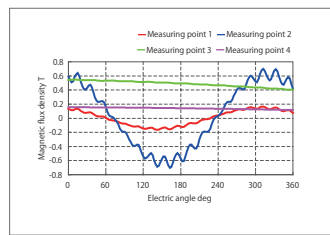


Fig. 2. Magnetic flux density waveforms (R-component)

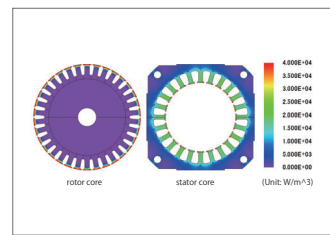


Fig. 5. Joule loss density distribution

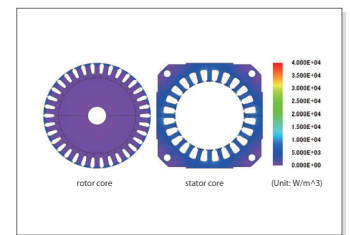


Fig. 6. Hysteresis loss density distribution

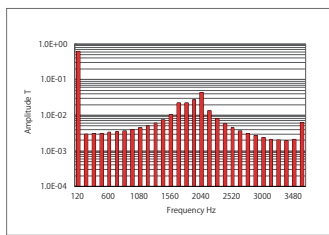


Fig. 3. Frequency components at measuring point 2

Rotation speed 3,300 r/min	Results
Torque (Nm)	0.37
Primary current (A)	1.5

Table 1. Reference results

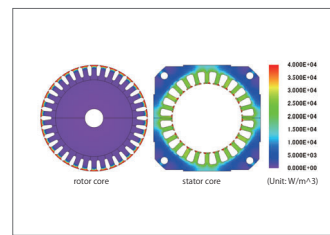


Fig. 7. Iron loss density distribution

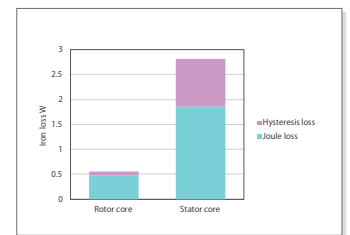


Fig. 8. Ratio of loss

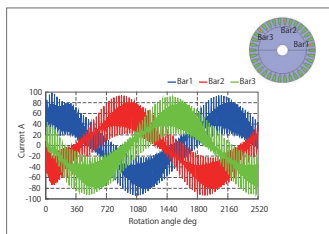
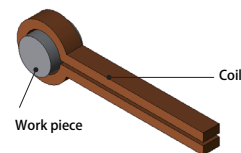


Fig. 4. Secondary current

Case 172 High-Frequency Induction Heating Analysis of a Test Piece (Rotational Induction Hardening)

module: FQ, HT



Overview

Machine parts like shafts and gears are made to be resistant to wear and tear. This is accomplished by giving them a certain degree of flexibility by maintaining their interior toughness while increasing the hardness of their surfaces. By using high-frequency induction heating, which is a type of surface hardening method, the part is heated rapidly on only its surface by a high frequency power source. This process also has many other benefits, such as providing a clean working environment because it uses electrical equipment, being very efficient, and providing uniform results for each product. This is why it is being aggressively implemented in the field.

With induction hardening like the kind used on the work piece in this analysis, the main requirement is to heat a given surface uniformly and increase rigidity. The high-frequency's varying magnetic field produces eddy currents with an offset in the surface of the work piece, so handling the phenomena inside the work piece with a numerical analysis based on the finite element method (FEM) is the most effective means analyzing the process in detail.

This Application Note explains how to create a numerical analysis model when obtaining the optimum coil geometry, current conditions (power supply frequency, current value), and rotation speed. It also shows how to evaluate whether the target temperature distribution is being achieved by analyzing the elevated temperature process.

Joule Loss Density Distribution

Figures 1 and 2 show the joule loss density distribution generated in the work piece and the coil. The magnetic field generated by the coil produces eddy currents in the work piece, which become heat sources in induction heating. The places where the heated part exceeds the Curie temperature lose their magnetism, so the eddy current loss density decreases, as well. The skin effect produced by the high frequency also causes the eddy current to be distributed near the work piece's surface.

Temperature Distribution and Variation vs. Time

Fig. 3 shows the work piece's temperature distribution, and fig. 4 shows its temperature variation versus time. In the surface facing the heating coil, the temperature is higher because more eddy currents are generated. As shown in fig. 4, induction heating causes the temperature in the surface of the work piece to rise first, and the temperature of the work piece's interior rises gradually due to thermal conduction.

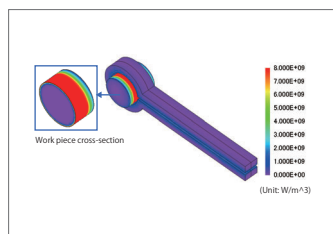


Fig. 1 Joule loss density distribution at 0.0 s

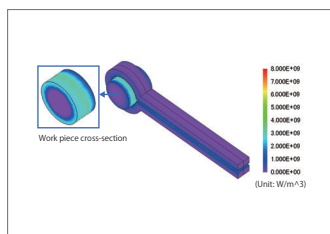


Fig. 2 Joule loss density distribution at 4.0 s

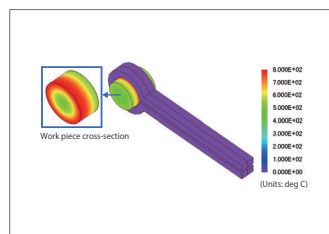


Fig. 3 Temperature distribution at 4.0 s

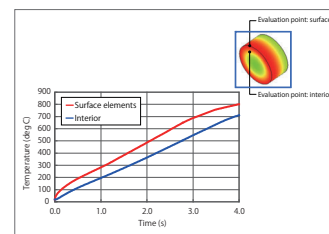


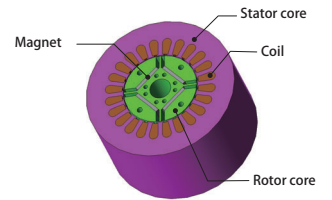
Fig. 4 Temperature variation of the work piece

Overview

Demand for higher efficiency and smaller size in motors has grown from the need to accommodate devices that incorporate miniaturization and energy efficiency in their designs. In order to meet this demand, motors have to improve their output density and reduce their losses. One type of loss commonly found in motors is iron loss, which increases drastically at high rotation speeds and high magnetic flux densities. This increase can lead to a rise in temperature and a reduction in efficiency. Consequently, it is growing more important to predict iron loss at the motor design stage.

Unfortunately, it is not possible to obtain iron losses accurately in studies that use the magnetic circuit method or rules of thumb. In order to obtain them accurately, one needs to find the distribution and time variations of the magnetic flux density in each part of the motor after accounting for a fine geometry and the material's nonlinear magnetic properties. Using the finite element method (FEM) is essential in order to carry out this kind of a detailed analysis.

This Application Note demonstrates an analysis in which an IPM motor's cogging torque, torque, magnetic flux density distribution, and iron loss in the stator core are obtained.



Torque Analysis (No-load)

The cogging torque waveform is shown in fig. 1, the magnetic flux lines where the cogging torque is 0 Nm at a rotation angle of 0 deg are shown in fig. 2, the induced voltage waveform is shown in fig. 3, the iron loss density distribution is shown in fig. 4, and the ratios of loss for the stator core are shown in fig. 5.

Torque Analysis (Load)

The current phase versus torque is shown in fig. 6, the magnetic flux density distribution and magnetic flux lines at current phase 10 deg are shown in fig. 7, the current phase versus loss is shown in fig. 8, and the iron loss density distribution at current phase 10 deg is shown in fig. 9.

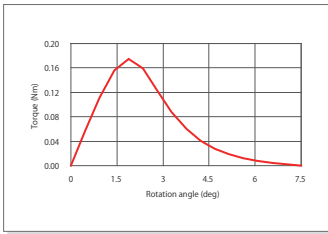


Fig. 1 Cogging torque waveform

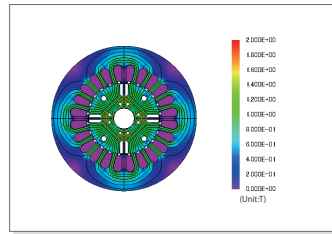


Fig. 2 Magnetic flux density distribution and magnetic flux lines (rotation angle: 0 deg)

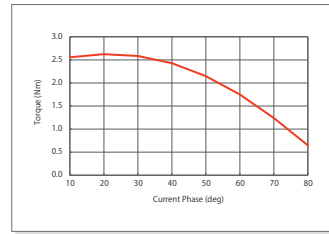


Fig. 6 Current phase versus torque

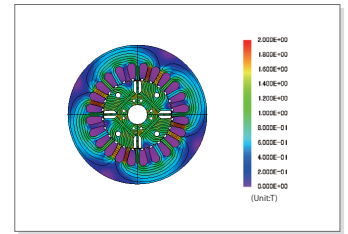


Fig. 7 Magnetic flux density distribution and magnetic flux lines (current phase: 10 deg)

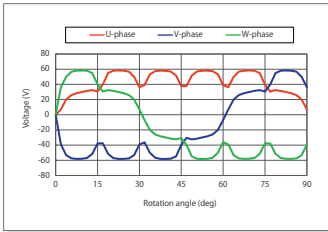


Fig. 3 Induced voltage waveform

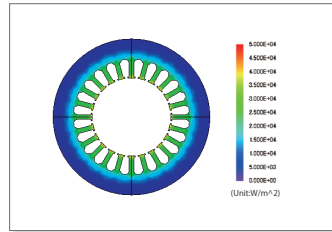


Fig. 4 Iron loss density distribution

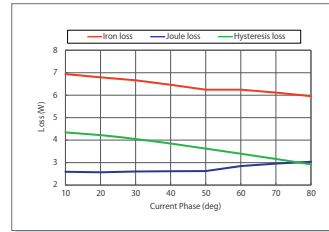


Fig. 8 Current phase versus loss

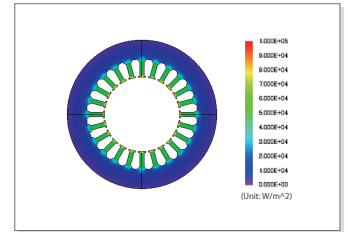


Fig. 9 Iron loss density distribution (current phase: 10 deg)

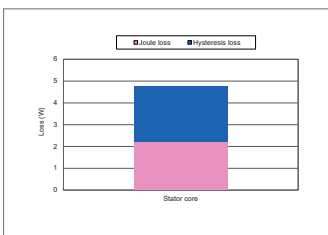
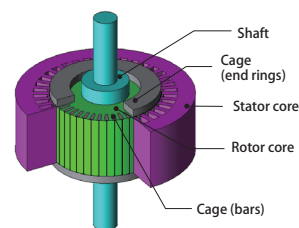


Fig. 5 Ratio of loss

Case 176 Drive Characteristic Analysis of a Three-Phase Induction Motor

module: DP, LS



Overview

An induction motor is a motor in which the rotating magnetic field of the stator coils causes induced current to flow in an auxiliary conductor, which exerts force on the rotor in the rotational direction and causes it to spin. Induction motors are widely used in everything from industrial machines to home appliances because they have a simple construction and are small, light, affordable, and maintenance-free.

In an induction motor, the current induced by the auxiliary conductor exerts a large influence on its characteristics. It also causes strong magnetic saturation in the vicinity of the gap, in particular. This is why a magnetic field analysis based on the finite element method (FEM) is useful when investigating the motor's characteristics for a design study.

This Application Note explains how to confirm drive characteristics such as torque, loss, and efficiency in an induction motor when its rotation speed changes.

Drive Characteristics (Voltage Control)

The primary current, primary copper loss, secondary copper loss, iron loss, torque, and efficiency with changing rotation speeds during voltage control are shown in figures 1 through 6. The eddy current density distribution, joule loss density distribution, hysteresis loss density distribution, and iron loss distribution at maximum efficiency are shown in figures 7 through 10.

Drive Characteristics (Current Control)

The primary voltage, primary copper loss, secondary copper loss, iron loss, torque, and efficiency with changing rotation speeds during current control are shown in figures 11 through 16. The eddy current density distribution, joule loss density distribution, hysteresis loss density distribution, and iron loss distribution at maximum efficiency are shown in figures 17 through 20.

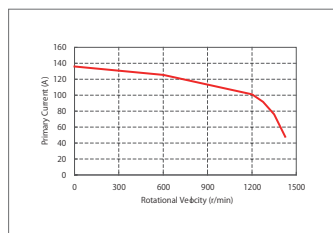


Fig. 1 Rotation speed versus primary current

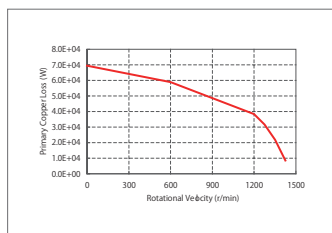


Fig. 2 Rotation speed versus primary copper loss

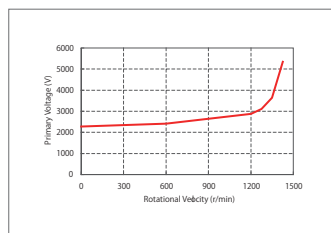


Fig. 11 Rotation speed versus primary voltage

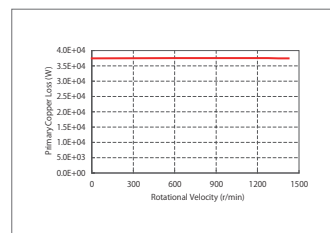


Fig. 12 Rotation speed versus primary copper loss

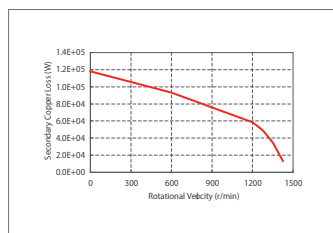


Fig. 3 Rotation speed versus secondary copper loss

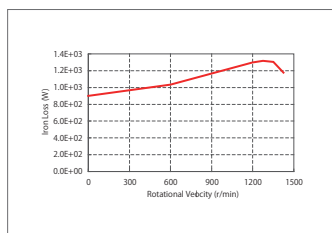


Fig. 4 Rotation speed versus iron loss

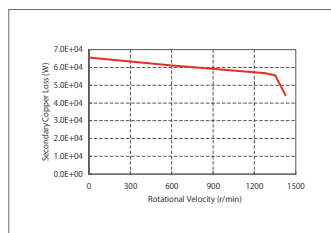


Fig. 13 Rotation speed versus secondary copper loss

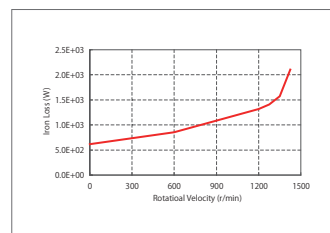


Fig. 14 Rotation speed versus iron loss

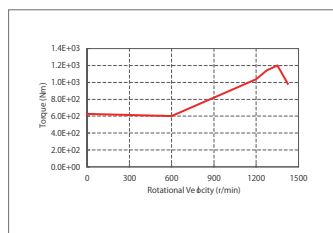


Fig. 5 Rotation speed versus torque

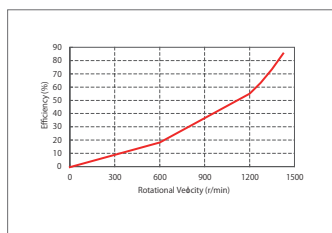


Fig. 6 Rotation speed versus efficiency

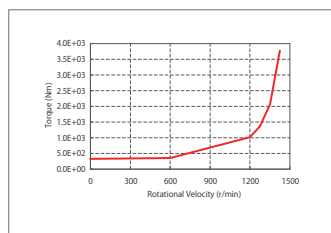


Fig. 15 Rotation speed versus torque

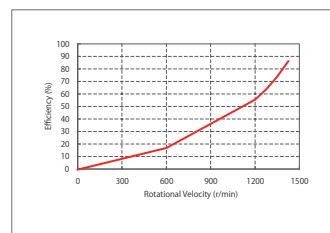


Fig. 16 Rotation speed versus efficiency

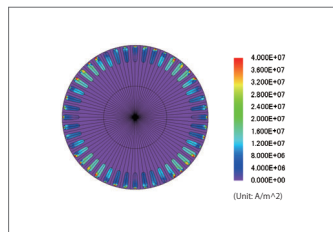


Fig. 7 Eddy current density distribution

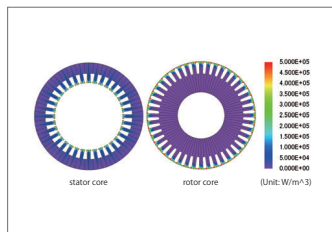


Fig. 8 Joule loss density distribution

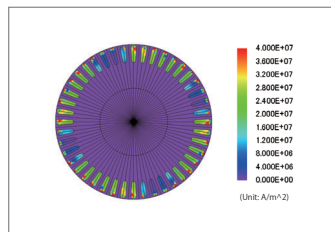


Fig. 17 Eddy current density distribution

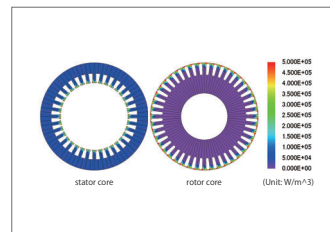


Fig. 18 Joule loss density distribution

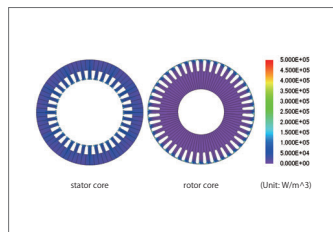


Fig. 9 Hysteresis loss density distribution

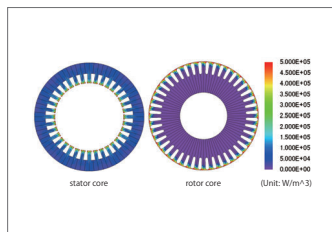


Fig. 10 Iron loss density distribution

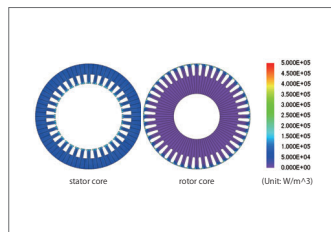


Fig. 19 Hysteresis loss density distribution

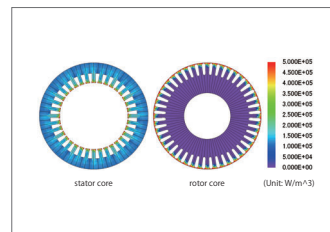
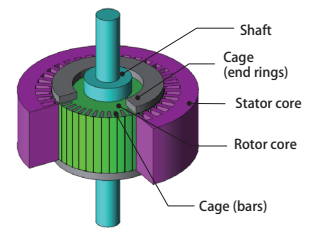


Fig. 20 Iron loss density distribution

Case 177

Torque Characteristic Analysis of a Three Phase Induction Motor

module: DP, LS



Overview

An induction motor is a motor in which the rotating magnetic field of the stator coils causes induced current to flow in an auxiliary conductor, which exerts force on the rotor in the rotational direction and causes it to spin. Induction motors are widely used in everything from industrial machines to home appliances because they have a simple construction and are small, light, affordable, and maintenance-free.

It is possible to drive an induction motor so that its slip is constant by adjusting the voltage or current against load variations. When this happens, each characteristic changes with influence from magnetic saturation and leakage flux because of the excitation variations in a specific slip.

This Application Note explains how to obtain the torque characteristics in an induction motor when the current amplitude has been changed in a specific slip.

Torque-Current Curve / Current-Voltage Curve

The Torque-Current curve and Current-Voltage curve when the current has been changed with a constant slip are shown in figures 1 and 2.

The figures show that the torque and voltage both rise when the current increases.

Eddy Current Density Distribution

The eddy current density when the current has been changed with a constant slip is shown in fig. 3. The figure shows that the eddy currents in the cage increase when the current value rises.

Joule Loss Density Distribution/Hysteresis Loss Density Distribution

The joule loss density distribution and hysteresis loss distribution in the stator core when the current has been changed with a constant slip are shown in figures 4 and 5, and the joule loss density distribution and hysteresis loss density distribution in the rotor core are shown in figures 6 and 7.

The figures show that all of the losses increase when the current value rises.

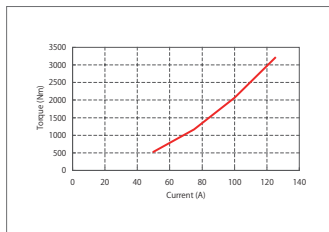


Fig. 1 Torque-Current curve

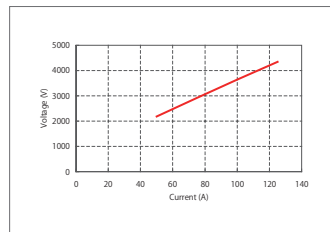


Fig. 2 Current-Voltage curve

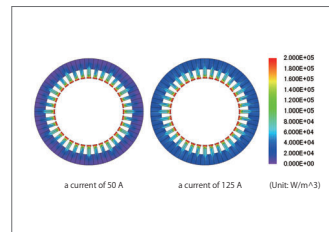


Fig. 4 Joule density distribution of the stator core

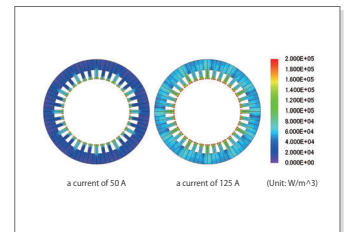


Fig. 5 Hysteresis loss density distribution of the stator core

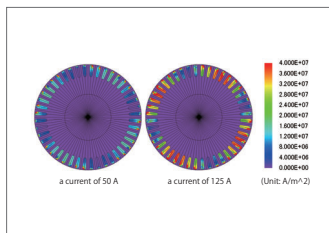


Fig. 3 Eddy current density distribution

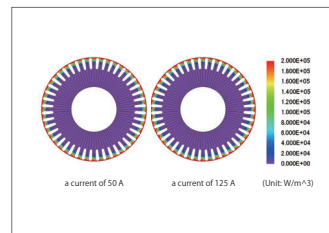


Fig. 6 Joule density distribution of the rotor core

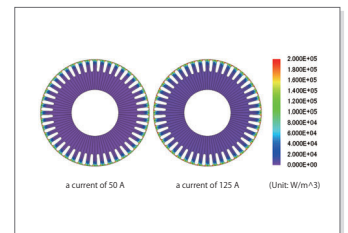
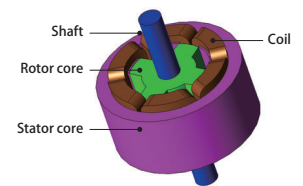


Fig. 7 Hysteresis loss density distribution of the rotor core

Case 178

Analysis of SR Motor I-Psi Characteristics

module: DP



Overview

With the skyrocketing prices of rare earth magnets, expectations have been rising for SR (switched reluctance) motors because they have a motor format that does not use permanent magnets. SR motors have a simple structure that can achieve solid performance at a low price. However, torque generation depends only upon the saliency between the stator and rotor, so torque variations are extremely large and cause vibration and noise, meaning that the use applications are limited. On the other hand, because of the skyrocketing prices of rare earth metals, the improvement in current control technology, the possibility of optimized designs thanks to magnetic field analysis, and the rising ability to reduce challenges, SR motors are being re-examined.

SR motors operate using the nonlinear region of a magnetic steel sheet, so because the inductance displays nonlinear behavior, it is impossible to carry out advanced projections that are accurate with calculation methods that follow linear formulas. Consequently, it becomes necessary to use the finite element method (FEM), which can handle nonlinear magnetic properties in material and minute geometry.

This example presents an evaluation of flux linkage, inductance and torque for each rotor position when the flowing current value is changed.

I-Psi Characteristics

Fig. 1 shows the SR motor's I-Psi characteristics, fig. 2 shows the current value 2 A and the magnetic flux density distribution for 10 A.

When the tooth is not facing to each other and is at 0 deg, because magnetic resistance is dominant in the main circuit, there is an almost linear increase in magnetic flux linkage in relation to the current. Also, we understand that particularly when the tooth is facing to each other, the more the current is increased, the more the amount of magnetic flux decreases. This is caused by influence from magnetic saturation of the core, as shown in fig. 2. In addition, the bigger the difference in the flux leakage (inductance) when the tooth is facing to each other and when it is not, increases torque so it is also possible to consider how this could be used.

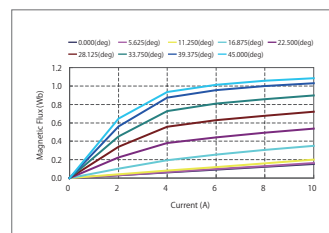


Fig. 1. I-Psi characteristics

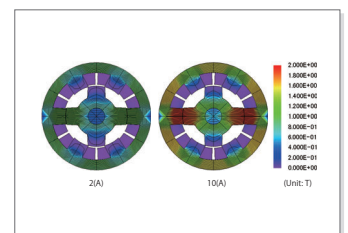


Fig. 2. Magnetic flux density distribution

Case
179

Analysis of SR Motor Static Characteristics

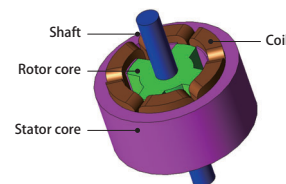
module: DP

Overview

With the skyrocketing prices of rare earth magnets, expectations have been rising for SR (switched reluctance) motors because they have a motor format that does not use permanent magnets. SR motors have a simple structure that can achieve solid performance at a low price. However, torque generation depends only upon the saliency between the stator and rotor, so torque variations are extremely large and cause vibration and noise, meaning that the use applications are limited. On the other hand, because of the skyrocketing prices of rare earth metals, the improvement in current control technology, the possibility of optimized designs thanks to magnetic field analysis, and the rising ability to reduce challenges, SR motors are being re-examined.

SR motors operate using the nonlinear region of a magnetic steel sheet, so because the inductance displays nonlinear behavior, it is impossible to carry out advanced projections that are accurate with calculation methods that follow linear formulas. Consequently, it becomes necessary to use the finite element method (FEM), which can handle nonlinear magnetic properties in material and minute geometry.

This example presents an evaluation for each rotor position of the effect on flux linkage (shown as I-Psi characteristics below) when excitation current is changed.



Flux linkage waveform/Inductance waveform/ Torque waveform

For each rotor's position change, the SR motor's flux linkage waveform is indicated in fig. 1, the inductance waveform in fig. 2, and the torque waveform in fig. 3.

From fig. 1 we understand that in the range of 45 deg when the tooth is facing to each other, the more the current is increased, the more the amount of magnetic flux decreases. As a result, as the current value increases, inductance decreases, which we also understand from fig. 2. These are due to the nonlinear properties of the core material. In fig. 3 it is possible to estimate the approximate average torque for each current value. Also, it is possible to consider geometry in accordance with setting specifications, such as peaks and reductions in the torque.

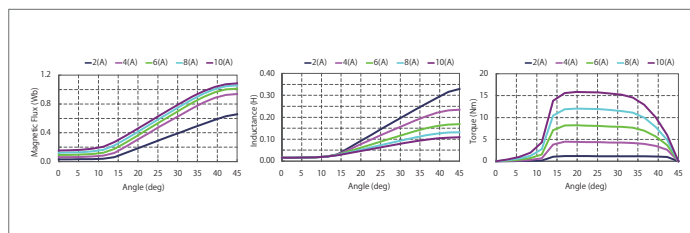
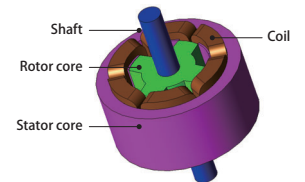


Fig. 1. Flux linkage waveform

Fig. 2. Inductance waveform

Fig. 3. Torque waveform



Overview

With the skyrocketing prices of rare earth magnets, expectations have been rising for SR (switched reluctance) motors because they have a motor format that does not use permanent magnets. SR motors have a simple structure that can achieve solid performance at a low price. However, torque generation depends only upon the saliency between the stator and rotor, so torque variations are extremely large and cause vibration and noise, meaning that the use applications are limited. On the other hand, because of the skyrocketing prices of rare earth metals, the improvement in current control technology, the possibility of optimized designs thanks to magnetic field analysis, and the rising ability to reduce challenges, SR motors are being re-examined.

SR motors create their excitation state by alternating between opening and closing switches in accordance with the position of the rotor's rotation, however the timing of the alternating causes major changes in the torque properties. Also, it is important not only to increase the torque average and torque constant, but also to consider the optimum switch timing to control vibration and noise.

This example presents how to carry out an analysis with different switch timings to evaluate torque and current in SR motors.

Torque Waveform

The torque waveform for each voltage application width θ_w with changing the voltage application start angle θ_s are shown in fig. 1 and fig. 2.

By changing θ_s and θ_w , we understand that the torque waveform has changed.

Current Waveform

The current waveform of the A-phase coil for each voltage application width θ_w with changing the voltage application start angle θ_s are shown in fig. 3 and fig. 4.

It is apparent that if the θ_w is 30 deg, it takes a longer time for the current to decrease to 0A. This is because the rotor tooth is nearing the stator and inductance has increased.

Copper Loss Waveform

The copper loss waveform for each voltage application width θ_w with changing the voltage application start angle θ_s are shown in fig. 5 and fig. 6.

It is apparent that depending on the voltage application width, there is a large difference in the waveform. We can understand that if θ_w is 30 deg, copper loss is bigger in the range of multiple phase currents flowing simultaneously.

Switching Properties

The average torque $T_{ave}(\theta_s)$, torque ripple $Tr(\theta_s)$, torque ripple rate $Tr(\theta_s)/T_{ave}(\theta_s)$, and torque constant K_t for each voltage application width θ_w with changing the voltage application start angles are shown in table 1 and table 2.

In this case, average torque and torque constant are at a maximum and the torque ripple rate is at a minimum at $\theta_w = 30$ deg, $\theta_s = 5$ deg. It is possible to consider optimum switch timing in accordance with required specifications.

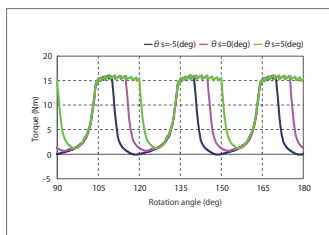


Fig. 1. Torque waveform (θ_w : 25 deg)

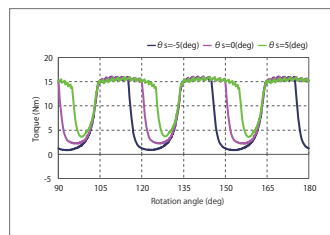


Fig. 2. Torque waveform (θ_w : 30 deg)

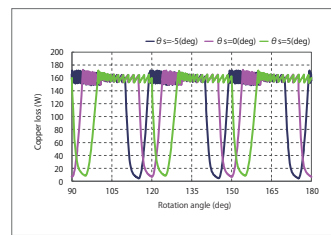


Fig. 5. Copper loss waveform (θ_w : 25 deg)

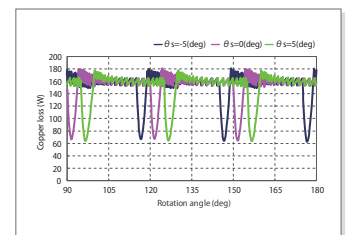


Fig. 6. Copper loss waveform (θ_w : 30 deg)

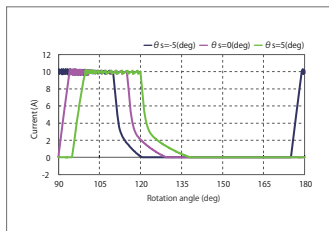


Fig. 3. Current waveform (θ_w : 25 deg)

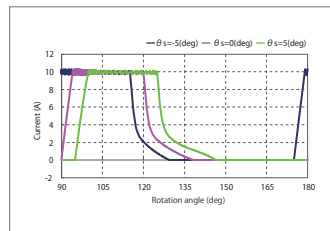


Fig. 4. Current waveform (θ_w : 30 deg)

θ_s (deg)	$T_{ave}(\theta_s)$ (Nm)	$Tr(\theta_s)$ (Nm)	$Tr(\theta_s)/T_{ave}(\theta_s)$ (%)	K_t (Nm/A)
-5	5.2	16.2	313	1.01
0	7.9	15.4	195	1.54
5	10.3	14.8	144	2.04

Table 1. Switching properties (θ_w : 25 deg)

θ_s (deg)	$T_{ave}(\theta_s)$ (Nm)	$Tr(\theta_s)$ (Nm)	$Tr(\theta_s)/T_{ave}(\theta_s)$ (%)	K_t (Nm/A)
-5	7.9	15.2	193	1.40
0	10.5	13.9	132	1.87
5	12.6	12.4	98	2.25

Table 2. Switching properties (θ_w : 30 deg)

Case 181 Analysis of SR Motor Drive Characteristics

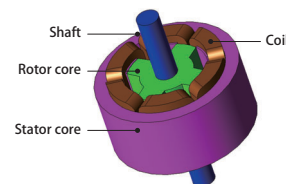
module: DP, LS

Overview

With the skyrocketing prices of rare earth magnets, expectations have been rising for SR (switched reluctance) motors because they have a motor format that does not use permanent magnets. SR motors have a simple structure that can achieve solid performance at a low price. However, torque generation depends only upon the saliency between the stator and rotor, so torque variations are extremely large and cause vibration and noise, meaning that the use applications are limited. On the other hand, because of the skyrocketing prices of rare earth metals, the improvement in current control technology, the possibility of optimized designs thanks to magnetic field analysis, and the rising ability to reduce challenges, SR motors are being re-examined.

SR motors sometimes drive while changing switch timing in accordance with rotation speed so it is useful to understand properties such as torque, current and iron loss in accordance with revolution speed.

This example presents how to confirm drive characteristics such as torque, loss, and efficiency in a motor when its switch timing changes for each rotation speed.



Drive Characteristics

The average torque, current, iron loss and efficiency with altered rotation speed and excitation specifications are shown in figures 1 through 4.

From fig. 1 we understand that whether iron loss is taken into account or not, there is almost no effect on torque. This is because the ratio of iron loss to output is small. From fig. 2 we understand that current does not drop gradually in relation to rotation speed. We understand that this is because switch timing has been changed in accordance with rotation speed, and switch timing exerts a large influence on its characteristics. In addition, we understand from fig. 4 that as rotation speed increases, efficiency rises and peaks at around 90%.

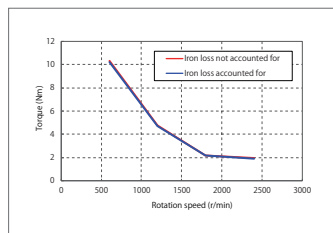


Fig. 1. Rotation speed versus torque

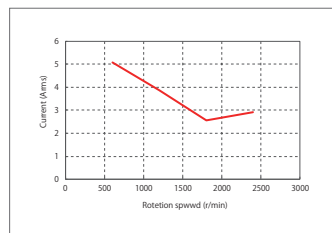


Fig. 2. Rotation speed versus current

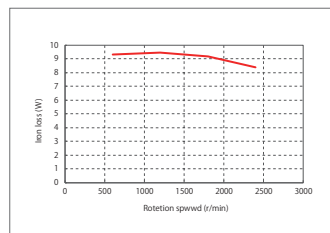


Fig. 3. Rotation speed versus iron loss

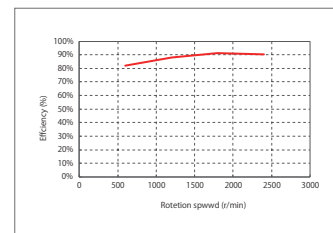


Fig. 4. Rotation speed versus efficiency

Case 183 Agitation Force Analysis of an Induction Furnace

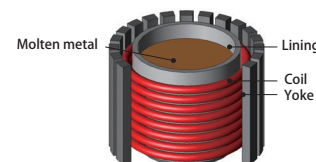
module: FQ

Overview

An induction furnace is an apparatus that uses high-frequency induction heating to melt metal. Running current through the coil surrounding the crucible starts electromagnetic induction phenomena, which generate current in the metal in the crucible. This current produces joule losses in the metal, which are used to heat and melt it. Magnetic yokes are arranged around the coil. The yokes are used as strong components that prevent the Lorentz force generated by the coil from damaging and deforming it. The magnetic yokes also reduce the leakage flux that flows out of the appliance, preventing unintended heating in surrounding structures. Keeping the amount of material used in the magnetic yokes to a minimum makes it possible to reduce the cost of the apparatus.

When evaluating to determine at what temperature does the molten metal in the crucible become uniform, the issue becomes one of what caused the molten metal to become agitated. As parts where heat was generated through induction heating are heated locally a gap in temperature with surrounding metals arises and sparks a convection phenomenon. Applying a large current and using the significant Lorentz force generated in the molten metal enables agitation of the molten metal.

This analysis will evaluate the size of Lorentz force required to agitate and where this is generated.



Magnetic Flux Density Distribution

The magnetic flux density distribution generated in the yokes and the air region is shown in fig. 1. The figure shows that Lorentz force is generated toward the inside of the molten metal. This enables confirmation of the size and direction of the agitation force.

Current Density Distribution

The current density distribution generated in the molten metal is shown in fig. 2. You can check the depth and size of the eddy current generated inside the molten metal. The Lorentz force distribution generated in the molten metal is shown in fig. 2.

Magnetic Flux Density Distribution

The magnetic flux density distribution generated in the molten metal is shown in fig. 3.

Lorentz Force of Molten Metal

The Lorentz force of the molten metal is shown in Table 1. We learned the force of the axis direction component Z is small and radial direction component R is large.

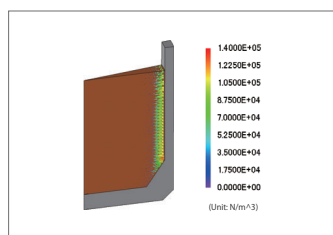


Fig. 1. Lorentz force density distribution

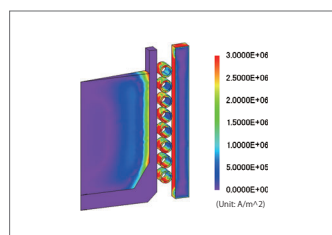


Fig. 2. Current density distribution

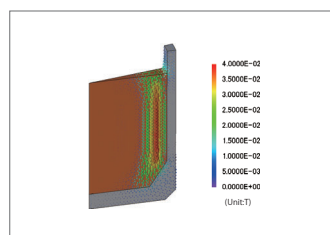
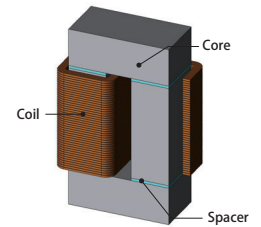


Fig. 3. Magnetic flux density distribution

Lorentz Force (R -component)	-21.7(N)
Lorentz Force (Z -component)	0.318(N)

Table 1. Magnetic flux density distribution



Overview

Reactors are used in all sorts of systems related to power systems. For example, they fill the role of making the current pulsation between an inverter and a motor smoother. Reactor vibration noise can also be an issue and countermeasures are sought from analysis. Among target reactors, vibration is not generated solely by electromagnetic force but also by magnetostriction force caused by magnetostriction. To evaluate this phenomenon with decent accuracy requires an accurate grasp of resonance phenomena with an eigen frequency by adding both electromagnetic force and magnetostrictive force to the vibratory force. These notes will conduct an analysis of changed vibratory force and show a case study of confirming the impact magnetostriction has on vibration noise.

Electromagnetic Force Distribution

Fig. 1 shows the distribution of the electromagnetic forces. It is apparent that the electromagnetic force is concentrated in the gap. This is because the air permeability in the core is different from the gap.

Magnetostrictive force distribution

Magnetostrictive force distribution dependent on magnetic flux density is shown in Fig. 2. As magnetostrictive force is larger than electromagnetic force, it needs to be added as a vibratory force, which is not just electromagnetic force alone.

Eigenmode

The eigenmode at around 10 kHz is shown in fig. 3. It was learned that the reactor has a mode in which it vibrates horizontally in the vicinity of 100 kHz. A great deal of vibration is likely to be caused by resonance phenomena between this eigenmode and the electromagnetic force.

Acceleration

Fig. 4 shows acceleration distribution. In this analysis data, confirm the results of analysis setting magnetic force only or magnetostrictive force only for the excitation force, and analysis when setting both of them for the excitation force. Looking at Fig. 4 shows that the degree of acceleration generated is greater in magnetostrictive force than in electromagnetic force. Taking both electromagnetic and magnetostrictive force into account with excitation force sees each cancel out the other and vibration reduced.

Sound Pressure Distribution

The distribution of the sound pressure level is shown in fig. 5. In this analysis data, confirm the results of analysis setting magnetic force only or magnetostrictive force only for the excitation force, as well as for analyses when setting both as the excitation force. Looking at Fig. 5 shows that sound pressure is greater in electromagnetic force than in magnetostrictive force as in the acceleration. Taking both electromagnetic and magnetostrictive force into account with excitation force sees each cancel out the other and sound pressure reduced.

Fig. 4 shows acceleration distribution. In this analysis data, confirm the results of analysis setting magnetic force only or magnetostrictive force only for the excitation force, and analysis when setting both of them for the excitation force. Looking at Fig. 4 shows that the degree of acceleration generated is greater in magnetostrictive force than in electromagnetic force. Taking both electromagnetic and magnetostrictive force into account with excitation force sees each cancel out the other and vibration reduced.

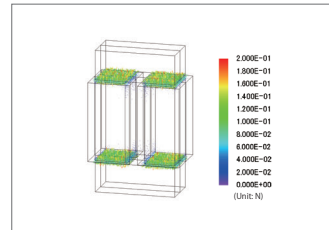


Fig. 1 Electromagnetic force distribution

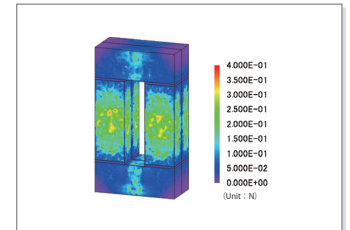


Fig. 2 Magnetostriction force distribution

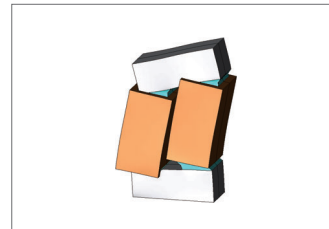


Fig. 3 The eigenmode of approximately 10 kHz

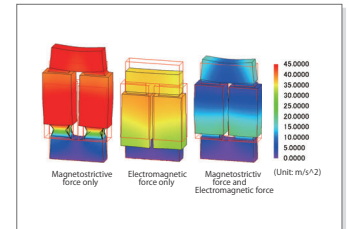


Fig. 4 Acceleration distribution

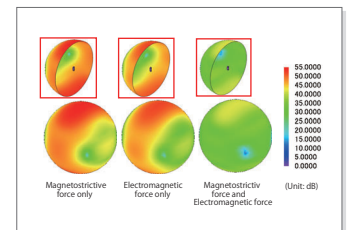


Fig. 5 Sound pressure distribution

Case 185

Analysis of Stray Loss in a Power Transformer

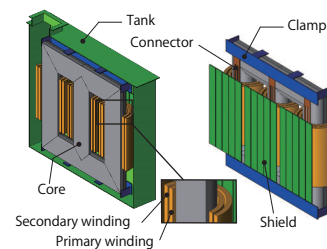
module: FQ, LS

Overview

Transformers are made to be used long-term, so it has become an important design policy to control running costs from losses. These losses include copper loss in the coil and iron loss in the core. In high-capacity transformers, however, there is also stray loss in the tank from flux leakage from the core. Stray loss is not only the total loss value, it also poses the risk of generating heat locally so there is a need to check loss distribution.

Predicting these losses and the heat that they generate is a vital component of transformer design, but it is difficult to estimate them from desktop calculations, so evaluations and detailed analyses using the finite element method (FEM) are indispensable.

This note obtains loss distribution for each component in drive condition and checks local overheating.



Joule Loss Density Distribution

Fig. 1 shows the magnetic flux density distribution, fig. 2 shows the current density distribution, and fig. 3 shows the joule loss density distribution in the tank. From fig. 1, it is apparent that magnetic flux is leaking from the transformer to the tank. This leakage flux generates eddy currents in the tank, as shown in fig. 2. Fig. 3 shows that joule losses get bigger in places with high current density.

Joule loss distribution on the shield, clamp and connector are displayed in figures 4 through 6. Check the danger of localized heating from joule loss distribution in each part.

Iron Loss Density Distribution

Fig. 7 shows the iron loss density distribution in the core. From fig. 7, it is apparent that iron losses increase in the inside corners. This is caused by the flow of magnet flux concentrating on the shortest path through the magnetic circuit.

Losses

Table 1 shows the losses in each part.

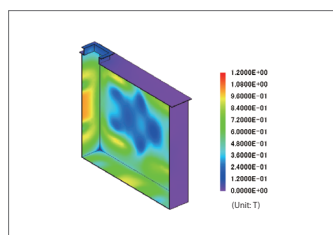


Fig. 1 Magnetic flux density distribution in the tank

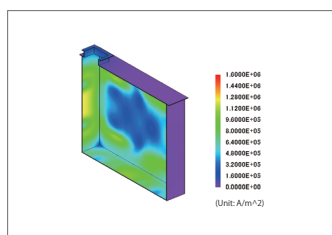


Fig. 2 Current density distribution in the tank

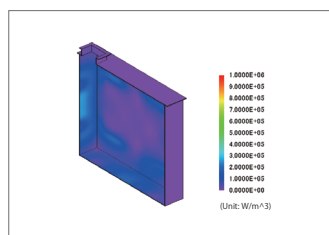


Fig. 3 Joule loss density distribution in the tank

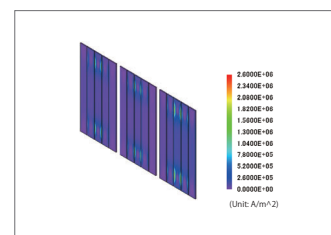


Fig. 4 Joule loss density distribution of the shield

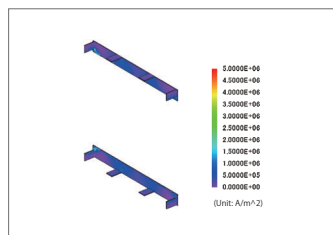


Fig. 5 Joule loss density distribution of the clamp

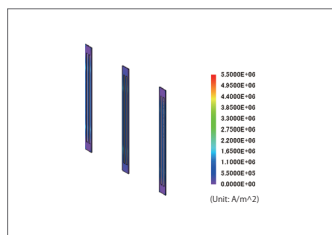


Fig. 6 Joule loss density distribution of the connector

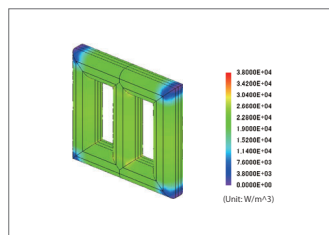


Fig. 7 Iron loss density distribution

Part	Iron losses (W)
Tank	7558.8
Core	80364.9
Secondary Winding	445566.9
Primary Winding	1111014.0
Shield	14190.7
Clamp	5444.7
Connector	5265.5

Table 1. Losses

Case 186

Gear Induction Hardening Analysis Using Two Frequencies

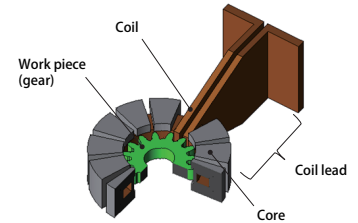
module: FQ, HT

Overview

Gears are created in such a way that the surfaces of their teeth are hard in order to resist the wear and tear that occurs when they come into contact with the teeth of other gears. However, this has to be accomplished while maintaining the gear's overall toughness. By using high-frequency induction heating, which is a type of surface hardening method, the teeth are heated rapidly on only their surface by a high frequency power source. This process also has many other benefits, such as providing a clean working environment because it uses electrical equipment, being very efficient, and providing uniform results for each product. This is why it is being aggressively implemented in the field. On the other hand, there are several factors that need to be studied in order to heat the gear's surface uniformly, such as how to adjust the heating coil's geometry, arrangement, current frequency and size.

The eddy currents generated by high-frequency varying magnetic fields are uneven in the tooth surface, so the material properties change a great deal as the temperature rises. In order to handle the detailed phenomena, it is necessary to calculate the heat generation amount in a numerical analysis based on the finite element method (FEM).

In this material, the validity of coil geometry used for quenching is evaluated by heating the gear top and bottom at high and low frequencies, respectively, to confirm uniform temperature distribution on the surface of the gear.



Eddy Current Loss Density Distribution of the Gear

Fig. 1 shows the eddy current loss density distribution of the surface of the gear and the cross-section of a tooth top. Each cross-section shown in the figure is the XY-plane at the midway position of the tooth width. The magnetic field generated by the coil produces eddy currents on the gear tooth surface. This eddy current is distributed on the surface of the gear due to the skin effect.

It's also possible to confirm the changes in the eddy currents due to different frequencies. Eddy currents are distributed on the gear bottom at low frequency and on the gear surface and tip at high frequency due to the skin effect.

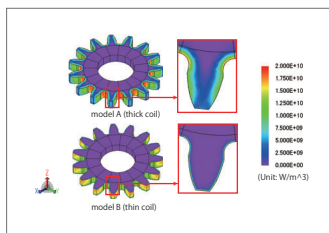


Fig. 1 Eddy current loss density distribution between 0.0 s and 0.2 s

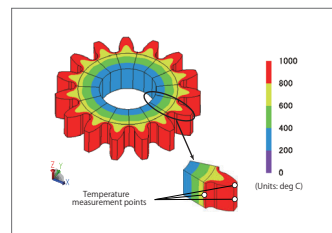


Fig. 2 Temperature distribution at 2.4 s

Temperature Distribution and Variation of the Gear

Temperature distribution in the gears is shown in Fig. 2. Fig. 3 shows the time characteristics of temperature variations at each temperature measurement point. From the temperature distribution, it is apparent that the eddy currents generate heat in the tooth top.

The difference in heat generation from the coil geometry can also be verified in Fig. 3. It is also possible to confirm at each measurement point that the temperature exceeds the Curie point of 800 deg C at around 2.0 sec.

Magnetic Flux Lines

The Magnetic flux lines are shown in fig. 4. It can be confirmed that magnetic flux is flowing from the core to the top of the gear.

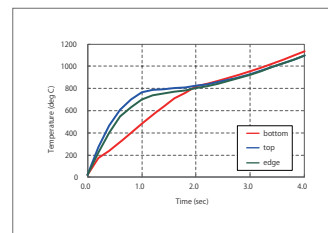


Fig. 3 Temperature versus time at tooth top

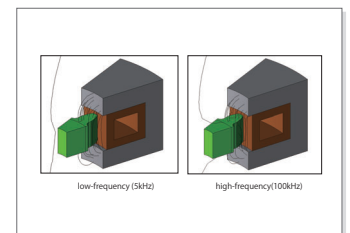


Fig. 4 Magnetic Flux Lines

Case 188

Thermal Demagnetization Analysis of IPM Motors Accounting for Coercive Force Distribution of Magnets

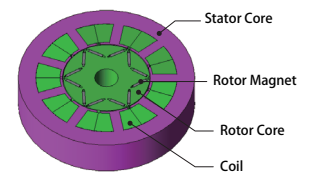
module: DP

Overview

The purpose of this Application Note is to help JMAG users understand the steps and settings used in a JMAG analysis. It is intended to help those who are working with a new analysis target better understand the analysis steps and the setting contents.

The actual JMAG model described in this Application Note is available for download from the JMAG Application Catalog. This model will allow you to view the model, settings and results. You can also create a template from the model to use as a starting point when analyzing your own geometry. They can be downloaded using the same method as the analysis model data. Please refer to the JMAG manual for more information on templates.

This example presents whether or not the demagnetization region can be smaller by assigning distribution to the coercive force of permanent magnets.



Torque

Fig. 1 indicates the reduction of torque when the temperature has changed. It can be confirmed that the reduction of torque can be controlled more than the original magnet by assigning coercive force distribution.

Demagnetizing Ratio Distribution

Fig. 2 shows the demagnetization ratio (*1) distribution after temperature increase with magnetization conditions prior to the raised temperature as a standard. By distributing high coercive force on the outer magnet surface, reduction in demagnetization ratio of the magnet can be confirmed.

(*1) The demagnetization ratio shows whether demagnetization has occurred from the specified standard magnetization.

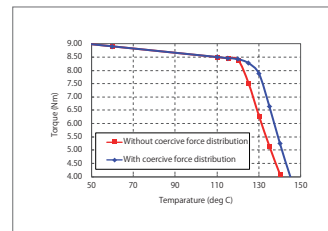


Fig. 1 Temperature versus Torque

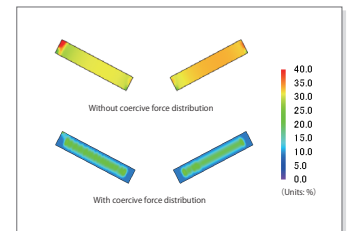
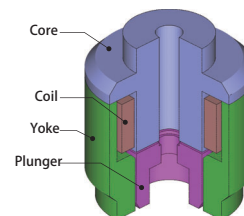


Fig. 2 Demagnetizing ratio distribution

Case 189 Response Characteristics Analysis of Injectors Accounting for Collision

module: DP



Overview

A solenoid type injector used in engines opens a valve and injects fuel by moving a plunger with magnetic force created by an electromagnet. Injectors in engines need to respond quickly for applied voltage to improve fuel consumption by maintaining the amount of fuel flow. In solenoid injectors, one of the reasons that the response is delayed is eddy currents, which are produced when the magnetic flux generated by current flow undergoes time variations. The eddy currents are generated in a direction that inhibits changes in the magnetic flux, causing a delay in the initial rise of the attraction force when the current begins to flow. This reduces the injector's responsiveness. Also, the reflection of the plunger at collision during open/close inhibits the open/close motion. By running a transient response analysis in JMAG, the responsiveness of the injector accounting for the effect of the collision of the plunger and the eddy current can be obtained. Identifying the places where eddy currents are generated enables a designer to study whether or not responsiveness can be improved. For this case, direct current voltage is applied to the solenoid type injector and the response characteristics is obtained after accounting for the effect of the collision and eddy current.

Position of Plunger and Coil Current

When accounting for collision and eddy current, the comparison of coil current and position of the plunger for each time is shown in Fig. 1. The position of the plunger is positive in the direction the valve opens, and the valve is fully open at position 100(μm) and closed at position 0(μm). The coil current value continues to rise to keep applying supply voltage to the coil until the time is 4(ms). To keep the current at a minimum while the valve is fully open during 4ms to 6ms, the voltage is controlled to maintain the coil current at 0.25 (A). The coil current is controlled so that it does not flow from 6(ms) and the valve will start to close due to fuel pressure, spring, and plunger weight.

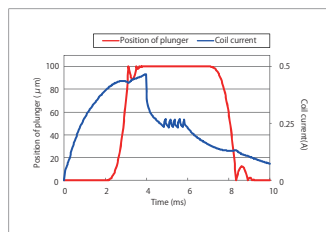


Fig. 1 Position of plunger and coil current

Current Density Distribution

Fig. 2 shows the current density distribution when current starts to flow at 0.05 (ms), when the plunger moves in the direction the valve opens at 2.2 (ms), when the plunger moves in the direction the valve opens at 7.1 (ms). By running current through the coil, eddy current will occur in the core, yoke and plunger. Eddy current will focus on the surface of each part since magnetic flux flow will suddenly increase at the start of current flow and because the power supply is direct current, eddy current will flow inside the parts as time passes. These eddy currents become the cause of the decrease in responsiveness.

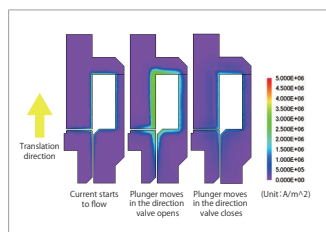


Fig. 2 Current density distribution

Comparison of Response Characteristics

Depending on whether you account for eddy current and collision, the comparison of response characteristics of the plunger for each time is shown in Fig. 3. The attraction force characteristics is shown in Fig. 4, and current characteristics is in Fig. 5. The position of the plunger is positive in the direction the valve opens and the valve is full open at position 100(μm) and the valve is closed at position 0 (μm).

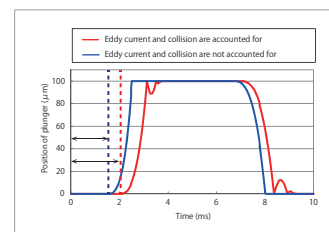


Fig. 3 Comparison of response characteristics

Fig. 3 shows that the plunger is bouncing near 3.2 (ms) due to the collision, when eddy current and collision are accounted for. Also, the responsiveness is slower compared to when they are not accounted for.

The slow responsiveness is caused by the reduced attraction force. In Fig. 4, the lower attraction force can be verified when eddy current and collision are considered compared to when they are not considered.

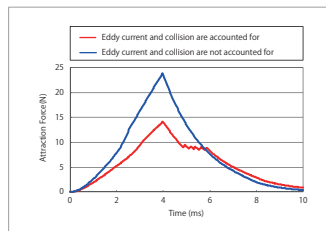


Fig. 4 Attraction Force Characteristics

As for the current characteristics, when the eddy current and collision are considered, the larger current value can be seen compared to when they are not considered. For more information about the cause, see the Application Note "66 - Operating Time Analysis of an Injector".

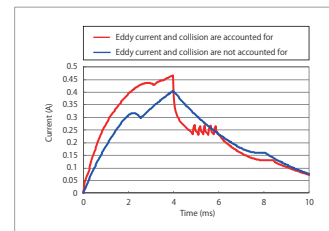


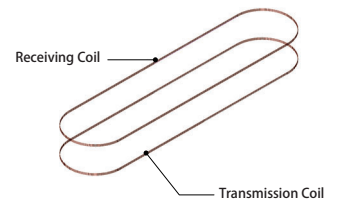
Fig. 5 Current Characteristics

When the plunger moves in the direction to open the valve, there will be a delay in response of approximately 1.5(ms) due to the fuel pressure, spring and the weight of the plunger in the case that eddy current and collision are not accounted for. In the case when eddy current and collision are accounted for, the delay in response is approximately 2 (ms) and it can be confirmed that the cause of delay in response is the decrease of the attractive force due to eddy current. The plunger will move to the direction of closing the valve from 7 (ms). Also, the eddy current caused magnetic flux and result in a delay of the plunger displacement. In addition, the plunger will collide and reflect, and it can be confirmed that more time is required for the open/close of the valve.

Overview

Originally there were only two types of wireless power transfer systems: proximity and long distance. However, recently mid-distance devices have been developed and has it made it possible for highly-efficient power transmission even when the transmission and receiving end are disconnected. Although there are charging devices for cellular phones that have already been released as products, research of charging large products such as automobiles and machine tools is currently in the process.

This document introduces the procedure in obtaining the optimum solution for geometries of transmission coils (angle that defines position) for simple magnetic resonance wireless power transfer system. Even if you are a user of applications excluding wireless power transfer systems, please use this document as a function reference material to get a grasp of the optimization procedure and the flow of result evaluation.



Efficiency

Fig. 1 shows the efficiency relative to the tilt calculated in optimization. This shows that efficiency is decreasing as the tilt gets bigger.

Coupling Coefficient

If the coupling coefficient, which is the coupling level of the transmission coil and the receiving coil, becomes poor, it will also decrease efficiency. The coupling coefficient in relation to the tilt is shown in fig. 2. The coupling coefficient will get smaller as the tilt gets larger. Fig. 3 shows the mutual inductance in relation to the tilt. It can also be confirmed that as the tilt gets larger, mutual inductance drops as well. This is because flux linkage to the receiving coil decreases, as shown in fig. 4.

Magnetic Flux Lines

Fig. 5 shows the magnetic flux line at 0 deg and 30 deg as the tilts of receiving coil. The magnetic flux line is displayed at 90 deg for phase settings, where transmission coil current will be the maximum value.

The receiving coil where tilt occurs has been marked with a circle. When comparing 0 degrees and 30 deg, the coil at 30 deg is outside the flux line. For this reason, the magnetic flux that links to the receiving coil drops. It can be said that adjusting parameters such as capacitance is required when creating models with tilts.

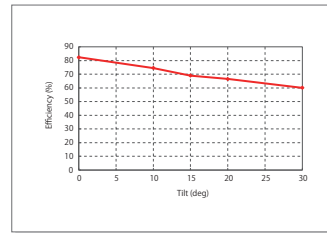


Fig. 1 Efficiency

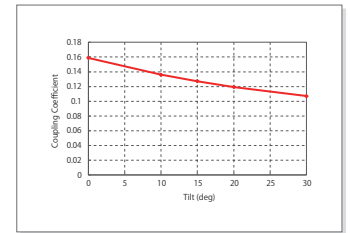


Fig. 2 Coupling Coefficient

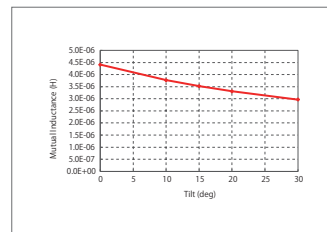


Fig. 3 Mutual Inductance

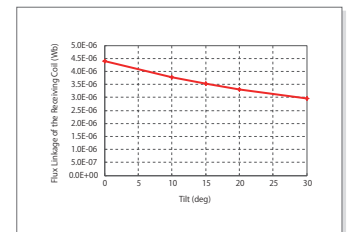


Fig. 4 Flux Linkage of the Receiving Coil

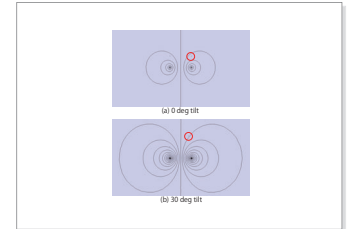
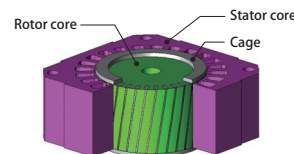


Fig. 5 Magnetic Flux Lines

Case 191 Torque Analysis of Three-Phase Induction Motors Accounting for the Skew Using the Multi-slice Method

module: DP



Overview

An induction motor can utilize skew easily because the cage is constructed by metallic casting such as die casting. When skew is applied, it arranges the variations in the magnetic flux that links to the cage in a sinusoidal wave. This makes it possible to eliminate the harmonic components from the induction current that cause negative torque and constrain things like the torque variations caused by influence from the slots. Generally when skew is applied, magnetic flux also flows in the axis direction, and this requires that a 3D analysis is performed in order to thoroughly evaluate skew effect. However, 3D analyses tend to cause an inordinate amount of calculation costs. The multi-slice method, representing skew approximately with a 2D cross-section superimposition, is effective.

In this document, the multi-slice method is used to compare torque waveforms of a cage three-phase induction motor with and without skew, and is then used to verify the effects of using skew to reduce torque variations.

Torque Characteristic

The harmonics of torque are significantly deleted due to skewing, showing that this is connected to a decrease in vibration and noise.

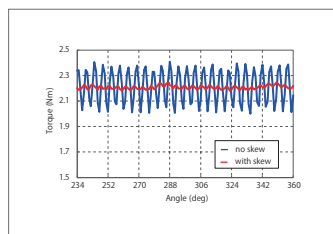


Fig. 1 Torque wave

With/without skew	Tave (Nm)	Tr (Nm)	Tr/Tave (%)
With skew	2.2	0.4	18
Without skew	2.2	0.1	3

Table 1 Torque characteristic

Current in the Secondary Conductor

Average current density distribution in one period of electric angle in the secondary conductor is shown in fig. 2 and 3, a section graph is shown in fig. 4, and current waveform and frequency components for the secondary conductor are shown in fig. 5 and 6.

As shown in fig. 2, 3 and 4, bar current without skewing is concentrated on the rotor surface, and with skewing, bar current enters almost to the inside. As shown in fig. 5 and 6, it is believed that this is due to the harmonic components in the secondary current decreases due to skewing, and the skin depth then becomes thicker. Slot harmonic components around 420(Hz), determined by the number of revolutions and slots, are greatly reduced.

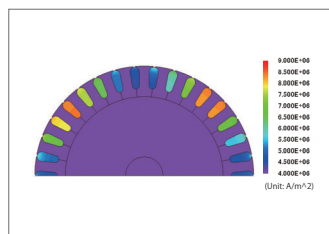


Fig. 2 Average current density distribution (no skew)

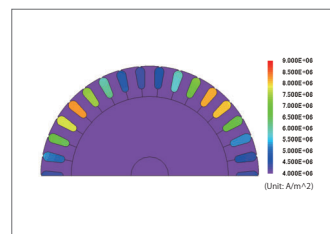


Fig. 3 Average current density distribution (with skew)

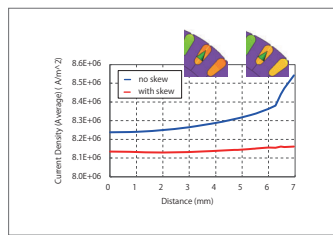


Fig. 4 Section graph of average current density

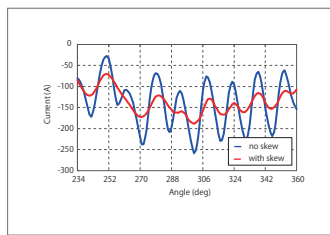


Fig. 5 Current waveform in the secondary conductor

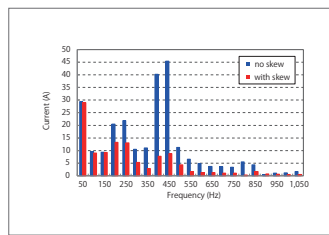
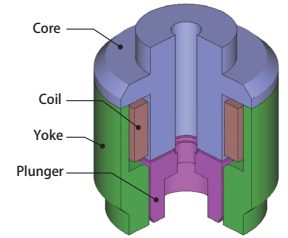


Fig. 6 Current in the secondary conductor (frequency component)



Overview

A solenoid valve becomes an electromagnet by applying current through the coil and moves the plunger by using electromagnetic force (attractive force) generated in the magnetic materials. Especially in products that require a quick response in the plunger, the time it takes for the valve to open and close is an evaluation indicator, and it is necessary to investigate in advance causes for decreases in responsiveness such as eddy current.

In this example, we will discuss the steps to investigate the effect on responsiveness caused by residual magnetization generated in the magnetic materials, and look at case examples.

Responsiveness

Fig. 1 shows a complete response graph comparing residual magnetization being accounted for and not accounted for, fig. 2 shows responsiveness when the valve opens, and fig. 3 shows responsiveness when the valve closes.

Fig. 1 demonstrates that responsiveness for the valve opening and closing differs depending if residual magnetization is accounted for or not. Fig. 2 and 3 demonstrates that responsiveness is lowered when residual magnetization is accounted for.

Responsiveness When Valve Opens

The cause behind a slower responsiveness when accounting for residual magnetization will be examined. Attraction force in the Y-axis direction when the valve opens is shown in Fig 4, and current values are shown in Fig. 5. We can verify that attractive force decreases in the Y-axis direction, and current values increase.

The cause behind a decrease in attractive force in this case is due to the difference in the how magnetic flux flows. Magnetic flux during the valve opening is shown in Fig. 6. It becomes clear that magnetic flux decreases when residual magnetization is accounted when compared to when it isn't accounted for. The root cause is not due to the effect of residual magnetization, but due to the handling of the magnetization properties when the valve opens.

Magnetization properties used when the valve opens are shown in Fig. 7. During an analysis, an initial magnetization curve is used when residual magnetization is accounted for, and an average magnetization curve is used when residual magnetization is not

accounted for, and then analysis is performed. In cases when average magnetization curves (not accounting for residual magnetization) are used, magnetic flux is generated easily when current flows, as shown in Fig. 7. As a result, attractive force in the Y-axis direction increases, and valve responsiveness improves compared to the initial magnetization curve (accounting for residual magnetization).

Furthermore, when residual magnetization is not accounted for, attractive force becomes larger than when residual magnetization is accounted for, but current values become smaller. For this case study, as shown in Fig. 8, using an average magnetization curve (not accounting for residual magnetization) results in a larger back electromotive force due to a lot of magnetic flux flow. Because of this, as shown in Fig. 9, as looking at the amount of magnetic flux generated per Ampere when the valve opens, the case where residual magnetization is not accounted for generates greater amount of magnetic flux per Ampere. Therefore, attractive force increases even if current values are small.

The cause for a decrease in responsiveness when the valve opens, as shown above, is not due to the effects of residual magnetization, but due to the differences in handling magnetization properties.

Responsiveness When Valve Closes

Magnetization contour plot when the valve closes at 0.005s is shown in Fig. 10. It shows that the yolk is magnetized while valve closes if residual magnetization is accounted for. Fig. 11 indicates that attractive force is maintained due to residual magnetization of yolk. This applied attractive force inhibits valve movement, and responsiveness decreases.

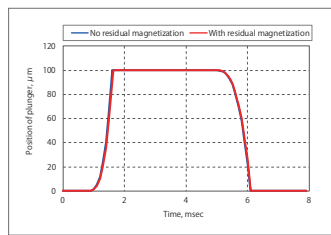


Fig. 1. Responsiveness

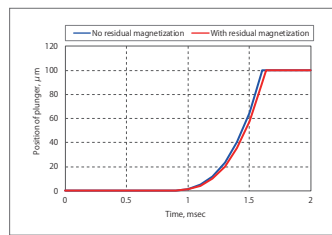


Fig. 2. Responsiveness When the Valve Opens

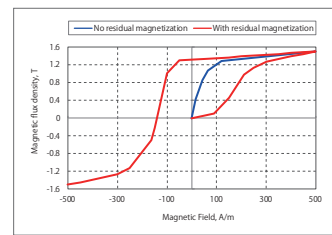


Fig. 7. B-H Curve

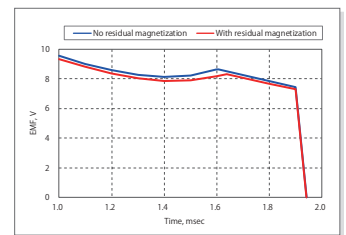


Fig. 8. Back Electromotive Force When the Valve Opens

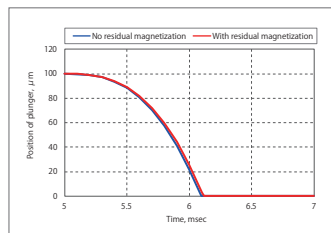


Fig. 3. Responsiveness When the Valve Closes

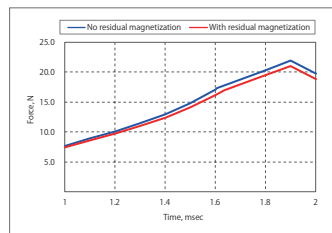


Fig. 4. Attractive Force When the Valve Opens (Y-axis Direction)

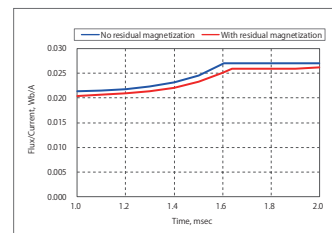


Fig. 9. Amount of Magnetic Flux Per Ampere

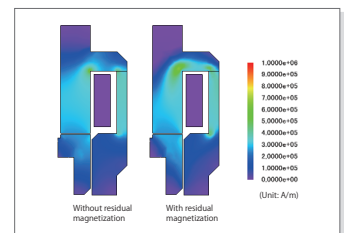


Fig. 10. Magnetization When the Valve Closes

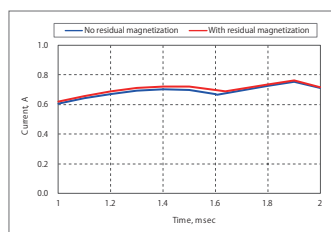


Fig. 5. Current Values When the Valve Opens

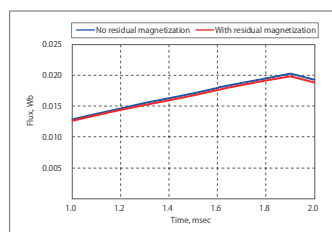


Fig. 6. Magnetic Flux When the Valve Opens

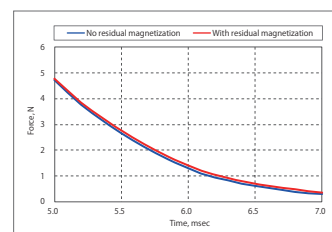
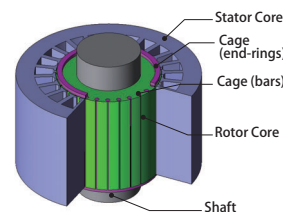


Fig. 11. Attractive Force When the Valve Closes

Case 193 Calculation of Equivalent Circuit Parameters in a Single-Phase Induction Motor

module: DP



Overview

Since single phase induction motors can be used with single-phase AC, which is common in general household power supply, it is widely used for electrical home and office appliances such as washers and fans as small power motors. However, unlike three-phase AC, single phase AC cannot independently create a rotational magnetic field, and since it cannot run a motor at this state, there is a need to develop a rotational magnetic field somehow and make it run.

Characteristics of single phase induction motors are affected by factors such as the secondary side and leakage inductance. These are called equivalent circuit parameters and they are important because they characterize the device's properties. Equivalent circuit parameters are greatly affected by current distribution induced by secondary conductors and magnetic saturation near the gap, and accurately understanding these characteristics using finite element analysis will be required.

In this example, We will be obtaining the secondary resistance, leakage inductance and excitation inductance of main coil winding of capacitor-start single-phase induction motor that has auxiliary winding.

Equivalent Circuit Parameter

The equivalent circuit parameter of 100V voltage and frequency 50Hz will be shown in fig. 1. In addition, the magnetic flux density (intensity) distribution of lock test analysis is shown in fig. 1, and the magnetic flux density (intensity) distribution of no-load test analysis in fig.2. Fig. 3 will show the current density (intensity) distribution of the lock test analysis bar.

Primary resistance	0.80 ohm
Secondary resistance	4.35 ohm
Primary, secondary leakage inductance	2.19 mH
excitation inductance	204 mH

Table 1 Each value of equivalent circuit parameters

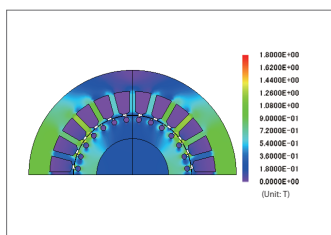


Fig.1 Magnetic flux density distribution (intensity) during lock test

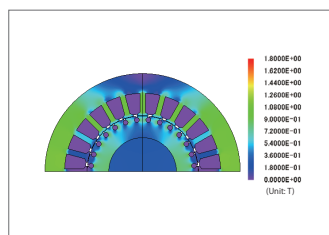


Fig. 2 Magnetic flux density distribution (intensity) during no-load test

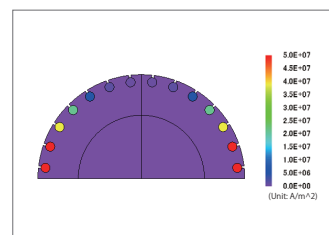
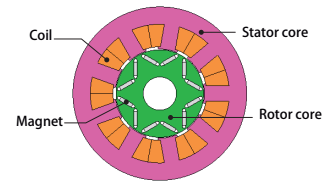


Fig. 3 Current density distribution during lock test

Overview

PM synchronous motors are used in HEV drives, air conditioner compressors, and various other industries. Especially in case of PM synchronous motors for HEV drives, high-speed rotation is advancing faster than ever to achieve a small size with high output density. The iron core of a PM synchronous motor is composed of magnetic steel sheets, and the iron loss generated in the magnetic steel sheets have generally been evaluated in the post processing of a magnetic field analysis. In this case, the effects of iron loss on the magnetic field analysis were not accounted for. However, the effects of iron loss on the magnetic field can no longer be ignored as rotation speeds are further increased, which causes the risk of not being able to accurately analyze the torque output by the motor when evaluating iron loss in post-processing.

Here we discuss the steps for accounting for eddy current loss occurring in the magnetic steel sheets during a magnetic field analysis, and then analyze the effects on torque.



Torque characteristics

Fig. 1 compares torques between one that does not account for eddy current inside the magnetic steel sheet during magnetic field analysis, and one that does. It shows that transient phenomena occur in the early stages of analysis when accounting for eddy current. When the revolution speed is high like in this motor, the torque is overestimated when eddy current is not accounted for in the magnetic steel sheet.

Line voltage

Fig. 2 shows the comparison between U-V line voltage when the eddy current inside the magnetic steel sheet is accounted for in the magnetic field analysis and when it is not. Like it is with torque, if eddy current inside the magnetic steel sheet is not accounted for, voltage will be overestimated. Fig. 2 shows that accounting for eddy current controls the harmonic component of voltage. This is because changes in the magnetic flux of magnets and current is controlled by the eddy current.

Iron Loss, Efficiency

Fig.3 shows the eddy current distribution (average value between electric angle of 180 to 360deg) obtained in the analysis accounting for eddy current of magnetic steel sheets. Large eddy currents occur in the tip of the teeth part and rotor surface of the stator. Next, the iron loss of analysis accounting for eddy current of magnetic steel sheets and one that is not will be summarized in fig 4. Iron losses are sum of the hysteresis loss and eddy current loss of magnetic steel sheet and eddy current loss of the magnet. However, even in an analysis accounting for eddy current, the hysteresis loss is calculated with post-processing of the magnetic field analysis.

The efficiency calculated from copper loss, iron loss and the output will be shown in fig 5. This table shows that there is when eddy current of magnetic steel sheets is not accounted for in the magnetic field analysis, efficiency is also overestimated by about 1%.

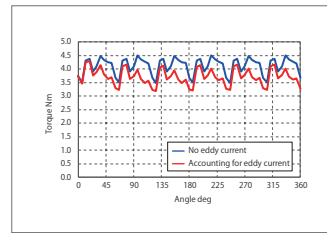


Fig. 1 Torque Wave

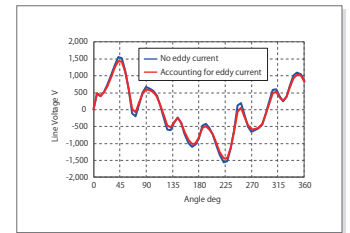


Fig. 2 U-V Line Voltage Waveform

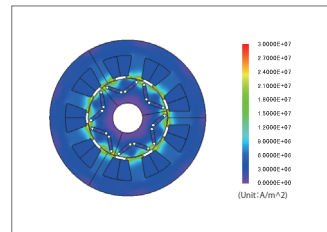


Fig. 3 Eddy current distribution

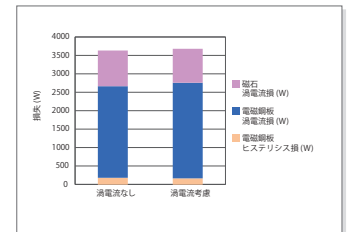


Fig. 4 Iron loss

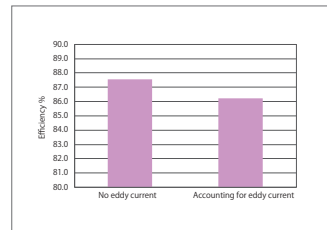


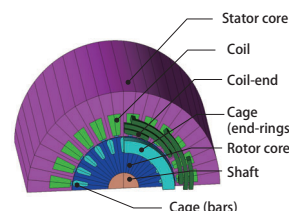
Fig. 5 Efficiency

Case 195 Torque characteristics analysis of three-phase induction motors using 3D correction function

module: DP, TR

Overview

An induction motor is a motor in which the rotating magnetic field of the stator winding causes induced current to flow in an secondary conductor, which exerts force on the rotor in the rotational direction and causes it to spin. In an induction motor, magnetic flux in the axis direction, such as leakage flux in the coil end, can have a large effect on motor characteristics. However, transient phenomena are strong in the inductance motor, and analysis time is needed in order to achieve a steady state solution. Due to this, being able to evaluate characteristics in a 2D analysis is desirable, but 3D effects such as leakage flux in the coil ends are ignored in a 2D analysis, and there are cases when an accurate analysis cannot be obtained. In JMAG, highly accurate results can be quickly obtained by performing corrections on 3D effects. This document introduces a case study which obtains inductance correction values, and then obtains N-T characteristics (revolution speed-torque characteristics) using the 3D correction function.



Self Inductance

Fig.1 shows the results of self inductance at lock tests. Fig.1 shows that inductance has decreased by approximately 25% in a 2D analysis when compared to a 3D analysis. This is because a 2D analysis cannot account for leakage inductance in the coil end.

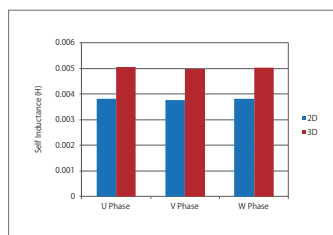


Fig. 1 Self Inductance

N-T Characteristics

Fig.2 shows those N-T characteristics of 2D, 3D and 2D analysis with 3D correction and fig.3 shows N-I characteristics.

Fig. 2 shows that N-T characteristics becomes the same as 3D by using 3D correction. As shown in fig.3, this is because current flowing in the coil has come closer by accounting for leakage inductance.

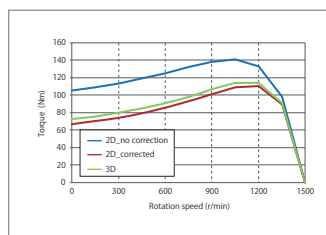


Fig. 2 N-T characteristics

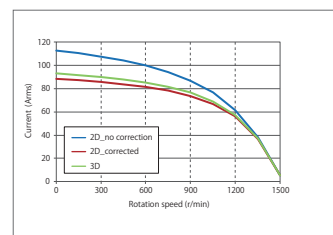


Fig. 3 N-I characteristics

Case 196 Analysis of coil stray capacitance

module: EL

Overview

In a high frequency application, not only the coil's inductance component but its capacitance component cannot be ignored and results in degradation of the circuit impedance characteristics and inconsistencies in resonance frequencies. Stray capacitance that occurs between the coil windings is one of them. For example, with a helical coil, electrical potential varies depending on its rotation so difference in electrical potential occurs between the neighboring windings. As a result, capacitance occurs between the windings and operates as a condenser component.

The stray capacitance that occurs in the coil depends on its geometry. To obtain the stray capacitance that occurs in various types of coils, a magnetic analysis using FEM is effective. By modeling the entire coil, stray capacitance accounting for the distance between windings and differences in winding pattern can be obtained.

This document introduces target on the helical coil, changes the distance between windings, and obtains stray capacitance that occurs in each coil.



Stray capacitance

Stray capacitance obtained from the analysis results are shown in Table 1. The stray capacitance is larger when the coil distance is shorter.

coil distance mm	1	5
Stray capacitance pF	1.42	0.89

Table 1 Stray capacitance

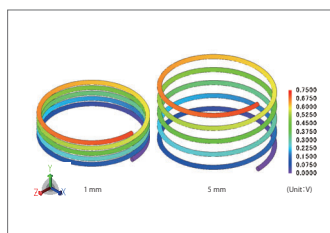


Fig. 1 Electric potential distribution (RMS)

Electric potential distribution, Current density distribution

Each electric potential (intensity) distribution of when electric potential of 1(V) is supplied between terminals of the coil with coil distance of 1.5 (mm) is shown in Fig.1, and current density distribution (intensity) is shown in Fig.2. It can be confirmed that the electric potential distribution inside the coil is solved from the supplied electric potential boundary condition (amplitude: 1V, 0V). It can be confirmed that current flowing in the coil depending on the electric potential difference is solved, and current density distribution is obtained.

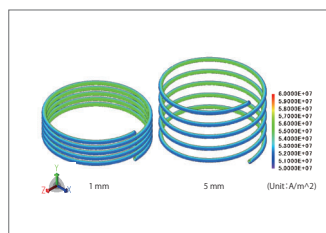


Fig. 2 Current density distribution (RMS)

Case 197

Electric field distribution Analysis of a Electroplating

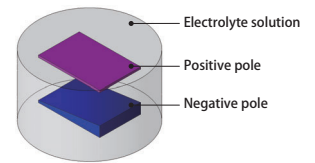
module: EL

Overview

Electroplating is a technology that forms a metal film on the surface of an object and is currently used in various fields from electric parts to automobiles.

When electroplating, use a solution that includes the component you wish to use. Within that solvent, set the board including the component you wish to electroplate at a positive pole, and set the board you wish to electroplate at the negative pole, and run voltage. Then, current will flow, and the component of the positive pole will melt in the solvent, and electroplating for the negative pole side will start.

This example will introduce the electric field distribution in a model with the negative pole geometry facing the positive pole that is not parallel but slanted.



Electric field distribution

Fig.1 shows the flat model and the slanted model in the electric field graph, and Fig.2 shows the contour of electric field distribution. Also, Fig.1 is measured along the electric pole.

For the flat model shown with the red line, Fig.1 shows that it is symmetrical at 15mm as the center. On the other hand, for the slanted model as shown with the blue line, it can be seen that the electric field gets larger as the distance between positive and negative poles becomes smaller.

Fig.2 shows that biases are occurring in the electric field for slanted model on the negative pole.

Current density distribution

Fig.3 shows the current density graph of the flat model and the slanted model, and Fig.4 shows the contour of the current density distribution.

For the flat model shown with the red line, Fig.3 shows that current density is symmetrical at 15mm as the center. On the other hand, for a slanted model as shown with the blue line, the current density close to the positive pole will be higher. In this case study, since the material property inside the solution is constant, the electric field intensity is in proportion with the amount of the current. For this reason, current density would have the same results.

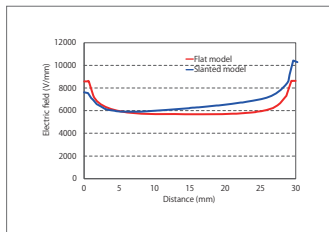


Fig.1 Electric field

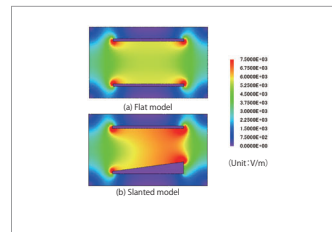


Fig.2 Electric field distribution

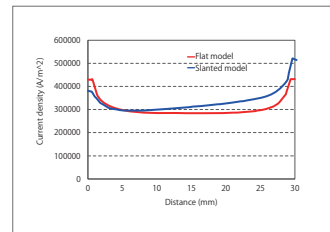


Fig.3 Current density

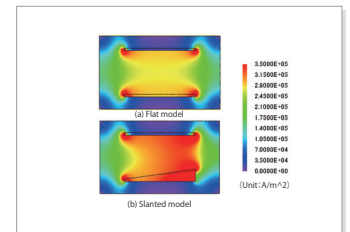


Fig.4 Current density distribution

Case 198

Busbar Thermal Stress Analysis

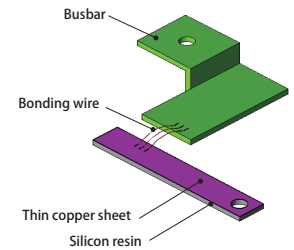
module: FQ, DS, HT

Overview

Current is supplied via busbars or wire bonding in power supply lines for power electronics devices such as inverters. Because inverters and similar devices operate with PWM carrier frequencies of several kHz, high-frequency current flows in their busbars. Influences from the skin effect cannot be ignored in this kind of high-frequency current, so increased resistance and loss become problems. Furthermore, when thermal strain is caused due to excessive heat generation, disconnections may occur in a worse case scenario of stress accumulating in the bonding wire connection region. This type of stress is called thermal stress. When thermal stress exceeds yield stress, irreversible changes to geometry occur, so verifying thermal stress distribution due to heat generation is important.

Because a busbar's geometry is complicated, it is difficult to predict in advance where there will be unevenness in the current's flow while current is running, and whether this will cause heat generation. With magnetic field analysis using the Finite Element Method (FEM), it is possible to correctly obtain the unevenness in current distribution and the joule loss, and then predict the temperature distribution with these as causes of heat generation.

Here, temperature distributions for busbars are obtained when the power supply frequency is changed.



Current Density Distribution

Fig.1 shows current density distribution. Distribution is occurring in current density for the bus bar and thin copper sheet due to the skin effect as indicated in Fig.1. As the section of the bonding wire where current flows is small, it is clear that current density is particularly getting higher, when compared to others.

Temperature Distribution

The temperature distribution of the bus bar is shown in Fig.2. Temperature is rising with the bonding wire and the copper thin sheets. The temperature of the bonding wire has increased especially at over 200 deg C.

Thermal Stress Distribution

Fig.3 shows thermal stress distribution of the bonding wire. There is distribution in thermal stress, and it also shows that large stress is put on the connection joint between the busbar and the copper thin sheet, as well as the top of the bending part. Caution needs to be taken because temperature increase will not only cause burn out, but it may also damage the wire due to local thermal stress.

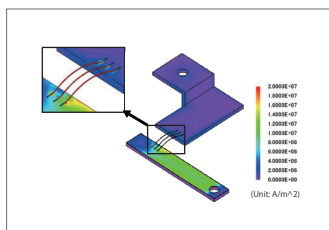


Fig. 1 Current density distribution

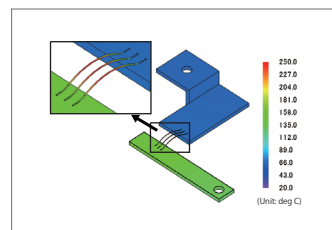


Fig.2 Temperature density distribution

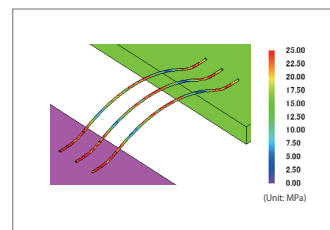


Fig. 3 Thermal stress distribution

Case 199 Efficiency Analysis of Wireless Power Transfer via Electromagnetic Induction Method using Resonance Circuits

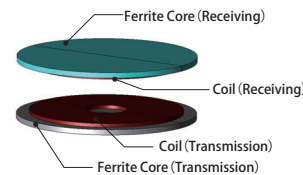
module: FQ

Overview

In recent years, electromagnetic induction type transmission is considered for applied use in wireless power supply systems for electric vehicles (hereinafter, referred to as EV) and plug-in hybrid cars (hereinafter, referred to as PHEV), which are demanded for practical use. As for wireless power supply systems for EV / PHEV, even if the car-equipped coil of the receiving end and the ground buried coil of the transmission end slip out of place in the horizontal position, electric power transmission needs to be retained with high efficiency. Recently, circuits with excitation condensers, which retain a large power supply of electric power is also considered.

Efficiency changes, which is triggered by change of positioning, is primarily because of the change in magnetic flux in the receiving end where the transmission coil is slightly shifted in relation to the receiving coil. Furthermore, run magnetic field analysis when evaluating power supply of electric power or capturing the variations in spatial magnetic flux.

This example presents, an electromagnetic induction-type wireless power supply system using an excitation circuit positioned with a parallel resonance condenser on the receiving end, and a series resonance condenser on the transmission end will be analyzed. An efficiency change in relation to the disposition in the horizontal direction is evaluated from both power transmission efficiency and the coupling coefficient.



Power Value / Power Transmission Efficiency

Graphs of power value and power transmission efficiency when changing the horizontal distance between the transmission and receiving coils are shown in Fig. 1.

When there are no displacements in the horizontal direction, power close to 4.7kW can be obtained with a maximum efficiency of 99%. The state where both the transmission and receiving coil centers match up is considered 0, and the distance that it moves in the horizontal direction (horizontal distance) is defined as displacement in the horizontal direction. As the horizontal distance between the transmission and receiving coil gets larger and displaced, both power supply and power transmission efficiency will decrease. Power transmission efficiency / power value will both be 0 at 180mm.

Since voltage of the transmission coil is constant in this model, the input voltage will change. Reduction of power value is thought to be because of the circuit design. With displacement in the horizontal direction, self-inductance of the coil will not change, but there will be a change in mutual inductance between coils. This causes the resonance frequency determined by the inductance and capacitor to be displaced, and power transmission efficiency will drop.

Coupling Coefficient

Fig. 2 shows the coupling coefficient when the horizontal distance between transmission and receiving coils is changed.

As with coupling coefficients, it will drop due to displacements in the horizontal direction.

Magnetic Flux Density

Fig.3 shows the magnetic flux density distribution when the horizontal distance is changed between the transmission and receiving coils. As horizontal distance changes, magnetic flux linked to the receiving coil (above) decreases. It is possible to confirm that these changes in flow of magnetic flux are the cause of decrease in power supply, efficiency, and coupling coefficient.

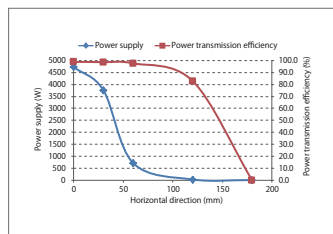


Fig. 1 Power supply and power transmission efficiency relative to the horizontal direction

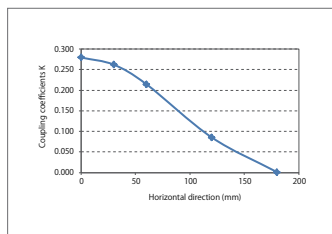


Fig. 2 Coupling coefficients relative to the horizontal direction

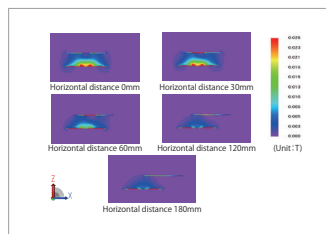
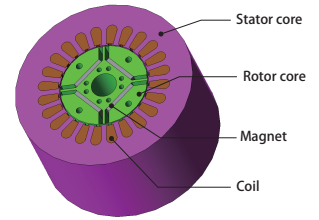


Fig. 3 Magnetic Flux Density



Overview

Recently, PM motors are being applied in home appliances and electric automobiles, and the demand for compactness and high power is increasing. On the other hand, small and high-power motors tend to be affected by high-frequency components due to magnetic saturation and high rotations, which results in increased loss in the motor; therefore, they are also expected to have increased efficiency. In the realization of highly-efficient motors, it will become increasingly important to accurately estimate loss.

In the drive circuit of a PM motor, there are times when current vector control using PWM control (pulse width modulation control) is run. Current waveform that is being supplied by PWM control have carrier harmonic current superimposed on the basic wave control, and with this carrier harmonic current, high-frequency of the magnetic field is applied to the motor core and iron loss occurs. With harmonic components and magnetic saturation of the iron core due to permanent magnets, it will be necessary to evaluate iron loss with magnetic flux density waveform that is different from the conventional sinusoidal alternating current. Also, in a high rotation PM motor, the variable frequency of magnetic flux density becomes increasingly high and the eddy current distribution of the depth direction of the laminated steel sheet due to skin effect becomes difficult to ignore. With these conditions, evaluation using the highly-accurate iron loss calculation function becomes required.

In this example, a hysteresis model accounting for minor loops of the direct current bias magnetism and the lamination analysis function accounting for eddy current distribution in the lamination direction are run simultaneously to evaluate iron loss due to high carrier harmonic components in the IPM motor.

Iron Loss

Iron loss is indicated in Fig. 1. The result of the hysteresis model and lamination analysis is compared with the loss analysis result of the conventional iron loss properties.

The eddy current loss obtained by conventional iron loss characteristics is underestimated. The magnetic flux density due to the carrier component during actual driving fluctuates more, so that the magnetic flux density peak is higher than the peak attained for the magnetic flux density used to obtain iron loss characteristics. It is thought that the loss increased because the magnetic permeability decreased, the skin effect was less, and eddy currents were greater. The hysteresis loss is larger than the iron loss in the rotor core. In the rotor core, the positions and areas of the minor loops change mainly due to DC superposition due to magnetic flux. It is thought that this is because the hysteresis model captured these effects more accurately.

Joule Loss / Hysteresis Loss Density Distribution

The distribution of joule loss density and hysteresis loss density is displayed in Fig. 2. It can be confirmed that hysteresis loss is higher in the rotor core surface. This is thought to be the effects of the minor loop. Furthermore, as with the results shown in Fig. 1, the Joule loss density is higher in the lamination analysis than the iron loss density.

Magnetic Flux Density Waveform

The waveform of magnetic flux density in the rotor core and stator core are displayed in Fig. 3.

Super imposed direct current components that affect the minor loop appear in the magnetic flux density waveform of the rotor core.

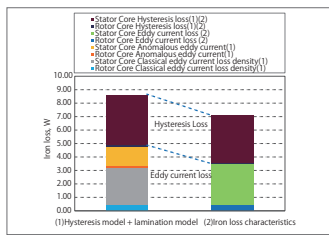


Fig. 1. Iron Loss

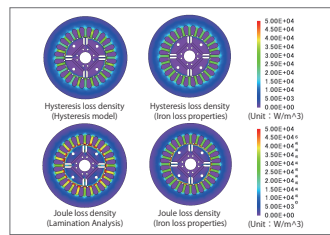


Fig. 2. Hysteresis Loss Density and Joule Loss Density Distribution

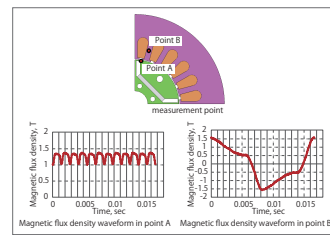
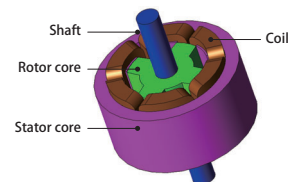


Fig. 3. Magnetic Flux Density Waveform of the Rotor Core and Stator Core

Case 201 Iron Loss Analysis of an SR Motor

module: DP, LS



Overview

With the skyrocketing prices of rare earth magnets, expectations have been rising for SR (switched reluctance) motors because they have a motor format that does not use permanent magnets. SR motors have a simple structure that can achieve solid performance at a low price. However, since they do not use permanent magnets, it is difficult to obtain the same efficiency as a permanent magnet motor, and efficiency increase is becoming an issue. Reduction of iron loss that occurs during drive is said to be a possible solution to this problem. This is where it becomes important to accurately obtain iron loss of SR motors.

The magnetic flux density waveform in each part of the SR motor is in a state where direct current magnetic flux is superimposed on the alternating current magnetic flux. Direct current bias magnetism, like in this case, has confirmed that the iron loss analysis method using the conventional Steinmetz empirical law produces underestimated evaluations of loss.

This example, to accurately capture iron loss that occurs in the SR motor, we will introduce hysteresis loss accounting for the hysteresis loop of the materials and the iron loss analysis methods accounting for eddy current loss on the inside of the lamination cross section.

Iron loss

Fig.1 shows the obtained iron loss value, and Fig. 2 shows the breakdown of hysteresis loss and joule loss of the rotor and stator. It is comparing with the analysis using the original iron loss properties. For more information about setting iron loss calculation using iron loss properties, see "JAC181 Analysis of SR Motor Drive Characteristics." It is confirmed that iron loss increases as power supply voltage gets larger. By using the hysteresis model and lamination analysis, larger iron loss is obtained from the iron loss properties, and as supply voltage gets large, the difference also increases. At 200V, a value higher by approximately 30% than the original iron loss properties is estimated. It can be confirmed that the hysteresis loss is largely increased in a hysteresis model although joule loss drops in the lamination analysis, when confirming the breakdown of iron loss at voltage of 100V to 200V.

Iron Loss Density Distribution

Fig.3 shows the iron loss density distribution at supply voltage of 100V, and Fig.4 shows the iron loss distribution at 200V. It can be confirmed that hysteresis loss density is high at the corner of the salient pole part of the rotor and stator in a hysteresis model. The density of joule loss is also high at the corner of the salient pole part, but the joule loss of iron loss properties is high.

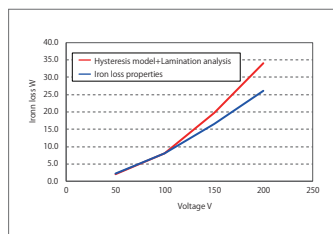


Fig. 1 Iron loss

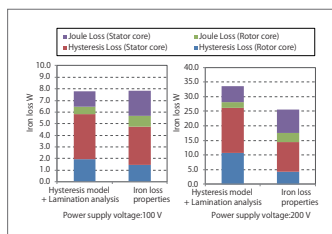


Fig. 2 Breakdown of iron loss

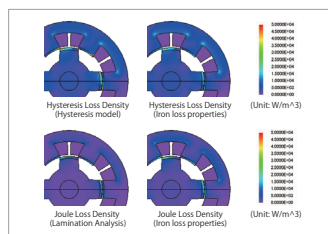


Fig. 3 Iron Loss Density Distribution (100V)

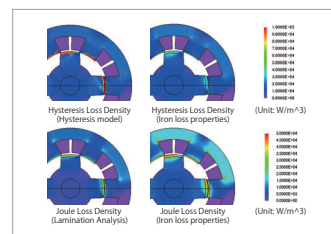
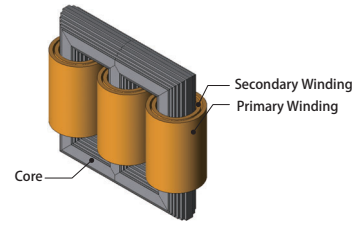


Fig. 4 Iron Loss Density Distribution (200V)



Overview

Stray loss is mainly caused by leakage flux from winding, but structures closer to the winding will tend to be affected easier by leakage flux. The ratio of stray loss relative to all losses may not necessarily be large but heat is generated in certain areas and may become an issue in the operation of transformers. In particular, stray loss occurring in the core tends to have effect on not only the core, but insulated items that construct the core, and may result in degradation of insulating oil due to burnout.

Stray loss of the core is physically iron loss, but the cause is not the main magnetic flux in the core. Categorically, it is considered stray loss as it is evaluated from short-circuit tests in the actual machine test and because it is caused by leakage flux from the winding.

This document introduces runs analysis by modeling the short-circuit test that is conducted when evaluating stray loss and obtains stray loss distribution in the core close to the winding.

Eddy Current Loss Density Distribution, Hysteresis Loss Density Distribution

Fig.1 shows the eddy current loss density distribution of the core, and Fig.2 shows hysteresis loss density distribution. It can be seen that the effects of leakage flux from the winding ends are large

Magnetic Flux Lines

Fig.3 shows the magnetic flux lines from the center foot section direction. As this is a short-circuit test, it can assume that all occurring magnetic flux are leakage flux. It can be seen that magnetic flux that is leaking from the winding ends are almost perpendicular to the core. This occurs because the permeability inside the core differs greatly from the permeability on the outside of the core. This leakage flux causes local eddy current loss in the core surface.

Magnetic Flux Density Distribution

Fig.4 shows magnetic flux density distribution of the core, and Fig.5 shows the current density waveform of 1 block in the lamination direction of the center foot. The block on the outermost layer of the core accounts for eddy current; therefore, with secondary magnetic flux occurring due to eddy current, magnetic flux density has become large on the steel sheet near the surface. On the contrary, as it is a short-circuit test, it can be seen the magnetic flux density is low as magnetic flux does not flow inside the core.

Eddy Current Loss Density Waveform

Fig.6 shows eddy current loss density waveform equivalent to 1 block of the lamination direction near the winding end part of the center foot. With the effects of leakage flux, it can be seen that there is strong heat generation on the core surface.



Fig.1 Eddy current loss density distribution

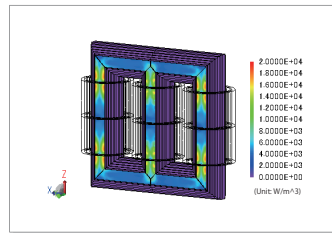


Fig.2 Hysteresis loss density distribution

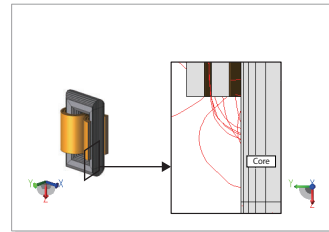


Fig.3 Magnetic Flux Lines

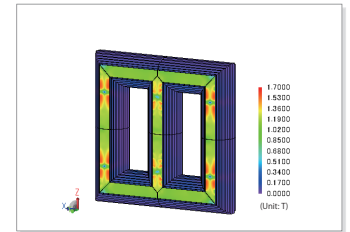


Fig.4 Magnetic flux density distribution of the core

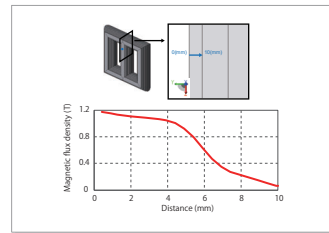


Fig.5 Magnetic flux density waveform

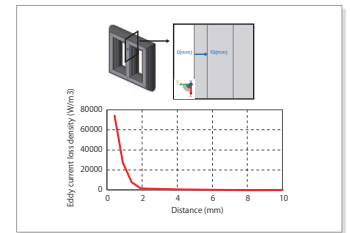


Fig.6 Eddy current loss density waveform

Case 203 No-Load Test Analysis of Power Transformer

module: FQ, LS

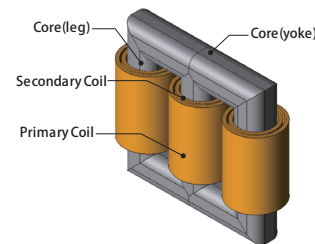
Overview

Large-scale power transformers are expected to be highly-reliable as machinery that will support the industry infrastructure, but unfortunately, it is impossible to conduct tests connecting to actual load. For this reason, tests of special circuit structure including no-load tests and contradiction tests are run.

No-load tests are tests that apply rated voltage in the primary side at the no-load state of the secondary side. Current only flows to the primary side in the no-load test, but this current causes excitation and iron loss of the iron core.

If it is an iron core that has a tripod structure, the magnetic circuit of each phase is not completely equivalent, and thus causes unbalanced current.

This example focuses on modeling in the analysis of no-load tests in JMAG and obtains the magnetic flux line, current, excitation conductance, and excitation susceptance that can be acquired from there.



Magnetic flux line

The magnetic flux line of the core is shown in fig. 1. According to the material properties of grain oriented steel, you can see that the magnetic flux line of the core is oriented along the easy axis of magnetization.

Iron Loss Current, Magnetization Current

Effective values for iron loss current and magnetization current are shown in table. 1. In the three-legged iron core, the center leg and the left/right legs are not equivalent in the magnetic circuit, so unbalanced current is generated between the three phases. In table. 1, the average values are taken for the current running through the three phases.

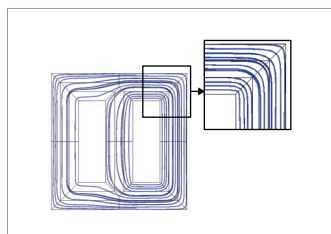


Fig. 1 Magnetic flux line of core

Iron loss current A	Magnetization current A
0.18	31.2

Table. 1 Iron loss current, magnetization current

Excitation conductance, Excitation susceptance

Excitation conductance and excitation susceptance are shown in table. 2, and the T-shaped equivalent circuit diagram in the transformer is shown in fig. 2. In the no-load test, the circuit constant in the dotted lines are obtained in the equivalent circuit shown in fig. 2. Voltage decreases due to the primary side coil resistance and the primary side leakage reactance are considered to be sufficiently small, so $V = V'$ is assumed.

Excitation conductance μS	Excitation susceptance μS
6.1	1042.3

Table. 2 Excitation conductance, Excitation susceptance

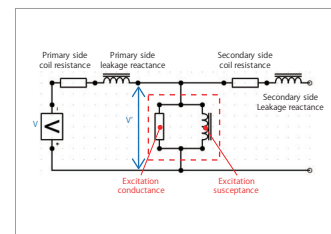


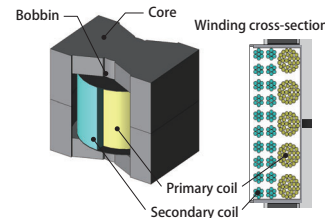
Fig. 2 T-shaped equivalent circuit diagram

Case 204 Copper Loss Analysis of Switching Transformers using Litz Wire

module: TS

Overview

Flyback converters are used for various applications such as power supply circuits, which is suitable for small electrical power that realizes switching power supply. Since there are not many parts and it is a very simple structure, it has realized power supply circuits that limit manufacturing cost. Power supply circuits require designs that limit the cost of operation but as portability becomes a focus and harmonics of switch frequencies become common, heating of the winding becomes an issue. To increase pressure resistance, there are times when gap is necessary for the core; however, with magnetic flux fringing near the gap, local heat generation may occur due to proximity effects in the winding. Local heat generation will not only drop the conversion efficiency of electrical power but it will also cause degradation in the insulating film so it is important to control it as much as possible. The Litz wire is one wire separated into multiple thin wires, painted with enamel film, and twisted together. Separating one wire into multiple thin wires controls the concentration of current due to the skin effect. By adding twisted structure to the bundle wire, it is expected that the current flows more evenly, and local heat generation is controlled. This document introduces the effects on copper loss due to the presence or absence of a twisted structure in the winding regarding the copper loss that occurs in the small switching transformer structured with PQ cores.



Current Waveform, Copper Loss Waveform

Fig. 1 shows primary and secondary current waveform depending on whether twisted wire is used or not, and Fig. 2 shows primary copper loss waveform. Fig. 1 shows that it has reached the steady state after 0.0006(sec) and whether or not it has twists, there are responses at approximately the same times. Also, Fig. 2 confirms that the average value of copper loss in winding for the primary winding has dropped by approximately 26(%) for the case with twists compared to the one without. It is assumed that with local flux linkage inside the winding dropping due to twist effects, local biases of eddy current caused by time variations have been resolved.

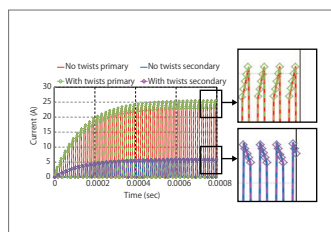


Fig. 1 Current Waveform

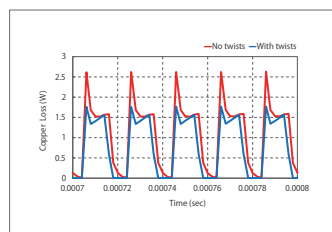


Fig. 2 Copper loss waveform

Joule Loss Density Distribution

Fig. 3 shows the time average of joule loss density distribution of winding at the steady state. In the results without winding, joule loss has increased as eddy current is induced by the reaction of the current in secondary winding, which occurs when the switch is off in the wires of the primary winding that is close to the secondary winding because of proximity effects. As opposed to this, the results with twists show that the impact of proximity effects from the secondary winding is controlled.

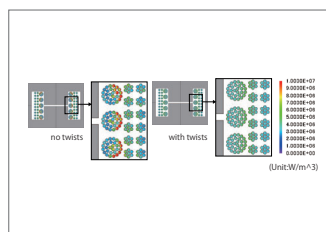


Fig. 3 Joule loss density distribution

Flux Linkage Waveform

Fig. 4 shows the winding flux linkage waveform. It can be confirmed that the transformer is operating regardless of whether there are twists or not, and without losing properties as a magnetic circuit.

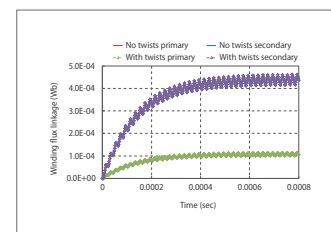
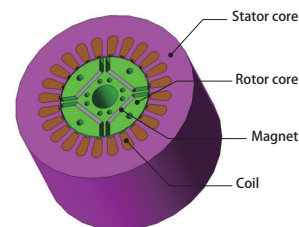


Fig. 4 Flux Linkage Waveform

Overview

In order to realize the high efficiency and high output of motors, it is necessary to understand the temperature increases that occur in each part of a motor. This is because coil resistance and magnet characteristics change with increases in temperature, and this may result in motor characteristics being largely affected.

Although it is difficult to understand the temperatures of each part in a real machine, the temperatures of each of these parts can be obtained with ease through simulations, and changes to characteristics due to increases in temperature can also be taken into account. As methods of analysis that account for the increases in temperature for each part, there exists the method of coupled analysis via magnetic field analysis and thermal analysis, as well as the method of performing magnetic field analysis that uses thermal equivalent circuits. Detailed evaluations that obtain temperature distribution are possible for coupled analysis. While the evaluation of temperature distribution is not possible when using thermal equivalent circuits, magnetic field analysis that accounts for temperature increases can be performed at high speeds with ease. In this example, magnetic field analysis is performed using a thermal equivalent circuit, and changes in average torque due to magnet demagnetization are confirmed.



Thermal Equivalent Circuit

The thermal equivalent circuit is displayed in Fig. 1.

Loss is expressed by heat source components. Heat sources are copper loss and the eddy current loss of magnets.

Coil temperature calculated with the thermal equivalent circuit is fed back into coil components. Coil components retain temperature dependency in resistance values, and copper loss values are updated. The feedback of coil temperature and updates to copper loss are repeated, and part temperatures during thermal equilibrium are obtained.

Magnets demagnetize due to heat generation from eddy current loss, in addition to heat transmitted from the coils through parts and air gaps.

Part Temperature, Copper Loss

The thermal equivalent circuit during thermal equilibrium and the heat flow vectors of each component are shown in Fig. 2.

The coil temperature, magnet temperature, external case temperature, and copper loss during initial temperature and during thermal equilibrium are shown in Table 1.

From Fig. 2 it is understood that heat is transferred from the magnet to the external case via the rotor core and the shaft, then dissipated to the ambient air. The magnet and heat dissipation path temperatures are as per Table 1; the ambient air is 20 deg C, the external case temperature is 134.5 deg C, and the magnet temperature is 136.1 deg C. Because the difference in temperature between the external case and the magnet is small, it can therefore be determined that the cause of the rise in temperature for the magnet is mainly the small heat dissipation that occurs from the external case to the ambient air.

It is understood from Table 1 that copper loss also increases in accordance with the rise in coil temperature. In this analysis there are no changes in current due to temperature because drive occurs with a specified current. Specifically, the temperature increases the coil electric resistance and copper loss.

Average Torque

The average torque of the initial temperatures and during thermal equilibrium is shown in Fig. 3.

It is understood that average torque decreases during thermal equilibrium. As mentioned previously, there are no changes in current due to temperature. It can therefore be determined that the decrease in average torque is due to the thermal demagnetization of the magnet.

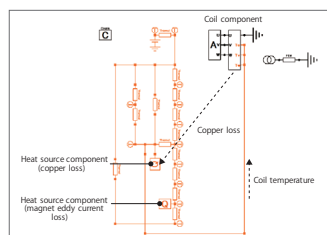


Fig. 1. Thermal Equivalent Circuit

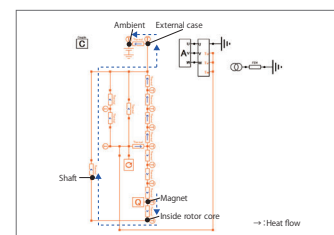


Fig. 2. Thermal Equivalent Circuit During Thermal Equilibrium

Item	External case temperature, deg C	Magnet temperature, deg C	Coil temperature, deg C	Copper loss, W
During initial temperature	20	20	20	24.7
During thermal equilibrium	134.5	136.1	144.2	36.4

Table 1. Temperature History

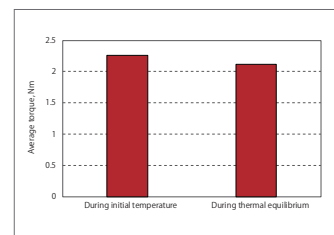


Fig. 3. Average Torque

Case 206 Temperature Analysis of an Oil-Immersed Transformer Using a Coupled Magnetic Field and Thermal Fluid Analysis

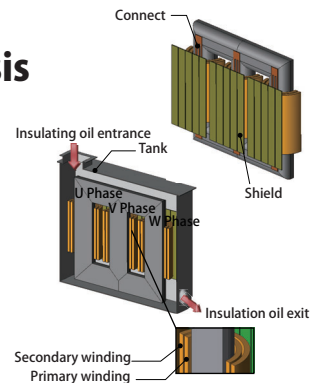
module: FQ, LS

Overview

Large power transformers are used to transform high voltage power generated at a power station into power that can be transmitted. For the structure of the transformer, oil-immersed transformers, which fill the inside of the tank that contains the transformer body with insulating oil for cooling and insulation, are often used. The insulating oil for the oil-immersed transformer is sometimes forced to circulate using a pump, and sometimes made to flow naturally.

In order to estimate the temperature of the winding and core of the oil-immersed transformer, heat transfer from the insulating oil must be estimated. Various structures exist inside the tank besides the core of the transformer and winding, such as clamps for supporting cores and shields for preventing magnetic field leakage. Whether circulation is forced or natural, the flow channel is complex, and estimating heat transfer is not an easy task. Especially in areas where structures block flow channels and other areas with large amounts of localized heat generation, hotspots with high temperatures may be formed. In order to understand and accommodate for these phenomena, a loss distribution analysis, as well as a thermal fluid analysis accounting for the flow path of the insulating oil are necessary.

This document introduces, examples and steps will be shown to obtain heat distribution in a magnetic field analysis for a forced circulation type oil-immersed transformer, map the thermal distribution to thermal fluid analysis model, and then obtain the temperature by handling the insulating oil as a fluid in a thermal fluid analysis.



Loss

Iron loss density distribution occurring in the core of the transformer obtained in the magnetic field analysis is shown in fig. 1, and distribution of copper loss and stray load loss (joule loss density distribution) occurring outside the core are shown in fig. 2. The main components for the loss amounts are iron loss in the core and copper loss in the winding, but when looking at the loss density, it shows that losses are also high in the connector.

Flow Rate Distribution (Streamline)

Flow rate (streamline, contour) of the insulating oil obtained in the thermal fluid analysis is shown in fig. 3. When looking at the streamline, the insulating oil flowing in from the entrance keeps moving downward, and flow rate in the U-phase winding is larger. On the other hand, we can see that flow rate is smaller in the W-phase winding side compared with the U-phase winding side. Furthermore, because the flow passage for the V-phase in the center is narrow, insulating oil cannot easily enter, and the flow rate is also very small.

Temperature

Temperature distribution that can be obtained in a thermal fluid analysis is shown in fig. 4. As estimated from the flow rate in fig. 3, looking at each phase shows the U-phase with the lowest temperature, and W-phase has a higher temperature than U-phase. Since the flow rate for V-phase is small and there is no thermal transfer to the tank side because it is located in the center, the temperature is extremely high, and the core temperatures rise locally by around 110 degC. It shows that there is a large amount of heat generation, and the temperature of the connectors between the core and the winding is extremely high.

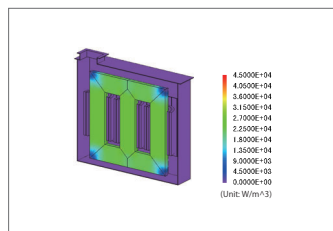


Fig. 1 Iron loss density distribution

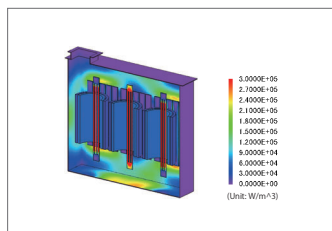


Fig. 2 Joule loss density distribution

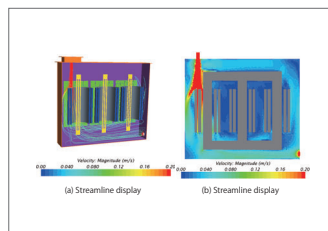


Fig. 3 Flow rate distribution

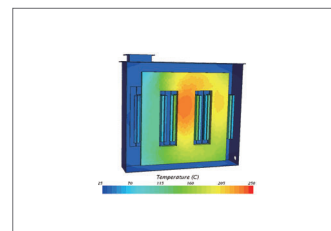
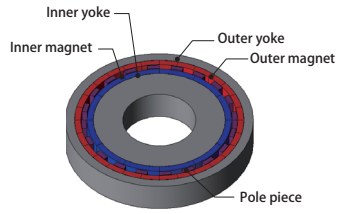


Fig. 4 Temperature distribution

Overview

Gears are used to transfer power. Velocity and torque are transformed depending on the gear ratio. Originally, mechanical gears using conventional wheels had issues with noise due to the meshing of wheels, and its maintenance requiring lubricating oil. As a gear to solve these issues, there is the magnetic gear. Magnetic gears are coupled with the magnetism of things like permanent magnets, and can transfer power without contact, as well as reducing noise and maintenance costs. When prioritizing the size of the transfer torque, rare earth sintered magnets with high energy product are selected for permanent magnets used in magnetic gear. However, since rare earth sintered magnets have high electric conductivity (not as strong as metals such as copper though), eddy current will occur in the permanent magnet and become the cause for decrease in transfer efficiency of magnetic gear. Eddy current of permanent magnets will occur due to variations in magnetic flux density of the gap; however, due to the principle of magnetic gears using pole pieces, the magnetic flux density distribution of gaps have various harmonics components, and for this reason, magnetic field analysis is effective in accurately estimating eddy current. In this example, the transfer torque and transfer efficiency are obtained with magnetic field analysis for the flux modulated type magnetic gear using permanent magnets for the inner and outer rotor and positioning a pole piece between the magnets. In addition, how transfer torque and transfer coefficient are affected due to revolution speed is researched.



Torque, Transfer Efficiency

As an example of a torque waveform that works on the inner and outer rotor, the results for the inner rotor with revolution speed of 2100 (rpm) will be shown in Fig. 1. The torque is negative for both the inner and outer rotor, but as the inner rotor is forcibly rotated in the counter-clockwise direction, which is the positive direction in terms of rotation direction, it shows that external force equivalent to torque is necessary for rotation. On the contrary, the outer rotor is rotated in the clockwise direction, which is the negative rotation direction. As torque is negative, it shows that the force rotating the inner rotor is transferred as the force rotating the outer rotor.

Table 1. shows the transfer efficiency from the inner rotor to the outer rotor. As it is with torque ratio, it can be seen that efficiency decreases with increase in revolution speed.

Joule Loss

As an example of joule loss (eddy current) density distribution occurring in the magnet, Fig 3 shows the results when the revolution speed of the inner rotor is 2100 (rpm). However, the contour plot shows the average rotation between 48 (deg) to 90 (deg) of the inner rotor. The figure shows that joule loss is high on the surface for the inner magnet and the side for the outer magnet.

Magnetic Flux Density Distribution, Magnetic Flux Line

As an example of magnetic flux density distribution and flux line, the results (final step) for inner rotor revolution speed of 2100 (rpm) is shown in Fig. 4. However, it is shown expanded to 1/1 (360 deg). It can be seen that the magnetic saturation in the pole piece is drastic.

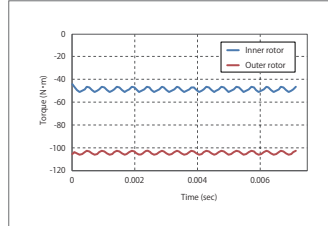


Fig. 1 Torque waveform (Inner rotor revolution speed 2100 rpm)

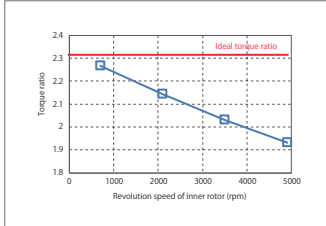


Fig. 2 Torque ratio – revolution speed

Revolution speed of inner rotor (rpm)	Transfer Efficiency (%)
700	97.2
2100	91.8
3500	87.1
4900	82.7

Table 1 Revolution speed

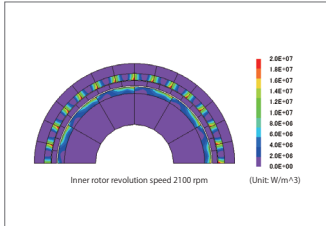


Fig. 3 Joule loss density

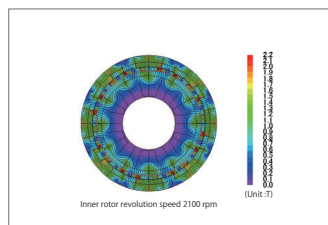
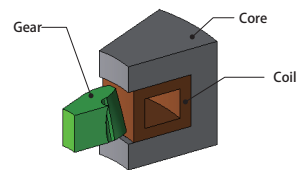


Fig. 4 Magnetic Flux Density Distribution, Magnetic Flux Line

Case 208 High Frequency Induction Hardening Analysis Accounting for Deformation (Abaqus Link)

module: FQ, ABAQUS2



Overview

Since gears are products that demand mechanical intensity, high frequency induction hardening is run for surface heat treatment. Since induction hardening can rapidly heat only the surface of the gear in a short amount of time, the hardness of the surface is continually increased while retaining the toughness inside. On the other hand, the surface of the gear is exposed to high temperatures in the heating process prior to induction hardening; therefore, there is a possibility of thermal expansion. This document introduces evaluates how heating ranges change depending on the deformation amount at high temperatures and deformation during heating, with heat generation analysis in JMAG and linking of heat transfer / deformation analysis in Abaqus.

Deformation Amount

The contour plot of the Z component of displacement is displayed in Fig.1, and the contour plot of the absolute value of displacement is displayed in Fig.2. With the rise in temperature, deformation where the tip of the helical gear is open up and down the Z-axis direction has occurred, and deformation expanding in the circumferential direction can be confirmed.

Temperature Distribution

The temperature distribution at the end of the heating process is displayed in Fig.3. Eddy current is flowing at the gear tip part close to the heating coil, and the process of temperature rise can be confirmed.

Time History of Temperature

The process in which temperature is rising in the center part of the top edge of the gear tip is displayed in Fig.4. After temperature has exceeded the Curie point, the process in which the speed of the temperature rise is decreasing can be confirmed.

Stress Distribution

Mises stress distribution at the end of the heating process is displayed in Fig.5. The process in which stress is concentrated at the gear bottom due to temperature increase / thermal expansion at the gear tip of the helical gear can be confirmed.

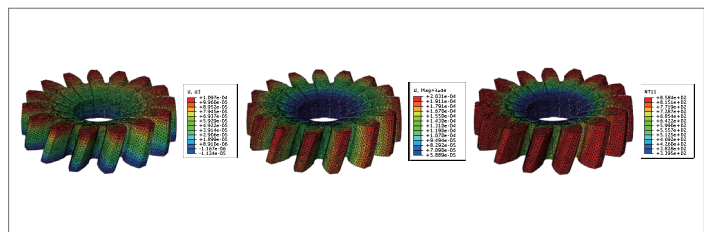


Fig.1 Displacement contour plot of the Z component

Fig.2 Contour plot of the absolute value of displacement

Fig.3 Temperature distribution

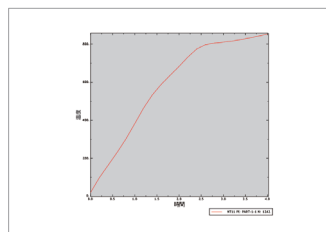


Fig.4 Temperature versus time

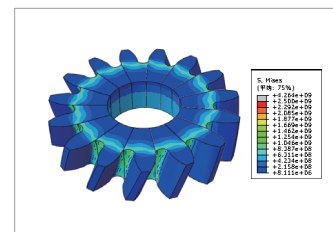


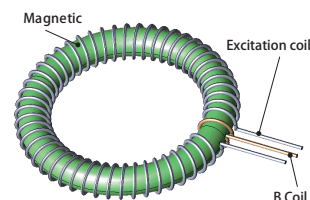
Fig.5 Mises stress distribution

Overview

Magnetic properties affect the performance of products composed of magnetic circuits using magnetic material. This requires that the magnetic properties are assessed accurately. The H-coil method and excitation current method can be used to measure magnetic properties of magnetic material. The excitation current method will be used in this Application Note.

An excitation coil is wrapped around a ring test piece and a current is run through it. Doing this generates a magnetic field inside the excitation coil, and magnetic flux flows through the test piece placed inside the coil. Output voltage will be measured in the B coil wrapped around the ring test piece. Magnetic flux is obtained from the output voltage waveform, and then magnetic flux density is calculated from a cross section of the target. When the excitation current frequency used in the measurement is high, eddy current is generated in the magnetic material, so effects also appear in the waveform of the measured magnetic properties.

In this example, an analysis model is created based on the excitation current method, and the differences in magnetic properties obtained when the frequency is changed are shown.



Relationship between Frequency and Magnetic Properties (B-H Curve)

The relationship between the average magnetic flux density and magnetic field of the magnetic materials obtained when changing the frequency of the alternating current passed through the excitation coil to 1Hz and 10Hz is shown in Fig. 1 (B-H curve), respectively. When eddy current is generated, responsiveness is lowered in the measured average magnetic flux density due to eddy current, and a hysteresis loop is drawn.

Current Waveform Flowing Through Excitation Coil

The current waveform passing through the excitation coil is shown in Fig. 2. In order to clearly show the areas with volatile changes in magnetic flux in the graph, time intervals where the current alternates between positive and negative are shortened.

Magnetic Waveform Produced by B Coil

The history graph of the B coil magnetic flux when the excitation current frequency is 1Hz is shown in Fig. 3.

Magnetic Flux Density Distribution Contour Plot

Magnetic flux density contour plot is shown in Fig. 4. Generated magnetic flux is nearly constant.

Eddy Current Density Contour Plot

Current density contour plot is shown in Fig. 5. Eddy currents concentrate on the outside perimeter of the magnetic material due to the skin effect.

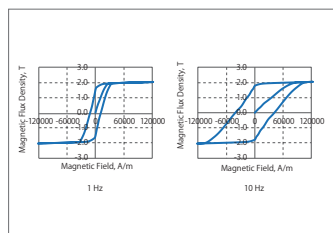


Fig. 1. Relationship Between the Magnetic Flux Density and the Magnetic

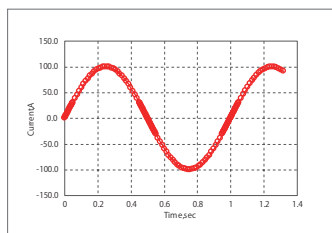


Fig. 2. Current Waveform Flowing Through Excitation Coil

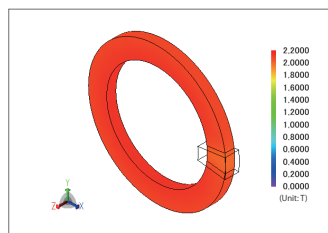


Fig. 4. Magnetic Flux Density Contour Plot

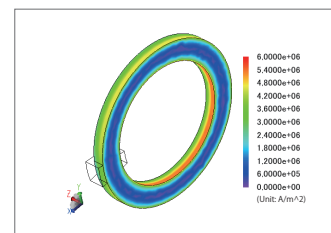


Fig. 5. Current Density Contour Plot

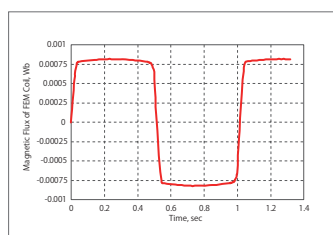


Fig. 3. History Graph of B Coil Magnetic Flux

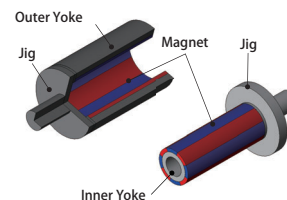
Case 210 Torque Decoupling of In-out Magnet Coupling

module: DP

Overview

Magnet coupling has two rotors, the driving side and the passive side. Unlike magnetic gears, the driving side and the passive side rotate synchronously. If torque exceeds the allowable torque, connection from the driving side to the passive side will slip, causing torque decoupling. The allowable torque is evaluated with the maximum value of the holding torque that keeps the relative positional relationship between the driving side and the passive side.

In this example, an analysis for finding holding torque and an analysis for transient response during torque decoupling.



Holding Torque

In general, the holding torque has a periodicity of two poles (90 deg), and maximum torque is reached when the relative position is shifted by 1/4 pole (22.5 deg). When the passive side is fixed and the driving side is rotated, relative position is changed and the holding torque waveform for 90 deg is obtained.

Fig. 1 shows the holding torque for 90 deg when the inner part is rotated. Peak torque at 22.5 deg is about 16.2 Nm.

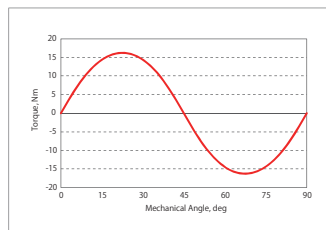


Fig. 1. Holding Torque

$$K_{att} = \frac{T_{load}}{\frac{RPM}{60} * 360}$$

K_{att} : Relaxation factor, Nm / (deg / sec)
 T_{load} : Load torque, Nm
 RPM : Rotation speed, r / min

Fig. 2. Conversion of Load Torque to Relaxation Factor

Starting Response and Delay Angle

Load torque given to the passive side is based on the supposition of load occurring from circumstances such as fluid in the pump. Also, load torque dependency on rotation speed is considered, and the equation shown in Fig. 2 is used to assign the equation of motion as the relaxation factor.

The rotation speed of the passive side is displayed in Fig. 3 for when the load torque assigned to the passive side is 10 Nm, 14 Nm, 16 Nm, 16.5 Nm, 17 Nm, and 18 Nm. The rotation speed of the driving side is also displayed in the figure as the "Reference" line. Notice that the passive side is able to follow the rotation of the driving side until a load torque of 16.5 Nm is reached. Values of 17 Nm and 18 Nm do not follow the rotation, and the sides become decoupled.

Fig. 4 shows the delay angle of the passive side at the time the driving side makes one rotation. The delay angle when the load torque is 16.5 Nm is about 22 deg. For load torque of 17 Nm and 18 Nm, it can be seen that slippage is about 90 deg.

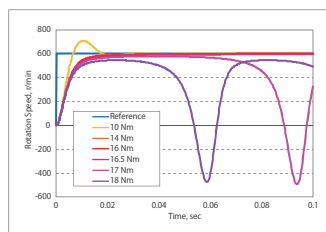


Fig. 3. Passive Side Rotation Speed When Load Changes

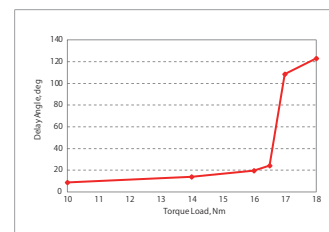


Fig. 4. Delay Angle on the Passive Side

Case 211 IPM Motor Wire Joule Loss Analysis

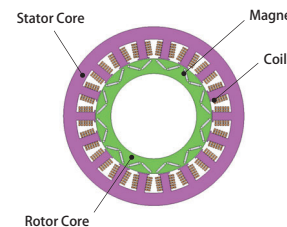
module: DP

Overview

The square wires and flat wires of segment coils and edgewise coils, etc., are being used for the purpose of improving lamination factors, the reduction of end parts, minimization, improvements in heat dissipation, and improvements in productivity in IPM motors. On the other hand, from the viewpoint of higher efficiency and increasing output, etc., motor coil resistance to loss is becoming a necessity as so to obtain a reduction of loss in electrical appliances in general.

When increasing the number of motor rotations, concentration of electric current occurs within the coil interior due to the eddy and current joule loss value increases. Especially at high rotation such as 10,000 r/min, joule loss may increase from 3 times to 4 times compared with low speed. In running accurate evaluations of joule loss and handling concentration of electric current within the wire correctly, it is also important to properly manage the eddy current generated by the distribution of magnetic flux density that links the wire and temporal changes to magnetic flux density. For these reasons, simulation via magnetic field analysis is a necessity.

In this example, evaluation of coil joule loss that includes eddy currents during motor rotation is introduced here.



Comparison of Winding Joule loss

Coil joule loss when using fundamental frequency and PWM waveforms as input at 10,000 r/min is displayed in fig. 1. It is understood that joule loss increases over 4 times more when the eddy current is accounted for, compared to when the eddy current is not accounted for.

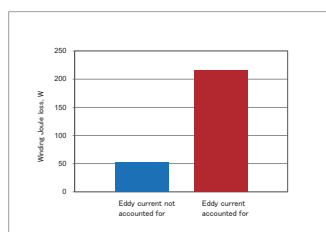


Fig. 1 Winding Joule loss

Joule Loss Density Distribution When Accounting for Eddy Current

Wire joule loss density distribution (at a time of maximum U phase current) when the eddy current is accounted for is displayed in fig. 2. It can be seen that gap side wire loss density is high and offset is large. From this it is understood that there is considerable eddy current generation at this position.

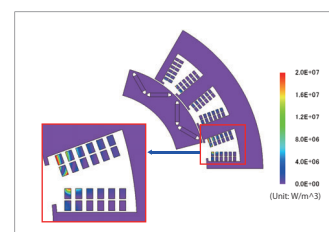


Fig. 2 Joule Loss Density Distribution

Flux Linkage per Component

Magnetic flux lines when eddy current is not taken into account are investigated and the relationship between magnetic flux linking the strand and its Joule loss is confirmed. Fig. 3 shows the flux lines.

In fig. 3, the rotor and the wires which are near the airgap are linked magnetically by the flux line. Observing PWM waveform on the other hand shows linkage with the entire wire. From this results, joule loss concentration within wires near the gap is thought to be caused by the link with fundamental frequency flux components.

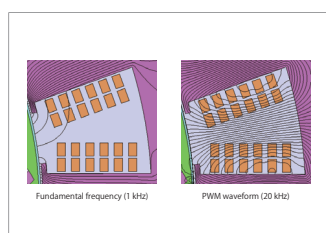


Fig. 3 Flux Line

Case 212 AC Loss Analysis of a Claw Pole Alternator

module: TR

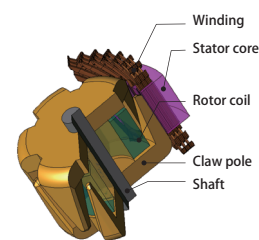
Overview

Electric Machines are affected primarily by 3 types of losses. Iron losses in steel lamination sheets, joule losses in the conducting components and joule losses in coils.

When we primarily focus on AC losses in coils, one way to reduce them is by using a "Bar winding". Bar winding is used large conductor bars, so this improves fill factor and reduces DC resistance which in turn reduce DC losses. Large cross section of these windings cause make them vulnerable to AC losses like skin effect and proximity losses. The AC losses are frequency dependent so if the machine operates on higher frequencies and higher speeds.

In order to examine the AC losses we use a bar wound claw pole alternator which is a three dimensional machine. This allows us to examine the AC losses in greater depth and get their full impact. These losses cannot be calculated via the equivalent circuit method. Hence finite element method has to be used.

In this example, we introduce the case study that evaluates AC losses in coils of claw pole alternator.



Loss Analysis

Fig. 1 shows AC losses vs DC losses. Fig. 2 shows loss distribution of coils. Fig. 3 shows loss distribution and flux line of end windings.

From fig. 1, we can observe that the effect of AC losses is significant on the overall efficiency, thus they cannot be ignored.

In fig. 2, most of the losses are concentrated on the edges of the coil geometry than the insides. This is one of the characteristics of AC Losses.

From fig. 3, we can confirm the relationship of loss distribution and magnetic flux in the end windings.

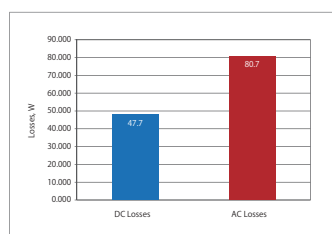


Fig. 1 AC Losses VS DC Losses

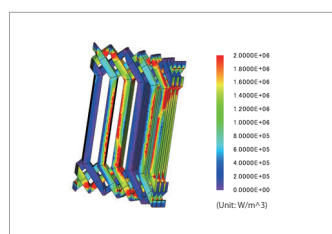


Fig. 2 Loss contour plot

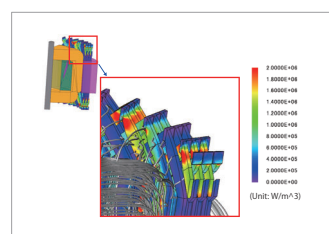


Fig. 3 End Winding Losses and Flux Line

Case 213 Circuit/Control Simulation of a Wound-Field Synchronous Motor

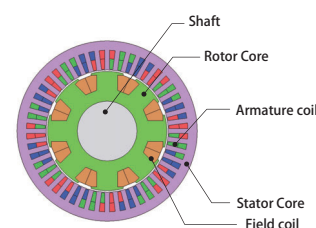
module: DP, RT

Overview

Traditionally, motor control design and motor design are often independent processes, with cooperative design being difficult. Meanwhile, for advanced motor control design, a plant model that is more detailed and behaves like the actual machine is required for control simulation.

In JMAG, it is possible to create a plant model (JMAG-RT motor model) suitable for the actual machine, taking into account magnetic saturation characteristics and space harmonics of the motor. By importing this plant model into a control/circuit simulator, it is possible to carry out coupled simulation taking into account both detailed motor characteristics such as magnetic saturation and space harmonics, and motor driver control characteristics.

In this example, JMAG-RT is used to obtain the torque of a wound-field synchronous motor (below WFSM) and the coil inductance current dependence, and the spatial harmonic components contained in them. Furthermore, we will simulate the WFSM current control by importing a JMAG-RT motor model created as a plant model into the control/circuit simulator.



Current Waveform, Torque Waveform, Inductance Waveform

The field current waveform when vector control is carried out is shown in Fig. 1, the armature current waveforms in Fig. 2, the torque waveform in Fig. 3, and the inductance waveforms in Fig. 4 and Fig. 5. From each waveform, it is understood that a large current flows momentarily immediately after turning on the power, and the torque also increases. Moreover, it can be confirmed that a steady-state condition is gradually converged to. On the other hand, since the JMAG-RT motor model takes into account the shape of the motor, the current and torque waveforms which include space harmonic components caused from the slot shape can be confirmed in steady state.

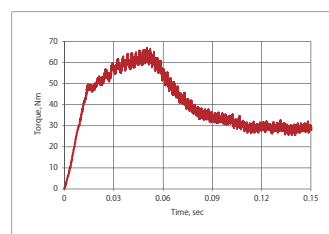


Fig. 3. Torque waveform

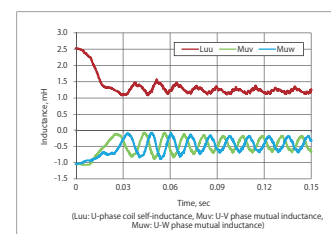


Fig. 4. Inductance waveform

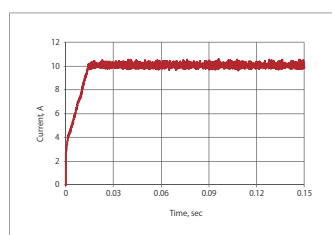


Fig. 1. Field current waveform

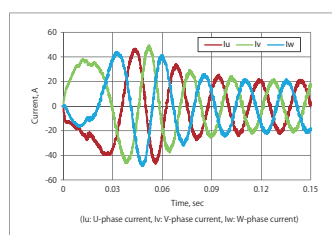


Fig. 2. Armature current waveform

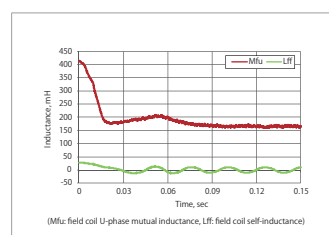


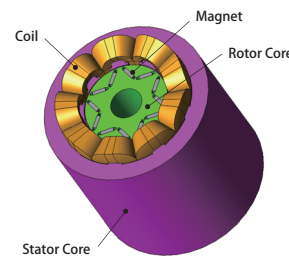
Fig. 5. Inductance waveform

Case 214 Monitoring the Radial Force Acting on the Teeth of IPM Motors Using Circuit Control Simulation

module: DP, RT

Overview

Motors used in electric vehicles are generally quieter than engines, but vibration and noise may be a problem because the drive range is wide. This vibration and noise also occur due to electromagnetic excitation forces and eigenmode resonances of the motor. Among the electromagnetic excitation forces, for the radial force acting on the teeth the second harmonic becomes dominant as the magnet passes by two poles in one electrical angle. On the other hand, it is known that the sixth harmonic can easily excite the zero-order ring mode which is the most likely mode to radiate sound because the excitation force of each tooth has the same phase. Because of this, for countermeasures against vibration and noise, it is useful to grasp the excitation force for each frequency component. In JMAG, it is possible to create motor models that can model actual machines in detail taking into account magnetic saturation characteristics and spatial harmonics in the motor. By capturing this motor model, the JMAG-RT model, in a control/circuit simulator, it is possible to perform coupled simulation taking into account both the magnetic saturation characteristics and spatial harmonics of the motor and the control characteristics of the motor driver. In addition, radial forces acting on the teeth when driving the motor can be monitored providing feedback for motor design and control design. In this example, an IPM motor as a JMAG-RT model is captured in a control/circuit simulator, and radial forces acting on the teeth during motor driving is monitored while changing the operating point (current phase).



Control Circuit

The control circuit uses the current amplitude and current phase command values, and a voltage command value is connected via an inverter to the motor. The control method specification realizes vector control from PI control. Fig. 1 shows the control section of the control circuit, and Fig. 2 shows the circuit section and the motor. The command values are current amplitude 84.8 A, and current phases of 0 deg, 45 deg, and 75 deg. The voltage command values are input to the motor via the inverter.

Current Waveform

Figures 3 to 5 show the current waveform for each current phase when the IPM motor is driven by vector control. By advancing the current phase, the magnetic field is weakened and the magnetic saturation is relaxed. As the magnetic saturation is relaxed and the inductance increases, the harmonic content contained in the current waveform decreases.

Radial Force Waveform Acting on the Teeth

Fig. 6 shows the radial force waveform acting on the teeth for each current phase when the IPM motor is driven by vector control, and Fig. 7 shows the frequency components. In Fig. 6, when a value is negative the radial force is acting in the direction toward the center axis of the motor. As the current phase changes, the positional relation between the stator magnetic poles and the rotor magnetic poles changes and the current waveform changes. This shows that the radial force acting on the teeth also changes. From Fig. 7, it is possible to check the radial force acting on the teeth for each frequency component.

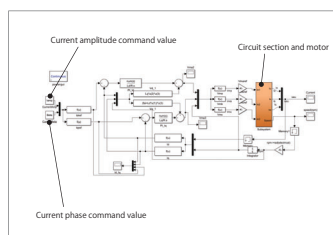


Fig. 1. Control Circuit (Control Section)

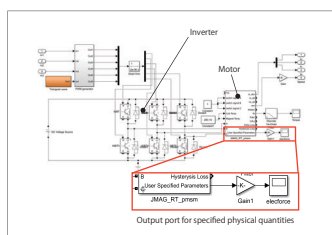


Fig. 2. Control Circuit (Circuit Section and Motor)

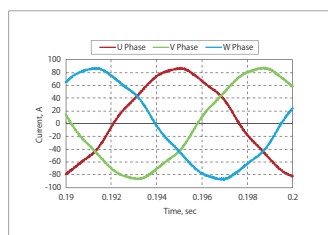


Fig. 5. Current Waveform (Current Phase: 75 deg)

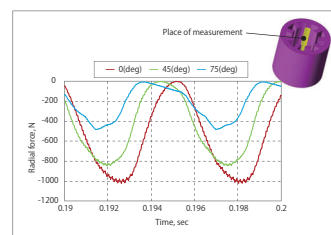


Fig. 6. Radial Force Waveform Acting on the Teeth

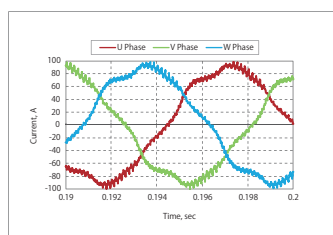


Fig. 3. Current Waveform (Current Phase: 0 deg)

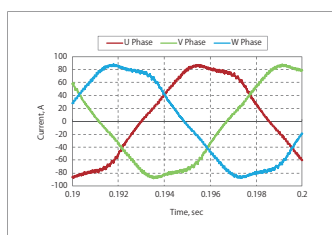


Fig. 4. Current Waveform (Current Phase: 45 deg)

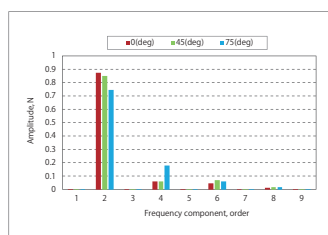


Fig. 7. Frequency Components of the Radial Force Acting on the Teeth

Case 215

Simulation of an IPM Motor with a Delta Connection Using a Control Simulator and JMAG-RT

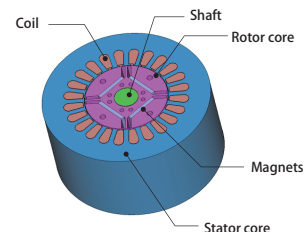
module: DP, RT

Overview

Traditionally, motor control design and design of the motor itself have mostly been performed independently, and cooperative designs have been difficult to carry out. Also, for advanced motor control design, a motor model showing more details and conformity to the behavior of the actual machine is required by control simulation.

In JMAG, it is possible to create a detailed model that conforms to the actual machine as well as account for spatial harmonics and magnetic saturation characteristics that are included in the motor. Importing this JMAG-RT motor model to a control/circuit simulator makes it possible to perform a linked simulation that accounts for a motor's magnetic saturation and spatial harmonics as well as a motor drive's control characteristics. Additionally, if the motor has a delta connection, cyclic currents will flow. This leads to an increase in copper loss and torque ripple, so it is beneficial to monitor cyclic currents while the motor is activated and feed back that information to control design and motor design.

In this example, the control and circuit simulator have been incorporated as a JMAG-RT model, and the cyclic current the IPM motor is monitored.



Control Circuit

The command value is set at 1,800 r/min and the d-axis current is set at 0 A, and the voltage command value is transmitted to the motor via the inverter.

Fig. 1 shows the control circuit, a control unit, and Fig. 2 shows the circuit and motor.

Rotation Speed Waveform, d-Axis Current Waveform

Fig. 3 shows the rotation speed waveform, and Fig. 4 shows the d-axis current waveform. It can be seen that both tend toward their command values.

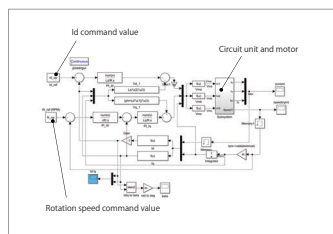


Fig. 1 Control Circuit (Control Unit)

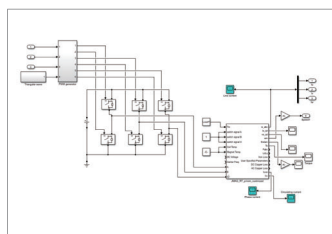


Fig. 2 Circuit and Motor

Current Waveform

Fig. 5 shows the line current waveform at steady-state, Fig. 6 shows the phase current waveform, and Fig. 7 shows the circulating current waveform.

In a motor with a delta connection, the imbalance of the back electromotive forces causes circulating current to flow, which can cause copper loss and torque ripple.

In this example, a circulating current of about half of the line current or phase current flows, and it can be seen that its contribution to loss is large.

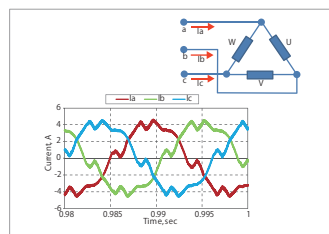


Fig. 5. Line Current Waveform

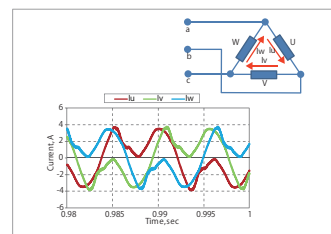


Fig. 6. Phase Current Waveform

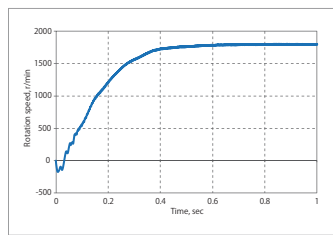


Fig. 3. Rotation Speed Waveform

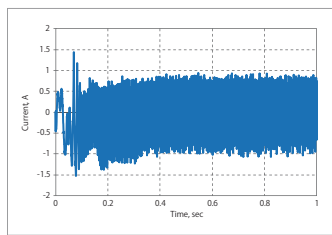


Fig. 4. d-Axis Current Waveform

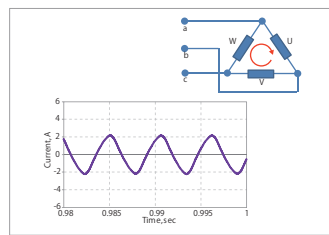


Fig. 7. Circulating Current Waveform

Case 216 Simulation of a Claw-Pole Type Alternator Using a Control Simulator and JMAG-RT

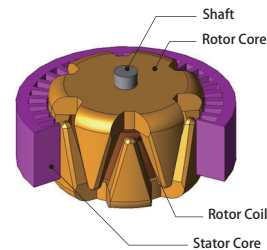
module: RT, TR

Overview

The demand for low fuel consumption of automobiles has been increasing every year, and types of auxiliary systems and devices such as power steering and cooling pumps are being electrified to support this. For this reason, the amount of electricity used has increased every year for general gasoline-powered vehicles, and the demand for higher output power for alternators which supply electricity is increasing. However, since it is not allowable to increase the vehicle size to increase the generating capacity, it is necessary to increase the power density. Furthermore, it is necessary to achieve high efficiency.

The rotation speed of the alternator changes as the vehicle speed changes while driving. But at the same time, the reference voltage of automotive electrical components is set at 12 V. Because of this, it is necessary to monitor the output voltage with a voltage regulator and control the field current considering the engine speed and electric load.

In this example, the output voltage and field current of a claw-pole type alternator is checked when the rotor speed is changed.



Control Circuit

The control circuit is shown in Fig. 1. The command value is set to a voltage of 12 V, and the current controller is connected to the field winding of the alternator. The initial value of the alternator is set at 2400 r/min, and at 0.1 sec later changed to 1800 r/min.

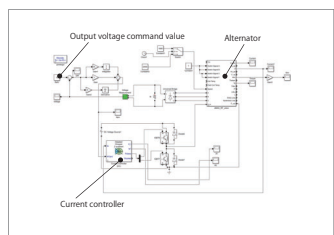


Fig. 1 Control Circuit (Control Section)

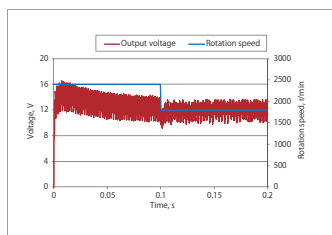


Fig. 2 Rotation speed waveform and Output voltage waveform

Rotation Speed Waveform, Output Voltage Waveform, and Field Current Waveform

Fig. 2 shows the rotation speed waveform and the output voltage waveform, and Fig. 3 shows the rotation speed waveform and the field current waveform.

From Fig. 2, it can be seen that the output voltage is kept at 12 V even if the rotation speed changes. This is because, as shown in Fig. 3, when the rotation speed decreases, increasing the field current increases the flux linkage of the coil and increases the output.

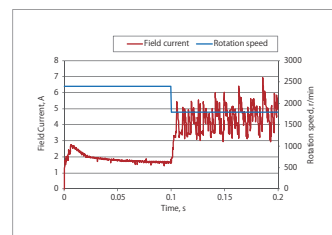


Fig. 3 Rotation speed waveform and Field current waveform

Case 217 Creating Efficiency Maps for 3-Phase Induction Motors

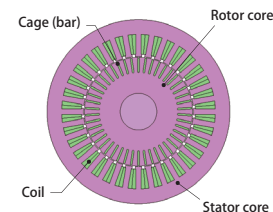
module: FQ, LS, EFFICIENCYMAP

Overview

Due to advances in the variable speed operation technology of induction motors, applications to areas requiring a wide range of operation are progressing. As an effective way to evaluate the characteristics of induction motors in such areas, efficiency maps can be used in the operating region.

To create efficiency maps using actual measurements or computations, it is necessary to search for the highest efficiency point by using voltage and slip as parameters for each rotation speed and load point. Doing this makes the analysis execution enormous, taking time to output the results as well. With JMAG, efficiency maps can easily be obtained by creating a JMAG-RT model which is a plant model and using the efficiency map creation function in JMAG-RT Viewer.

In this example, JMAG-RT Viewer is used to create efficiency maps of a 3-phase induction motor when the driving temperature has been changed.



Efficiency Map

Fig. 1 and Fig. 2 show the efficiency maps when the drive temperature is changed to 20 deg C and to 120 deg C respectively. From the figures, the efficiency for each drive condition can be understood. Also, as the temperature rises, it can be seen that the efficiency becomes worse.

Loss Map

The stator copper loss map for when the drive temperature is changed to 20 deg C and to 120 deg C is shown in Fig. 3 and Fig. 4 respectively, and the rotor copper loss map is shown in Fig. 5 and in Fig. 6.

When the temperature is high, it can be seen that the copper loss on the primary side and the secondary side is large. This is because the electrical characteristics of the primary coils and the secondary conductors deteriorate and the electrical resistances increase, which leads to a decrease in efficiency.

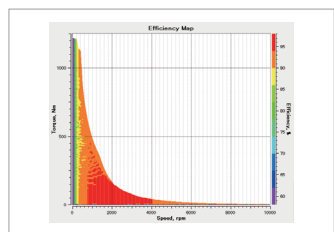


Fig. 1. Efficiency Map (20 deg C)

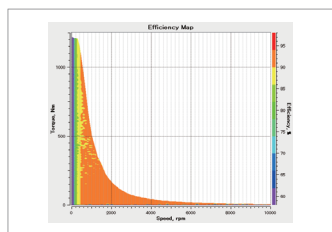


Fig. 2. Efficiency Map (120 deg C)

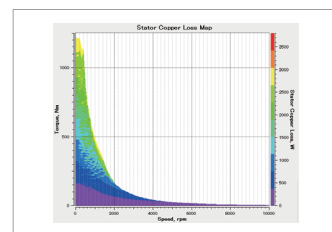


Fig. 3. Stator Copper Loss Map (20 deg C)

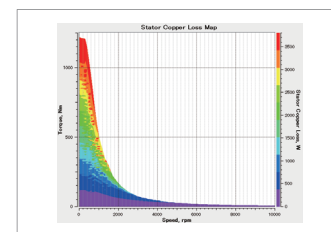


Fig. 4. Stator Copper Loss Map (120 deg C)

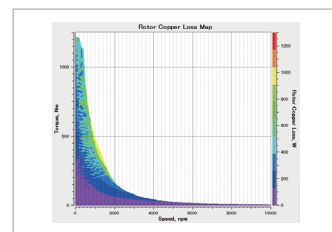


Fig. 5. Rotor Copper Loss Map (20 deg C)

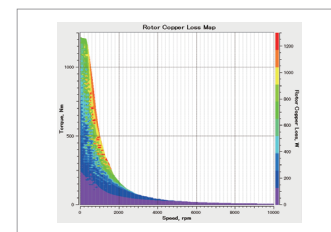


Fig. 6. Rotor Copper Loss Map (120 deg C)

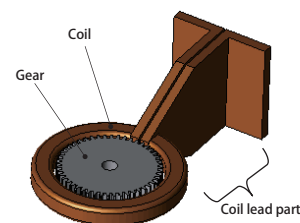
Overview

Gear surfaces are generally hardened to ensure abrasion resistance of the tooth surfaces, but it is necessary to harden the surfaces while maintaining the overall toughness of the gear. For high-frequency induction heating, which is one of the surface hardening methods, it is possible to harden only the tooth surfaces by rapidly heating only these surfaces using a high-frequency power supply.

On the other hand, in order to uniformly heat the surfaces of the gear, it is necessary to consider several factors such as how to adjust the geometry, arrangement, frequency, and size of the heating coil.

Eddy currents generated by high-frequency varying magnetic fields are generated near the surface of the teeth. As temperature rises material characteristics change drastically, and the object heated is thermally deformed by thermal stress. It is necessary to compute heat generation amounts and deformation amounts in numerical analysis using finite element methods (FEMs).

In this example, using the JMAG magnetic field - thermal stress coupled analysis function, analysis is performed evaluating gear deformation from induction heat hardening.



Eddy Current Loss

A high-frequency (30 kHz) current flows in the coil causing a magnetic field fluctuation which induces induced current in the gear. Due to the skin effect, current concentrates on the tooth tips of the gear.

Skin thickness can be calculated by the equation shown in Fig. 1.

From magnetic field analysis, induced current in the model can be checked. The loss due to the induced current is used as a heat source for thermal stress analysis. The temperature distribution in and on the gear and deformation of the gear obtained from thermal stress analysis are input as conditions in magnetic field analysis.

Fig. 2 shows the eddy current loss density distribution on a cut surface of a gear tooth tip.

$$\delta = \frac{1}{\sqrt{\pi f \mu \sigma}}$$

δ : skin depth, m
 f : frequency, Hz
 μ : magnetic permeability, H/m
 σ : electrical conductivity, S/m

Fig. 1. Equation of the Skin Depth

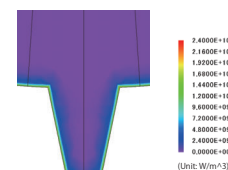


Fig. 2. Eddy Current Loss Density Distribution over 0 to 0.2 sec

Temperature Distribution

Loss due to induced current acts as a heat source increasing temperature. In thermal stress analysis, the loss obtained from magnetic field analysis is set as an input condition. Since losses concentrate primarily on the tooth tips which are outside the model, this region naturally becomes the region of maximum temperature change. Material magnetization characteristics and temperature characteristics of electrical characteristics are taken into account using an obtained temperature distribution as an input condition for magnetic field analysis.

Fig. 3 shows the temperature distribution on the gear, and Fig. 4 shows the temperature vs. time of a tooth tip. Fig. 4 shows the change in temperature at the tooth width center shown in Fig. 3.

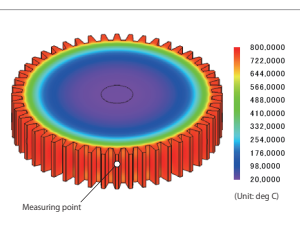


Fig. 3. Gear Temperature Distribution

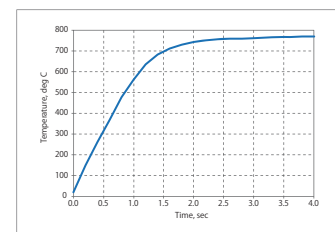


Fig. 4. Tooth Tip Temperature vs. Time

Thermal Stress (Deformation)

The deformation of and temperature distribution on the gear at a 4 sec are shown in Fig. 5, and the deformation of the gear is shown in Fig. 6. The thermal expansion deformation of the model is confirmed at 100 times magnification.

As the gear temperature changes, deformation occurs due to thermal expansion and thermal contraction. During this time, thermal stress is produced due to for example constraints and an uneven temperature distribution. From the figure, it can be seen that the areas of highest temperature expand the most. After heating for 4 sec, the tips are deformed to a maximum of 0.18 mm. Furthermore, the gear is drawn toward the ground by gravity. The influence of gravity on the deformation can also be confirmed.

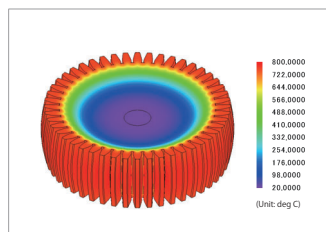


Fig. 5. Gear Temperature Distribution

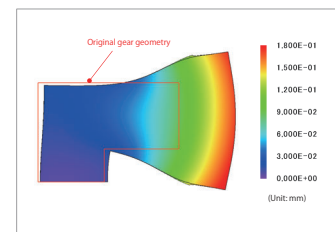


Fig. 6. Gear Deformation

Case 219

Axial Gap Type Motor Cogging Torque Analysis

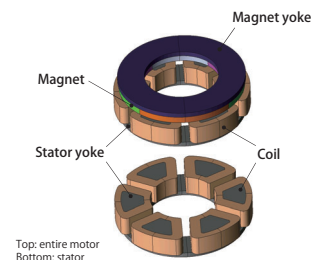
module: TR

Overview

An axial gap motor has a motor structure in which the rotor and stator are arranged in a disk shape facing each other and rotate using magnetic flux in the axial direction. The advantages of this motor are that this motor can be made thinner than a radial gap motor, and that higher torque can be obtained for a given magnetic flux density if properly designed. This motor has been developed for a variety of uses including automobiles, and can respond to market demands with its unique design.

In an axial gap motor, 3D electromagnetic field simulation is necessary because the magnetic flux passing through the facing rotor and stator is a 3D magnetic circuit.

In this example, presents an example of cogging torque analysis of an axial gap type motor.



Cogging Torque Waveform

A cogging torque waveform is shown in Fig. 1.

This result shows that the amplitude is approximately 0.044 Nm. The cogging torque period is determined by the number of slots and the number of poles. Since this analysis target has 8 poles and 6 slots, the cogging torque period is 15 deg obtained by dividing 360 by 24, the least common multiple of 6 and 8. The torque waveform result is periodic and has a period of 15 deg as well, and since the coils are not excited the torque waveform has half-wave symmetry.

Magnetic Flux Density Distribution

Fig. 2 shows the magnetic flux density distribution for a rotation angle of 0 deg and for 3.75 deg.

The symmetry of the magnetic flux density distribution seen at the rotation angle of 0 deg is not seen at the rotation angle of 3.75 deg. Cogging torque is generated by this phenomenon.

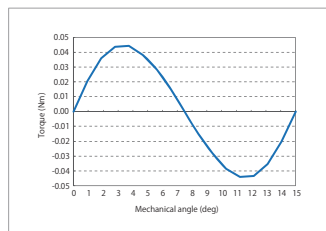


Fig. 1. Cogging Torque Waveform

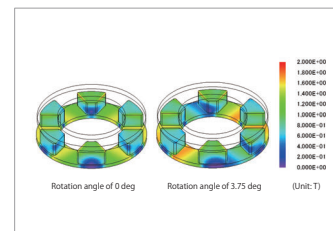


Fig. 2. Magnetic Flux Density Distribution

Case 220

Analysis of the High-Frequency Induction Hardening and Cooling of a Gear

module: FQ, HT

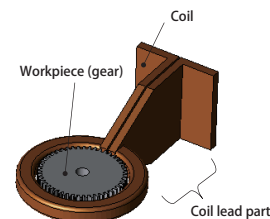
Overview

In order to ensure the abrasion resistance of teeth surfaces where teeth are in contact with each other, a gear must maintain the toughness of each entire tooth while increasing the hardness of the surface, necessitating making the teeth with tenacity. Inductive hardening, which is one of a number of surface hardening methods, can locally and rapidly heat and harden just the teeth surfaces.

In the induction hardening heating process, it is required to uniformly heat the surface of the gear. Also, to suppress oxidation, decarbonization, and deformation in the cooling process, it is necessary to complete the cooling in a short time. Therefore, the cooling rate is an important factor affecting the mechanical properties of the gear heated.

In order to accurately obtain the temperature change in the gear from induction heating analysis, it is necessary to not only accurately express the heat generated in the gear by electromagnetic induction, but also to obtain temperature distributions taking into account the change in temperature and physical characteristics due to heat generation. Because of this, electromagnetic field analysis - thermal analysis two-way coupled analysis is essential.

In this example, deals with induction heating and cooling analysis. An example is presented where the cooling rate for a gear differs depending on the cooling conditions.



Temperature Distribution of the Gear and the Change in Temperature vs. Time

The temperature distribution of the gear at the end of the heating process is shown in Fig. 1, and the change in temperature vs. time at the tooth tip is shown in Fig. 2. From the temperature distribution, it can be seen that the tooth tip is generating heat due to eddy currents. Fig 2 shows the change in temperature at the tooth tip width center (point of measurement). It can be seen that water cooling is faster than air cooling so the effect from water cooling is higher.

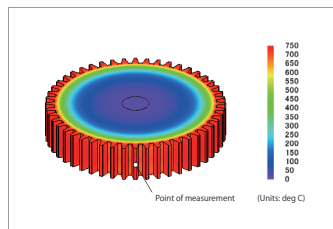


Fig. 1. Temperature Distribution After 4.0 Sec

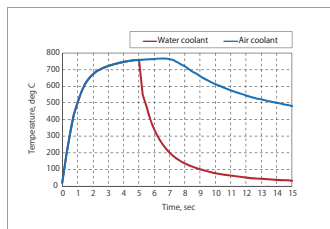


Fig. 2. Temperature vs. Time at Tooth Tip

Change Among the Gear Temperature Distributions in the Cooling Process

Fig. 3 shows the temperature distribution at various times in the cooling process. It can be seen that in the vicinity of the teeth tips significant cooling can be achieved with water cooling in a short time.

In addition, when comparing the temperature distribution between water cooling and air cooling, it can be seen that with water cooling the cooling of the teeth tips proceeds more quickly than the more interior portion of the gear. This is thought to be because the heat dissipation from the teeth tips in contact with the cooling water proceeds faster than the heat conduction interior to the gear.

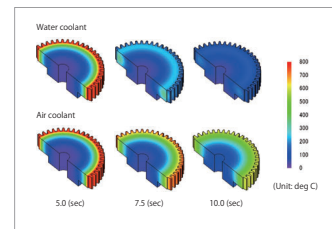


Fig. 3. Changes Among Temperature Distributions vs. Time

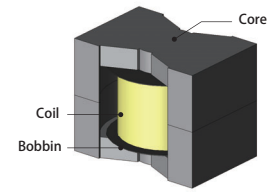
Confirmation of the Influence from the Reduction of High-Frequency Resistance of a Magnetically Plated Wire Choke Coil

module: TS, FQ

Overview

A choke coil is an electronic component aimed at filtering high frequency current. The current generated inside a choke coil has a distribution in a single wire, and among the wires, due to current bias from the skin effect, proximity effect, and leakage flux near the gap. By using a magnetically plated copper wire with a ferromagnetic thin film layer for the coil wire, high frequency loss can be reduced compared to conventional polyurethane copper wire. This is due to the proximity effect generated in the coil being reduced by the magnetic plating layer, and due to the effective resistance of the conductor being lowered.

In this example, high frequency resistance values are obtained from choke coil copper loss analysis results using JMAG's layer coating mesh function, and the effectiveness of reducing the resistance value of the coil using magnetically plated wire is confirmed.



Specification of Copper Wire

Fig. 1 shows the specification of copper wire used in this case study.

Comparisons of AC Resistance Value Frequency Characteristics

In fig. 2, the frequency resistance values from the Joule loss values of the coil when polyurethane copper wire and when magnetically plated wire are used are calculated, and the frequency resistance values at each frequency are compared.

From fig. 2, it can be seen that when using magnetically plated wire, the AC resistance is lower than when polyurethane copper wire is used.

Comparison of Copper Loss Density Distributions

Fig. 3 show the Joule loss density distribution and isolines for polyurethane copper wire and magnetically plated wire at a frequency of 75 kHz.

From fig. 3, it can be seen that joule loss when using magnetically plated wire is lower than when using polyurethane copper wire.

This shows that there is an influence from the proximity effect of coil wire being reduced when magnetically plated wire is used.

Comparison of Magnetic Flux Density Distributions

Fig. 4 shows the magnetic flux density distributions in coil wires near the gap when using polyurethane copper wire and magnetically plated wire.

The figure shows that the magnetic flux density in the copper wire when using magnetically plated wire is smaller than when using polyurethane copper wire.

As shown in the figure, when magnetically plated wire is used, the number of isolines in the copper wire is large indicating that the magnetic flux concentrates on the copper wire surface, and the difference in the magnetic flux density between the copper wire interior and surface is higher than that for polyurethane copper wire.

Since a magnetic circuit is formed around the copper wire in the magnetic layer when a magnetically plated wire is used, and since the magnetic flux generated by the proximity effect in the wire interior is lower, it is seen that this is effective in reducing current bias.

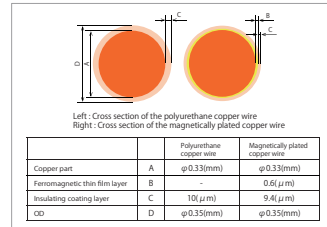


Fig. 1 Specification of Copper Wire

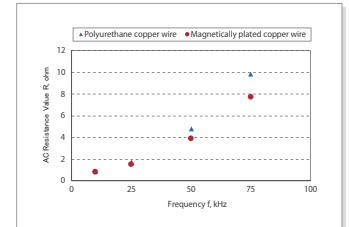


Fig. 2 Comparisons of AC Resistance Value Frequency Characteristics

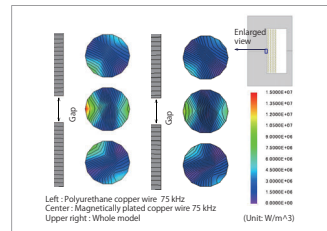


Fig. 3 Comparison of Copper Loss Density Distributions (Copper wire expansion near the gap)

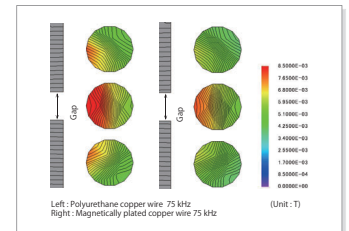


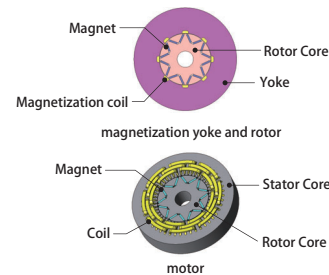
Fig. 4 Comparison of Magnetic Flux Density Distributions (Copper wire expansion near the gap)

Case 222 Irreversible Thermal Demagnetization Analysis of Incompletely Magnetized Magnets

module: DP, ST

Overview

It is important to solve the problem of temperature rise in order to achieve high motor efficiency and high output. Magnets are used in motors and display large variation in their properties verse temperature. For rare earth magnets at temperatures over hundred degrees demagnetization can occur. Since the presence or absence and degree of demagnetization are determined by a combination of the demagnetizing field and the temperature applied, it is necessary to pay attention to magnetic circuit design in addition to the heat resistance of magnets themselves. In particular, since it is easier for demagnetization to occur at locations where the coercive force is not sufficient due to incomplete magnetization, it is desirable to at the same time evaluate the coercive force distribution of magnets. Using magnetic field analysis simulation that uses finite element method analysis, it is possible to evaluate motor characteristics at high temperatures and high loads by taking into account the thermal demagnetization characteristics verse coercive force distribution values obtained from magnetization analysis. In this example, analysis is performed while varying the temperature of magnetized magnets, and then the influence on the torque waveform and magnetic flux density distribution is evaluated.



Magnetizable Material with Thermal Demagnetization Information

Since demagnetization characteristics after magnetization also depend on temperature, a characteristic table was prepared verse several different temperatures where the temperature is for after magnetization from an magnetizing magnetic field. This table was created for magnetizing magnetic field, temperature, and demagnetization characteristics (Fig. 1).

When used as magnet material after magnetization, a table of temperature - demagnetization characteristics verse magnetizing magnetic field at the time of magnetization is referenced. Since the magnetizing magnetic field is not uniform inside the magnet, the demagnetization characteristics vary in the magnet.

Magnetic Field Distribution After Magnetization

Fig. 2 shows the magnetic field distribution of two magnets magnetized in place (in the rotor core) at input currents of 25 kA, 35 kA, and 45 kA. As the input current becomes larger the portion of the magnets near the bridge, which is least magnetized, becomes more magnetized. Where magnetization is low the magnetization is insufficient.

Induced Voltage Waveform

Fig. 3 shows the U-phase induced voltage waveform when the magnets are magnetized in place with an input current of 25 kA, 35 kA, and 45 kA. The rms value of the induced voltage over this time is shown in Table 1. From an evaluation of only the induced voltages it can be confirmed that there is a difference of about 5 % between the 25 kA case and the other cases.

Change in Torque Due to Thermal Demagnetization

Using magnetized magnets in place for input currents of 25 kA, 35 kA, and 45 kA the torque waveforms are shown in Fig. 4 for when the magnet temperature changes from 60 to 125 deg C at the first 1/2 electrical angle period (mechanical angle of 45 deg) and from 125 to 60 deg C at the second 1/2 electrical angle period.

From Fig. 4, it can be seen that the average torque decreases due to thermal demagnetization when the magnets are heated to 125 deg C. In addition, even if returned to 60 deg C, since the average torque decreases by 3 to 11 % compared to with before the temperature increase, it can be seen that irreversible demagnetization occurred during the temperature rise. Furthermore, it can be confirmed that the degree of deterioration of torque characteristics due to demagnetization is dependent on the input current during magnetization.

Demagnetization Ratio Distribution

Fig. 5 shows the demagnetization ratio distribution when the temperature is returned to 60 deg C referenced to the magnetization state before the temperature rise. The demagnetization shown here is irreversible demagnetization caused by exceeding the knee point, which is an indicator of the deterioration of the magnet characteristics. From the figure, even if returned to 60 deg C, significant demagnetization appears over a wider region than before the temperature rise. Moreover, when the input current during magnetization is small, it can be confirmed that large demagnetization occurs near the bridge.

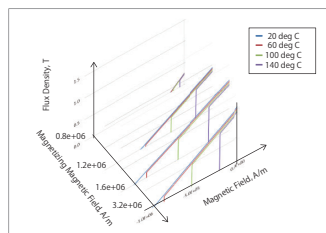


Fig. 1. Magnetizing magnetic field - temperature - demagnetization characteristics

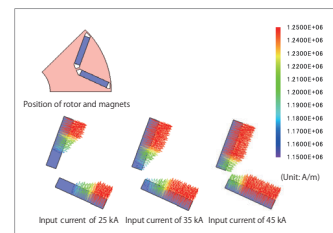


Fig. 2. Magnetization distribution after magnetization

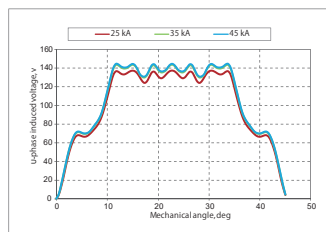


Fig. 3. Induced voltage

Item	Specification		
Induced voltage-rms value, V	25	35	45
Magnetization current, kA	108.3	113.2	114.2

Table 1. Applied current during and induced voltage rms values over the magnetization period

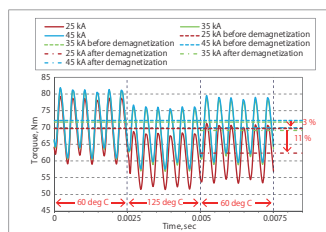


Fig. 4. Torque waveform

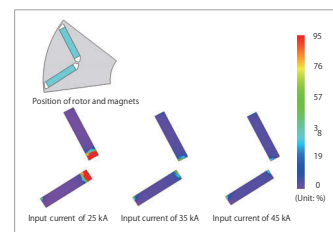
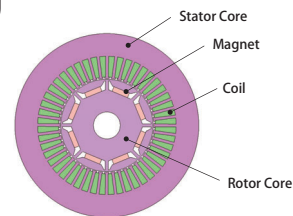


Fig. 5. Demagnetization ratio distribution

Multi-Objective Optimization of an IPM Motor Accounting for Stress at High-Speed Rotation

module: DP, DS



Overview

As so to prevent mechanical issues from occurring during high-speed rotation for IPM motors, it is necessary to realize highly accurate designs accounting for the trade-off between torque and the stress that generates from centrifugal force at high-speed rotations. The phase at which maximum torque can be obtained will also change alongside changes to geometry, and it is necessary that optimization calculations account for this. FEA is essential for accuracy in these circumstances, and the use of genetic algorithms is recommended as a tool for handling the issues in this trade-off relationship.

In this example, the optimum current phase that achieves high torque per each geometry is obtained, and the torque characteristics (1,000 r/min) and stress due to centrifugal force at high-speed rotation (10,000 r/min) obtained with that optimum phase are both taken as objective functions for a multi-objective genetic algorithm used to carry out the optimization of rotor geometry.

Optimization Conditions

Design variables in Fig. 1 are displayed in Table 1. 6 rotor shape design variables are selected. Magnet positions, magnet geometry, and flux barrier geometry that are considered to have a large influence on von Mises stress and torque are parameterized. This time obtains geometry with high torque at 1,000 r/min and low von Mises stress within the rotor during rotations at 10,000 r/min. In accordance with this, 2 evaluation items shown in Table 1 are used and the performance of rotor geometry is evaluated.

Optimization Results

Fig. 2 shows the result of multi-objective optimization using genetic algorithms with the maximum value of von Mises stress and average torque objective functions. Performance improvements can be confirmed from a comparison of all individuals from the initial and 10th generations. It can also be observed that von Mises stress and torque are in a trade-off relationship in the 10th generation.

The case with the lowest von Mises stress (1) and the case with the highest average torque (2) in the initial generation are emphasized. Cases A and B are 10th generation cases with the maximum average torque for approximately the same maximum von Mises stress as cases (1) and (2) respectively, and are shown in Table 2. While each have approximately the same maximum von Mises stress, it can be confirmed that average torque improves between (1) and A by 93 %, and by 16 % between (2) and B.

Selecting Rotor Phase

Fig. 3 shows a graph of the phase of each geography and torque. From the maximum phase geometry obtained from the torque formula, it is understood that the phase showing maximum torque differs. The phase showing the maximum torque value is shown in red.

Rotor Interior Magnetic Flux Flow

The magnetic flux density distribution and magnetic flux lines of each geometry are shown in Fig. 4. For thick-bridge geometry (A), it is thought that the magnetic flux flows through the bridge to the adjacent magnetic pole, causing a decrease in torque. Conversely, for thin-slit geometry (B), a high torque value is obtained because the short-circuited rotor interior magnetic flux is suppressed and flows to the stator.

Rotor Interior Magnetic Flux Flow

The magnetic flux density distribution and magnetic flux lines of each geometry are shown in Fig. 4. For thick-bridge geometry (A), it is thought that the magnetic flux flows through the bridge to the adjacent magnetic pole, causing a decrease in torque. Conversely, for thin-slit geometry (B), a high torque value is obtained because the short-circuited rotor interior magnetic flux is suppressed and flows to the stator.

Von Mises Stress Distribution

The von Mises stress distribution of geometry A and B shown in Fig. 5. It can be confirmed that for thin-bridge geometry (B), there is a tendency for stress to be higher at those locations, while von Mises stress remains low for thick-bridge geometry (A). From this it can be observed that maintaining bridge thickness is effective in controlling von Mises stress.

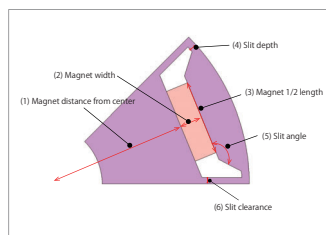


Fig. 1 Optimization Design Parameters

Design variable range		
Item	Minimum value	Maximum value
(1) Magnet distance from center, mm	26	36.6
(2) Magnet width, mm	2	5.49
(3) Magnet length, mm	3	9.15
(4) Slit depth, mm	0.1	1.83
(5) Slit angle, deg	45	140
(6) Slit clearance, mm	0.1	1.6

Evaluation Items	
Evaluation Items (Objective Functions)	Description
Torque average value	Torque characteristics are evaluated using average torque values.
Von Mises stress maximum value	It is considered that the lower the von Mises stress maximum value is in the model, the less likely breakage will occur. The von Mises stress maximum value in the model is used for evaluations.

Table 1. Design Variable Ranges, Evaluation Items

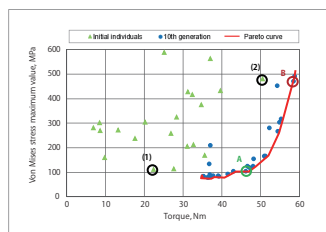


Fig. 2. Initial Generation and 10th Generation Population Performance

Item	Speed 10,000 r/min Von Mises stress maximum value, MPa	Low speed 1,000 r/min Average torque, N·m
Initial individuals (1) (low stress)	110.5	22.3
Initial individuals (2) (high torque)	479.0	50.5
10th generation A	105.0	43.0
10th generation B	470.6	58.5

Table 2. Comparison of Performance of Individuals

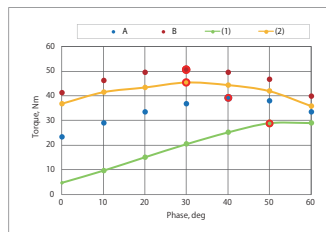


Fig. 3 Mises Stress Distributions for 10th Generation Individuals

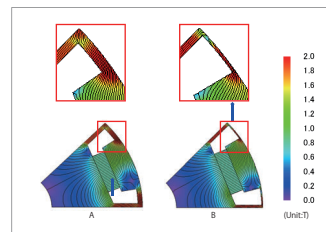


Fig. 4. 10th Generation Rotor Geometry and Magnetic Flux Density Distribution

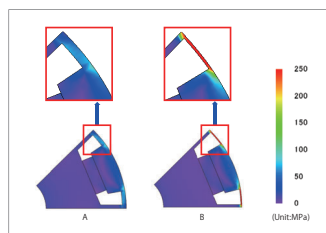


Fig. 5. The Von Mises Stress Distribution of 10th Generation Individuals

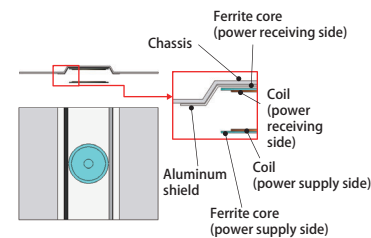
Case 224 Wireless Power Transfer Device Stray Loss Analysis

module: FQ

Overview

In recent years, using electromagnetic induction type power supply systems for wireless power transfer systems for electric vehicles (hereinafter referred to as EVs) and plug-in hybrid cars (hereinafter referred to as PHEVs), for which practical applications are sought, have been investigated. Wireless power transfer systems for EVs and PHEVs are required to maintain power transmission with high efficiency. Many studies on magnetic resonance coupling (magnetic resonance) schemes with resonance capacitors have been performed. Considering corrosion resistance and strength, steel plates such as SUS steel plates are used for the casings of wireless power transfer equipment. Because of this, if the leakage magnetic flux component generated from the power supply device interlinks with the metal casing, stray loss occurs resulting in a decrease in efficiency. Therefore, when the loss component is high, it is necessary to suppress the loss by providing for example an aluminum shield.

Since in order to accurately calculate stray loss it is necessary to accurately calculate the flow of magnetic flux interlinking with steel plates or aluminum shields and the eddy current distribution caused thereby, electromagnetic field analysis using finite element methods is necessary. In this example, an example is presented investigating by using electromagnetic field analysis whether stray loss can be suppressed using an aluminum shield.



Stray Loss Distribution

Fig. 1 shows the Joule loss distributions of the chassis and aluminum shield. Regardless of the presence or absence of the aluminum shield, it can be seen that Joule loss due to leakage flux is generated around the ferrite cores. After installing an aluminum shield on the surface of the chassis, it is possible to confirm that almost no loss is generated in the chassis due to this shielding with loss occurring only on the aluminum shield surface. In addition, it can be confirmed that there are places with higher Joule loss density with the aluminum shield installed as compared to before the aluminum shield was installed.

Difference in Stray Loss With and Without an Aluminum Shield

Table 1 shows Joule loss values due to eddy currents. It can be confirmed that the stray loss could be reduced when an aluminum shield was installed even though the Joule loss density on the surface was higher. This is because the skin thickness decreased and the volume where the loss occurred decreased since aluminum was used which has higher conductivity than the SUS material used for the chassis.

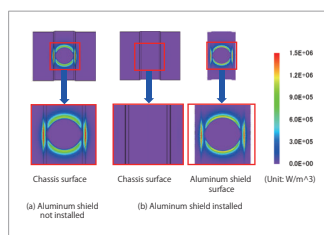


Fig. 1. Joule Loss Density Distribution

	Stray loss, W		
	Chassis	Aluminum shield	Total
Aluminum shield not installed	77.7	-	77.7
Aluminum shield installed	0.5	15.5	16.0

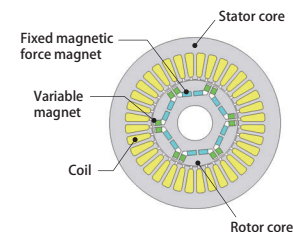
Table 1. Comparison of Joule Loss Values

Case 225 Induced Voltage Analysis on Memory Motors Using Variable Magnets

module: ST, DP

Overview

There are many kinds of variable flux motors, but the kind that makes a permanent magnet magnetization variable is called a memory motor. The magnetic field for magnetizing and demagnetizing memory motor magnets is generated by the same three-phase coil current as in the drive system, so the magnetic force can be changed without adding any special devices. In this example, the change in motor characteristics are checked as the memory motor variable magnet magnetization is changed using the three-phase coil current. One example of modeling using a variable magnet user subroutine is presented as well.



Alteration of Variable Magnetized Magnet Induced Voltage

Fig. 1 shows the induced voltage when the variable magnets are fully magnetized, then demagnetized, and then magnetized again. In Table 1, the induced voltage state for each interval in Fig. 1 is shown as well. In interval (3) in Fig. 1, from demagnetizing the variable magnets, only the induced voltage due to the fixed flux magnets can be seen. The maximum change of induced voltage from this model is approximately 50%.

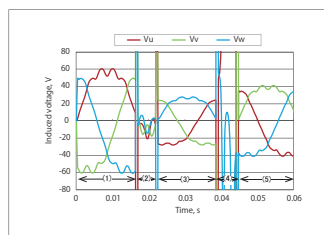


Fig. 1. Change in Variable Magnet Magnetization State and Induced Voltage

Interval	KI (A)	Current state	Variable magnet magnetization state
(1)	0	No-load	Magnetization
(2)	-10	Demagnetizing current applied	Demagnetization
(3)	0	No-load	Demagnetization
(4)	+200	Magnetizing current applied	Magnetization
(5)	0	No-load	Magnetization

Table 1. Induced Voltage State

Flux Line Changes Under No-load

Fig. 2 shows the flux lines at no-load when the variable magnets are magnetized and demagnetized. The left is when magnetized and the right is when demagnetized. When the variable magnets are demagnetized, it can be seen that the magnetic flux from the magnets flowing in the stator is decreased. Also, from the enlarged views of two variable magnets it can be seen that in the left view for the magnetization state several flux lines penetrate the variable magnets passing from one magnet core to the other and returning back again. On the other hand in the right view for the demagnetization state, the flux lines do not penetrate the variable magnets, and it can be seen that the flux lines generated from the fixed magnetic force magnets flow around the variable magnets. This means that a stronger magnetic flux is generated from the fixed magnetic force magnets than from the variable magnets.

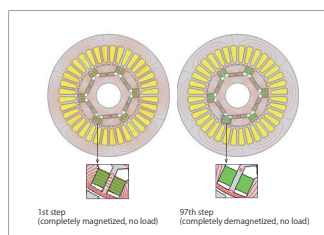


Fig. 2. Flux Lines at No-load

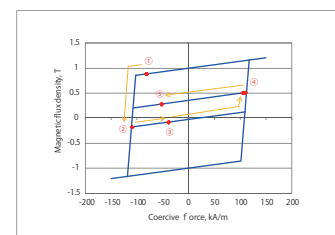


Fig. 3. Variable Magnet Operating Points

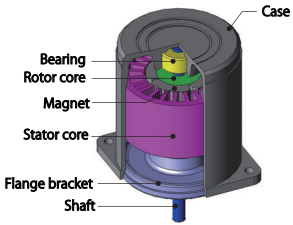
Variable Magnet Operating Points

The variable magnet operating points are shown in Fig. 3. While changing the input magnetization characteristics, it can be seen that the residual magnetic flux density Br changes when a magnetization/demagnetization current is applied.

Overview

Electromagnetic force acting on a motor causes vibration and noise in the form of electromagnetic excitation force. Vibration and noise also are produced when this electromagnetic excitation force resonates with an eigenmode of the motor. In order to accurately evaluate this phenomenon, it is necessary to ascertain each frequency and spatial mode in detail about the electromagnetic force and eigenmodes of the motor.

In this example, the acceleration is evaluated by obtaining the electromagnetic force generated in the stator core of the SPM motor at multiple rotation speeds and coupling with the eigenmodes of the motor. In addition, the frequency components of the electromagnetic force and eigenmodes and the spatial modes are analyzed, and the resonance modes are confirmed.



Eigenmodes

Notice the spatial 4th-order mode is focused on. From the eigenmode analysis results, the eigenfrequency for each vibration mode is found. The spatial 4th-order mode results are shown in Fig. 1 and Table 1.

Rotation Speed, Frequency, and Acceleration Graphs

Coupled analysis of magnetic field transient response analysis and structural frequency response analysis is performed to evaluate the acceleration of the vibration excited by the electromagnetic force generated in the stator.

Fig. 2 shows a radar graph of the cylindrical coordinate system R component of the acceleration at a measurement position with a phase of 0 deg. As a measurement example, the graph shows the acceleration computed from the electromagnetic force 2nd-order component. Also, the amplitude of the acceleration is plotted on graphs with axes of rotation speed and frequency shown in Fig. 3 and Fig. 4.

Among the plotted accelerations, some particularly large values can be seen. The electromagnetic forces which are the excitation forces of these vibrations are 22nd-, 26th-, and 34th-order, and the acceleration increases because the rotation speed rises and the electromagnetic force 22nd-, 26th-, and 34th-order frequencies become close to the 4th-order mode eigenfrequency. This is due to specific frequency components of electromagnetic force strongly resonating with certain eigenmodes.

The 22nd-, 26th-, and 34th-order vibration modes at 12 kHz are shown in Fig. 5. All the spatial 4th-order vibration modes are shown.

For the 22nd, 26th, and 34th-order components of the electromagnetic force, when the cylindrical coordinate R component at phase 0 deg is shown in a radar graph similar to the acceleration radar graph above, it can be seen that there is a strong correlation between the acceleration and the electromagnetic force (Fig. 6). On the other hand, there are frequency components close to the spatial 4th-order mode eigenfrequency, but it can be seen that for small order vibrations there are different spatial modes as shown in Fig. 7.

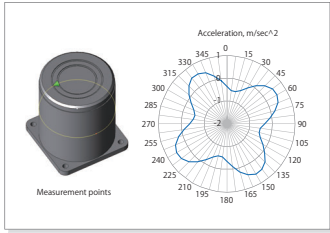


Fig. 3. Amplitude of Acceleration of Vibration Due to Excitation from Electromagnetic Force

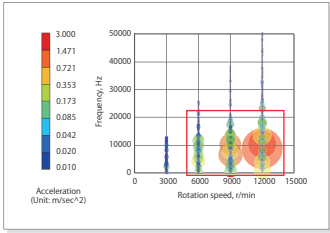


Fig. 3. Amplitude of Acceleration of Vibration Due to Excitation from Electromagnetic Force

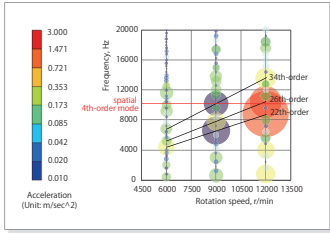


Fig. 4. Eigenmodes Dependent on Electromagnetic Force Order and Number of Poles

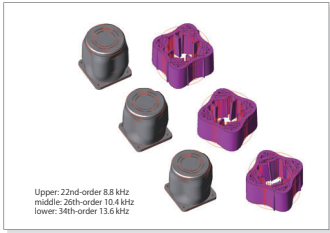


Fig. 5. Resonance Vibration Modes at 12,000 r/min

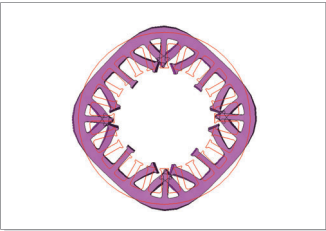


Fig. 1. Spatial 4th-order Mode Eigenmodes

Eigenmode	Orders	Eigenfrequency
spatial 4th-order	42, 43	10.8 kHz

Table 1. Eigenfrequencies

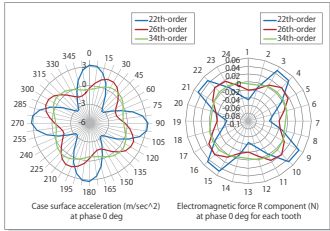


Fig. 6. Spatial 4th-Order Mode Vibration and Electromagnetic Force

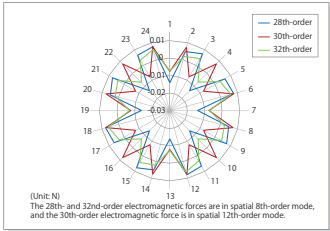


Fig. 7. Spatial Non-4th-Order Electromagnetic Force

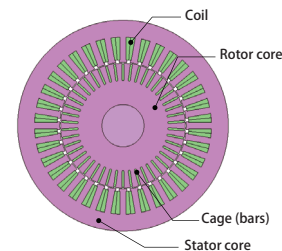
Case 227 Circuit Control Simulation for Three-Phase Induction Motor

module: FQ, RT

Overview

Since control design and motor design are designed by different designers, coordination of the designs is difficult. However, in order to realize the sophisticated demands of recent years, it is important to identify problems during the coordination between motor design and control/circuit design in the early stages of development. In cooperative design, it is possible to utilize circuit simulation using a highly accurate plant model.

Characteristics of the induction motor depend on motor shapes, materials, and drive states. For example, it is necessary to calculate the resistance of the secondary side by taking into account the current distribution in the secondary conductor, but the phenomenon is complicated and it is difficult to calculate manually. JMAG-RT can create a highly accurate plant model (JMAG-RT model) by calculating the FEA while taking the motor shape, material, and driving condition into account, then extracting the characteristics of an induction motor. In this example, we conduct a circuit simulation to control current and speed by incorporating the JMAG-RT model of an induction motor into the control/circuit simulator.



Control Circuit

The control circuit is shown in Fig. 1. The command values are 2,000 r/min for rotation speed and 30 A for the d-axis current, and the voltage command value is connected to the motor via the inverter.

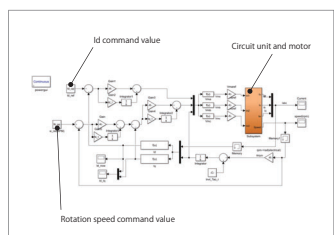


Fig. 1 Control Circuit (Control Unit)

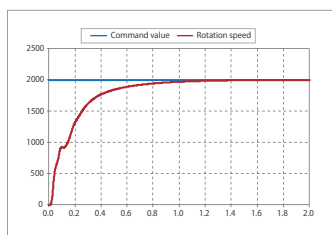


Fig. 2. Rotation Speed Waveform

Rotation Speed Waveform and d-Axis Current Waveform

Fig. 2 shows the rotation speed waveform and Fig. 3 shows the d-axis current waveform. It can be seen that both become steady at their command values.

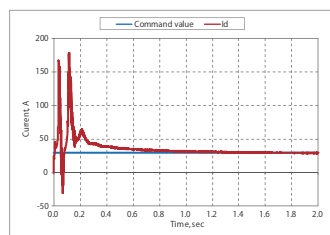


Fig. 3. d-Axis Current Waveform

Case 228 Induction Motor Thermal Analysis

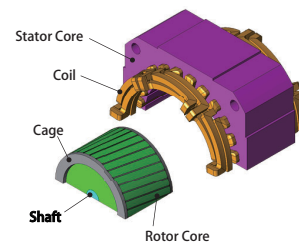
module: HT, LS, TR

Overview

Induction motors can be found in a wide number of uses, from industrial machines to home appliances, as they are simple construction in addition to being small, light, affordable, and maintenance-free. An induction motor is a motor in which a rotating magnetic field in the stator winding causes an induced current to flow in an auxiliary conductor. This current and magnetic field exert force on the auxiliary conductor in the rotation direction and cause the motor's rotor to rotate. When this occurs, a large amount of joule heat is generated in the motor due to the influence of induced currents.

In order to correctly evaluate increases in temperature induction motor joule loss and iron loss, the use of coupled analyses is advantageous as so to obtain temperature distribution from thermal analyses using iron loss density distribution obtained from magnetic field analysis. This makes it possible to confirm overall temperature distribution and locations where temperatures grow particularly high.

In this example, evaluating induction motor temperature distribution.



Loss Density Distribution

The joule loss density of the cage and windings is displayed in Fig. 1 and Fig. 2 respectively. A large portion of joule loss is distributed in the end ring.

Iron loss analysis results for the stator and rotor are displayed in Fig. 3 and Fig. 4.

Temperature Distribution

Stator temperature distribution is displayed in Fig. 5, and rotor temperature distribution is displayed in Fig. 6.

For the stator, each part is a heat source, and it is understood that temperatures rise until approximately 63 deg C. On the other hand, the main source of rotor heat is the cage, and it can be confirmed that heat is transferred to the rotor core. Because it is additionally difficult to emit the heat trapped within the stator, this becomes a high temperature of 156 deg C or above.

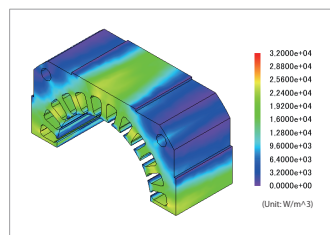


Fig. 3. Stator Iron Loss

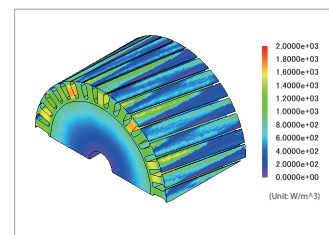


Fig. 4. Rotor Iron Loss

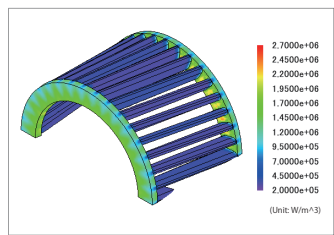


Fig. 1. Cage Joule Loss

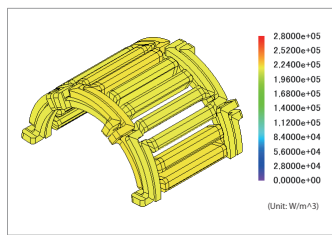


Fig. 2. Winding Joule Loss

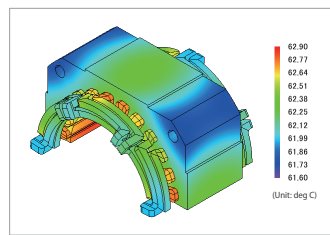


Fig. 5. Stator Temperature

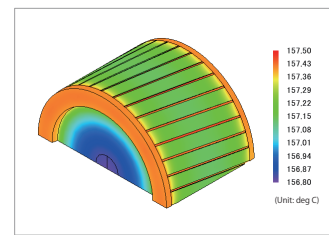


Fig. 6. Rotor Temperature

Analysis of the Effect of PWM on the Iron Loss of an Induction Motor

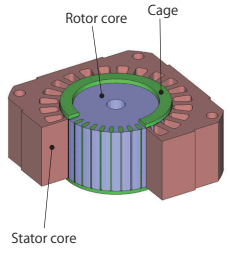
module: DP, LS

Overview

An induction motor is a motor in which the rotating magnetic field of the stator coils causes induced current to flow in an auxiliary conductor, which produces force in the rotational direction. Induction motors are widely used in everything from industrial machines to home appliances because they have a simple construction without parts that experience wear from abrasion, and can be used simply by connecting them to a power source.

Usual simulation use sinusoidal inputs for their studies of induction motors but in reality electrical machines are generally fed using Inverter drives that generates PWM signals. For this reason looking at PWM input in FEA simulation would allow to give us a better idea of the losses in an induction motor.

In this example, we introduce a case study to obtain the iron losses of the induction motor that accounts for the PWM input.



PWM

The PWM of the induction motor will be generated using a modified macro of the standard PWM Inverter of JMAG. The PWM Inverter uses the angular position of the rotor to create the PWM but this cannot be used in a Induction machine setting as the machine does not turn at synchronous speed. We need therefore to Set the PWM to be synchronized with a frequency, in our case 120 Hz and give us a voltage of 40.8 V. The switching frequency was set at 10 kHz.

Fig.1 illustrates the circuit used to create the PWM and fig 2 shows the waveform.

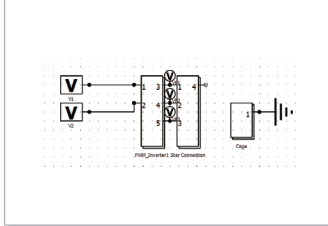


Fig. 1 PWM Circuit

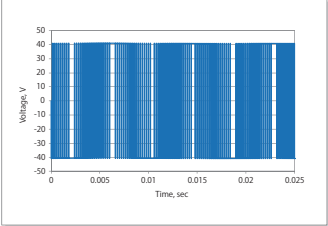


Fig. 2 PWM Inverter waveform

Losses in Induction Motor

The study was set so that induction machine rotating at a speed of 3,300 r/min (a slip of 0.0833). To obtain the currents and magnetic flux density in the induction machine we will use a magnetic transient study. The time step was set so that each period of PWM has at least 30 points.

Fig. 3 shows the magnetic flux density of the induction machine. This highlights the areas where the magnetic filed is the most concentrated. The higher magnetic field flux density will also induce more Iron losses.

Fig. 4 and fig. 5 shows the FFT of magnetic flux density at the rotor teeth and stator teeth with PWM and without. These show that the losses considering PWM will probably increase due to the harmonics present in the iron.

Fig. 6 shows the iron loss density distribution.

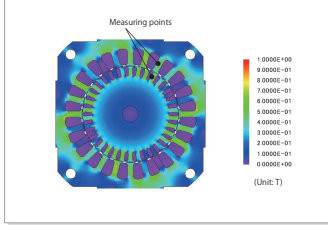


Fig. 3 Magnetic Flux Density

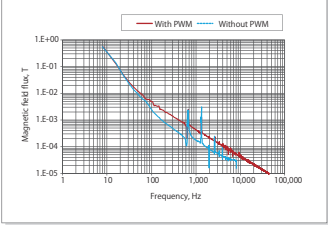


Fig. 4 Magnetic Flux in Rotor Teeth

Iron Loss Study

An iron loss study will then be applied on the results of the magnetic study. Here, compare the iron losses in the induction machine with and without the use of PWM. Table 1 shows the different losses in the rotor and stator iron. We can observe that the total losses in the rotor iron increased by 28 % and 17 % in the stator iron.

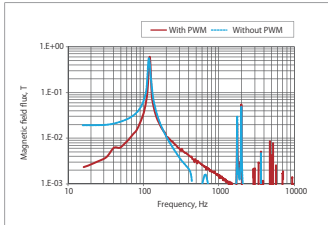


Fig. 5 Magnetic field flux In Stator Teeth

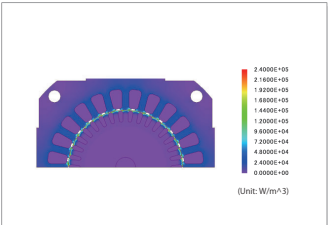


Fig. 6 Iron Loss Density

Part	Iron Loss (Total)			Joule Loss			Hysteresis Loss		
	With PWM	Without PWM	Diff	With PWM	Without PWM	Diff	With PWM	Without PWM	Diff
Rotor	0.69 W	0.54 W	+28 %	0.60 W	0.47 W	+28 %	0.09 W	0.07 W	+28 %
Stator	3.23 W	2.76 W	+17 %	2.23 W	1.81 W	+23 %	1 W	0.95 W	+5 %

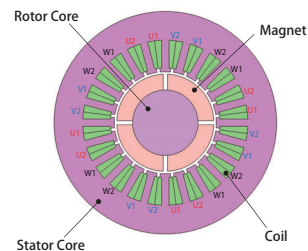
Table 1 Iron Loss Comparison

Case 230 6-Phase SPM Motor Inverter Fault Simulation

module: DP, RT

Overview

In recent years, multiphase design has been adopted for automotive motors due to the merits of cost reduction and improvement in functions. For example, for power supplies there are 6-phase motors with 3-phase double windings that use two inverters, having a 30 deg phase shift in electrical angle. From this, by using multiple inverters, enhanced redundancy of the in-vehicle motor system is achieved. The motor system can be stopped safely without falling to be in an uncontrollable state even if a failure occurs in a part of an inverter. However, circuit simulation is necessary to accurately evaluate safety. When an inverter malfunctions, from overcurrent flowing and from the range of the magnetic field in and around the steel plate where the magnetization properties are nonlinear, inductance exhibits nonlinear behavior as well. Because of this, a highly accurate plant model cannot be created using only linear methods. In JMAG, it is possible to create a plant model that models actual motors in detail taking into account magnetic saturation characteristics and spatial harmonics exhibited in motors. In this example, a JMAG-RT model of a 6-phase SPM is loaded into a control/circuit simulator, and circuit simulation for an inverter failure is carried out.



Control Circuit

The control circuit is shown in Fig. 1. A command value of current amplitude of 8 Apeak and current phase of 0 deg is used, and the voltage command value is sent to the motor via the inverter. Inverter 1 is connected to the U1, V1, and W1 phase terminals, and inverter 2 is connected to the U2, V2, and W2 phase terminals. In addition, a fault alarm is set to go off at 0.02 sec after the start of simulation execution.

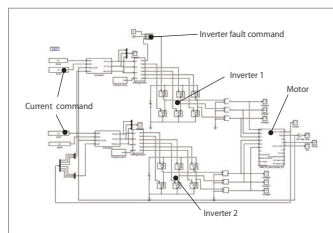


Fig. 1. Control Circuit

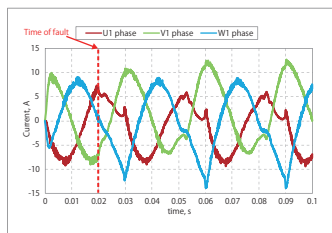


Fig. 2. Current Waveform (U1, V1, and W1 Phases)

Current Waveform, Torque Waveform

The currents for the U1, V1, and W1 phases, for the U2, V2, and W2 phases, and the torque waveform are shown in fig. 2, fig. 3, and fig. 4 respectively.

From fig. 2, it can be seen that the U1-phase current decreases somewhat after the occurrence of the fault, and overcurrent flows through the V1-phase and W1-phase coils. Meanwhile, from fig. 3 it can be seen that the U2-phase, V2-phase, and W2-phase currents are stable.

As shown in fig. 4, although the torque exhibits a large periodic ripple after the fault, its size remains steady. From this, it can be judged that the motor system can safely be brought to a stopped state without falling into an uncontrollable state.

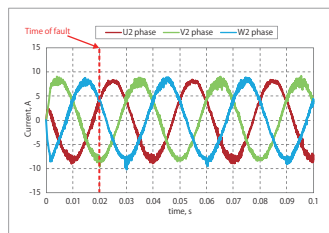


Fig. 3. Current Waveform (U2, V2, and W2 Phases)

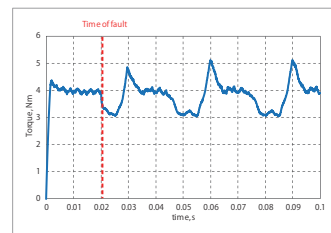


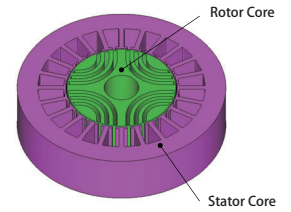
Fig. 4. Torque Waveform

Overview

Since control design and motor design are designed by different designers, cooperative design is difficult. However, in order to meet the sophisticated demands in recent years, it is important to identify problems while coordinating motor design and control/circuit design at the early stages of development. In cooperative design, it is possible to utilize circuit simulation using a highly accurate plant model.

When operating a synchronous reluctance motor (hereinafter referred to as a SynRM), since the nonlinear range of the magnetization properties of an electromagnetic steel plate is used, inductance also exhibits nonlinear behavior. Because of this, a highly accurate plant model cannot be created using only linear methods. In JMAG, it is possible to create a plant model that models actual motors in detail taking into account magnetic saturation characteristics and spatial harmonics exhibited in motors.

In this example, circuit simulation is carried out simulating the control of current and speed by loading a JMAG-RT model for a SynRM into a control/circuit simulator. In addition, comparison with an ideal motor model is performed.



Control Circuit

The control circuit is shown in fig. 1. The rotation speed command value is set to 600 r/min and the d-axis current command value is set to -5 A, and the voltage command value is sent to the motor via the inverter.

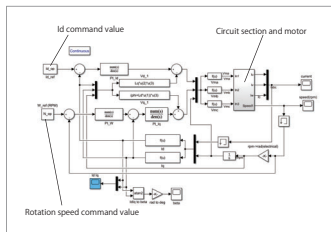


Fig. 1. Control Circuit (Control Section)

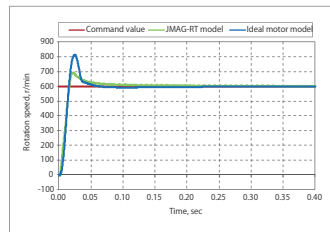


Fig. 2. Rotation Speed Waveform

Rotation Speed Waveform, d-Axis Current Waveform

Fig. 2 shows the rotation speed waveform for a JMAG-RT model and an ideal motor model, and fig. 3 shows the d-axis current waveform.

It can be seen that both converge to the command value. Moreover, it can be seen that there is a difference in behavior between the two as regards the overshoot.

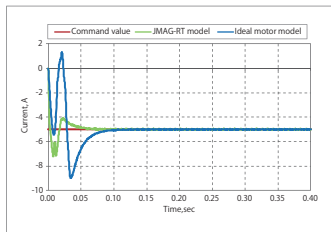


Fig. 3. d-Axis Current Waveform

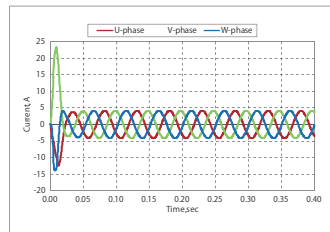


Fig. 4. Coil Current Waveform (JMAG-RT Model)

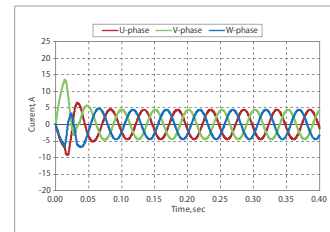


Fig. 5. Coil Current Waveform (Ideal Motor Model)

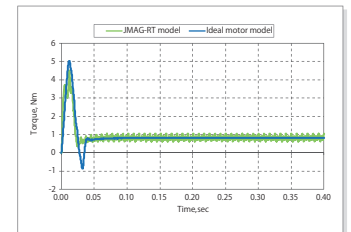


Fig. 6. Torque Waveform

Coil Current Waveform, Torque Waveform

The coil current waveforms when using the ideal motor model and the JMAG-RT model are shown in fig. 4 and fig. 5, and the torque waveform is shown in fig. 6.

Regarding the rise, the JMAG-RT model has more current flowing, but the torque being generated is lower. This is due to the magnetic saturation of the core being precisely taken into account. In addition, looking at the steady-state torque waveform, it can be seen that there is torque ripple due to spatial harmonics.

Case 232 Reactor Joule Loss Analysis

module: FQ

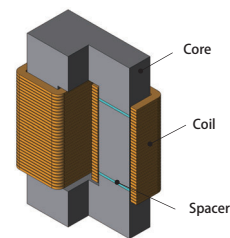
Overview

When designing a high-frequency reactor which is a key component in a converter, inductance and loss, which are parameters required for voltage conversion, are important factors.

By setting gaps in the core of the reactor, it becomes difficult for the core to become magnetically saturated making a stable inductance obtainable. However, the position of the air gaps may affect Joule loss and eddy currents in the coil.

Therefore the position of the air gaps is an important issue in the design of a reactor. It takes however an inordinate amount of time and much cost to perform studies in trial production. By using FEA, it is easy to visualize leakage magnetic flux and compare Joule losses against air gap positions easily.

In this example, investigating Joule loss with respect to the positions of air gaps in a reactor is presented.



Flux Leakage

A sine wave current of 0.5 A at 10 kHz is supplied to the reactor. If there are spacers (air gaps), there is leakage magnetic flux. In addition, this leakage magnetic flux induces current in the coil, generating Joule loss.

The leakage magnetic flux in a certain area is shown in Fig. 1, and the induced current generated in the coil is shown in Fig. 2.

Joule Losses Comparison

Next, losses are compared when changing the spacer positions over 19 intervals.

Fig. 3 shows a Joule loss comparison graph and Fig. 4 shows leakage magnetic flux comparisons.

From Fig. 3 it can be seen that the position of the spacers greatly affects the Joule loss in the coil.

When the two spacers are placed side by side, some of the magnetic flux leaks from the core center.

As shown in Fig. 4a, when the two spacers are placed close to each other, it is seen that the magnetic flux leaks to the sides, is short-circuited, and flows near the core center. In addition, as shown in Fig. 4b, if spacers are placed at the mid-interval position from the center, though leakage magnetic flux is generated, it can be seen that it is over a smaller region. However in Fig. 4c it can be seen that the leakage magnetic flux extends to the nearby portion of the core as with the magnetic flux short-circuit portion of the core in Fig. 4a.

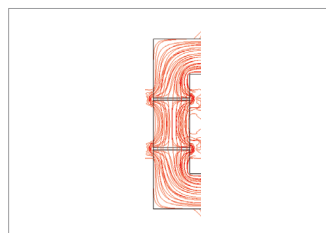


Fig. 1. Leakage Magnetic Flux

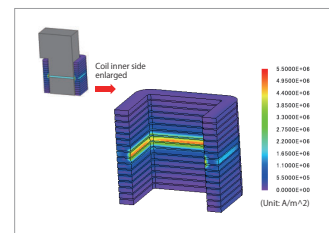


Fig. 2. Induced Current Generated in a Coil

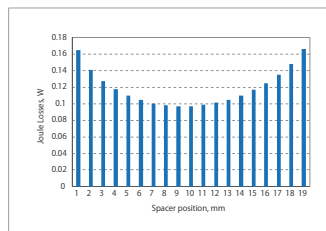


Fig. 3. Joule Losses Comparisons

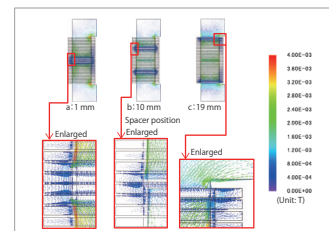
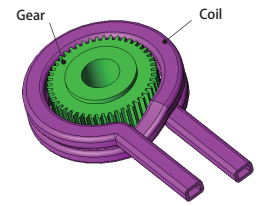


Fig. 4. Leakage Magnetic Flux Comparisons



Overview

As one of the surface hardening techniques for steel, high-frequency induction hardening has been applied to many kinds of mechanical parts. In general, prototyping and testing high-frequency induction hardening equipment requires a great deal of time and money, and is sometimes accompanied by danger. Moreover, in addition to the complex phenomenon called induction heating, material properties also change greatly due to heating exceeding the Curie point, making it difficult to estimate the heating state. For this reason, simulation based on finite element analysis which can model detailed phenomena is useful.

When hardening is performed, uniform heating is desirable, but there are significant factors to consider such as the geometry and arrangement of heating coils and the adjustment of current frequency and amount. When there are many design variables or items to evaluate, applying automatic computation using an optimization function for simulation can greatly reduce the workload.

In this example, an example of using an optimization function to design a coil to use for induction hardening a gear is presented.

Coil Design Variables

The coil has two turns, the distance from the center of the workpiece, CPosition, and the coil width CWidth are design variables. In addition, input current lamp is also defined as a design variable.

Fig. 1 shows the coil dimension design variables, and Table 1 shows all the design variables and range settings.

Fig. 2 shows the temperature evaluation points, and Table 2 shows the objective functions for coil optimization. The objective functions have the following three objectives.

- Minimizing input current
- Minimizing the standard deviation Tdev from the target temperature T_R using the evaluation point temperatures T_i (Fig. 2)
- Minimizing the bias Tbias from the target temperature T_R using the evaluation point temperatures T_i (Fig. 2)

Initial Design

Fig. 3 shows the temperature distribution with the initial design.

As shown in Fig. 3, the workpiece temperature is high at the temperature evaluation points T2 and T4 at the center of the workpiece, and low at the temperature evaluation points T1 and T3 near the end faces of the workpiece.

In the initial design, since the difference in temperature among the temperature evaluation points is large, improvements need to be made.

Pareto Curve Produced From a Multi-objective Optimization

Optimization using a multi-objective genetic algorithm with a population size of 15 and 10 generations is performed. Fig. 4 shows a graph of input current Input and the standard deviation of temperature, Tdev, obtained by the multi-objective optimization.

The standard deviation of temperature, Tdev, one of the design variables with the objective of being minimized, is shown. The optimized value case, the case with the minimum Tdev value, may lower the input current value, and also reduces the standard deviation compared with the initial design.

Whether the current is lower after the optimization is checked. As shown in Fig. 4, if the current value is lowered, the temperature does not rise sufficiently at any of the four evaluation points, and the standard deviation Tdev is larger.

Fig. 5 shows a comparison of the temperature distribution for an optimized geometry vs. input current.

Sensitivity Evaluation Using a Correlation Matrix

Fig. 6 shows a correlation matrix, Fig. 7 shows a CPosition-Tdev scatter plot, and Fig. 8 shows a comparison of two temperature distributions from two optimization cases with the same current where in one case Tdev is larger.

As seen in Fig. 6, CPosition is the most sensitive among the design variables, and the coil width CWidth has low sensitivity. In addition, as in Fig. 7, as CPosition increases, Tdev also increases.

From Fig. 8, it can be seen that as the coil positions move to the ends of the workpiece, the temperature also becomes higher near the ends of the workpiece and the temperature variation becomes larger.

From these results, it can be seen in this Fig. 8 example that CPosition has high correlation with Tdev, heating occurs more uniformly for cases when CPosition is small, and CWidth has low correlation with Tdev.

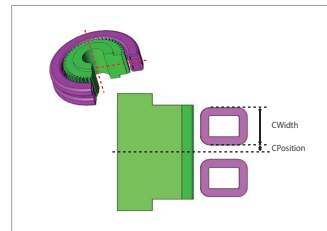


Fig. 1. Design Variables (Coil Dimensions)

Variable name	Minimum value	Maximum value
lamp	3	8
CPosition	1	20
CWidth	10	25

Table 1. Design Variables

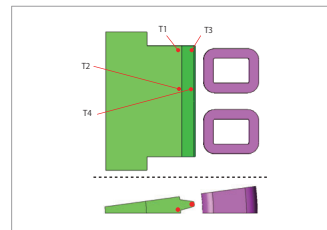


Fig. 2. Temperature Measurement Points

Item	Expression	Objective
Input current, kA Input	$3 \leq \text{Input} \leq 8$	Minimum value
Standard deviation Tdev	$T_{dev} = \sqrt{\frac{1}{4} \sum_{i=1}^4 (T_i - T_R)^2}$	Minimum value
Bias Tbias	$T_{bias} = \frac{1}{4} \sum_{i=1}^4 T_i - T_R $	Minimum value

T_i : temperature at a measurement point
T_R : target temperature = 850(deg C)
T_{dev} : standard deviation
T_{bias} : bias

Table 2. Objective Functions

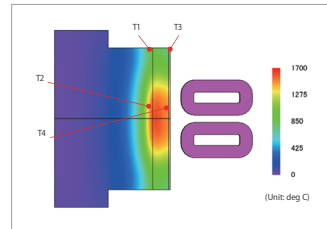


Fig. 3. Initial Design Temperature Distribution Contour Plot

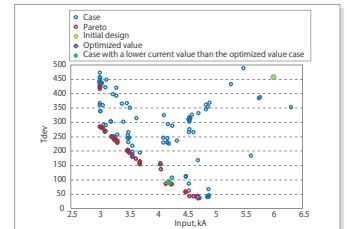


Fig. 4. Input Current Input vs. Temperature Standard Deviation Tdev

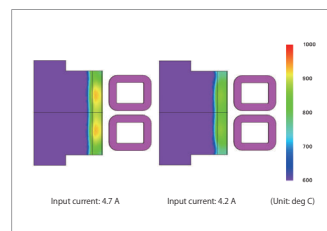


Fig. 5. Temperature Distribution Comparison for an Optimized Geometries vs. Input Current

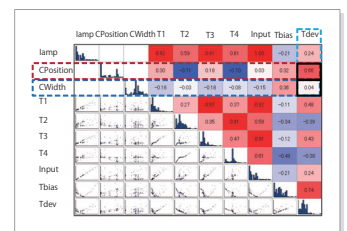


Fig. 6. Correlation Matrix

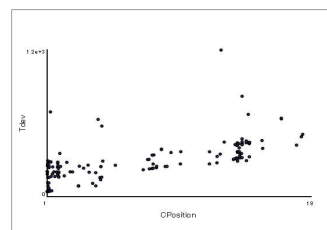


Fig. 7. Scatter Plot

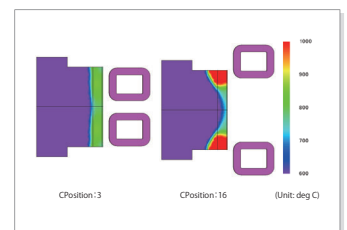


Fig. 8. Temperature Distribution Comparison vs. CPosition

Case 234 Vibration Characteristics Analysis of an Induction Motor

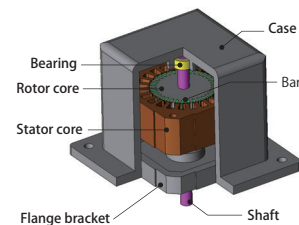
module: DP, DS

Overview

Because the construction of induction motors is simple, easy, durable, and highly effective, they have been widely used throughout industry in general for an extensive period of time. In recent years however, there has been an increase in words raised concerning issues of pollution and improvements to work environments, and the noise that emanates from induction motors is also becoming an issue. Electromagnetic force acting on the induction motor is the source that generates torque, but at the same time the excitation force of the motor itself generates electromagnetic noise.

To favourably evaluate both noise caused by electromagnetic force and vibrations, it is necessary to accurately grasp the electromagnetic force distribution acting on the stator core which is the source of radiated sound, and to obtain the eigenmode of the entire motor that includes the connected case. Because electromagnetic force distribution and eigenmode are dependent on the geometry of the stator core, it is necessary to obtain this via analyses such as the finite element method.

In this example, electromagnetic force generated in the induction motor stator core is obtained, and an example of evaluating sound pressure by linking it with the eigenmode of the motor is shown.



Eigenmode

Attention is paid to the mode of vibration depending on the number of poles. Because a 4-pole model is being used, it is understood that this mode exists near 3,700 Hz by confirming the rectangular vibration mode. The condition of deformities is shown in Fig. 1.

Acceleration at Each Frequency Generated by Electromagnetic Force

The frequency dependence of acceleration generated by electromagnetic force during rotation is displayed in Fig. 2. One side is chosen for evaluation points in the diagram for the case shown, maximum value is extracted from the effective value of each point and is taken as the evaluation value of that frequency. It is confirmed that acceleration is at maximum when near eigenmode at 3,700 Hz as shown in Fig. 1, and resonance is considered to occur also.

Acceleration and Sound Pressure Distribution in Square Form Eigenmode

Acceleration at 3,700 Hz and sound pressure levels are each displayed in Fig. 3 and Fig. 4. It can be seen that both acceleration and sound pressure levels are high due to resonance. It can be additionally confirmed that eigenmode spatial characteristics are reflected in the distribution of both.

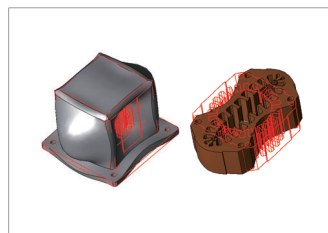


Fig. 1. Square Form Eigenmode

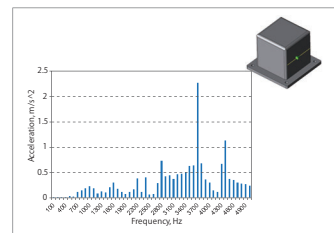


Fig. 2. Acceleration Frequency Dependence

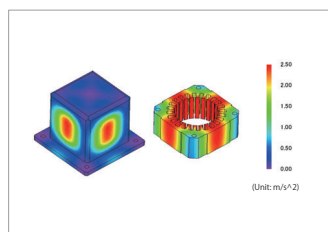


Fig. 3. Acceleration Distribution at 3,700 Hz

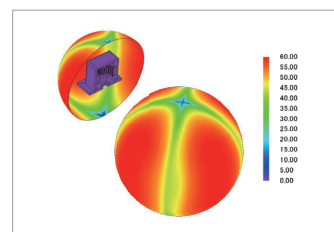


Fig. 4. Sound Pressure Level Distribution at 3,700 Hz

Case 235 Reactor Core Stray Loss Analysis

module: LS, TR

Overview

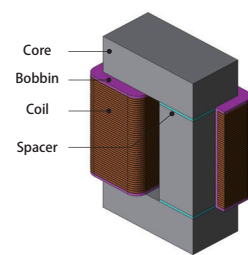
When designing a high-frequency reactor which is a key component in a converter, inductance and loss, which are parameters required for voltage conversion, are important factors.

Copper loss is dependent on coil resistance and current, and iron loss is classified as eddy current loss or hysteresis loss. Other losses are called stray loss.

Stray loss is a loss caused by eddy currents in the core portions near coil ends and conductive parts near the coils which in turn are caused by mainly leakage flux from the coil ends.

Although the stray loss is not always a large part of the entire loss, heat generation may occur locally sometimes causing operational problems. Although it is difficult to capture stray loss by actual measurement and calculation by hand, it is possible to visualize core surface eddy currents which result in stray loss or leakage flux from the coils to the core by JMAG transient analysis.

In this example, reactor core stray loss is described.



Leakage Flux and Eddy Currents

Fig. 1 shows the flux lines near a gap and a core eddy current distribution. From the enlarged view of the flux lines, it can be confirmed that fringing occurs in which the magnetic flux bulges due to the magnetic flux cross sectional area becoming larger than the core cross sectional area at the core gap. In addition, in-plane eddy currents are generated on the surface right under the right coil near the gap, and it can be seen that the magnetic flux is generated perpendicularly to the laminating direction.

Reactor Loss

Fig. 2 shows the loss in the reactor. By performing magnetic field analysis and iron loss computations together, analysis results can be obtained by separating out hysteresis loss, eddy current loss, stray loss, and loss.

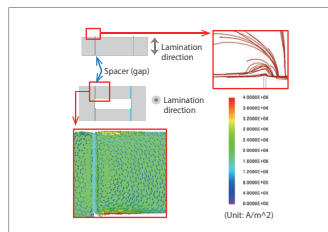


Fig. 1. Leakage Flux and Eddy Currents

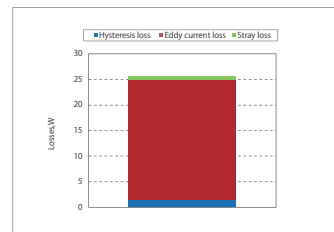


Fig. 2. Reactor loss

Magnetic Circuit Optimization for Plastic Magnets in an Axial Magnetic Field

module: ST

Overview

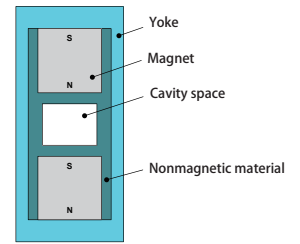
Plastic magnets are characterized by light weight with high strength and have a high degree of freedom in shaping, and very suitable for mass production.

Anisotropic plastic magnets with good magnetic properties need magnetic field orientation. For this reason, a magnetic circuit is created to generate the magnetic flux necessary for magnetic field orientation in the product cavity in the mold used.

Design requirements for the magnetic circuit are that the magnetic flux generated in the cavity has the magnitude necessary and sufficient for the magnetic field orientation, that flux parallel to the analysis target main axis be produced, and that the magnetic circuit be formed as small as possible.

In the case of simple magnetic circuits, these requirements can be met by hand calculation, but FEA is effective for obtaining a generated spatial magnetic flux density distribution, angles, etc. in detail in the cavity. In addition, since trial and error cannot be avoided in an optimum design that minimizes geometry size while satisfying the above requirements, and time is consumed, automation of analysis combined with optimization tools is widely used.

In this example, a use case is presented in which a magnetic circuit of a product-forming mold, in a magnetic field aligned with the mold's main axis, is optimized, with the mold's dimensions used as design variables.



Optimization Conditions

Fig. 1 shows design variables and objective functions as optimization conditions.

The design variables are the magnet radius a , the non-magnetic material width b , and the yoke width c . Settings are performed for an optimization function that gives the highest priority to minimizing the magnetic circuit radius $a+b+c$.

In addition, the angle formed by the magnetic flux density B generated in the cavity with respect to the Y-axis and the threshold for the magnitude of B are specified.

In this example, the angle is within an error of 5 deg and the value of B is 0.3 T or more. Also, these variables are used in objective functions.

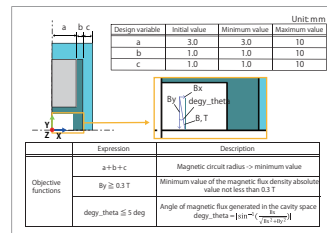


Fig. 1. Optimization Conditions

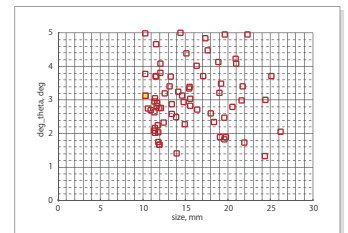


Fig. 2. Magnetic Circuit Radius and Cavity Magnetic Flux Angle (When Satisfying the Objective Function Constraints)

Optimization Results

The response graphs for the results after optimization is shown.

Fig. 2 and Fig. 3 show graphs of B_{\min} and degy_theta from the objective functions, respectively, vs. the radius of the magnetic circuit. The yellow plot is the optimum value. The optimum value is the minimum value of the radius of the magnetic circuit when the objective function constraints are satisfied. The optimum value plot shown in Fig. 2 and in Fig. 3 are for the same case.

Fig. 4 shows the results magnetic flux density contour plots and flux lines obtained with the initial geometry and with the optimum geometry. The initial values of the variables a , b , c and the values obtained after optimization. It can be seen that in the region of the cavity surrounded by the red rectangle, for the initial geometry some of the flux enters at an angle, however, for the optimized geometry obtained the flux has parallel flux lines and is nearly uniform.

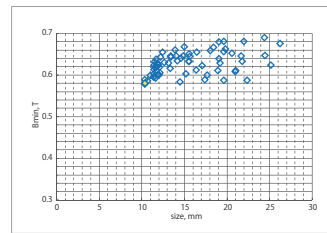


Fig. 3. Magnetic Circuit Radius and Cavity Magnetic Flux Density (When Satisfying the Objective Function Constraints)

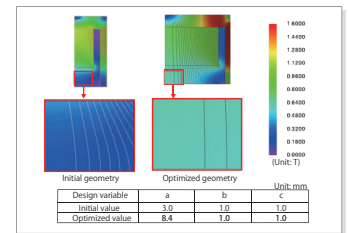
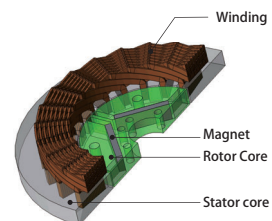


Fig. 4. Optimized Results (Magnetic Flux Density Contour Plots, Magnetic Flux Lines)

Case 237 AC Loss Analysis of an IPM Motor

module: TR



Overview

Primary power loss drivers in PM machines are iron, magnets and the winding. The main focus of this analysis is the winding losses, particularly those which occur in the end winding. The flux patterns occurring in the end winding region are different from those within the core winding length. These losses can be defined by their two components namely DC and AC losses, DC winding loss is easily analyzed by circuit analysis of the windings and are within the realm of arithmetic calculation. The AC loss components are caused due to various effects of the magnetic fields generated by the conductors in proximity of each other. This used to be estimated by creating prototypes and doing tedious measurements on the coil parts. This used to make the design workflow expensive and time consuming. However by using a 3-D Finite Element Analysis on these coils the losses can be analyzed relatively quickly and economically. In this example, we introduce the case study that evaluates AC losses in coils of an IPM motor.

Loss Analysis

The difference between DC and AC losses can be gleaned from Fig. 1. After considering AC losses and subsequently adding DC and AC losses we get a total increase of 45 % in losses. This is quite a significant amount of increase. The AC losses in the end winding as seen in Fig. 2 depend on the shape of the winding as well as the flux leakage through the end windings. This happens due to mutual flux linkages between individual conductors which create eddy currents flowing through system.

In Fig. 3, the flux linkages between the stator end (fringing effect) and the coil and mutual flux linkages in the conductors can be observed. These are the main drivers behind AC losses in the end winding.



Fig. 1 AC Losses VS DC Losses

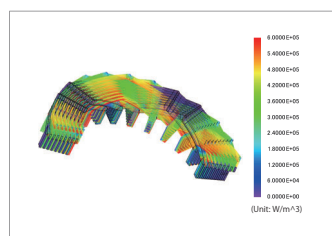


Fig. 2 Joule Loss Density Distribution

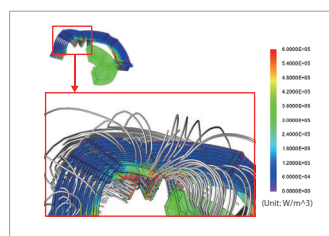
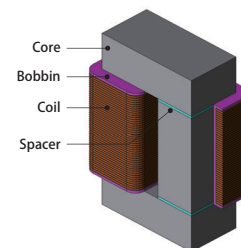


Fig. 3 End Winding Loss and Flux Line

Case 238 Hysteresis Loss Analysis in a Reactor with DC Bias

module: DP, LS



Overview

When designing a high-frequency reactor which is a key component in a converter, inductance and loss, which are parameters required for voltage conversion, are important factors. A reactor are usually used in power electronics and experience high frequency signals. Therefore they will be subject to hysteresis losses that we can calculate with JMAG. In this example, we will observe the difference between the hysteresis losses calculation method loop count and the play model for the model that is subjected to a DC bias filed on top of a AC field.

Hysteresis Loss Comparison

Table 1 shows a difference between the two method of calculations. This is due to the way the method calculate the hysteresis losses in the Iron core. The loop count method uses a Steinmetz method which takes in account only AC variation of the field. Whereas the play model takes in account the AC variation on top of the any DC component that may be present. This will be highlighted in the Fig. 1.

Play Model

The Reactor is supplied by a 10 kHz, 2 A sinusoidal current as well as 20 A DC current. This provides us with a Magnetic field flux containing an AC and DC component, as illustrated in Fig.1.

The core being laminated each of them will be subjected to a 1D lamination FEA study to find the eddy currents induced in the plates at different depths. From there we can extract the average Magnetic Field Flux depending on the depth as shown in Fig.2. We observe that the field is the highest around the skin of the laminated sheets.

The play model will take in account even the DC component of the field as Illustrated in Fig.3 where we can observe the hysteresis loops of the Magnetic field flux at different depths in the steel sheets. This is the main difference between the loop count and play model. Since loop count only considers AC fields we have a difference in the resulting hysteresis loops.

Therefore for an accurate estimation of those losses in a system that includes an AC and DC component of magnetic field flux, it is recommended to use a play model hysteresis loss calculation especially since in this case the hysteresis losses represent more than half of the AC losses in the core. 2.75 W of eddy current loss compared to the 3.08 W of hysteresis loss.

Play Model	Loop Count
3.08 (W)	0.55 (W)

Table 1 Hysteresis Loss Comparison

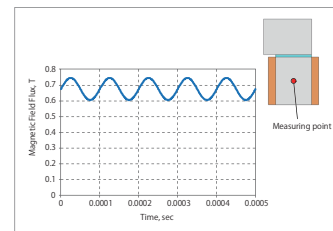


Fig. 1 Magnetic Field Flux in the Reactor

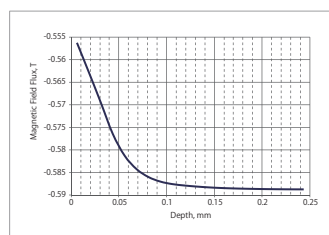


Fig. 2 Hysteresis loop (Average Field Flux)

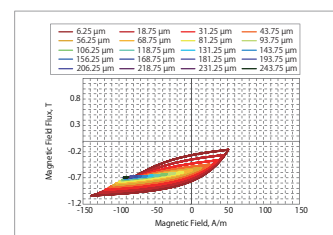


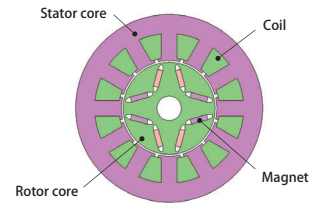
Fig. 3 Hysteresis loop

Overview

Electrical faults are a commonly occurring conditions during operation of machines. These can cause an adverse effect on the power electronics or the power system connected to these machines. It is necessary to run many test cases with changing fault conditions for a comprehensive analysis of motor behavior during a fault.

JMAG-RT Model can simulate the effect of harmonics on the system and magnetic saturation effect that are calculated from FEA.

In this example, we introduce the case study that simulate the fault of an IPM motor using JMAG-RT. The fault simulated in this case study is an open circuit fault which is caused due to failure of an IGBT, this is one of the most commonly occurring faults in PMSM operation.



Fault Description

The Motor is a 4 pole machine rated at 1 kW. It is operating at 600 r/min and 10 A.

The fault occurs due to an IGBT failure at 0.3 sec into operation start.

This causes an open circuit in the six step inverter. This causes the current through that particular IGBT to fall to zero.

We are particularly looking for the effect of this kind of fault on the torque and current characteristics of this motor.

Fault Analysis

There is a fundamental difference between the high fidelity model (JMAG-RT Model) and low fidelity model (LdLq (Constant) Model). The JMAG-RT model take into account the angular position of the current vectors. This requires FEA. Thus with JMAG-RT model it is possible to capture torque ripple before and during fault.

This is beneficial in prediction of motor behavior due to a IGBT fault while doing a system analysis. The torque behavior is demonstrated in Fig. 3. The point at which the fault occurs is also visible. By running higher time resolution analysis on such a model it is also possible to predict the phenomenon while reclosing or after fault is resolved.

This difference can also be observed in the current waveform after the fault occurs. From Fig. 3, the difference in currents is minimal this causes the difference in the average values of torque for two models to be minimal.

Fault analysis at higher loading

There is a difference between the average values of torque when using LdLq (Constant) Model and JMAG-RT Model in Fig. 4. This difference is however not observed in Fig. 2. The main difference here being the supply currents. Fig. 2 has 10 A while Fig. 4 has 28.3 A.

The reason behind this difference is the saturation effect, this can only be observed in the JMAG-RT Model and not the LdLq (Constant) Model.

From Fig. 5, the values of Ld and Lq decrease as the input current increases. This happens due to the cores being saturated. Due to saturation the Iron in the cores starts acting like air. This causes a decrease in the average torque observed in Fig. 5. The saturation can be observed in FEA from Fig. 6.

The behavior prediction in the fault thus also depends on characteristics not observed by a simple LdLq (Constant) Model thus it is useful to use a High Fidelity one.

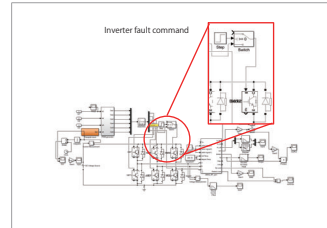


Fig. 1 Motor Control Circuit

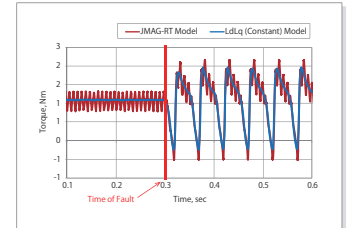


Fig. 2 Torque Characteristic comparison (10 A)

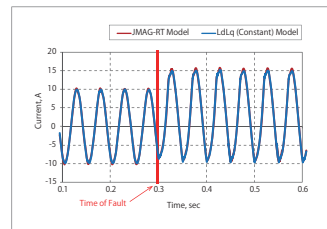


Fig. 3 Current characteristic comparison

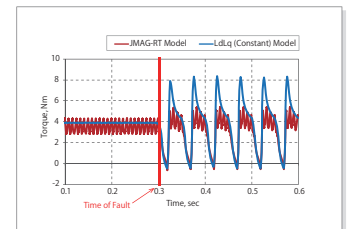


Fig. 4 Current characteristic comparison

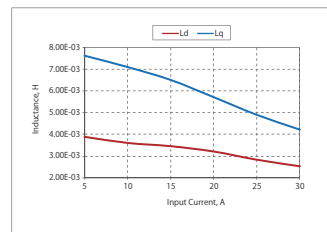


Fig. 5 Inductance Analysis

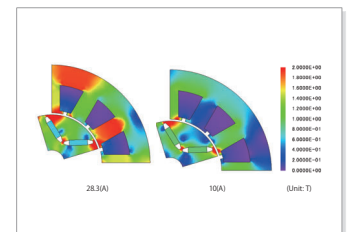


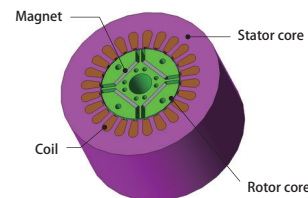
Fig. 6 Magnetic Flux Density Distribution

Case 240 NT Characteristics Analysis of an IPM Motor Using PAM Drive

module: DP

Overview

A PMSM usually requires a drive system to operate. There are various types of drive systems such as PAM drive and PWM drive systems. The concept of PAM drive is simple: a carrier signal modulates a supply signal to generate pulses and controls the amplitude of these pulses by controlling the amplitude of the supply signal. By applying appropriate switching control, this concept can be used in a PMSM drive device. Furthermore, due to the simplicity of the switching control, PAM drive tends to be cheaper and more robust than PWM drive. In addition, with IPM the back electromotive voltage increases during high-speed rotation, which reduces the torque and the current flowing to the coils. When designing a motor, it is necessary to understand the characteristics for a wide range of operating points. The evaluation of NTI characteristics with FEA at the design study stage contributes greatly to development speed. In this example, an example of evaluating the performance of an IPM with PAM operation is presented.



PAM Drive

Fig. 1 shows the magnetic flux density distribution at a rotation speed of 1,800 r/min. It can be seen that the teeth near the coils being excited have a magnetic flux density close to saturation. Fig. 2 and Fig. 3 show the torque and current waveforms respectively at an operating point of 1,800 r/min when using PAM drive. Fig. 4 shows the NTI curves, which predicts motor performance at various operating points. The torque of the IPM motor decreases as the rotation speed increases and increases as the current increases.

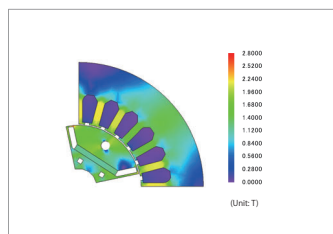


Fig. 1. Magnetic Flux Density Distribution (1,800 r/min)

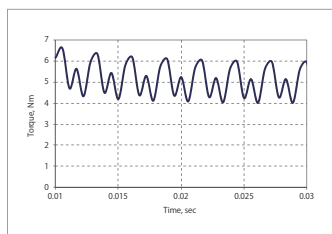


Fig. 2. Torque Waveform (1,800 r/min)

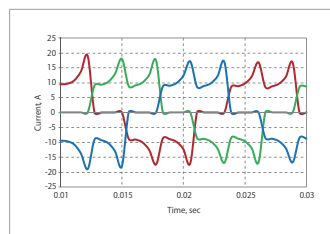


Fig. 3. Current Waveform (1,800 r/min)

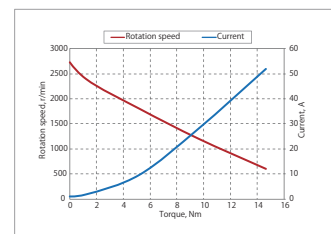


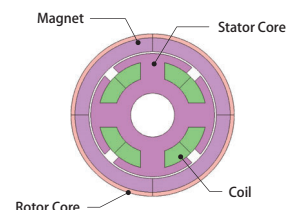
Fig. 4. N-T-I Curve

Case 241 Single-Phase Synchronous Motor N-T-I Characteristics Analysis

module: DP

Overview

The widely used three-phase synchronous motor can be driven efficiently and stably but costs tends to increase due to using an inverter. Whereas since single-phase synchronous motors do not require inverters, they can reduce costs. Furthermore, because they are brushless, maintenance costs can also be lowered. In a single-phase synchronous motor, the back emf and the current flowing through the coils change in accordance with the rotation speed of the rotor. At low rotation speed, since the back emf is small, a large current flows through the coils, and magnetic saturation occurs in the magnetic circuit. On the other hand, the back emf increases at high speed, so the current flowing through the coils and torque decrease. Because of this when designing a motor it is important to understand characteristics for a wide range of operating points. Obtaining N-T-I characteristics from performing analysis in JMAG at the design study stage contributes greatly to the speed of motor development. In this example, a use case in which the N-T-I characteristics for a single-phase synchronous motor are obtained is presented.



N-T-I Characteristics

Fig. 1 shows an N-T-I characteristics graph. From Fig. 1, torque for each rotation speed, maximum driving rotation speed, and so on can be seen. The current and torque are roughly proportional.

Magnetic Flux Density Distribution

Fig. 2 shows the magnetic flux density distribution at 2,000 r/min and at 12,500 r/min. Since a large current flows at a low driving speed, magnetic saturation can be seen in the stator core as well. On the other hand, the current flowing through the coils decreases at high driving speeds, so it can be seen that the magnetic saturation in the stator core is relaxed.

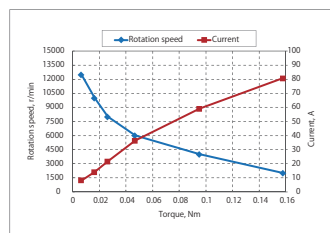


Fig. 1. N-T-I Characteristics (Rotation Speed - Torque - Current Characteristics)

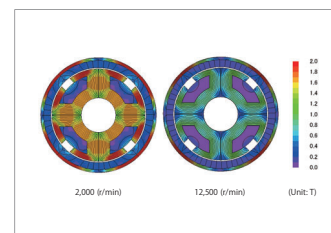


Fig. 2. Magnetic Flux Density Distribution

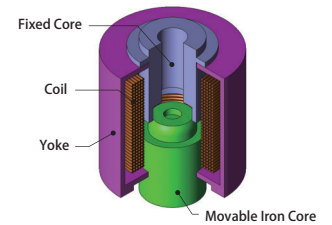
Overview

Solenoid valves are used to adjust the inflow or outflow of liquids or gases by translational movement of the iron core. If an electric current is passed through the coil, an electromagnet is created and an electromagnetic attractive force is generated between the movable part and the fixed parts. Since high responsiveness is required for valve opening and closing, an important item to evaluate is whether or not the power source used for driving and the solenoid valve meets the required responsiveness and attractive force.

Solenoid valves are often used for hydraulic valves and injectors, and the movable part itself is placed in high pressure liquid and encounters flow resistance. Since the movable part uses a guide to move, there is error with the possibility to cause an inclination. In the case of inclination, the electromagnetic attraction force is unbalanced, so it is necessary to confirm beforehand whether or the force acts in the proper direction.

It is useful to examine by FEA beforehand whether there is a change in the attractive force when there is an inclination and whether an unbalanced force causes the movable part to become unaligned.

In this example, an example is presented where the influence on the electromagnetic force by the presence or absence of inclination is confirmed at each position of the movable part.



Position and Inclination of The Movable Part

Fig. 1 shows the position and inclination of the movable part. The position of the movable part is considered for three gap lengths - 3.6 mm, 1.9 mm, and 0.2 mm. At each position, there is an inclination of the movable part. Comparisons to the situation of having no inclination is carried out. The center axis of the inclination is not dependant on the position of the movable part and has fixed coordinates. The inclination is 2 deg.

Influence on Electromagnetic Force

Fig. 2 shows the attractive force from the inclination at each movable part position, and Fig. 3 shows the torque around the center axis of the inclination.

As can be seen in Fig. 2, the inclination has almost no effect on the attractive force at the gap length of 3.6 mm, but the attractive force increases by 20% without inclination compared with inclination at 1.9 mm, and decreases by 3% at 0.2 mm.

As shown in Fig. 3, with inclination it can be seen that the torque becomes larger as the gap length becomes shorter. In this example, since the positive direction of the torque and the direction of the center axis of inclination are made to coincide with each other, it is seen that the unbalanced force generated in the movable part acts in a direction to increase the inclination.

Electromagnetic Force Distribution

Fig. 4 to Fig. 6 show the electromagnetic force distribution around the movable part at each position.

As shown in Fig. 4, at the gap length of 3.6 mm almost no change in electromagnetic force due to inclination is observed. On the other hand as shown in Fig. 5, it can be seen that the electromagnetic force increases at the position where the fixed iron core and movable iron core are closest with an inclination at the gap length of 1.9 mm. As a result, the attractive force has increased. With the gap length of 0.2 mm shown in Fig. 6, the electromagnetic force acts not only in the motion direction but in the horizontal direction due to the inclination of the movable part. It can be seen that this is the reason for the decrease in the attractive force.

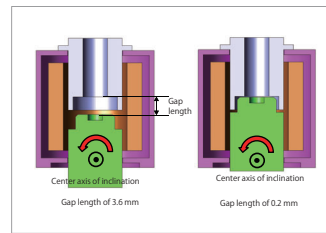


Fig. 1. Position and Inclination of the Movable Iron Core

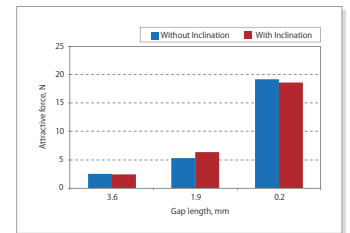


Fig. 2. Attractive Force

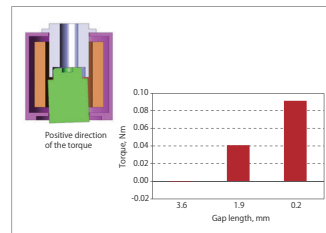


Fig. 3. Torque

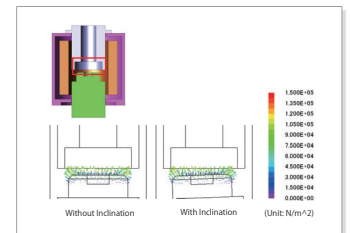


Fig. 4. Electromagnetic Force Distribution (Gap length 3.6 mm)

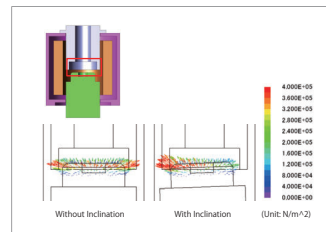


Fig. 5. Electromagnetic Force Distribution (Gap length 1.9 mm)

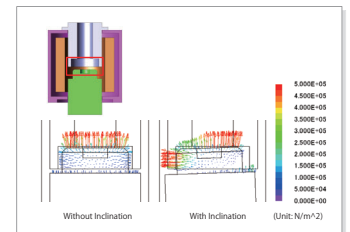


Fig. 6. Electromagnetic Force Distribution (Gap length 0.2 mm)

Case 243 Voice Coil Motor Control Simulation Using a Control Simulator and JMAG-RT

module: DP, RT

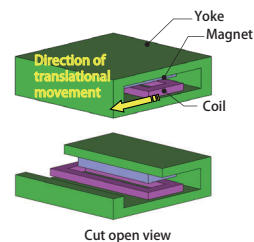
Overview

Linear actuators are used in machine tools and other applications because they can achieve high speed and high acceleration/deceleration, and because they have high positioning accuracy. In particular, coreless type linear actuators have a small driving force compared to linear actuators having a core, but because they do not generate cogging their driving force fluctuations are small. Utilizing this characteristic, they are used in environments requiring high-precision positioning such as head drives for electronic component mounting machines and for very fine movements when precision is needed.

The change in driving force from the change in actuator positions greatly affects the positioning accuracy. Furthermore, the driving force is controlled by the current. Moreover, because of the nonlinearity of the material and due to the magnetic path not being fully contained in the magnetic material, it is difficult to calculate by hand the driving force for each current value and position of the voice coil motor. Therefore, taking into account dynamically changing characteristics, in order to control the voice coil operating at high speed, a plant model containing characteristics dependent on magnetic saturation and the position of the mover is required.

JMAG-RT can create a highly accurate plant model in a JMAG-RT model by performing FEA taking into account the geometry, materials, and driving conditions, and extracting the characteristics of the voice coil motor.

In this example, circuit simulation is performed to control the position of a mover by loading a JMAG-RT model for a voice coil motor into a control/circuit simulator.



Control Circuit

The control specifications are shown in Table 1. The control circuit control section is shown in Fig. 1.

Item	Details
Control method	Position control realized by chopping control

Table 1. Control Specifications

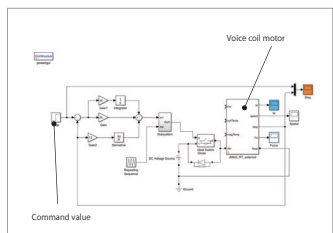


Fig. 1. Control Circuit

Coil Position vs. Time

Fig. 2 shows the coil position vs. time, and Fig. 3 shows the excitation current vs. time.

As shown in Fig. 2, the movement from the 0-mm position to the 0.8-mm position and the movement from the 0.8-mm position to the 1.6-mm position are both a movement of 0.8 mm, but the electromagnetic force is different, and the trajectory of the movement is different because it is dependent on inductance current and on position and is influenced by the spring.

From Fig. 3, it can be seen that a surge current is generated the moment the coil starts to move. Since surge current may damage peripheral electrical equipment, examination of this equipment is necessary when it is excessive.

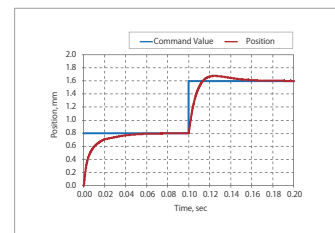


Fig. 2. Change in Coil Position vs. Time

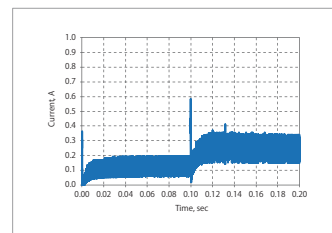


Fig. 3. Change in Excitation Current vs. Time

Case 244 Magnetic Field Strength Analysis at a Sensor Position

module: DP

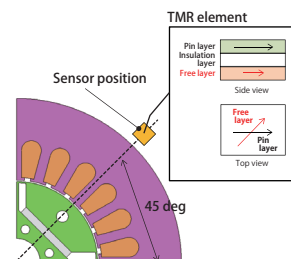
Overview

To control the position or speed of a motor or actuator, it is necessary to accurately detect the position of the mover and calculate command values based on that position. To detect the position, a method to detect leakage flux produced from an analysis target is widely used.

There are various detection methods, from using electromagnetic induction from a pickup coil to using the Hall effect or the magneto resistive effect. The latter methods have begun to be used in recent years because they can obtain a signal corresponding to the magnitude of the magnetic flux density regardless of the frequency.

To predict the signal produced in a sensor by the magnetic flux density generated at the sensor position and apply it to the displacement and speed control of the mover, electromagnetic field analysis that can accurately calculate the magnetic flux density and magnetic field distribution generated from the analysis target is useful.

In this example, with the analysis target being a motor and the detection sensor being a TMR sensor, an example where a detection signal waveform is obtained that is based on magnetic field values computed from electromagnetic field analysis is presented.



Magnetic Field Radial Component at the Sensor Position

Fig. 1 shows the magnetic field strength radial component at the sensor position. Together with this value increasing as the motor current is increased, it can be confirmed that the rotor position achieving the maximum value shifts to a lower angle.

Resistance Change Rate of Each Sensor

Fig. 2 shows the percentage change in resistance when the sensor pin layer is fixed in the radial direction, and the free layer magnetization direction is the same as the external magnetic field direction. The TMR ratio maximum value is 100 %, and the percentage change in resistance is for when the angle between the pin layer magnetization direction and the free layer magnetization direction is 90 deg.

When the current changes, it can be confirmed that the percentage change in resistance shifts to a lower rotation angle, and it can be seen that the relationship between the field strength and the position of the motor changes with the current amplitude. It can be seen that it is necessary to ascertain the relationship between the sensor output and the rotor position when the current changes in order to detect the rotor position accurately.

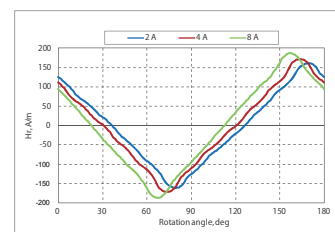


Fig. 1. Magnetic Field Radial Component at the Sensor Position

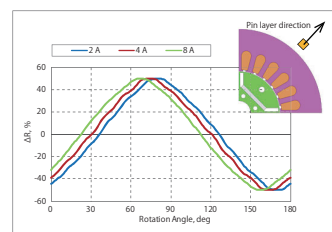


Fig. 2. TMR Ratio vs. Rotor Rotation Angle

Case 245

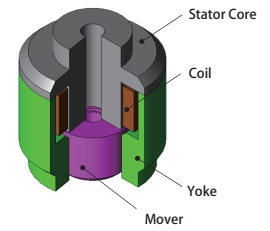
Injector Control and Eddy Current Effects

module: DP

Overview

Solenoid injectors used in engines open a valve by injecting fuel as a plunger moves from the magnetic force of an electromagnet. For injectors in engines, high responsiveness to applied voltages is required for suppressing flow rate fluctuations and improving fuel economy. MATLAB/Simulink and JMAG can be linked directly when performing injector circuit control simulations. Taking into account eddy current effects as well, this allows injector characteristics to be reflected in more detail and allows evaluation of control systems that accurately model actual control systems.

In this example, an example of evaluating the difference in responsiveness of an injector when eddy currents are taken into account or not is presented.



Control Circuit

The 18-V DC power supply of the circuit energizes the coil via a switch controlled by MATLAB/Simulink.

The switch is controlled by hysteresis band control and maintains the current in a range around a reference current.

When current flows through the injector, the reference current is maintained until the plunger reaches its end position. After that the reference current is lowered to maintain the plunger at a specified position and finally the current value is returned to 0 after a certain time as shown in Fig. 2.

Fig. 1 shows the control circuit specifications, and Fig. 2 shows the control model.

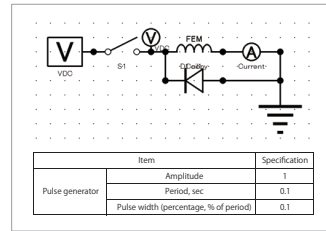


Fig. 1. Circuit Diagram, Control Specifications

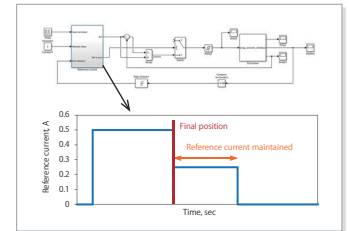


Fig. 2. Control Model

The Position of the Plunger and the Force Acting on the Plunger

Fig. 3 shows the plunger position and Fig. 4 shows the force acting on the plunger.

Looking at the position of the plunger in Fig. 3, it is seen that when taking into account eddy currents, it takes longer to reach the final position and return to the initial position.

This is because as seen from the force acting on the plunger in Fig. 4, when eddy currents are taken into account, the force generated on the plunger becomes smaller. The rate of change in force is also smaller. This phenomenon is caused by the generation of eddy currents which impede fluctuations of the magnetic field.

Effects on Coil Current Due to Eddy Currents

Fig. 5 shows the current.

The model taking into account eddy currents has 30 % or more current flowing in the injector. That is, the power consumption increases.

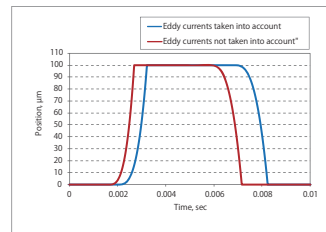


Fig. 3. Plunger Position

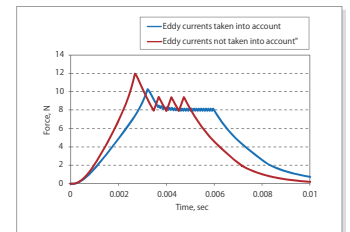


Fig. 4. Force Acting on the Plunger

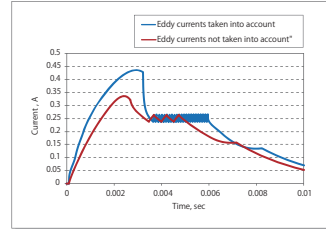


Fig. 5. Current

Case 246 Analysis of Electromagnetic Force Acting Between a Coil and a Magnet

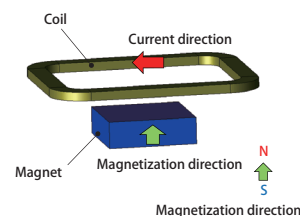
module: ST

Overview

With the miniaturization of electrical equipment, even effects from very small interactions are a concern. Therefore, it is important to ascertain the magnetic and electromagnetic forces acting on parts. Moreover, in an analysis model where the magnetic circuit extends into the air region, it is necessary to use a sufficiently fine mesh over a large region since obtaining an accurate magnetic field distribution in the air region is directly related to electromagnetic force computation accuracy.

In circumstances such as these, the adaptive mesh function can be used to again subdivide mesh from air region error distribution, and mesh that obtains a high analysis accuracy can be generated. By additionally using electromagnetic force calculation correction methods, it is possible to obtain the electromagnetic force acting between parts that would otherwise be difficult to calculate.

This case study obtains electromagnetic force acting between a coil and magnet using the electromagnetic force calculation correction method and the adaptive mesh function.



Attractive Force Acting Between Coil and Magnet

The current flows in a direction perpendicular to the attractive force acting between the coil and the magnet. During such a time, the forces acting between the coil and the magnet are balanced. Fig. 1 shows the attractive and repulsive forces acting between the coil and the magnet.

Forces Acting on the Magnet

Upon confirming the electromagnetic force distribution generated on the magnet shown in Fig. 1, both magnetic forces, one acting on the lower face and the other acting on the upper face of the magnet, differs by 4 order of magnitude from the net force on the entire magnet. The forces acting on the two magnet faces are obtained from the nodal forces. Since the net force on the entire magnet is obtained from the cancellation of the electromagnetic forces distributed in this way, the electromagnetic force must be computed with very high accuracy. The forces acting on the magnet are shown in Fig. 2.

Magnetic Field Lines Extending in Air

Since magnetic flux lines giving rise to electromagnetic force extend far in the air, accurate computation is required over a wide region. Fig. 3 shows the lines of magnetic force extending in the air.

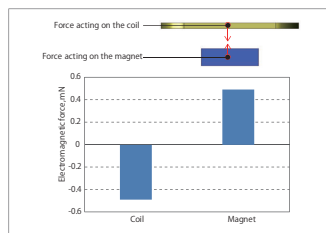


Fig. 1. Attractive and Repulsive Forces Acting Between Coil and Magnet

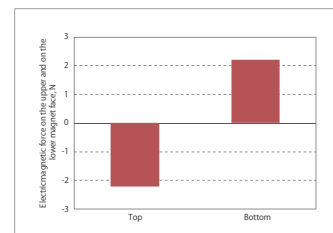


Fig. 2. Forces Acting on the Magnet

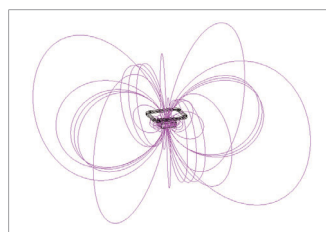


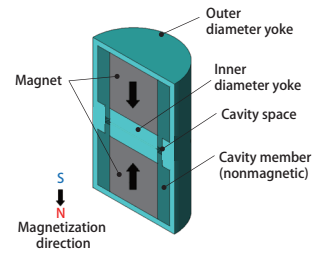
Fig. 3. Magnetic Field Lines Extending in Air

Magnetic Circuit Optimization for Plastic Magnets in a Radial Magnetic Field

module: ST

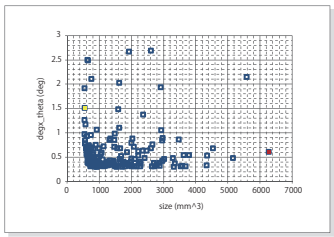
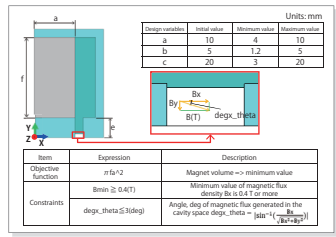
Overview

Plastic magnets are magnets formed from pellets made by mixing magnetic powder and resin binder. Depending on the manufacturing method, compression molding, extrusion molding, or injection molding are used. Plastic magnets are light weight with high strength and have a high degree of freedom in shaping, and very suitable for mass production. Anisotropic plastic magnets with good magnetic properties need magnetic field orientation. For this reason, a magnetic circuit is created to generate the magnetic flux necessary for magnetic field orientation in the product cavity in the mold used. The design requirements of the magnetic circuit are that the magnetic flux generated in the cavity obtain a necessary and sufficient magnitude for magnetic field orientation, that uniform and parallel magnetic flux can be obtained, and that the magnetic circuit be formed as small as possible. Furthermore, the price of the magnetic circuit magnets are high compared to the other magnetic circuit components, so reducing the size of the magnets is effective for lowering the cost. In the case of simple magnetic circuits, these requirements can be met by hand calculation, but FEA is effective for obtaining a generated spatial magnetic flux density distribution, angles, etc. in detail in the cavity. In addition, since trial and error cannot be avoided in an optimum design that minimizes geometry size while satisfying the above requirements, and time is consumed, automation of analysis combined with optimization tools is widely used. In this example, a use case of magnetic circuit optimization in a metal mold with radial magnetic field orientation used for ring-shaped magnet production is presented.



Optimization Conditions

Fig. 1 shows the design variables, objective function, and constraints used for optimization conditions. The design variables are a radius a and a height f of one magnet and e is the height of the yoke. The objective function is defined so that the volume πfa^2 of the magnet is minimized. The constraints specify the maximum limit of the angle formed by the magnetic flux density B generated in the cavity with respect to the X -axis, and the minimum limit of the magnitude of B . In this use case, two constraints are defined. One is that the angle formed with the X -axis be within ± 3 deg and the other is that B_x be greater than or equal to 0.4 T.



Optimization Results

Fig. 2 and Fig. 3 show the graphs of the response values $degx_theta$ and $Bmin$ vs. size obtained by optimization. The cases where the $Bmin$ and $degx_theta$ constraints are not satisfied are not included in the graphs. The initial value is shown in red and the optimum value is shown in yellow. For the initial value shown in red, size indicating the volume of the magnet is approximately $6,300$ mm^3 . Whereas for the optimum value shown in yellow the volume of the magnet is 555 mm^3 , which is about 11 times smaller than the initial value. The optimum value plot shown in Fig. 2 and in Fig. 3 are for the same case. Fig. 4 shows the magnetic flux density contour plot and flux lines for the initial geometry and for the optimized geometry. It can be confirmed that the magnetic flux density of the cavity satisfies both the $Bmin$ and $degx_theta$ constraints, and that a parallel and uniform magnetic flux density can be obtained. Table 1 shows the initial values of the variables a , e , and f and the same values obtained from optimization.

Fig. 1. Optimization Conditions

Fig. 2. Magnet Volume and Angle Graph (Cases Satisfying Constraints)

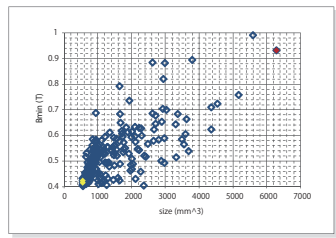


Fig. 3. Magnet Volume and Magnetic Flux Density Graph (Cases Satisfying Constraints)

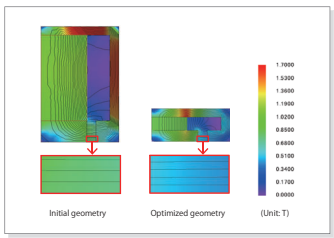


Fig. 4. Optimized Results (Magnetic Flux Density Contour Plots, Magnetic Flux Lines)

Design variables	a	e	f
Initial value	10.0	5.0	20.0
Optimized values	7.7	2.6	3.0

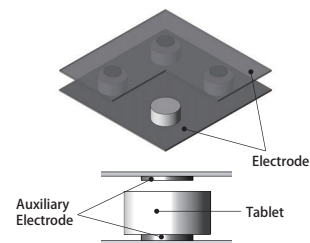
Table 1. Initial Values and Optimized Values

Case 249 Dielectric Heating Analysis of a High-Frequency Preheater with Parallel Plate Electrodes

module: EL, HT

Overview

When creating a resin mold with thermosetting resin, there is a method to beforehand raise the resin temperature to just before the curing temperature. This allows molding using a small molding pressure. To raise the resin temperature, a high-frequency preheater using dielectric heating is used. The electrodes of the high-frequency preheater consist of parallel plate electrodes and roller electrodes. The parallel plate electrodes are suitable when there are many heating materials, and by using auxiliary electrodes it is possible to control the range where temperature is raised. Since the temperature distribution is dependent on for example the shape of the auxiliary electrodes, it is necessary to check whether the target temperature is reached in a range containing the high temperatures of interest. With FEA, it is possible to visualize the temperature distribution inside a material which is difficult to actually measure, making evaluations easy. In this example, a use case evaluating the influence on the temperature distribution of materials (tablets) with and without auxiliary electrodes is presented.



Positional Relationship Between a Tablet and Its Associated Electrodes

Fig. 1 shows the positional relationship between a tablet and its associated electrodes. The generated electric field is affected greatly by the distance between the electrodes. The distance between an electrode and the tablet is fixed whether or not an auxiliary electrode is used.

Electric Field Loss Density Distribution

The dielectric loss density distribution is shown in Fig. 2, and the electric field strength distribution is shown in Fig. 3.

From Fig. 2, it can be seen that when there is no auxiliary electrode the loss on the side surface (perpendicular to the radius) is high, and when there is an auxiliary electrode the loss toward the center radially is high.

From Fig. 3, it can be seen that the electric field concentrates toward the center radially with an auxiliary electrode. The dielectric loss is affected by the physical characteristics, frequency, and electric field. In this use case since the physical properties and frequencies are the same with and without an auxiliary electrode, the difference in the dielectric loss distribution with and without an auxiliary electrode can be said to be due to the difference in the electric field strength distribution with and without auxiliary an electrode.

Temperature Distribution

The temperature distribution after heating for 90 sec is shown in Fig. 4. Differences also appear in the temperature distribution with and without an auxiliary electrode. From this it can be seen that with an auxiliary electrode it is possible to concentrate greater heat near the center of an electrode extending the greater heat area to the center of the tablet.

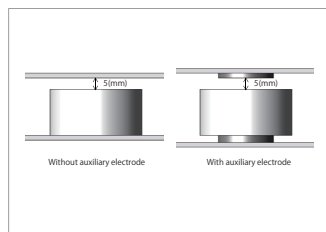


Fig. 1. Positional Relationship Between Electrode and a Tablet

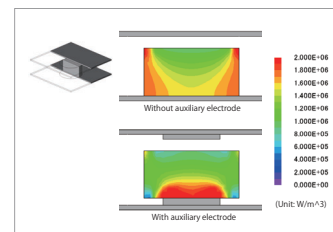


Fig. 2. Dielectric Loss Density Distribution

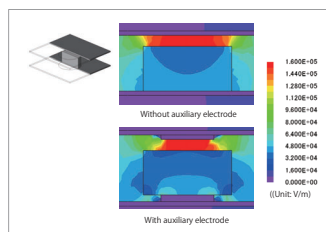


Fig. 3. Electric Field Intensity Distribution

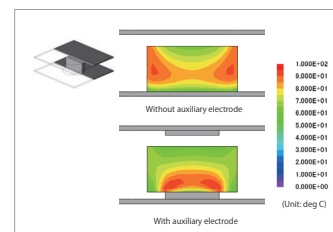


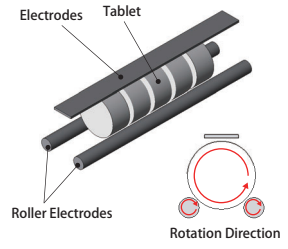
Fig. 4. Temperature Distribution (After 90 sec)

Case 250 Dielectric Heating Analysis of a High-Frequency Preheater with Roller Electrodes

module: EL, HT

Overview

When creating a resin mold with thermosetting resin, there is a method to beforehand raise the resin temperature to just before the curing temperature. This allows molding using a small molding pressure. To raise the resin temperature, a high-frequency preheater using dielectric heating is used. The electrodes of the high-frequency preheater consist of parallel plate electrodes and roller electrodes. The roller electrodes rotate the tablets and heat them, so they are suitable for uniform preheating. Furthermore, by changing the pitch of the roller electrodes, the temperature distribution can be controlled. With FEA, it is possible to visualize the temperature distribution inside a material which is difficult to actually measure, making evaluations easy. In this example, a use case is presented where the influence of the pitch of roller electrodes on the temperature distribution of a material (tablets) is evaluated.



Roller Electrode - Tablet Positional Relationship

Fig. 1 shows the positional relationship between the roller electrodes and the tablets. The pitch of the roller electrodes is set to 90 deg and 40 deg. Also, the distance between the roller electrodes and the tablets is fixed.

Dielectric Loss Density

The dielectric loss density distribution is shown in Fig. 2, and the electric field strength distribution is shown in Fig. 3. From Fig. 2, it can be seen that when the pitch of the roller electrodes is 90 deg the loss at the circumferential surface of the tablets is high, and when the pitch is 40 deg the loss interior to the circumferential surface of the tablets is high. From Fig. 3, it can be seen that by reducing the pitch of the roller electrodes, the electric field inside the tablets concentrates interior to their circumferential surfaces. The dielectric loss is affected by the physical characteristics, frequency, and electric field. In this use case, since the physical characteristics and frequency are common for both analysis targets, the difference in the dielectric loss distribution from the difference in the pitch of the rollers can be said to be due to the difference in the electric field strength distribution.

Temperature Distribution

The temperature distribution during heating is shown in Fig. 4 to Fig. 6, and the temperature change between the radial centers and circumferential surfaces of the tablets is shown in Fig. 7 and Fig. 8. Due to the differences in pitch of the roller electrodes, a difference also is exhibited among the temperature distributions. It can be seen that when the pitch is 90 deg, heating is more prominent towards the circumferential surface of the tablets, but when the pitch is 40 deg the temperature difference between the radial centers and at the circumferential surfaces of the tablets is small during heating.

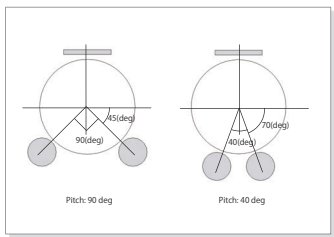


Fig. 1. Positional Relationship Between Roller Electrodes and Tablets

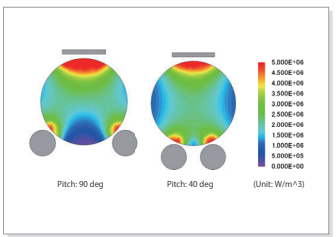


Fig. 2. Dielectric Loss Density Distribution

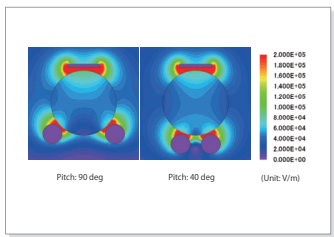


Fig. 3. Electric Field Intensity Distribution

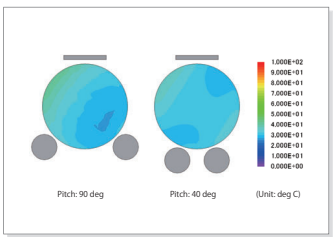


Fig. 4. Temperature Distribution (After 10 sec)

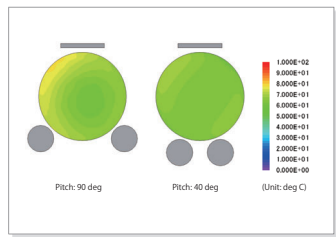


Fig. 5. Temperature Distribution (After 40 sec)

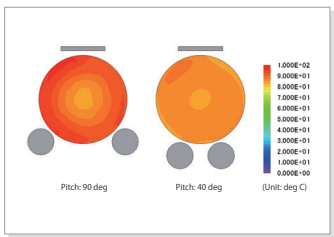


Fig. 6. Temperature Distribution (After 60 sec)

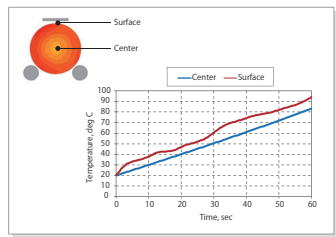


Fig. 7. Temperature Change (Pitch: 90 deg)

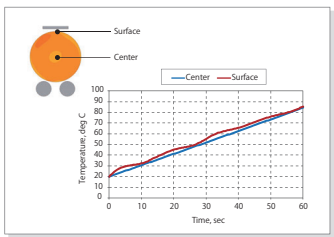


Fig. 8. Temperature Change (Pitch: 40 deg)

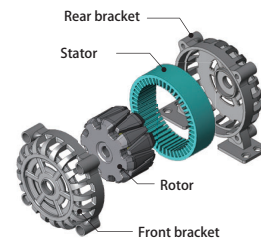
Case 251 Alternator Vibration Analysis

module: DS, TR

Overview

Electromagnetic force in the form of an electromagnetic excitation force acting on a motor or an alternator causes vibration and noise. Vibration and noise are produced when this electromagnetic excitation force resonates with an eigenmodes of the motor. In order to accurately evaluate this phenomenon, it is necessary to ascertain each frequency and spatial mode in detail about the electromagnetic force and eigenmodes of the motor. FEA is useful in advance at the design stage for ascertaining the situations where large vibrations and noise occur, and for analyzing the factors involved and taking countermeasures.

In this example, the electromagnetic force generated in the stator core of a claw pole alternator is obtained, and acceleration is evaluated with an electromagnetic force - structural coupled analysis on the alternator. In addition, the frequency components of the electromagnetic force and the eigenmodes and spatial modes are analyzed to obtain the sources of resonance.



Electromagnetic Force

The electromagnetic force distribution for one electrical angle period at steady-state is obtained. When rotating a 16-pole rotor at 1,500 r/min, 200 Hz is the fundamental frequency. Fig. 1 shows the electromagnetic force frequency components.

In general, the electromagnetic force acting on a stator tooth has a frequency component (secondary component) which is twice the fundamental frequency, but if the rotor is a claw-pole rotor, since the N-pole and S-pole widths are different, the fundamental component is included as well. In particular, the magnitude of the fundamental component included differs between the axial center and either end of a claw pole. Fig. 2 shows the electromagnetic force time history.

Eigenmode

The stator is fixed between the front and rear brackets. Since each part is connected using bolt holes, rigid body conditions are used to model these connections. In addition, the bolt holes for mounting the rear bracket are completely constrained simulating a mounted bracket.

Fig. 3 shows the constraint conditions. Fig. 4 shows the 2nd- to 4th-order ring modes and their eigenfrequencies of the stator.

Sound Pressure Level Evaluation and Vibration Analysis

Vibration analysis is performed for each electromagnetic force frequency component obtained from magnetic field analysis in order to determine sound pressure levels. Fig. 5 shows the sound pressure levels.

The ring modes can be checked by computing the vibration spatial modes from accelerations of the stator outer circumference at 3.6 kHz and 7.2 kHz. Fig. 6 shows the spatial mode order analysis.

It can be seen that the effects from the 3rd- and 4th-order ring modes are large. Fig. 7 shows the sound pressure level distribution.

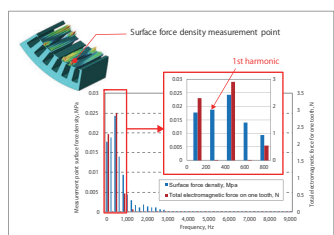


Fig. 1. Surface Force Density and Electromagnetic Force Frequency Components

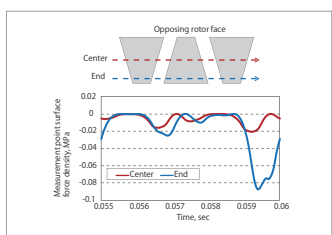


Fig. 2. Electromagnetic Force Time History

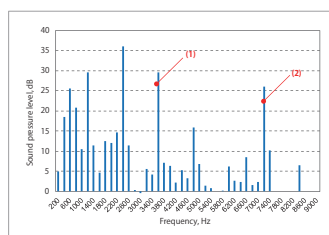


Fig. 5. Sound Pressure Levels

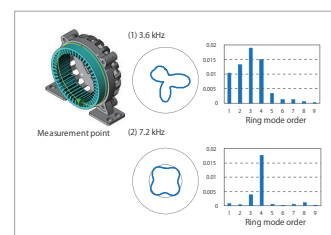


Fig. 6. Spatial Mode Order Analysis

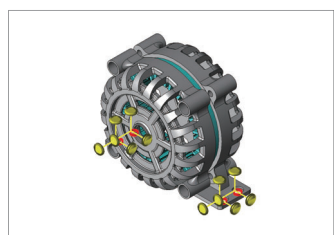


Fig. 3. Constraint Conditions

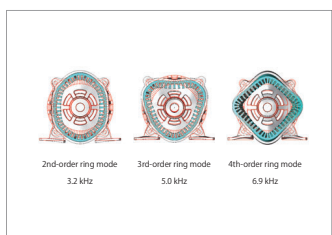


Fig. 4. Eigenmodes

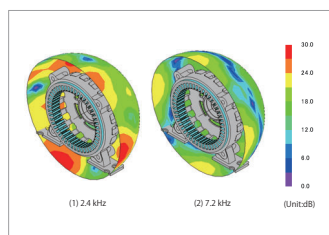
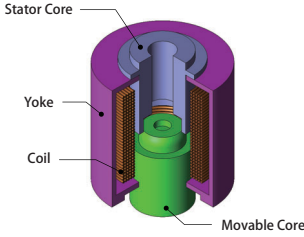


Fig. 7. Sound Pressure Level Distribution

Overview

For the good functioning of a solenoid valve, we want that the solenoid valve is as responsive as possible to the opening and closing commands. For this, we want to optimize the rise time of the solenoid valve's mover. But at the same time we want to make sure that the volume of the solenoid valve doesn't increase much. In this example, we introduce the case study that optimize the shape of a solenoid valve using a multi-objective optimization algorithm.



Optimization Conditions

The rise time of the mover is measured from the time the coil is feed to the time the mover reaches its final position.

We will therefore look at the impact of shape of the mover has on the rise time of mover. Fig. 1 shows geometrical design parameters that will be changed in the solenoid valve. The dimensions presented are all defined by two parameter: Radius and Shoulder_coefficient. Equations in shows the relation between all the geometric parameters.

For this case study, we will set the optimization to minimize the rise time of the mover as well as the volume of the mover. The constraint and set in this optimization study are all described in Table 1.

Stator Radius = Radius
 Shoulder Radius = Radius × Shoulder_coefficient
 Shoulder Stator = 1.125 × Radius × Shoulder_coefficient

Results

Looking simply at the rise time depending on the volume of the valve in Fig. 2. We can see that increasing the Radius / Volume decreases the time needed for the mover to reach its final position. The minimal rise time being set 12.8 msec with a Radius of 7.9 mm and a Volume of 15.6 cm³.

This represent an decrees of 50 % in Rise time but an increase of 56 % in Volume from the base model.

To find the best compromise between rise time and volume we introduce a volumetric rise time. It will be the product of the rise time of a geometry by its volume.

This is illustrated in Fig. 3 where we found that the best compromise is a rise time of 14.6 msec and a Radius of 6.1 mm. It increases the volume of the valve by 20 %. but on the other hand, it decreases the rise time by 40 %. Giving a better rise time for the space used.

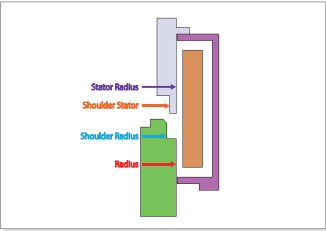


Fig. 1 Geometrical design parameters

Design parameters	Min. value	Max. value
Radius	5 mm	8 mm
Shoulder_coefficient	0	0.8
Constraint		
Radius × Shoulder_coefficient ≥ 2		

Table 1 CAD constraint

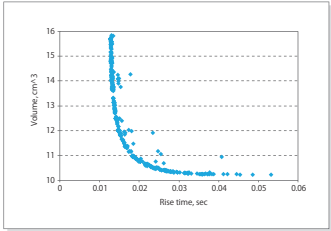


Fig. 2 Rise time - Volume

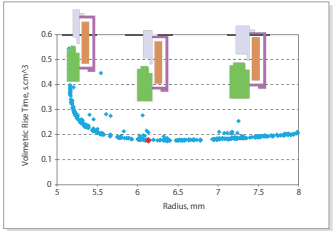


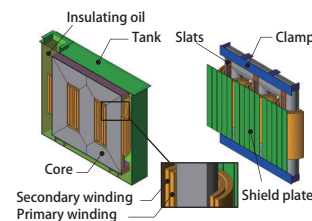
Fig. 3 Radius - Volumetric Rise Time

Case 254 Vibration Analysis of a Large Oil-Filled Transformer

module: DS, FQ

Overview

Fig. 1 shows the electromagnetic force distribution of the core, Fig. 2 shows the magnetostrictive force distribution of the core, and Fig. 3 shows the electromagnetic force distribution for the tank. Also, the leakage flux and eddy current distribution for the tank are shown in Fig. 4. The core and tank excitation sources are focused on. The excitation sources of the core are the electromagnetic and magnetostrictive forces generated in and on the core. Furthermore, the vibration source of the tank is the electromagnetic force affecting eddy currents generated in and on the tank which are generated from leakage flux from the core reaching the tank. From Fig. 1 to Fig. 3, it is clear that the magnetostrictive force is the dominant force in the excitation force. From Fig. 4, it can be seen that the leakage flux interlinks with the tank generating eddy currents.



Excitation Force Distribution

Core electromagnetic force distribution is displayed in Fig. 1, core magnetostrictive force distribution is displayed in Fig. 2, and tank electromagnetic force distribution is displayed in Fig. 3. Tank magnetic flux leakage and eddy current is additionally displayed in Fig. 4. It is understood that magnetostrictive force is dominant as the magnitude of the excitation force, as indicated Fig. 1 to 3. From Fig. 4, it can be seen that a generation of eddy currents follows the linkage of tank magnetic flux leakage. The electromagnetic force acting on these eddy currents is the tank's main source of vibration.

Acceleration Distribution

Fig. 5 shows the acceleration distribution of the core, and Fig. 6 shows the acceleration distribution of the tank. The excitation force was dominated by the magnetostrictive force of the core, but the vibration is seen to be larger in the tank than in the core. It is thought that this is due to the low rigidity of the tank. In addition, since the vibration on the side where the shielding plates are not installed is large, it is thought that by adding shielding plates to this side as well excitation force and vibration can be reduced.

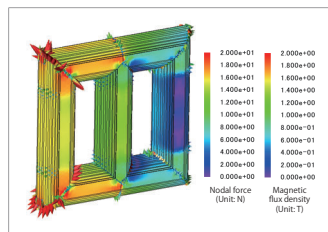


Fig. 1. Core Electromagnetic Force Distribution

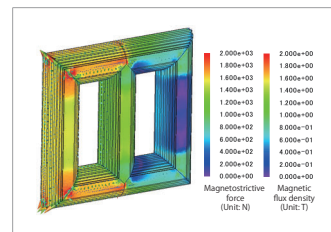


Fig. 2. Core Magnetostrictive Force Distribution

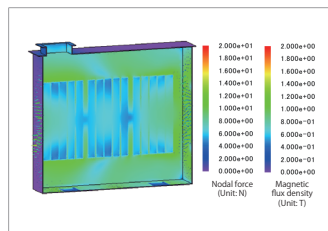


Fig. 3. Tank Electromagnetic Force Distribution

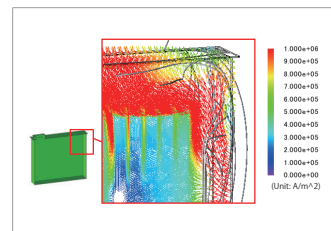


Fig. 4. Tank Leakage Flux and Eddy Currents

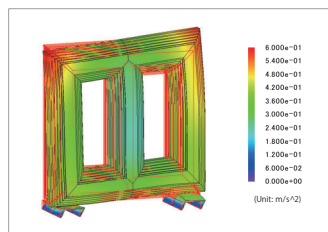


Fig. 5. Core Acceleration Distribution

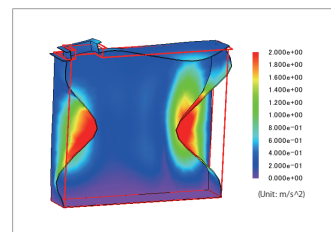


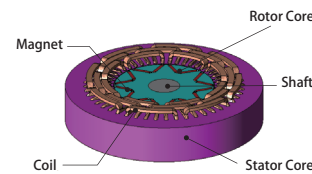
Fig. 6. Tank Acceleration Distribution

Case 255 Evaluating the N-T Curve of an IPM motor Using 3D Correction

module: TR

Overview

Since control design and motor design are designed by different designers, cooperative design is difficult. However, in order to meet the sophisticated demands in recent years, it is important to identify problems while coordinating motor design and control/circuit design at the early stages of development. In cooperative design, it is possible to utilize circuit simulation using a highly accurate plant model. In JMAG, it is possible to create motor models that can model actual machines in detail taking into account magnetic saturation characteristics and spatial harmonics in the motor. By incorporating the JMAG-RT motor model into a control/circuit simulator, it is possible to perform coupled simulation taking into account both the magnetic saturation characteristics and spatial harmonics of the motor and the control characteristics of the motor driver. In recent years, due to motors becoming thinner and power output increasing, 2D model approximations during plant model creation are no longer able to be used. However, by performing 3D analysis for some operating points and correcting the characteristics of the plant model used, it is possible to improve the model accuracy while suppressing the computation time. In this example, obtains N-T curves using the correction function.



N-T curves

An N-T curve for a 3D model, a 2D model, and a 2D model with correction are shown in Fig. 1. It can be seen that there is a large difference in the maximum torque at low speed between the 3D model and the 2D model. This is because for the 2D model the torque is overestimated because the magnetic saturation at the motor end is underestimated. N-T curve becomes the same as 3D by using correction.

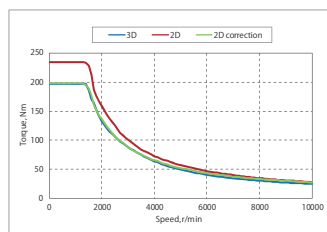
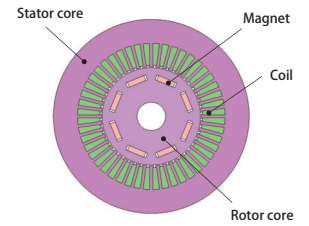


Fig. 1. N-T curves

Case 257 IPM Motor Topology Optimization

module: DP, DS



Overview

Motor design requirements are becoming more sophisticated. While satisfying torque ripple and back electromotive voltage, line voltage limits, magnet demagnetization resistance, the stress on cores, and displacement constraints due to centrifugal force, it is required that torque is maximized at both low and high speeds.

Optimization that uses FEA is effective in satisfying these strict requirements. Parameter optimization that can change dimensions to parametrics depends on the topology of the initial geometry that is the optimum geometry. Topology optimization capable of making significant changes to part layout can make changes to topology and perform searches in wider design spaces.

In this example, rotor core maximum stress and radial direction maximum displacement in the radial direction are set to certain values or less, and rotor geometry is designed that minimizes the torque ripple and maximizes the average torque value. Sensitivity analysis is then performed afterwards.

Optimization Conditions

Fig. 1 shows the design region, and Table 1 shows the evaluation items and objective function.

Fig. 1 shows that the design region is situated near the magnet and the gap which are considered to have a large effect on von Mises stress and torque.

Optimization Results

The transitions in the torque average values and torque ripple rates for the best cases of each generation are shown in Fig. 2. The von Mises stress distribution for the best cases throughout all generations are shown in Fig. 3, with various quantities shown in Table 2.

A state of convergence where torque average values grow larger with each generation and torque ripple rates grows smaller can be confirmed.

It is understood that in the best cases, results that satisfy von Mises stress and radial direction displacement constraints are obtained.

Sensitivity Analysis Results

Torque waveforms and magnetic flux lines are shown in Fig. 4 and Fig. 5 respectively for when grooves are present and absent in the rotor core surface for the geometry obtained with optimization. Unlike case optimization, no smoothing is performed for the boundary faces between materials, meaning that results with grooves differ from optimization results.

Although optimization uses the grooves because the torque ripple rate improves when the grooves are present, the effect is rather small, and no significant changes to magnetic flux flowing from the rotor to the stator teeth can be observed. As such, it is thought that even an absence of grooves is acceptable for the design.

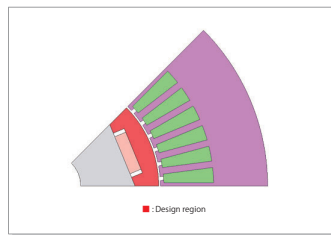


Fig. 1. Design Region

Evaluation item	Objective function
Torque average value	Maximize the torque average value.
Torque ripple	Torque ripple rate is minimized.
Von Mises stress maximum value	Rotor core internal von Mises stress is a maximum value of 200 MPa or less.
Displacement maximum value	Rotor core radial direction displacement is a maximum value of 200 MPa or less.

Table 1. Evaluation Items and Objective Functions

Item	Value
Average torque, Nm	20.7
Torque ripple, %	2.47
Stress maximum value, MPa	86.4
Displacement maximum value, mm	0.00915

Table 2. Various Evaluation Value Quantities

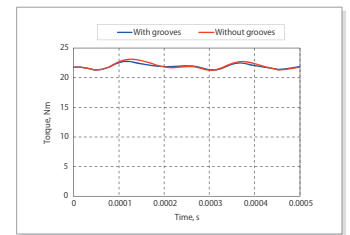


Fig. 4. Torque Waveform

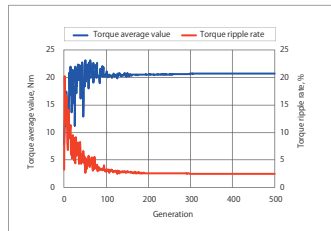


Fig. 2. Transitions in Torque Average Values and Torque Ripple

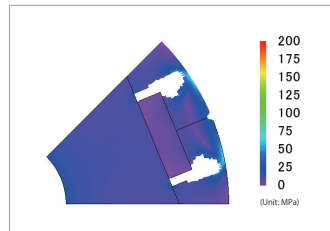


Fig. 3. Von Mises Stress Distribution

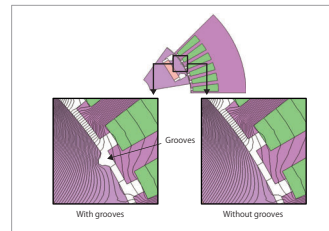


Fig. 5. Magnetic Flux Lines

Case 258 Magnetic Shield Geometry Optimization

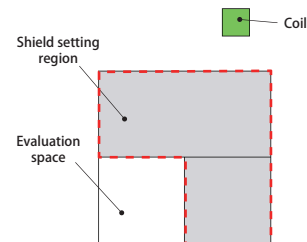
module: ST

Overview

In electrical device design, due to increasing demand, optimal design using trial and error is being studied. In recent years, topology optimization that can significantly change the geometry itself has been attempted, and novel designs heretofore not considered are being created.

By using FEA, it is possible to optimize a sensitivity analysis (density method) topology using the material density in the design region as a design variable. For relatively simple problems, from evaluating the influence (sensitivity) of design variables on objective functions such as for maximizing torque or minimizing loss it is possible to speed up convergence and achieve a topology optimization with a small number of cases.

In this example, a case study in which the geometry of a magnetic shield is optimized using topology optimization that uses a sensitivity analysis (density method) is presented. Due to the material density distribution, topology changes, magnetic energy changes, and the optimal case magnetic flux lines can be checked.



Changes in Topology

Fig. 1 shows the material density distribution (during changes in topology) during topology optimization calculation process.

As the optimization progresses, the geometry gradually gets determined, resulting in a multi-layer shield geometry from minimizing the magnetic energy in the evaluation region.

Changes in Magnetic Energy During Optimization Processing

Fig. 2 shows the history of magnetic energy changes during the topology optimization. From the air layer and the magnetic layer alternating going from the outermost layer to the innermost layer, it can be seen that the magnetic resistance increases and the magnetic energy decreases in the direction of the magnetic flux.

Optimal Case Magnetic Flux Lines

Fig. 3 shows the magnetic flux lines flowing in the shield design region for the optimal case.

It can be seen that the most of the magnetic flux flows along the shield. Also, it can be seen that the leakage magnetic flux has not entered the evaluation region due to the innermost layers.

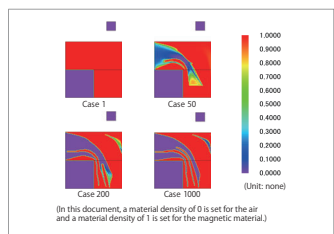


Fig. 1. Material Density Distributions During Optimization Processing

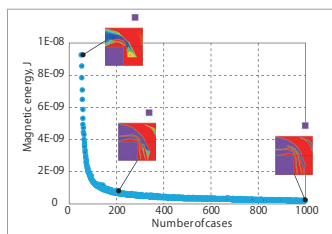


Fig. 2. The Progressing of Optimization Processing and Changes in the Magnetic Energy

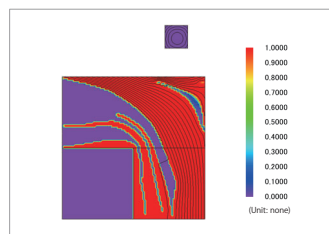
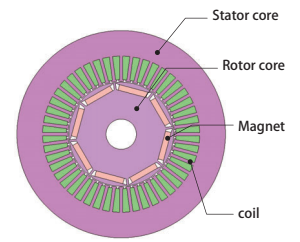


Fig. 3. Optimal Case Magnetic Flux Lines



Overview

In the low speed side of an N-T curve, there is a region where the maximum torque is constant regardless of the rotation speed because of current limitations. In this region, the current phase that maximizes torque is selected. When designing motor components, many designs are compared using dimensions as design variables. In such situations, the current phase with maximum torque will differ depending on motor geometry. In order to obtain this, what is required is an evaluation of the phase with maximum torque per geometry in advance using FEA.

When comparing a large number of designs using simulations, torque characteristics can be evaluated by automatically searching for the current phase that provides the maximum torque.

In this example, a search is performed for the current phase that maximizes torque for each of 3 rotor geometries. Motor average currents and torque ripples are evaluated using the obtained current phases.

Evaluation Details

Inductance values are calculated at 10 deg increments in the current phase range of 0 to 60 deg calculated from 3 rotor geometry cases, obtaining values L_d , L_q , l_d , l_q , and φ .

From inductance evaluation results, torque is obtained with torque formulas for each rotor geometry, and a search is performed for the current phase that obtains maximum torque. Motor torque analysis is performed with the obtained current phase, from which the average torque and ripple ratio are obtained. Fig. 1 shows the evaluation flow.

Current Phase - Torque Graph

Fig. 2 shows the current phase - torque graph. From this, the current phase where the torque is maximum is found for each rotor geometry. The current phases for the maximum torque for cases 1 to 3 are shown in red.

Average Torque and Ripple Ratio

Fig. 3 shows the average torque and ripple ratio at the current phase for maximum torque. These values are calculated from the current phase showing maximum torque obtained from the inductance shown in Fig. 2.

Comparison Between Torque Values Obtained With the Torque Formula and FEA

Fig. 4 shows the graph comparing the torque value obtained with the torque formula at each current phase for Case 1 geometry, and the average torque value obtained with FEA. Because the torque value obtained with the torque formula is of a fixed inductance, the value is high when compared to the FEA results that account for the influence of magnetic saturation. In this model, torque shows the maximum at a current phase of 30 deg for both FEA and the value obtained from the torque formula, and it can be confirmed that current phase values match.

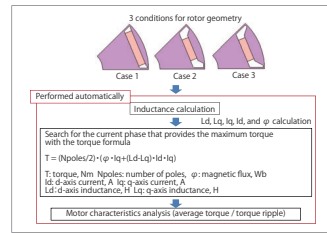


Fig. 1. Evaluation flow

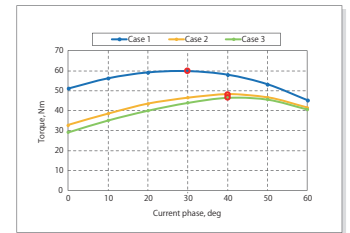


Fig. 2. Current Phase - Torque Graph

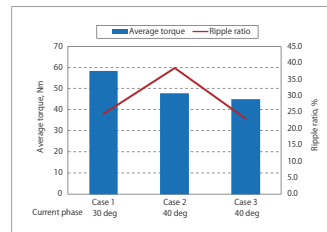


Fig. 3. Average Torque and Ripple Ratio at the Current Phase Showing Maximum Torque

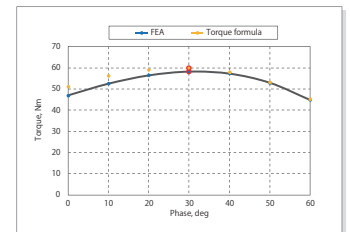


Fig. 4. Comparison Between Phase and Torque Curve from FEA and the Torque Formula (Case 1 geometry)

Case 260 Creating Axial Gap-Type Motor Efficiency Maps

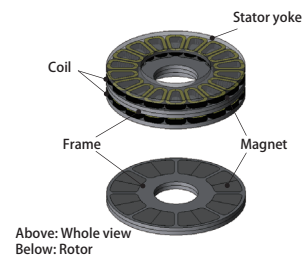
module: LS, TR

Overview

Axial gap-type motors can consist of a thinner construction than that of radial gap-type motors, and are used for in-vehicle motors where available space is otherwise compromised. Because in-vehicle motors are additionally driven at a wide range of operating points, motor performance is evaluated using efficiency maps.

Efficiency maps require a significant amount of calculations, and organizing results can also take a considerable amount of time. Although it is possible to estimate efficiency by calculating the torque, voltage, and current from motor voltage equations and torque equations, there exists several issues in the difficulty involved in using this method to estimate loss and account for the effects of the nonlinear magnetization characteristics of the motor iron core, as well as accurately calculating efficiency, which can also prove to be similarly challenging.

Through simulations using the finite element method, however, efficiency maps that account for the effects iron loss and nonlinear magnetization characteristics can be written with ease. Comparing motor performance in varying design proposals is also a simple process. In this example, the motor performance of axial gap-type motors with changes made to the flatness ratios.



Comparison Conditions

Flatness ratios are defined by axial length/diameter. Design proposal A that has a flatness ratio of 0.24 is compared with design proposal B that has a flatness ratio of 0.42. Motor volume, gap length, magnet quantity, and windings remain the same for both design proposals.

Efficiency Maps

The efficiency maps for design proposals A and B are shown in Fig. 2, while the copper loss maps are shown in Fig. 4.

From Fig. 2, it is understood that maximum torque is large in low-speed regions for design proposal A, and design proposal B reaches high efficiency in high-speed regions. A low flatness ratio means a larger gap surface area where torque can be generated, therefore increasing maximum torque. A high flatness ratio decreases the field magnetic flux that occurs due to permanent magnets, and the load d-axis current required for weakening magnetic flux decreases. This leads to a reduction in copper loss, thus leading to high efficiency (Fig. 3, Fig. 4).

It is thereby understood that motor performance can be adjusted by making changes to the flatness ratio of axial gap-type motors.

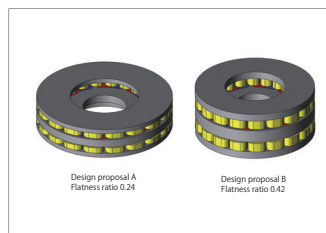


Fig. 1. Design Proposals and Flatness Ratios

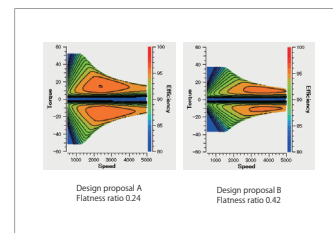


Fig. 2. Efficiency Maps

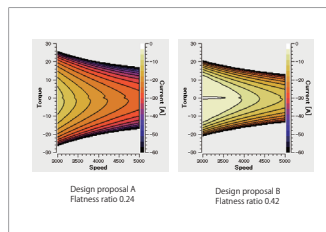


Fig. 3. Id Maps (High-Speed Region Magnification)

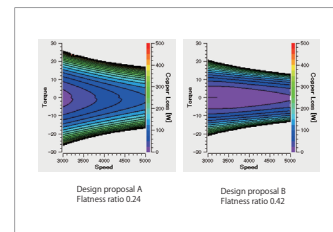
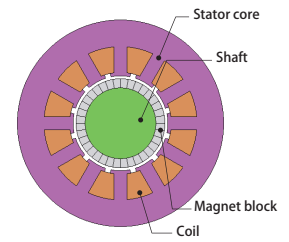


Fig. 4. Copper Loss Maps (High-Speed Region Magnification)



Overview

In general, when the magnetic flux density of a gap approaches a sine wave, harmonic components are suppressed and efficiency improves. A method exists to locally change the coercive force of magnets used in SPM to bring magnetic flux density closer to a sine wave. However, the proper coercive force of magnets is difficult to find through a process of trial and error. In situations such as these, by using optimization, coercive force distribution can be obtained effectively.

In this example, a magnet is segmented into blocks and coercive force is defined. The coercive force of each block is calculated so that the induced voltage waveform approaches a sine wave through optimization. The voltage waveforms are compared between the case where the coercive force distribution obtained by the optimization is used and the case where the same coercive force distribution is used for all magnet blocks.

Rotor Magnetization

The number of poles of the target motor is 4. Therefore, the angle between two poles is 90 degrees.

1 pole uses a magnet block divided into 9 every 10 deg. These are magnetized in the radial direction.

Fig. 1 displays the rotor magnet orientation direction.

Spatial Magnetic Flux Density Evaluation

Fig. 2 shows the spatial magnetic flux density evaluation.

The spatial magnetic flux density is found when the rotor is fixed at no load.

To determine whether close to a sine wave, the total harmonic distortion (THD) that represents the degree of signal distortion is used. Since THD is the ratio of the square root of the sum of the squared harmonic components to the fundamental component, the smaller the THD the closer the induced voltage waveform is to a sine wave.

A different coercive force for each magnet block is set and the THD value is evaluated.

Optimization Conditions

Fig. 3 shows magnet blocks as design variables, design variable ranges, and objective functions.

Design variables are the coercive forces of each magnet block, and the minimum and maximum values indicate the search range.

The primary goal is to minimize THD, but in order to prevent sufficient torque not being obtained due to low spatial magnetic flux density, a constraint is imposed to maximize the fundamental.

By satisfying these, the generated magnetic flux density is at a maximum and the waveform is close to a sine wave.

Objective functions are set to maximize the fundamental and minimize THD using the above gap magnetic flux density evaluation formula.

Pareto Curve

Fig. 4 shows the Pareto curve of the optimization results.

The point shown in green is the initial design, and the points shown in blue are the results obtained from optimization. Here, the design proposal with the smallest THD among the design proposals on the Pareto curve is adopted. The design proposal obtained by optimization is smaller in both fundamental and THD compared to the initial case.

Magnet Block Coercive Force

Fig. 5 shows the magnet block coercive force at the blue point obtained with optimization.

It is understood from the graph that coercive force near the pole center increases.

THD of the Initial Case and Optimized Case

Both initial case and optimized case THD is shown in Table 1.

Compared to the initial case, optimized case THD becomes a value of 1/2 or less. From this, it can be described that the optimized case has a lower ratio of spatial harmonics to the fundamental wave than the initial case, and is a waveform close to a sine wave.

Spatial Magnetic Flux Density Waveform

Radial direction spatial magnetic flux density waveforms are displayed in Fig. 6.

Peaks and valleys are thought to be produced by the positions and angles of the magnets. However, by optimizing the magnet block coercive forces, it can be confirmed that the spatial magnetic flux density has become a waveform close to a sine wave. This is consistent with the results in Table 1 above.

Induced Voltage Waveform

Fig. 7 shows the induced voltage waveform, and Fig. 8 shows the induced voltage frequency components.

Similar to the prior THD and spatial magnetic flux density waveform evaluation results, it can be confirmed that this nears a sine wave through optimization.

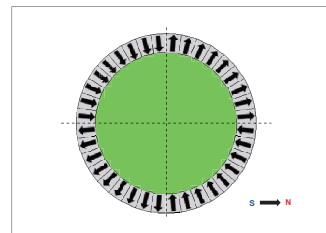


Fig. 1. Rotor Magnet Orientation Direction

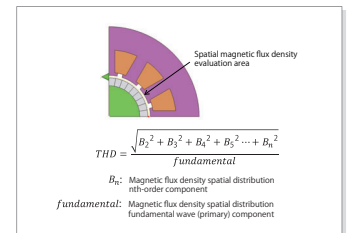


Fig. 2. Spatial Magnetic Flux Density Evaluation

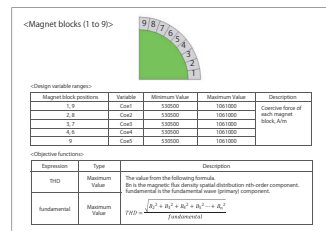


Fig. 3. Optimization Conditions

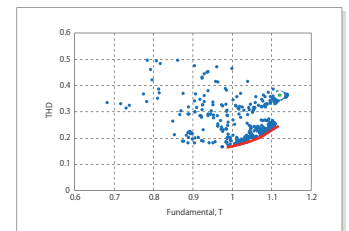


Fig. 4. Pareto Solution

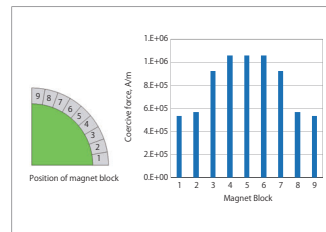


Fig. 5. Magnet Block Coercive Force

	Initial case	Optimized case
THD	0.37	0.17

Table 1. THD

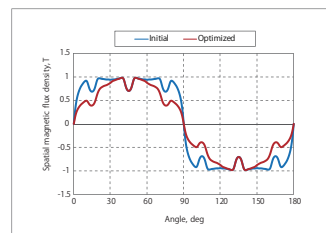


Fig. 6. Spatial Magnetic Flux Density Waveform

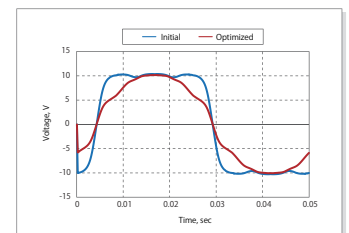


Fig. 7. Induced Voltage Waveform

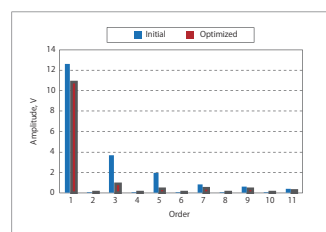


Fig. 8. Induced Voltage Frequency Components

Case 262 IPM Motor Thermal Demagnetization Analysis Accounting for Dy-Diffusion Magnet Incomplete Magnetization

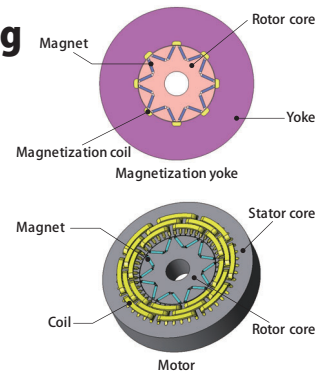
module: DP, ST

Overview

Dy-diffusion magnets can increase demagnetization resistance by distributing a high coercive force on their magnet surfaces. On the other hand, if the magnetization is incomplete, the coercive force is reduced creating areas where demagnetization is likely. Therefore, it is important to consider both the effect of Dy diffusion and the effect of incomplete magnetization.

Using finite element methods, it is possible to define the coercive force distribution and thermal demagnetization characteristics with incomplete magnetization. Motor performance at high temperatures can be evaluated using defined magnet characteristics.

In this example, the thermal demagnetization resistance of a motor is analyzed using Dy-diffusion magnets with a coercive force distribution under incomplete magnetization.



Magnetization Material Determined from Demagnetization Data

Since the demagnetization characteristics after magnetization also depend on the temperature, prepare a characteristic table based on the applied magnetic field during magnetization and the temperature to be used after magnetization. Since the applied magnetic field is not uniform in the magnet, each element has different demagnetization characteristics.

Fig. 1 shows the table of applied magnetic field-temperature-demagnetization characteristics.

Dy-diffusion Magnet Coercive Force Distribution

The Dy-diffusion magnet maximum coercive force is distributed inside the magnet. Fig. 2 shows the coercive force distribution (complete magnetization) of a Dy-diffusion magnet used in this case study.

During incomplete magnetization, the coercive force distribution changes vs. the applied magnetic field.

Magnetization Distributions

Fig. 3 shows the magnet magnetization distributions obtained by in-place magnetization at input currents of 25 kA and 45 kA. The smaller the input current, the smaller the magnet magnetization near the bridge. Incomplete magnetization results where the magnetization is small.

In addition to the effect of the magnitude of the magnetization, the Dy-diffused magnets are also affected by the coercive force distribution. Demagnetization is likely to occur where there is low coercive force and incomplete magnetization.

Torque

Fig. 4 shows the average torque when the magnet temperature is varied.

When the magnetization current is 25 kA, it can be seen that even at 100 deg C the torque is lower than with complete magnetization. From this it is predicted that compared with complete magnetization a decrease in the overall torque over the entire temperature range results due to the entire magnet not being sufficiently magnetized due to the effect of incomplete magnetization at the magnetization current of 25 kA.

Also, the magnetization characteristics change as the temperature rises. Even with complete magnetization, when the temperature is 130 deg C or more, the torque decreases greatly and thermal demagnetization occurs. At the magnetization current of 45 kA, the torque up to 130 deg C is almost the same as that at complete magnetization, but when 130 deg C is exceeded, the torque decreases more than at complete magnetization. This is because with incomplete magnetization there is an area where demagnetization is large, thus at high temperature there is more demagnetization than with complete magnetization. From this the average torque is reduced.

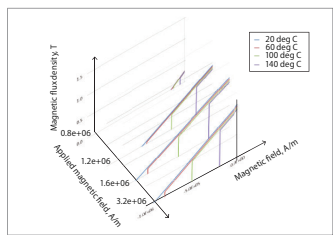


Fig. 1. Applied Magnetic Field - Temperature - Demagnetization Characteristics Table

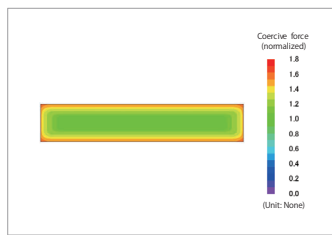


Fig. 2. Dy-diffusion Magnet Coercive Force Distribution (Complete Magnetization)

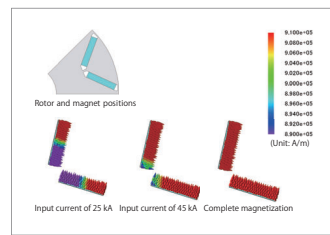


Fig. 3. Magnetization Distributions (Under No-Load)

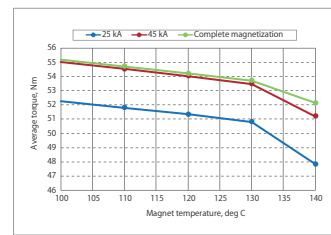


Fig. 4. Magnet Temperature - Average Torque Characteristics

Case 263

IPM Motor Stress Analysis Taking Into Account Friction between Magnets and the Rotor Core

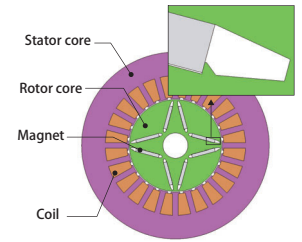
module: DS

Overview

In an IPM motor, magnets experience centrifugal force during high-speed rotation, generate friction while sliding, and are pressed against the rotor core, generating large stress. If the stress acting on a part exceeds its yield stress, plastic deformation occurs, which may cause a change in its properties or cause it to break. Therefore, it is necessary to create a design where yield stress is not exceeded even with centrifugal force.

By using simulation, the effects of centrifugal force can be checked and reflected in design before actually making the motor. During simulation, it is important to accurately simulate plastic deformation and part contacts.

In this example, in order to evaluate how the contacts between the magnets and the rotor core in an IPM motor affect the stress distribution, the von Mises stress is checked when there are rigid contacts and when the magnets are allowed to slide while the friction taken into account.



Core Material Characteristics

Fig. 1 shows the core material characteristics. The yield stress of the material used is 330 MPa.

Von Mises Stress Distribution

Fig. 2 shows a comparison between von Mises stress distributions. Since for a rigid connection there is no slipping, a large stress is generated at the contacts. When taking into account friction, the magnet slides tangentially along contact area with the rotor core, generating large stress at the bridge. The distribution differs between the rigid connection case and the case when friction is taken into account. In actual phenomena, since it is thought that there is sliding and not a contact with a continuous rigid connection, it is understood that it is necessary to correctly model the contact state for accurate evaluation.

The von Mises stress maximum value exceeds the yield stress of 330 MPa. If left as is, plastic deformation occurs and the geometry changes, which may result in changes in characteristics or breakage, indicating that measures such as changing the material are necessary.

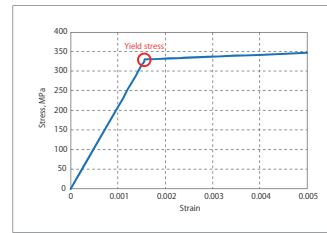


Fig. 1. Core Material Characteristics

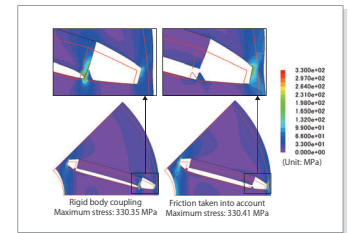


Fig. 2. Von Mises Stress Distribution

Case 264

Creating 6-Phase IPM Motor Efficiency Maps

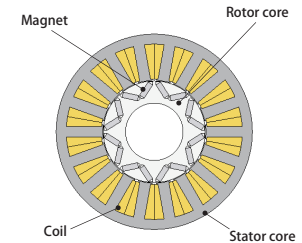
module: DP, LS

Overview

For traction motor, multi-phase design is sometimes employed with the objective of improving redundancy and reducing torque ripple during drive. multi-phase design includes the likes of 6-phase drive using two inverters. Efficiency maps are created for both motor design and control design in order to fully comprehend the characteristics of motors such as Traction motors that are capable of drive within such a wide range.

Torque, voltage, and current can be calculated from motor voltage equations and torque equations for estimating efficiency, but there exists the issue of difficulty in estimating iron loss, as well as accounting for the nonlinear magnetization characteristics of the iron core. Through simulations using FEA, however, efficiency maps that account for the effects of iron loss and nonlinear magnetization characteristics can be obtained with ease.

In this example, the efficiency map of a 6-phase IPM motor is created with loss ratios at each operating point also evaluated.



Efficiency Map and Power Factor Map

The efficiency map is displayed in Fig. 1, and the power factor map is displayed in Fig. 2. Motor mode and generator mode efficiency can be understood from Fig. 1. It can be seen that the high-efficiency region for this motor on the motor mode extends to the high-speed area on the generator mode.

For this motor, it can be understood from Fig. 2 that the ratio of reactive power becomes larger at a low rotation speed in high-torque regions, and the ratio of reactive power becomes smaller in low-torque regions.

Loss Ratios at Each Operating Point

Fig. 3 displays pie charts showing loss ratios at low speed and high load, low speed and medium load, medium speed and medium load, and lastly, high speed and low load. Copper loss decreases in accordance with load. It can be seen that the loss of both the stator core and the rotor core increases in accordance with rotation speed, with eddy current loss increasing in particular.

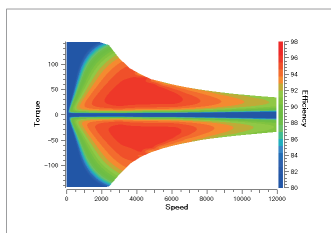


Fig. 1. Efficiency Map

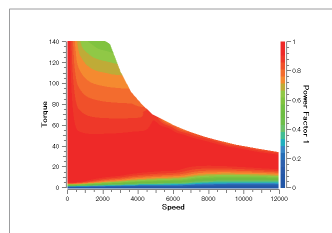


Fig. 2. Power Factor Map

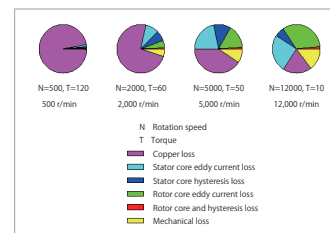


Fig. 3. Loss Ratios at Each Operating Point

Case 265 Creating Synchronous Reluctance Motor Efficiency Maps

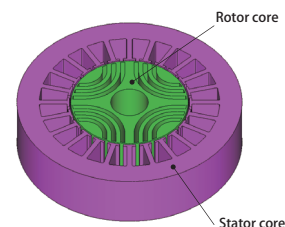
module: DP

Overview

With the increase in price for rare earth magnets, synchronous reluctance motors that do not utilize permanent magnets have been attracting attention for the likes of industrial purposes. Because they do not use permanent magnets or secondary conductors, synchronous reluctance motors can be anticipated to be variable speed motors that are both inexpensive and highly efficient. Efficiency maps are created for both motor design and control design in order to fully comprehend the characteristics of these motors that are capable of drive within such a wide range.

Torque, voltage, and current can be calculated from motor voltage equations and torque equations for estimating efficiency, but there exists the issue of difficulty in estimating iron loss, as well as accounting for the nonlinear magnetization characteristics of the iron core. Through simulations using FEA, however, efficiency maps that account for the effects of iron loss and nonlinear magnetization characteristics can be obtained with ease.

In this example, the efficiency map of a synchronous reluctance motor is created with loss ratios at each operating point also evaluated.



Efficiency Map and Power Factor Map

The efficiency map is displayed in Fig. 1, and the power factor map is displayed in Fig. 2. Motor mode and generator mode efficiency can be understood from Fig. 1. It can be seen from Fig. 2 that this motor has a power factor of 0.7 or less, which is particularly low in both the high-torque region and the low-torque region.

Loss Ratios at Each Operating Point

Fig. 3 displays pie charts showing loss ratios at low speed and high load, low speed and medium load, medium speed and medium load, and lastly, high speed and low load. Copper loss decreases in accordance with load. It can be seen that the loss of both the stator core and the rotor core increases in accordance with rotation speed, with eddy current loss increasing in particular.

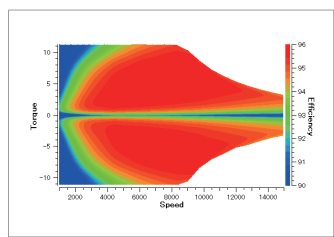


Fig. 1. Efficiency Map

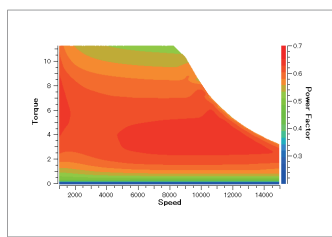


Fig. 2. Power Factor Map

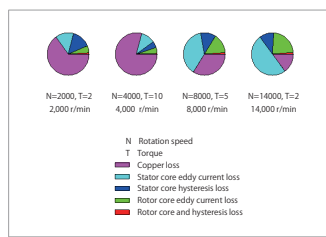


Fig. 3. Loss Ratios at Each Operating Point

Case 267 IPM Motor Topology Optimization Using the Density Method

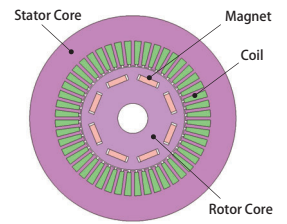
module: DP, DS

Overview

Motor design requirements are becoming more sophisticated. While satisfying the torque ripple rate and back electromotive voltage, line voltage limits, magnet demagnetization resistance, the stress on cores, and displacement constraints due to centrifugal force, it is required that torque is maximized at both low and high speeds.

Optimization that uses FEA is effective in satisfying these strict requirements. Design proposals can be obtained with a high degree of freedom because topology optimization in particular can perform searches that are not dependent on initial shapes.

Magnetic field and structural coupled analysis is run in this example. While accounting for rotor core strength, topology optimization that uses the density method is used to perform searches for a rotor shape that maximizes average torque.



Optimization Conditions

Fig. 1 shows the design region, Table 1 shows the evaluation item and objective functions. The red frame shown in Fig. 1 is the design region. Topology accounts for the symmetry per each 1/2 pole while accounting for the rotor strength.

Optimization Results

The graph for the average torque-torque ripple rate for all cases when both accounting for and not accounting for rotor strength is shown in Fig. 2, and the optimum case average torque and torque ripple rate are shown in Table 2.

Average torque increases when rotor strength is not accounted for.

The results showing the optimum case material density distribution contours and magnetic flux lines when both accounting for and not accounting for rotor strength are shown in Fig. 3.

Flux barriers are generated in either circumstance to suppress the magnetic flux that short-circuits in the rotor, which results in larger average torque. When accounting for rotor strength, however, the formation of a bridge makes it easier for the magnetic flux to short-circuit. It is therefore thought that average torque is larger when not accounting for rotor strength.

The results showing R direction displacement contours for the optimum case when both accounting for and not accounting for rotor strength are shown in Fig. 4.

Not accounting for rotor strength means that the bridge is not generated, and there exists the structural issue of the increasingly large rotor displacement. Accounting for rotor strength means that the bridge is generated, and the displacement is suppressed.

From this we understand that optimization accounting for rotor strength can be useful.

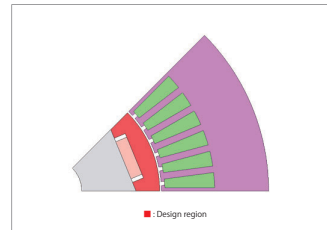


Fig. 1. Design Region

Evaluation item	Objective functions
Average torque	Torque average is maximized.
Torque ripple rate	Torque ripple rate is minimized.
Mean compliance	Mean compliances is minimized.

Table 1. Evaluation Items and Objective Functions

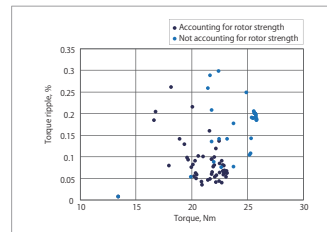


Fig. 2. Average Torque-Torque Ripple Rate for All Cases

Item	Rotor strength accounted for	Rotor strength not accounted for
Average torque, Nm	23.141	25.799
Torque ripple rate, %	0.064	0.187

Table 2. Optimization Case Average Torque and Torque Ripple Rate

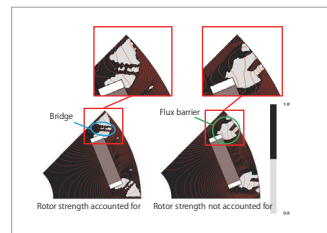


Fig. 3. Optimization Case Material Density Distribution Contours and Flux Lines

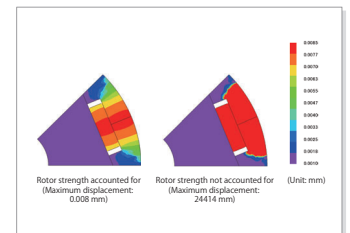


Fig. 4. Optimization Case R Direction Displacement Contours

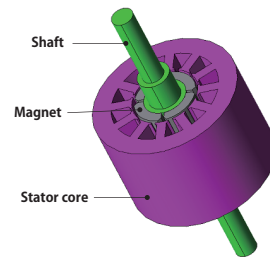
Case 268 SPM Motor Teeth Geometry Topology Optimization

module: DP

Overview

Basic policies for motor design are the maximization of torque and low oscillation. The smaller the torque ripple, the lower the vibrations of the motor. Torque ripple is generally affected by stator teeth geometry. Due to the complexity of the magnetic flux distribution in gap vicinities, expressing detailed teeth geometry with magnetic equivalent circuits can prove to be of considerable difficulty. Performing optimization that uses FEA capable of analyses based on actual geometry can be effective in satisfying these requirements. Optimization results can be obtained with a high degree of freedom because topology optimization additionally performs searches that are not dependent on initial geometry.

In this document, the on / off method is used to search for stator teeth geometry that maximizes average torque and minimizes torque ripple with the entire areas of stator teeth tips as the design region.



Optimization Conditions

Fig. 1 shows the design region, and Table 1 shows the objective functions.

As shown in Fig. 1, the design region is the stator teeth parts, which are thought to have a large influence on torque and torque ripple.

Optimization Results

Fig. 2 shows a correlative diagram between the torque average value and torque ripple rate, and Fig. 3 shows a larger view of the range for the maximum torque and minimum torque ripple from Fig. 2. In Fig. 3, the maximum torque average value is shown at point A as the best case, and the minimum torque ripple rate is shown at point B.

Topology optimization geometries for best cases A and B are shown in Fig. 4 and Fig. 5 respectively.

For best case A which has the maximum torque, material inside the teeth consists entirely of electromagnetic steel sheets. The presence of slot opening parts can also be observed here, whereas in best case B where torque ripple is at a minimum, teeth are connected around the entire arc, and there are no slot opening parts.

Sensitivity Analysis

As so to confirm the influence of teeth geometry on the torque characteristics, sensitivity analysis is performed for each best case.

Consider best case A, which has maximum average torque. Analysis patterns are shown in Table 2, and analysis results are shown from Fig. 6 to Fig. 8. From a comparison between A pattern 1 and A pattern 3, it is understood that the presence or absence of slot opening parts has a small effect on torque characteristics. In A pattern 2, the end parts of the teeth tips are thick, and it can be considered that torque ripple increases because of the steep permeance with the slot opening parts. In A pattern 4, it can be considered that the average torque decreases because the magnet magnetic flux short-circuits at the teeth tip parts.

Consider best case B, which has the minimum torque ripple rate. Compare best case B and A pattern 3 which share similar geometry. Table 3 shows the geometry of A pattern 3 and best case B, and the analysis results are shown from Fig. 9 to Fig. 11. Because magnetic flux flows easier in the iron region for A pattern 3, the maximum torque increases. It can be considered that the reason the torque ripple rate increases is because the magnetic flux where force acts in the opposite direction of rotation flows easily.

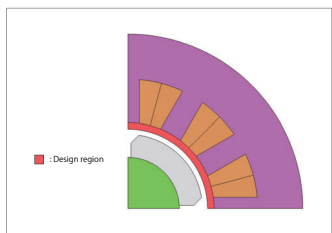


Fig. 1. Design Region

Evaluation item	Objective
Average torque	Maximize
Torque ripple	Minimize

Table 1. Objective Functions

Name	A pattern 1	A pattern 2
Description	Geometry with maximum average torque	Electromagnetic steel sheets other than the slot opening part
Diagram		
Name	A pattern 3	A pattern 4
Description	No slot opening part	Teeth parts are entirely electromagnetic steel sheets
Diagram		

Table 2. Best Case A Sensitivity Analysis Patterns

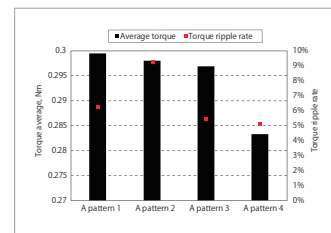


Fig. 6. Torque Characteristics (Best Case A Sensitivity Analysis)

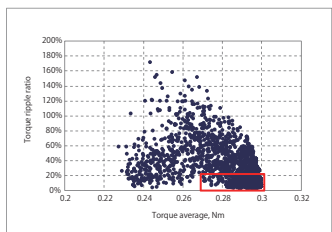


Fig. 2. Correlation Curve Between Torque Average Value and Torque Ripple

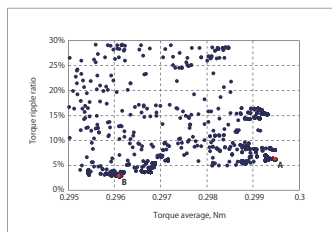


Fig. 3. Correlation Curve Between Torque Average Value and Torque Ripple

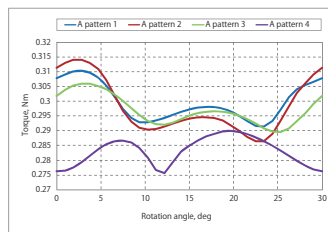


Fig. 7. Torque Waveform (Best Case A Sensitivity Analysis)

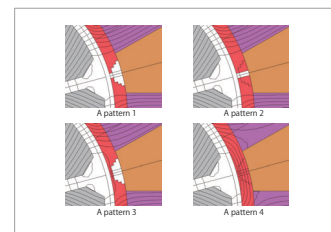


Fig. 8. Air Gap Vicinity Magnetic Flux Lines (Best Case A Sensitivity Analysis)

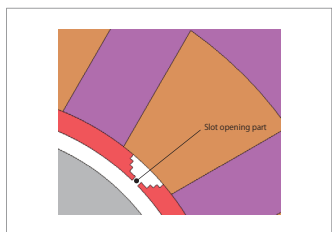


Fig. 4. Topology Optimization Geometry (Best Case A)

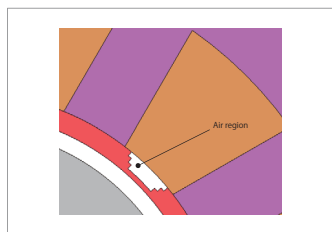


Fig. 5. Topology Optimization Geometry (Best Case B)

Name	A pattern 3	B
Description	No slot opening part	Geometry with minimum torque ripple rate
Diagram		

Table 3. A Pattern 3 and Best Case B

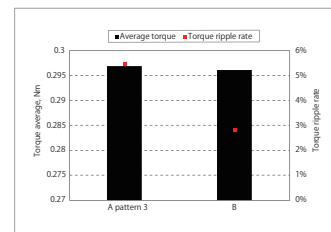


Fig. 9. Torque Characteristics (A Pattern 3 and Best Case B)

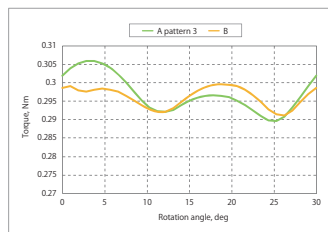


Fig. 10. Torque Waveform (A Pattern 3 and Best Case B)

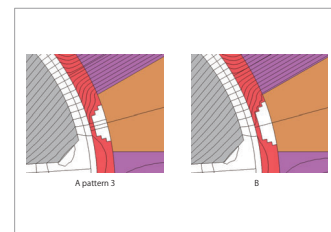


Fig. 11. Air Gap Vicinity Magnetic Flux Lines (A Pattern 3 and Best Case B)

Creating Three-Phase Induction Motor Efficiency Maps Accounting for Harmonics

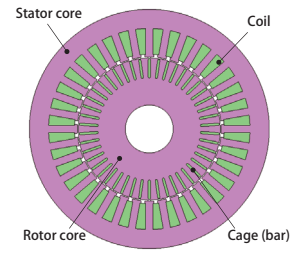
module: DP, LS

Overview

With advances in variable speed operation technology for induction motors, progress is being made in applications to fields where wide operating regions are required. An effective method of evaluating the characteristics of induction motors in fields like these is to create efficiency maps for the operating regions.

Simple calculations that do not account for harmonics that enable the faster creation of efficiency maps are effective for concept designs that are narrowed down from a larger number. When concept designs have then been narrowed down to a certain extent, efficiency maps can then be created which do account for harmonics, which then allows for more accurate evaluations to be run.

In this example, efficiency maps are created for a three-phase induction motor accounting for PWM carrier and slot harmonics. These are compared with efficiency maps when harmonics are not accounted for.



Circuit Diagram

The circuit diagram of the induction motor is shown in Fig. 1. Control is accounted for by the circuit.

Efficiency Map, Ratio Map

An efficiency map not accounting for harmonics is shown in Fig. 2 and an efficiency map accounting for harmonics is shown in Fig. 3. Ratio maps for the total loss, iron loss, and copper loss are shown in Fig. 4, Fig. 5, and Fig. 6 respectively when harmonics are or are not accounted for.

Efficiency at operating point 1600 rpm, 180 Nm is 96.5% when harmonics are not accounted for and 94.7% when harmonics are accounted for, showing a 1.8 point difference. A look at the high-speed region shows a large difference in loss for both iron and copper.

High-Speed Region Loss Components

The breakdown of loss components when harmonics are or are not accounted for in the high-speed region (1600 rpm, 180 Nm) is shown in Fig. 7. When harmonics due to PWM carriers and slots are accounted for, both iron and secondary copper losses are larger than when harmonics are not accounted for because the corresponding iron and secondary copper losses are included.

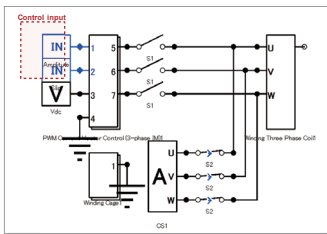


Fig. 1 Induction motor circuit

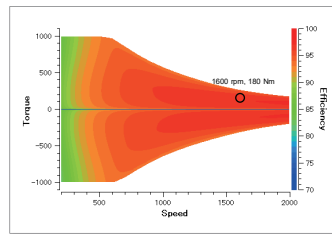


Fig. 2. Efficiency map not accounting for harmonics

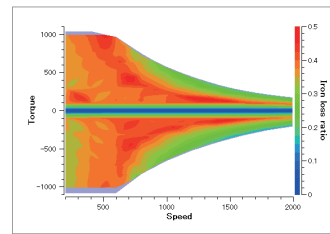


Fig. 5. Iron loss ratio map

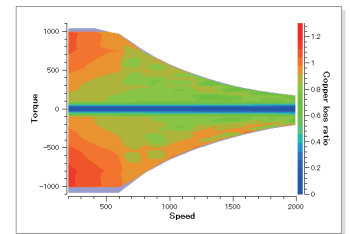


Fig. 6. Copper loss ratio map

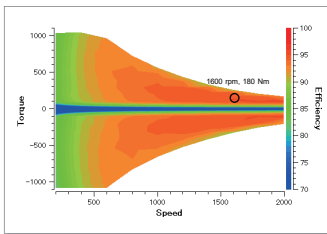


Fig. 3. Efficiency map accounting for harmonics

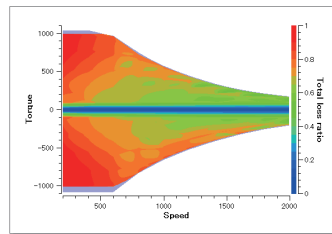


Fig. 4. Total loss ratio map

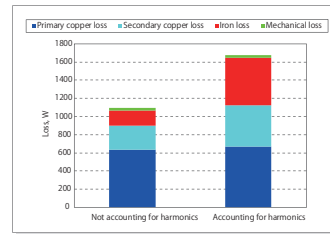


Fig. 7. Breakdown of both loss components in the 1600 rpm, 180 Nm

Axial Gap Type Motor AC Copper Loss Analysis

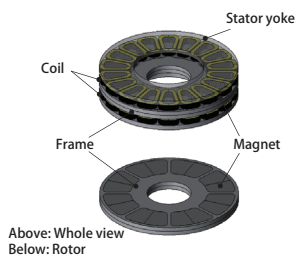
module: TR

Overview

The primary loss of axial gap type motors occurs in the core, magnets, and coils. This document focuses on the loss that occurs within coils. Coil loss can be defined in accordance with both DC copper loss and AC copper loss. It is entirely possible to calculate DC copper loss with relative ease from the coil geometry, electrical resistivity, and the current. Conversely, AC copper loss is influenced by the likes of magnetic fields generated by conductors that are positioned close together. There are instances of using square wire to increase the coil fill factor, but in this circumstance, because the coil wire cross section is large, the current is easily distributed, and making estimates from calculations done manually can prove difficult.

By using finite element analysis, coil loss can be visualized, and analysis is made entirely possible without the need for prototyping any real machines.

In this example, the AC copper loss of an axial gap type motor using square wire is evaluated.



Above: Whole view
Below: Rotor

AC Copper Loss

Coil AC copper loss is shown in Table 1, and coil cross section loss density distribution and magnetic flux density distribution are both shown in Fig. 1.

It can be understood from Fig. 1 that loss becomes larger in the vicinity of the air gap. It can be considered that the distribution of loss occurs due to flux leakage in the vicinity of the air gap linking with the coils.

AC copper loss (W)	1,344
--------------------	-------

Table 1. AC Copper Loss

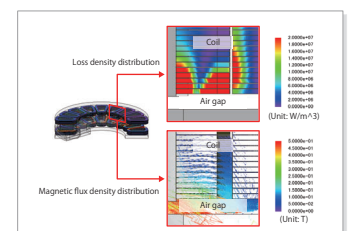


Fig. 1. Coil Cross Section Loss Density Distribution and Magnetic Flux Density Distribution

Case 272 Thrust Analysis of Linear Actuator with a Curved Section

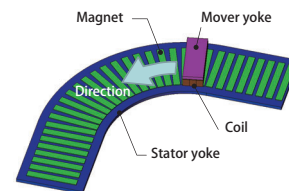
module: TR

Overview

Linear motors are used for machine tools and similar devices because of their ability to exhibit high speeds, high acceleration and deceleration, in addition to high-accuracy positioning. Among them, linear actuators with curved sections also possess the ability to realize curved motions in addition to straight motions. High thrust that is also stable is required as a matter of improving performance, but because high thrust is affected by curved motion sections, prior investigations are necessary.

Differences in gap magnetic flux density between linear motion sections and curved motion sections can be difficult to comprehend in virtual calculations. High-accuracy estimations are possible through the use of FEM, which can take into account the effects of material non-linearity and magnetic flux leakage in space.

In this example, the thrust characteristics of a linear actuator with a curved section are obtained via analysis, and thrust at the transition from a linear motion to a curved motion is evaluated.



Thrust Characteristics

Thrust characteristics are shown in Fig. 1.

It is understood that thrust in the curved section is lower compared to the straight section.

This is because, as shown in Fig. 2 and Fig. 3, the space between magnets becomes narrower on the inner diameter side of the curved section and widens on the outer diameter side, so the area where the mover and the stator are situated opposite each other is reduced, and the effective magnetic flux is also reduced.

It is understood that changes in the amount of thrust are large in the curved section. Similarly, as changes occur where the mover and the stator are situated opposite each other, the magnetic field of magnets becomes non-sinusoidal, but because coil magnetomotive force is a sine wave, this results in the generation of unintended thrust.

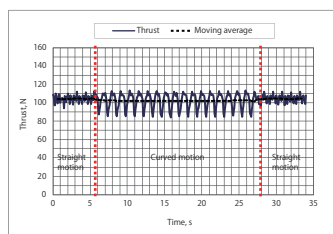


Fig. 1. Thrust Characteristics

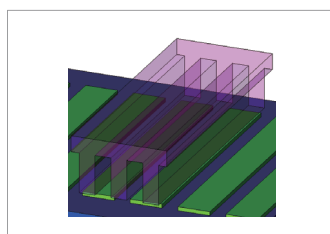


Fig. 2. Mover and Stator Situated Opposite Each other in a Straight Section

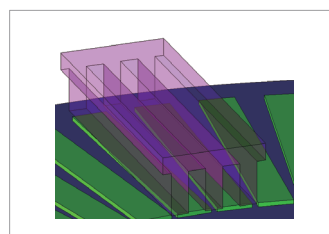


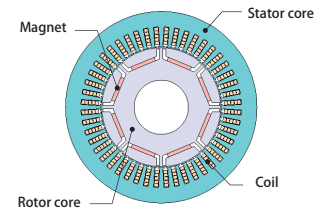
Fig. 3. Mover and Stator Situated Opposite Each other in a Curved Section

Overview

IPM motors use rare-earth sintered permanent magnets with strong magnetic forces, and in addition to the magnet torque that occurs as a result of the magnetic fields of magnets as well as rotating magnetic fields, IPM motors are also capable of using reluctance torque generated from the difference between d-axis inductance and q-axis inductance. IPM motors are therefore in possession of wide operating regions, and are highly efficient. It is for these reasons that IPM motors are used for the likes of traction motors for electric vehicles. Creating efficiency maps for both motor design and control design can be useful due to the fact that motor efficiency varies in accordance with rotation speed and load.

An example of creating efficiency maps is shown in JAC165. PWM iron loss is accounted for in JAC165 in pre-processing, but input is sinusoidal, and coil AC loss is ignored. Because power electronics are used for traction motors, ignoring the effects from PWM can lead to the possibility of overestimating motor performance.

In this example, an IPM motor efficiency map that accounts for AC loss from a PWM is created, and a comparison with an efficiency map that does not account for AC loss is performed.



Efficiency Map Not Accounting for AC Loss

The efficiency map not accounting for AC loss is shown in Fig. 1, and the operating points extracted to create an efficiency map that does account for AC loss are shown in Fig. 2.

In order to create the efficiency map accounting for AC loss from the PWM, an efficiency map not accounting for AC loss, similar to that of Fig. 1, is created first. Refer to JAC165 for more information on efficiency maps not accounting for AC loss.

It is from this efficiency map that operating points for the purpose of creating an efficiency map accounting for AC loss are extracted.

This document categorizes three regions consisting of a low speed region, a medium speed region, and a high speed region. Operating points are selected to include maximum torque points.

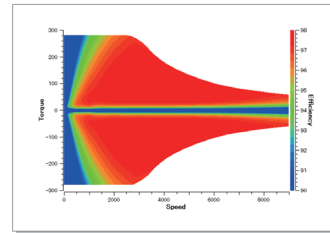


Fig. 1. Efficiency Map Not Accounting for AC Loss

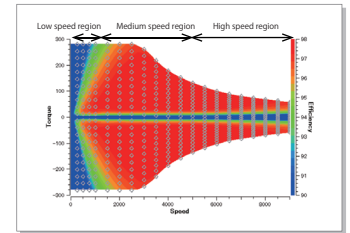


Fig. 2. Operating Points to Extract

Modeling to Account for AC Loss

The control circuit is shown in Fig. 3.

The control circuit is created to account for the influence of the PWM. As so to additionally calculate AC loss, the coils model wire geometry similar to the schematic diagram.

A JMAG-RT model is used in the control circuit. Calculations of a transient state at the start of analysis are performed with the JMAG-RT model, and by performing FEA only with an electric angle period after reaching a steady state, analysis time can be reduced.

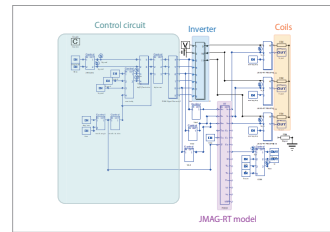


Fig. 3. Control Circuit

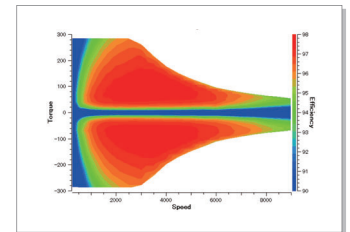


Fig. 4. Efficiency Map Accounting for AC Loss

Efficiency Map Accounting for AC Loss

The efficiency map accounting for AC loss from the PWM is shown in Fig. 4. Additionally, as a comparison between accounting for AC loss and not accounting for AC loss, an efficiency difference map is shown in Fig. 5, and a copper loss comparison map is shown in Fig. 6.

From Fig. 5, it is understood that the difference between accounting for AC loss and not accounting for AC loss is approximately one point in low speed and medium speed regions. There is also a difference of two to five points or more in the high speed region. When there is a desire to reach high efficiency of 90% or higher like that of a traction motor, there exists the possibility that this difference could have an effect on accuracy.

From Fig. 6, it is understood that whether AC loss is accounted for or not results in a large difference in copper loss in the high speed region. It is thought that the differences in efficiency shown in Fig. 5 occur as a result of this.

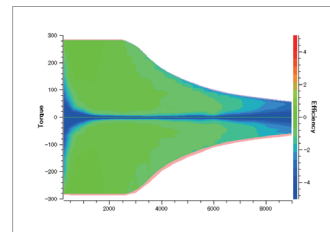


Fig. 5. Efficiency Difference Map

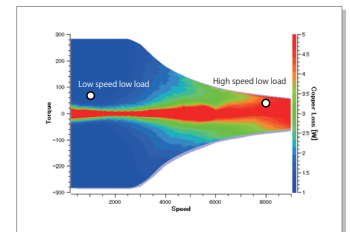


Fig. 6. Copper Loss Comparison Map

Loss Component Breakdown

Confirm the loss that occurs during low-speed, low-load and high-speed, low-load shown in Fig. 6.

A breakdown of loss components during low-speed, low-load is shown in Fig. 7, and the stator core eddy current loss frequency components when accounting for AC loss are shown in Fig. 8.

PWM carrier frequency is 6,000 Hz. From Fig. 7 and Fig. 8, it is understood that the PWM harmonic components have a large effect on eddy current loss at low-speed, low-load. For analysis not accounting for AC loss, PWM iron loss is obtained in post-processing. This reduces the difference from when accounting for AC loss.

A breakdown of loss components during high-speed, low-load is shown in Fig. 9, and flux lines and current density distribution frequency components when accounting for AC loss are shown in Fig. 10.

From Fig. 9, it is understood that the influence of eddy current loss from the PWM at high-speed, low-load is small, but also that whether AC loss is accounted for or not results in a large difference in copper loss. From Fig. 10, it can be considered that the difference in this copper loss is due to the eddy currents that occur as a result of the leakage flux within the slots.

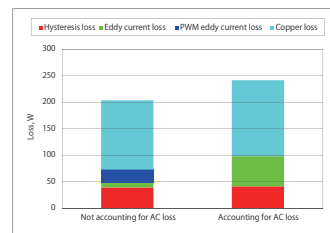


Fig. 7. Breakdown of Loss Components at Low-Speed, Low-Load

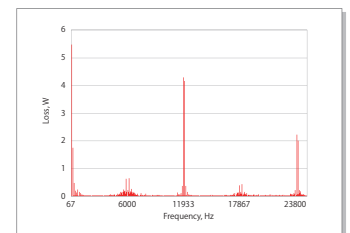


Fig. 8. Stator Core Eddy Current Loss Frequency Components at Low-Speed, Low-Load

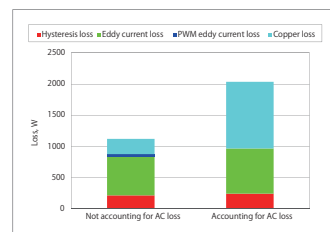


Fig. 9. Breakdown of Loss Components at High-Speed, Low-Load

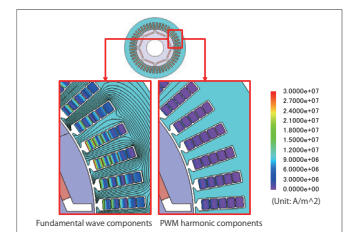


Fig. 10. Frequency Components for High-Speed, Low-Load Flux Lines and Current Density Distribution

Case 274 SPM Motor Thermal Demagnetization Analysis Using Bonded NdFeB Magnets

module: DP

Overview

Because SPM motors are, due to their structure, susceptible to demagnetizing fields from rotor magnets, it is necessary to consider the influence of magnet demagnetization on motor characteristics. In order to properly grasp this demagnetization, the demagnetizing characteristics that magnets possess should be correctly accounted for. When there exists magnetization characteristics that make it difficult to observe knickpoints on demagnetization curves like those of bonded NdFeB bonded magnets, it becomes difficult to recreate demagnetization curves with linear approximation. By correctly expressing demagnetization curves using point arrays, the influence of demagnetization on various characteristics can be accounted for at a high level of accuracy. In this example, an SPM motor thermal demagnetization analysis is performed using bonded NdFeB magnets. Both the influence on torque waveforms when changing rotor magnet temperatures and the distribution of the demagnetization ratio within the magnets are evaluated.

Demagnetization Curves

Fig. 1 shows the demagnetization curves of the rotor magnets used in this document. The blue lines show characteristics at 60 deg C, and the red lines show characteristics at 140 deg C. The dashed lines are the demagnetization curves obtained with bilinear approximation, and the solid lines are the actual demagnetization curves plotted with point arrays.

It can be observed that differences exist in the demagnetization curves obtained with bilinear approximation compared to the actual demagnetization curves. From this, it can be considered that a difference in results occurs when accounting for thermal demagnetization using the two types of demagnetization curves shown.

Effect on Motor Characteristics

The influence on torque characteristics was evaluated when magnet temperatures were changed from 60 deg C to 140 deg C and back to 60 deg C again when running at an excitation condition of a phase current amplitude of 5 A at an angle 80 deg.

Fig. 2 and Fig. 3 shows the demagnetization ratio of the rotor magnets after irreversible demagnetization with contours. The demagnetization ratio is defined as the amount of variation for magnet residual magnetic flux density prior to additional load and heating. It is understood that a difference occurs between the bilinear approximation of the demagnetization curves and using the actual demagnetization curves.

Fig. 4 shows torque characteristics, where it is understood that differences in torque characteristics occur. Compared to the average torque after irreversible demagnetization, it is understood that there is an error of 8 % that occurs when using the bilinear approximation demagnetization curves.

This shows that demagnetization can be correctly accounted for by specifying demagnetization curves with arbitrary point arrays when using magnets where knickpoints on demagnetization curves are difficult to observe.

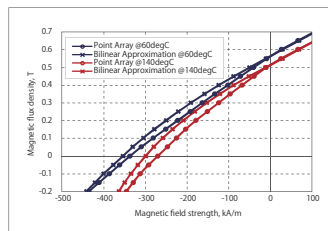
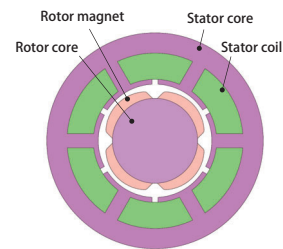


Fig. 1 Magnetization Curves

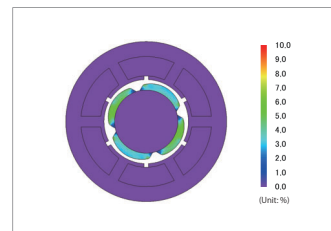


Fig. 2 Demagnetization Ratio Using Demagnetization Curves Obtained with Bilinear Approximation

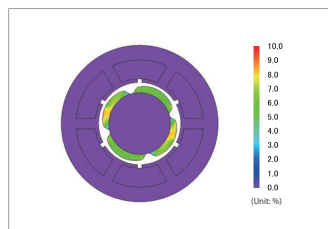


Fig. 3 Demagnetization Ratio Using Actual Demagnetization Curves

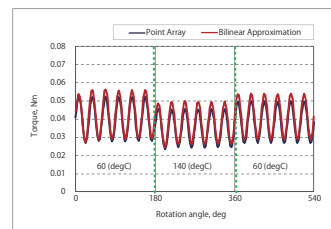
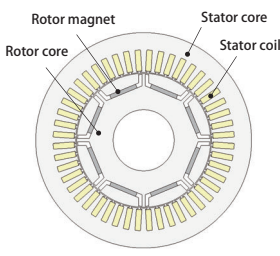


Fig. 4 Torque Characteristics



Overview

As electromagnetic appliances become more and more efficient, evaluations of iron loss at a high accuracy also become increasingly sought after. Actual manufacturing sees processes of electromagnetic steel sheets being punched out with a press, laminated, fixed into place with caulking, welding, with bolts tightened, etc., with the laminated iron core either press-fitted into frame or shrink-fitted. Stress and residual strain can occur as a result of these processes, which compared to more ideal conditions, causes increases in iron loss. In simulations using the finite element method, iron loss can be calculated taking into account the effect of this stress and distortion. In this example, an analysis of an IPM motor accounting for the residual strain that occurs as a result of punching processes, and evaluates the effect on torque, magnetic flux density, and iron loss.

Expressing Deterioration as a Result of Residual Strain

The deterioration that occurs as a result of residual strain is expressed via the deterioration coefficient in the cut plane, and the deterioration function from the surface. Fig. 1 shows the permeability deterioration coefficient of the magnetic field dependency, and Fig. 2 shows the hysteresis loss correction coefficient of the magnetic flux density dependency.

Effect on Magnetic Flux Density and Torque

Fig. 3 shows differences in magnetic flux density due to the presence or absence of residual strain, while Fig. 4 shows the comparison of average torque. It can be understood from Fig. 3 that by accounting for residual strain, magnetic flux density grows smaller in the vicinity of the core cut plane. This is because permeability deteriorates due to manufacturing. From Fig. 4, it can be understood that the effect on average torque from residual strain is approximately 1%.

Effect on Iron Loss

Fig. 5 to Fig. 8 show the differences in the breakdown of iron loss, iron loss density, and hysteresis loss density, all from the presence or absence of residual strain. It is understood from Fig. 5 that iron loss increases by approximately 13% by accounting for residual strain. From Fig. 6 to Fig. 8, it is understood that differences occur not only in hysteresis loss, but Joule loss also. The increase in Joule loss occurs as a result of the deterioration of magnetization characteristics at the edges due to residual strain, as well as the increase in magnetic flux density at the center of the teeth.

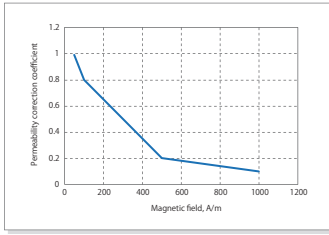


Fig. 1. Permeability Correction Coefficient

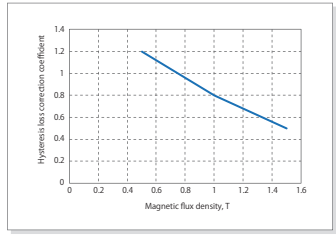


Fig. 2. Hysteresis Loss Correction Coefficient

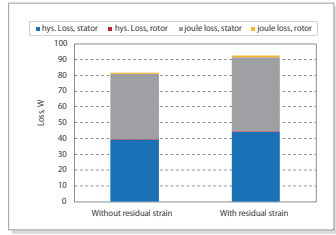


Fig. 5. Iron Loss Breakdown

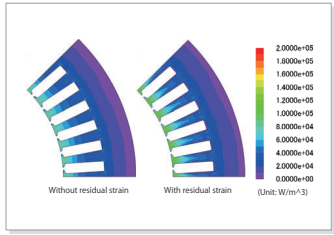


Fig. 6. Iron Loss Density Distribution

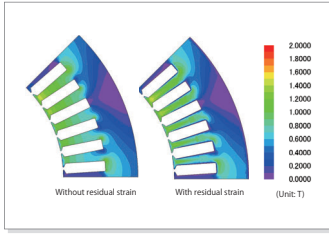


Fig. 3. Magnetic Flux Density Distribution

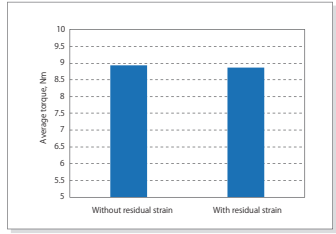


Fig. 4. Average Torque

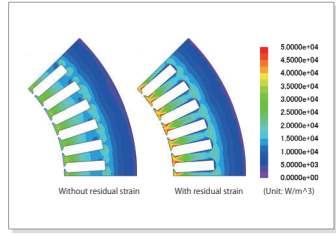


Fig. 7. Hysteresis Loss Density Distribution

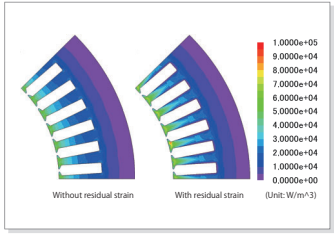


Fig. 8. Joule Loss Density Distribution

Case
276

Six-Phase IPM Motor Harmonic Iron Loss Analysis

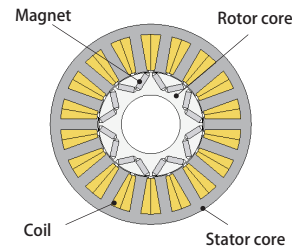
module: DP, LS

Overview

For traction motors, polyphase design is sometimes used with the objective of improving output density, increasing redundancy during drive, and reducing torque ripple. In polyphase design, six-phase drive with two inverters are used. The typical control method is current vector control, and PWM motors are widely used to create command currents.

It is necessary to be aware of iron loss to increase the efficiency of motor drive systems. When power is converted using PWM, carrier harmonics produced by PWM are superimposed on the current and IPM motor core magnetic flux density waveforms, causing an increase in iron loss. Iron loss accounting for PWM carrier harmonics can be evaluated by modeling control circuits that include PWM inverters and coupling them with magnetic field analysis.

In this example, confirming the effects of carrier harmonics on the iron loss of a six-phase IPM motor are explained here.



Operating Point to Evaluate

The efficiency map and the operating point for evaluating this motor are shown in Fig. 1. This evaluates harmonic iron loss at an operating point where rotation speed is 2,800 r/min and torque is 75 Nm. This operating point also has a current amplitude of 76.6 A and a current phase of 36 deg.

Modeling to Account for Harmonic Iron Loss

The control circuit is shown in Fig. 2. The control circuit is created to account for the influence of the PWM. A JMAG-RT model is used in the control circuit. Calculation is performed with the JMAG-RT model when analysis begins in a transient state. Analysis time is then reduced by switching to FEA after reaching a steady state.

Loss Breakdown

Hysteresis loss and Joule loss that occurs during sinusoidal current drive and PWM inverter drive are shown in Fig. 3.

Loss increases during PWM inverter drive for both the rotor core and the stator core. In particular, there is a large increase in Joule loss approximately 30% more increase for both the rotor core and stator core.

Joule Loss/Loss Density Distributions

Joule loss frequency components are shown in Fig. 4 and Fig. 5 and loss density distributions are shown in Fig. 6 and Fig. 7. Note that, the vertical axis for Fig. 4 and Fig. 5 are deliberately narrowed to clarify the difference.

Iron loss mainly increases in the secondary component of the PWM carrier frequency (12 kHz) (the red frame in the center of the diagram). It is recognized that the increase in Joule loss during PWM inverter drive is caused by the carrier frequency. Therefore, it is necessary to account for the effects of carrier harmonics when evaluating detailed motor characteristics.

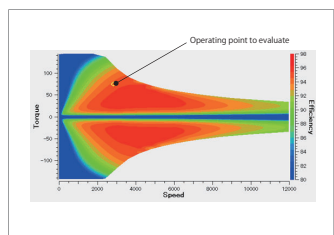


Fig. 1. Efficiency Map and Operating Point for Evaluation

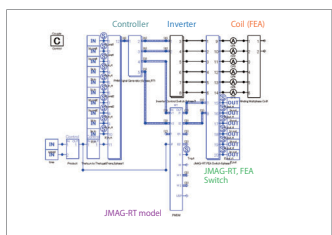


Fig. 2. Control Circuit

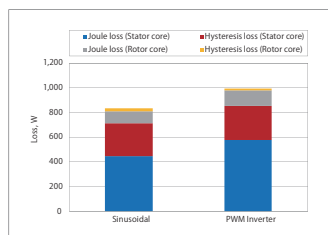


Fig. 3. Loss Breakdown

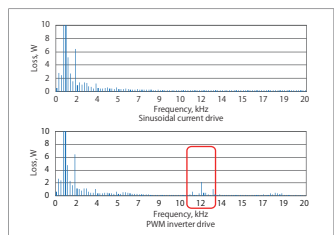


Fig. 4. Rotor Core Joule Loss Frequency Component

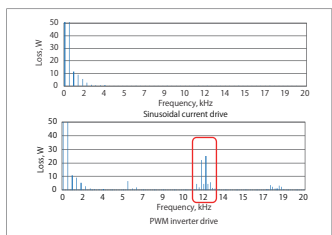


Fig. 5. Stator Core Joule Loss Frequency Component

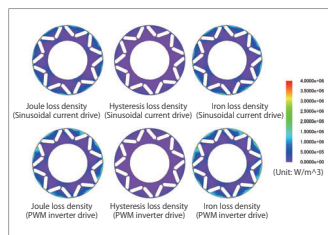


Fig. 6. Rotor Core Loss Density Distributions

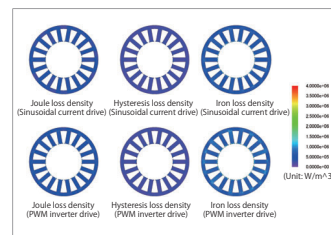
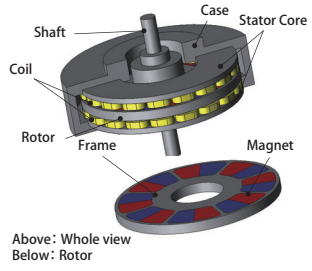


Fig. 7. Stator Core Loss Density Distributions

Overview

Axial gap type- motors can be can have a thinner construction than radial gap-type motors, and are used for in-vehicle motors where space is limited. In general, the motor is quiet compared to the engine, however, the wide rotation speed range may at times cause the vibration noise to be a problem. In order to evaluate noise/vibration caused by electromagnetic force, it is necessary to accurately obtain the source of sound radiation, the total eigen mode of the motor, including the cases it is linked to must be perceived and taken into account at the same time. It is effective to use the finite element method in simulations before creating a prototype to assess the level of vibration caused by air distribution from electromagnetic force and eigen mode. In this example, phenomena confirmed in axial gap-type motors that occur at maximum sound pressure level, from an electromagnetic excitation force and eigen mode perspective.



Frequency Characteristics of Maximum Sound Pressure Level

Sound pressure level target plane for stress evaluation is shown in Fig. 1 and frequency characteristics of maximum sound pressure level is shown in Fig. 2. As shown in Fig. 1, sound pressure level target plane for stress evaluation is on a 200 mm diameter sphere. As shown in Fig. 2, sound pressure level reaches maximum at 1,333 Hz. The phenomena that occur when reaching maximum sound pressure level is confirmed from an electromagnetic excitation force and eigen mode perspective.

Spatial Mode of Electromagnetic Force Acting on Teeth

The spatial mode of electromagnetic mode with large frequency component of 1,333 Hz is shown in Fig. 5. The circumferential figures represent the teeth numbers and the radial direction figures represent the size of the electromagnetic force. Note that, the size of magnetic force is normalized at maximum value. Since there are 6 peaks in one period, you can see that the sixth spatial component is dominant in the magnetic force at 1,333 Hz. As shown in Fig. 6, this is thought to be because the winding arrangement is made so there are six phases in the circumferential direction.

Electromagnetic Force History Acting on Teeth / Frequency Component

Electromagnetic force history acting on stator teeth wrapped with U phase coil is shown in Fig. 3 and frequency components are shown in Fig. 4. In Fig. 3, you can see that the historical waveforms of electromagnetic force are not the same even for teeth wrapped in the same phase coil. Note that, the waveform for teeth wrapped in V phase or W phase coils will be out-of-phase. In Fig. 4, you can see that the electric angle secondary component 1,333 Hz, is dominant in both teeth. This is because two rotor magnetic poles pass through in one electrical angle period.

Acceleration Distribution

The acceleration distribution by frequency at maximum noise pressure level is shown in Fig. 7. You can see that acceleration of the case is larger in the area connecting to the stator. Note that, spatial distribution of acceleration is in spatial 2nd order and is different from spatial distribution of electromagnetic force.

Eigen Mode

Eigen modes that are similar to acceleration distribution and change in spatial 6th order are shown in Fig. 8. Electromagnetic force distribution is in spatial 6th order, but the natural frequency of eigen mode in spatial 6th order is extremely high at 18 kHz. Therefore, the natural frequency is thought to be greatly affected by the eigenmode of spatial 2nd order (9 kHz) which is closer to the electromagnetic excitation force frequency.

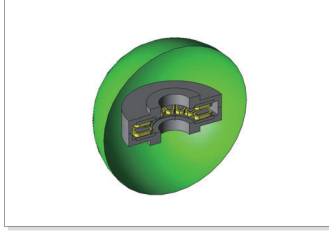


Fig. 1. Sound Pressure Level Measured Part

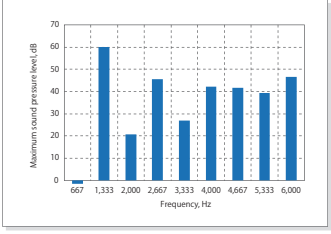


Fig. 2. Frequency Characteristics of Sound Pressure Level

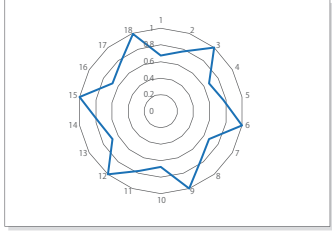


Fig. 5. Spatial Mode of Electromagnetic Force

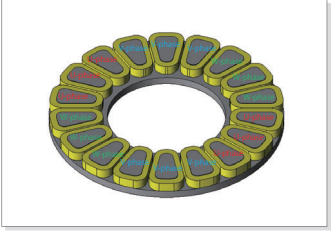


Fig. 6. Winding Wire Arrangement

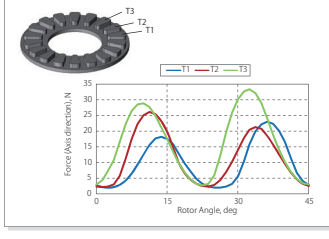


Fig. 3. Electromagnetic Force History Acting on Teeth

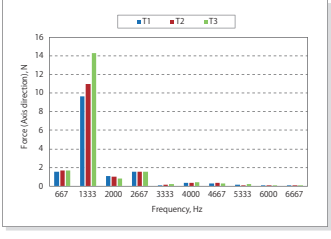


Fig. 4. Frequency Component of Electromagnetic Force Acting on Teeth

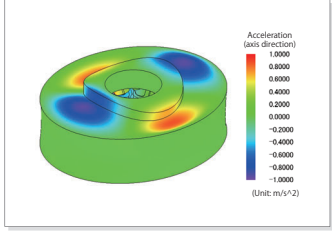


Fig. 7. Acceleration Distribution (1,333 Hz)

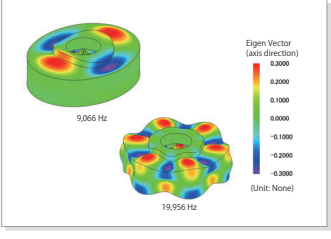


Fig. 8. Eigen Mode

Case 278 Creating Six-Phase Induction Motor Efficiency Maps

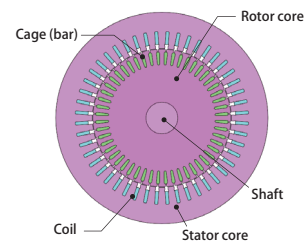
module: FQ, LS

Overview

With advances in variable speed operation technology for induction motors, progress is being made in applications to fields where wide operating regions are required. With this, polyphase design may be used for the purpose of enhancing redundancy. Polyphase design includes the likes of six-phase drive using two inverters. Efficiency maps are created for both motor design and control design in order to fully comprehend the characteristics of these motors that are capable of drive within such a wide range.

It is necessary that operating region rotation speed and each loss point results are obtained as so to draw efficiency maps with actual measurements and calculators. This means that a large amount of calculations and time to organize the results are required. In concept design, evaluating efficiency maps within short amounts of time is also required. In JMAG-Designer, however, efficiency maps that account for the effect of iron loss and nonlinear magnetization characteristics can be created with ease.

In this example, a six-phase induction motor efficiency map is created in the concept design stage, and each operating point slip and iron loss are evaluated.



Efficiency Map, Slip Map

The efficiency map is displayed in Fig. 2, and the slip map is displayed in Fig. 3. Efficiency can be understood from Fig. 2.

Slip can be understood from Fig. 3. Slip with maximum efficiency at each operating point can also be understood.

Loss Ratios at Each Operating Point

Fig. 4 displays pie charts showing loss ratios at low speed and low load, low speed and high load, medium speed and low load, medium speed and high load, and lastly, high speed and low load.

It is understood that iron loss dominates more than copper loss during high rotation speed.

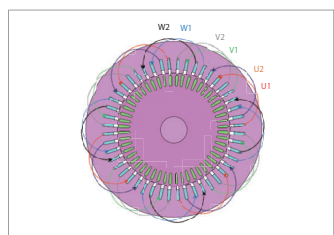


Fig.1 Distributed Winding

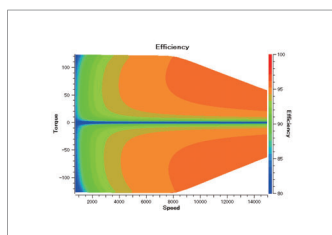


Fig. 2. Efficiency Map

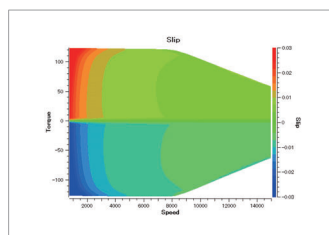


Fig. 3. Slip Map

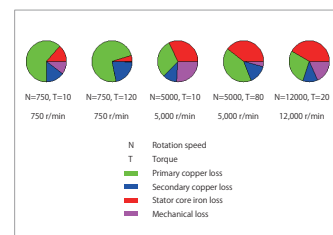


Fig. 4. Loss Ratios at Each Operating Point

Thermal Analysis Accounting for Cooling of the IPM Motor

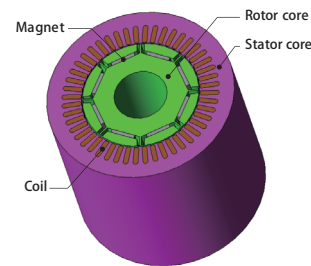
module: ExpressFR

Overview

EV/HEV traction motors operate at ranges such as high torque and high power ranges. When running at such operating points, the temperature of parts rises as the loss becomes the heat source. Cooling system design using water jackets and ATF is put into practice as normal cooling by air allows the parts to exceed their heat resistant temperature.

It is possible to run an analysis that takes into account the cooling and the heat resistance between the parts by using the thermal equivalent circuit.

In this example, thermal equivalent circuit is used to run thermal analysis of a 3-phase IPM motor that accounts for cooling, and check the temperature change in the coil.



Cooling Specifications

Cooling specifications are shown in Fig. 1.

The water jacket is installed on the upper 90 deg sector of the stator.

Assume that oil in the ATF pool accumulates inside the lower 90 deg sector of stator.

Housing, coil end and shafts are modeled in the thermal equivalent circuit.

Thermal Equivalent Circuit

The thermal equivalent circuit is shown in Fig. 2.

The heat transfer boundary component labeled as FEM is connected to the finite element model.

The sides of stator core are divided into three parts: the water jacket part, the ATFpool part, and the rest of the remaining parts, which are connected to the housing and outside air through thermal resistance component.

Core surfaces other than the above and coil ends are thermally connected to the shaft and the housing through the air inside the housing.

Temperature Change in Coil

The temperature evaluation point of the coil is shown in Fig. 3, the temperature change of the coil is shown in Fig. 4, and the temperature 15 minutes after the motor starts is shown in Table 1.

You can determine whether the temperature is within the allowable temperature range of the heat resistance class by checking the coil temperature.

In this case study, the ATF pool part is cooler than the water jacket part when checking the temperature 15 minutes after the motor starts. You can see that the ATF has a higher cooling effect.

In the ATF pool part, the end portion is cooler than the central portion. You can see that cooling through the coil end is more effective than cooling through the core.

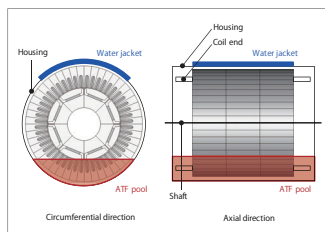


Fig. 1. Cooling Specifications

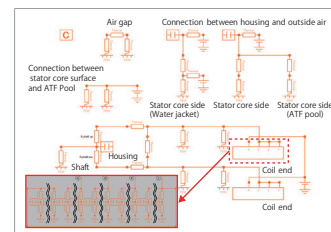


Fig. 2. Thermal Equivalent Circuit

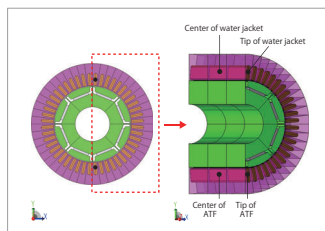


Fig. 3. Temperature Evaluation Point of Coil

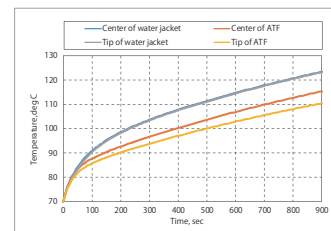


Fig. 4. Temperature Change of Coil

Item	Center of water jacket	Center of ATF	Tip of water jacket	Tip of ATF
Temperature (deg C)	123.5	115.4	123.4	110.5

Table 1. Coil Temperature 15 Minutes After the Motor Starts

Case 280 Topology Optimization of Induction Heating Coil

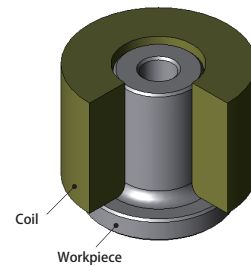
module: FQ, HT

Overview

When designing an induction heating coil, it is necessary to investigate both the heating time and the coil shape in order to uniformly heat the workpiece. Such investigations are run through a process of trial and error based on both the knowledge and experience of skilled engineers, as well as experiments with actual machines.

Optimization using FEA is effective in reducing prototyping costs and reducing the construction period. In parameter optimization using design variables and dimension ranges, although knowledge and experience is required to determine parameters, because searches can be performed for topology optimization without depending on the initial shape, design proposals with a high degree of freedom can be obtained.

In this example, magnetic field and thermal coupled analysis is run, and using topology optimization, searches are performed for a heating coil that maximizes the power factor and minimizes the apparent power.



Optimization conditions

The design region is shown in Fig. 1, the constraint conditions are shown in Table 1, and the objective functions are shown in Table 2.

Define the following four points in the objective functions.

Power factor maximization

Apparent power minimization

Minimizing the standard deviation Tdev from the target temperature T_i using the evaluation point temperature T_i (Fig. 2)

Minimizing the bias Tbias from the target temperature T_i using the evaluation point temperature T_i (Fig. 2)

The temperature evaluation points are shown in Fig. 2.

Optimization Results

The correlation diagram between the coil power factor and the temperature standard deviation Tdev is shown in Fig. 3.

The case with the minimum temperature standard deviation Tdev is Optimum solution 1, the case with the maximum power factor is Optimum solution 3, and the one case between Optimum solution 1 and Optimum solution 3 is Optimum solution 2.

The topology optimization shapes for optimum solutions through 1 to 3, and the temperature distribution contours during heating at 7.0 sec are both shown in Fig. 4.

In each optimum solution, the coil surface facing the workpiece has a wavy shape, whereas the lower part of the coil has a shape that follows along the workpiece. It is understood that the workpiece surface is heated evenly in each case.

Sensitivity Analysis

In order to confirm the effect that the wavy coil shape on the surface facing the workpiece has on the temperature distribution of the workpiece, sensitivity analysis is run for the best case.

Fig. 5 shows Optimum solution 1 which is the case where the temperature standard deviation Tdev is the minimum value, as well as the temperature distribution of the case where the coil surface facing the workpiece is changed to a shape that is near to a straight line.

In the case where the coil surface is changed to a shape that is near to a straight line, the upper part of the workpiece is heated first. The workpiece surface temperature is not uniform even if heat transfer occurs within the workpiece. Conversely, in Optimum solution 1, multiple points where the coil is asymptotic to the workpiece are heated first. The workpiece surface temperature then becomes uniform due to the heat transfer. It is understood that the wavy shape of the coil surface is important for uniform temperature.

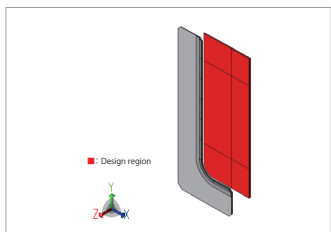


Fig. 1. Design region

Item	Objective
Workpiece surface minimum temperature HT_min	900 deg C or more
Workpiece surface maximum temperature HT_max	1300 deg C or less

Table 1. Constraint conditions

Item	Expression	Objective
Power factor PF	ActiveP/ActiveP3	Maximize
Apparent power ActiveP3	ActiveP3	Minimize
Standard deviation Tdev	$T_{dev} = \sqrt{\frac{1}{m} \sum_{i=1}^m (T_i - T_t)^2}$	Minimize
Bias Tbias	$T_{bias} = \frac{1}{m} \sum_{i=1}^m T_i - T_t $	Minimize

ActiveP1: Active power
 ActiveP2: Apparent power
 m : Number of evaluation points
 T_i : evaluation point temperature
 T_t : target temperature = 1000(deg C)
 T_{dev} : Standard deviation
 T_{bias} : Bias

Table 1. Objective functions

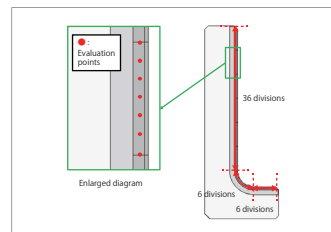


Fig. 2. Temperature evaluation points

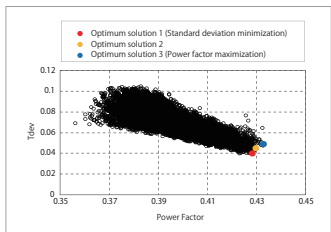


Fig. 3. Power factor vs temperature standard deviation Tdev

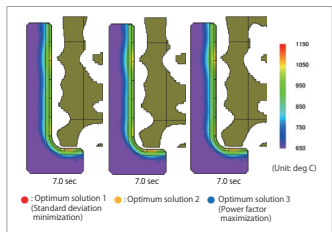


Fig. 4. Optimum solution temperature distribution

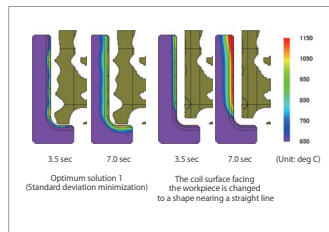


Fig. 5. Sensitivity analysis temperature distribution

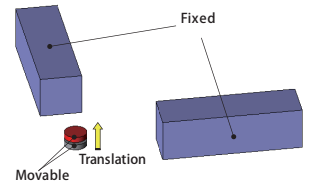
Case 284

Analysis of Minute Electromagnetic Forces Acting on a Magnet

module: TR

Overview

With the miniaturization of electrical equipment, the amount of equipment that uses minute electromagnetic forces is increasing. Therefore, it is important to understand the minute electromagnetic forces that act between parts, such as between multiple magnets. With magnetic field analysis, you can estimate minute electromagnetic forces at a high accuracy. In this example, we obtain the minute electromagnetic forces acting on a magnet that is moving translationally.



Electromagnetic Forces Acting on the Magnet

The electromagnetic force acting on the movable magnet in the direction that it moves in is shown in Fig. 1. The movable magnet is moving translationally away from the fixed magnets. As a result, as the distance moved increases, the electromagnetic forces acting on the movable magnet decrease. You can check these trends even with minute electromagnetic forces.

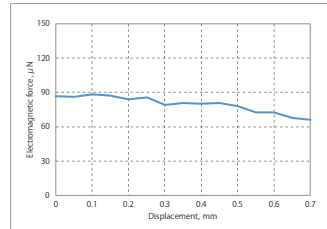


Fig. 1. Electromagnetic forces acting on the magnet

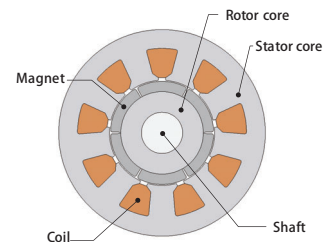
Case 285

Integrated Magnetization Analysis of an SPM Motor by Magnetizing Multiple Times

module: DP

Overview

Permanent Magnet Synchronous motors (PMSM) sometimes use a method known as integrated magnetization. This is where magnets are assembled without magnetization then magnetized after the assembly. Depending on the combination of the number of poles and slots, the magnets may not be sufficiently magnetized by just one magnetization. The magnets are then magnetized more than once by rotating the rotor or changing the current values. In situations like these, the design must prevent the irreversible demagnetization of the magnets that have been previously magnetized. By using a magnetic field analysis simulation which uses the finite element method, you can check the magnetization distribution that occurs in the magnets as the result of the magnetization conditions. By accounting for magnetic hysteresis during this process, the magnetization distribution in the magnets can be evaluated at a higher accuracy. In this example, the magnets are magnetized more than once with the rotor at different positions to evaluate the magnetization distribution in the magnets while also accounting for hysteresis.



Magnetization Field Distribution

The magnetization field distribution and the magnetic flux line diagram when the magnetization current is 1 kA are shown in Fig. 1. The magnets are evaluated for the 1st and 2nd magnetizations. In the analysis, the magnets are evaluated as being arranged in the same positions. In the diagram, the stator side is shown as having been rotated. Note that the magnets are arranged in a radially outward orientation direction. In the 1st magnetization, the magnetic fields are weak in the center of the magnet because the center of the magnetic pole faces the slot opening part. To ensure that the magnets are fully magnetized, for the 2nd magnetization, the magnetic pole instead faces the center of the tooth. Looking at the magnetization distribution of the 2nd magnetization, we see this occurring in the opposite direction of the orientation direction at the ends of the magnet.

Magnetization Distribution of the Magnet Positioned in the Air

The magnetization distribution (radial component) of the magnet positioned in the air when the 1st and 2nd magnetizations end respectively is shown in Fig. 2. Looking at the magnetization distribution when the 1st magnetization ends, we understand that the magnetization is weaker at the center of the magnetic pole. Looking at the magnetization distribution when the 2nd magnetization ends, the magnetization has increased at the center of the magnetic pole, but compared to the 1st magnetization, magnetization has reduced at the ends of the magnet. From this we understand that irreversible demagnetization has occurred. As shown by the magnetization field distribution in Fig. 1, this is because magnetic fields are generated in the opposite direction in the 2nd magnetization.

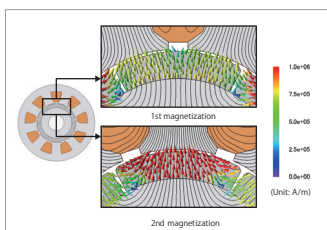


Fig. 1. Magnetization field distribution and magnetic flux diagram

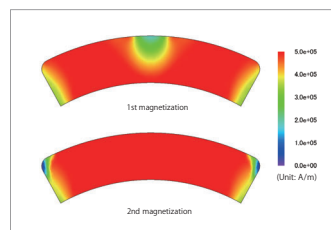


Fig. 2. Magnetization field distribution and magnetic flux diagram

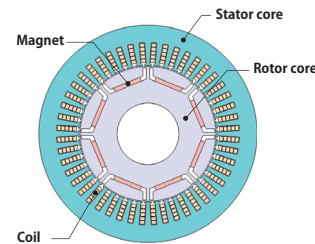
Case 286 IPM Motor Iron Loss Analysis Accounting for PWM : Evaluation with Different Modulation Methods

module: DP, LS

Overview

PWM control is widely used in the control of IPM motors. Because currents include carrier harmonics, this results in an increase in iron loss. Many different types of control methods are available. Modulation methods are selected according to the objective and application of the control. The carrier harmonic components of a current will vary depending on the modulation method. Assessing iron loss is essential in improving the efficiency of IPM motors, and the modulation method must also be accounted for in order to evaluate the iron loss accurately. By using a magnetic field analysis simulation that accounts for control, the iron loss accounting for the PWM control carrier harmonics can be assessed.

In this example, the effects on iron loss when the modulation method for PWM control is changed are evaluated.



Current Waveforms

The current waveforms for the PWM 3-phase modulation and 2-phase modulation are shown in Fig. 1, and the frequency components of the current are shown in Fig. 2. In this example, we compare the components at approximately 6,000 Hz, which is the carrier frequency of the PWM inverter. The carrier amplitude of the 2-phase modulation is larger than that of the 3-phase modulation.

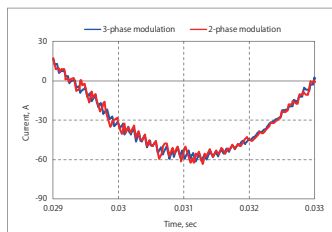


Fig. 1. Current waveforms

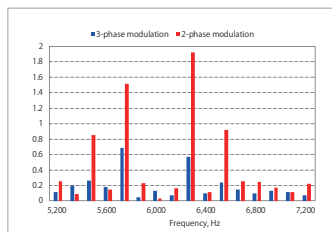


Fig. 2. Frequency components

Iron Loss

The iron losses for the PWM 3-phase modulation and 2-phase modulation are shown in Fig. 3.

The iron loss of the 2-phase modulation increases compared to that of the 3-phase modulation. This may be due to the carrier amplitude of the 2-phase modulation current, which is larger than that of the 3-phase modulation.

In general, switching loss is smaller with the 2-phase modulation. However, looking at the analysis results, we see that the iron loss of the 2-phase modulation increases. When considering overall system efficiency, the effect that different modulation methods have on iron loss must be obtained correctly.

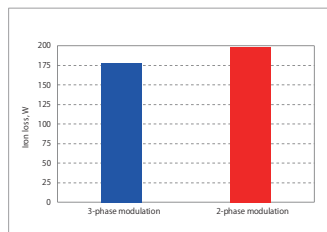


Fig. 3. Iron loss

Case 287 Analysis of Current Conditions for the Maximum Efficiency of a WFSM

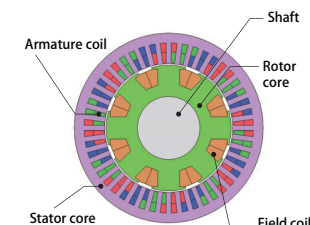
module: DP, LS

Overview

Wound-field synchronous motors (hereinafter referred to as WFSM) possess the capability of varying field magnetomotive force and feature characteristics where high efficiency can easily be achieved in the mid-to-high speed and low torque range. In recent years, one area of applying WFSM is in traction motors for electric vehicles, where there is demand for improved motor efficiency.

In designing high-efficiency motors, it is important to understand the combination of field current and armature current that can achieve maximum efficiency. However, understanding these by using actual measurements requires great effort. On the contrary, by using simulations, these can be understood with ease in a short amount of time.

In this example, we determine the motor efficiency in relation to the field current for a WFSM when the motor output is kept constant.



Relationship Between Field Current, Motor Efficiency, and Loss Breakdown

The motor efficiency in relation to the field current when the rotation speed is 600 r/min and the torque is 28 Nm is shown in Fig. 1, and the loss breakdown for when the field current is 3, 6, and 10 A are shown in Fig. 2.

From Fig. 1, motor efficiency is reaching maximum when the field current is 6 A. From Fig. 2, it can be seen that the copper loss is taking a large proportion in the motor loss. When reducing the field current to less than 6 A, copper loss of the armature increases and efficiency goes down since it is necessary to increase the current amplitude of the armature in order to maintain the same output. On the other hand, when increasing the field current to over 6 A, the efficiency goes down likewise since the copper loss of the field increases.

From these results, it can be concluded that determining the optimal combination of the armature and field currents is important in order to achieve maximum efficiency in the WFSM. Moreover, by using simulations, it is possible to comprehend the details of the loss which is a determinant of motor efficiency.

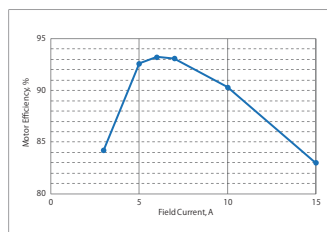


Fig. 1. Motor efficiency in relation to field current

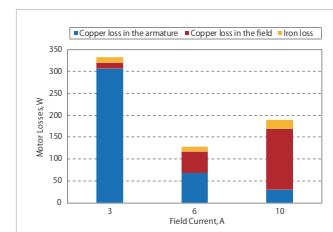
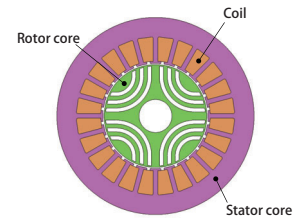


Fig. 2. Loss breakdown in relation to field current

Overview

The synchronous reluctance motor is a low-cost, highly efficient variable speed motor because it does not use permanent magnets or secondary conductors. Since its torque characteristics are particularly affected by the flux barrier shape, optimization with the flux barrier shape as a design variable is most effective in improving torque characteristics. Topology optimization allows for bold changes in material arrangement when exploring the design region, and is an effective method for generating concepts at the early stages of design when there are few geometry constraints. In this example, topology optimization is used to minimize the torque ripple and maximize the average torque when exploring the rotor geometry.



Optimization Condition

Fig. 1 shows the design region and Table 1 shows the evaluation items and objective functions. Fig. 1 shows that the rotor perimeter and area near the shaft are excluded from the design region with consideration for the actual manufacturing of the motor.

Optimization Results

Fig. 2 shows the transitions in the torque average values and torque ripple rates for the best case of each generation. Fig. 3 shows the rotor core geometry in conventional design and the best case throughout all generations, with various quantities shown in Table 2. As the generation progresses, it can be seen that the torque average value grows larger and the torque ripple rate becomes smaller as they converge. It is understood that in the best case, a comparison to the conventional design shows that the average torque is raised by 4 % and the torque ripple rate is lowered by 70 %.

Reluctance Torque

Fig. 4 shows the torque formula for reluctance torque. In a reluctance torque, the average value is larger when the difference between the d-axis inductance and q-axis inductance is large, and the ripple decreases as the change in difference is small.

q-axis Inductance

Fig. 5 shows the waveform of the q-axis inductance. Fig. 6 shows the magnetic flux line near the q-axis for each timing with Position A (0 deg) as the timing when magnetic flux flows most easily in the q-axis direction and with Position B (20 deg) as the timing when magnetic flux is least likely to flow in the q-axis direction in a conventional design. In Fig. 5, it can be seen that in the best case the change in q-axis inductance is small compared to conventional designs. In Fig. 6, it can be seen that magnetic flux flows easily when the core on the q-axis is facing the teeth and does not flow well when it is not facing the teeth. In the best case, compared to the conventional design, the flux barrier generated on the q-axis makes it difficult for the magnetic flux to flow easily when the q-axis is facing the teeth and makes it flow easily when it is not facing the teeth. It can be seen that the change is kept small and this reduces the torque ripple.

d-axis Inductance

Fig. 7 shows the waveform for the d-axis inductance. Fig. 8 shows the magnetic flux lines near the d-axis with Position C (22.5 deg) as the timing when magnetic flux flows most easily in the d-axis direction in a conventional design. In Fig. 7, it can be seen that the d-axis inductance is smaller in the best case compared to the conventional design. In Fig. 8, it can be seen that the magnetic flux flowing in the d-axis direction is suppressed by the flux barrier which extends in the q-axis direction in the best case. This increases the difference between the d-axis and q-axis inductance, resulting in a higher average torque.

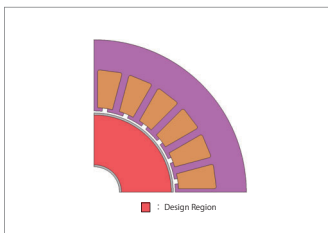


Fig. 1. Design region

Evaluation item	Objective function
Torque average value	Maximize the torque average value
Torque ripple	Minimize the torque ripple rate

Table 1. Evaluation items and objective functions

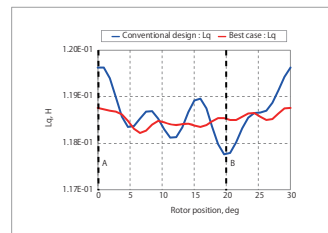


Fig. 5. q-axis inductance

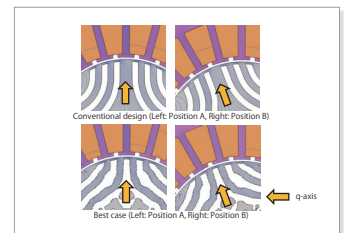


Fig. 6. Magnetic flux lines near the q-axis

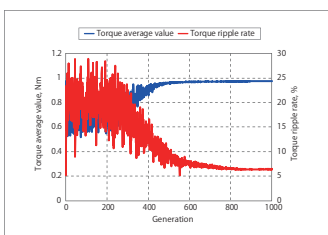


Fig. 2. Transitions in torque average value and torque ripple rate

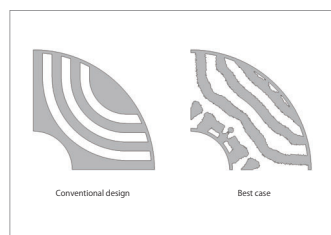


Fig. 3. Geometry of rotor core

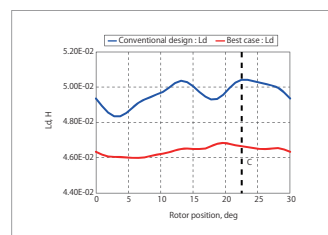


Fig. 7. d-axis inductance

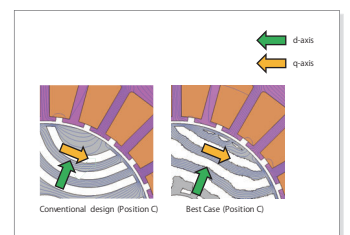


Fig. 8. Magnetic flux lines near the d-axis

Item	Conventional design	Best case
Average torque, Nm	0.93	0.97
Torque ripple rate, %	21.2	6.4

Table 2. Various evaluation value quantities

$$T_r = P_n (L_d - L_q) I_d I_q$$

T_r : reluctance torque, Nm
 P_n : pole logarithm
 L_d : d-axis inductance, H
 L_q : q-axis inductance, H
 I_d : d-axis current, A
 I_q : q-axis current, A

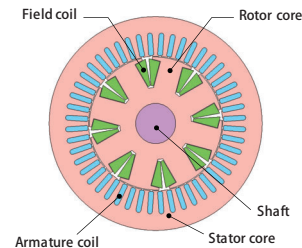
Fig. 4. Torque Formula

Case 289 Efficiency Map Creation for Wound-Field Synchronous Motors

module: DP, LS

Overview

Wound-field synchronous motors are gaining attention as traction motors for electric vehicles that require a wide drive range because the field can be strengthened or weakened simply by adjusting the current. In motor design and control design, efficiency maps are created to understand the characteristics of motors that are driven over a wide range. A wound-field synchronous motor has many different combinations of currents to obtain the same torque, and from within those combinations, the most efficient (lowest loss) combinations must be found. When using FEA, you can account for detailed geometry and also run calculations for multiple operating points at the same time. You can obtain efficiency maps easily by also automating the results processing. In this example, efficiency maps for a wound-field synchronous motor are created to check the combinations of currents that result in maximum efficiency. In addition, the loss breakdowns are also evaluated for the representative operating points.



Efficiency Map

Fig. 1 shows the efficiency map. It can be seen that for this motor, the maximum torque is 280 Nm, the maximum rotation speed is 12,000 rpm, and the maximum efficiency is 95 %.

Loss and Current Maps

Fig. 2 shows the iron loss map, Fig. 3 shows the field coil copper loss map, Fig. 4 shows the stator copper loss map, Fig. 5 shows the field current map, Fig. 6 shows the current amplitude map, and Fig. 7 shows the current phase map.

Loss Breakdowns at Each Operating Point

Fig. 8 displays pie charts showing the loss breakdowns at low speed and high load (2,000 r/min, 150 Nm), low speed and medium load (2,000 r/min, 30 Nm), medium speed and medium load (8,000 r/min, 30 Nm), and lastly, high speed and medium load (12,000 r/min, 30 Nm).

The DC copper loss breakdown for the stator core is large at low speed and high load. The AC copper loss breakdown for the stator core is large at medium speed and medium load, as well as high speed and medium load. Among the iron losses for the stator core, the eddy current loss in particular increases with rotation speed, but at 12,000 r/min, the AC copper loss is more dominant. On the contrary, it can be seen that the breakdown for the entirety of the rotor core loss is small.

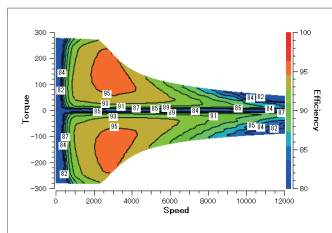


Fig. 1. Efficiency map

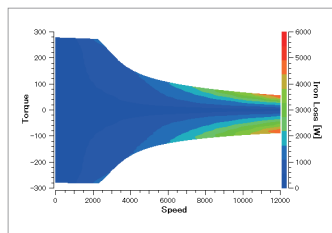


Fig. 2. Iron loss map

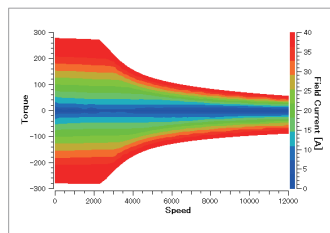


Fig. 5. Field current map

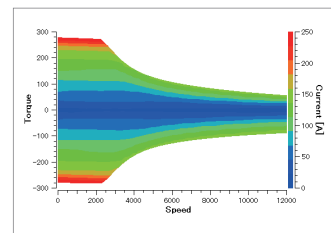


Fig. 6. Current amplitude map

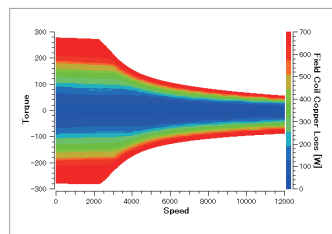


Fig. 3. Field coil copper loss map

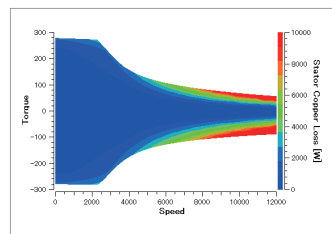


Fig. 4. Stator copper loss map

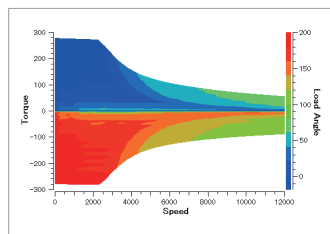


Fig. 7. Current phase map

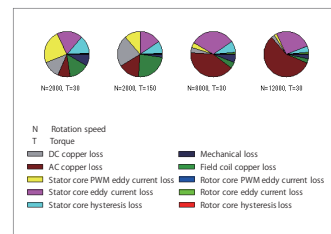


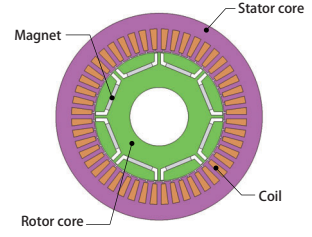
Fig. 8. Loss breakdowns at each operating point

Case 290 Design Exploration of IPM Motors, Including Evaluating Part Temperature and Stress

module: ExpressFR

Overview

In the initial stages of motor design, if only the magnetic design is completed and the design proceeds to the later stages, rework may occur when it is discovered that the part temperature and stress do not meet the requirements. Such rework can be reduced by running multifaceted evaluations from the initial design stages, including not only magnetic design but also thermal and stress. By using the templates included in JMAG-Express, you can create motor models and evaluate design plans both quickly and easily. In addition, by combining the prepared scenarios, you can run magnetic design, thermal design, and structural design all at the same time. In this example, the part temperature and stress are evaluated at the same time for the motor design plan, and a design plan that meets the requirements is explored.



Design Requirements, Design Variables

Table 1 shows the design requirements, Fig. 1 shows the rotor core and geometry that are the design variables, and Table 2 shows the cooling specifications. The rotor core slit depth and the cooling jacket flow velocity are also design variables.

Initial Design Plan Evaluation

Fig. 2, Fig. 3, and Fig. 4 show the efficiency map, average temperature of each part, and maximum stress position, respectively, for a rotor core slit depth of 0.5 mm and a cooling jacket flow velocity of 0.5 msec. Table 3 shows the maximum stress value. From Fig. 2, it can be seen that the maximum torque exceeds the requirement of 280 Nm and the efficiency at the rated point exceeds the requirement of 95%. On the contrary, Fig. 3 shows that the coil temperature is 130 deg C, and Fig. 4 and Table 3 show that the maximum stress occurs at the bridge where it exceeds 200 MPa. This indicates that adjustments are necessary in terms of the temperature and stress.

Design Plan Adjustments

The design variables are adjusted based on the results of the initial design plan. In this example, the evaluation is run again with the rotor core slit depth changed to 1.5 mm and the cooling jacket flow velocity changed to 2 msec. Fig. 5, Fig. 6, and Fig. 7 show the obtained efficiency map, average temperature of each part, and maximum stress position, respectively. Table 4 shows the maximum stress value. From Fig. 5, it can be seen that the maximum torque exceeds the requirement of 280 Nm and the efficiency at the rated point exceeds the requirement of 95%. Fig. 6 shows that the coil temperature is 130 deg C or less, and Fig. 7 and Table 4 show that the maximum stress occurs at the bridge, where it is 200 MPa or less. From this, it can be seen that the design plan meets the requirements after the adjustments have been made.

Evaluation item	Objective
Maximum torque	280 Nm or more
Efficiency at rated point	95 % or more
Coil temperature (°C)	130 deg C or less
Magnet temperature (°C)	100 deg C or less
von Mises stress	200 MPa or less

*1 1,800 sec during continuous operation at rated point

Table 1. Design requirements

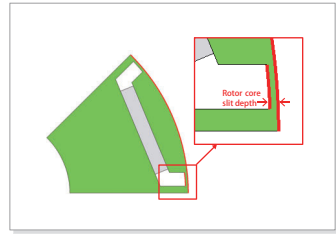


Fig. 1. Design variables

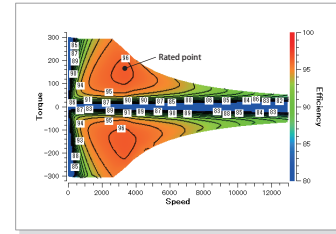


Fig. 5. Efficiency map (Adjusted design plan)

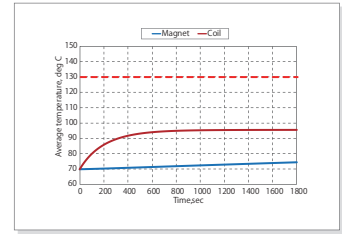


Fig. 6. Average temperature of each part (Adjusted design plan)

Item	Value
Housing cooling method	Cooling Jacket
Coolant Type	Water

Table 2. Cooling specifications

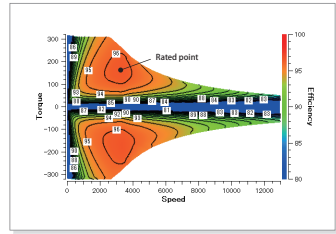


Fig. 2. Efficiency map (Initial design plan)

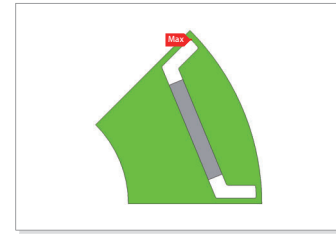


Fig. 7. Maximum stress position (Adjusted design plan)

Item	Value
Maximum stress value	175 MPa

Table 4. Maximum stress value (Adjusted design plan)

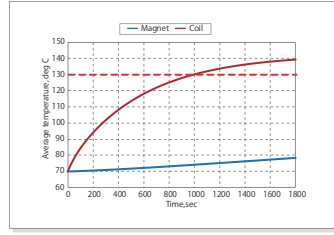


Fig. 3. Average temperature of each part (Initial design plan)



Fig. 4. Maximum stress position (Initial design plan)

Item	Value
Maximum stress value	220 MPa

Table 3. Maximum stress value (Initial design plan)

Case 291 Control Simulation of Switching Number of Poles in a 6-Phase Induction Machine

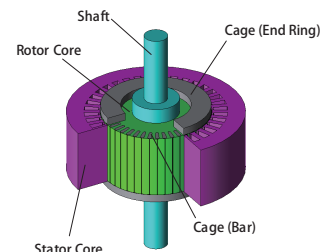
module: DP, RT

Overview

Multiphase design may be used in drive motors to increase high power density, enhance redundancy during operation and reduce torque ripple. In a cage inductance motor, the number of poles is determined by the rotating magnetic field generated by the stator side. A wide range of motors with good characteristics can be built by switching the number of poles at both the low and high-speed sides. For practical use, we want to minimize the change in torque when switching the number of poles.

To accurately evaluate the behavior of switching the number of poles during a simulation, the motor model to be controlled must also be highly accurate. The JMAG-RT model is a high-accuracy behavior model created by FEA-based calculations that can express motor characteristics that account for magnetic saturation and slip dependency.

In this document, the behavior of a 6-phase induction motor during the switching of the number of poles is evaluated by simulation.



Control Circuit

The control circuit is shown in Fig. 1.

A controller and inverter are arranged for both the 4-pole and 8-pole drive. Use only the 8-pole drive for the time between 0 to 4 sec. For each current command value between 4 and 6 sec, decrease the values for the 8-pole drive and increase the values for the 4-pole drive. After 6 sec and beyond, use only the 4-pole drive.

The switching pattern is shown in Fig. 2. The linear and exponential switching patterns are evaluated here.

Coil Current Waveform (Steady State)

The coil waveforms in the steady state for both the 8-pole drive and 4-pole drive are shown in Fig. 3 and Fig. 4.

In an 8-pole drive, the phase difference is off by 120 deg, similar to a 3-phase sine wave, and in a 4-pole drive, the phase difference is off by 60 deg, similar to a 6-phase sine wave.

Current Waveform on the Controller Side

The current command value and current waveform for a linear switching pattern is shown in Fig. 5 and the current command value and current waveform for an exponential switching pattern is shown in Fig. 6.

It can be seen that, the current waveform follows the current command value in each switching pattern.

Torque Waveform

The torque waveform is shown in Fig. 7.

There is a large fluctuation when the number of poles are switched and you can see that the fluctuation is smaller when the switching pattern is linear. However, for practical use, it is necessary to design a system that can further reduce this fluctuation.

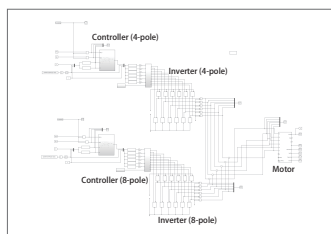


Fig. 1. Control circuit

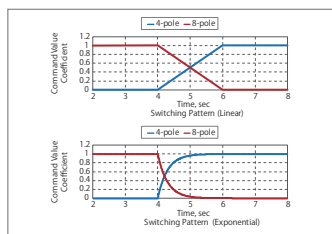


Fig. 2. Switching pattern

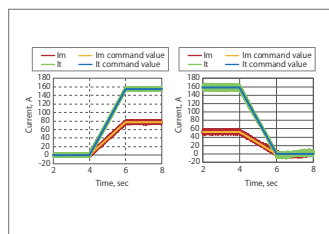


Fig. 5. Current command value and current waveform (Switching pattern: linear)

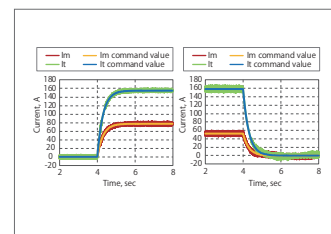


Fig. 6. Current command value and current waveform (Switching pattern: exponential)

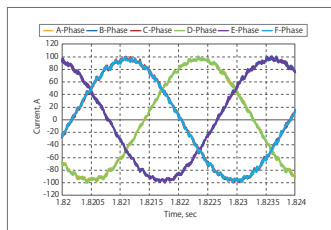


Fig. 3. Coil current waveform (8-pole drive)

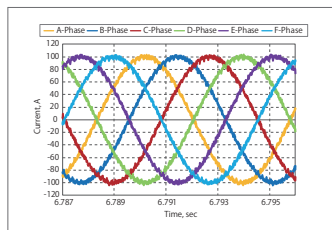


Fig. 4. Coil current waveform (4-pole drive)

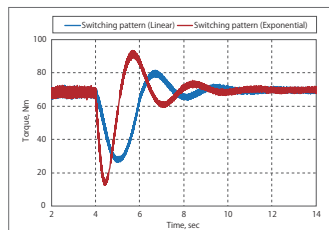


Fig. 7. Torque waveform



For more information about JMAG, visit : <https://www.jmag-international.com>

JSOL CORPORATION

KUDAN-KAIKAN TERRACE 11th Floor
1-6-5, Kudanminami, Chiyoda-ku, Tokyo 102-0074, Japan
TEL +81(0)3-6261-7361
E-mail info@jmag-international.com

*The names of products and services described herein are the trademarks or registered trademarks of the respective owners.

